Micro-mechanical study of sand fabric during earthquake

Ali Momeni

Submitted in accordance with the requirements for the degree of

Doctor of Philosophy

The University of Leeds

School of Civil Engineering

December, 2014

Declaration

The candidate confirms that the work submitted is his/her own and that appropriate credit has been given where reference has been made to the work of others.

Acknowledgements

Foremost, I would like to express my sincere gratitude to my dear supervisor Prof. Barry G. Clarke sparing his priceless time patiently and sharing his immense knowledge generously, for the continuous support of my study and research. I could not have imagined having a better supervisor and mentor for my PhD study. My thanks also go for my co-supervisor Dr. Sheng for his consultant during this PhD.

I would like to thank all academic and support staff of the school of Engineering for providing a perfect environment for all students and researchers.

I would like to thank my parents for dedicating their life for providing their children with the support needed in order to continually push themselves to succeed. I also like to thank them for being a constant source of inspiration.

Last but not the least, I would like to thank my wife who had to spend all our moment of togetherness lonely in order to support me.

Ali Momeni

December, 2014

This PhD is fully dedicated to my Dear Father.

Abstract

The seismically induced interface friction capacity of piled foundations is a function of the soil-pile interface friction, the relative stiffness of the pile and the soil and the volume changes in the soil adjacent to the pile which affect the strength and stiffness of the soil. In order to fully understand this interface it is necessary to study the behaviour at the micro level which is possible with Discrete Element Modelling. A 2D DEM model was developed that simulated a section of an inflexible pile in a coarse grained soil that was subject to cyclic shear load. The model had to be representative of typical soil behaviour so it was necessary to carry out a sensitivity analysis to investigate the effect the micro behaviour had upon the macro properties, properties that are typically interpreted from laboratory tests such as triaxial tests. It was necessary to develop appropriate boundary conditions that allowed shear to be applied and dynamic deformable boundary particles to absorb some of the energy. In order to appreciate the stability of the particles, a new fabric quantity called the “symmetric geometric deviation index” was developed to show the deviation of the contact points from a symmetric, stable distribution.

The results of the sensitivity analysis showed that the macro stress strain response and dilation behaviour with deformable boundary particles is more representative of actual behaviour than that with rigid boundaries. Further, the symmetric geometric deviation index was constant post peak for deformable boundaries, suggesting critical state conditions whereas it continued to change with rigid boundaries.

A study of the impact of size of the element and the boundary conditions led to the development of DEM model which could be used to simulate the effect of a horizontal cyclic shear load applied to the base of the element. A comparison between a soil element with deformable boundaries and a soil element adjacent to a pile showed that the pile increased the shear stress in the soil which would lead to greater deformation consistent with observations in practice.

Keywords: Discrete Element Method, biaxial test, idealized sand, earthquake, deformable boundary particles, dynamic deformable boundary particles

Table of Symbols

A Particle area

C Bulk damping matrix

D_n Normal contact damping force

D_s Shear contact damping force

E_p Elastic modulus of particle

E_{50} Second Elastic modulus

F Total resultant force

F_f Failure load

F_n Total normal contact force

F_s Total shear contact force

$|\mathcal{F}_x|$ Particle's unbalanced force in x-direction

$|\mathcal{F}_y|$ Particle's unbalanced force in y-direction

F_x^d Local damping force in x-direction

F_y^d Local damping force in y-direction

G Gain parameter

G_{max} Maximum shear modulus

K Bulk stiffness matrix

K^n Normal particle stiffness

K^s Shear particle stiffness

M Bulk mass matrix

$\dot{U}_x$ Input velocity-time history in x direction

$\dot{U}_y$ Input velocity-time history in y direction

V RVE's volume

V_p Particle volume

V_P Primary wave velocity

V_S Shear wave velocity

I Dimensionless inertia parameter

I Inertial moment of particle

c_n Normal contact viscous damping ratio

c_s Shear contact viscous damping ratio

d Particle diameter

$d_M^{S^n}$ Radial distance

f Frequency

f^c Contact force

k Wave number

k_n Normal contact stiffness

k_s Shear contact stiffness

l_c Branch vector

m Particle mass

n Bulk porosity

t_i Shear unit vector

v_n Normal contact velocity

v_s Shear contact velocity

v_x Particle velocity in x-direction

v_y Particle velocity in y-direction

x^c Contact position vector

$\dot{x}$ Particle velocity in x direction

$\dot{y}$ Particle velocity in y direction

z Average coordination number

α Impedance ratio

α Damping constant

α Relaxation factor

β Contact viscous constant

γ Shear strain

ε_{xx} Normal strain in x-direction

ε_{yy} Normal strain in y-direction

ε_{11} Axial strain

ε_{22} Minor principle strain

ε_v Volumetric strain

$\dot{\varepsilon}$ Strain rate

θ Angle of friction

θ Angular rotation of particle

θ_a Normal contact direction

θ_n Normal contact force direction

θ_t Shear contact force direction

$\dot{\theta}$ Rotational particle velocity

$\ddot{\theta}$ Particle angular acceleration

λ Lame parameter

λ Average symmetric geometric deviation index

λ Wavelength

μ Lame parameter

μ Inter-particle coefficient friction

v_{50} Second Poisson's ratio

ν_p Particle's Poisson's ratio

ρ_{bulk} Bulk density

ρ Particle density

p_y Limiting contact pressure

σ_{11} Major principle stress

σ_{22} Minor principle stress

σ_t Tensile strength of disk particle

σ_{xx} Normal stress in x-direction

σ_{yy} Normal stress in y-direction

τ Shear stress

ω Angular frequency

Δ_n Incremental normal displacement

Δ_t Incremental shear displacement

Δ_t Time step

ΔF^n Incremental normal contact force

Table of Contents

Table of Figures

Table of tables

Chapter 1

1 Introduction

1.1 Background of the thesis

Granular materials such as sands are made up of frictional discrete particles in contact. Sands in nature are three-dimensional with agglomerate shapes. However, as discussed by O'Sullivan (2011), it is useful to consider a two-dimensional idealized system, where particles are disk shape, in fundamental research studies. A two-dimensional granular system is also particularly useful as particle motion is restricted to one plane, enabling clear visualisation. Many researchers, the most notable (Oda et al., 1985, Rothenburg and Bathurst, 1989) have also illustrated that invaluable insight can be attained from considering two-dimensional models of idealized sand.

The static and seismic macro-mechanical behaviours of granular materials are greatly dependent on the inter-particle interactions and the geometrical distributions of these interactions along with the geometrical distribution of the contacts. The inter-particle interaction forces, including normal and shear contact forces, are related through the contact model to the inter-particle properties (such as particles stiffness and friction). The continuum approaches which are commonly applied to study the behaviour of granular sand under static and dynamic loads cannot take into account the inter-particle interactions and the geometrical distributions of these interactions along with the geometrical distribution of contacts in their frameworks.

The discrete element method (DEM) simulations provide an opportunity to study in-depth the macro-mechanical behaviour of granular systems from inter-particle interactions. The DEM model has been also shown to be capable of capturing the macro-mechanical variables of granular system from inter-particle properties (e.g. more recentlly Kozicki et al., 2014, Belheine et al., 2009), but it has not been fully addressed in the case of two-dimensional system. The DEM algorithm was developed for *PFC*^{2D} software (Itasca, 2008).

The geometrical distribution of contact networks and inter-particle contact forces in particulate systems are referred to as the fabric (e.g. Yimsiri and Soga, 2010, Rothenburg and Bathurst, 1993, O'Sullivan and Cui, 2009). Indeed, fabric is a collective term which is applied to characterize the spatial arrangement of granular particles and their interactions. However, geometrical data such as contact position, contact orientation, particle centroid and particle radius along with the inter-particle interaction forces such as normal and shear contact forces at the microscopic level, which are required to analysis the fabric evolution quantitatively during loading, are difficult to measure experimentally (Luo, 2012, Yimsiri and Soga, 2010, Rothenburg and Bathurst, 1989). DEM is able to predict both the spatial arrangement of sands and their inter-particle interaction forces at any time during loading. These data are then used to compute the fabric of sand through a number of fabric quantities such as “average normal contact distribution”, “average normal contact force distribution”, “average shear contact distribution” and “average coordination number”. Thus, with the help of DEM, the relation between macro-mechanical responses and fabric quantities of sands can be investigated quantitatively so that studying the fabric evolution of granular system during loading increases our insight from changes in macro-mechanical behaviour.

1.2 Problem definition

The normal approach to studying effects of earthquakes in soil media and soil-pile system is to consider them as wave propagation problems in solid semi-infinite continuum space. Although sands are particulate materials, they are treated as a continuum. This has proved acceptable for geotechnical structures provided an adequate factor of safety is applied so that there is no risk of failure (e.g. Zordan et al., 2011, Vasheghani-Farahani et al., 2010, Spyrakos and Loannidis, 2003, Zhang, 2006, Shamsabadi et al., 2007, Dicleli and Erhan, 2010, Huang et al., 2008, Pugasap et al., 2009, Thippeswamy et al., 2002, Khodair and Hassiotis, 2005, Karantzikis and Spyrakos, 2000, Mylonakis et al., 1997b, Springman et al., 1996, Kim and Laman, 2010, Civjan et al., 2007, Arsoy et al., 1999, Novak and Nogami, 1977, Makris and Gazetas, 1992, Mylonakis and Gazetas, 1999). However, a continuum

approach does not explain the mechanism of inter-particle interactions and fabric evolution which can have a significant influence on the macro behaviour of soil and soil-pile system, which is still not properly understood due to the effects of nonlinear behaviour, possible separation between the pile and soil and possible sliding of the pile. Ideally sand should be modelled as a particulate material using DEM but the number of particles involved is such that this is not possible because of the scale of geotechnical problems. DEM can be used to model elements of sand with and without the pile element to help understand the effect of fabric on the overall performance of a soil mass and soil-pile system qualitatively both during static and dynamic loading. This is discussed in this work to show how the contact properties between soil particles and fabric evolution influence the mass behaviour. This requires a new approach to describing soil at the micro level to show how DEM can be used to model soil under different boundary conditions and apply that knowledge to mass behaviour.

To date, most DEM analyses in soil mechanics and granular materials have considered quasi-static material response. However, the influence of inter-particle properties on the macro-mechanical parameters such as elastic modulus, Poisson's ratio and angle of friction in the case of two-dimensional cannot be fully addressed.

The use of DEM for dynamic problems in geotechnical earthquake engineering is restricted to a small number of published works (O'Donovan et al., 2012, Marketos and O'Sullivan, 2013, Zamani and El Shamy, 2011, El Shamy and Zamani, 2012, Zamani and El Shamy, 2012, El Shamy and Denissen, 2010, Hazzard et al., 1998, Toomey and Bean, 2000). However, the fabric evolution during an earthquake is not addressed in these works. As the particulate pack in the works of O'Donovan et al. (2012), Marketos and O'Sullivan, (2013), Hazzard et al. (1998) and Toomey and Bean, (2000) was homogeneous, hexagonal packing, the contact force network was also effectively homogeneous. Therefore, no hypotheses can be developed on the effect of fabric on the seismic macro-mechanical behaviour of sand as the contact networks in sands are neither hexagonal nor homogeneous. For the rest, the vertical gravitational acceleration increased to 25 to reduce the

dimensions of the model and time of simulation significantly. This leads to increase the contact forces and the overlap between them significantly increases during the process of particle generation. Since, the fabric is a microscopic term, changes at particle levels such as inter-particle contact forces leads to change the fabric of particulate system. Thus, studying the seismic fabric evolution by this approach cannot be accurate. This research will describe the static and seismic modelling of soils and the results obtained.

1.3 Research objectives

To better understanding the effect of inter-particle properties such as normal and shear contact stiffness and inter-particle coefficient friction on the macro-mechanical behaviour of idealized two-dimensional sands such as elastic modulus, Poisson's ratio and angle of friction using DEM, a sensitivity analysis is required to be performed. The macro-mechanical parameters of sand are generally obtained from triaxial tests but the number of tests and range of parameters to be assessed are limited. Further, the results are affected by the particle shape as well as their distribution. DEM biaxial tests allow the effect of particle size distribution to be studied in more detail giving greater scope to vary the porosity and inter particle properties thus developing an understanding to the impact micro mechanical behaviour has upon macro behaviour. This also establishes a series of relationships between micro parameters and macro parameters, which have neither been fully understood nor taken into account in continuum mechanics. From this, the proper inter-particle properties can be extracted for further works. The following objectives are required for this aim to be achieved:

1. Sourcing the inter-particle properties of single quartz sand particle from literature (see Appendix 2).
2. DEM modelling of a biaxial test using *PFC*^{2D},
   2.1. The assumptions and limitations of *PFC*^{2D},
   2.2. Comparing the methods of particle generations,
   2.3. Applying confining pressure,
   2.4. Applying deviatoric stress,

2.4.1. Boundary conditions,

2.4.1.1. Rigid boundary,

2.4.1.2. Deformable boundary particles,

2.5. The sensitivity of the macro-mechanical behaviour of sand to the normal contact stiffness,

2.6. The sensitivity of the macro-mechanical behaviour of sand to the shear contact stiffness,

2.7. The sensitivity of the macro-mechanical behaviour of sand to the inter-particle coefficient friction,

2.8. The sensitivity of the macro-mechanical behaviour of sand to the confining pressure,

2.9. The sensitivity of the macro-mechanical behaviour of sand to rigid boundaries,

2.10. The sensitivity of the macro-mechanical behaviour of sand to deformable boundary particles,

To use *PFC*^{2D} to simulate biaxial tests, a suitable code has to be written. The programming language used for this software is Fish. 44 DEM biaxial tests were executed. 4800 lines of code were written, including 1500 lines of this code were related to boundary deformable particles.

By studying the fabric evolution of sand media during the propagation of the shear component of an earthquake, a better understanding of the fundamental behaviour of sand was obtained. The following objectives are required for this aim as follows:

1. DEM modelling of two-dimensional earthquake using *PFC*^{2D},

1.2. Generating the particles using the radius expansion approach,

1.3. Assigning the proper inter-particle properties obtained from the first aim,

1.4. Applying dynamic deformable boundaries,

1.4.1. Comparing the effects of rigid boundaries and dynamic deformable boundaries on the overall shear wave propagation in sands,

1.4.2. Verification of the dynamic deformable boundaries,

1.5. Applying shear seismic force to the base particles,

1.5.1. Simulating shear wave propagation through the sand,

2. Comparing the shear wave velocity against different earthquake frequencies,
3. The effect of different sample ratios on the average shear particles velocity,
4. The sensitivity of the sand fabric and seismic macro-mechanical behaviour to the different sample ratio,
5. The sensitivity of the sand fabric and seismic macro-mechanical behaviour to different earthquake frequencies,
6. The sensitivity of the sand fabric and seismic macro-mechanical behaviour to different earthquake amplitudes,
7. The sensitivity of the sand fabric and seismic macro-mechanical behaviour to different normal contact stiffnesses,
8. The sensitivity of the sand fabric and seismic macro-mechanical behaviour to different normal inter-particle friction,
9. The sensitivity of the sand fabric and seismic macro-mechanical behaviour to different confining pressures.

Overall, 30 DEM tests were executed. 1500 lines of code were written for creating dynamic deformable boundary particles.

By studying the fabric evolution of sand media near the pile element during the propagation of the shear component of earthquake, a better understanding of the fundamental effect of pile on the seismic macro-mechanical behaviour of sand can be attained. The following objective is required for this aim as follows:

1. DEM modelling of two-dimensional soil-pile system subjected to earthquake using *PFC*^{2D},
   1.2. Generating the particles using radius expansion approach,
   1.3. Applying dynamic deformable boundary,
   1.4. Defining rigid pile,
   1.5. Applying shear seismic force to the base particles,
2. Studying the fabric evolution and seismic macro-mechanical behaviour of sand

A development in fabric quantity which is called “average symmetric geometric deviation index” is also introduced in this work.

1.4 Thesis structure

The background of the thesis, problem definition, research objectives and thesis structure are presented in chapter 1.

Chapter 2 covers the concept, limitation and assumptions of DEM and reviews in homogenization method, which is needed to make a bridge between inter-particle contact force and particle displacement and average stress and strain tensor.

Chapter 3 presents a review of previous DEM research on seismic wave propagation and soil-structure interaction and the boundary conditions which are required to define the deformable boundary particles for chapter 6 are discussed. The fabric quantities required to study the sand media are discussed in this chapter.

Chapter 4 presents the development of a sensitivity analysis using *PFC*^{2D}. An equation based on contact mechanics principle is provided to compute the normal contact stiffness, k_n, for disk particles. An algorithm is proposed to develop a biaxial test simulation. Two different boundary conditions were applied, which are rigid wall and deformable boundaries, to maintain confining pressure during deviatoric loading. The algorithm is based on directed graph theory to update the deformable boundary particles at each time step. A new fabric quantity is also developed to measure the configuration of contact points of each particle from geometry symmetric deviation.

In chapter 5, the results of sensitivity analysis are shown. Based on the results, the combination of inter-particle properties such as ($K_n, K_s\ and\ \mu$) which provide reasonable values of macro-mechanical quantities such as elastic modulus, Poisson’s ratio and angle of friction of dense and medium sand were obtained. These values were used to simulate the dense sand with DEM.

In chapter 6, the assumptions and limitations of dynamic deformable boundary particles which should be applied for seismic problems are discussed. The effect of different earthquake frequencies on the shear wave velocities and fabric evolution and consequently the seismic macro-mechanical behaviour are also investigated. The effect of different earthquake amplitudes and various confining pressures, inter-particle coefficient friction, normal contact stiffnesses on the fabric evolution and consequently the seismic macro-mechanical behaviour are also investigated.

The conclusion and recommendations are presented in chapter 7.

Chapter 2

2 The analysis of granular sand media

2.1 The Discrete Element Method

DEM is an advanced numerical algorithm, which is able to dynamically simulate and track the micro-macro scale behaviour of granular materials subject to quasi-static and dynamic loads. The central explicit finite difference scheme is used in this code to solve the dynamic equilibrium of each particle at each time step. The stability of the solution is dependent on the magnitude of the time step. That is, the value of this time step should be small enough so that the effects of incremental contact force and displacement (i.e. disturbance) cannot be transmitted through the particle during each time step. The framework of this method is based on both motion equations and contact mechanics. Motion equations are used to determine the location of each individual particle at every time step and contact mechanics used to determine the inter particle force and displacement. This algorithm must be applied through the *DEM* computer codes such as *BALL*, *TRUBAL* and *Particle flow code 2D* (*PFC*^{2D}). *BALL* and *TRUBAL* are early versions of *DEM* computer codes and are rarely employed by researchers for simulating particulate systems. It may be because the instinct functions provided in these codes are not comprehensive enough in comparison with those provided by *PFC*^{2D} (Itasca, 2008). In addition, the special language programming, called *FISH*, is embedded into *PFC*^{2D} to make this code more useful as it allows a user to provide any subroutine. Thus, this computer code is used in this research. The main advantage of this method is the generation of abundant information at particle scale, which can be used to comprehend the physics of granular systems. This method is proven to be a comprehensive method to study the sand medium (e.g. Iwashita and Oda, 1998, Oda and Iwashita, 1999, Thornton and Zhang, 2003, Sitharam, 2003, Rothenburg and Kruyt, 2004, Potyondy and Cundall, 2004, O'Sullivan et al., 2003, O'Sullivan, 2011). More in depth studies of particulate behaviour have taken place in chemical engineering where particulate performance is critical

in process engineering (e.g. Antony, 2007, Thornton and Antony, 2000, Antony and Kruyt, 2009, Tardos et al., 2003). As with all numerical methods, this method has its assumptions and limitations. The assumptions and limitations of this method are presented in section 2.1. The limitation of DEM in dealing with seismic analysis of granular systems is presented in section 2.2. Section 2.3 presents the application of DEM in soil mechanics and soil dynamics. A DEM mechanical calculation cycle is illustrated in section 2.4. The interpretation of the DEM results into average continuum stress and strain tensors is discussed in section 2.5. The conclusion is presented in section 2.6.

2.1.1 The limitations and assumptions of *DEM*

The main limitations and assumptions of *DEM* are as follows:

2.1.1.1 Computer speed-dependent

Since *DEM* is computer speed-dependent, it has an explicit limitation to generate soil particles. For example, in a two dimensional study of the particulate regions adjacent to a pile foundation subjected to seismically movement of bedrock, a large number of sand particles should be generated to transfer bedrock movement, which is in 100 meters below the surface, to the particulate regions adjacent to the pile foundation. The largest computers yet built would not be able to handle these number of particles because the number of equations to be solved in each time step. Therefore, it is unrealistic to solve them in a reasonable time frame. For this reason, the application of *DEM* simulations in soil mechanics is restricted to small elements of soil medium (e.g. Yang et al., 2014, Gao et al., 2013).

2.1.1.2 Rigid particle with soft contact

In reality, single sand particle deforms when it is subjected to contact forces. Since the rigidity of a sand particle is relatively high, the change in particle geometry is assumed to be restricted to the contact area. Therefore, a contact model is required to link the stress and strain for the contact area. Additionally, calculations are required to compute the updated geometry of the particle including central mass and contact geometry. Thus, the time of simulations increases significantly. Instead, in *DEM*, it is assumed that

particles are rigid with soft contact points and contact overlap is considered instead of contact deformation (Cundall and Strack, 1979). The amount of this overlap is dictated by a contact model. By using this assumption, the degrees of freedom of a particle are restricted to only contact points. The calculation volume decreases dramatically and force-displacement contact model is used instead of stress-strain contact model. Moreover, the geometrical characteristics and mass properties of particles are calculated in a straightforward analytical manner. However, the assumption of rigid particles with soft contact is acceptable if the contact deformations represent the particle deformations. This condition is more applicable for those particles with disk and spherical geometry undergoing elastic deformation (Johnson, 1985).

2.1.1.3 Particle geometry

Sand particles have complex shapes including spheres, ellipsoids, cylinders, tubes and others (e.g. Bardet, 1998, Lambe and Whitman, 1969). However, only round geometrical particle shapes including disks and spheres are considered in *DEM*. The main reason is that the calculations related to these types of geometrical shapes are more straightforward reducing the processing time. However, in some *DEM* computer codes such as *PFC*^{2D} and *PFC*^{3D} it is possible to create agglomerate particles (or clumped particle) combining either disks or spheres particles (Cundall and Strack, 2008, Potyondy and Cundall, 2004).

2.1.1.4 Particle asperity

In DEM, particle friction and particle roughness are considered as two different issues. The friction term resists against particle sliding due to applied shear load. The particle asperity resists against particle rolling. However, the conventional *DEM* algorithm ignores the effect of particle roughness in the angular motion equation. That is, particles will be free to roll over together if the conventional *DEM* algorithm is used. (Iwashita and Oda, 1998, Belheine et al., 2009) by using DEM simulations showed that the rolling resistance play a minor role on the micro-deformation mechanism controlling the dilatancy and strength of granular materials. (O'Sullivan, 2012) showed experimentally that if the size of particle is bigger than 0.1 [mm], the

size of particle asperity will be negligible in comparison to the particle inertia. Therefore, the surface roughness will have a minor effect on the material behaviour in comparison with the particle inertia. However, for those particles whose sizes are less than 0.1 [mm] the rolling resistance component should be considered in the *PFC*^{2D} simulation by adding a *C*$^{++}$ subroutine into the target *Fish* code. This results in increasing the time of simulation because at the start of each mechanical cycle, the *PFC* compiler should compile this subroutine function for all contact points.

2.1.1.5 Particle crush

Sand particles deform and crush under compressive load in triaxial and odometer tests (e.g. Nakata et al., 1998, Nakata et al., 2001c, Nakata et al., 2001a, Nakata et al., 2001b, Fukumoto, 1992). The failure takes place when the tensile stress along the line connecting the top and bottom of single a particle shown in figure 2-1, which is subjected to the compression load diametrically, reaches the tensile strength of that particle which is defined $\sigma_t = \frac{F_f}{d^2}$ (Lee, 1992).

where F_f is the failure load and d is particle diameter. At this stage, the particle being considered split into small rigid portions. (Bolton et al., 2008) using the DEM simulations on the agglomerate particles assemblies of quartz sand (a clump of spherical particles are bonded with together) showed that the majority of agglomerate particles will crush and split into the single rigid spherical particles at the peak stress. This fact is ignored in the DEM code; that is particles do not split.

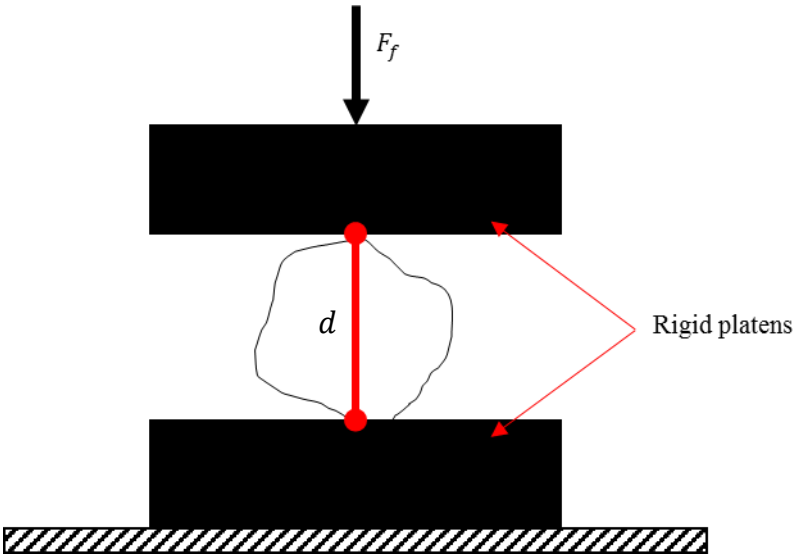

Figure 2-1 Particle tensile strength test

2.1.1.6 Strength of single disk and spherical particle

As mentioned above, an agglomerate particle is defined as a group of disks (in 2D) or spherical (in 3D) which are bonded together at their contact points to form a single particle (see figure 2-2). The strength of an agglomerate particle is based on its tensile strength while the strength of each single rigid particle is based on the shear strength at the contact zone which can be computed from Tresca and van Mises criterion (Thornton and Ning, 1998, O'Sullivan, 2011). The limiting contact pressure of each material is a material property-dependent.

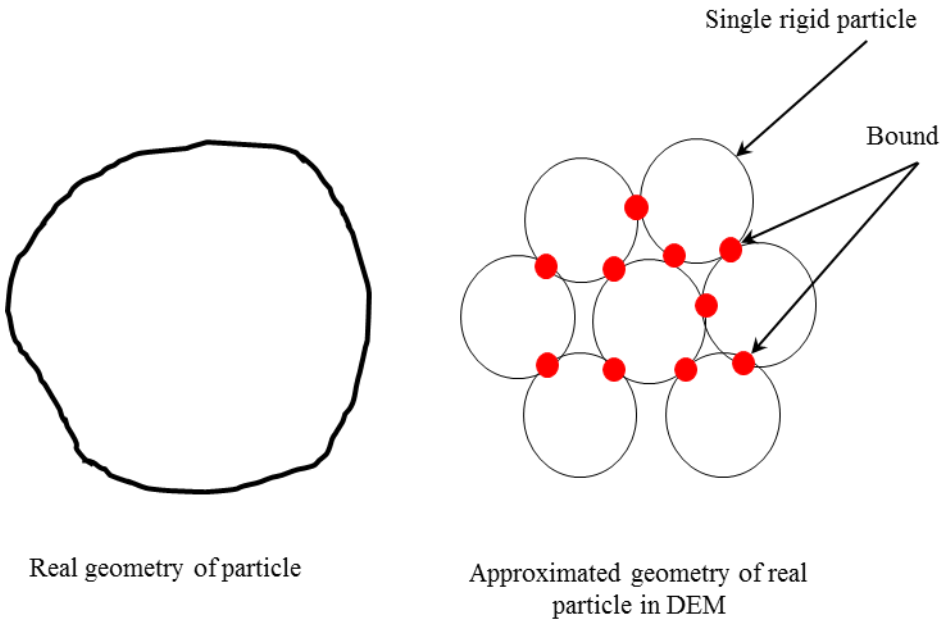

Figure 2-2 Real geometry of particle and approximated geometry of agglomerate particle in DEM

2.1.2 The main of limitation of DEM in dealing with seismic analysis of granular systems

One of the important seismic features of soil is to find its fundamental (or resonance) frequencies. This helps us to find the resonance frequencies of the soil deposit. To find the fundamental frequencies of a system, the free vibration equation of the system must be solved in numerical manner (see below equation).

$$M\ddot{x} + C\dot{x} + Kx = 0 \qquad 2.1$$

where M, C, K and x is mass, damping and stiffness matrices of each particle and contact deformation, respectively. This equation simply shows that the free vibration of a dynamic system at each time step is dependent on considering the response of whole system into three matrices simultaneously. The vibration modes are then obtained by applying transfer functions. However, these matrices cannot be directly formed by DEM, since DEM only obtains the response of each particle at each time step, which is executed by computing resultant forces on particles and applying Newton's second law to each particle to capture the deformation of the system at each

time step. Therefore, the DEM model cannot a priori give information on natural frequencies of granular system. However, DEM model can provide each component of Eq. 2.1 at each time step such that at the end of each mechanical time step this equation can be solved. For more details readers can be referred to (Marketos and O'Sullivan, 2013)

2.1.3 Application of Discrete Modelling in soil mechanics

Hertz (1882) established a link between contact normal pressure and contact deformation of two contacting spheres. (Dantu, 1957) and (Schneebeli, 1956) by idealizing real soil as assemblies of rigid rod found some striking similarities between the macro-mechanical stress and strain responses of these idealized assembly and those obtained from real soils. (Duffy and Mindlin, 1956), (Deresiewicz, 1958, Deresiewicz, 1957), and (Thurston and Deresiewicz, 1958) studied the responses of soil idealized by rigid spheres. (Biarez, 1962) by employing glass beads and duralumium rods estimated the elastic and plastic behaviour of soils. These observations were applied to study the practical problems in soil mechanics. These pioneering works were later pursued by photoelastic studies (e.g. Drescher, 1976, Drescher and De Josselin de Jong, 1972) to visualize stresses within particulate systems. However, by increasing the speed of computers in early of 1970's, the first discrete element method code, called BALL, was developed by (Cundall, 1971) for simulating progressive large scale movements in blocky rock systems. (Cundall, 1978) and Cundall and Strack (1979) used this method in BALL software for modelling sand. The results were found to correspond well with experimental work of (Jong and Verruijt, 1969) and Dantu (1957) and (Wakabayashi, 1957). However, limited memory and storage capacity of the computers at the time meant that the number of particles was limited. For instance, the number of particles used by (Cundall and Strack, 1979) to simulate sand was 85. However, the significant increase in computing speed and storage capacity of computers in the last decade has resulted in developing *DEM* computer codes for simulating granular systems. Among them, *Particle flow code 2D* (*PFC*^{2D}) which is one the powerful *DEM* code, has been used by many researchers to study sand behaviour. Owing to intrinsic *Fish* functions provided in this code, the speed of computations

increases considerably, and allows users to apply the desired subroutines. For example, (Cheung et al., 2013, O'Sullivan and Cui, 2009, Belheine et al., 2009, Yimsiri and Soga, 2010, Sitharam and Vinod, 2010, O'Sullivan, 2011, Soroush and Ferdowsi, 2011, Liu et al., 2012, Fan et al., 2013, O'Sullivan et al., 2008, Tannant and Wang, 2007, Momeni et al., 2012) used *PFC^{2D}* to study the microscopic behaviour of sand subjected to monotonic and cyclic loads. The results show that *PFC^{2D}* is an appropriate code to examine the microscopic behaviour of sand media. (Jensen et al., 1999, Zeghal et al., 2002) conducted a series of *2D DEM* simulations to study the behaviour of sand-structure interface under monotonic load. In this work, soil particles were enclosed between four rigid walls with only the bottom wall moving horizontally. The results show that the displacements of those particles in contact with rigid wall are different from other particles. Also the different types of wall roughness have a significant effect on the particles displacements in contact with it. (Zamani and El Shamy, 2012, El Shamy and Zamani, 2012) used *PFC^{2D}* to analyse the seismic response of soil–foundation–structure systems. (Zamani and El Shamy, 2011, Sadd et al., 2000) used *PFC^{2D}* to analyse one dimensional wave propagation in dry granular soils. The results show that DEM is able to derive the seismic properties of soils such as shear wave velocity, the degradation of shear modulus and hysteretic damping curve. Additionally, the conducted PFC simulations are able to capture a number of fundamental characteristics of wave propagation in soil media such as motion amplification and occurrence of resonance.

2.1.4 The *DEM* calculation process

The process of DEM calculation is schematically shown in figure 2-3.

- After generating the initial configuration of an assembly (see figure 2-3a), at the start of a time step, the contact detection process is implemented to detect contacting particles and location of each particle (see figure 2-3b).
- The incremental contact forces, that is the contact normal and shear forces, of each contact point due to the incremental contact

deformation (i.e. overlap) resulted from boundary excitation is then computed by a contact model $\Delta \mathrm{F} = K(\Delta \mathrm{U})$ (see figure 2-3c).

- If contact viscous dashpots are applied for simulation at this stage some portions of kinetic energy obtained from incremental normal and tangential contact forces is dampened. If contact viscous dashpots are not applied to the simulation the incremental normal and shear force are not changed.
- The incremental resultant forces and moment in Cartesian directions due to these incremental forces obtained at current time step are then computed (see figure 2-3d). From these incremental forces and moment and by applying Newton's second motion law the incremental accelerations in Cartesian directions (i.e. x and y) and angular acceleration are computed.
- If local viscous damping is applied to this simulation, this term will be added to the unbalanced forces and moment to absorb some portions of kinetic energy of the particle.
- The incremental normal and tangential force at each contact at the current time step are added to the total normal and tangential contact force at each contact since contact has been established. Then, the updated total contact shear force is compared to the Coulomb sliding friction criterion to check whether the sliding has occurred. If it has taken place, all data related to this contact point including geometry and contact forces is removed and the contact is broken.
- Using a central explicit finite difference integration from acceleration, particle velocity is extracted and by central explicit finite difference integration from this velocity, particle displacement including translation and rotation is obtained (see figure 2-3e).
- From this new displacement, the updated position of each particle can be obtained at the end of the time step. Figure 2-3f shows schematically the new configuration of the assembly.
- This mechanical cycle is repeated until the code reaches to the termination criterion. Therefore, DEM has time-marching algorithm to solve the motion equation.

If local damping is applied, the incremental contact forces are not damped. It is because this type of damping only influences the incremental resultant forces. Thus, if the applied strain rate on the DEM model is relatively high, the contact force will be large. Therefore, the use of contact viscous damping seems to be a priority to absorb some contact force at each time step.

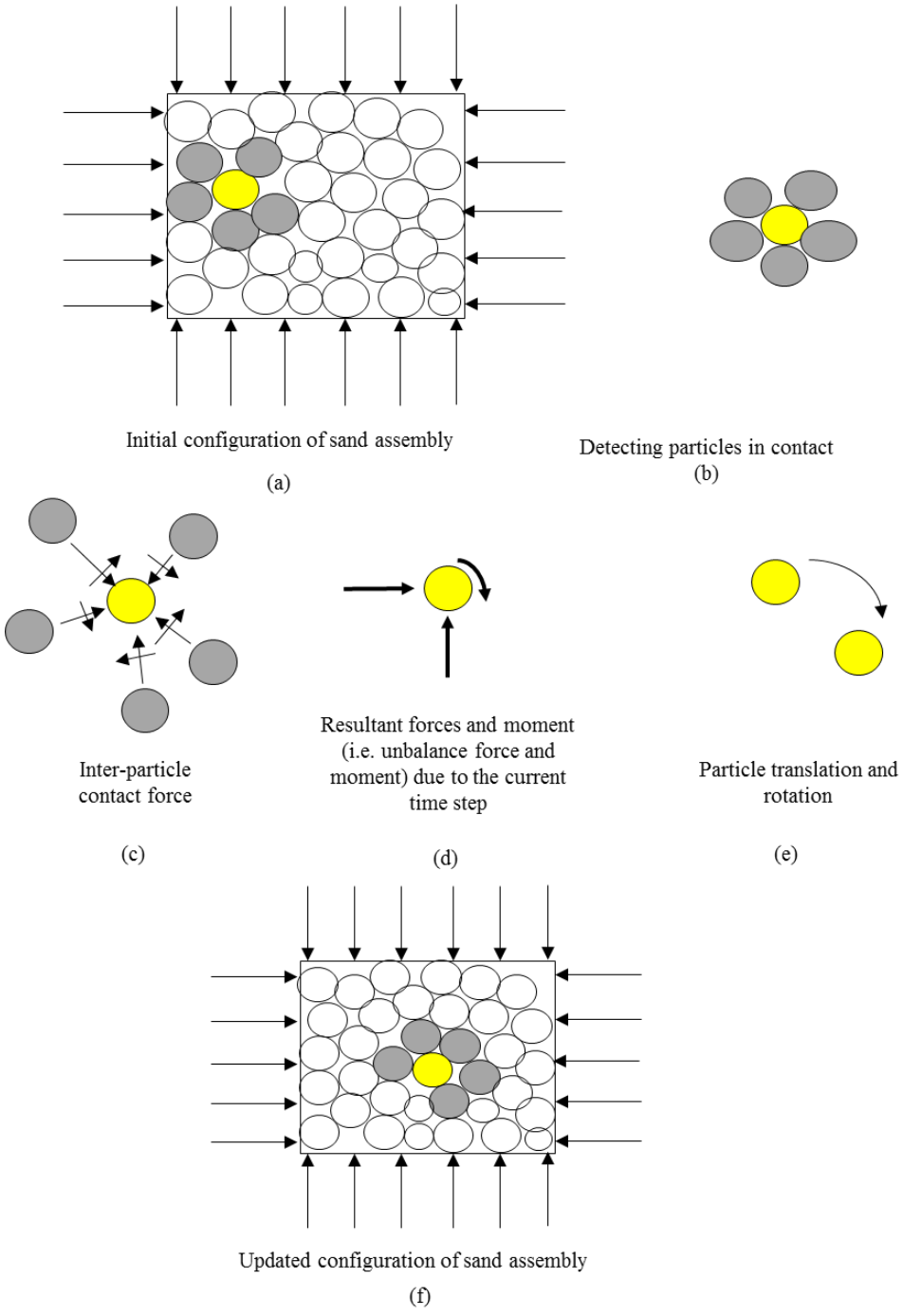

Figure 2-3 The calculation process in DEM

2.1.4.1 Contacts

In the previous section an overview of DEM calculation was discussed. In this section, those parts of contact mechanics which are related to DEM calculations such as contact detection, contact kinematics, contact kinetics and contact models are discussed.

2.1.4.1.1 Contact detection mechanism

Before describing the contact detection mechanism, some notations are described. A contact between pairs of disk particles, a and b, takes place if the following criterion is met (see figure 2.4):

$$d < R^a + R^b \quad \text{where } d = \left|x_i^a - x_i^b\right| \qquad 2.2$$

in which $\mathrm{x_i^a and\ x_i^b}$ are the coordinates of particles centroid. $\mathrm{R^a and\ R^b}$ are the radius of particles a and b, respectively. $x_i^c \text{and } n_i$ are the vector position of contact and normal unit vector obtained by the following equation:

$$x_i^c = x_i^a + \left(R^a - \frac{1}{2}U^n\right)n_i; \quad \text{where} \quad n_i = \frac{x_i^a - x_i^b}{d} \qquad i = 1,2 \qquad 2.3$$

U^n is contact deformation or overlap and obtained from:

$$U^n = R^a + R^b - d \qquad 2.4$$

For complicated particle shapes the computation of overlap becomes more complicated (e.g. (Ting et al., 1993).

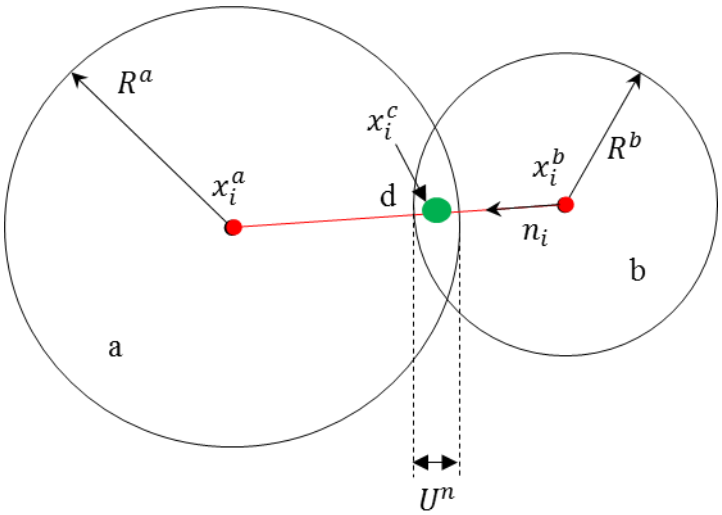

Figure 2-4 Notation used to characterize particle-particle contact

The contact detection process in particulate systems is one of the most time-consuming and complicated parts in DEM. It will be more time-consuming and complex the more particles are being used. One of the robust and efficient contact detection algorithms, which are compatible for explicit nature of mechanical calculations was proposed by Cundall (1988). This technique is utilized in *PFC*^{2D}. There are five steps to this technique:

- **Data element:** each entity such as a particle, a wall or a contact point is represented by a data element (i.e. they are converted into *PFC*^{2D} language). Each data element contains geometric and mechanical data (e.g. particle size, contact stiffness, particle and contact coordinate).
- **Data structure:** all data elements are then linked in a list to data structures by memory addresses. The advantage of using linked-list scheme is that it takes very little computer time to maintain.
- **Grid the space of granular system:** The next step is to divide the space containing the particles and walls into rectangular two-dimensional cells (see figure 2-5). Then each entity and wall is mapped into a cell or cells. Each cell stores the addresses of all entities that map into it in linked-list form. It is difficult to provide an appropriate relationship for optimum cell size. However, the optimum cell density is ideally one cell per entity.
- **Identification of neighbours:** Once all entities have been mapped into the cell space, the adjacent entities for a single entity are identified. Since the data of each entity is in the linked-list of cells, it is easy to detect the neighbours of each entity.
- **Contact detection:** when neighbours of each entity are recognized, Eq. 2.2 is applied to check whether the pairs of entity are in contact (and touch) or not. In addition to Eq. 2.2, a heuristic algorithm is utilized in *PFC*^{2D} to find those pairs of entities that may come in contact in a future time step, called potential contact, during the course of a simulation. For this reason, if incremental displacement of each entity becomes less than a pre-set tolerance value, the contact between two entities is considered as a potential contact. If two

entities are found to be separated by a gap that is equal to or less than a pre-set tolerance value, a potential contact is created. If an existing contact acquires a separation that is greater than a pre-set tolerance value, the contact is deleted.

It is noted that the necessary computation time to perform the map and search functions for each entity depends on the size and shape of the entity. The overall computation time for neighbour detection is directly proportional to the number of entities.

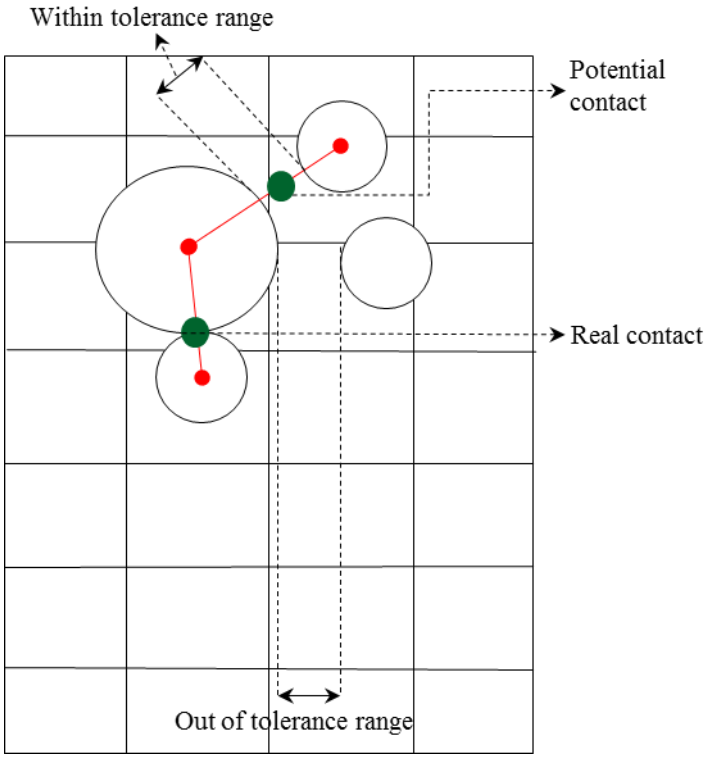

Figure 2-5 Uniform grid for contact detection between pairs of particles Contact kinematics

When two particles a and b come into contact at *c* (see figure 2-4) due to boundary excitation, the kinematics at this contact such as relative displacement (or overlap) is determined from the relative displacement of pairs of particles. The explicit central finite difference method of relative displacement at the contact point at time step Δ_t is as follows:

$$(\Delta_n)_{t+\frac{\Delta_t}{2}} = \left[\left(\dot{x}_i^b - \dot{x}_i^a\right)_{t+\frac{\Delta_t}{2}}\right] n_i^c \Delta_t \qquad i = 1,2 \qquad 2.5$$

$$(\Delta_s)_{t+\frac{\Delta_t}{2}} = \left\{\left[\left(\dot{x}_i^b - \dot{x}_i^a\right)_{t+\frac{\Delta_t}{2}}\right] t_i^c - \left(\dot{\theta}^a |l_c^a| + \dot{\theta}^b l_c^b\right)_{t+\frac{\Delta_t}{2}}\right\} \Delta_t \qquad i = 1,2$$

where $\dot{x}^a$, $\dot{x}^b$ **,** $\dot{\theta}^a$ and $\dot{\theta}^b$ are translational and rotational particle velocities of particle *a* and *b*, respectively. $l_c^a \; and \; l_c^b$ are the vectors connecting the centre of masses of two particles to contact point "*c*". n_i^c and t_i^c are the i^{th} vector of normal and tangential components' contact plane at contact point of two particles; Δ_n and Δ_s are the relative normal and tangential displacements of two particles over the time step, respectively. The kinematics of the contact is updated at the beginning of each cycle by applying Eq. 2.3.

2.1.4.1.2 Contact kinetics

The relative displacement at contact, *c*, leads to the contact force and moment between the particles, F_i and M_i. However, the contact deformation between pairs of disk particles is restricted to an infinitesimal area (contact point) in DEM. That is, the contact moment cannot transmit significant moment due to the small contact area (Bardet, 1998, O'Sullivan, 2011). Therefore, contact kinetic energy is reduced to contact force. The contact force is resolved into normal, F_i^n, and shear, F_i^s, components with respect to the contact plane as:

$$F_i = F_i^n + F_i^s \qquad 2.6$$

The magnitude of the normal contact force is calculated by

$$\Delta F_t^n = k_n(\Delta_n)_t \qquad i.e. \;\; (F_{totall}^n)_t = \; (F_{totall}^n)_{t-1} + (\Delta F_n)_t \qquad 2.7$$

in which k_n is the normal stiffness [force/displacement] at the contact at current time step and relates incremental normal contact displacement and force. The value of this parameter will be determined by the contact model in further section. The magnitude of the shear contact force is calculated by

$$\Delta F_t^s = k_s(\Delta_s)_t \qquad i.e. \;\; (F_{totall}^s)_t = \; (F_{totall}^s)_{t-1} + (\Delta F_s)_t < \mu(F_{totall}^n)_t \qquad 2.8$$

in which k_s is the shear stiffness [force/displacement] at the contact at current time step and relates incremental shear contact displacement and force. The value of this parameter will be determined by the contact model in further section. μ is the inter-particle friction coefficient, assigned by user. If contact viscous damping is applied, a new term will be add to each component of Eq. 2.7 and 2.8.

$$\Delta F_t^n = k_n(\Delta_n)_t + D_n \quad and \quad \Delta F_t^s = k_s(\Delta_s)_t + D_s$$

$$D_i = c_i|\mathrm{v}_i|: \ i = n, s \quad and \quad c_n = \beta k_n \ \ c_s = \beta k_s \tag{2.10}$$

in which c_n, c_s, β, v_n, v_s and D_n, D_s are contact normal and shear damping coefficients, contact viscous constant, normal and shear contact velocities, normal and shear contact damping forces.

At the end of each time step the total tangential contact force at each active contact point is compared to Coulomb sliding friction criterion. If $F_{totall}^s > \mu(F_{totall}^n)_t$ the contact is broken, but the two particles will be checked at a future time step by the contact detection mechanism for potential contact. If $F_{totall}^s < \mu(F_{totall}^n)_t$, the two particles will be still in contact although the position of contact point may has been changed. At the end of each time step the resultant or out-of-balanced force and moment for each particle due to its contact points are computed. If local damping is required for simulation, a new term, F_i^d, is added to both resultant force and moment by following equation:

$$(F_i)_t^K = \sum_{\mathrm{n}=1}^{\mathrm{n_k}}[(\mathrm{F_n})_\mathrm{t}\,\mathrm{n}_i^\mathrm{c} + (\mathrm{F_s})_\mathrm{t}\mathrm{t}_i^\mathrm{c}] + F_i^d \qquad i = 1{,}2 \tag{2.11}$$

$$(M)_t^K = |l^K|\sum_{\mathrm{n}=1}^{\mathrm{n_k}}[\,(F_s)_t] + F_i^d \qquad i = 1{,}2$$

where $\mathrm{n_k}$ is number of contact points per particle. F_i^d is obtained as:

$$F_i^d = -\alpha|\mathcal{F}_i|sign\,(\mathrm{v}_i) \tag{2.12}$$

where F_i^d, $\alpha, |\mathcal{F}_i|$ and $sign\,(\mathrm{v}_i)$ are local damping force, damping constant, unbalanced force on the particle i^{th} and particle velocity, respectively.

2.1.4.1.3 Contact models

In order to compute the contact forces including normal and shear, the normal and tangential contact stiffnesses are required. These parameters are determined from contact normal and tangential models, which show how two particles interact together in normal and tangential directions. In general, the framework for these relationships is $K(P,\delta) = \frac{\partial P}{\partial \delta}$.

in which *P* is the component of contact force (normal or tangential) and δ is its corresponding normal or tangential displacement. Various types of contact models such as linear elastic, non-linear elastic Hertz and Elasto-plastic are proposed (e.g. Misra, 1995, Thornton and Ning, 1998, Cundall and Strack, 1979, Johnson, 1985). However, only elastic models have been used by *DEM* analysts in soil mechanics disciplines. It may be because the compression stiffness of soil particles is so much greater than the mass stiffness that particles cannot reach to the plastic zone. *PFC*^{2D} uses these models. Further assumptions are considered to produce the constitutive contact models:

- The surface of a particle is smooth,
- There is no friction between the particles
- There is no adhesion at the contact
- There is no viscosity

For more complicated constitutive models readers can refer to (Johnson, 1985).

2.1.4.1.4 The motion relationships

After obtaining the resultant forces and moments of each particle at each time step from Eq. 2.11 and adding the gravitational force and external loads (e.g. for those deformable boundary particles), Newton`s second law and the conservation law of angular momentum is applied to each particle to obtain the particle acceleration:

$$m(\ddot{x}_i)_t = (F_i)_t \quad i = 1,2 \qquad 2.13$$

$$I(\ddot{\theta})_t = (M)_t$$

where m and I are the mass and inertial moment of the particle respectively, $(F_i)_t$ and $(M)_t$ are the total resultant forces and moment at the central mass of each particle at time *t.* Based on the principles of DEM, the linear acceleration ($\ddot{x}$) and angular acceleration ($\ddot{\theta}$) of the particle during the time step $t-\frac{\Delta_t}{2}$ to $t+\frac{\Delta_t}{2}$ are constant. By using the formulation of central explicit finite difference method, the linear velocities and angular velocities of a particle can be obtained from the following equation:

$$(\dot{x}_i)_{t+\frac{\Delta_t}{2}} = (\dot{x}_i)_{t-\frac{\Delta_t}{2}} + \frac{(F_i)_t}{m}\Delta_t \qquad i = 1,2 \qquad 2.14$$

$$\left(\dot{\theta}\right)_{t+\frac{\Delta_t}{2}} = \left(\dot{\theta}\right)_{t-\frac{\Delta_t}{2}} + \frac{(M)_t}{I}\Delta_t \qquad i = 1,2$$

The coordinate of central mass of particle, (x_i) and the rotation (θ) at $t+\Delta_t$ is obtained from the following equation:

$$(x_i)_{t+\Delta_t} = (x_i)_t + \left[(\dot{x}_i)_{t+\frac{\Delta_t}{2}}\right]\Delta_t \qquad i = 1,2 \qquad 2.15$$

$$(\theta)_{t+\Delta_t} = (\theta)_t + \left[\left(\dot{\theta}\right)_{t+\frac{\Delta_t}{2}}\right]\Delta_t \qquad i = 1,2$$

These equations are updated at each time step by the *PFC* compiler to obtain the new positions of particles.

2.2 Homogenization method

The stress and strain tensors of a representative volume element (RVE) of a particulate assembly are generally measured by averaging procedures from inter-particle forces and displacements calculated from DEM. The methods to translate inter-particle forces and displacements into continuum mechanics stress and strain tensors are called homogenization techniques (or often called volume averaging methods). The transition from micro-scale to the macro-scale is associated with multi-scale modelling. Thus, homogenization technique is associated with multi-scale modelling. Applying this method to compute stress and strain tensors of a representative volume element of a

particulate assembly subjected to loading increases our understanding from the effect inter-particle force and displacement and their changing on the macro-mechanical behaviour of *RVE*. However, the homogenization method is dependent on the flow regime of the granular system being simulated (i.e. quasi-static regime, transient regime and rapid flow regime) (O'Sullivan, 2011). Based on these flow regimes, three different averaging methods are used: volume averaging, time-volume averaging and weighted time-volume averaging (Zhu and Yu, 2002). The first one, which is appropriate for quasi-static regimes and the other two are appropriate for transient and rapid flow regimes.

2.2.1 Micro-mechanical stress tensor

A stress tensor is one of the continuum variables, which do not exist at each contact point of discrete media. Instead, a contact force over an infinitesimal point, (i.e. contact point) is obtained from DEM. Calculating the average micro-mechanical stress tensor from a RVE region within a particulate assembly can be undertaken in three ways:

- Average macro stress tensor derived from boundary forces
- Average stress tensor derived from inter-particle forces

These methods will be compared in this section to detect their positive and negative aspects. In the case of static equilibrium (Chang and Kuhn, 2005) showed that the average macro stress is equivalent to the Cauchy stress tensor.

2.2.1.1 Average macro stress tensor derived from boundary forces

This approach is the quickest way to compute the stress tensor from DEM simulations. As shown in figure 2-6 the average stress along the rigid wall boundary or boundary particles is obtained by summing the inter-particle-wall or inter-particle-boundary particles contact force ($f_{c_{ij}}^{pw}$) of N_p number of particle over the length of sample, l, (for 2D case):

$$\sigma_{ij} = \frac{\sum_{N_p} f_{c_{ij}}^{pw}}{l} \quad where \;\; i,j = 1,2 \qquad 2.16$$

This method is also used for validating and calibrating the DEM simulations with laboratory tests such as biaxial and triaxial tests (e.g. Belheine et al., 2009). However, this method is only suitable for a *RVE* that has rigid wall boundaries. Therefore it is necessary to develop another method has to be developed for a RVE that represents a region within the DEM model since the boundary of the RVE is defined by particles.

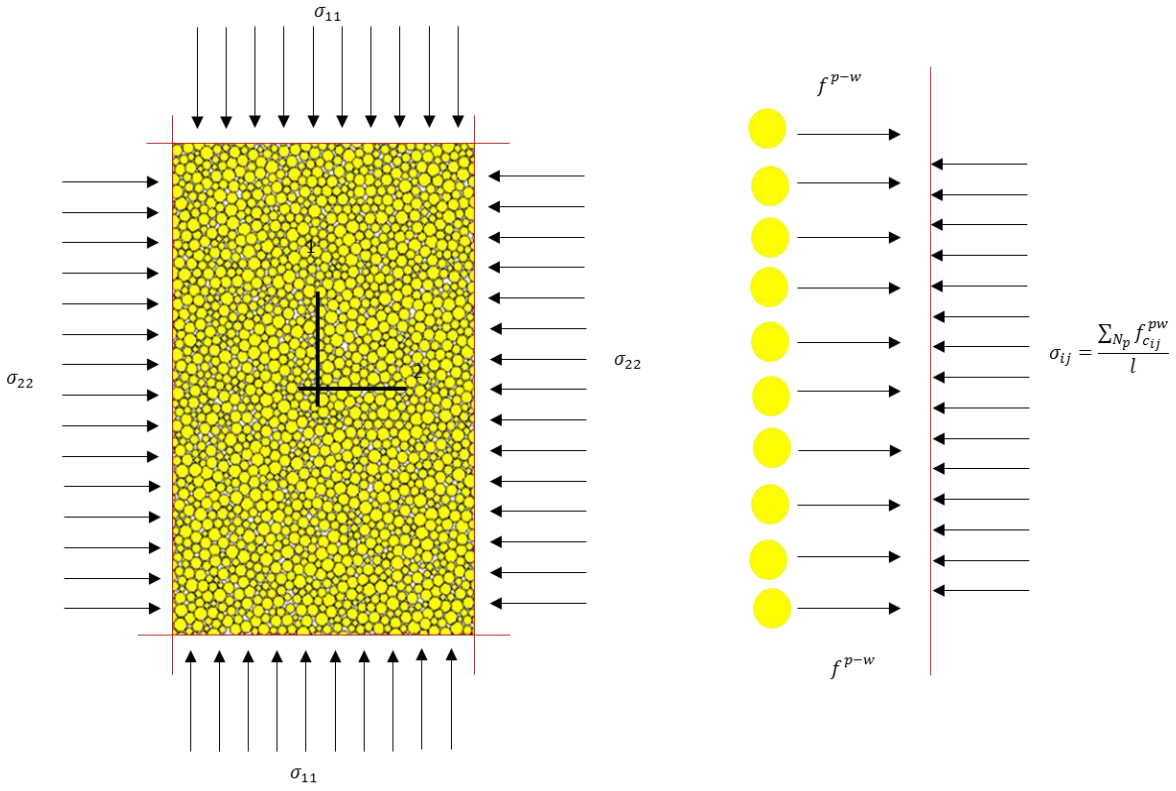

Figure 2-6 Computing the average macro stress from the boundary of sample

2.2.1.2 Average stress tensor derived from inter-particle forces

The aim of this method is to compute the average stress tensor, $\overline{\sigma}_{ij}$, of a *RVE* of a particulate system through the contact forces and position vectors of contact points of all the particles are in this element. A number of approaches were proposed by researchers to derive this relationship (e.g. Potyondy and Cundall, 2004, Rothenburg, 1980, Bagi, 1996, Li et al., 2009, Bardet and Vardoulakis, 2001). The basis of these methods is to measure the macro stress tensor of *RVE*, $\overline{\sigma}_{ij}$, from volume average of average particle stress tensor, $\bar{\sigma}_{ij}^{p}$,:

$$\overline{\sigma}_{ij} = \frac{1}{V}\sum_{N_p} \bar{\sigma}_{ij}^{p} V_P \quad where \quad \bar{\sigma}_{ij}^{p} = \frac{1}{V_p}\sum_{N_p} x_i^c f_j^c \tag{2.17}$$

where V_P is the volume of disk with unit thickness. V is the volume of *RVE* with unit thickness. x_i^c is the position vector of contact point. f_j^c is the inter-particle force. N_p is the number of contact points for each particle (see figure 2-7). As particles are assumed to be rigid in a DEM simulation, the idea of an average stress tensor for the particles seems to be somewhat misleading. However, $\bar{\sigma}_{ij}^{p}$ is used to define a term that has units of stress. The average stress tensor, $\overline{\sigma}_{ij}$, within *RVE* proposed by Potyondy and Cundall (2004) is as follows:

$$\overline{\sigma}_{ij} = \frac{1-n}{\sum_{N_p} V^p}\left(\sum_{N_p}\sum_{N_c^p} (x_i^c - x_i^p) n_i^c f_j^{c,p}\right) \quad i,j = 1,2,3 \tag{2.18}$$

where the summations are taken over the N_p particles. n is the porosity of the *RVE*, N_c^p is the number of contacts of each particle. $x_i^c \text{and } x_i^p$ are the position vectors of particle centroid and its contact points respectively. $f_j^{c,p}$ is contact force acting on particle, *p*, at contact *c*. This relationship is often used to calculate the average stress tensor of a group of particles that from a RVE. From this equation, it is quite clear that the microscopic average stress tensor of a particulate region is greatly dependent on the geometry of particle, contact coordinate and inter-particle forces. This method is embedded into *PFC*^{2D} (Itasca, 2008). The advantages of this method over that based on the boundary forces is that the contact forces between all the particles are considered and variation of the macro stress tensor within a DEM model can be calculated. However, there is a limit to the size of the region if the output is to have any meaning. For instance, if particle size distribution (PDE) is various, some particles are big and some is very small over the boundaries such that some of which may not have contact with others. Therefore, the macro average stress tensor obtained might be wrong. Rothenberg (1980) only took those particles lying along an *RVE* boundary (not the element boundary) to compute the average macro stress tensor:

$$\overline{\sigma}_{ij} = \frac{1}{V}\sum_{\beta \in S} x_i^{\beta} f_j^{\beta} \quad i,j = 1,2,3 \qquad 2.19$$

where x_i^{β} and f_j^{β} is the i^{th} component of the position vector of contact at point β and f_j^{β} is i^{t} component of the force vector at this point respectively (grey particles in figure 2-7). The main disadvantage of this method is that only those particles lying along the *RVE*'s boundary are considered. In addition, the deviation between the stress tensor attained using this method and that obtained by above method may be considerable, especially when the *RVE* is near boundaries. At these regions the fabric anisotropy may be significant because of particles movement and changing interaction forces.

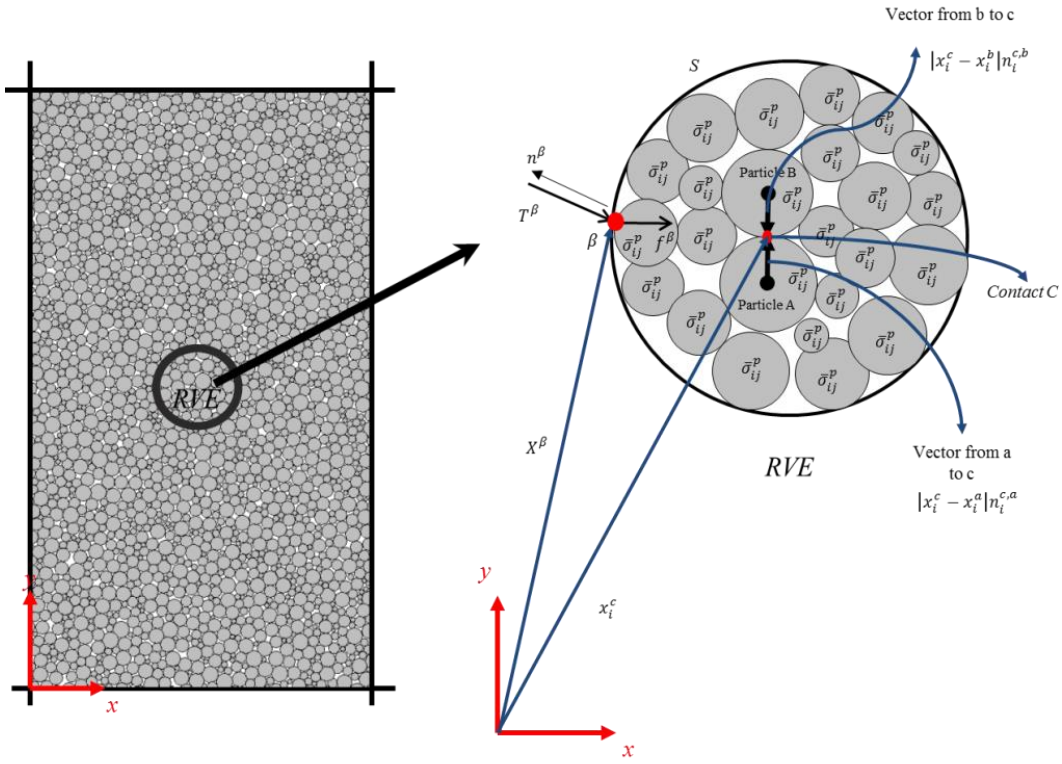

Figure 2-7 Introducing a typical representative volume element (RVE)

The structure of macro stress tensor proposed by (Bagi, 1996) is equal to the stress tensors derived using the method proposed by (Potyondy and Cundall, 2004). However, instead of considering a particle, a continuum cell is defined using the tessellation shown in figure 2-8. Applying this method increases the

time of simulation. It is because at each time step the cells are updated. In addition, the discrete space in this method is considered as a continuum space. This method is not used by other researchers who are interested in granular soil mechanics.

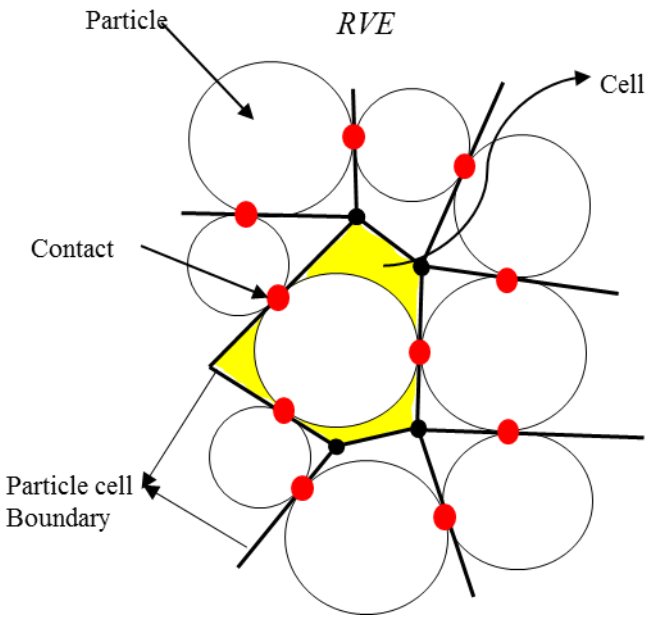

Figure 2-8 Particle cell diagram proposed by (Bagi, 1996)

It is worth mentioning that in deriving the average stress tensor from the mentioned methods, the effect of particle rotation is not considered.

(Bardet and Vardoulakis, 2001) proposed a method based on energy and virtual work methods to derive an average stress tensor. According to this study, the average stress tensor is anti-symmetric due to inter-particle moments. The amount of anti-symmetry in the average stress tensor is dependent on ratio of particle volume (or area in 2D case) to its circumference such that by increasing this value, the average stress tensor become more symmetric. However, the use of this method results in increasing the time of simulation because most of the time step portion is taken to compute the energy and virtual work for each particle.

2.2.1.3 Macro-mechanical strain tensor

The strain tensor, ε_{ij}, is a fundamental concept in continuum mechanics, which is used to calculate the relative displacement of each element from its gradient displacement tensor field.

$$\varepsilon_{ij} = \frac{1}{2}\left(U_{i,j} + U_{j,i}\right) = \frac{1}{2}\left(F_{ij} + F_{ji}\right) \qquad \text{where i, j} = 1,2 \qquad 2.20$$

where U_i is the displacement in i direction. $F_{ij} = U_{i,j}$ is the gradient displacement tensor field of each point within a continuum domain. By using Gauss divergence theorem, the volume integral is converted to the surface integral. Therefore,

$$F_{ij} = \frac{1}{V}\int_V \frac{\partial U_i}{\partial x_j} dV = \frac{1}{V}\oint_S U_i n_j dS \qquad 2.21$$

where dS is the differential surface area and V is volume. n_j is the j^{th} component of unit normal vector at each node. x_j is the position vector of each point.

Based on gradient displacement tensor field definition several methods have been suggested to compute the strain tensor such as Cauchy-Green, Piola, Green-Lagrange, Euler-Almansi strain tensors in continuum mechanics. For example, a gradient displacement tensor field used in finite element method (FEM) is based on linear interpolation between the relative displacements of mesh nodes.

In contrast, granular assemblies consist of discrete particles with finite size, such that each particle has its own translational and rotational degrees of freedom. These translations and rotations are greatly heterogeneous such that their magnitude and orientation vary from one particle to other particle. Therefore, the estimation of the particle displacements with a continuously differentiable gradient displacement tensor field is impossible.

However, in geotechnical engineering the interpretation of soil behaviour is done by using stress and strain tensors terms. Hence, establishing an approximate constitutive relationship between particles displacements within

a RVE and macro strain tensor is needed. The most important factor to establish this homogenized link is to find the approximate gradient displacement tensor field in terms of particle-level displacement. Hence, the aim of the existence macro-mechanical strain tensor methods is to estimate this gradient displacement tensor field. These methods are generally classified into two categories:

- Strains based on continuum approach
- Strains based on best-fit

These methods will be compared in this section.

2.2.1.3.1 Strains based on continuum approach

The basis of this approach is to replace the *RVE* with a triangulation graph, a line connecting the particles centroids (see figure 2-9). The interior space of this region is then assumed to be a continuum. The next step is to specify the displacement gradient tensor for each triangle by considering linear variation from relative displacement values at nodes (see Eq. 2-20 and 2-21). The average displacement gradient tensor for each triangle is assumed to be constant in this method. The size of RVE is changing during loading as particles within RVE are moving. The average homogenized macro-mechanical strain tensor for this domain is then determined by the two following methods:

- Average of each element strain tensor
- Average of boundary particles' strain tensor

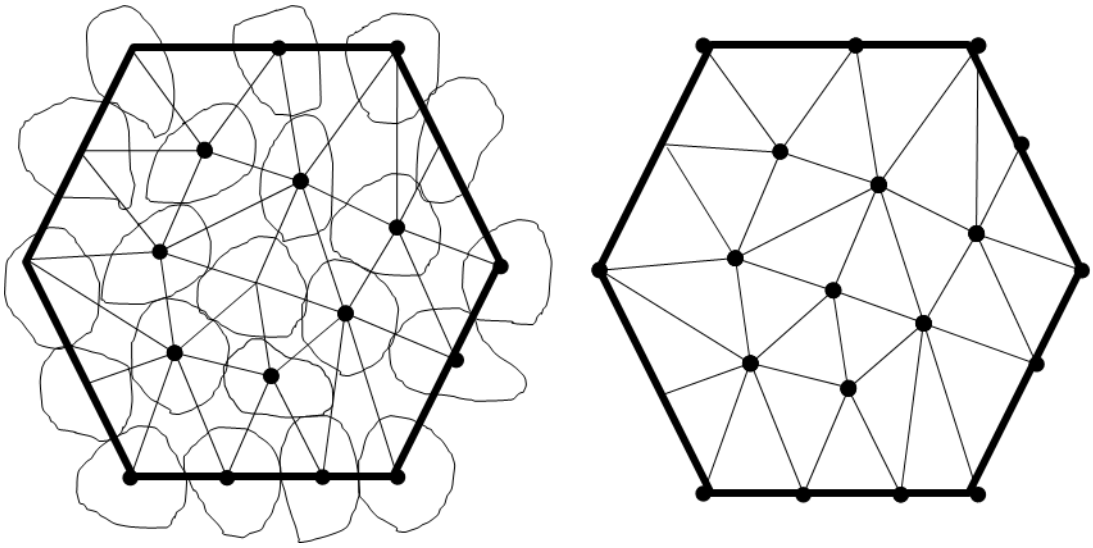

Figure 2-9 The configuration of RVE and its equivalent continuum domain at time t

2.2.1.3.1.1 Average of each element strain tensor

In this approach, a mesh is created as in FEM for the equivalent continuum polygon at each time step. Thus, the shape of particles is not important if this method is used. The node of each mesh is the particle centroid. Therefore, the nodal displacement can be extracted at each time step from DEM outputs. The strain tensor for each element, ε_{ij}^{e}, is then estimated from the nodal displacements of that element using Eq. 2-20 and 2-21. Eventually the average strain tensor of the equivalent continuum domain $\bar{\varepsilon}_{ij}$ is calculated by weighted average method:

$$\bar{\varepsilon}_{ij} = \frac{1}{V}\int_{V} \varepsilon_{ij}^{e}\, dV \qquad 2.22$$

where V is the volume of the equivalent continuum domain in *3D* or it is area in *2D*. A number of researchers (e.g. Bagi, 1996, Bagi, 1993, Kruyt and Rothenburg, 1996, Kuhn, 1997, Kuhn, 1999, Cambou et al., 2000, Dedecker et al., 2000, Kruyt, 2003, O'Sullivan et al., 2003) applied this method to find out a more accurate average strain tensor. Although the fundamental of these methods is the same, they do differ.

Bagi method: this method which is applicable for both *2D* and *3D* assemblies of particles with any arbitrary shape was proposed by (Bagi,

1996, Bagi, 1993). The strain tensor for each element is based on its vertices displacement. Due to this constant displacement gradient, the displacement of each point within this triangular element is found by using linear interpolation. The RVE's boundary passes through the centres of boundary particles (see figure 2-10). That is, the condition of connecting boundary particles with together is not necessary. The particle rotation or anti-symmetric part of the strain tensor is not considered in this method. At each time step the nodal displacement for each mesh is calculated by DEM code such as PFC, the strain tensor for each element (i.e. Eq. 2-20 and 2-21) can be computed by directly by DEM code by adding a subroutine to this code. Finally the average strain tensor of the RVE is calculated from Eq. 3.31 directly from DEM model. Thus, all calculations are performed by DEM code and there is no need to use another method in corporation with DEM code. This is one of the advantage if this approach.

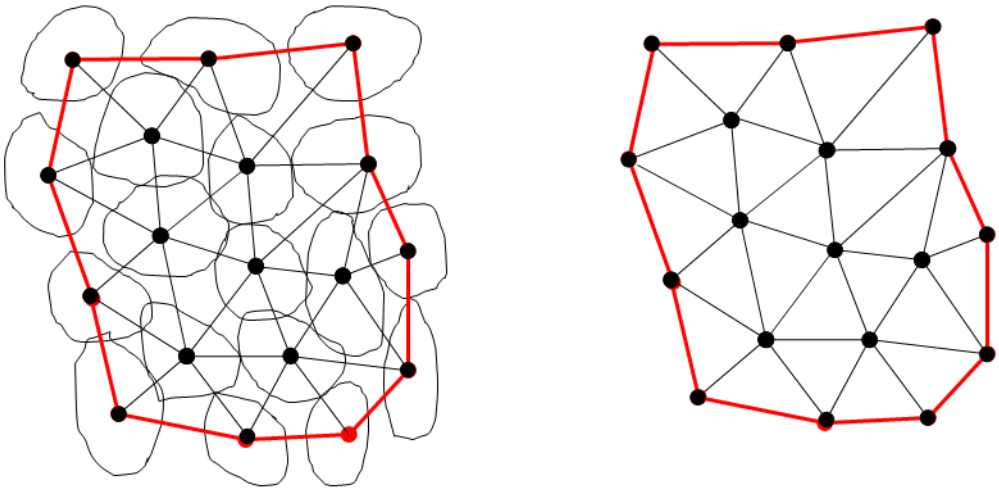

Particle configuration: Red line is boundary of RVE

Bagi equivalent continuum zone along with mesh

Figure 2-10 Bagi method

The Kruyt–Rothenburg method: this macro-structural strain tensor method which is only applicable for 2D particulate systems with any arbitrary shape was proposed by (Kruyt and Rothenburg, 1996).The triangulation of *RVE* in

this method goes through the centres of particles that are in contact (see figure 2-11).The strain tensor for each element is determined from the vertices displacement. The particle rotation or anti-symmetric part of the strain tensor is not also considered in this method. The disadvantage of this method is its high volume of calculations.

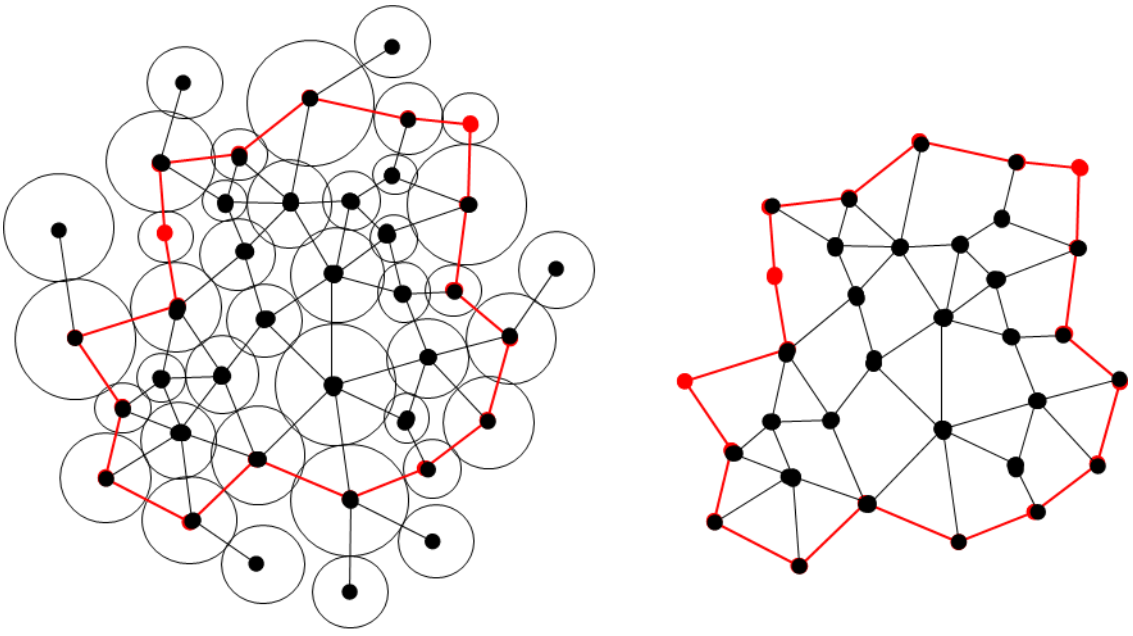

Particle configuration: Red line is boundary of RVE

Kruyt–Rothenburg equivalent continuum zone along with mesh

Figure 2-11 The Kruyt–Rothenburg equivalent continuum

Kuhn method: the framework of this method is the same as Kruyt–Rothenburg method. The only difference is that the triangulation of the equivalent continuum domain in this method is restricted only to those particles that take part in the load-bearing framework (Kuhn, 1997, Kuhn, 1999). The disadvantage of this method is its high volume of calculations.

Cambou method: this method which was proposed by (Cambou et al., 2000) and (Dedecker et al., 2000) in terms of mathematical structure is almost the same as Bagi method. The only difference between those

methods is in the detail of triangulation of *RVE*. The disadvantage of this method is its high volume of calculations.

Kruyt method: this micro-structural strain tensor method is only applicable for *2D* assemblies of circular particles (Kruyt, 2003). The triangulation of the equivalent continuum domain in this method is the same as Kruyt–Rothenburg method but the strain tensor determined in this method includes the particle rotation or anti-symmetric part. The disadvantage of applying this method is its high volume of calculations.

O'Sullivan et al. method: This method was proposed by (O'Sullivan et al., 2003). The geometry of *RVE* in this method is restricted to a rectangular geometry (see figure 2-12). A rectangular mesh is created within the *RVE*. The nodes of the mesh are referred to as grid points. The interpolated displacements and displacement gradients are calculated at these grid points using the mesh free interpolants. The displacement of the particle centroids are known from the DEM analysis. Each particle within the RVE has a zone of influence, the compact support. It is simply a multiple of the radius of the particle and will include some grid points. The displacement gradient tensor, including translation and rotation, for each compact support is calculated using the reproducing kernel particle method (RKPM). The advantage of this method is to have a smoother continuous gradient displacement field for the RVE. However, applying this method increases the time of simulation.

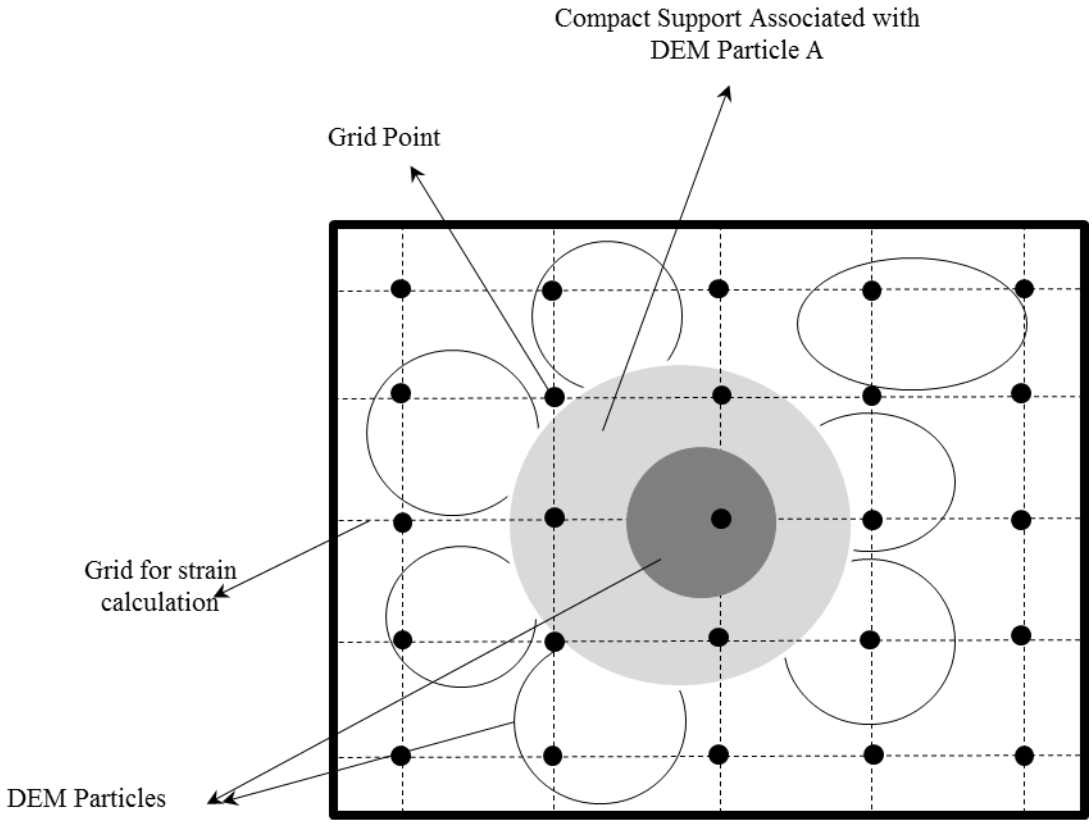

Figure 2-12 A compact support (After O'Sullivan et al. (2003)

A common feature of these methods is to assign a gradient displacement tensor field to the void spaces, which leads to unrealistic macroscopic response of particulate assemblies. In addition, the use of any of these methods using *PFC*^{2D} requires a *C*$^{++}$ subroutine. The *PFC*^{2D} compiler should then compile this subroutine at each time step. This increases the time of simulation.

2.2.1.3.1.2 Average of boundary particles' strain tensor

The estimation of the displacement gradient field in this approach is only dependent on RVE's boundary vertices displacements. That is, the displacements of the particles within RVE are not considered. The size of RVE changes during loading. The continuous boundary in this method is broken into a number of straight lines as shown in figure 2-13. The average stress tensor, ε_{ij}^{e}, and displacement gradient tensor for each line is then computed. A number of researchers (e.g. Bardet and Proubet, 1991, Bonilla,

2004) applied this method to find out a more accurate average strain tensor and displacement gradient tensor.

Bardet and Proubet method: (Bardet and Proubet, 1991) proposed a method to calculate the strain tensor based on vertices displacement of the equivalent continuum domain. This method is more applicable for studying the shear band or localization phenomena in two dimensions. The particle rotation or anti-symmetric part of the strain tensor is also considered. In this method, the circumference of the equivalent continuum domain is broken into the straight lines such as *AB*, *BC* and others with their lengths S_k (see figure 2-13). Assuming the displacement for each line on each boundary piece such as *AB* is a linear function of the end points, Eq. 2-21 are becomes:

$$F_{ij} = \frac{AB}{2}\left(U_i^A + U_i^B\right)n_j^{AB} + \frac{BC}{2}\left(U_i^B + U_i^C\right)n_j^{BC} \qquad 2.23$$

n_j is the j^{th} component of unit normal vector of each line.

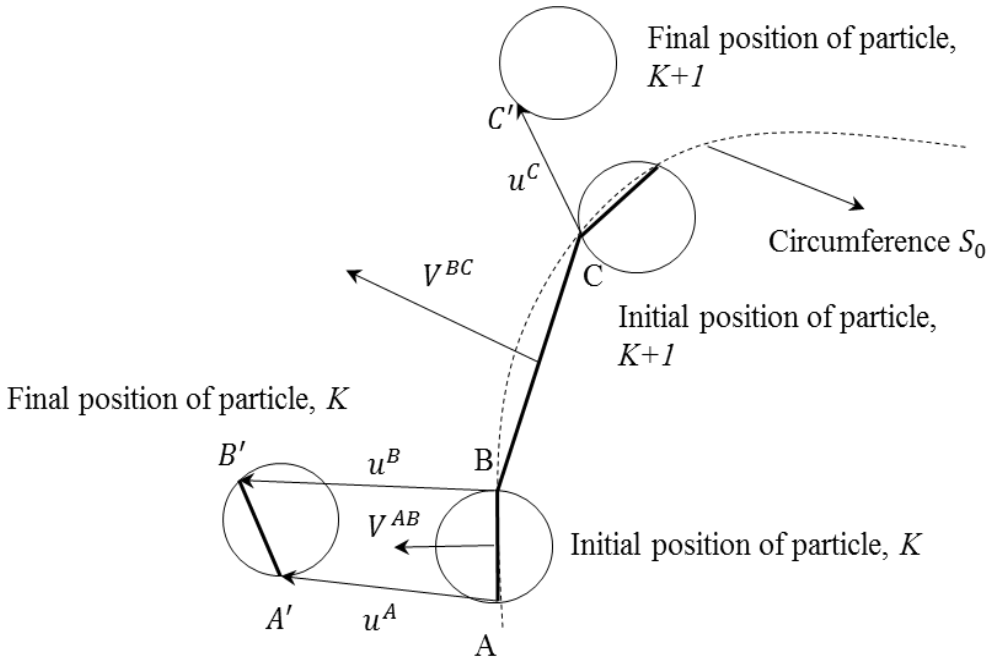

Figure 2-13 Calculating the average displacement gradient tensor considering the particle rotation (After Bardet and Proubet, 1991).

Bonilla method: the framework of this method is the same as Bardet and Proubet method expect that particle rotation is not considered (Bonilla, 2004). Therefore, the obtained average strain tensor by this method is as follows:

$$\varepsilon_{ij} = \frac{1}{V}\sum_{\beta=1}^{n_\beta}[\frac{1}{2}\left\{\Delta x_i^\beta + \Delta x_i^{\beta+1}\right\}e_j^\beta S^\beta] \;\; i,j = 1,2 \qquad 2.24$$

The parameters in this equation are shown in figure 2-14. *V* is the volume or area (in *2D* analysis) of the polygon of the equivalent continuum domain with sides' length of S^β. The vertices of this polygon correspond with the boundary particles. Each side of this polygon is defined by the coordinate of its two adjacent particles, *β* and *β+1*, with their displacement in *i* direction is Δx_i^β and $\Delta x_i^{\beta+1}$ respectively. The quantity of e_j^β is also the j^{th} component of unit normal vector on the side S^β.

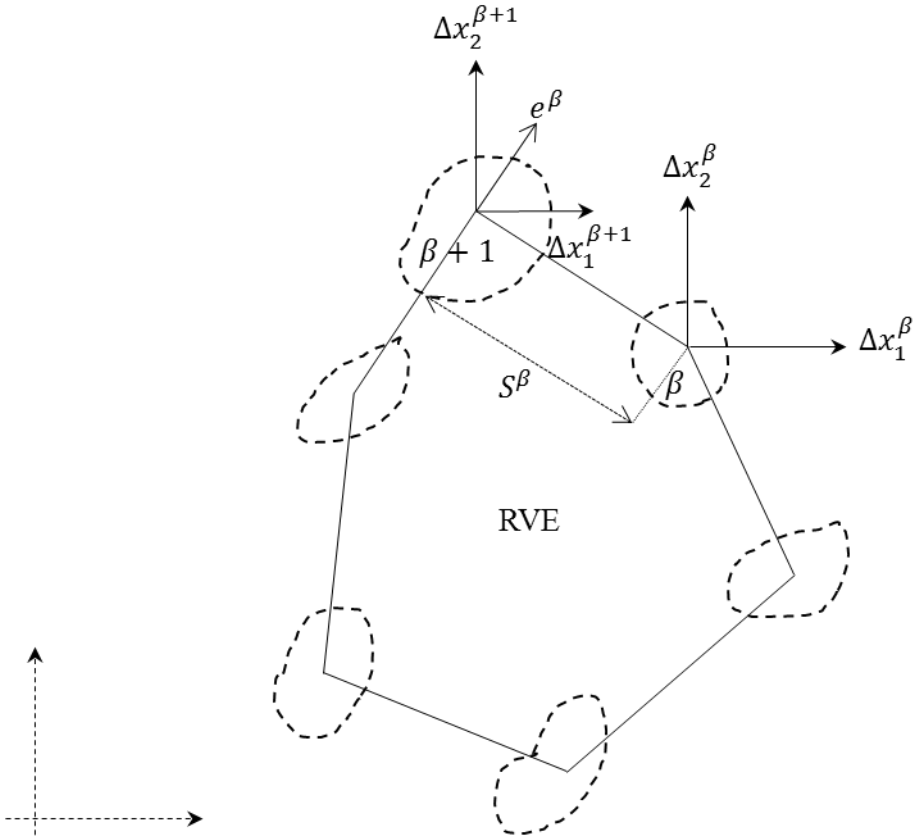

Figure 2-14 Calculating the average strain tensor is based on boundary particle translation (After Bonilla, 2004)

Only the displacements of the particles on the boundary of a RVE are used to compute the average strain tensor of the RVE. The displacements of the interior particles are not taken into account when calculating the strain tensor. This can lead to erratic displacement vector fields for those particles near the boundary boundaries producing an unrealistic strain tensor for the region.

In addition, the real contact between boundary particles of a RVE is not considered in these methods, care has to be taken in selecting the size of RVE. The number of boundary particles for a RVE is constant which means that a *RVE* deforms the particles may separate from one another leading to an erratic distribution of the strain tensor on the boundary giving an unrealistic strain tensor for that region. Thus this method may be acceptable for small regions where the displacements at the boundary are limited but inappropriate where displacements are much greater.

The average strain tensor obtained from the boundary particles is not the same as the average stress tensor obtained from each particle within an RVE.

However, in both approaches, the average of each element strain tensor and the average of boundary particles' strain tensor, the volume of RVE is changing during loading. Thus, tracking the strain tensor for a constant position of RVE within a particulate system by applying these methods is impossible. If static and lower quasi-static loading is applied for a particulate system such that unbalanced forces are nearly zero, these methods can be applied with caution. In addition, these methods apply a strain tensor field to the void spaces and do not consider the granular media. Moreover, the strain tensor components obtained from these methods are based on continuum mechanics assumption while the stress tensor components are obtained from the inter-particle forces. Thus, the stress and strain tensors may not compatible because they obtained from two different spaces (i.e. continuum and discrete). Hence, an approach is required to track the strain tensor for a constant position of RVE within a particulate system, using an individual particle displacement to extract the strain tensor that is compatible with

average stress tensor. In the following section this approach will be described.

2.2.1.3.2 Strains based on best-fit

The gradient displacement tensor in this method is only allocated to those particles where are a RVE. The volume and location of the RVE change as the DEM model deforms therefore it is not possible to track the strain tensor at a particular location. Further the strain tensor is based on a continuum whereas the stress tensor is based on the contact forces between the particles thus they are not compatible.

Since only one accurate displacement vector field and one displacement gradient tensor can be determined for each particle within an RVE, the average displacement vector field is based on the best-fit method to derive a displacement vector field equation which most describes the characteristic displacements of RVE to obtain the displacement gradient tensor of that region. The characteristic displacements of that RVE can be the displacements of particle centres (with or without considering the rigid-body rotation) or the relative translations at the contact points. A number of researchers (e.g. Potyondy and Cundall, 2004, Liao et al., 1997, Cambou et al., 2000) used this method to provide a more accurate average strain tensor.

Potyondy and Cundall method: this method is proposed by (Potyondy and Cundall, 2004). An average strain tensor is defined instead of specifying a form to compute the average strain tensor. The average strain-rate tensor in this method is based on the velocities of particle centres without considering the effect of particle rotation velocity (i.e. rigid-body-like rotation velocity). In this method, the velocity and position vector of each particle is firstly calculated as a relative velocity and position vectors with respect to the mean velocity and position vectors of N_p particles centres (see Eq. 2.26 and 2.28). As only one accurate displacement vector field and one displacement gradient tensor can be specified for each particle within the RVE, a best-fit method (i.e. a first-order polynomial equation or higher order polynomial equation) is applied to predict a gradient velocity field and gradient translation field from those calculated data; (Itasca, 2008) and (Potyondy and Cundall,

2004) suggested a linear equation in order to obtain the gradient velocity tensor (or strain-rate tensor), $\dot{\varepsilon}_{ij}$, which is as follows:

$$\tilde{v}_i^{P,rel} = \dot{\varepsilon}_{ij} x_j^{P,rel} \tag{2.25}$$

$$x_i^{P,mea} = X_i^P - \frac{1}{N_p}\sum_{i=1}^{N_p} X_i^P \tag{2.26}$$

where $\tilde{v}_i^{P,rel}$, X_i^P and $x_i^{P,rel}$ are the relative velocity vector, position vector and the relative position vector of each particle, respectively and N_p is the number of particles within the measurement region. For the particulate assemblies, this velocity gradient tensor,$\dot{\varepsilon}_{ij}$,is calculated in such a way that the velocity gradient tensor has the minimum deviation from the data on which it is based (i.e. $\tilde{V}_i^{P,mea}$). Therefore:

$$\frac{\partial E}{\partial \dot{\varepsilon}_{ij}} = 0 \tag{2.27}$$

$$\tilde{V}_i^{P,mea} = V_i^P - \frac{1}{N_p}\sum_{N_p} V_i^P \tag{2.28}$$

$$E = \sum_{N_p} \left|\tilde{v}_i^{P,rel} - \tilde{V}_i^{P,mea}\right|^2 = \sum_{N_p} \left|\dot{\varepsilon}_{ij} x_i^{P,rel} - \tilde{V}_i^{P,mea}\right|^2 \tag{2.29}$$

where E, V_i^P and $\tilde{V}_i^{P,mea}$ is the approximation error, the translation velocity vector and the measured relative velocity of particle respectively. The minimization process is the least squares approach. Solving Eq. 2.29 leads to the system of equations (for *2D* case):

$$\begin{bmatrix} \sum_{N_p} \tilde{x}_1^{P,\tilde{V}_i^{P,mea}} \tilde{x}_1^{P,\tilde{V}_i^{P,mea}} & \sum_{N_p} \tilde{x}_1^{P,\tilde{V}_i^{P,mea}} \tilde{x}_2^{P,\tilde{V}_i^{P,mea}} \\ \sum_{N_p} \tilde{x}_2^{P,\tilde{V}_i^{P,mea}} \tilde{x}_1^{P,\tilde{V}_i^{P,mea}} & \sum_{N_p} \tilde{x}_2^{P,\tilde{V}_i^{P,mea}} \tilde{x}_2^{P,\tilde{V}_i^{P,mea}} \end{bmatrix} \begin{pmatrix} \dot{\varepsilon}_{i1} \\ \dot{\varepsilon}_{i2} \end{pmatrix} = \begin{Bmatrix} \sum_{N_p} \tilde{V}_i^{P,\tilde{V}_i^{P,mea}} \tilde{x}_1^{P,\tilde{V}_i^{P,mea}} \\ \sum_{N_p} \tilde{V}_i^{P,\tilde{V}_i^{P,mea}} \tilde{x}_2^{P,\tilde{V}_i^{P,mea}} \end{Bmatrix} \tag{2.30}$$

These equations can only be solved (i.e. components of strain-rate tensor $(\dot{\varepsilon}_{11}, \dot{\varepsilon}_{12}, \dot{\varepsilon}_{21} \text{and } \dot{\varepsilon}_{22})$) if there exist at least three particles whose centres are not co linear.

This average strain tensor (see Eq. 2.30) is compatible with the average stress tensor derived from discrete particles within RVE the same *RVE* (see Eq. 2.25). This method is compatible for PFC^{3D} and PFC^{2D} softwares. Unlike continuum methods, the number of boundary particles of *RVE* in not restricted in this method. Therefore the number of particles within a *RVE* can freely change. Therefore, the effects of fabric anisotropy on the average strain tensor are considered in this method. There is no need to add a C^{++} subroutine to the *PFC* code in order to calculate the average strain tensor.

Liao et al. method: The main difference between this method (Liao et al., 1997) and Potyondy and Cundall method is to include the rigid body motions of each particle.

Cambou et al. methods: (Cambou et al., 2000) proposed two methods which are the result of improving the Liao et al. method. In the first method, the effect of rigid body motion is not taken into account and in the second method the effect of neighbouring particles is considered in the equations in order to predict the strain tensor.

2.3 Conclusion

In this chapter, the concepts of the Discrete Element Method to analyse granular media is described. In DEM, the motions of each particle are calculated through an explicit time integration scheme that operates under the principle that during a small time step the change in velocities and accelerations is so small that they can be assumed constant within that time step. During a calculation cycle, the interaction between particles is tracked and the contact forces are updated based on the contact laws. The particle equations of motion are then integrated to obtain new particle positions. As a result, in each time step, new contacts are formed and some existing contacts are deleted. The main advantages of this method are to provide abundant information at particle scale such as contact force and contact deformation, which can be used to comprehend the physics of granular systems. It was seen that this method has been applied by many researchers to study the sand medium.

In terms of average stress tensor methods, the average macro stress tensor derived from boundary forces (Eq. 2.16) is the quickest way to compute the macro stress tensor from DEM simulations and properly validate and calibrate the DEM simulations with laboratory tests such as biaxial and triaxial tests. However, if the aim is to study the average stress tensor from a RVE within a particulate system, this method is not appropriate. Thus, other methods are required to compute the average stress tensor within a particulate region. The method proposed by Bardet and Vardoulakis results in increasing the cost of simulation. It is because most of the time step portion is taken to compute the energy and virtual work for each particle. Applying the method of Bagi increases the cost of simulation. It is because at each time step, cells should be recognized then the mechanical calculation should be performed. In addition, a stress tensor field assigned to the void spaces in this method. The method proposed by (Potyondy and Cundall, 2004) is more appropriate to compute the average stress tensor within a particulate region because this method considers only the effect of all individual particles within a *RVE*, while the method proposed by (Rothenburg, 1980) only considers those particles lying along the *RVE*'s circumference.

In terms of strain tensor, two general approaches were discussed: strains based on continuum approach and Strains based on best best-fit. The former approach, which assumes the interior space of RVE is continuous, is then split into two separate methods: average of each element strain tensor and average of boundary particles' strain tensor. Based on these two approaches, several methods were illustrated. The main disadvantage of these methods is that the volume of RVE is changing during loading. Thus, tracking the strain tensor for a point within a particulate system by applying these methods is impossible. If static and quasi-static loading applied to a particulate system such that unbalanced forces are nearly zero, these methods can be applied with caution. In addition, these methods apply a strain tensor field to the void spaces and cannot consider the granular media. Since, the average strain tensor components obtained from these methods are based on continuum mechanics assumption, this average strain tensor may not be compatible with average stress tensor extracted from inter-

particle forces because they obtained from two different spaces (i.e. continuum and discrete).

In the best-fit approach, the disadvantages of applying continuum methods are solved by considering the discrete space of RVE. The Potyondy and Cundall method may estimate the realistic strain tensor for sand media because it considers particle displacement to derive the average strain tensor while Liao et al. and Cambou et al. methods consider particle deformation instead of particle displacement to derive the average strain tensor. However, for those granular systems that impact behaviour (i.e. particle deformation) is dominant such as fluid and gas media these average strain methods, obtained from particle deformation, would be proper. Additionally, in this approach the location of RVE is constant during particle movement. Thus, we can track the average strain tensor for a constant position of RVE within a particulate system during loading.

Chapter 3

3 The literature review

3.1 Introduction

Piled foundations in seismic hazardous regions are damaged by earthquakes due to the effect of seismic loads on the soil-pile interaction and the development of soil particles' instability adjacent to the pile. The interface friction capacity plays a major role on the seismic pile capacity. To understand how a seismic load affects the capacity of a pile, it is necessary to study the changes in that interaction to the soil fabric. Since the pile capacity is a function of the interaction between individual soil particles and the pile the discrete element method of analysis is considered to be the most appropriate method. Thus, a comprehensive review in the concepts of wave propagation in solid media is carried out to address the appropriate boundary condition for seismic problems. It follows by reviewing in the concepts of seismic behaviour of pile to address the gap. The current development in DEM model for earthquake wave propagation and soil-pile interaction is carried out. The importance of monitoring of fabric quantities during loading will be discussed.

3.2 Literature review of seismic shear wave propagation through the soil using DEM

3.2.1 Introduction

Wave propagation through a particulate system is dispersive if the wavelengths of induced seismic wave approach to the mean particle size of granular system. Since the wavelength of earthquake waves is much longer than the size of sand particles, the wave propagation through a particulate system can be assumed to be similar to that in a continuous elastic medium (Toomey and Bean, 2000, Itasca, 2008, Marketos and O'Sullivan, 2013). In contrast to continuum mechanics, in which the wave propagation through a solid system is simulated by applying wave propagation equation (see section 3.2), the phenomena of wave propagation using DEM is simulated by

considering the physics of individual particle vibration. Due to the computational cost of DEM simulations, granular media is discretized into small parallelepiped cells. Each cell is then simulated by DEM. By applying the homogenization method (i.e. average method), the macro-scale behaviour of each cell is then computed. Thus, the continuum definitions applied in seismic wave propagation field such as shear wave velocity, impedance ratio and dynamic or viscous damping boundary concepts can be used in DEM simulations. These issues will be required to develop the dynamic deformable boundary particles discussed in chapter 6. They are discussed in following sections.

3.2.2 The overview of seismic wave propagation through the infinity solid continuum media

The rational approach to analytical study of earthquakes effects in soil deposits is to consider them as wave propagation problems in solid infinite continuum space. This leads to consider the attenuation and radiation of seismic energy from the excited zone to each point within the model. It is to be noted that the infinity term is a mathematical concept and it is considered when the aim is only to find the closed form analytical solutions for a system with simple geometrics.

Due to the seismic excitation, the acceleration, velocity and displacement vector fields, which are time-dependent, are developed in three directions within a solid media (Pujol, 2003). These time-dependent variables result in development of stiffness, inertia and viscous forces on elements. Depending on the received amplitude and frequency of displacement vector fields (or acceleration and velocity vector fields) of seismic loading to each element, changes in the geometry and characteristic behaviour of solid elements including volumetric deformation, and distortion will be taken place. (Ishihara and Knovel, 1996) categorized dynamic events base on time of loading and number of repetitions of each sinusoidal impulse (see figure 3-1). In terms of an earthquake event, each sinusoidal displacement, velocity or acceleration impulse during an earthquake involves 10-20 times cycles. In addition, earthquakes generate low-frequency seismic waves (Marketos and O'Sullivan, 2013).

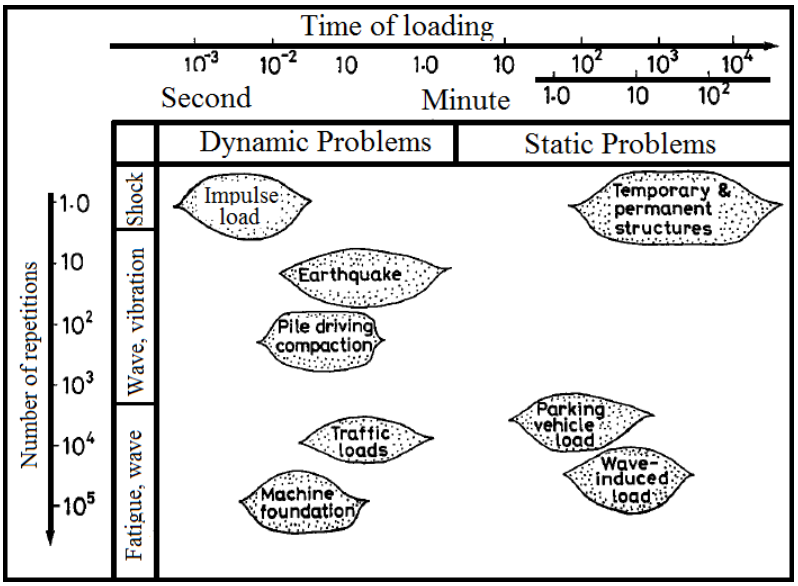

Figure 3-1 Categorizing dynamic events base on time of loading and number of repetitions of each sinusoidal impulse (After Ishihara, 1996)

The induced gradient of stress tensor on the element due to received displacement vector fields on it ($\boldsymbol{u}_1$, $\boldsymbol{u}_2$ and $\boldsymbol{u}_3$) is shown at figure 3-2.

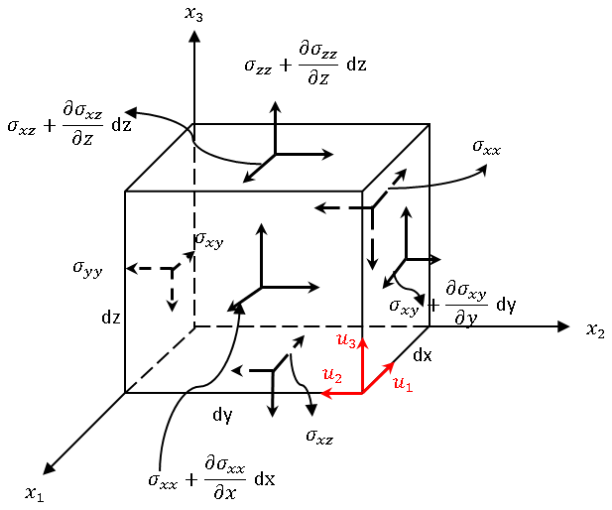

Figure 3-2 The gradient of stress tensor on the typical soil element due to displacement vector field $\boldsymbol{u}_1$, $\boldsymbol{u}_2$ and $\boldsymbol{u}_3$ at three directions.

Applying the dynamic equilibrium equation at three perpendicular directions (i.e. for 3D analysis) for this element due to these three perpendicular

displacement vector fields leads to the wave propagation equations in three directions (see Eq. 3.1).

$$\rho_{bulk}\frac{\partial^2\vec{u}}{\partial t^2}=\frac{\partial\sigma_{ij}}{\partial x_j}+\rho_{bulk}f_i \qquad \vec{u}=\begin{bmatrix}\vec{u}_1\\ \vec{u}_2\\ \vec{u}_3\end{bmatrix} \tag{3.1}$$

where ρ_{bulk} is bulk density and term $\rho_{bulk}f_i$ represents body force. The above equation can be used for any type of constitutive model. However, elastic wave propagation is widely used in research to illustrate the behaviour of soil under seismic load. For this purpose, the viscous-elastic constitutive model applied for soil (Kramer, 1996; Ishihara, 1996; Prakash, 1981; Zamani and El Shamy, 2011; Novak and Nogami, 1977; Makris and Gazetas, 1992; Mylonakis et al., 1997). By combining Hooke's law ($\sigma_{ij}=\lambda\delta_{ij}\varepsilon_{kk}+2\mu\varepsilon_{ij}$) and the relation between strain tensor field and displacement vector field ($\varepsilon_{ij}=\frac{1}{2}[\frac{\partial u_i}{\partial x_i}+\frac{\partial u_j}{\partial x_i}]$, the displacement vector field of a typical element of a general isotropic elastic solid can be obtained. However, for an inhomogeneous material where the Lame parameters are not constant, the analytical close-form solution for a displacement vector field of the element is impossible. The problem can be analytically solved with the following assumptions:

- The material is homogeneous,
- The material is linear elastic and
- Deformations are small.

Considering these assumptions and limitations, the displacement equation of an element during the wave propagation is as follows:

$$\frac{\partial^2\vec{u}_i}{\partial t^2}=\left[\frac{\lambda+\mu}{\rho_{bulk}}\right]\frac{\partial\varepsilon_V}{\partial x_i}+\left[\frac{\mu}{\rho_{bulk}}\right]\nabla^2\vec{u}_i+f_i \tag{3.2}$$

where λ and μ are the Lame parameters and ∇^2 is Laplacian operator and that is:

$$\nabla^2=\frac{\partial^2}{\partial x^2}+\frac{\partial^2}{\partial y^2}+\frac{\partial^2}{\partial z^2} \tag{3.3}$$

The close-form solution of Eq. 3.2 leads to two sets of independent answers (see Eq. 3.4 and 3.5). That is, only two types of seismic waves can generate and propagate within an infinity space: Primary wave and Secondary wave. The response of element due to P-wave propagation is as follows:

$$\frac{\partial^2 \varepsilon_V}{\partial t^2} = \left[\frac{\lambda + 2\mu}{\rho_{bulk}}\right] \nabla^2 \varepsilon_V + \sum_{i=1}^{3} f_i \qquad 3.4$$

where term $\left[\frac{\lambda+2\mu}{\rho_{bulk}}\right]$ represents Primary (or compressive) seismic wave velocity. By considering the fact that the ε_V, volumetric strain, is the result of isotropic stress applied on the element, it can be concluded that the propagation of P-wave only leads to an isotropic stress, σ_P, and volumetric strain within a solid element (see figure 3-3).

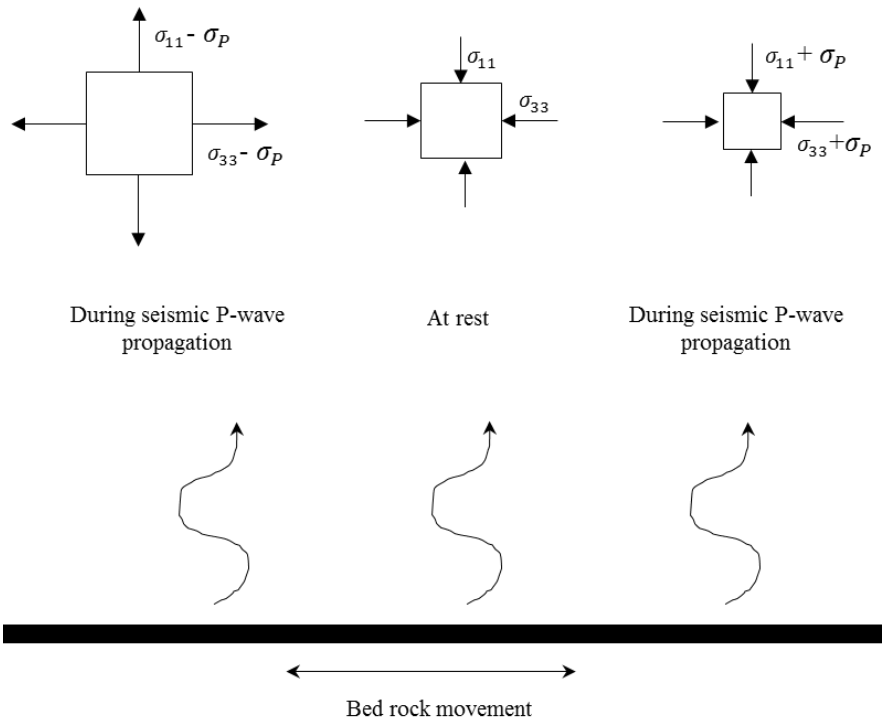

Figure 3-3 The vertical propagation of P-wave within a soil media and the reaction of soil element to this wave schematically

The response of an element due to S-wave propagation is as follows:

$$\frac{\partial^2 \omega_1}{\partial t^2} = \left[\frac{\mu}{\rho_{bulk}}\right] \nabla^2 \omega_1$$

$$\frac{\partial^2 \omega_2}{\partial t^2} = \left[\frac{\mu}{\rho_{bulk}}\right] \nabla^2 \omega_2 \qquad 3.5$$

$$\frac{\partial^2 \omega_3}{\partial t^2} = \left[\frac{\mu}{\rho_{bulk}}\right] \nabla^2 \omega_3$$

where term $\left[\frac{\mu}{\rho_{bulk}}\right]$ represents shear seismic wave velocity. By considering this fact that $\omega_1 = \frac{1}{2}[\frac{\partial u_3}{\partial y} - \frac{\partial u_2}{\partial z}]$, $\omega_2 = \frac{1}{2}[\frac{\partial u_1}{\partial z} - \frac{\partial u_3}{\partial x}]$ and $\omega_3 = \frac{1}{2}[\frac{\partial u_2}{\partial x} - \frac{\partial u_1}{\partial y}]$ are the rotation tensor of each side of element, it can be concluded that the propagation of an S-wave leads to distortion of element with constant volume such that pure shear stress is developed on the sides of element (Prakash, 1981, Kramer, 1996, Ishihara, 1996) (see figure 3-4).

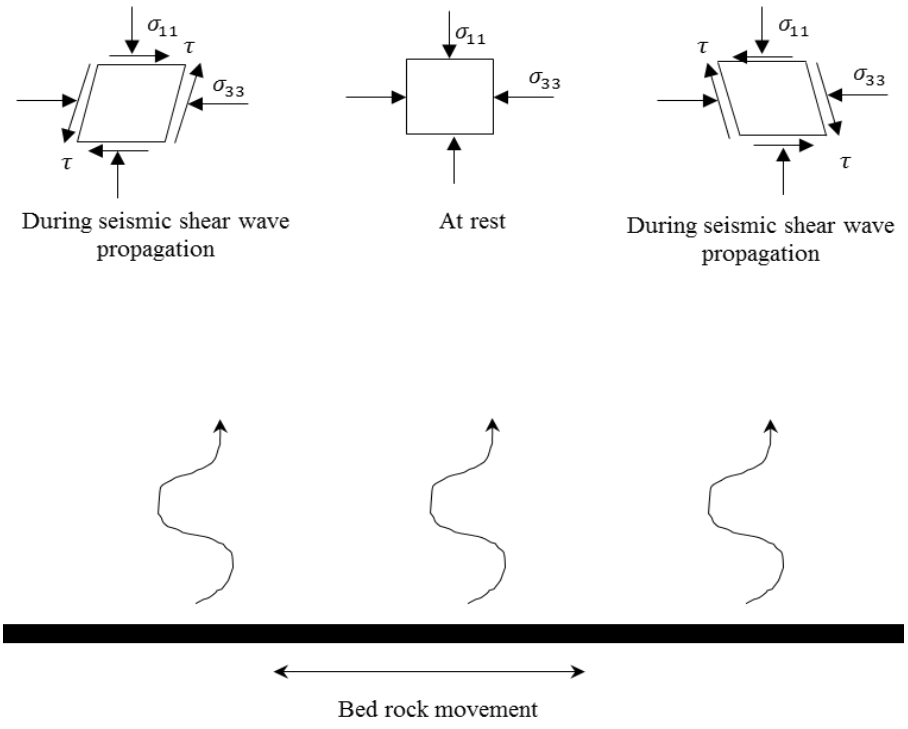

Figure 3-4 The vertical propagation of S-wave within a soil media and the reaction of soil element to this wave.

This leads to this conclusion that seismic P-wave and S-wave propagation cannot influence the gravity acceleration field as seen in figures 3-3 and 3-4. Thus, the static vertical and horizontal in-situ stresses applied on the boundaries of a solid continuum element do not alter during earthquakes. Rather a dynamic stress tensor field which will be further discussed should be superimposed on them. Another conclusion can be met from Eq. 3.4 and 3.5 is that the propagation of P-wave in solid continuum media does not generate S-wave and vice versa.

3.2.3 Dependency of deformation characteristics upon shear strains

The deformation characteristics of soils depend upon the shear strains to which soils are subjected. Based on the induced shear strains, soil behaviour can be categorised into three stages: elastic, elasto-plastic and failure states of stress (see figure 3-5).

3.2.4 The range of shear strain

Soil is assumed to be linear elastic, providing the shear strain is less than 10^{-5} (Ishihara, 1996). The shear modulus is, therefore, a key parameter to properly model the stress–strain behaviour of soil. However, based on experimental tests carried out by, (Okur and Ansal, 2007), some energy dissipates during cyclic loading which implies hysteresis. This fact is neglected in the linear elastic analytical approach. If the magnitude of the induced amplitude of cyclic shear strain is between 10^{-5} and 10^{-2}, the soil behaviour will be elasto-plastic. The shear modulus decreases as the shear strain increases and energy dissipation occurs during the cyclic loading. The damping ratio represents the energy absorbing capacity of soils at this stage. Within this range of shear strain, the shear modulus and damping ratio are functions of the shear strain and independent of the progression of cycles (visco-elastic model). For shear strains exceeding 10^{-2}, the mechanical soil properties such as the shear modulus and damping ratio change with both the shear strain and the progression of cycles. The current methods to achieve the stress–strain response of soil in this range of the shear strain are based on a numerical procedure involving step-by-step integration techniques (i.e. non-linear plastic method). Most of these techniques couple

a backbone curve (also called skeleton curve) with a series of constitutive laws such as a hyperbolic constitutive model. Consequently, the stress-strain relations can be specified at each step of loading, unloading, and reloading phases Ishihara (1996).

Shear Strain	10^{-5}		10^{-2} $>10^{-2}$
	Small Strain	Medium Strain	Failure Strain
Elastic			
Elasto-plastic			
Failure			
Model	Linear elastic	Elasto-plastic Visco-elastic (for dynamic loading)	Non-linear plastic

Figure 3-5 the typical range of shear strains for different soil models (after Ishihara, 1996).

3.2.5 The input earthquake motion

The amplitude and frequency of a dynamic load has a significant effect on the seismic macro mechanical behaviour of granular sand (e.g. Amin, 1976). To import the earthquake motion to the model, an acceleration time-history of a specific earthquake is applied to the base of the model. However, the seismic site responses vary. Thus, an acceleration time-history of a specific earthquake cannot be applied to other sites. Instead a simplified periodic sinuous function with different amplitude are generally considered e.g. (El Shamy and Denissen, 2010). However, due to high computational cost of DEM simulations only a single sine impulse is considered in this research. Marketos and O'Sullivan (2013) and O'Donovan et al. (2012) studied the seismic shear wave propagation through idealized sand using DEM by applying a single period sine load. To find the typical frequencies and amplitudes for this ideal input motion, the lower and higher bound of amplitude and frequency within a strong ground motion is required. For this purpose, the frequency content of a series of well-known earthquake extracted by applying Discrete Fourier Transfer (DFT) is required. DFT is able to extract the amplitude and frequency contents of earthquake signals.

The acceleration time-history of ten well-known earthquakes along with their frequency contents obtained from open source website “Seismo signal” are shown in Appendix 1. The figures show that the maximum amplitudes of earthquake seismic waves is between the frequency range 1 to 6 [Hz] approximately. Also, the lower and higher bound of Fourier acceleration amplitudes within this range is between 0.03 [m/s^2] and 0.5 [m/s^2] approximately. The average duration of earthquakes is 40 [sec] with most of the shaking more likely in the first 10 [sec].

3.2.6 Impedance ratio

In reality, the seismic waves travel within different soil layers. When the incident seismic waves approach to the boundary of two layers, depending on the material properties of these layers such as density and Elastic modulus, whole or part of the seismic energy will reflect or transmit to the immediate neighbouring media (see figure 3-6). Impedance ratio, α, adjusts the effect of incident seismic energy at the interface of two different materials. By definition, Impedance ratio is:

$$\alpha = \frac{\rho_B V_B}{\rho_A V_A} \qquad 3.6$$

where ρ and V are the bulk density and wave velocity propagation (P or S) for the two media. Table 3-1 shows the effect of various Impedance ratios on the displacement amplitude of transmitted and reflected waves. It is to be noted that this material is taken from (Aki, 1980).

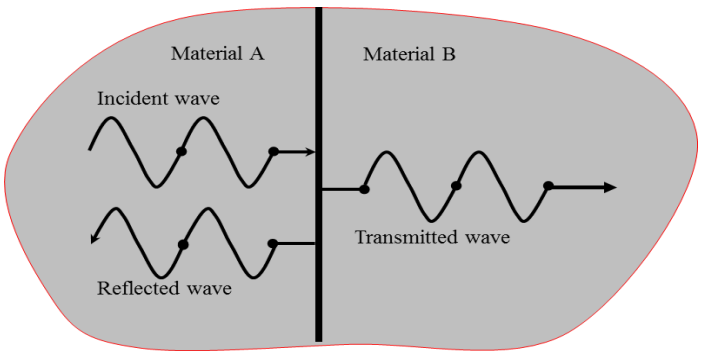

Figure 3-6 The reaction of incident wave at the interface

Impedance ratio (α)	Acceleration, Velocity or Displacement amplitude		
	Incident wave	Reflected wave	Transmitted wave
0	A	A	2A
1	A	0	A
∞	A	-A	0

Table 3:1 The effect of Impedance ratio on the displacement amplitude of reflected and transmitted waves

α=0 implies that the incident wave reaches to the free surface. At this state, the wave will reflect with the same amplitude of incident wave and transmit with two times bigger than the amplitude of incident wave. α=1 means the material A and B are the same. That is, the incident wave will fully transmit into material B without any reflection taking place at the boundary. α=∞ shows that incident wave meets solid material. At this point, the wave will fully reflect back to the media but with opposite sign of incident wave. For a 2D element of sand at depth, α=1 for all four boundaries.

3.2.7 Dynamic boundary

It is assumed that all seismic energy will decay at infinity. Due to the complicated geometries of soil media and the excited zone encountered in reality, it is unlikely to find the close form solutions for wave propagation phenomenon for such an infinite system. For this purpose, numerical methods such as the finite element method (FEM) are used (e.g. Anandarajah et al., 1995, Guéguen et al., 2000, Lysmer, 1969, Semblat, 2009, Wolf and Song, 1996) and the boundary element method (BEM) (e.g. Aubry and Clouteau, 1991, Bonnet, 1999, Dangla, 1988). However, as a finite number of nodal points can be defined for these methods and, in situ, faults are kilometres from the geotechnical application zones of interest, the numerical methods are not directly appropriate for infinite systems (Lysmer, 1969). Therefore, an infinite half-space should be approximated to a finite half-space. A special dynamic boundary condition (called viscous boundary or absorb boundary) is superimposed to the boundary of the model to model this (White et al., 1977, Lysmer, 1969).

Consider Figure 3-7. This figure displays two different boundaries: an imaginary infinity boundary (i.e. green dash lines), where it encloses all excited zones. Dynamic boundaries (i.e. blue dash lines) used to reduce the dimensions and discretization of space in order to study it within an infinity space. The boundary condition applied at viscous boundary should absorb t the P and S waves so that no energy reflection takes place at the boundary. That is, when the seismic energy arrives at the viscous boundary it is assumed that it fully travels onto infinity. By applying the following normal and shear stresses to each node along that boundary, the arrival seismic waves will fully travel into infinity without reflection waves:

$$\sigma_{lateral} = \alpha * \rho * V_P * \dot{x}$$

$$\tau_{lateral} = \alpha * \rho * V_S * \dot{y} \qquad 3.7$$

where α, ρ, V_P, V_S, $\dot{x}$ and $\dot{y}$ are impedance ratio, bulk density, primary wave velocity, shear wave velocity and nodal velocity in the normal and shear directions. α will be set to 1.0 if the material properties within the interior finite half-space and exterior zone are the same.

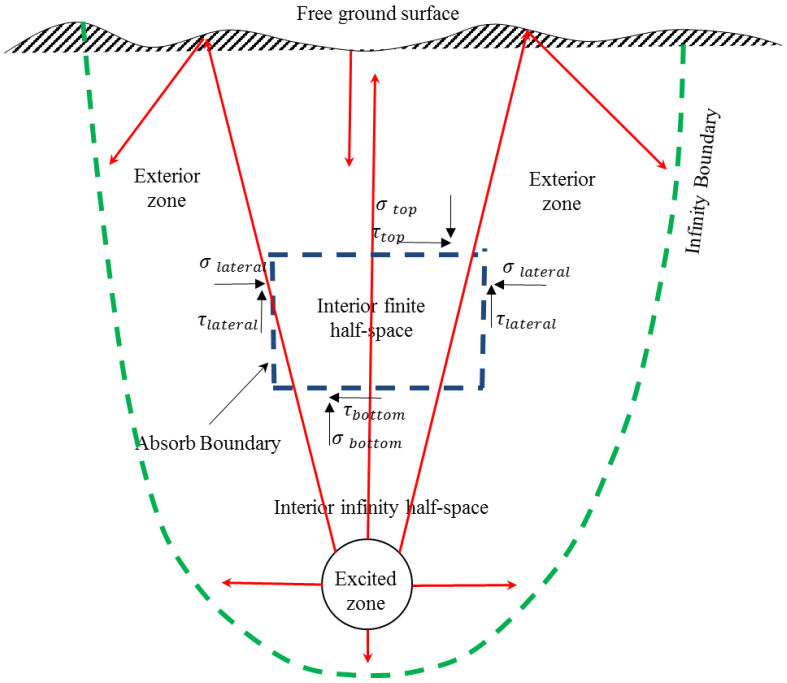

Figure 3-7 Schematic infinite and finite half-space

Since a finite half-space is considered, the excited seismic zone cannot be taken into account within this zone. To consider the effect of the excitation zone to the model being considered, an input motion (e.g. velocity-time history) should be applied at the base of the model. For this purpose, an appropriate dynamic boundary must be employed at the base of model to consider both the imaginary infinite media below the model and the input motion. Such boundary is able to absorb the reflecting waves (Joyner and Chen, 1975, Itasca, 2008, Zamani and El Shamy, 2011). The following normal and shear stresses are applied to each node of the base dynamic boundary to remove reflected energy:

$$\sigma_{bottom} = \alpha * \rho * V_P * (2 * \dot{U}_y - \dot{y})$$

$$\tau_{bottom} = \alpha * \rho * V_S * (2 * \dot{U}_x - \dot{x}) \qquad 3.8$$

where $\dot{U}_x$ and $\dot{U}_y$ are the input velocity-time history in horizontal and vertical directions. If the top boundary is ground surface, the dynamic stresses are zero because α is zero. If the top boundary is placed at depth, the impedance ratio will be between 0 and 1. These boundary conditions are applicable for linear and non-linear systems (Joyner and Chen, 1975). These conditions

correspond to a situation where the finite media boundary is supported on dashpots oriented in normal and tangential directions to provide viscous tractions that remove all or part of the energy of the propagating wave at the boundary (see figure 3-8).

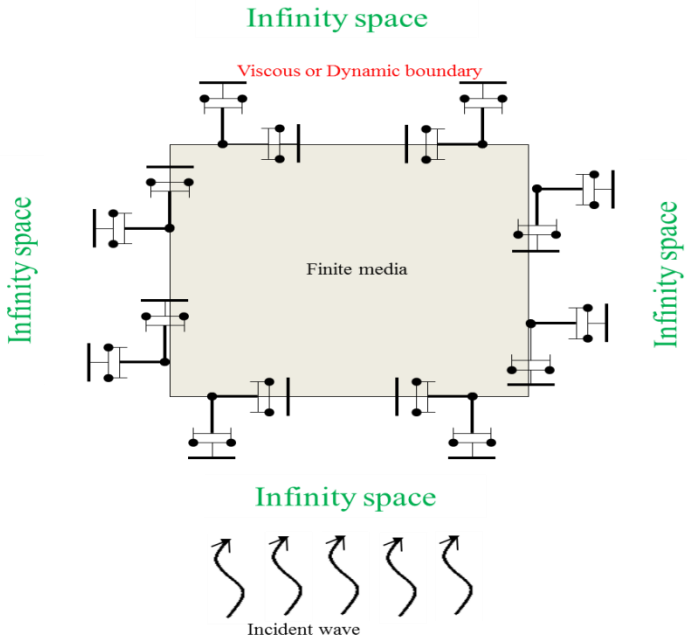

Figure 3-8 a schematic of dynamic boundary by applying normal and shear viscous damping on the finite media

3.2.8 Seismic behaviour of pile

Piled foundations in seismic hazardous regions are damaged by earthquakes because of the effect of seismic loads on the soil-pile interaction (Zafeirakos et al., 2011, Zhang and Zhang, 2009, Zhang, 2008, Zhang and Zhang, 2006, Cheung and Lee, 1991, Kucukarslan et al., 2003, Novak and Nogami, 1977, Mylonakis et al., 1997a, Mylonakis and Gazetas, 2000, Mylonakis and Gazetas, 1999, Gazetas and Mylonakis, 1998, Makris and Gazetas, 1992) and the development of sand particles' instability adjacent to the pile. This interaction is affected by the volume changes in the soil (Wolf, 1985). The pile capacity is formed of the interface friction and end bearing capacity. Therefore, the pile capacity due to the interface friction capacity (Poulos and Davis, 1980) alters. This fact fails to be addressed by continuum mechanics. Since interface friction capacity is a function of the interaction between individual soil particles and the pile as well as particles' stability the discrete

element method of analysis is considered to be the most appropriate method. This research focuses on the interface friction and particles' stability because the visual evidence suggests that a seismic load has a dramatic effect on the volume of the soil adjacent to a pile.

3.2.9 Literature review of earthquake wave propagation through sand using DEM

DEM has been proved to be a tool to study the quasi-static behaviour of granular sand at the micro and macro scale. The use of DEM for dynamic problems in geotechnical earthquake engineering is restricted to a small number of published works (e.g. O'Donovan et al., 2012, Marketos and O'Sullivan, 2013, Zamani and El Shamy, 2011, El Shamy and Zamani, 2012, Zamani and El Shamy, 2012, El Shamy and Denissen, 2010, Hazzard et al., 1998, Toomey and Bean, 2000). The aim of this section is to examine the advantages and disadvantages of DEM models employed by them in order to develop a novel DEM code.

The early work of applying DEM for seismic wave propagation is that of Hazzard et al. (1998). They investigated the acoustic emission produced when failure occurs in a hexagonal lattice rock medium during an earthquake. However, this experience is of interest in the area of dynamic rock mechanics failure. The post seismic behaviour of rock mass after breaking the bond between discrete particles was also studied in this work.

Toomey and Bean (2000) studied the dispersive properties of granular systems during seismic wave propagation. For this purpose, a lattice of uniformly bonded particles was created. This model was then vertically excited by applying a single periodic load to propagate a seismic primary wave. They derived an important relationship relating angular frequency to the wave number for lattice packing with contact linear stiffness. This equation is:

$$\omega = 2\sqrt{\frac{K_n}{m}}\sin\left(\frac{k*r}{2}\right) \;\; ; \; k = \frac{2\pi}{\lambda} \;\; ; \lambda = V_P * \mathrm{T} \Longrightarrow \; V_P = \frac{\omega}{k} \qquad 3.9$$

where ω, K_n, m, k, r, λ, V_P and T are angular velocity, normal contact stiffness, particle mass, wave number, mean particle diameter of system, wavelength, P-wave speed and period of loading. Figure 3-9 shows the relationship between angular frequency and wave number.

Based on this figure, if the wavelength is much larger than the mean particle size the dispersion becomes practically undetectable (i.e. waveform cannot be changed within the particulate system). For shorter wavelengths, the waveform begins to be affected by discrete particles. That is, the wave is being dispersed during wave propagation. This leads to the conclusion that for those wavelengths that are much larger than mean particle diameter of a granular system, the wave propagation through them can be assumed to be similar to that in a continuous elastic medium.

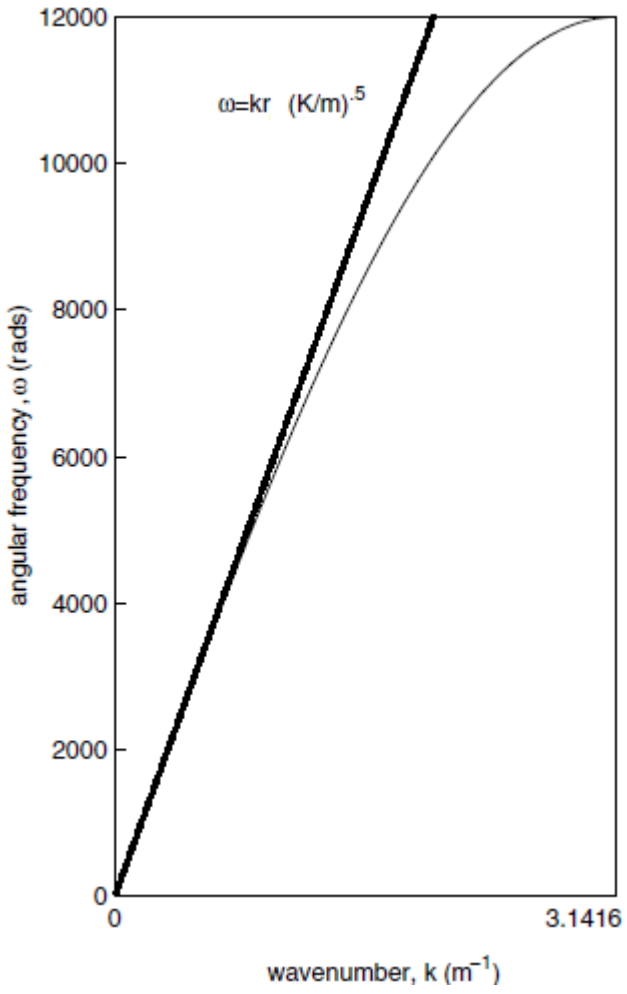

Figure 3-9 Investigation of dispersion phenomena by drawing a relationship between angular frequency and wavenumber (after Toomey and Bean (2000))

(O'Donovan et al., 2012) studied seismic S-waves propagation within an idealized frictional uniformly-radius sized disks 0.0029 [m] in a hexagonal packing using a series of *PFC*^{2D} simulations. They applied the idea of bender element test, originally proposed by (Shirley and Hampton, 1978) used in experimental soil mechanics such as standard triaxial tests to measure the P and S wave velocities and small strain shear modulus of soil (e.g. Kuwano and Jardine, 2002), for their DEM simulations. It is to be noted that a bender element is made of a small piezoceramic plate and can generate ultrasonic waves when a signal is sent through it. Pairs of these bender elements are inserted at the centre of the bottom and top of soil DEM model as a transmitter and receiver of a signal wave. The lateral boundaries applied in this work were static membrane particles to maintain constant confining pressure on them during the wave propagation simulation. It is done by applying an external force to each membrane particle. The algorithm of applying external force is based on the work proposed by (Cheung and O'Sullivan, 2008). The top and bottom boundaries were rigid walls according to this algorithm (see figure 3-10).

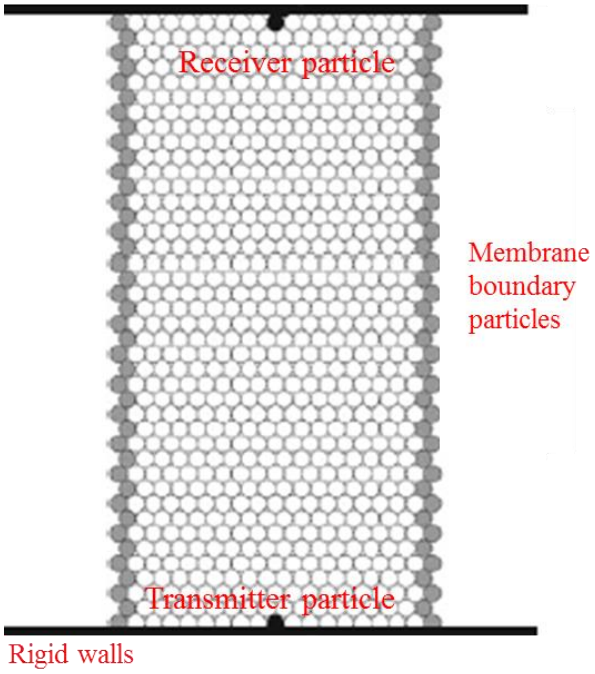

Figure 3-10 the DEM model used by O'Donovan et al., (2012) and Marketos and O'Sullivan, (2013) to simulate bender element test.

It is to be noted that the algorithm of membrane particles proposed by Cheung and O'Sullivan, (2008) was originally created to simulate membrane latex in a biaxial test. Connectivity between membrane boundary particles was not considered in this algorithm. That is, a number of the membrane particles are unlikely to be in contact with its immediate membrane particles, while the membrane latex in standard triaxial test is continuus. Thus, the use of this algorithm for seismic research is restricted to hexagonal packs. Another limitation of this code is that once one of the membrane particles loses its contact with its immediate membrane boundary particles as the boundary is deflected, it is removed and a new particle with the same material properties and size is inserted into the membrane boundary. The place of this new particle in the membrane is the place of the deleted particle which was already in contact with other membrane particles before losing its contact. Removing a boundary particle from a dynamic system leads to chaos in the average un-balanced system of forces being considered. This chaos propagates through the model within a number of time steps and the current particles velocities will be changed. Thus, the amplitude of periodic load applied to the base of this model should be very small to prevent this issue. However, the use of membrane boundary particles in this work leads to a reduction in the impedance mismatch between the particles and the deformable boundary particles because of the forces applied to the boundary particles. Since there is no restriction applied to membrane particles adjacent to a rigid wall, they can move more freely. That is, more energy is absorbed at the deformable boundaries. This leads to a reduction of reflecting waves through the deformable boundaries. Applying rigid walls at the top and bottom of the model results a large impedance mismatch between rigid boundaries and the particulate system. Therefore, the whole of the energy wave is reflected back into the system. This shows that the use of rigid walls boundaries to simulate the wave propagation with DEM results in reflection of energy to the sample being considered. Therefore the seismic responses obtained by this condition should be used with caution.

The input seismic energy to the system which was applied to the transmitter particles was a horizontal pulse sinuous displacement with amplitude 1.25

(μm) with frequencies between 4 and 12 [kHz]. Due to this perturbation, the seismic waves including P and S waves that propagated through the sample and were measured at the receiver particle. The propagation of the wave in this work was tracked by demonstrating both the particle velocities and the mean normal and shear particle stresses at different times.

In spite of applying this idealized hexagonal pack, the response of the system was in good agreement with lab data. The results show that under small seismic perturbations in shear direction, no change in contact configuration of hexagonal pack took place. That is, the material seems to be elastic as plasticity is related to contact breakage and sliding. Thus, the system being considered is fully homogeneous with lattice packing such that the contact force network is homogeneous. This is in contrast with soil packing configuration in reality where the size of particles varies, chains force are highly inhomogeneous and contact can break and slide in the course of loading. Additionally, the effect of dynamic boundary is not applied in this work to artificially consider the presence of infinity media.

Marketos and O'Sullivan, (2013) created the stiffness and mass matrices of a un-damped granular sand from *PFC^{2D}* data to compute its vibration modes, natural frequencies and transfer function. The DEM assumption applied for this work is the same as that of O'Donovan et al., (2012). However, the input frequancy was 40 [kHz]. Marketos and O'Sullivan, (2013) said "*Consideration is restricted here to a very simple system, that of a two-dimensional damped crystalline assembly of dry, uniformly sized grains. The conclusion drawn here are likely to be applicable to more random and three-dimensional packings; confirmation this requires future development of a more sophisticated model."*

The results show that applying pure shear wave force at the transmitter particle results in both horizontal and vertical motion of the receiver particle. That is, applying pure shear wave propagates P-wave and S-wave within a sample. They said the reason of this is a combination of the granular packing and boundary conditions. Since the transmitter particle was excited, and because the contacts with the next row of particles were at angles of 60° and

120° these were forced to move vertically as well as horizontally. This was also observed by O'Donovan et al., (2012). The effect of different boundary conditions such as full rigid boundaries and mixed rigid top and bottom boundaries and lateral membrane boundary particles during a pure shear pulse excitation on the particles motions were also studied. It was seen that rigid walls leads to fully reflect the wave and increase the amplitude of receiver displacement. Changing the input frequency from 4 [kHz] to 40 [kHz] caused a big difference in the received signal shape at the receiver particle. An interesting result obtained from this work is that the minimum natural frequancy of granular sand is inversely proportional to the number of particles at the base of the model, while the maximun natural frequency of granular sand increases by increasing the number of particles at the base of the model.

El Shamy and Denissen (2010) investigated liquefaction phenomena using a series of DEM simulations. They monitored the energy components of saturated sand including friction, viscous damping, kinetic, strain, and drag energies during a periodic loading. It was found that at the onset of liquefaction, the loss of energy increased remarkably. They increased the vertical gravitational acceleration to 25 to reduce the dimensions of the model and cost of simulation significantly. That is, the dimensions and time scales in the computational model declines by a factor of 25 while the acceleration amplitude and frequency of the seismic motion in the simulations will be 25 times larger than those of the prototype. However, increase in gravity acceleration leads in increase the weight of individual particles and its inertial force. Increase in the weight of particles results in increase in the initial overlap between contacting particles before applying dynamic loading. Thus, to move the particle from its static equilibrium position during earthquake excitation more displacement is required. Additionally, an increase in the initial value of overlap between contacting particles increases the contact forces between the particles forming the granular system. Thus, the initial condition of the system will be completely different from the real one. Thus, the results at the prototype scale cannot be simply obtained by multiplying the results obtained from the model by a factor of 25. The initial fabric

condition plays an important role on the response of the granular system. As will be seen in section 3.3, the fabric quantities are dependent on the geometry of contact points. The geometry of contact points will be different for a model with an applied gravitational acceleration of -9.81 [m/s^2] and a model with an applied gravitational acceleration of -25g [m/s^2].

In terms of boundary conditions, periodic boundaries were used to simulate a semi-infinite media in the two lateral directions in this work. The top of the model was the ground surface and the base of the model was rigid wall (see figure 3-11a). The use of periodic boundaries has the following effect on the physics of wave propagation. When a seismic wave reaches to the lateral boundary, it does not reflect but it also does not transmit to the infinite media. Rather, a wave with the same properties enters to the system from the adjacent virtual system on the opposite side. When this boundary condition is applied, the expansion of model during loading cannot be take place because the dimension of periodic space is already set to a constant value. When the system expands, the displacement of boundary particles may exceed the set periodic space. At this stage, those boundary particles will be removed automatically and the same particle enters to the system from the adjacent virtual system on the opposite side. This leads to change in the normal shear force distribution on the boundary. It will be seen further any unexpected changes in boundary particles result in change in the average un-balanced force system. That means the significant and permanent chaos in un-balanced forces and particles velocities will be take place. Thus, the magnitude of periodic load imported to the base of system should be small enough to prevent a boundary particles flying over the periodic boundary.

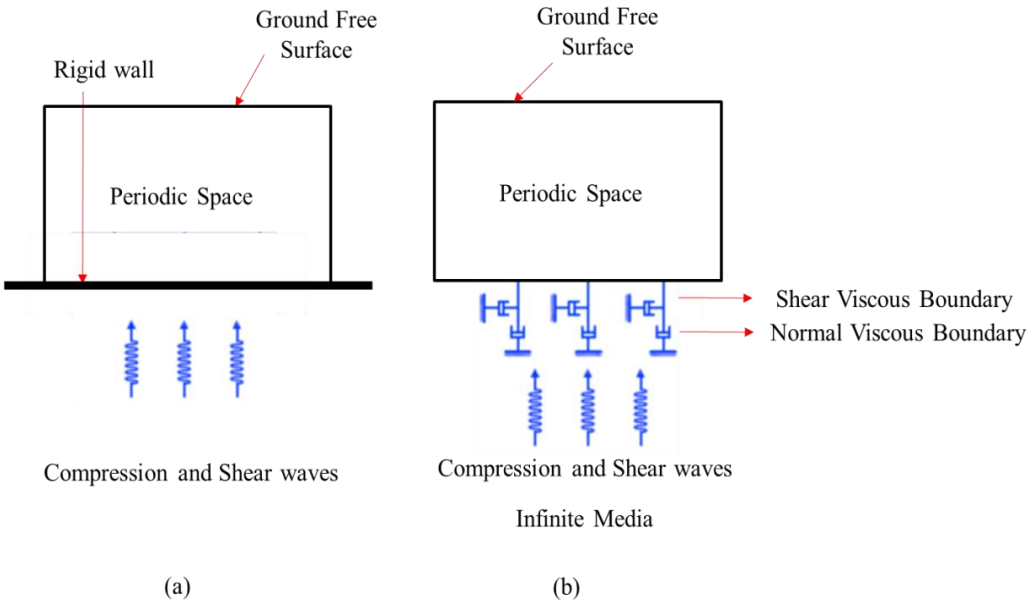

Figure 3-11 The boundary condition used by Zamani and El Shamy (2011), El Shamy and Denissen (2010) and Zamani and El Shamy (2012).

Zamani and El Shamy (2011) studied earthquake seismic wave propagation through the dry granular soil using *PFC*^{3D} qualitatively. The same conditions applied by El Shamy and Denissen (2010) were used for this work. Three types of base conditions were studied in this work to investigate the effects of base material on the macroscopic behaviour of system: rigd bedrock, elastic bedrock and infinite base (see figures 3-11a and 3-11b). It was seen that applying a rigid base condition results in amplification in particle acceleration though the sample, while applying infinite base boundary condition does not cause the amplification in particle acceleration through the sample. However, the amplification in particle acceleration through the sample due to an elastic base boundary condition produces amplification but it is significantly lower than those introduced by a rigid base.

Zamani and El Shamy (2012) studied seismic response of dry soil-shallow foundation interaction using *PFC*^{3D} qualitatively. The same conditions applied by El Shamy and Denissen (2010) were used for this work. The results showed that DEM can be used to study the complex seismic soil-structure interaction problems.

3.3 The analysis of fabric of sand

3.3.1 Introduction

Particles are in static equilibrium until an earthquake occurs. A drift in displacement of any particle having one or more contacts about its equilibrium position during earthquake loading induces additional normal and shear contact forces at each contact point (called additional normal and shear dynamic contact forces) at each time step. These new contact forces generate an additional un-balanced force for each particle. This results in accelerating the particles. Depending on the magnitude of this acceleration at each time step, the fabric quantities change. These alterations may result in lost contacts or new contacts between particles. The energy applied to a granular system is lost as particles move a collide. Sand is considered as a collection of frictional discrete particles in which each particle has its own morphology and contact stiffness. The static and dynamic macro-mechanical behaviour of such granular material is influenced by its fabric evolution (e.g. contact configuration). Studying the fabric evolution of a sand assembly during the seismic loading with and without a pile element opens a new window to advance our understanding on the responses of sand element. It is because, the boundary excitation propagates through the contact network.

However, analysing the sand fabric and its effect on the macro-micro mechanical stress-strain behaviour of the element whether the element is subjected to static or dynamic loading by means of experimental tests or analytical methods is difficult (Luo, 2012, Yimsiri and Soga, 2010, Rothenburg and Bathurst, 1989).

Alternatively, *DEM*-based simulations can provide the particle-level information such as particle movements and rotations, contact forces, contact directions, particle velocities, average coordination, porosity, relative density, specific volume and particle size distribution. Thus, this method can be used to study the evolution of sand fabric under seismic loading with or without the presence of a pile. Although, many efforts have been made to describe the fabric and macro-mechanical behaviour of sand under monotonic and quasi-static cyclic loading using *DEM* such as (Luo, 2012, O'Sullivan et al., 2008,

Sitharam, 2003, Soroush and Ferdowsi, 2011, Belheine et al., 2009, Sazzad and Suzuki, 2010, Iwashita and Oda, 1998, Rothenburg and Kruyt, 2004, Thornton and Zhang, 2003, Mahmood and Iwashita, 2010, Yimsiri and Soga, 2010, O'Sullivan and Cui, 2009, Cui et al., 2007, Cheung and O'Sullivan, 2008, Yan and Zhang, 2013), no study has been carried out to examine the evolution of sand assembly fabric under seismic loading and no evaluation of the evolution of sand assembly fabric in presence of a pile under seismic loading.

3.3.2 The history of studying sand fabric

The early works related to the study of sand fabric was by (Arthur and Menzies, 1972, Miura et al., 1986, Oda, 1972). In these works, the fabric evolution and its effect on the macro-mechanical behaviour of sand subjected to static load were experimentally studied. Monitoring the evolution of contact configuration at different stages of loading process is, however, difficult to observe. Optical technology such as X-ray diffraction and electronic measurement techniques was used by a number of researchers (e.g. Lee et al., 1992, Hasan and Alshibli, 2010) to study the evolution of granular materials for quantitative and qualitative studies (Ng, 2001). However, the experimental methods are time consuming and difficult to apply. Thus, an alternative method is required to quantitatively and qualitatively study the fabric of sand.

Void ratio, porosity and specific volume are fabric quantities (Brewer, 1964) in classical soil mechanics. The overall response of sand subjected to loading in *DEM* simulations can be partly estimated by void ratio and the mean effective stress of the specimen (Lamb and Whitman, 1969). However, such fabric descriptors used to quantify the packing density of the granular materials cannot explicitly describe the internal structure of granular materials during loading. Therefore, a micro-mechanical study should be conducted to examine sand fabric, including contact configuration, contact force configuration, using the microscopic quantities.

The analysis of sand fabric is generally performed by micro-mechanics. Micro-mechanics is a field of geo-mechanics trying to statistically interpret the

fabric of granular materials and study the macro-mechanical behaviour of granular materials by applying a number of fabric quantities. The use of fabric quantities, however, is needed to extract particle-level information such as particle movements and rotations, contact forces, contact directions and number of contacts per particle. These data are obtained from *DEM* simulations.

3.3.3 Average coordination number

One of the key microscopic parameters, which are defined at particle-level, is the average coordination number. This parameter is the average number of contacts per particle within a specific volume of a particulate assembly and consequently it provides a measure of packing density or packing intensity of fabric at particle-level. For a specific volume of particulate assembly with N_p particles and total number of contacts, N_c, the simplest definition of average coordination number C_n is given by:

$$C_n = \frac{2N_c}{N_p} \qquad 3.10$$

Since each contact is shared between two particles, the actual number of contacts is multiplied by 2. From the micro-mechanical stability perspective, the stability and equilibrium of each particle within a particulate system is dependent on its coordination number and arrangement of contact points. Therefore, as outlined by (Thornton, 2000) and (Kuhn, 1999) only active contacts should be considered for calculating the average coordination number. (Maeda, 2009, Rothenburg and Kruyt, 2004) have shown that average coordination number should be at least three for each disk when a granular system is in quasi-static equilibrium. However, this average fabric quantity cannot show how contact points are distributed. Thus, a number of tensor quantities are needed to statistically describe the orientation of contacts and contact force during loading.

3.3.4 Contact normal distribution

An early study on contact normal distribution and contact force distribution for an idealized particulate system during loading was by (Dantu, 1957). Photo-elasticity was used. The distribution of both normal contact orientations and

normal contact forces was monitored during these tests. Clear biases in orientation of contacts during loading were noted. (Oda, 1972), using drained triaxial test on resin-impregnated samples of sand, showed that soil strength and stiffness was highly anisotropic because the number of contacts in the direction of major principle stress axis was higher than those in the direction of the minor axis. Thus, the re-arrangement of particles during loading from an isotropic state to an anisotropic state leads to "*anisotropy of contact orientation*" or "*fabric anisotropy*" in a granular system. (Oda et al., 1980) showed that the extent of this anisotropy can be found by studying the standard deviation of each particle coordination number at different time of triaxial test. However, this approach is time-consuming to apply.

Since the contact normal and contact force are simply extracted from *DEM* outputs at any time-step, the study of fabric anisotropy, including average normal contact distribution, average normal contact force distribution and average shear contact force distribution, by using DEM outputs is possible. These fabric quantities can be shown either in tensorial form or in polar diagram form. The "polar diagram" is often used by those working with DEM.

The contact normal, n^c, is the unit normal vector at a contact point between two particles (see figure 3-12a). The vector connecting the centroid of two particles is called the branch vector or contact vector. However, for circular particles in contact, the branch vector coincides with the line connecting the centres of the two particles (see figure 3-12b).

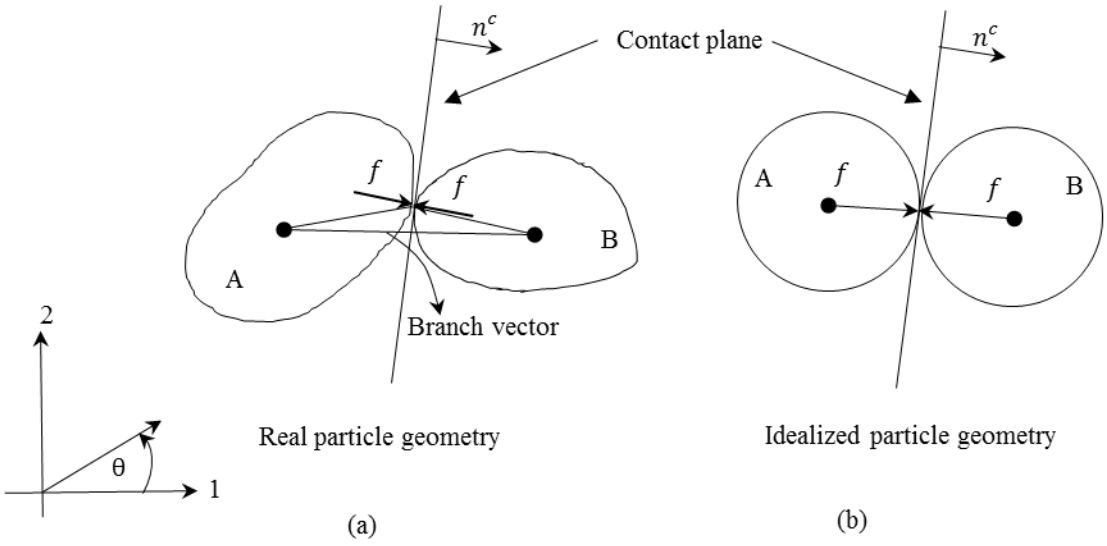

Figure 3-12 Defining contact normal vector for real and circular particles

To show the statistical distribution of contact normal vectors within a representative volume element (*RVE*) (see figure 2-7) (see figure 3-13) the direction of each unit normal vector is plotted in the form of a polar diagram using an angular interval to define the range of direction θ).

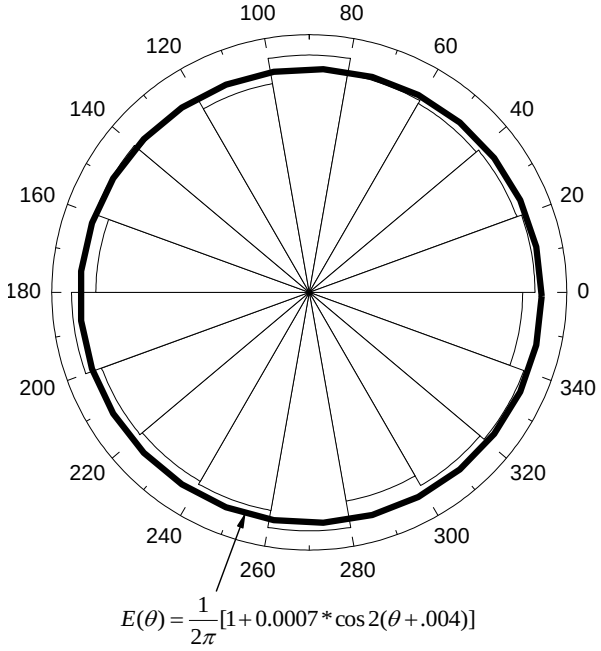

Figure 3-13 Polar diagram of normal contact distribution along with approximate continuous function

Increasing the number of particles within a *RVE* produces a smoother polar diagram. As a result, the polar diagram can be estimated with a continuous function $E(\theta)$ (i.e. probability distribution function of unit normal vectors for disk assemblies). (Rothenburg, 1980) proposed a closed form solution to estimate the normal contact distribution histogram. The key feature of this function is that $E(\theta) = E(\theta + \pi)$:

$$E(\theta) = \frac{1}{2\pi}[1 + a\cos 2(\theta - \theta_a)] \qquad 3.11$$

Where a represents a "*geometrical anisotropy*" in a granular system, depending on the number and density of unit normal vectors in principles axes. For example, if $a = 0$, $E(\theta)$ will be a circle such that the state of the system being considered is in an isotropic state. $\theta_a\ is$ the direction of aanisotropy. Parameters, $a\ and\ \theta_a$, are obtained by the following equations:

$$a = \frac{2\sin\Delta\theta}{N\Delta\theta}\sqrt{\left[\sum_{g=1}^{n_g} N_g \sin\big((2g-1)\Delta\theta\big]\right.^2 + \left[\sum_{g=1}^{n_g} N_g \cos((2g-1)\Delta\theta\right]^2} \qquad 3.12$$

$$\theta_a = \frac{1}{2}\tan^{-1}\frac{\sum_{g=1}^{n_g} N_g \sin((2g-1)\Delta\theta}{\sum_{g=1}^{n_g} N_g \cos((2g-1)\Delta\theta}$$

where N is the total number of contact. $\Delta\theta = \frac{360}{n_g}$, n_g the number of segments and N_g is the number of contacts within the g^{th} segment. It is seen that $a\ and\ \theta_a$ obtained from Eq. 3.12 are $\Delta\theta$-dependent such that changing the value of angular interval results in changing these parameters. In fact, these fabric anisotropy parameters show the ability of granular systems to create the anisotropy state in normal contact distribution and normal force distribution quantities. There are a number of *DEM* studies which have examined the influence of anisotropy of contact orientation on the macro-mechanical sand. More recently (Sazzad and Suzuki, 2010, Yimsiri and Soga, 2010, Mahmood and Iwashita, 2010) using monotonic and cyclic *2D* biaxial and *3D* triaxial *DEM* simulations showed that the initial fabric and

preferential or induced fabric plays an important role on the overall macro-mechanical behaviour of sand.

3.3.5 Contact force distribution

Parameters $a\ and\ \theta_a$ can statistically show the deviation between the unit normal vector at any step during loading and that for an isotropic arrangement of the particles. The same idea can be used to draw the polar diagram of contact force distribution, which shows the deviation between the geometry of contact force distribution at any step during loading and the isotropic geometrical contact force distribution of a granular system. Contact forces can be expressed as average normal forces, $\bar{f}_n^c(\theta)$, and average tangential forces, $\bar{f}_t^c(\theta)$.

The distribution function of average normal contact force, $\bar{f}_n^c(\theta)$, and tangential forces, $\bar{f}_t^c(\theta)$ was initially proposed by (Rothenburg, 1980) for disk particles.

As the normal force component is perpendicular to the contact plane (see figure 3-12), the form of probability distribution function of average normal contact force is the same as “normal contact distribution” equation:

$$\bar{f}_n^c(\theta) = \bar{f}_0^c[1 + a_n \cos 2(\theta - \theta_n)] \qquad 3.13$$

where a_n is the normal contact force anisotropy. θ_n is a direction of the normal contact force anisotropy. The same method used to compute the contact normal distribution is used here to specify a_n and θ_n:

$$\bar{f}_0^c = \frac{1}{2\pi}\sum_{g=1}^{n_g} f_n^c(g)\Delta\theta$$

$$a_n \sin 2\theta_n = \frac{1}{\pi \bar{f}_0^c}\sum_{g=1}^{n_g} f_n^c(g)\sin((2g-1)\Delta\theta)\Delta\theta$$

$$a_n \cos 2\theta_n = \frac{1}{\pi \bar{f}_0^c}\sum_{g=1}^{n_g} f_n^c\,(g)\cos((2g-1)\Delta\theta)\Delta\theta \qquad 3.14$$

$$f_n^c(g) = \sum_{i=1}^{nc_g} f_n^{c_i}$$

where nc_g and $f_n^{c_i}$ are the number of contacts within g^{th} segment and the normal contact force of i^{th} contact from g^{th} segment respectively. If $a_n = 0$, $\bar{f}_n^c(\theta) = \bar{f}_0^c$. That is, if the deviation of contact forces from average value of contact forces is small, the system is likely to be isotropic (O'Sullivan, 2011).

The distribution function of average shear contact force is defined as follows:

$$\bar{f}_t^c(\theta) = -\bar{f}_0^c[a_t \sin 2(\theta - \theta_t)] \qquad 3.15$$

where a_t and θ_t are the magnitude of shear contact force anisotropy and the direction of the shear contact force anisotropy respectively which are obtained by the following equation:

$$a_t \sin 2\theta_t = \frac{1}{\pi \bar{f}_0^c}\sum_{g=1}^{n_g} f_t^c(g)\sin((2g-1)\Delta\theta)\Delta\theta$$

$$a_t \cos 2\theta_t = \frac{1}{\pi \bar{f}_0^c}\sum_{g=1}^{n_g} f_t^c\,(g)\cos\big((2g-1)\Delta\theta\big)\Delta\theta \qquad 3.16$$

$$f_t^c(g) = \sum_{i=1}^{nc_g} f_t^{c_i}$$

where $f_t^{c_i}$ is the shear contact force of i^{th} contact from g^{th} segment. (Kruyt, 2003), by comparing the results obtained from DEM biaxial tests on two separate samples, where one of them was filled with 1000 particles and other filled by 20000 particles, showed that increasing the number of particles produces results which are similar to those from continuum analysis. This fact was also proved by (Momeni et al., 2012, Rothenburg, 1980) who implemented a series of sensitivity *DEM* biaxial tests. Thus, an increase in the number of particles within a *RVE* (i.e. applying particles with finer size) results in $E(\theta)$, $\bar{f}_n^c(\theta)$ and $\bar{f}_t^c(\theta)$ become smoother. It also leads to the estimated average stress and strain tensors within a *RVE* become more representative of the average stress for the whole sample provided each particle has at least three contact points.

3.3.6 Sand particle morphology

Particle morphology (e.g. shape and surface roughness) is one of the fabric quantities, and has a significant effect on the fabric and subsequently on the macro-mechanical behaviour of particulate system (Iwashita and Oda, 1998, Sazzad and Suzuki, 2010, Oda et al., 1985, O'Sullivan et al., 2002, O'Sullivan, 2011, O'Sullivan, 2012, Mitchell and Soga, 2005).

In terms of particle roughness, (Iwashita and Oda, 1998) using *DEM* biaxial simulations showed that particle roughness has a significant effect on the fabric and macro-mechanical behaviour of disk sand assemblies. It is because the effect of rolling resistance is considered for the dynamic equilibrium of each particle ($I\ddot{\theta} + C\dot{\theta} + \sum K_\theta \theta = M$). $I, C, K_\theta, \theta \; and \; M$ are particle moment of inertia, damping ratio, rolling stiffness of particle, angular displacement of particle and resultant moment. The effect of particle shape on the fabric and macro-mechanical behaviour of granular material was also studied by (Sazzad and Suzuki, 2010). In their work, the macro-mechanical behaviour of sand specimens, with oval roughness shape, was studied by implementing a series of *DEM* biaxial simulations. It was found that the particle rotation, which is due to shear and normal contact force, decreases and subsequently the Young's modulus, peak stress and Poisson's ratio of sand increases.

(O'Sullivan, 2012) showed that if the particle size is larger than 0.1 mm, the surface roughness will have a minor effect on the material behaviour in comparison with the particle inertia. That is, the effect of rolling resistance in the dynamic equilibrium of each particle can be ignored.

3.3.7 Stress-force-fabric relationship

The relationship between fabric quantities and average stress tensor for a system with idealized circular particles was first suggested by (Rothenburg, 1980).

$$\sigma_{xx} = \frac{m_v \bar{l}_0^c \bar{f}_0^c}{2}[1 + \frac{a a_n}{2} + \frac{a + a_n + a_t}{2}\cos 2\theta_a]$$

$$\sigma_{yy} = \frac{m_v \bar{l}_0^c \bar{f}_0^c}{2}[1 + \frac{a a_n}{2} - \frac{a + a_n + a_t}{2}\cos 2\theta_a] \qquad 3.17$$

$$\tau = \frac{m_v \bar{l}_0^c \bar{f}_0^c}{2}[\frac{a + a_n + a_t}{2}\sin 2\theta_a]$$

where $\bar{l}_0^c$ is the mean of particle radius within a *RVE*. m_v is the "average contact density" defined as follows (Rothenburg and Bathurst, 1989):

$$m_v = \frac{2N_c}{V} \qquad 3.18$$

where V is the volume of *RVE*. Other parameters such as a, $\theta_a, a_n, \bar{f}_0^c$ and a_t, are obtained from Eq. 3.12, Eq. 3.14 and Eq. 3.16. t invariants of stress tensor, isotropic stress, s, and internal mobilized friction are:

$$s = \frac{\sigma_{xx} + \sigma_{yy}}{2} = \frac{m_v \bar{l}_0^c \bar{f}_0^c}{2}\left[1 + \frac{a a_n}{2}\right]$$

$$t = \sigma_{xx} - \sigma_{yy} = \frac{m_v \bar{l}_0^c \bar{f}_0^c}{2}[a + a_n + a_t] \qquad 3.19$$

$$\sin(\theta) = \frac{t}{s} = \frac{\sigma_{xx} - \sigma_{yy}}{\sigma_{xx} + \sigma_{yy}} \cong \frac{[a + a_n + a_t]}{2}$$

Eq. 3.17 and 3.19 shows that the macro-stress tensor components have a direct relationship with fabric quantities such as a, a_n, a_t, θ_a and m_v and inter-

particle forces. These equations also show that the angle of friction, θ, of a granular system depends on how much this system is able to develop anisotropy in its fabric. That is, an increase or decrease in the values of fabric anisotropy parameters result in an increase or decrease in the shear strength parameters of a particulate system. At each time step the required *DEM* outputs are extracted and the fabric quantities computed using Eq. 3.12 to Eq. 3.16. Therefore, monitoring the stress tensor components using this approach increases the time of computation.

However, the fabric quantities addressed above are a collective terms and fails to address the individual particles' instability. As the failure of pile during earthquake is because of individual particles' stability where are adjacent to it, a new fabric quantity is required to investigate at each time step the stability of both each single particle and bulk. This term, called "symmetric geometric deviation index", will be introduced in chapter 4.

3.4 Conclusion

In this chapter, the impact of a seismic event was considered by assessing how a wave propagates through a simulated granular system. Due to the computational time of DEM simulations, the granular media is discretized into small parallelepiped cells or RVEs. DEM simulation is then applied to simulate each cell. Special conditions should be applied for the boundary particles to simulate the effect of infinite media. A literature review of the impact of the boundary conditions on wave propagation in a using continuum was done was used to provide the deformable boundary particles algorithm used in Chapter 6.

A literature review on the phenomena of wave propagation using DEM was done. It was seen that the number of works using DEM for seismic problems was limited. Frequencies higher than those observed in earthquakes and hexagonal pack media rather than random packing were considered. Other works increased the gravity to decrease the time of simulations. However, the boundary conditions applied for these work was also based on the static boundary. Thus, a new algorithm was required to for a boundary in dealing with dynamic problems.

Studying how seismic waves propagate through the contact networks helps gain an insight into the fabric evolves during an earthquake and how that fabric evolution affects the macro-mechanical behaviour. For this purpose, a literature review on the both fabric quantities and the application of fabric on seismic behaviour of soil was carried out. It was found that there was no work carried out to investigate the effect of fabric evolution on the macro-mechanical behaviour of sand.

Chapter 4

4 The development of the DEM model

4.1 Introduction

The macro-mechanical behaviour of granular sand is related to the parameters that affect the inter-particle interaction forces. The Discrete Element Method takes into account the discrete nature of sand (Antony, 2007, O'Sullivan et al., 2002, O'Sullivan, 2011). As with any numerical method, assumptions still have to be made such as inter-particle properties, particle shape, size and configuration in *DEM* simulations. The former is addressed through the contact model. As a *DEM* model's response is based on inter-particle forces and displacements, the homogenization approach is used to obtain the average macro-mechanical response. The macro mechanical response is then validated against appropriate experimental data.

The accuracy of this validation depends on replicating the geometric properties of the sample and selecting the appropriate inter-particle properties. The former means creating a configuration of particles that has the same geometry including boundary conditions and particle size distribution as the experimental sample. However, this cannot be achieved because of the nature of the particles; the number, the shape, the size and the distribution will be different between the numerical model and the experimental sample. Therefore, any model can be similar but not the same as the real sample.

The second issue, and fundamentally more important, is the inter-particle relationship, which is based on a number of variables including the particle stiffness, particle size and the inter-particle friction. It is possible to fit a single experimental curve with a number of combinations of these variables. However, not all the combinations will be valid because there can be some interdependencies between the parameters and there are limits to the range of the parameters.

A sensitivity analysis will identify which are the critical parameters and the range over which the parameters impact on the mass behaviour. Mass behaviour is used as the outcome as it provides a link to experimental behaviour, which provides the macro mechanical properties.

The main aim of this chapter is to develop a DEM model to perform biaxial test simulation with different boundary conditions such as rigid and deformable boundary particles using *PFC*^{2D}. This model is then used in chapter 5 for sensitivity analysis. A review of the assumptions and limitations of *PFC*^{2D} is presented. A new method to define deformable boundary particles is presented. Also a method which is required to define the normal contact stiffness is discussed. A new fabric quantity term, called “symmetric geometric deviation index” is also defined.

4.2 The *DEM*-based biaxial tests

The macro-mechanical characteristics of sand are found from field and laboratory tests. The triaxial test is the most common laboratory method used to determine the stress strain characteristics. However, many problems in geotechnical design assume plane strain (e.g. Lambe and Whitman, 1969, Wood, 1990). Therefore, a biaxial test may be more appropriate assuming that the soil response is different between triaxial and biaxial behaviour. For this purpose, biaxial test simulations are needed to reproduce the macro-mechanical behaviour of sand. To simulate a biaxial test using *PFC*^{2D}, an algorithm written using the *Fish* language programming code is required. Before describing this algorithm and its assumptions and limitations, it is essential to illustrate the assumptions and limitations of *PFC*^{2D}.

4.2.1 Assumptions and limitations of *PFC*^{2D}

The two-dimensional version of *particle flow code* or *PFC*^{2D} (Itasca, 2008) is based on the *DEM* numerical algorithm. The accuracy of this programme has been already approved by other researchers (e.g. Belheine et al., 2009, Bhandari et al., 2014). As with any numerical method, it is necessary to consider the limitations and assumptions when using *PFC*^{2D}. These limitations and assumptions are as follows:

4.2.1.1 Two-dimensional simulations

Providing a two-dimensional *DEM* simulation using *PFC*^{2D} requires two in-plane force components and one in-plane moment. Stress and strain tensors exist at each point within a continuum media, they cannot be determined within a granular media. An averaging method is used to estimate the average stress and strain tensors within an RVE. Since the in-plane contact force components are considered to calculate the average stress tensor in *2D* case and the out-of-plane force component is not taken into account in the motion equation - i.e. the out-of-plane constraint factor which is essential to enforce a state of plane strain or plane stress is not present, the interpretation of *PFC*^{2D} results in terms of either plane strain or plane stress will be a controversial issue.

The two-dimensional assumption, however, has an advantage. The dynamic response of a particulate system is greatly dependent on the number of degrees of freedom of each particle within these systems. In *3D DEM* simulations, each idealized particle has six degrees of freedom while in *2D* cases there are three degrees of freedom per particle. The computational effort in *2D DEM* simulations will be less than *3D* simulations and therefore faster. Furthermore, the number of documented *2D DEM* studies published annually shows that *2D DEM* simulations are able to capture the key complex mechanical response features of soil medium. Moreover, many problems in geotechnical design are assumed to be plane strain. Therefore, the two-dimensional analysis may be more appropriate.

4.2.1.2 Particle geometry

In morphological terms, sand particles have a complex geometry such that a particle may have more than one contact point with its neighbouring particle (see figure 4-1). When a particle is squeezed by their surrounding particles during loading, their geometry will change. Therefore, finding the current geometry characteristics of a deformed particle such as particle centroid and contact geometry in the framework of a simple analytical manner will be difficult. To overcome this difficulty, as mention in the previous chapter all particles are assumed to be rigid with soft contact. This condition is applicable only for disk and spherical particles which behave elastically. It is

because the contact deformation for such particles based on the principle of contact mechanics can properly demonstrate the particle deformation in elastic domain behaviour (Johnson, 1985). However, for complex particle geometry, this assumption may results is unrealistic contact behaviour (Bardet, 1998).

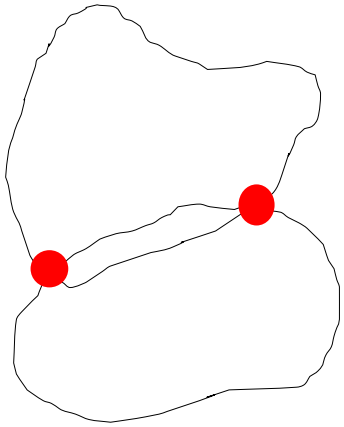

Figure 4-1 A possible shape of sand particles showing multiple contact points for two particles

4.2.2 Elastic normal contact model

The response of soil systems is dependent on both relative movement of particles and contact deformations. The normal contact model is a relationship between the normal contact force, F_n, and normal contact deformation, U^n, $F_n = f(U^n)$. To find the contact deformation, it is vital to define a proper contact model which must be compatible with the assumptions and the limitations of both DEM and *PFC*^{2D}. All particles are rigid disk with soft contact. This restricts the simulations to an elastic contact model. For quartz sand material, the Young's modulus is relatively high compared to the soil skeleton (Nakata et al., 2001a), therefore, it can be assumed that a particle might behave elasticity during loading (Nakata et al., 2001b) since most of the deformation will be due to the movement of the particles.

When modelling the behaviour of sand subject to quasi static loads

- Contact velocity is low since the unbalanced force is small,
- The particle rigidity is much greater than the rigidity of the particle skeleton.

Some sand grains may undergo plastic deformation and possibly fail but the macro failure mode of the sample is dominated by the relative displacement between the sand grains (e.g. Nakata et al., 2001b). Therefore, a simplified contact model such as elastic contact model can be used. Two types of elastic normal contact models are generally used by researchers in soil mechanics and soil dynamics: the modified Hertz model and the linear elastic contact model.

The limitations and assumptions of these two contact models are dependent on the limitations and assumptions of the Hertz contact model. The Hertz contact model is originally obtained for two spherical particles in contact. The assumptions of Hertz contact model are:

1- The strains are small and within the elastic limit,
2- The radius of contact area is much smaller than the particle radius,
3- The width of contact zone is infinitesimal,
4- The particle surface is continuous,
5- The particles are frictionless,
6- The particles are spherical,
7- The particles are considered as an elastic half-space,
8- Failure criterion is not applied.

However, as this analysis is 2D, the particles are disks and assumed to be elastic the following assumptions are considered:

1- Particles are assumed to be rigid with an elastic soft contact zone,
2- Contact point is considered rather than contact area between two particles,

The contact models link contact forces to contact deformation not contact stress to contact strain. This reduces the degrees of freedom to one.

4.2.2.1 Hertz contact model

In the Hertz contact model (see figure 4-2a), the normal contact stiffness at the interface of two particles (i.e. k_n) is dependent on the elastic modulus, Poisson's ratio and geometry of the two particles (see Eq. 4.1 to Eq. 4.4). These material properties are defined by the user.

$$k_n = \left\{ \frac{2G^* \sqrt{2R^* U^n}}{3(1-\upsilon^*)} \right\} \tag{4.1}$$

$$R^* = \frac{2R_1 * R_2}{R_1 + R_2} \tag{4.2}$$

$$G^* = \frac{1}{2}(G_1 + G_2) \tag{4.3}$$

$$\nu^* = \frac{1}{2}(\nu_1 + \nu_2) \tag{4.4}$$

In which U^n is contact deformation or overlap and computed by *PFC*^{2D} compiler at each time step from (Eq. 3.3). The other symbols are shown in figure 4.2. Typical values of shear modulus and Poisson's ratio of quartz sand particles can be found from the literature or acquired from a uniaxial compression test on a quartz sand particle (i.e. the change in diameter, both in line with the load and perpendicular to the load will be used to obtain the compression stiffness of that grain. However, the latter is difficult to perform (e.g. McDowell and Bolton, 1998).

As particles are rigid with a soft contact zone (see figure 4-2b), the contact deformation between two particles is restricted to the soft contact zone interface. Therefore, the rheological model (figure 4-2c) shows the behaviour of contact subjected to the normal contact force and deformation $F^n = f(U^n)$. It should be noted that the soft contact zone drawn in figure 4-2 is scaled up to show the details of rheological modified Hertz contact model.

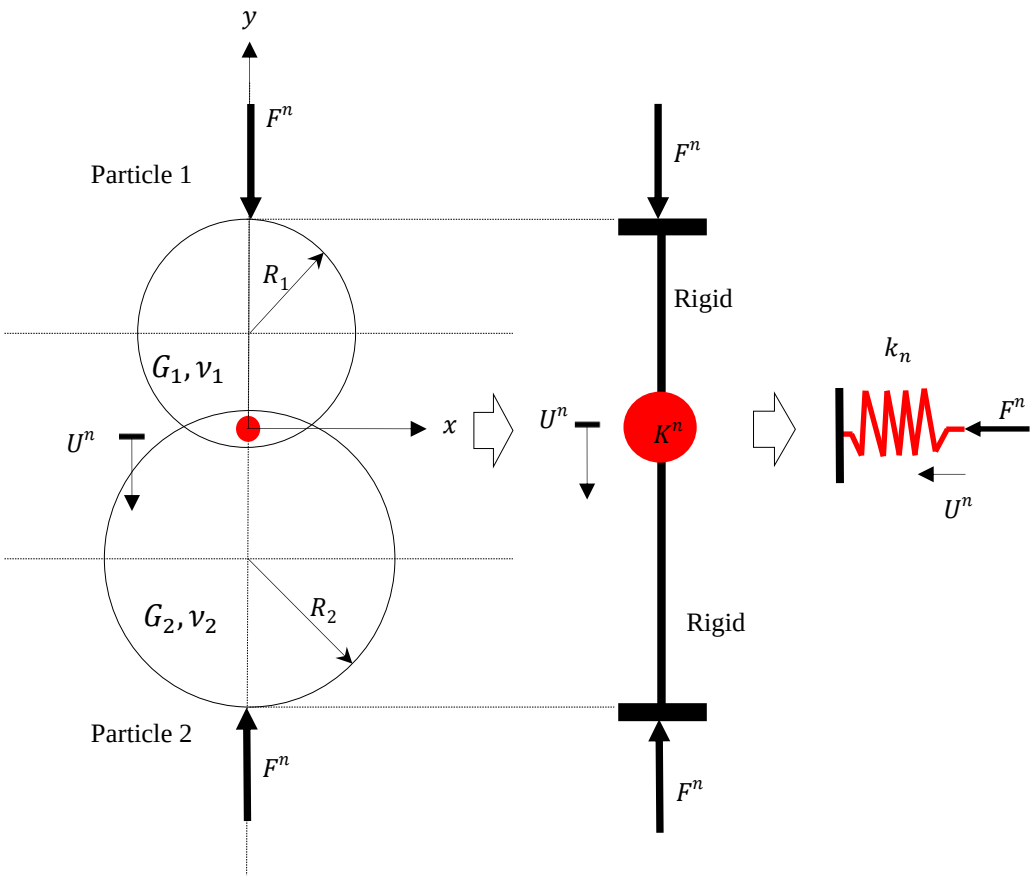

Figure 4-2 Modified Hertz contact model used in *PFC*^{2D}

This model is appropriate for spherical particles but not disk particles. The linear elastic contact model has been used by a number of researchers to study the two dimensional behaviour of soil. This model links the normal contact force to the normal contact deformation by the constant normal contact stiffness, (i. e. k_n) (see figure 4-3). To find the normal contact stiffness, the normal stiffnesses of two contacting particles are required. Therefore, other methods are needed to determine the stiffness of disk particles. These methods should be able to take into account disk radius, contact radius and material properties. Two methods can be used to compute normal stiffness for disk particles:

- Equivalent rectangular approach, and
- Deformable disk method.

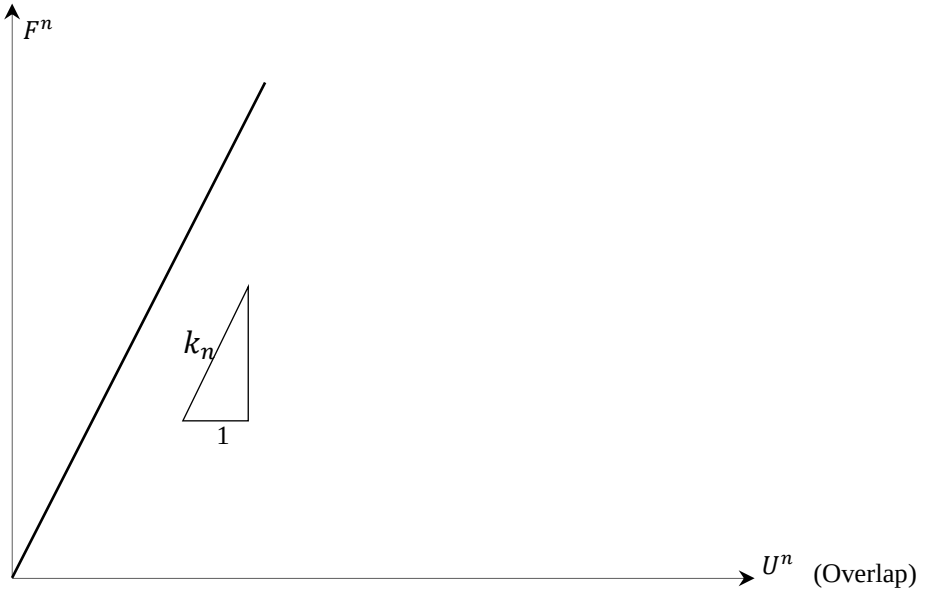

Figure 4-3 Schematic linear normal contact stiffness model used by *PFC*

4.2.2.2 Equivalent rectangular approach

This method (Figure 4-4) is proposed by Itasca (2008). As shown in figure 4-4a and 4-4b, a compressive force exists between two disk particles. The size of these two particles is assumed the mean particle size. As particles are assumed rigid, the load applied at the contact points, F, is transferred to the particles centroid (see figure 4-4c and 4-4d). The area of contact is obtained from Eq. 4.6. Since the particles are subject to a normal load they can be replaced by a column or beam of length equal to the distance between the centres of the particles, axially loaded and with a stiffness K^n.(see figure 4-4e). From this figure, the value of normal contact stiffness is:

$$K^n = \frac{AE_p}{L} \tag{4.5}$$

$$A = 2Rt \tag{4.6}$$

$$L = 2R \tag{4.7}$$

in which t and R are the particle (or disk) thickness and radius of particle, respectively (i.e. geometry components). E_p is the intrinsic elastic modulus of

the particle material, which is independent of the particle size. By default t is equal one (***SET disk t = 1.0***) in PFC^{2D}.

In *PFC*, the normal contact stiffness, k_n, is computed at each time step by assuming that the stiffnesses of the two contacting particles, $K_1^n \text{and } K_2^n$, act in series (see figure 4-4f):

$$k_n = \frac{K_1^n * K_2^n}{K_1^n + K_2^n} \qquad 4.8$$

Generally the stiffness of the particles is assumed to be the same (i.e. $K_1^n = K_2^n = K^n$) such that Eq. 4.8 becomes:

$$k_n = \frac{K^n}{2} \qquad 4.9$$

From Eq. 4.9, the normal particle stiffness is twice the normal contact stiffness, which is computed from Eq. 4.5. The normal particle stiffness is provided by the user. The normal contact stiffness then is calculated by computing Eq. 4.8. The intrinsic elastic modulus of a particle, which is independent of particle size, is obtained from the literature. The main advantage of applying this contact model is that it is a straightforward method to give the initial value for the normal contact stiffness. However, the main disadvantages of this approach are as follows:

- The stiffness is independent of the geometry,
- The size of contact is the same as diameter of particle and it is constant even though the actual contact area is much smaller,
- Only the normal force at a contact is considered, and
- Only the elastic modulus is considered.

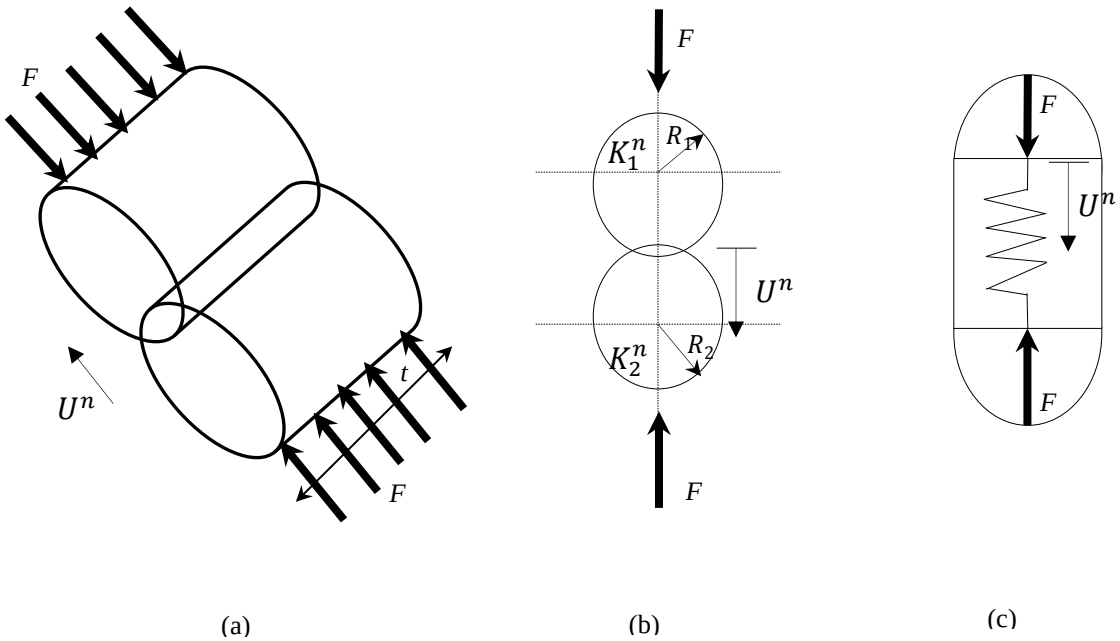

(a) Two disk particles are in contact

(b) Cross section

(c) Elastic Beam

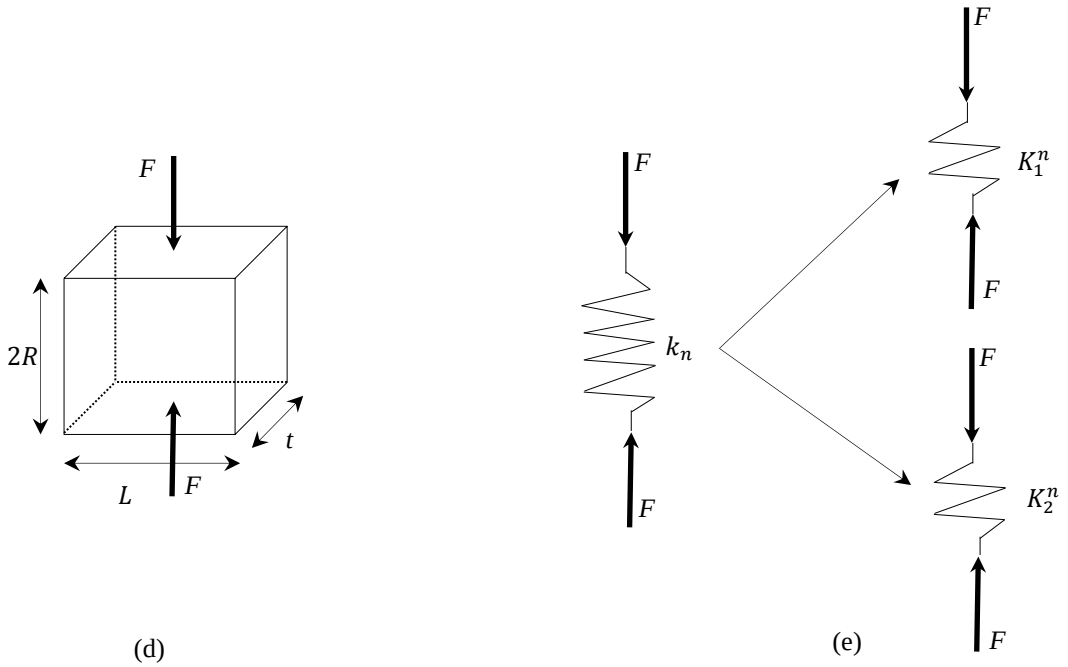

(d) Elastic Beam

(e) Rheological Model

Figure 4-4 Linear elastic normal contact model used in *PFC*^{2D}

4.2.2.3 Deformable disk method

The aim of this method is to find a proper contact stiffness of two disks in contact based on the principle of contact mechanics. The normal contact stiffness of two disks in contact is dependent on their normal stiffness which is in series. Two disks in contact with elastic properties E_1, ν_1 and E_2, ν_2 are subject to a compressive load to determine the normal contact stiffness (see figure 4-5 (a)). The relative displacement, U^n, of the disk, C_1 C_2, is obtained by integrating by ε_z from $z = 0$ to $z = 2R$ (see figure 4-5 (b)):

$$U^n = \int_0^{2R} \varepsilon_z \, dz = \int_0^{2R} \frac{2F(1-\nu^2)}{\pi E}\left(2Ln\left(\frac{4R}{a}\right) - 1\right) \qquad 4.10$$

In plane strain, the vertical strain obtained by following equation:

$$\varepsilon_z = \frac{1-\nu^2}{E}\left\{\sigma_z - \frac{\upsilon}{1-\upsilon}\sigma_x\right\} \qquad 4.11$$

$$\sigma_z = \frac{F}{\pi}\left\{\frac{1}{R} - \frac{2}{2R-z} - \frac{2}{\sqrt{a^2+z^2}}\right\} \text{ and } \sigma_x = \frac{F}{\pi}\left\{\frac{1}{R} - \frac{2(a^2+2z^2)}{a_1^2\sqrt{a^2+z^2}} + \frac{4z}{a^2}\right\} \qquad 4.12$$

$$a = \sqrt{\frac{4FR}{\pi E^*}} \quad \text{where } \frac{1}{E^*} = \frac{(1-v_1^2)}{E_1} + \frac{(1-v_2^2)}{E_2} \qquad 4.13$$

In the case of identical elastic properties, $E^* = \frac{E}{2(1-\nu^2)}$. The tangential disk stiffness then is obtained by:

$$K_{disk}^n = \frac{F}{U^n} = \frac{\pi E}{\ln(4RE^*\pi) - \ln(F) - \ln(e)} \qquad 4.14$$

Figure 4-6 shows the variation of normalized normal load with normalized relative displacement for disk-disk and sphere-sphere in contact with the same properties. Figure 4-7 shows the variation of normalized normal stiffness with normalized relative displacement for disk and sphere. For more details reader can refer to (Bardet, 1998, Johnson, 1985).

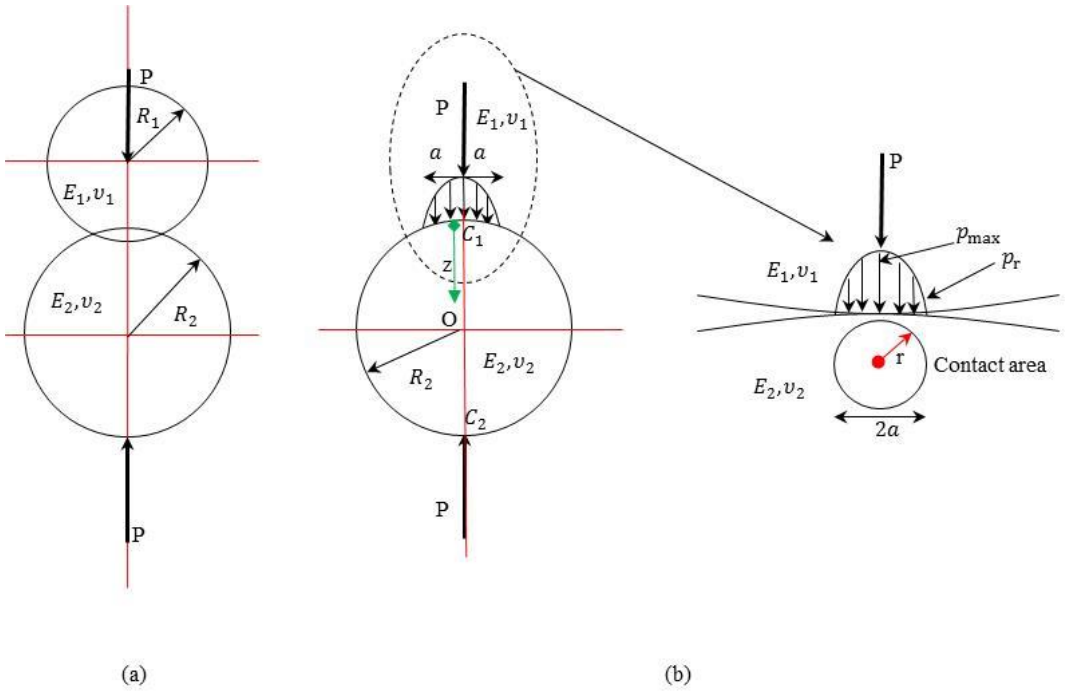

Figure 4-5 Compression of deformable disk particle due diametrically opposed point loads

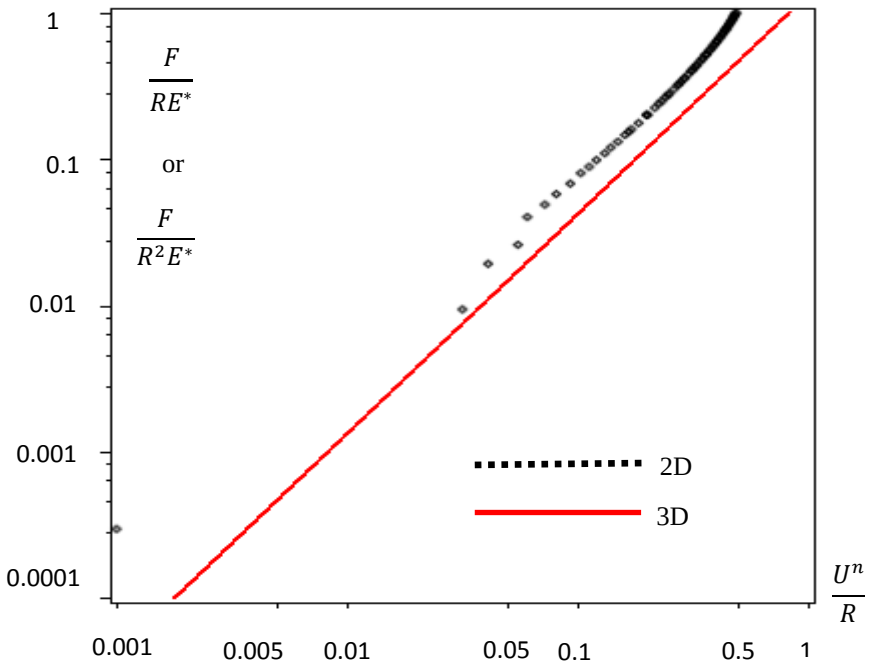

Figure 4-6 The variation of normalized normal load with normalized relative displacement for disk and sphere

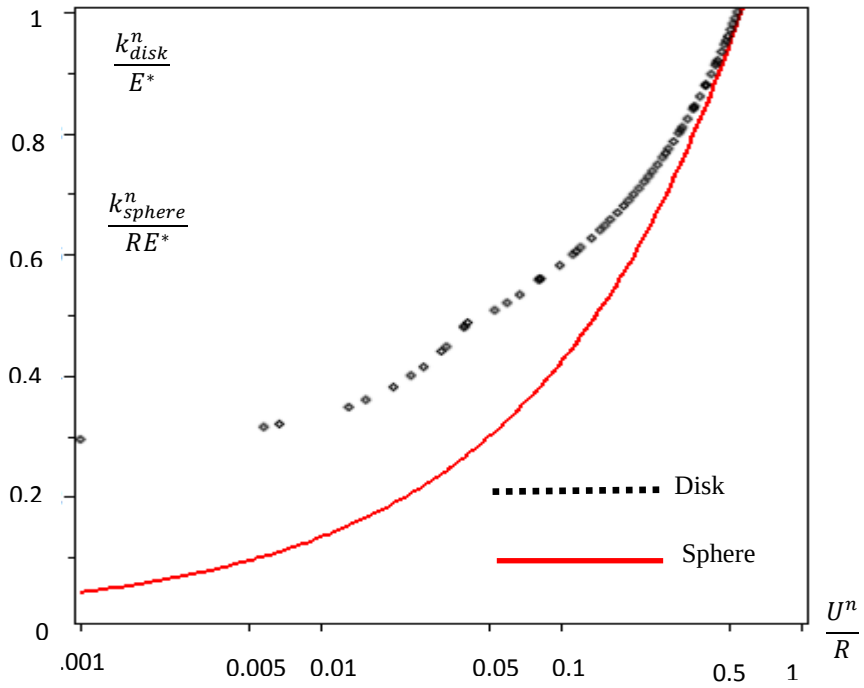

Figure 4-7 The variation of normalized normal stiffness with normalized relative displacement for disk and sphere

The graphs show that the use of Eq. 4.1 to compute the normal contact stiffness of two disks in contact results in to produce unrealistic response.

By using mean theory, the average particle stiffness of a disk can be obtained from Eq. 4.14-

$$K^n = \int_0^x \frac{\left(\frac{\pi E}{\ln(4RE^*\pi) - \ln(x) - \ln(e)}\right)}{x - 0} \qquad 4.15$$

where *x* is the upper bound of applied force, which can be infinite. Instead, the initial stiffness is used from figure 4-7. When the initial normal or average stiffness of two disks in contact obtained from figure 4-7 or Eq. 4.14 respectively, the contact stiffness is then computed using Eq. 4.8. The advantage of using this approach is to consider the geometry of particle and contact area. In addition, the force is considered in this approach. This leads to the conclusion that the contact stiffness obtained from this approach is more realistic in comparison with the Equivalent rectangular approach.

4.2.3 Elastic tangential contact model

Unlike the normal contact models, the parameters for the tangential contact model are numerous; contact geometry, the intrinsic material property, normal contact traction, normal contact deformation, inter particle friction, particle roughness, loading and unloading cycles and tangential deformation (see chapter two). Two types of tangential contact models are generally used by researchers in soil mechanics and soil dynamics: the modified Mindlin and the tangential linear elastic contact model.

The original Mindlin contact model can compute the tangential stiffness, k^{s}_{Mindlin}, between two frictional spherical particles in contact (Mindlin and Deresiewica, 1953). The assumptions considered in the Hertz model are also considered in this model. This contact model is also a function of contact force history, including normal and tangential force:

$$k^{s}_{\text{Mindlin}} = k_s \left\{ 1 - \frac{F^{t}_{t-1}}{(\mu F^{n}_{t})} \right\}^{\frac{1}{3}} \qquad 4.15$$

where k_s is tangential shear stiffness and obtained from Eq. 4.16. μ is the minimum inter-particle friction, $F^{tangential}_{t-1}$ is the total tangential contact force at the prior time step and F^{n}_{t} is the total normal contact force at the current time step.

This contact model has been modified by (Cundall, 1988) in such way that the tangential contact force and particle friction terms are ignored. The modified tangential stiffness is as follows (see figure 4-8):

$$k_s = \left\{ \frac{2[\frac{E^2}{4(1+\nu)^2} 3(1-\nu)\tilde{R}]^{\frac{1}{3}}}{(2-\nu)} \right\} |F^n|^{\frac{1}{3}} \qquad 4.16$$

$\tilde{R}$, E and ν are particle radius, Elastic modulus and Poisson's ratio . $|F^n|$ is the magnitude of the normal contact force at each time step.

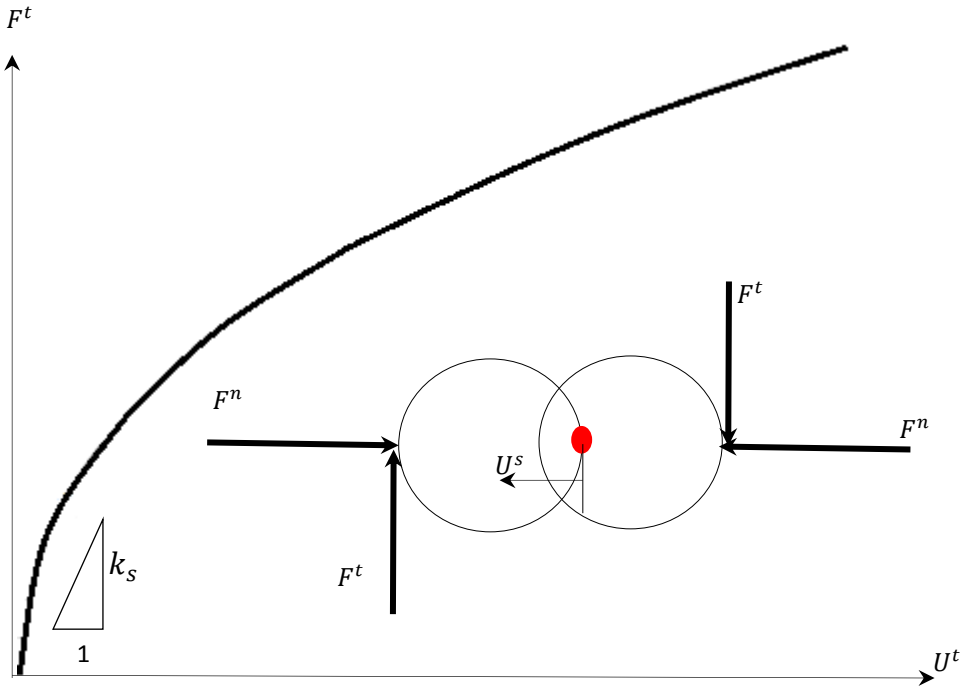

Figure 4-8 Modified Mindlin contact tangential force vs. tangential deformation used in *PFC*

Next, the incremental tangential force is obtained by applying

$$\Delta F^{tangential} = k_s \Delta U^s \qquad 4.17$$

where ΔU^s is the relative tangential contact deformation and computed by *PFC*^{2D} compiler from Eq. 3.4. The incremental tangential contact force at the current time step is then added to the total tangential contact force when the contact point was formed ($F_t^{tangential} = \Delta F^{tangential} + F_{t-1}^{tangential}$). This total tangential contact force is then compared to the sliding criterion to check whether the contact is lost or not.

The Hertz normal contact model and Mindlin tangential contact model, so called Hertz-Mindlin contact model, is activated in *PFC*^{2D} by specifying the keyword hertz command. That is, these two contact models are coupled in *PFC*. The main advantage of applying this tangential contact model is to consider normal contact force component in order to evaluate the tangential contact stiffness. The main disadvantage of this contact model is that at each time step, the tangential contact stiffness should be derived from Eq. 4.15.

Thus, by increasing the number of particles the time of simulation will increase. The ratio of $\frac{k_s}{k_n}$ based on Hertz-Mindlin contact model is:

$$\frac{k_s}{k_n} = 2\frac{1-\nu}{2-\nu} \qquad 4.18$$

By changing the Poisson' ratio from zero to 0.5, the value of $\frac{k_s}{k_n}$ will vary between one and two third.

The linear elastic tangential contact model links the shear contact force to the shear contact deformation by using the constant tangential stiffness (i.e. k_s). The same assumptions used to derive the elastic beam are considered here to derive the linear tangential contact stiffness (see figure 4-9). The linear tangential stiffness value for a contact point between two particles is obtained from:

$$K^s = \frac{12IE_p}{L^3} \qquad 4.19$$

in which $I = \frac{1}{12}t(2R)^3$ is moment of inertia. In *PFC*, the tangential contact stiffness, K^s, is computed at each time step by assuming that the stiffnesses of the two contacting particles, K_1^s and K_2^s, act in series (see figure 4-9f):

$$K^s = \frac{K_1^s * K_2^s}{K_1^s + K_2^s} \qquad 4.20$$

Generally the user-defined value of normal stiffness for all the particles within a model is assumed to be the same (i.e. $K_1^s = K_2^s = K^s$) such that:

$$k_s = \frac{K^s}{2} \qquad 4.21$$

From Eq. 4.21, it is deduced that the tangential particle stiffness is twice the tangential contact stiffness, which is computed from Eq. 4.19. The tangential particle stiffness is specified by the user. The tangential contact stiffness is then calculated by computing Eq. 4.20.

(Cundall and Strack, 1979) recommended that for the linear elastic contact model the $\frac{k_s}{k_n}$ ratio is between two third and one.

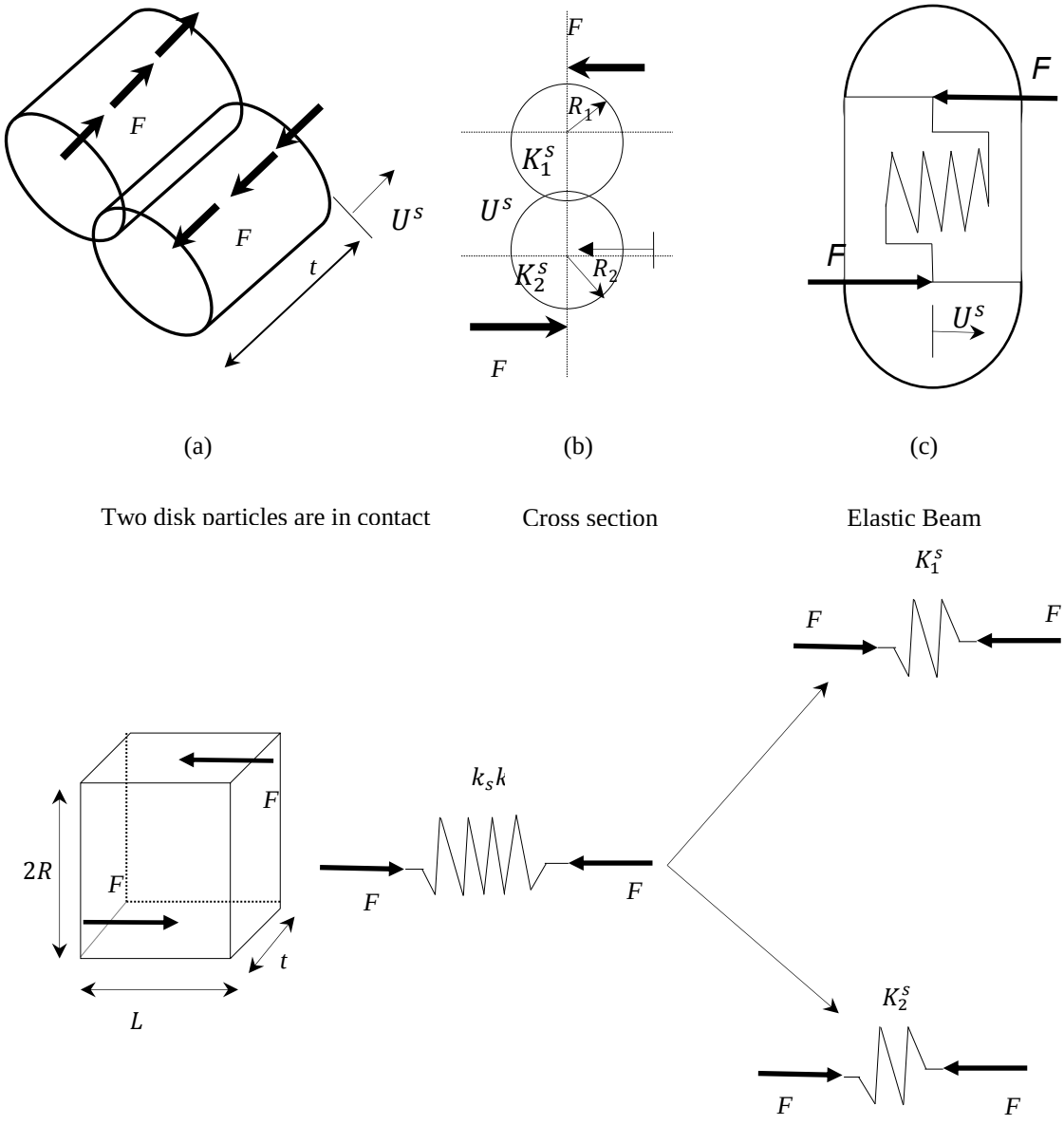

(a) (b) (c)

Two disk particles are in contact | Cross section | Elastic Beam

(e) (f)

Elastic Beam | Rheological Model

Figure 4-9 Tangential linear elastic contact model

Although the use of Mindlin contact model for simulating the elastic normal and tangential behaviour of contact points leads to more appropriate results, applying this contact model will increase the time of simulation in comparison with the linear elastic contact model. Additionally, the majority of papers published in *DEM* in soil mechanics use the linear elastic contact model for

modelling the inter-particle contact behaviour. This contact model is applied in this research.

4.2.4 Sliding criterion

As sand particles are frictional and cohesionless, the continuous shearing deformation at the contact point should be limited. The failure criterion used to restrict the tangential force in *PFC* is the Mohr-Coulomb criterion:

$$F_{max}^{t} = \mu |F^{n}| \qquad 4.22$$

where μ is particle friction and F^{n} is total contact normal force. At each time step the total tangential force, $F_t^{tangential}$, is compared with Eq. 4.22. If $F_t^{tangential}$ is more than F_{max}^{t}, $F_t^{tangential}$ is set to F_{max}^{t} (see figure 4-10).

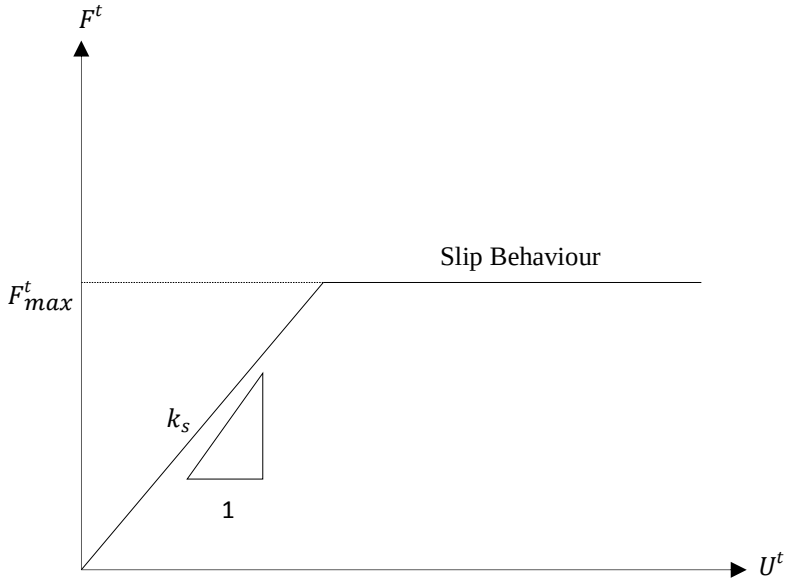

Figure 4-10 Shear contact force vs. shear contact deformation

4.2.5 Damping

The mechanism of stress wave propagation within particulate systems, subjected to boundary excitation, is based on an individual particle vibration, which act on its translational and rotational degrees of freedom. A particle starts to vibrate due to imposed kinetic energy when the wave front reaches it. However, this kinetic energy and particle vibration is naturally damped in

real granular material such as sand due to the mass, plastic deformation, crush and slippage of particle establishing static equilibrium. Since the elastic contact model is applied in this work, absorbing a portion of kinetic energy due to plastic deformation and particle crushing cannot be met. Therefore, the damping mechanism associated with applying the elastic contact model is only concentrated on the frictional slippage and mass of particles.

- Frictional slippage: this term is only applied at the contact points. When the tangential contact force exceeds the Coulomb failure criterion, the slippage mechanism is activated to absorb some of the kinetic energy.

The stress wave propagation tends to move the particles from their stationary positions based on motion law. The frictional damping which is applied to absorb the release energy due to the slippage of particles cannot be adequate for non-slippage of particle movement. The rate of particle movement is naturally dampened due to viscosity of system. Since this movement is the result of unbalanced force and unbalanced force is the result of the sum of contact forces, this viscosity damping is generally separated based on the local damping, which is compatible with unbalanced force of each particle mass, and contacts viscous damping, which is compatible with each contact force of particle mass.

- Local viscous damping: it is assumed that the particles are immersed in a viscous liquid. This reduces the particle inertial force or unbalanced force which acts on translational and rotational degrees of freedom on a particle by adding a virtual damping force against the particle movement rate. The damping is applied equally to all particles (Cundall, 1989). The magnitude of the local damping force is proportional to the unbalanced force acting on each particle. By applying this type of damping, the F_i^d term applied in equation of motion Eq. 3.10 becomes:

$$F_i^d = -\alpha |F_i| sign(\mathrm{v}_i);\ i = 1,2 \qquad sign(\mathrm{v}) = \begin{cases} +1, & \text{if } \mathrm{v} > 0 \\ -1, & \text{if } \mathrm{v} < 0 \\ 0, & \text{if } \mathrm{v} = 0 \end{cases} \tag{4.23}$$

where v is particle velocity and α is the local damping ratio.

Since in quasi-static deformation the acceleration of all particles is very small, the use of local damping means that all particles are equally dampened. This results in the particulate system reaching the static state quickly. For the quasi-static deformation such as biaxial and triaxial test (Bardet and Proubet, 1991) by using Adaptive Dynamic Relaxation method (ADR) on an assembly of 163 spherical particles surrounded by four rigid walls shows that this value fluctuates between 0.5 and 0.8 (see figure 4-11). (Potyondy and Cundall, 2004) suggested for quasi-static regime this value is 0.7.

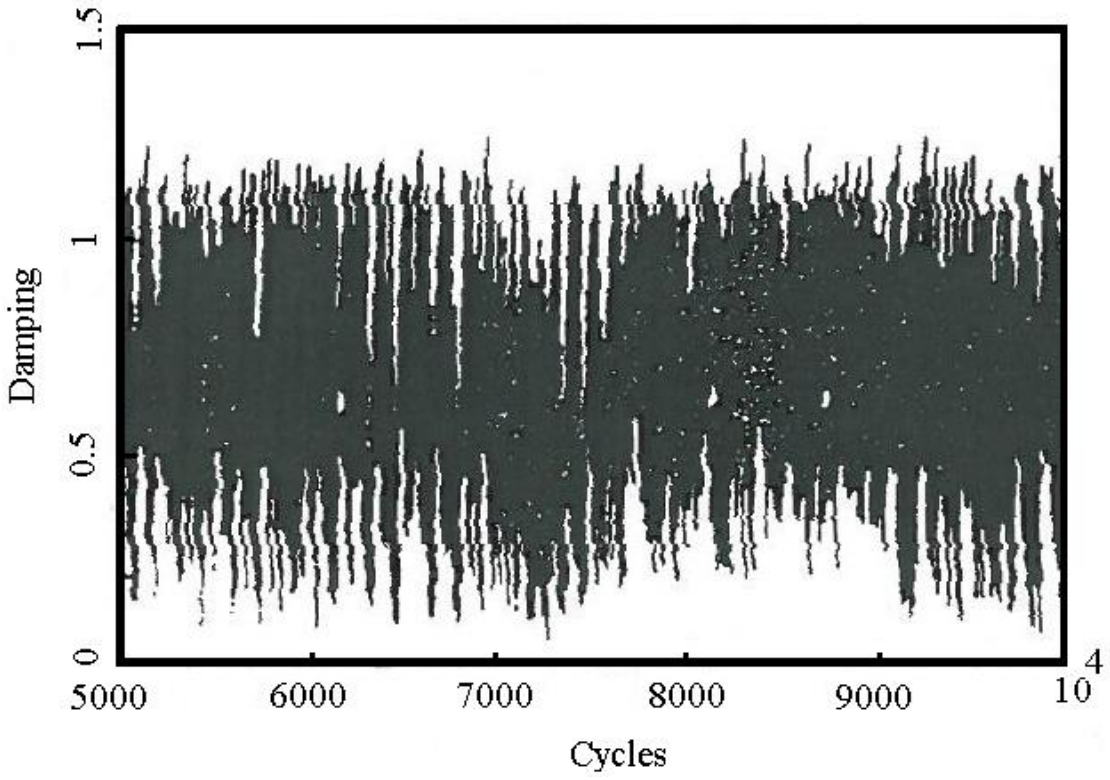

Figure 4-11 Variation of α calculated by Adaptive Dynamic Relaxation method during deviatoric load After (Bardet and Proubet, 1991)

This form of damping has the following advantages:

1- Only accelerating motion is damped. Therefore, no erroneous damping forces arise from steady-state motion.
2- The damping constant, α, is non-dimensional.

3- Since damping is independent of frequency, regions of the assembly with different natural periods are damped equally, using the same damping constant.

However, for dynamic loading such as that due to earthquakes where the particle acceleration is relatively high and is not uniform within a sample contact viscose damping is used to show the dynamic behaviour of system. For these simulations, the small value for contact viscose damping in normal and tangential direction appropriate to energy dissipation of dynamic waves is applied.

- Contact viscous damping: it is assumed that only contact points are immersed in a viscous liquid. Therefore, normal and tangential damping forces (dashpots) are added to the normal and tangential contact forces, respectively to diminish the value of contact forces in those directions. As this resistance force is only applied on those entities that have a velocity, it can resist against unbalanced force and contact force. The normal and tangential damping force is obtained by following equation:

$$F_i^d = \beta_i c_i^{critical} |\mathrm{v}_i| : \quad i = n, s \quad \text{where} \quad c_i^{critical} = 2\sqrt{m k_i} \qquad 4.24$$

$c_i^{critical}$ is the critical contact viscous damping constant and k_i (i.e. k_n and k_s) is the contact stiffness, and m is the particle mass. β_i (i.e. β_n and β_s) are the critical damping ratio, defined by user. Based on the principle of dynamic structure (e.g. Humar, 2012), when β_n and β_s = 1, the system is said to be critically damped (i.e. the response decays to zero at the most rapid rate). When β_n and β_s < 1 the system is said to be underdamped with oscillation behaviour and when β_n and β_s > 1, the system is said to be overdamped, or heavily damped with no oscillation behaviour. Appropriate viscous damping constants have to be determined for the simulation to produce a realistic response.

In the case of particle-wall contact, *m* is taken as the particle mass; in the case of particle-particle contact, $m = \frac{m_1 * m_2}{m_1 + m_2}$, where m_1 and m_2 are the

mass of particle *1* and particle *2*, respectively are. In case of applying contact viscous damping the equation of motion Eq. 3.10 becomes:

$$(M)_t^K = |l^K| \sum_{\mathrm{n=1}}^{\mathrm{n_k}} [\,(F_s - F_s^d)_t$$

4.25

$$(F_i)_t^K = \sum_{\mathrm{n=1}}^{\mathrm{n_k}} [(F_n - F_n^d)_{\mathrm{t}}\, \mathrm{n}_i^{\mathrm{c}} + (\mathrm{F_s} - F_s^d)_{\mathrm{t}} \mathrm{t}_i^{\mathrm{c}}$$

4.2.6 Non-crushable particle

The failure mode of spherical sand particles under compression in reality is based on tensile failure (McDowell and Bolton, 1998). This fact is not considered in *PFC*^{2D} because grains are assumed to be rigid and non-crushable. Therefore, single particles do not fail.

4.2.7 Rolling resistance

One of the main limitations associated with *PFC*^{2D} is to not consider the rolling resistance. (O'Sullivan, 2012) experimentally showed that if the particle size is larger than 0.1 mm, the surface roughness will have a minor effect on the material behaviour in comparison with the particle inertia. That is, the effect of rolling resistance on the dynamic equilibrium of each particle can be ignored. As the particle size in this research is between 1 mm and 2mm, this assumption in particle size met the above condition.

4.2.8 Forced-vibration and free-vibration of single degree of freedom

When the boundaries of a biaxial test are excited, those particles that are in contact with those boundaries start to oscillate due to either forced-vibration or free-vibration framework, depending on the boundary condition: rigid wall or deformable boundary. If the boundaries of biaxial test are rigid, the vibration mode for all boundary particles will be free-vibration. Figure 4-12 shows the biaxial test with rigid horizontal boundaries and flexible vertical boundaries. In *PFC*^{2D}, the velocity of the rigid walls is defined by the user. The mode of vibration for those particles that are in contact with rigid walls

(i.e. green particles in figure 4-12) is based on a free-vibration framework, while that for the boundary particles (red particles in the figure 4-12) due to the external pressure (e.g. isotropic confining pressure) is based on a force-vibration framework.

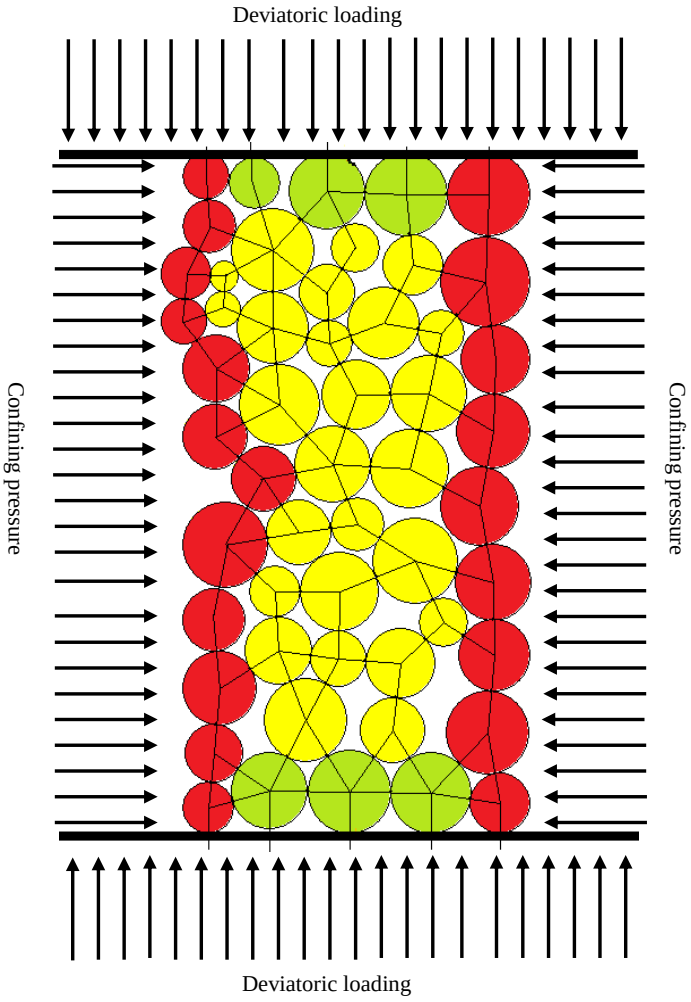

Figure 4-12 The schematic biaxial test with mixed the boundary excitation

By vibrating the boundary particles the forces are propagated through the contact network to the neighbouring particles thus generating a stress wave throughout the model.

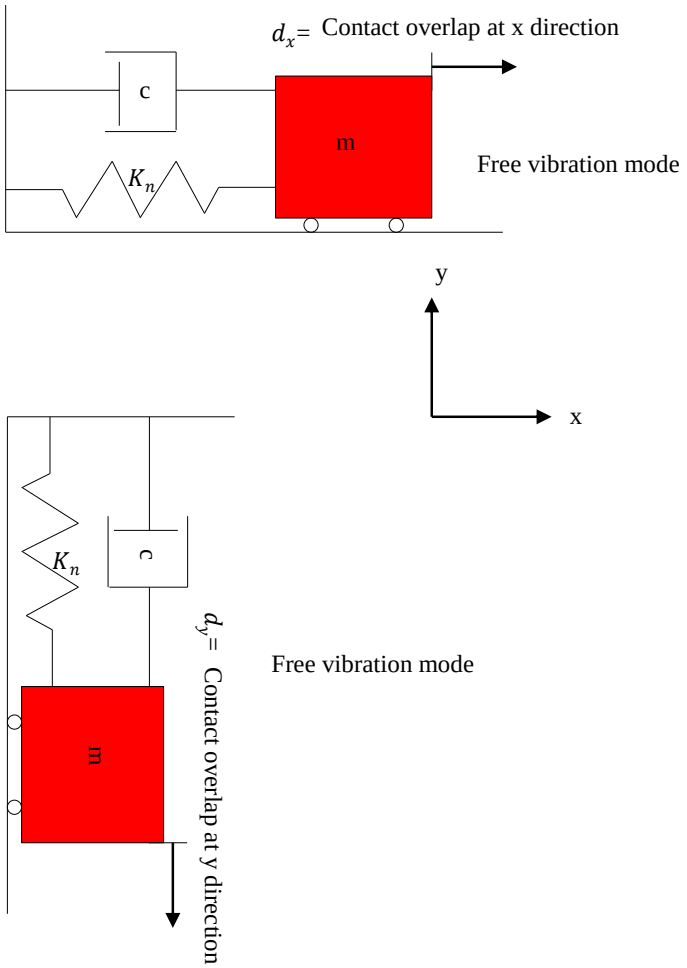

Figure 4-13 Free-vibration of red particles after encountering the halt *PFC* command

In contrast, when the boundary movement encounters the halt *PFC* command, the forced-vibration of boundary particles is changed to the free-vibration mode (i.e. the external confining forces applied on the boundaries particles, such as F_X and F_Y, are set to zero: $m\ddot{x}_x + c\dot{x}_x + \sum_{i=1}^{ng} f_x = 0$ and $m\ddot{x}_y + c\dot{x}_y + \sum_{i=1}^{ng} f_y = 0$ (see figure 4-13). In which n_g is the number contact of each grain.

Those particles (i.e. yellow particles) far from the source of boundary will still be vibrating whereas even though the boundary excitation has been halted. It is because the stress wave travels from boundaries with time lag (i.e. explicit solution). Thus, additional number cycles are needed to damp the free-vibration of particles in order reach a quasi-static state.

4.2.9 Time step

A centred finite-difference formula is used in *PFC*^{2D} to explicitly solve both the free and forced-vibration equation of each individual particle. In order for the solution to converge it is necessary to use a time step that is a fraction of the critical time step. Otherwise, the solution does not converge. A critical time step of a particulate system at the current time step is, however, dependent on the minimum Eigen-period of the system at the current time step. The accurate way to obtain the minimum Eigen-period of the particulate system at the every time step is to solve the $M\ddot{X} + C\dot{X} + KX = F(t)$ using matrix analysis. Where $M, C\ and\ K$ are the mass, damping ratio and stiffness matrix of the particles, respectively. $F(t)$ is the external boundary forces matrix. X is the inter-particle overlap matrix of particles. The matrix analysis of the system is, however, impractical to apply to the large and constantly changing systems typically encountered in *PFC*^{2D} simulations. A simplified approach is needed to predict the minimum period of the system. Having attained the minimum period, the critical time step is obtained. Based on this method, the minimum period of whole system is attained by applying Eq. 4.26. The critical time step is then found by using Eq. 4.27.

$$T_{min} = 2\pi\sqrt{\frac{m_{min}}{k_{max}}} \qquad 4.26$$

in which m_{min} is the minimum mass of particle within a system and k_{max} is the maximum contact stiffness within a system either normal or tangential.

$$\Delta_{t\ crit} = \frac{T_{min}}{\pi} \qquad 4.27$$

Motion is based on one-dimensional simple harmonic motion. Thus, the used time step in *PFC*^{2D} is taken as a fraction of the critical time step at each cycle. This fraction is characterized by using the **SET safety_fac** *PFC* command. The amount of this parameter by default is 0.8.

$$\Delta_t = \mathbf{safety\_fac} * \Delta_{t\ crit} = 2 * \mathbf{safety\_fac} * \sqrt{\frac{m_{min}}{k_n}} \qquad 4.28$$

In *PFC*^{2D}, the time step can be determined either by user or it can be computed automatically at each time step from by solving Eq. 4.28.

4.2.10 Equilibrium condition

DEM is a dynamic method. Controlling the quasi-static condition of each grain at the end of each time step is of great importance when the quasi-static state of the granular materials is required. The following key assumptions are made:

1- The load is applied slowly on the boundaries,
2- A damping term is applied to each grain.

When the net force vector at each grain centroid is zero, a *DEM* model is in equilibrium. That is, the right side of Eq. 3.10 becomes zero (i.e. out-of-balanced force is zero, $m\ddot{x} + c\dot{x} = \cancel{F_{body}} - \sum f_{contact\ force}$). However, this condition is unlikely to be satisfied because the unbalanced force will never reach zero. For this purpose, the "*relative equilibrium*" term is used. That is, if the right side of that equation approaches to zero, it will be assumed that the particle is in equilibrium. The criteria which show that particles are in relative equilibrium will be discussed at this section. If the out-of-balance force approaches a constant non zero value, this may indicate that failure and granular flow are occurring within the *DEM* model. The criterion used to show whether the *DEM* simulations are in relative equilibrium or not is:

- Restricting the ratio of the average unbalanced force to the average contact force of grains to the specific value (i.e. $\frac{|F|_{ave}}{|C|_{ave}} \leq \chi$),

in which $|F|_{ave}$ and $|C|_{ave}$ are the average unbalanced force (or out-of-balanced force) and the sum of average contact forces of a particle, respectively. χ is the limited value of each criterion. For example, in *PFC*^{2D}, it is 0.005.

4.3 *PFC*^{2D}-based biaxial test

There are four stages to a *PFC*^{2D}-based biaxial test simulation in this research: initial condition, boundary condition, applying deviatoric stress and interpreting the results (see figure 4-14).

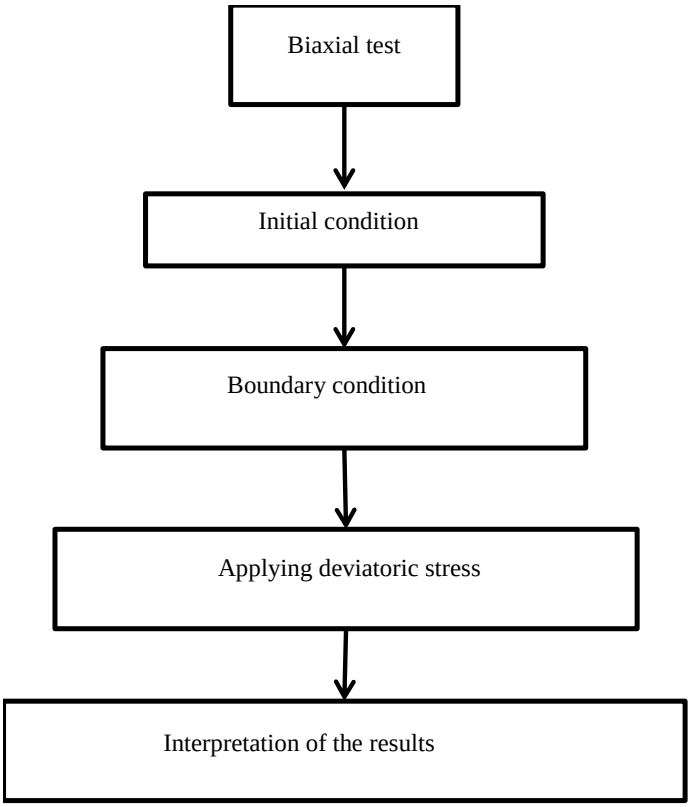

Figure 4-14 The diagram of biaxial simulation test in this research.

4.3.1 Initial condition

As the stress wave that reaches a particle is the result of earlier responses of the system, the initial condition (i.e. the initial geometry, manner of particle generation and the micro-mechanical properties) plays a major role in the response of the granular system.

4.3.1.1 Initial geometry

In general, the initial particle configuration of a soil is generated by allowing the particles to fall under the gravity force. It is also presumed that they are in static equilibrium under gravitational force such that each particle will have enough contact points (i.e. constrains) with another particles (O'Sullivan, 2011) to satisfy the static equilibrium condition. In this way forces are transmitted through the model. The initial geometry of a biaxial test in this work is created using the following stages (see figure 4-15):

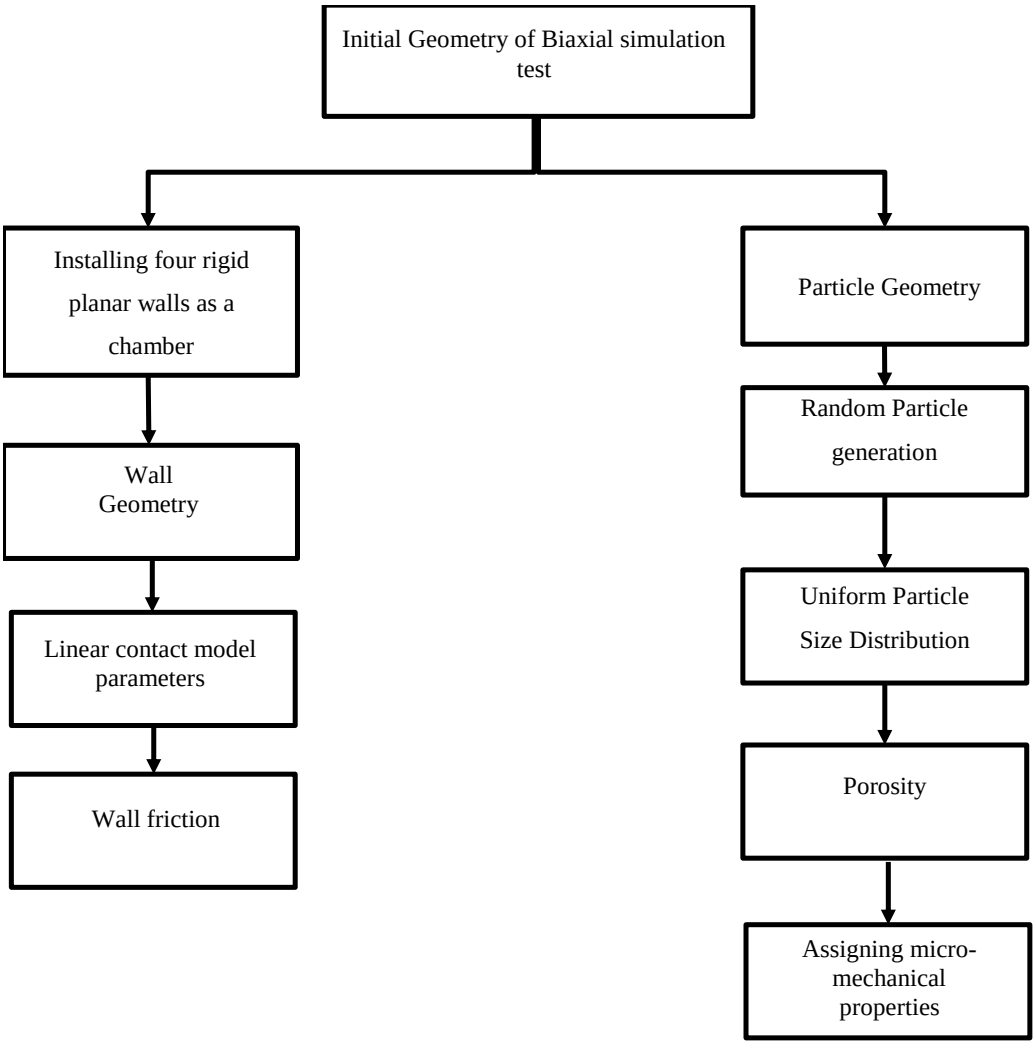

Figure 4-15 The initial geometry of creating biaxial test

4.3.1.2 Rigid walls

The first step to set up the initial geometry of a biaxial test is to generate the geometry of four rigid planar walls as the boundaries of the biaxial test chamber (see figure 4-16).

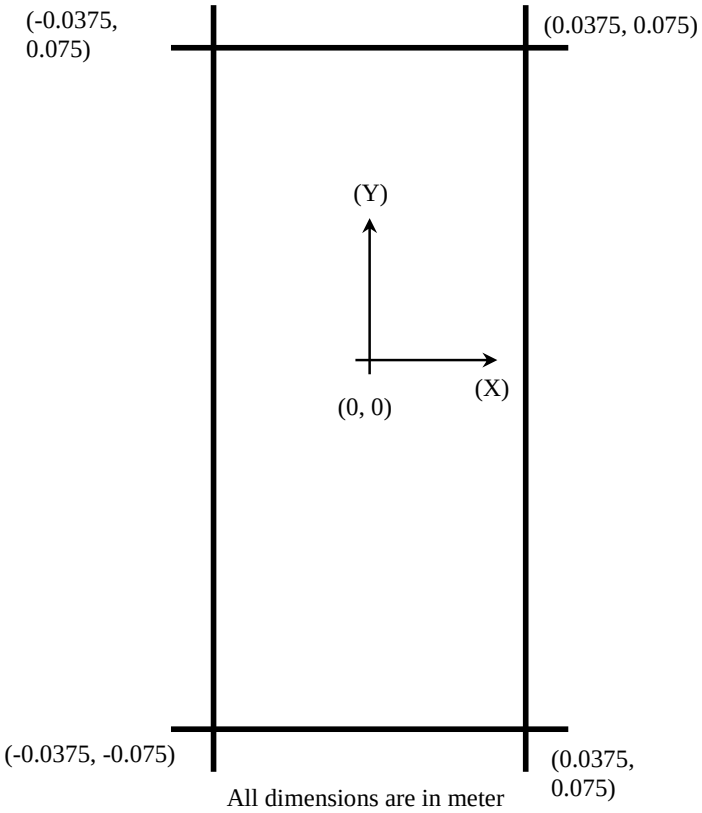

Figure 4-16 The initial dimention of the biaxial test‘s chamber

These walls by default are fixed. Generally, these platen walls are smooth and frictionless (Belheine et al., 2009). Therefore, the wall friction is set to zero in the code. The tangential stiffness of wall is assumed to be the same as particle tangential stiffness. The value of normal stiffness for each wall in this work is, however, computed by *Fish* compiler in such a way that normal stiffness of walls are ten times the average of the normal stiffness of those particles in contact with each wall. In *PFC*^{2D}, if the value of the overlap between a wall and a particle exceeds half of the particle size, the particle will cross over the boundary. Hence applying a higher normal stiffness prevents particles crossing the wall during loading. If the particle does cross the boundary there is disturbance in the chain forces and instability of the particulate system within the boundaries zones. Increasing and decreasing the wall normal stiffness increases or decreases the particle acceleration in a given time step such that it effects the vibration mode of particles in contact with the wall. Thus, the further response of particulate systems, including

fabric and macro-mechanical behaviour, will be influenced by this issue. The advantages and disadvantage of applying rigid walls to simulate the biaxial test are mentioned in the previous chapter.

The following features are considered in this DEM model:

- As the walls are considered to be inflexible, they do not deform during loading,
- It is assumed that the walls have no inertia,
- The velocity of the wall can be specified directly by the user either as a constant value or as a time-dependent values,
- The particle-wall interaction forces do not influence the wall movement.
- the equations of motion are not satisfied for walls since the wall motion is specified by the user,
- The use of walls in *PFC*^{2D} requires only defining the force-displacement law.

4.3.1.3 Random particle generation and particle size distribution

Sand particles sizes vary in nature. To generate the various sizes of sand particles in *PFC*^{2D}, a random function generation is required (see Eq. 4-29). In this equation the term $\tilde{X}$ is randomly selected by the software within range 0 and 1.

$$r = r_{min} + (r_{max} - r_{min})\tilde{X} \qquad with \qquad \tilde{X} = (0,1) \tag{4.29}$$

However, the mechanism of choosing this random number is dependent on the particle size distribution. The distribution of well graded soil particles is normal for most sands so the PSD is linear in a logarithm graph (Van Baars, 1996) (see figure 4-17). Considering the smaller sizes for sand particles leads to a reduction in the time step in *DEM* simulations and increase the number of particles within a chamber (see Eq. 4.28). To decrease the cost of simulation it is preferred to filter out the small sizes of particles. By doing this, the PSD supposed to be more uniform. Thus, the maximum and minimum radii of particles in this research were restricted between 0.25 to 1.0 [mm]. That is, $\bar{R} =$ 0.625 [mm]. Repeated calls to the function (Eq. 4.29) will

generate different particle size between a minimum and maximum particle radii based on uniform PSD.

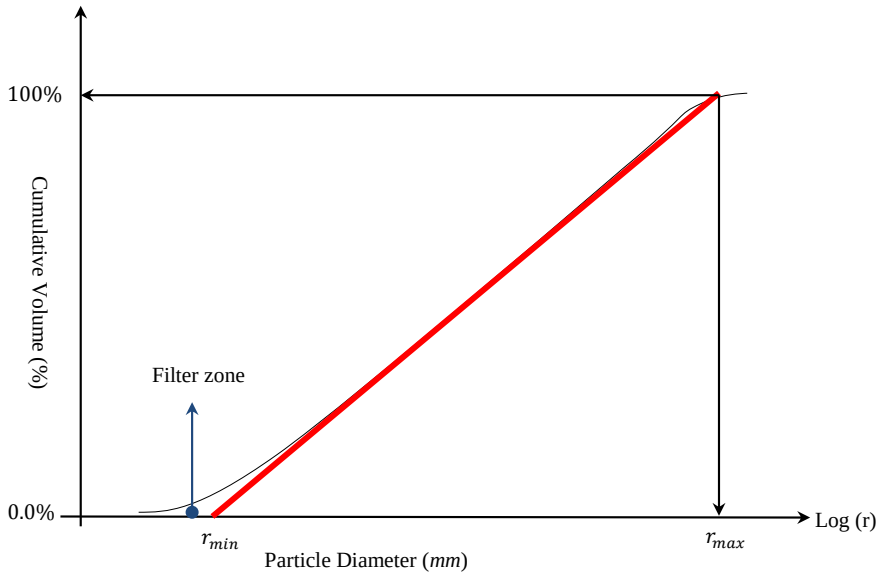

Figure 4-17 Sand particle size distribution

4.3.1.4 The methods of filling the biaxial chamber

After generating each particle, the chamber of biaxial test should be filled. There are two methods for fill the chamber: gravitational and radius expansion method.

4.3.1.4.1 Gravitational method

The particles are typically deposited as particles under gravitational vector field. This process will have been continuing when the particles reach to the state of equilibrium (e.g. dry pluviation method). At static equilibrium each disk particle will need enough constraints to satisfy the static equilibrium equations. That is, the minimum average coordination number for each disk will be three. This is a fundamental key feature to generate the assemblies of sand grains numerically. In this method, all of the particles cannot be deposited simultaneously because there is not enough space to accommodate them. Rather they will be deposited in stages (see figure 4-18). Therefore, the process of filling of biaxial chamber is time-consuming. During the deposition time, soil grains undergo large displacements. They also collide with other particles entering the model. Therefore, the initial force

will be anisotropic before applying the confining stress. This leads to non-uniform chain forces within a system (see figure 4-19 and figure 4-20).

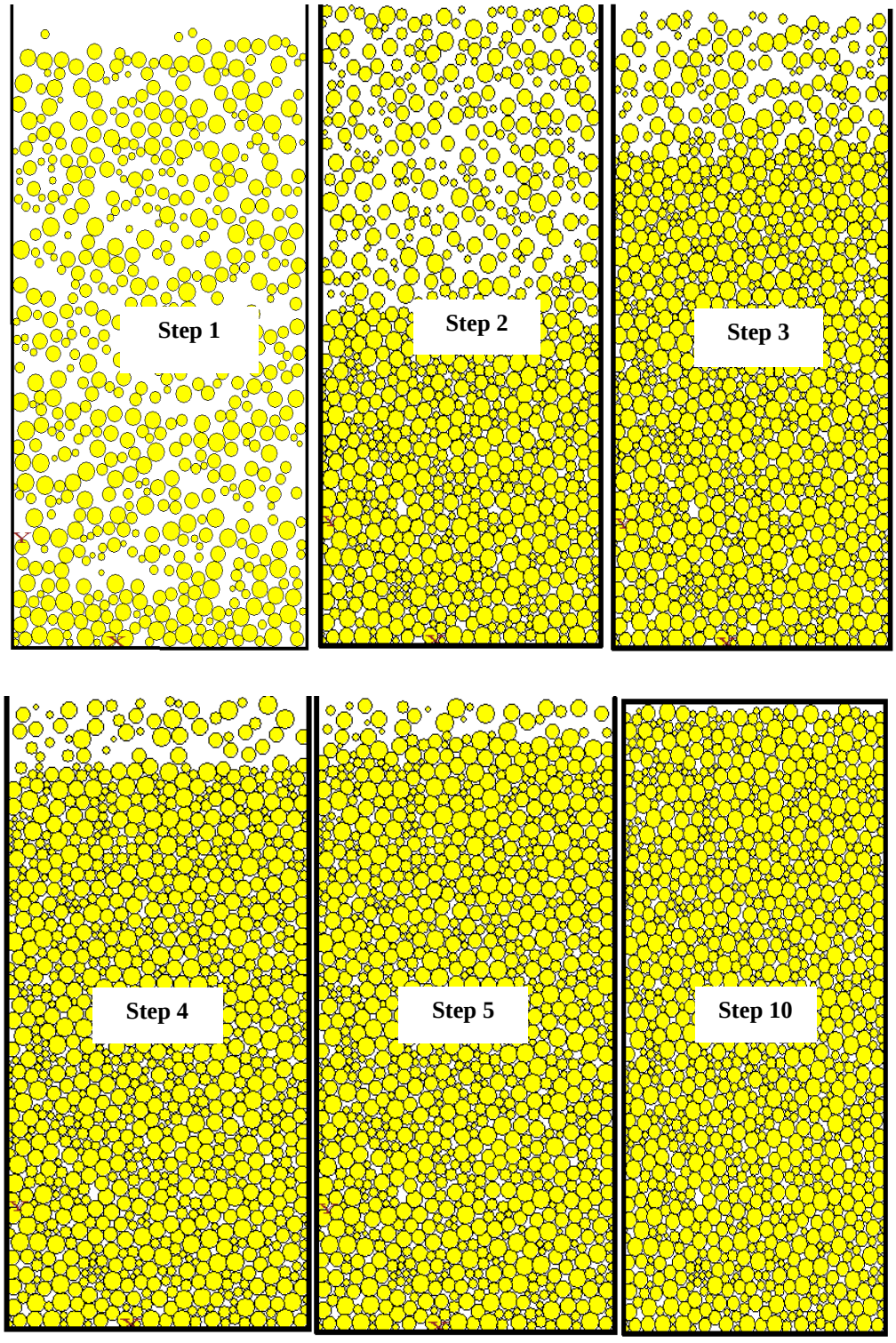

Figure 4-18 Particles generation based on gravity method

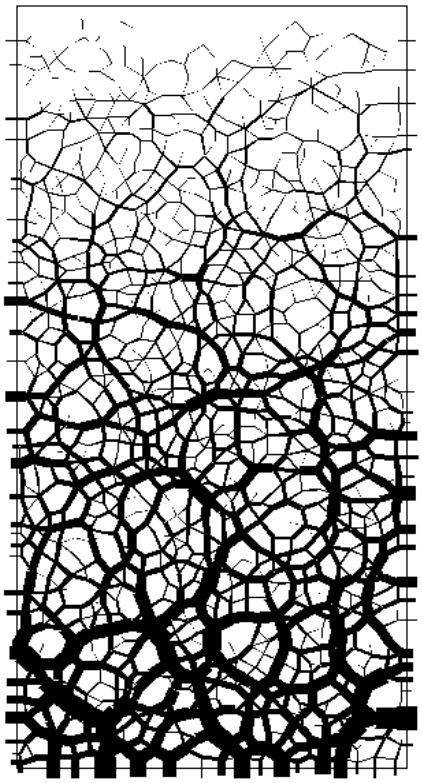

Figure 4-19 Contact normal force chains

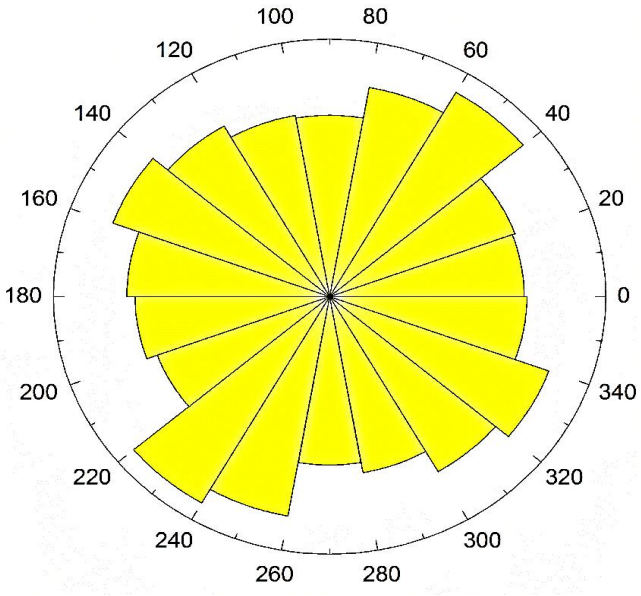

Figure 4-20 The initial fabric anisotropy of pack generated based on gravity method

The disadvantages of this method are:

- The user does not control the desired number of particles, target porosity and stress state during deposition,
- This method is time-consuming. It is because filling the chamber has to be carried out in stages. As more particles are added more contact points are generated increasing the time of computation to reach equilibrium.

4.3.1.4.2 Radius expansion method

The alternative method, which is in common use, is to use a radius expansion method. This reduces the computational time significantly. This method covers those disadvantages of prior method. That is, the number of particles and target porosity are the user-defined. The first stage is to define the required number of particles to fill the chamber based on a uniform particle distribution. All of the particles are generated in one stage (see figure 4-21). The number of particles required are based on the target porosity, n, chamber area, A, and average particle radius, $\bar{R}$, by the following equation:

$$N = \frac{A(1-n)}{\pi \bar{R}^2} \; with \; \bar{R} = \frac{R_{min} + R_{min}}{2} \qquad 4.30$$

In which R_{min} and R_{min} are the minimum and maximum particle radii, which is defined by the user, and dependent on the chosen particle size distribution. Based on Eq. 4.30, the number of particles needed to fill the chamber is inversely related to the average particle size. However, it is unlikely that all of the particles will fit into the biaxial chamber and, given that the walls are fixed, will cause the particles to overlap. Therefore, to generate the required number of particles, they start at half their final size. Then all particles are uniformly expanded to reach to the target porosity.

Other advantages of using this approach are as follows:

- The number of cycles needed to strain a system with the same chamber size and PSD to equilibrium using this approach is

significantly less in comparison with the gravitational method (Zamani and El Shamy, 2011).

- It takes more time to establish the contacts in the gravity method compared to the radius expansion approach.
- The particulate system after generation is shown in figure 4-21.
- The force chains are shown in figure 4-22.
- Figure 4-23 shows the development of macro stresses on walls during the particles expansion. The graph shows the stresses on the four walls at the end of expansion are the same; that is an isotropic state.
- The initial fabric provided by this method is in an isotropic state (see figure 4-24).

Some disadvantages of using this approach are as follows:

- During the expansion, it is seen for the number of simulations that the magnitude of walls stresses are greater than would be expected in geotechnical problems

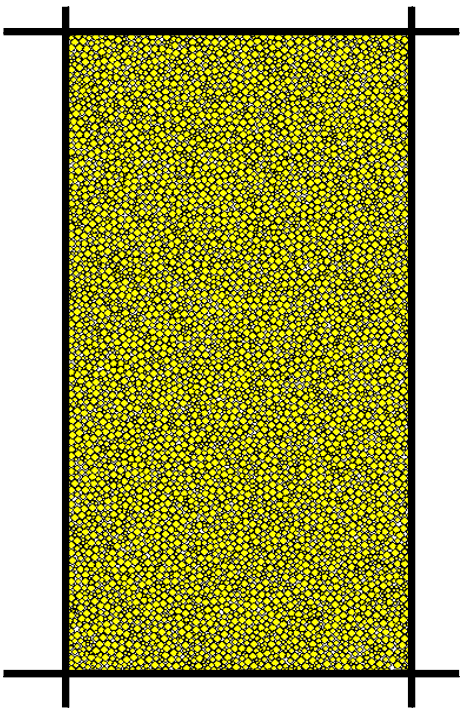

Figure 4-21 Particle generated using radius expansion method

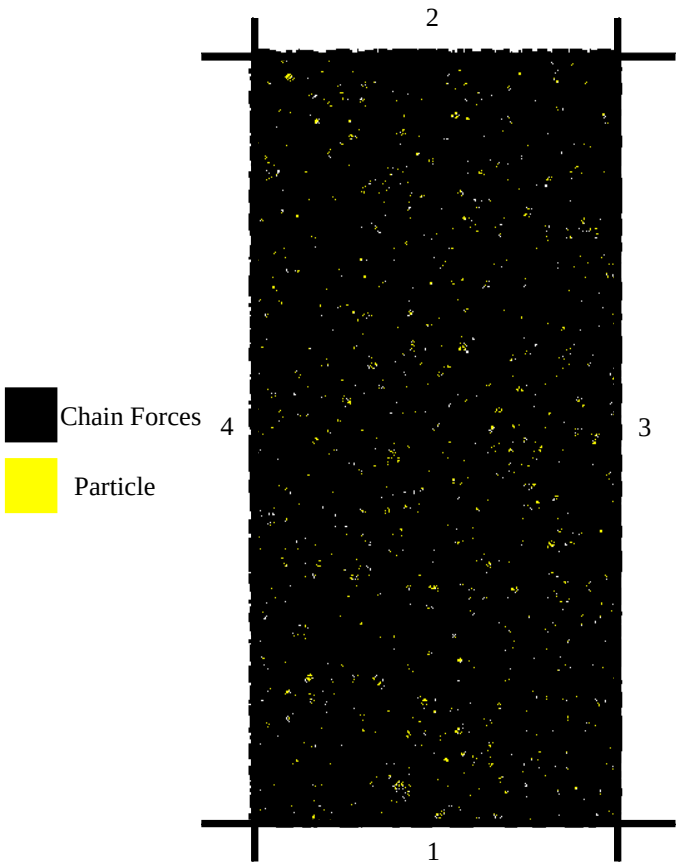

Figure 4-22 Normal contact chain forces

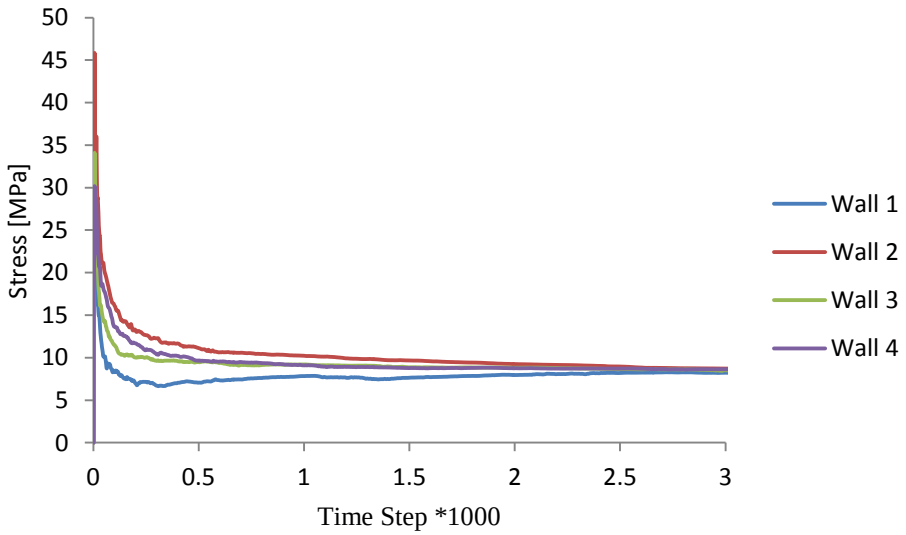

Figure 4-23 The development of macro stresses on four wall vs. time step during particle expansion

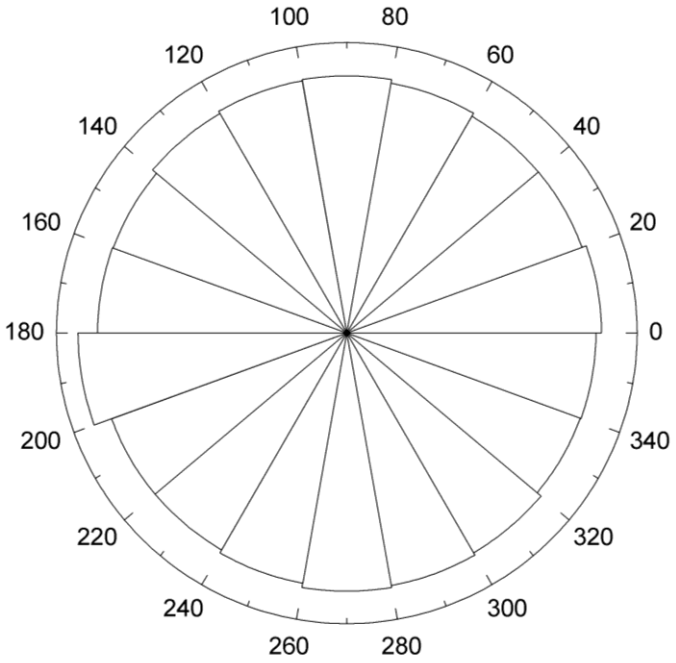

Figure 4-24 The normal contact distribution at the end of expansion

4.3.2 Symmetric geometric deviation index

The fabric quantities such as average coordination number and contact normal distribution provide average data from bulk packing during loading. These global fabric quantities cannot provide information such as the drift from the past contact configurations of a particle to the current contact configurations and how this develops for each single particle during loading. In addition, the stability of each single particle cannot be addressed using these fabric terms. For example consider figure 4-25. The fabric anisotropy for this configuration is zero (i.e. a=0). Although particle A in this figure is stable for the current contact configuration, any imposed force in the x-direction may cause it to be unstable. Thus, a proper fabric quantity should define the deviation of the current contact geometry of each particle from a symmetric geometry or the stables contacts configuration.

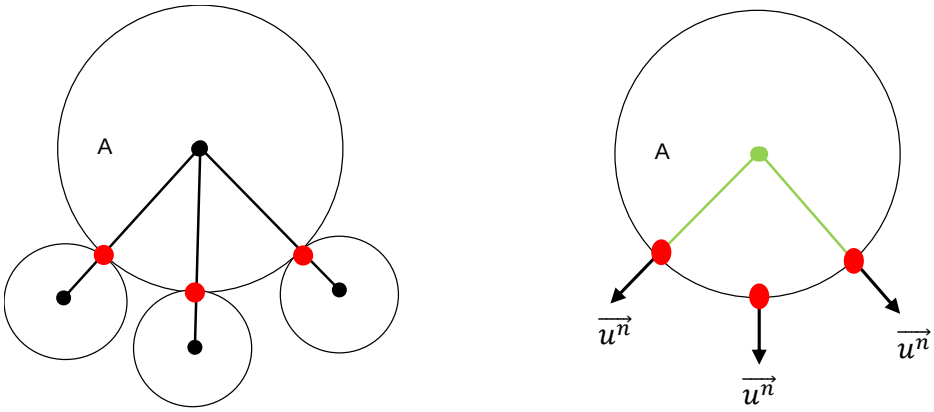

Figure 4-25 A particulate system

A set of n symmetric contact points on a particle is called n-symmetry, if the radial distance between them is $\frac{2\pi}{n}$. Consider figure 4-27. In this figure, the set of 3 blue contact points and 4 red contact points are called 3-symmetry and 4-symmetry.

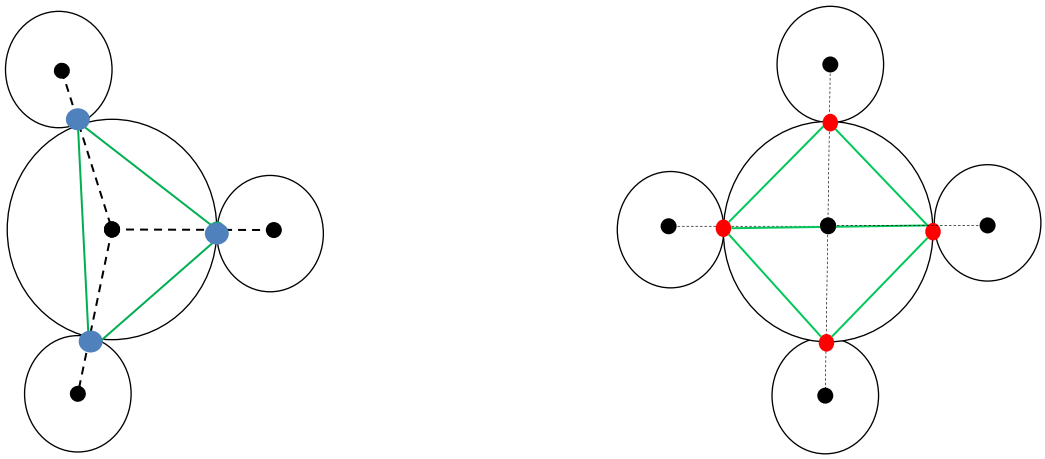

Figure 4-26 A set 3 and 4 of symmetric configurations

An arbitrary set of n-symmetry is shown by S^n and the class of such all sets is shown by $\bar{S}^n$.

Let *M* be a set of *k* contact points of m_j where $j = 1..k$. The radial distance of set M with an arbitrary n-symmetry set is defined as follows:

$$d_M^{S^n} = \sum_{i=1}^{n} d(S_i^n, M) \tag{4.31}$$

in which:

$$d(S_i^n, M) = \min\{d(S_i^n, m_j) |\ \ m_j \in M\} \tag{4.32}$$

in which S_i^n are the contact points for the n-symmetry set.

$$D_M^n = \min\{d_M^{S^n} \,|\, S^n \cap M \neq \phi \ and\ \ S^n \in \bar{S}^n\} \tag{4.33}$$

$$D_M = \min\{D_M^n | n = 3 \dots k\} \tag{4.34}$$

$$\lambda = \frac{D_M}{360} \tag{4.35}$$

in which λ is geometry symmetric deviation index.

Figure 4-27 shows that particle A is in contact with four particles. Therefore, this contact configuration can be compared with 3-symmetric and 4-symmeteric sets as *j*=4. First this contact configuration is compared with 3-symmetric sets (figure 4-27(a)). One of the vertexes in the 3-symmetric set is placed at the one of the contacts (No. 1 in red network). The radial distances (i.e. $d_M^{S^3}$) are then computed for this 3-symmetric set. This applies for other contacts. Then $D_M^3 = \min[d_M^{S^3}, d_M^{S'^3}, d_M^{S''^3}, d_M^{S'''^3}]$ is computed.

This procedure is also applied for 4-symmetric sets (figure 4-27(b)) to compute D_m^4. The best n-symmetric set (i.e. D_M) which is the close to the current contact arrangement of this particle is the minimum of $d_M^{S^3} and\ D_M^3$. To make this quantity dimensionless, it is divided to 360˚. Therefore, λ is the deviation of the current contact arrangement of particle from the best possible symmetric configuration or the stablest contacts configuration.

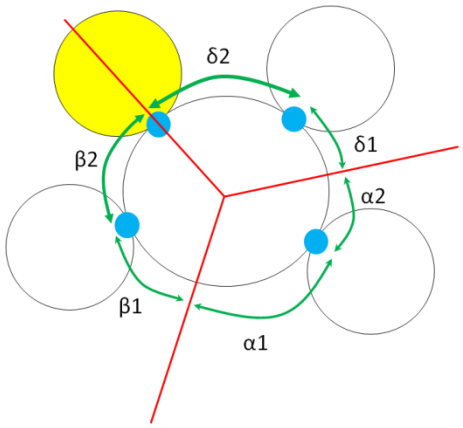

(1)

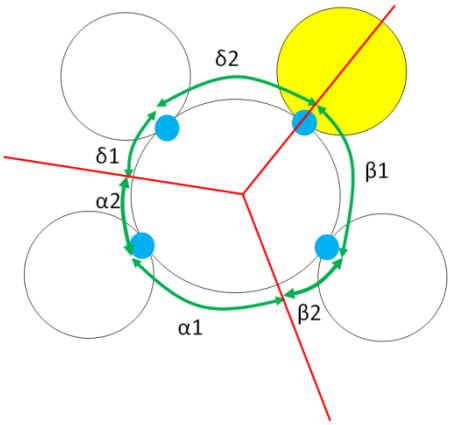

(2)

$d_M^{S^3} = 0 + \min(\beta 1, \beta 2) + \min(\delta 1, \delta 2) + \min(\alpha 1, \alpha 2)$ $d_M^{S'^3} = 0 + \min(\beta 1, \beta 2) + \min(\delta 1, \delta 2) + \min(\alpha 1, \alpha 2)$

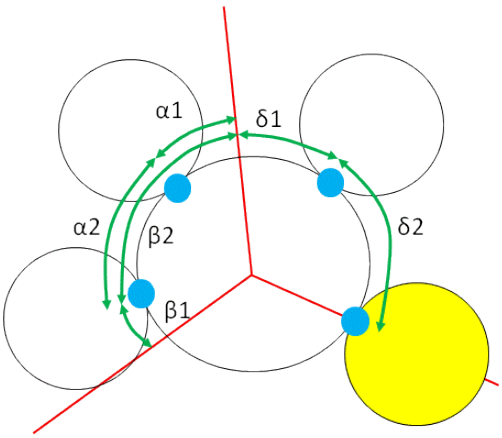

(3)

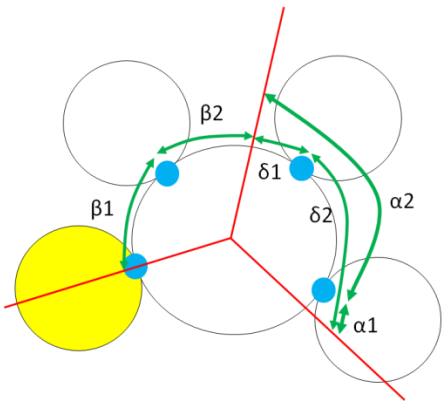

(4)

$d_M^{S''^3} = 0 + \min(\beta 1, \beta 2) + \min(\delta 1, \delta 2) + \min(\alpha 1, \alpha 2)$ $d_M^{S'''^3} = 0 + \min(\beta 1, \beta 2) + \min(\delta 1, \delta 2) + \min(\alpha 1, \alpha 2)$

$$D_M^3 = \min\{d_M^{S^3}, d_M^{S'^3}, d_M^{S''^3}, d_M^{S'''^3}\}$$

(a) Comparing with 3-symmetry sets

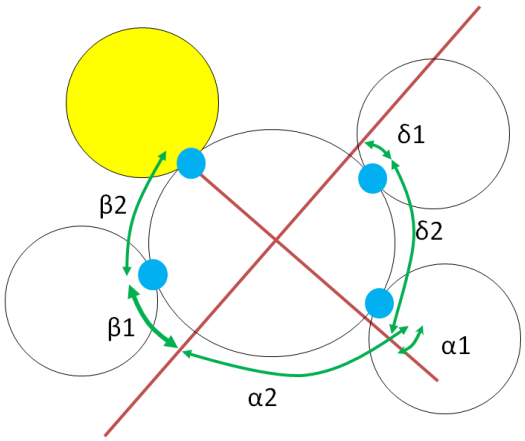

(1)

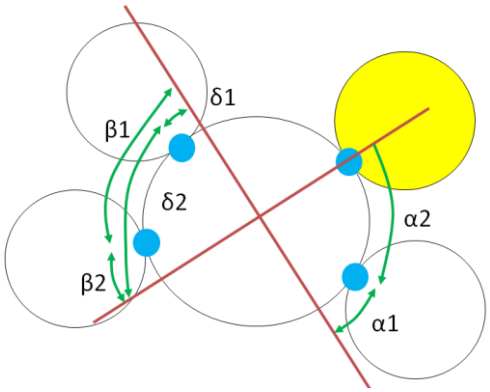

(2)

$d_M^{S^4} = 0 + \min(\beta 1, \beta 2) + \min(\delta 1, \delta 2) + \min(\alpha 1, \alpha 2)$ $d_M^{S'^4} = 0 + \min(\beta 1, \beta 2) + \min(\delta 1, \delta 2) + \min(\alpha 1, \alpha 2)$

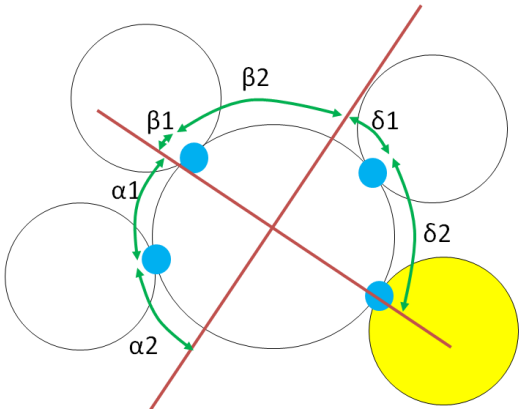

(3)

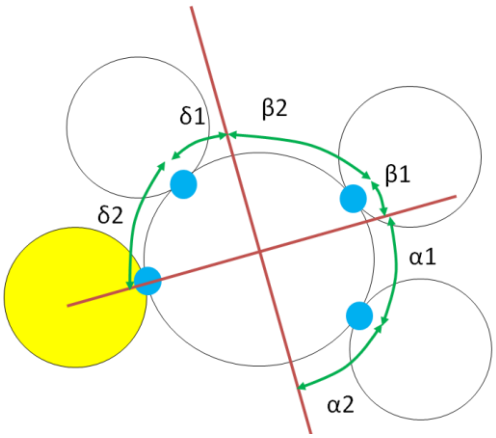

(4)

$d_M^{S''^4} = 0 + \min(\beta 1, \beta 2) + \min(\delta 1, \delta 2) + \min(\alpha 1, \alpha 2)$ $d_M^{S'''^4} = 0 + \min(\beta 1, \beta 2) + \min(\delta 1, \delta 2) + \min(\alpha 1, \alpha 2)$

(b) Comparing with 4-symmetry sets

$$D_M^4 = \min\{d_M^{S^4}, d_M^{S'^4}, d_M^{S''^4}, d_M^{S'''^4}\}$$

$$D_M = \min\{D_M^3, D_M^4\}$$

$$\lambda = \frac{D_M}{360}$$

Figure 4-27 An example of a contact arrangement to apply Eq. 4-31 to 4-35- (a) Comparing with 3-symmetry sets, (b) Comparing with 4-symmetry sets

4.3.3 Porosity

Ideally there should be at least three contact points per particle to achieve the maximum density. This means that there is no zone of instability within a sample. Based on Eq. 4.30, the number of particles needed to fill the chamber is directly related to the target porosity. The number of half-sized particles is placed in the chamber and then expanded to achieve the target porosity. However, some particles, i.e. floating particles, do not have enough contacts to be stable. Therefore, a sensitivity study to establish which porosity values can provide a stable system with a minimum number of floating particles, i.e. a particle with one and zero contact point. For this reason, 43 *PFC*^{2D} simulations, including irregular and hexagonal packing, were carried out. A hexagonal packing is created using single sized particles. The inter-particle properties and mean particle size for all these tests are the same. The simulations were spilt into two groups. In the first group, 33 irregular simulations with different porosities were carried out. The nominal radius of the particles varied between 0.25 and 1.0 [mm]. In the second group, 10 hexagonal packing simulations with equal particles radii but with different porosity were carried out to find the densest packing. The results are drawn in figures 4-28 and 4-29. The results show that there is a reasonable relationship between porosity and coordination number and between coordination number and geometric deviation index such that a decrease in porosity results in an increase in active coordination number and a decrease in geometric deviation index such as:

$$n = -0.0012z^4 + 0.009z^3 - 0.0194z^2 + 0.0081z + 0.1775 \qquad 4.36$$

According to figure 4-28, for a porosity greater than 0.1680, the system will be unstable because the average active coordination number for the model is less than three. Therefore, all values of porosity less than 0.1680 may be appropriate. However, a review of the results based on geometric symmetric deviation index and floating particles obtained from simulation shows that that porosity is more appropriate having less geometric symmetric deviation index and floating particles, such as from 0.08 to 0.12. A porosity of 0.12 was used in this research. It is worth mentioning that the average coordination number obtained from Eq. 3.15 cannot distinguish potential contact and real

contact engaged in chain forces. Thus, another method is required to make distinguish potential contact and real contact. The method proposed by (Thornton, 2000) used to compute the active coordination number is as follows:

$$z = \frac{2 * (N^c - N_1^C)}{N^P - N_1^C - N_0^C} \qquad 4.37$$

in which N^c, N_1^P, N_0^P and N^P are total active contact points, the number of particle with one contact, the number of particle with zero contact and total number of particles.

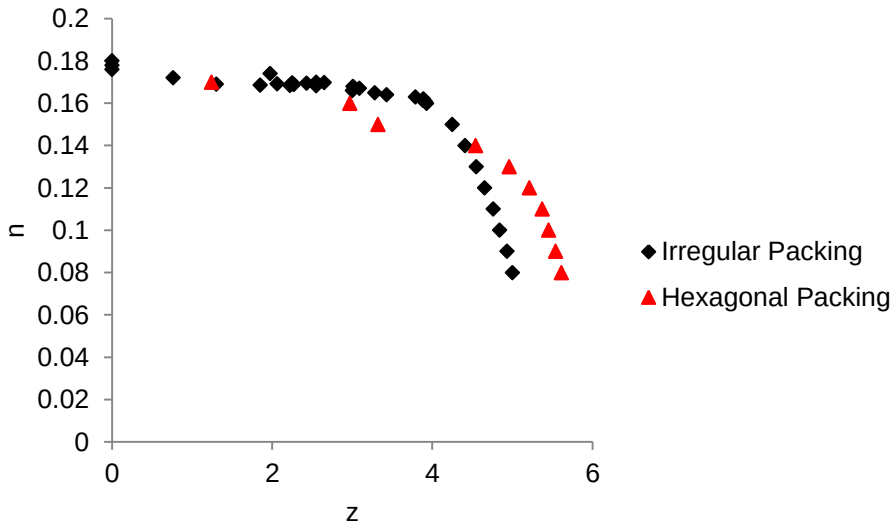

Figure 4-28 The sensitivity study between coordination number and porosity

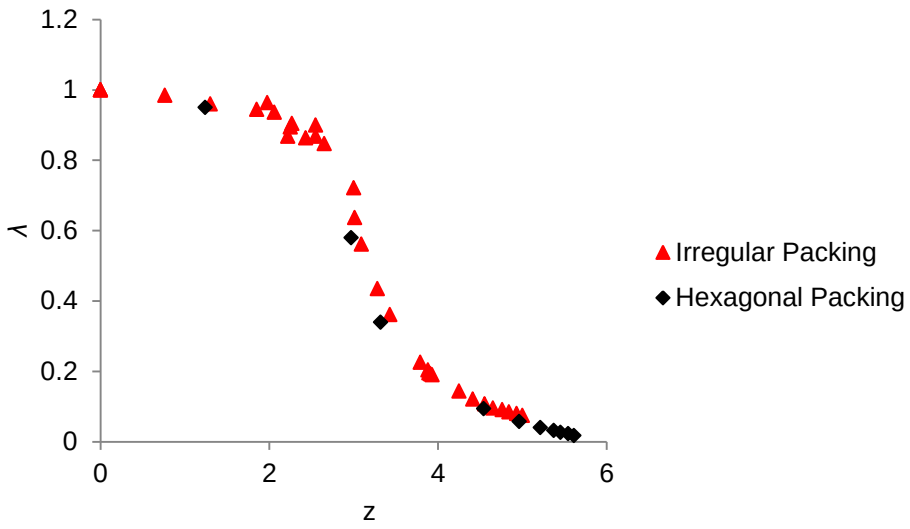

Figure 4-29 The sensitivity study between coordination number and geometry symmetry deviation index

4.3.4 Soil data

The inter-particle parameters of the linear elastic contact model, i.e. normal and tangential stiffnesses and inter-particle friction, must be assigned. The values of elastic modulus, Poisson's ratio and inter-particle friction can be found from literature (see Appendix 2). Inter particle friction is set to zero when the model is created in order to create the porosity required. The internal particle friction coefficient is set to the desired value when the model is created. The tables in Appendix 2 show that quartz sand data vary. If the macro soil properties depend on the inter particle properties then an analysis needs to be undertaken. This will demonstrate that how much each inter-particle property has an effect on the macro-mechanical parameters such as elastic modulus, Poisson's ratio and angle of friction. (Belheine et al., 2009) showed that the inter-particle properties have a significant effect on the macro-mechanical parameters of three-dimensional sand. However, this effect has not been addressed for two-dimensional configurations.

4.3.4.1 The values of inter-particle parameters for PFC^{2D} biaxial tests

The initial values for normal and tangential stiffnesses, which are shown in table 4-1, were obtained from Eq. 4.15 and figure 4-7 at $\frac{U^n}{R} = 0.001$ for various elastic moduli and Poisson's ratio, respectively. The values of inter-

particle coefficient friction are also listed in table 4-2. These values were used for the sensitivity analysis.

E_p [Pa]	Mean size[mm]	k_n (N/m)					k_s (N/m)				
		v_p=0.12	v_p =0.15	v_p =0.2	v_p =0.25	v_p =0.35	v_p =0.12	v_p =0.15	v_p =0.2	v_p =0.25	v_p =0.35
5.40e8	0.625	1.36e7	1.38e7	1.40e7	1.44e7	1.54e7	1.27e7	1.27e7	1.24e7	1.234e7	1.23e7
4.00e9	0.625	1.01e8	1.02e8	1.04e8	1.06e8	1.14e8	9.45e7	9.38e7	9.24e7	9.08e7	8.98e7
8.34e9	0.625	2.11e8	2.13e8	2.17e8	2.22e8	2.38e8	1.97e8	1.95e8	1.92e8	1.90e8	1.87e8
2.32e10	0.625	5.88e8	5.95e8	6.04e8	6.18e8	6.61e8	5.50e8	5.46e8	5.36e8	5.29e8	5.20e8
7.00e10	0.625	1.78e9	1.79e9	1.83e9	1.87e9	2.00e9	1.66e9	1.64e9	1.63e9	1.60e9	1.57e9
7.83e10	0.625	1.98e9	2.00e9	2.03e9	2.08e9	2.23e9	1.85e9	1.83e9	1.80e9	1.78e9	1.75e9
8.00e10	0.625	2.03e9	2.04e9	2.08e9	2.13e9	2.28e9	1.90e9	1.87e9	1.84e9	1.82e9	1.79e9
8.30e10	0.625	2.10e9	2.12e9	2.16e9	2.21e9	2.36e9	1.96e9	1.95e9	1.92e9	1.89e9	1.75e9
8.50e10	0.625	2.15e9	2.17e9	2.21e9	2.27e9	2.42e9	2.01e9	1.99e9	1.96e9	1.94e9	1.91e9

Table 4:1 The normal and tangential stiffnesses values for sensitivity analysis

μ	Particle-wall friction
0.46	0°
0.57	
0.70	
0.90	
1.20	

Table 4:2 The Inter-particle coefficient friction values for sensitivity analysis

4.3.4.2 Selection of data for the sensitivity analysis

The methodology of sorting out the various range of inter-particle values (see table 4-1 and 4-2) for sensitivity analysis in this research is as follows.

For each pair of normal and tangential stiffnesses obtained from the same elastic modulus and Poisson's ratio, the inter-particle coefficient friction is changed from 0.36, 0.46, 0.57, 0.7 and 1.20. This leads to 225 simulations.

For each simulation, the macro-mechanical behaviour such as axial stress vs. axial strain, volumetric strain vs. axial strain and macro-mechanical parameters including elastic modulus, E, and Poisson's ratio, v, and angle of friction, θ, are determined using the theory discussed in Chapter 5. The simulation time required for each test using the current computer takes nearly eight days, performing all of these 225 DEM biaxial simulations proved impossible in the time available. To decrease the number of biaxial tests to an acceptable number of simulations, only the normal and shear stiffnesses based on Poisson's ratio of 0.12 are used. Additionally, only the $\frac{k_s}{k_n}$ =1 and 0.5 are used for this research. The effect of a variation of Poisson's ratio is recommended for further work. In terms of inter-particle coefficient friction only the lower, middle and higher bounds are considered. The inter-particle properties used for this research are listed in tables 4-3 and 4-4.

E_p [MPa]	Mean size [mm]	v_p=0.12		
		k_n (N/m) *10^7	k_s/k_n =1	$\frac{k_s}{k_n}$ =0.5
			k_s (N/m) *10^7	k_s(N/m) *10^7
540	0.625	1.24	1.24	0.62
4000	0.625	8.45	8.45	4.22
8340	0.625	17.1	17.1	8.55
23200	0.625	46	46	23.0
70000	0.625	133	133	66.5
78300	0.625	150	150	75.0
85000	0.625	160	160	80.0

Table 4:3 The revised inter-particle values for the sensitivity analysis

μ	Particle-wall friction
0.5	0°
0.9	0°
1.2	0°

Table 4:4 The revised Inter-particle friction values for the sensitivity analysis

4.3.5 Boundary condition

Having assigned the values of normal and tangential stiffnesses for each particle and wall, the simulation is ready for isotropic consolidation. In order to reach a stable condition, the particle and wall friction are set to zero during this process. At this stage, the constraint of wall fixity, which had been applied at the particle formation stage, is released to allow the walls to move freely. To reach to desired isotropic stress at the boundaries of a sample, a proper servo mechanism code is required. Note that the term servo mechanism is used by Itasca (2008), the software developers. Thus, a Fish code was developed for a servo mechanism to maintain the confining pressure on four boundary walls.

4.3.5.1 The rigid wall-basis servo-control mechanism

Isotropic stresses are maintained during consolidation and a deviatoric stress is applied during the loading stage. The vertical walls are maintained at constant pressure. At the start of each time step, the value of the wall stress, $\sigma^{(w)}$, obtained from Eq. 3.22 is compared with $\sigma^{(t)}$. If the wall stress is equal to $\sigma^{(t)}$, the wall velocity will be set to zero; otherwise the wall velocity, $\dot{u}^{(w)}$, should be adjusted through the following relation:

$$\dot{u}^{(w)} = G\left(\sigma^{(w)} - \sigma^{(t)}\right) \quad \text{where} \quad G \leq \frac{\alpha A}{K_n \Delta t} \tag{4.38}$$

where G, α, A, k_n and Δ_t is the gain parameter, the relaxation factor, wall area, average normal contact stiffness of those particles in contact with wall and time step. In practice, the relaxation factor, α, is set to 0.5 (Itasca, 2008). For stability, the absolute value of the change in wall stress must be less than the absolute value of the difference between the measured and target stresses. This prevents overshooting of the target stress, which would lead to an oscillation about the target stress that would grow in an unbounded fashion and lead to instability.

4.3.5.2 The deformable boundary particles-basis servo-control mechanism

The algorithm to provide a deformable boundary is more complex in comparison with that for a rigid wall. When the granular system reaches the isotropic state in a biaxial test, the vertical rigid walls are removed.

The boundary particles should form two continuous chains at the edge of the model connecting the horizontal walls. This means that the centroid of a particle (i) is above the centroid of particle (i – 1) and below the centroid of particle (i + 1). However, this is not always the case as shown in figure 4.32. This means that some particles at the edge of the model are not part of the deformable boundary. This means that the deformable boundary lies within a boundary zone shown in Figure 4.31. Trial and error showed that the zone was ten times the mean particle size.

To identify the boundary particles, a path is followed from the base wall (figure 4.30) using the centroid criteria. It starts with the particle (A in figure 4.31) to the left of the model. The pathway to the left is followed until it reaches particle D. At this point the path comes to the top boundary. Particle D is defined as a degenerate particle which is not part of the deformable boundary. The degenerate particles were identified throughout the boundary zone (the yellow particles in figure 4.31). Once the degenerate particles are identified, those particles connected to them as shown in figure 4.33.The clear particles in figure 4.33 are particles that could form the deformable boundary. The actual deformable boundary for the left side of the sample, the grey particles, is shown in figure 4.34. This is the continuous chain of particles to the furthest left of the sample.

The inter particle friction of the boundary particles is set to zero because it is assumed that these particles from the interface between the external pressure and the soil model and only transmit lateral pressure. In practice, latex is used which is considered a frictionless material (O'Sullivan, 2007). While in practice a uniform pressure is applied, in the DEM model a force is applied to each boundary particle (figure 4.34b). The force divided by the effective area is equal to the external pressure. The effective area is defined

by the line connecting the two contact points which define the pathway though the particle.

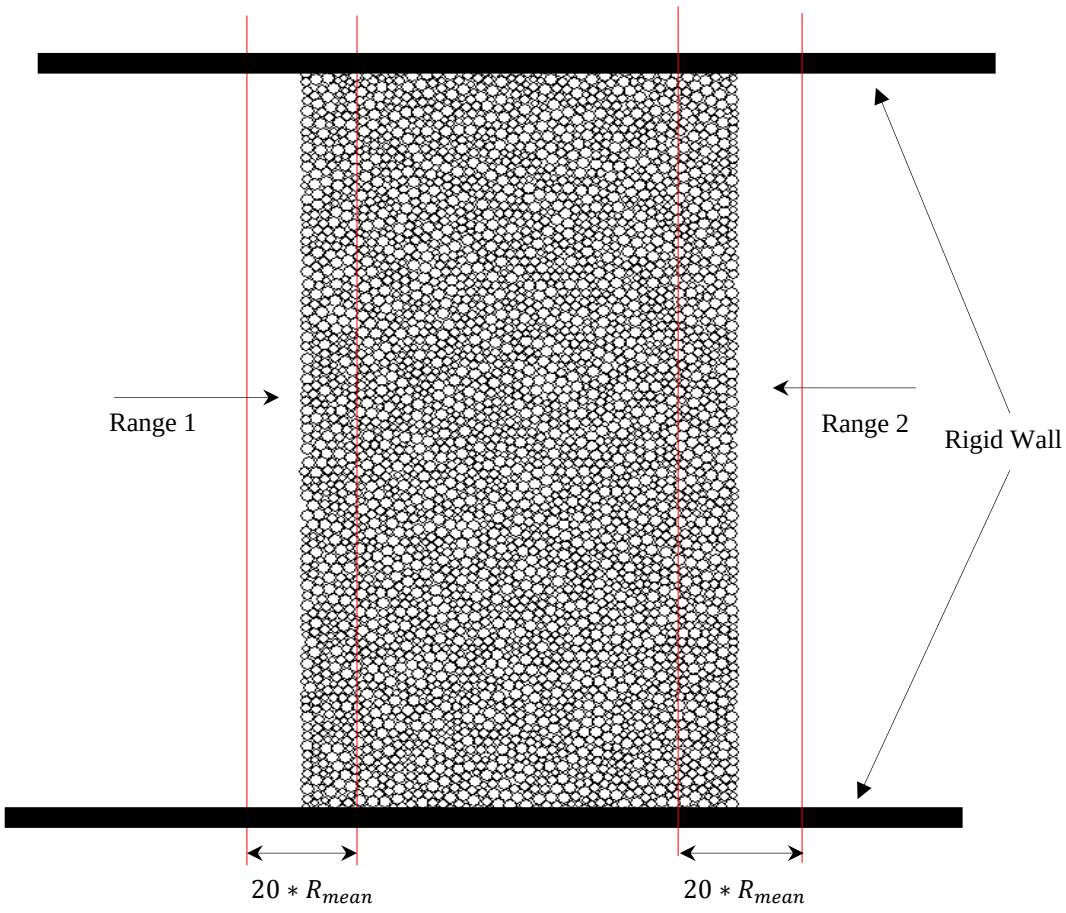

Figure 4-30 Define two separate ranges for left and right hand side of the sample

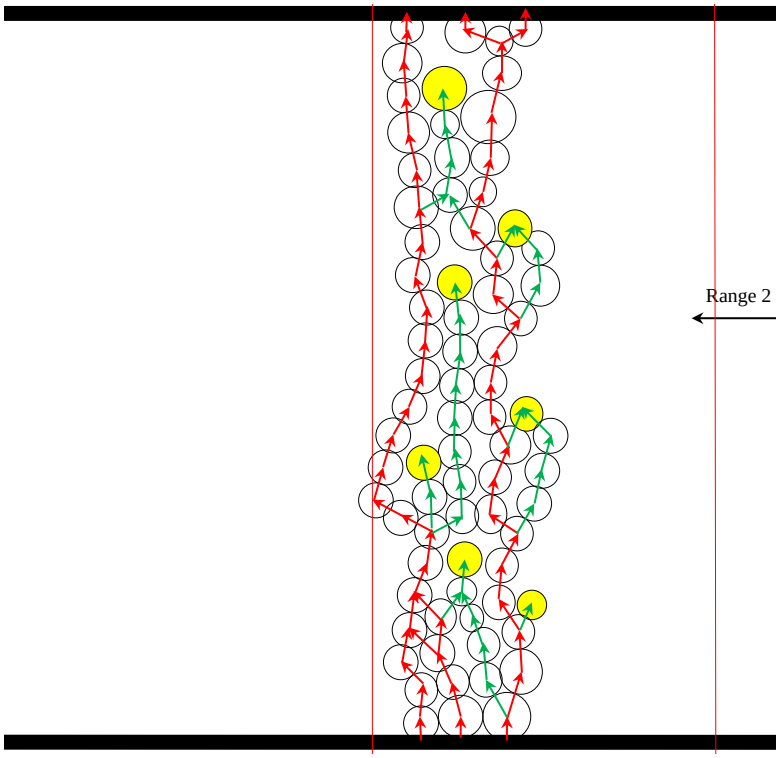

Figure 4-31 Finding the degenerate particles on left boundary schematically

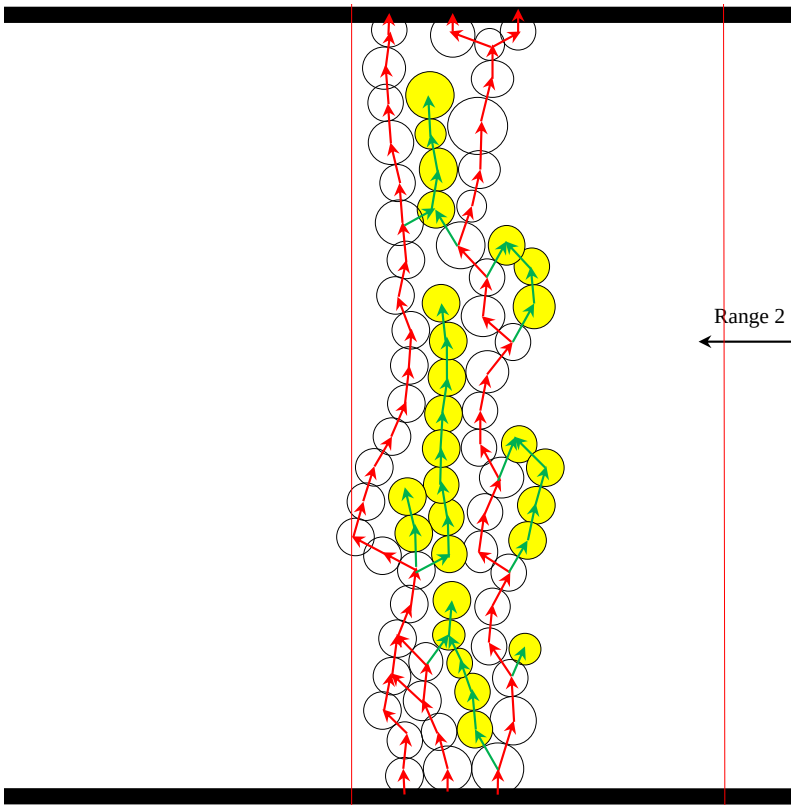

Figure 4-32 Determination of all degenerate particles and paths within Range 2 (left range) schematically

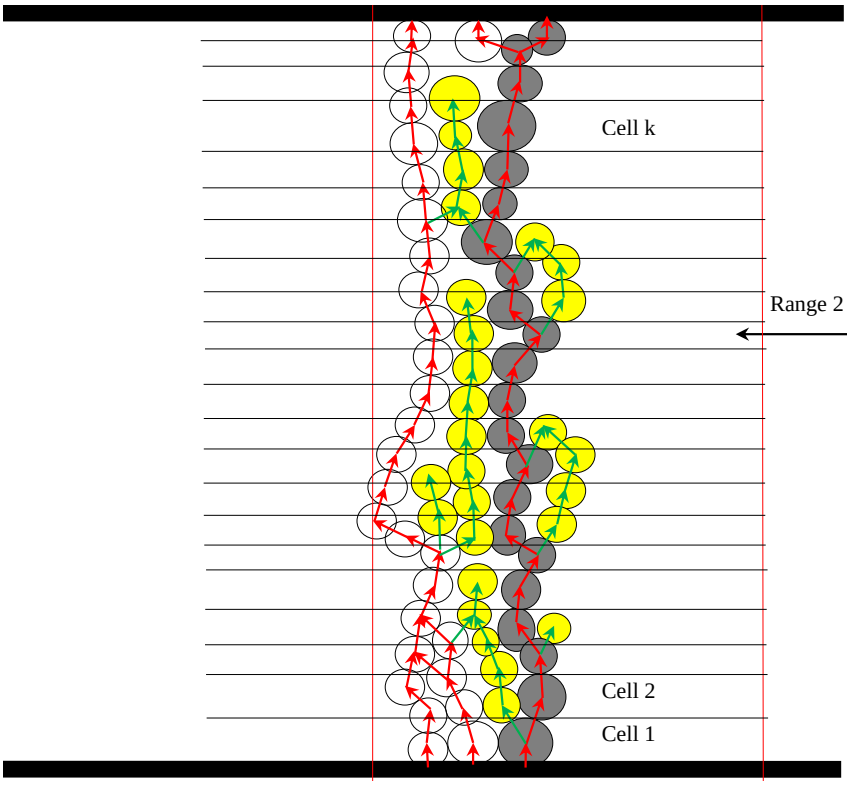

Figure 4-33 Determination of boundary particles

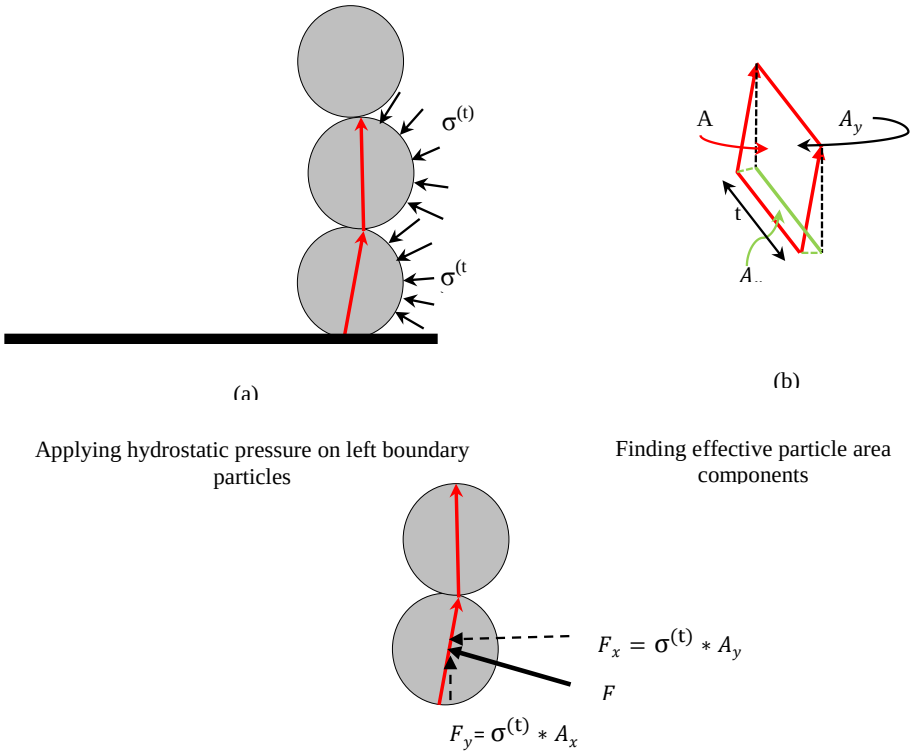

Figure 4-34 Applying hydrostatic forces on left boundary particles schematically

As the deviatoric loading proceeds, some particles escape from the model. A force is applied to those particles to push them back to edge of the model. Once these particles come into contact with the model, their velocity is set to zero. The process to identify the boundary particles is repeated.

The advantages of this approach over those mentioned in chapter three are that the boundary particles are always in real contact though the actual particles forming the boundary may change between time steps and the boundary is updated every time step.

4.3.5.3 Deviatoric loading

When the system reaches an isotropic stress state, the top and bottom platens are moved inward at a constant velocity to perform a biaxial test. For a quasi-static problem, the strain rate should be applied very slowly to the top and bottom walls of chamber (e.g. $2.2*10^{-5}$ (1/s)) such that the incremental acceleration of each particle on left hand side of Eq. 3.12 at each time step is small. However, completing the simulations with such small strain rate value may take several days due to the very small time step, obtained from Eq. 4.28. As the critical time step is proportional to the particle mass (see Eq. 4.28), a mass scaling is adopted to increase both the critical time step and local viscous damping. This reduces the computational time of DEM simulations significantly. For a quasi-static state in which particle acceleration is nearly zero and no body force is applied, the contact forces and displacements are not sensitive to the mass density (Soroush and Ferdowsi, 2011). To consider the effect of mass scaling, a dimensionless parameter has been introduced, called dimensionless inertia parameter, I (e.g. Sheng et al., 2004, Agnolin and Roux, 2007).

$$I = \sqrt{\frac{\dot{\varepsilon}^2 \rho r_{min}^2}{p_y}} \qquad 4.36$$

where $\dot{\varepsilon}$, r_{min}, p_y and ρ are the strain rate, the minimum radius of the particles, the limiting contact pressure between particles and the density of the particles. There is a transition zone in the behaviour of the materials near $I = 10^{-3}$ for which higher values of I leads to a transient and dynamic behaviour, and the behaviour maintains a quasi-static response for lower

values. In these simulations, I is used to control the density scaling effect and maintain the behaviour of the assembly in the quasi-static response range. For example, Soroush and Ferdowsi (2011) applied this method to study the cyclic behaviour of sand. The value of particle density in this work was $2*10^{18}$ (kg/m^3). To ensure the effect of mass density on the macro-mechanical behaviour is negligible, four simulations with different particle densities were implemented. The value of ρ is shown in table 4-6-

Test number	ρ (kg/m^3).
Test 2	2650 (real value of quartz sand particle)
Test 3	$2*10^8$
Test 4	$2*10^{12}$
Test 5	$2*10^{18}$

Table 4:5: The value of ρ

The results of sensitivity analysis are shown in chapter 5.

4.4 Conclusion

In this chapter the development of a DEM model, which is required for the sensitivity analysis performed in Chapter 5 using *PFC^{2D}*, was discussed. The main assumptions and limitations of *PFC^{2D}* were also presented. The numerical stages which were required to prepare the idealized sand sample including the generation of the particles and the methods of filling the biaxial chamber were discussed. It was seen that the use of radial expansion to fill the chamber was much faster than the gravitational method. It was also seen that the use of Hertz model which was originally based on spherical particles to model the normal contact stiffness of disk particle produces an unrealistic response. The new normal contact stiffness model developed for disk particles was able to take into account the non-linear elastic behaviour of the contact. However, a C^{++} code would have to be developed for this contact model so only the initial normal contact stiffness obtained from this method was used.

An investigation into the properties of quartz sand was undertaken to establish the range of inter particle properties to be considered in the sensitivity analysis. Given the time for simulation the actual number of analyses was limited.

The simulations were carried out using deformable boundaries. A description of the generation of these boundaries for the quasi static simulations was provided. The criteria for the deformable boundary is formed of a continuous chain of particles such that the centroid of each particle was above the centroid of the particle below. This meant that some particles in the boundary zone were degenerate particles which fell outside the deformable boundary. The number of these particles was limited and was assumed to have little effect on the overall analysis.

A new fabric quantity term called “symmetric geometric deviation index” was also defined. This term is able to investigate the stability of each single particle by comparing the current contact configurations with the possible symmetric states.

Chapter 5

5 The results of biaxial tests

5.1 Introduction

The sensitivity of macro-micro mechanical properties of sand (i.e. Young's modulus, Poisson's ratio, angle of internal friction, to the micro-mechanical parameters (i.e. $k_n, k_s \; and \; \mu$) of a single sand particle, presented in table 4-3 and table 4-4 was studied by performing a series of quasi-static DEM biaxial tests using rigid boundary. The effects of applying deformable boundary particles to maintain the confining pressure at the vertical sides on the macro-micro response of sand was also investigated and compared with those obtained from an analysis based on rigid boundary. The analyses were used to investigate the effects of confining pressure.

The pre-peak and peak behaviour of the sand material was studied. Interpretation of sand behaviour at the critical state obtained from these simulations is beyond the scope of this thesis, though the macro-mechanical behaviour and micro-mechanical behaviour i.e. fabric quantities evolution at these stages are shown. The *PFC*^{2D} biaxial simulations are performed under the limitations and assumptions explained in the previous chapter. The micro-mechanical properties used for the simulations are taken from table 4-3 and 4-4. It is to be noted that only those normal stiffnesses based on Poisson's ratio of particle 0.12 are considered in this work due to the time of simulation.

As mentioned in chapter four (see section 4.2.1), an important aspect with respect to biaxial tests is to interpret their results. Since a two-dimensional *DEM* code is used, what happens in the third dimension is not known. Thus, the results should be interpreted assuming either a plane-strain or a plane-stress situation. Both situations are discussed and compared in this chapter.

Section 5.2 gives the difference between the plane-strain and plane-stress situation. The typical behaviour of dry medium and dense sand are discussed in Section 5.3. The results of sensitivity analysis are shown in Section 5.4. Conclusions are presented in Section 5.5.

5.2 Plane-strain and plane-stress behaviour

The behaviour of the majority of geotechnical problems such as tunnels, retaining walls, earth dams, strip foundations, slope stability is assumed to be dependent on the vector displacement field in two dimensions and the effect of vector displacement field in third dimension is not very evident on the behaviour. This situation in continuum mechanics is called plane-strain. From this situation, the three-dimensional problem is analysed as a two-dimensional problem where the values of the strain tensor components in the third dimension are set to zero (i.e. $\varepsilon_{33} = \tau_{31} = \tau_{32} = 0$). In some cases in continuum mechanics, the stress tensor field is also two-dimensional. In this case, the stress in the third dimension is the intermediate stress. This situation is called plane-stress. This does not apply in DEM analysis because no stress and strain tensor exists in DEM models. Instead, in two-dimension DEM only two in-plane force components and one out-of-plane moment (see figure 2-3d) exists. By applying an averaging method an average stress and strain tensor can be computed. However, only the in-plane forces and displacements are used to calculate the average stress and strain tensor (see chapter 2) and the out-of-plane force and displacement are not taken to calculate the average stress and strain tensor. Therefore, the out-of-plane constraint which is essential to enforce a state of plane strain or plane stress cannot be present. Hence, the interpretation of *PFC*^{2D} results in terms of either plane strain or plane stress will be a controversial issue. In this section the formulations of plane-stress and plane-strain needed to describe both situations are explained. The macro parameters (i.e. Elastic modulus, Poisson's ratio and angle of internal friction) obtained from these two situations will be compared, in order to view the differences between both interpretations.

5.3 The typical behaviour of dry sand

As schematically shown in figure 5-1, the general macro–mechanical behaviour of dry sand subjected to the static deviatoric loading in a standard triaxial test is characterized by:

- The initial Young's modulus, E_0 (the value of Young's modulus at very small axial strains usually of the order of 10^{-5}) is an important characteristic of soil deformability and plays an important role in dynamic and static response of soil. This is usually estimated using laboratory or field tests which are related to seismic wave propagation and stiffness degradation curves based on cyclic tests conducted in the laboratory (Okur and Ansal, 2007). Instead, E_{50}, the secant modulus at 50% of peak stress is often used to predict ground movements (Holtz et al., 1981).
- The slope of the volumetric strain vs. axial strain curve at a strain corresponding to half of peak stress is used to compute Poisson's ratio υ_{50} both plane-strain and plane-stress.
- The slope of the volumetric strain vs. axial strain curve at the strain at which the stress is maximum in used to compute the maximum dilatancy angle ψ, where the material starts to show mechanical instabilities (Bolton, 1986).
- In the case of dense and medium sand, the characteristic point, M, corresponds to $\frac{\partial \varepsilon_v}{\partial \varepsilon_{11}} = 0$, where the dilation of the sample starts. The axial strain corresponding to this point varies between sands, and is likely to be between of the order 10^{-4} and 10^{-2} (Atkinson, 2007, Belheine et al., 2009).
- Small strains: these correspond to those ranges of strains which are generally between 0.00001 and 0.1. At this range, the stress-strain curve is highly non-linear and E is strain-dependent. In the case of dense and medium sand, the peak stress ratio or deviatoric stress occurs within this range.
- Large strains: these correspond to strains generally larger than 0.1, where the soil is approaching failure and the shear stiffness becomes small.

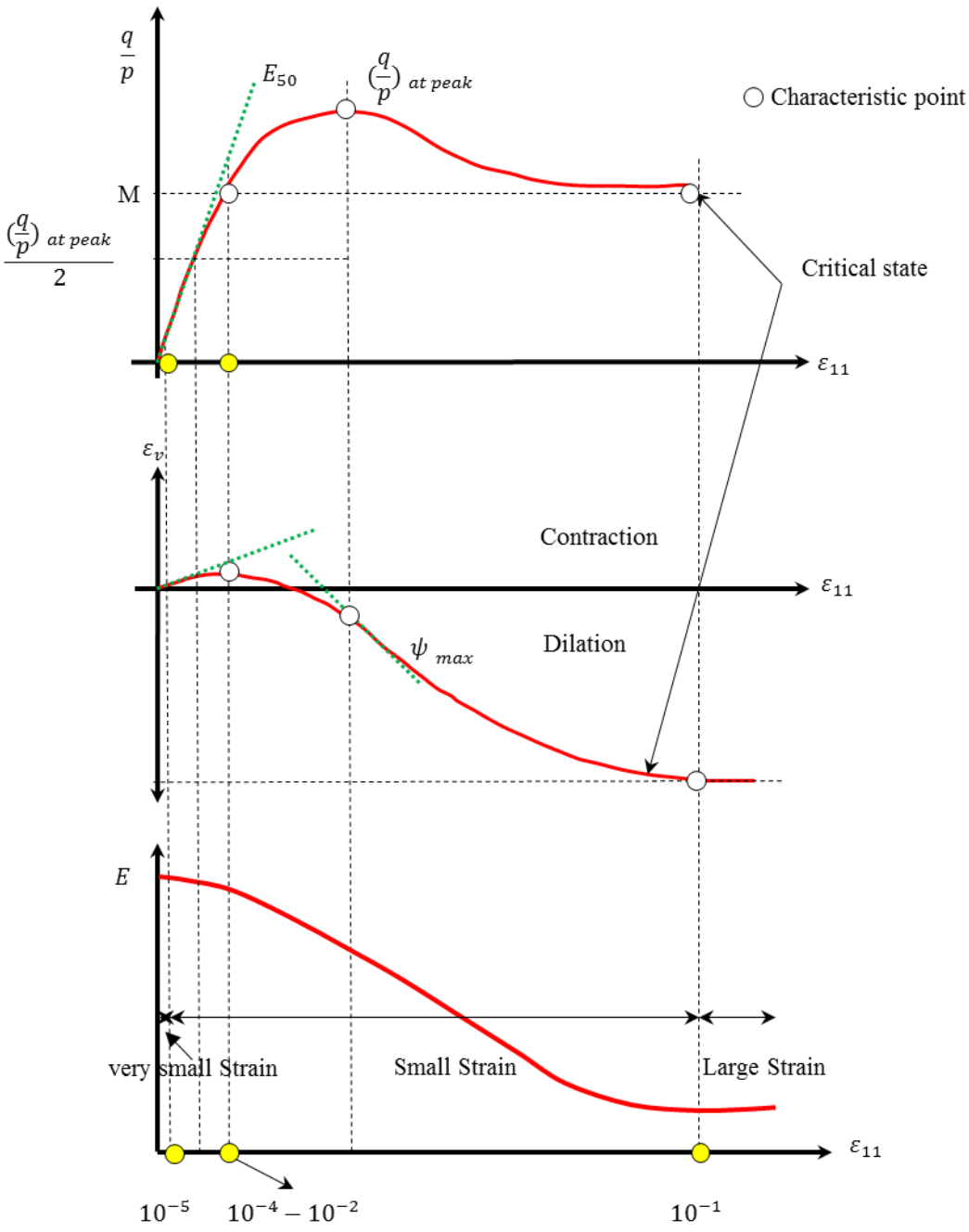

Figure 5-1 The typical behaviour of medium and dense sand

These characteristics are derived from triaxial tests.

5.3.1 Elastic parameters

In soil mechanics it is assumed that at the start of a triaxial test the material is linear elastic. In principal stress space the behaviour is as follows:

$$\begin{pmatrix}\varepsilon_{11}\\ \varepsilon_{22}\\ \varepsilon_{33}\end{pmatrix}=\frac{1}{E}\begin{bmatrix}1 & -v & -v\\ -v & 1 & -v\\ -v & -v & 1\end{bmatrix}\begin{pmatrix}\sigma_{11}\\ \sigma_{22}\\ \sigma_{33}\end{pmatrix} \quad 5.1$$

In terms of plane-strain, the stress-strain relation is as follows:

$$\begin{pmatrix}\varepsilon_{11}\\ \varepsilon_{33}\end{pmatrix}=\frac{1}{E}\begin{pmatrix}1-v^2 & -v(1+v)\\ -v(1+v) & 1-v^2\end{pmatrix}\begin{pmatrix}\sigma_{11}\\ \sigma_{33}\end{pmatrix} \quad 5.2$$

In terms of plane-stress, the stress-strain relation is as follows:

$$\begin{pmatrix}\varepsilon_{11}\\ \varepsilon_{33}\end{pmatrix}=\frac{1}{E}\begin{pmatrix}1 & -v\\ -v & 1\end{pmatrix}\begin{pmatrix}\sigma_{11}\\ \sigma_{33}\end{pmatrix} \quad 5.3$$

The elastic modulus and Poisson's ratio are important characteristics when predicting ground movements as it is often assumed that soil is isotropic and homogenous and behaves elastically. There are numerous methods available to determine these characteristics but the most common is the triaxial test. In this test, using local strain measurements it is possible to measure the stress strain response of the sample of soil subject to a variety of load paths. The values of stiffness obtained are stress path dependent and vary with strain range over which they are measured as well as being a function of the confining stress, the particle geometry and the density of packing. In this study only monotonic compressive loading is monitored. Further, the triaxial test is three dimensional, whereas the DEM analysis used in this study is two dimensional. However, as soil assumed to be isotropic and homogenous material, the material properties obtained from triaxial test can be applied for two-dimensional analysis. In two dimensional studies it is necessary to consider plane stress or plane strain conditions which lead to small different values of stiffness.

In plane-strain situation, the secant Elastic modulus is:

$$E=(1-v^2)\frac{\sigma_{11}}{\varepsilon_{11}} \quad 5.4$$

where σ_{11} is the deviatoric stress value at 50% of peak stress. (ε_{11}) is the corresponding axial strain (see figure 5-1).

In plane-stress situation, the Elastic modulus is:

$$E = \frac{\sigma_{11}}{\varepsilon_{11}} \qquad 5.5$$

It can be seen that when Poisson's ratio is zero, the elastic modulus is equal for the plane-stress and plane stain situations. Also when Poisson's ratio is 0.5 the elastic modulus of plane-strain is 75% the elastic modulus of plane-stress.

Poisson's ratio is obtained from the slope of the horizontal strain vs. axial strain curve. In two-dimensional analysis volumetric strain is $\varepsilon_v = \varepsilon_{11} + \varepsilon_{33}$. In plane-stress condition, Poisson's ratio is obtained from the following equation:

$$\upsilon = -\frac{\varepsilon_{33}}{\varepsilon_{11}} \qquad 5.6$$

where ε_{33} is the horizontal strain and ε_{11} is the axial strain. In plane-strain situation it is:

$$\upsilon_{Plane-strain} = \frac{\upsilon}{1+\upsilon} \qquad 5.7$$

The equations of 5.4, 5.5, 5.6 and 5.7 are converted into Fish language to compute the elastic parameters for the plane-strain and plane-stress cases.

If the slope of the volumetric strain vs. axial strain curve is changed from 0 (lower extreme) to 1.0 (higher extreme) (see figure 5-1), the corresponding values for Poisson's ratio for the plane strain and plane stress situations can be calculated. Table 5-1 shows these values.

Slope of volumetric strain vs. axial strain	υ (Plane-strain)	υ (Plane-stress)
0.0	0.5	1.0
0.5	0.3	0.5
1.0	0.0	0.0

Table 5:1 Values of Poisson's ratio obtained from the slope of the volumetric strain vs. axial strain curve for plane strain and plane stress situations

From this table it is seen that when the slope has such values, Poisson's ratio for the plane strain case has realistic values between 0 and 0.5 while Poisson's ratio in case of plane stress situation has unrealistic values larger than 0.5.

5.3.2 Plastic parameters

Angles of friction, θ, are related to the plastic and failure behaviour of non-cohesive material. For non-cohesive sand the following relationship can be used to compute the angle of friction:

$$\frac{t}{s} = Tan^2(45 + \frac{\theta}{2}) \qquad 5.8$$

where *t* is the deviatoric stress and *s* is the isotropic stress.

5.4 The sensitivity analysis

The macro behaviour of frictional sand is related to its inter-particle properties. A sensitivity analysis will identify which are the critical parameters and the range over which the parameters impact on the macro-mechanical behaviour. Macro-mechanical behaviour is used as the outcome as it provides a link to experimental behaviour, which provides the macro mechanical properties.

The inter-particle properties for each biaxial test are obtained from tables 4-3 and table 4-4. A total of forty two biaxial tests were conducted for this part. The initial condition such as the initial geometry of biaxial chamber, particle size distribution, particle shape, contact model, porosity and isotropic stress state condition and the lateral boundary condition for all of these tests were similar. The initial porosity of system, which was 0.12, was based on section 4.3.3. After generating the particles, the system was allowed to reach static equilibrium. Next, the rigid boundaries of biaxial cell were moved based on the applied strain-control, see section 4.3.5.1., to approach the stress at the boundaries to the 100 [kPa] (see figure 5-2). Once the system was isotropically consolidated, further cycles were needed to reach system equilibrium (i.e. $\frac{|F|_{ave}}{|C|_{ave}} < 0.05$). Due to the time of simulation at this stage, the particle friction was set zero. It is because particles can move freely in an

isotropic state in a reasonable time. Figure 5-3 shows the system met the static equilibrium condition of uniform boundary stresses. Figure 5-4 shows the average velocities of all particles are about zero when the system is in static equilibrium.

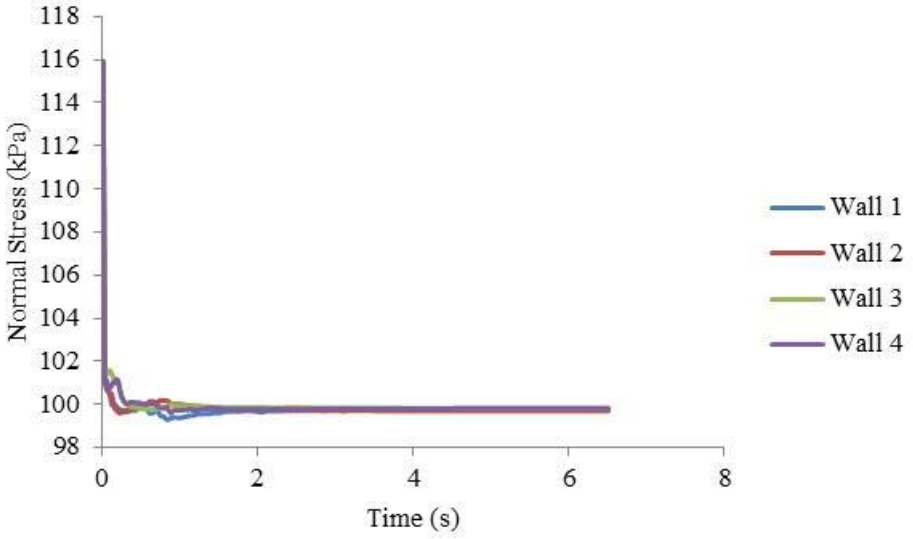

Figure 5-2 The normal stresses on the walls at isotropic consolidation state.

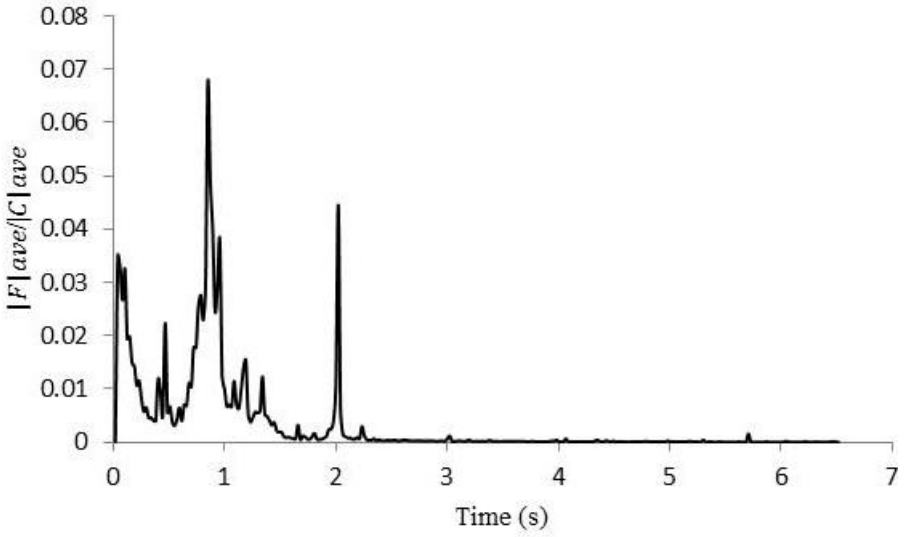

Figure 5-3 The variation of $\frac{|F|_{ave}}{|C|_{ave}}$ by time to show the system reaches to the relative equilibrium.

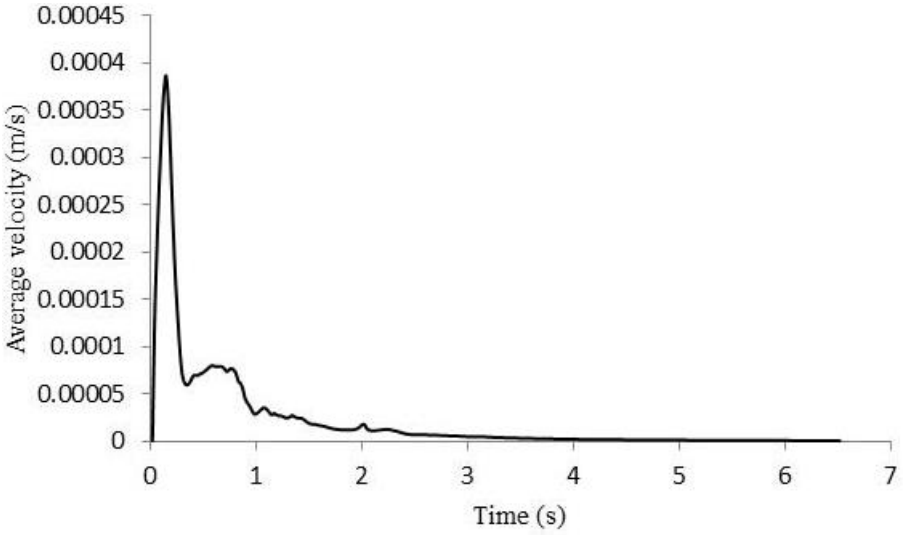

Figure 5-4 The variation of average particles velocity by time to show how the system reaches equilibrium.

The variation of average coordination number of system during isotropic consolidation is shown in figure 5-5.

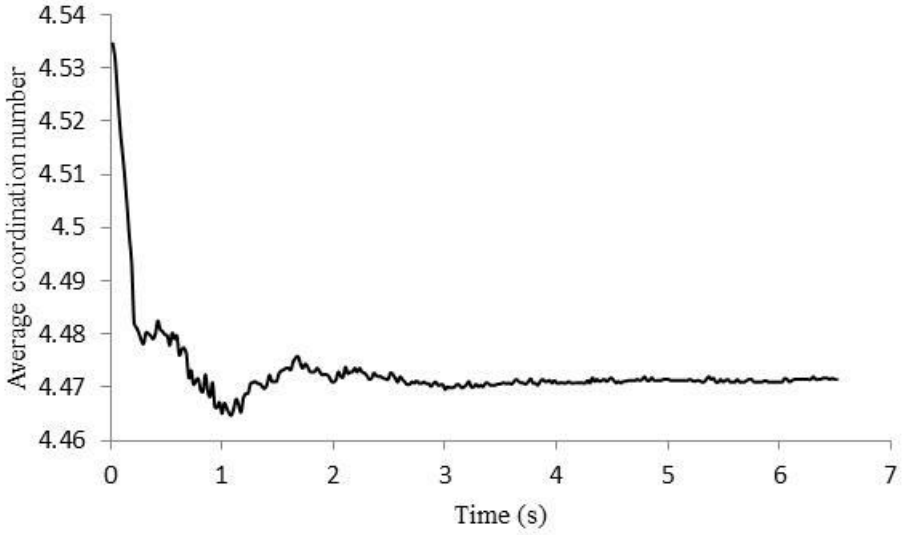

Figure 5-5 The variation of average coordination number by time

The polar diagrams of normal contact distribution and normal contact force distribution at isotropic consolidation are shown in figure 5-6 and 5-7. To draw these polar diagram 18 bins were considered with an angular interval $\Delta\theta = 20^{\circ}$. The radius of each bin in the polar diagram of normal contact and

normal contact force distribution corresponds to the number of contacts and summation of normal contact forces within each angular interval. If polar diagram of is fully circle, it shows that the distribution of normal contact and normal contact force is in isotropic state. That is a and a_n = 0 (see Eq. 3.12 and 3.14). Since, the friction between the particles was zero during isotropic consolidation, no shear contact force distribution was drawn at this stage. Although the macro state of stress shows that the system is in an isotropic state, it can be seen from figures 5-6 and 5-7 that the fabric of the system at this stage is not in an isotropic state because a=0.0034 and a_n=9*10^{-8}.

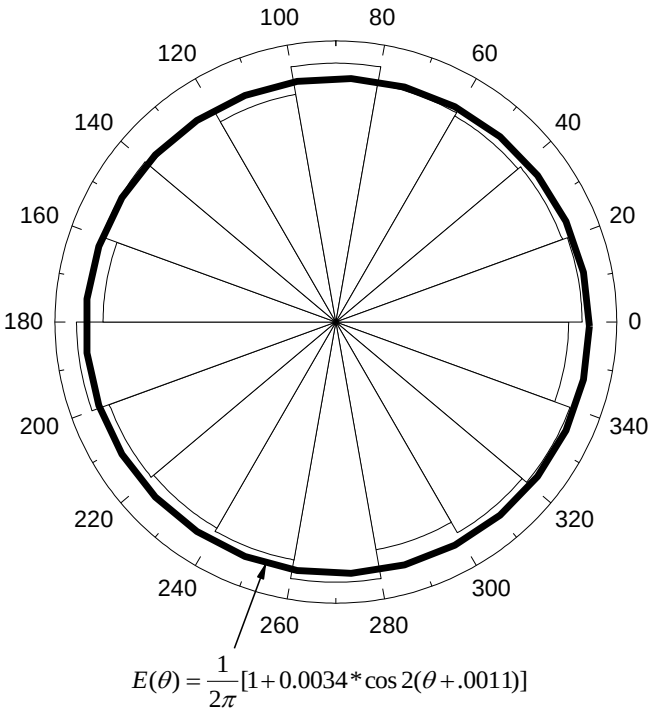

Figure 5-6 Normal contact distribution at the isotropic state.

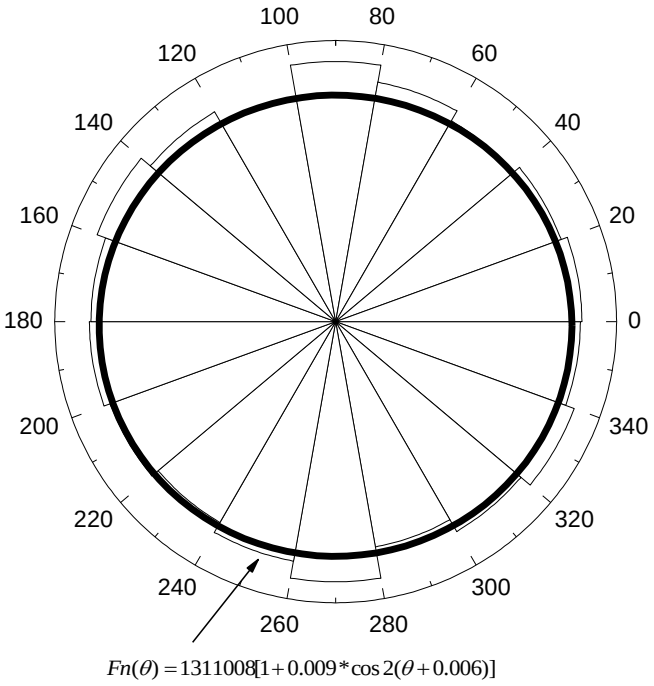

Figure 5-7 Normal contact force distribution at the isotropic state.

Next, the confining pressure on the vertical rigid boundaries was kept constant while the top and bottom rigid boundaries move towards each other to apply a deviatoric stress. In the calibration method (e.g. Belheine et al., 2009) the inter-particle properties (i.e. $k_n, k_s \; and \; \mu$) are attained so that the obtained stress-strain curve from DEM simulations fits to that from triaxial test. However, in the sensitivity analysis the critical parameters and the range over which the parameters impact on the macro-mechanical behaviour is investigated. From each combination of $k_n, k_s \; and \; \mu$, the macro parameters of elastic modulus, Poisson's ratio and angle of internal friction were computed. These values will be then compared with typical Elastic modulus, Poisson's ratio and angle of internal friction of sand obtained from literature (see table 5-2). Additionally, the sensitivity analysis displays that effect of each inter-particle property to the macro-micro behaviour.

Elastic parameter	Medium sand	Dense sand
E [MPa]	30~50 (Obrzud, 2010) 25~50 (Bowles, 1988)	50~80 (Obrzud, 2010) 50~81(Bowles, 1988)
v	0.2~0.35 (Bowles, 1988)	0.3~0.4 (Bowles, 1988)
Friction angle (°)	30~36 (Obrzud, 2010)	36~41 (Obrzud, 2010)

Table 5:2 Typical bulk properties of sand

5.4.1 The methodology of sensitivity analysis

Three inter-particle properties, the normal and shear stiffnesses and inter particle friction, were considered in this research. It was necessary to establish a methodology to measure the effect of each parameter on the macro-micro behaviour expressed in terms of the angle of friction and stiffness of the sample. Each of the inter particle properties were varied keeping the others constant to determine the impact on the macro properties.

5.4.1.1 The sensitivity of sand system to the various particle densities under the quasi static simulation

The time step required to simulate the biaxial test has to be very small in order to prevent instability of the model. To increase the time step, the density scaling approach was used in this work in such a way to realise a sensible time for the simulation. This method is only applicable for quasi-static simulation. That is, I, in Eq.4-36 must be less than 10^{-3} (see 4.3.5.3.) (Sheng et al., 2004). For example, for typical properties of sand, (see Table 5-3),

$\dot{\varepsilon}$ (typical strain rate applied in triaxial test) ($\frac{1}{s}$)	$\frac{2\%}{min}$
ρ (typical sand particle density) ($\frac{kg}{m^3}$)	2650
R_{min} (minimum rounded sand particle radius) (m)	0.000236
p_y (typical limiting contact pressure) (MPa) (Goodman, 1980)	150

Table 5:3 The values are required for *I*.

$I = 3.30^{-10}$. Eq. 4.28 shows a stable time step is also related to the particle mass and particle stiffness. Based on table 4-1, three different orders of magnitude of particle stiffness were considered for quartz sand particle, 10^7, 10^8 10^9 were considered. The initial packing density, number of particles, particle size distribution, and inter-particle properties for these three set of simulations were the same. In the first group of simulations, the sensitivity of macro-mechanical behaviour of idealized sand system to the various particle densities when the particle stiffness was 10^7 $[\frac{N}{m}]$ is examined. The micro-mechanical properties, initial porosity and D_{50} is presented in table 5-4. 13 simulations based on table 5-5 were performed to find an appropriate density for each particle for further simulations. The macro-mechanical behaviour of sand including deviatoric stress vs. strain, volumetric stain vs. axial strain and fabric quantities such as average coordination number vs. axial strain, degree of anisotropy vs. axial strain and average geometric symmetric deviation index vs. axial strain for the first group of simulations are presented from figures 5-8 to 5-12.

Initial porosity	0.12
D_{50} (m)	0.000625
k_n $(\frac{N}{m})$	$1.25*10^7$
k_s $(\frac{N}{m})$	$1.25*10^7$
μ	0.2
v_p	0.15

Table 5:4 The initial porosity and micro-mechanical properties to measure the sensitivity of system to the various particle densities

Test number	ρ (kg/m^3)	I
Test 1	2650 (real value of quartz sand particle)	$3.30*10^{-10}$
Test 2	$2*10^{4}$	$9.07*10^{-10}$
Test 3	$2*10^{6}$	$9.07*10^{-9}$
Test 4	$2*10^{7}$	$2.87*10^{-8}$
Test 5	$2*10^{8}$	$9.07*10^{-8}$
Test 6	$2*10^{9}$	$2.87*10^{-7}$
Test 7	$2*10^{10}$	$9.07*10^{-7}$
Test 8	$2*10^{11}$	$2.87*10^{-6}$
Test 9	$2*10^{12}$	$9.07*10^{-6}$
Test 10	$2*10^{13}$	$2.87*10^{-5}$
Test 11	$2*10^{14}$	$9.07*10^{-5}$
Test 12	$2*10^{15}$	$2.87*10^{-5}$
Test 13	$2*10^{16}$	$9.07*10^{-4}$

Table 5:5 The various values of density for the sensitivity analysis

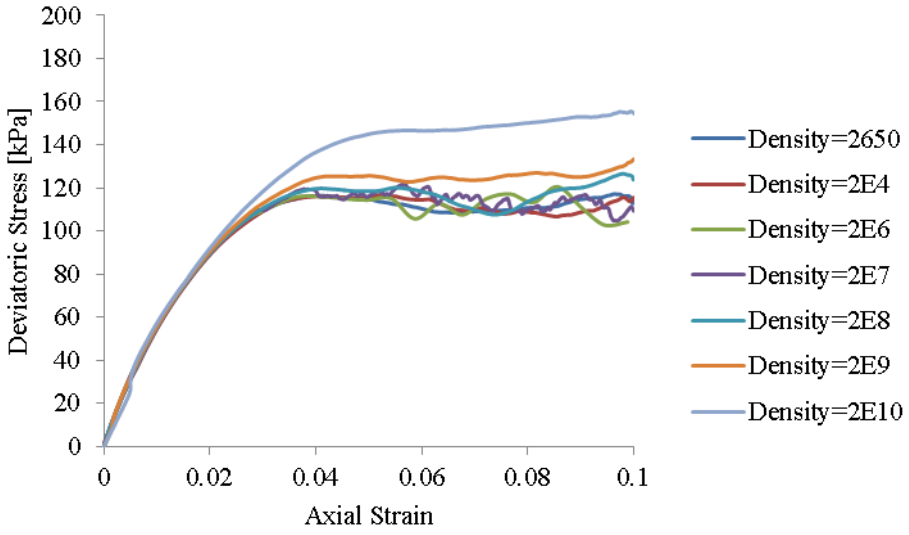

Figure 5-8 The sensitivity of sand response to the different particle density when the normal stiffness of particle was 10^7: deviatoric stress vs. axial strain

Figure 5-8 shows that the stress strain behaviour when ρ is between 2650 $[\frac{kg}{m^3}]$ and $2*10^8$ $[\frac{kg}{m^3}]$ are similar. When the density exceeds $2*10^8$ $[\frac{kg}{m^3}]$ the results indicate hardening behaviour which is not consistent with real sand behaviour (Mitchell and Soga, 2005). Since the rate of applying deviatoric

loading is very small also the density of particles is very high, the tendency of particles to move decreases. That is, the particles' velocity decreases (see figure 5-9). This decrease in particles' velocity is more evidence for the higher particle density (i.e. 2*10^8 [$\frac{kg}{m^3}$]).

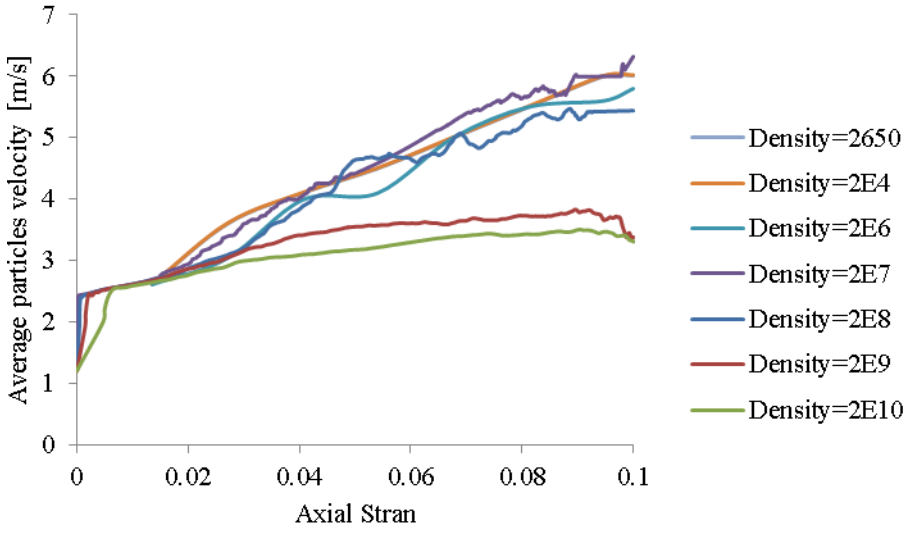

Figure 5-9 The sensitivity of average particle velocity to the various particle density when the normal stiffness of particle was 10^7

Therefore, the shear capacity of the bulk corresponding to the particle density 2*10^8 [$\frac{kg}{m^3}$] is more than others. This fact also shows in figure 5-10 where for the higher particle density the ability of system to develop normal contact anisotropy (or anisotropy degree) increases, while increasing ρ between 2650 [$\frac{kg}{m^3}$] and 2*10^9 [$\frac{kg}{m^3}$] has a slight effect on this fabric. As the particle inertia increase, the tendency of losing contacts per particles decrease especially in the case of 2*10^{10} [$\frac{kg}{m^3}$]. Thus, the average coordination number in the case of higher particle density slightly increases (see figure 5-11).

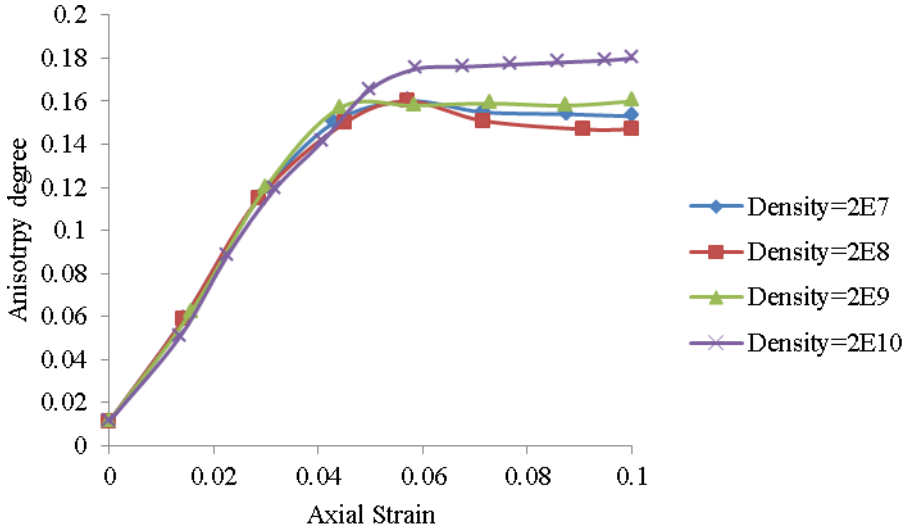

Figure 5-10 The sensitivity of average anisotropy degree to the various particle density when the normal stiffness of particle was 10^7

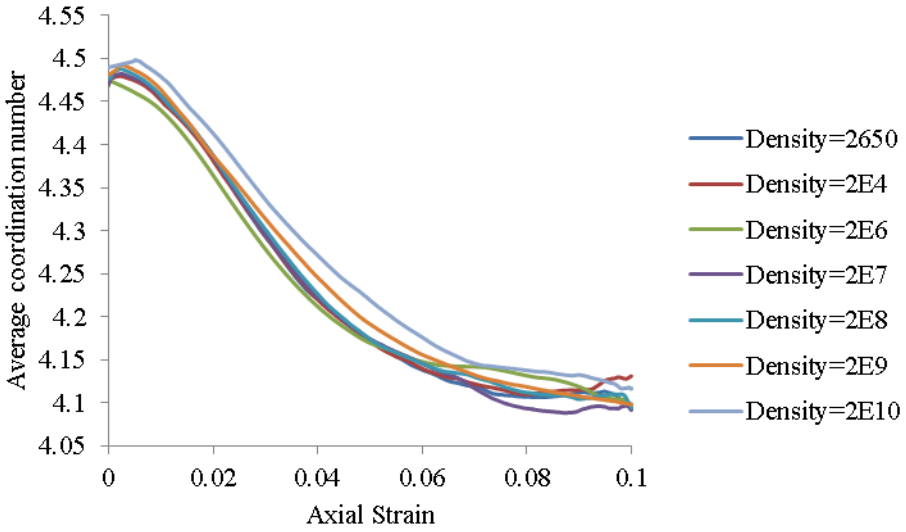

Figure 5-11 The sensitivity of average coordination number to the various particle density when the normal stiffness of particle was 10^7

Figure 5-12 shows that the average stability of bulk increases by increasing the particle density. It was seen around axial strain 0.3 a significant change in the slope of λ takes place which corresponds with the maximum deviatoric stress (see figure 5-8). This inflection point is consistent with change in the slope of average particles velocities (see figure 5-9).

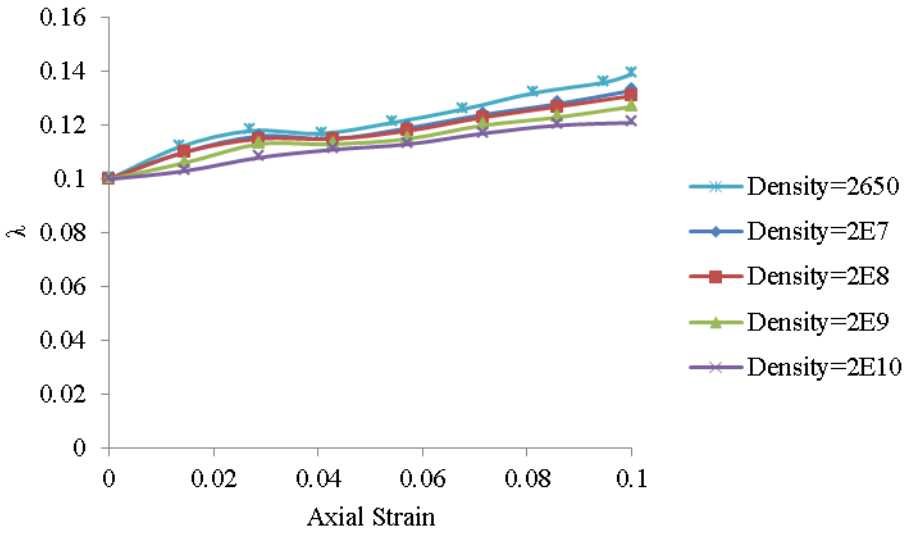

Figure 5-12 The sensitivity of average geometric symmetric deviation index, λ, to the various particle density when the normal stiffness of particle is of order 10^7

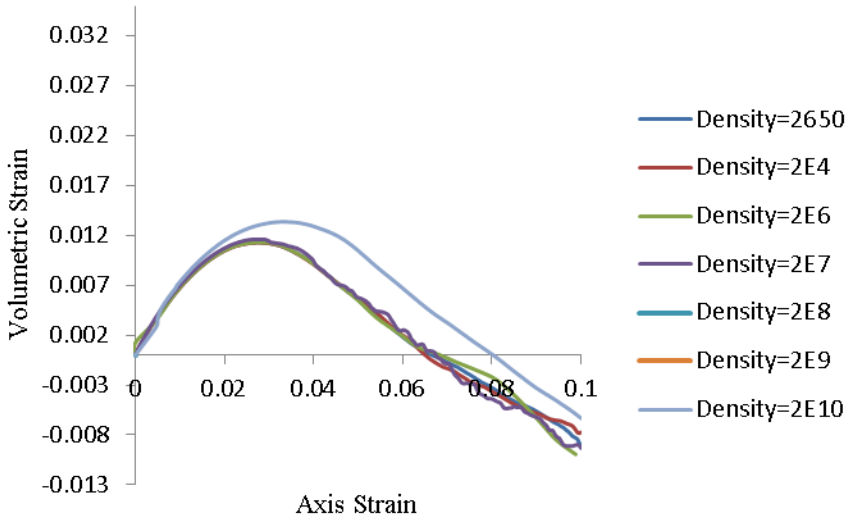

Figure 5-13 The sensitivity of sand response to the different particle density when the normal stiffness of particle was 10^7: volumetric strain vs. axial strain

Figure 5-13 shows that the volumetric behaviour when ρ is between 2650 $[\frac{kg}{m^3}]$ and 2*10^9 $[\frac{kg}{m^3}]$ is similar. However, for density 2*10^{10}, the starting of bulk dilation takes place at the higher value of axial strain. It is because the tendency of particles movement over each other in order to show the expansion reduces. These results show that a density of 2*10^8 $[\frac{kg}{m^3}]$ gives similar results to the natural density of 2650 $[\frac{kg}{m^3}]$, therefore, 2*10^8 $[\frac{kg}{m^3}]$ was used for further simulations if the normal stiffness of the particles is of order 10^7 $[\frac{N}{m}]$ to reduce the time of processing.

For the second group of simulations, the sensitivity of macro-mechanical behaviour of idealized sand system to the various particle densities when the particle stiffness is 10^8 $[\frac{N}{m}]$ was examined. The micro-mechanical properties, initial porosity and D_{50} are presented in table 5-6.

Initial porosity (n)	0.12
D_{50} (m)	0.000625
k_n ($\frac{N}{m}$)	4.62*10^8
k_s ($\frac{N}{m}$)	4.62*10^8
μ	0.2
v	0.15

Table 5:6 The initial porosity and micro-mechanical properties to measure the sensitivity of system to the various particle densities.

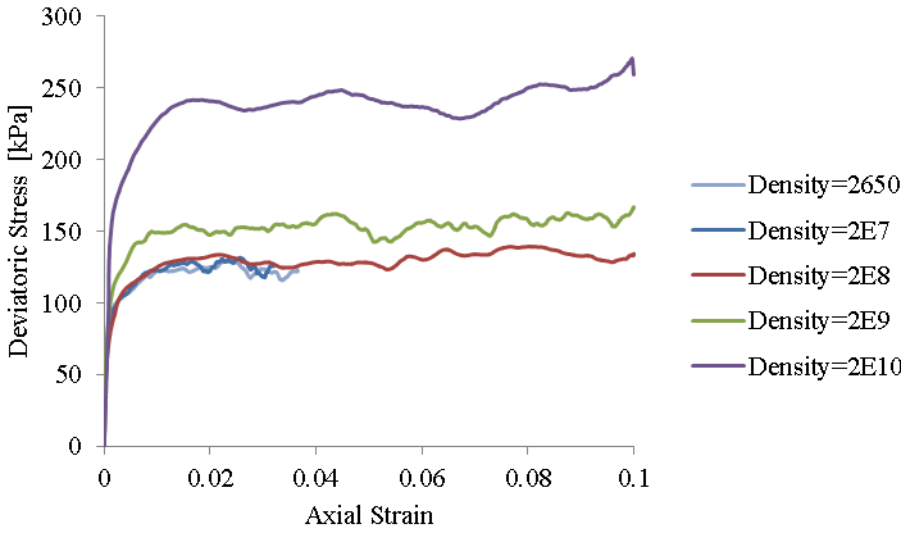

Figure 5-14 The sensitivity of sand response to the different particle density: deviatoric stress vs. axial strain when the normal stiffness of particle is of order 10^8

The figures 5-14 and 5-15 show that the macro-mechanical behaviour of this particulate system is independent of the particle density if it is between the range of 2650 $[\frac{kg}{m^3}]$ and 2*10^8 $[\frac{kg}{m^3}]$. Therefore, ρ = 2*10^8 $[\frac{kg}{m^3}]$ is used for the further simulations for a particle stiffness of 10^8 $[\frac{N}{m}]$. As seen increase in particle stiffness leads to that the slope of deviatoric stress become more deeper in comparison with that for a particle stiffness of 10^7 $[\frac{N}{m}]$. It is because the normal contact forces significantly increases. Therefore, the shear capacity of single particle remarkably increases. This fact will be discussed in details at section 5.4.1.3. As the shear capacity of system increases, the tendency of particle to move decreases considerably. Thus, The threshold of dilation behaviour significantly decreases for a particle stiffness of 10^8 $[\frac{N}{m}]$.

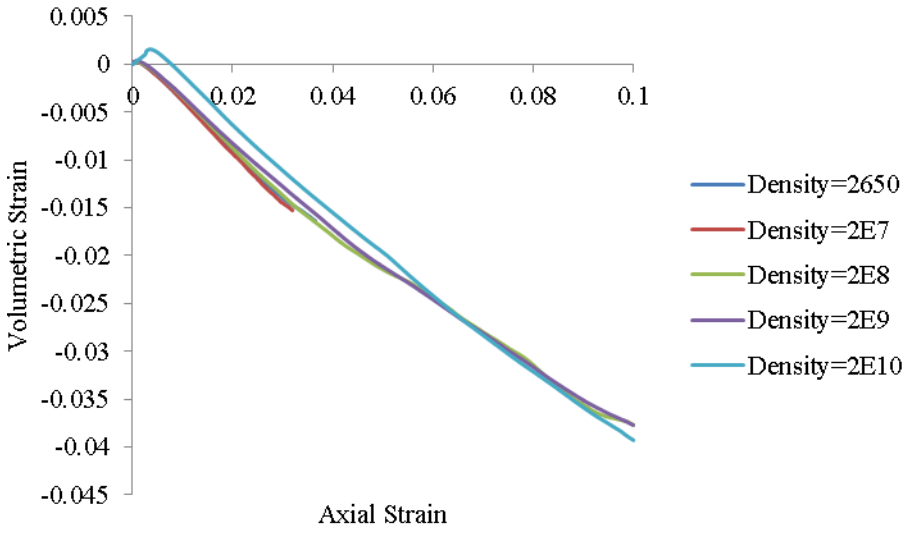

Figure 5-15 The sensitivity of sand response to the different particle density: volumetric strain vs. axial strain when the normal stiffness of particle is of order 10^8

For the third group of simulations, the sensitivity of macro-mechanical behaviour of idealized sand system to the various particle densities when the particle stiffness was 10^9 $[\frac{N}{m}]$ is examined. The micro-mechanical properties, initial porosity and D_{50} are presented in table 5-7.

n	0.12
D_{50} (m)	0.000625
k_n $(\frac{N}{m})$	$1.5*10^9$
k_s $(\frac{N}{m})$	$1.5*10^9$
μ	0.2
v	0.15

Table 5:7 The initial porosity and micro-mechanical properties to measure the sensitivity of system to the various particle densities

Figures 5-16 and 5-17 clearly show that the macro-mechanical behaviour of this particulate system is independent of the particle density if it is between the range of 2650 $[\frac{kg}{m^3}]$ to $2*10^8$ $[\frac{kg}{m^3}]$. Therefore, $\rho = 2*10^8$ $[\frac{kg}{m^3}]$ is used for the further simulations for a particle stiffness of 10^9 $[\frac{N}{m}]$.

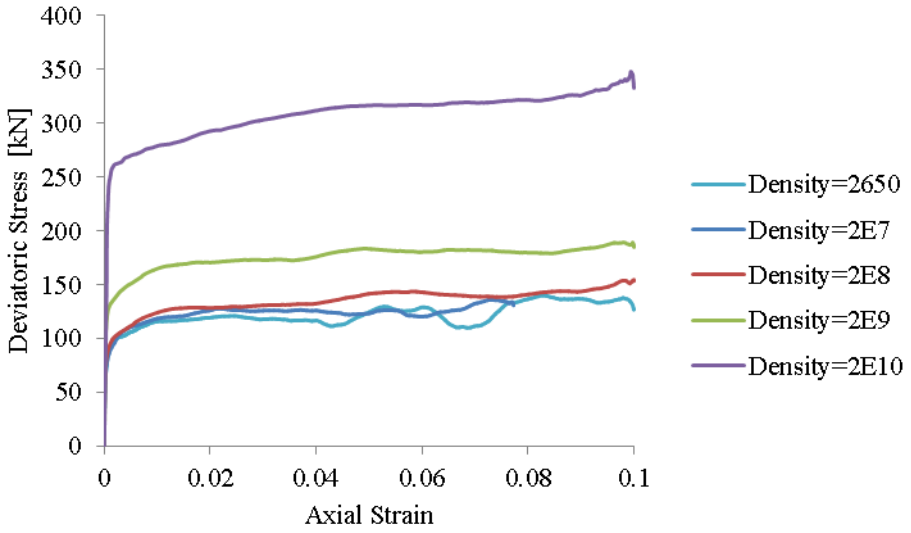

Figure 5-16 The sensitivity of sand response to the different particle density: deviatoric stress vs. axial strain when the normal stiffness of particle is of order 10^9

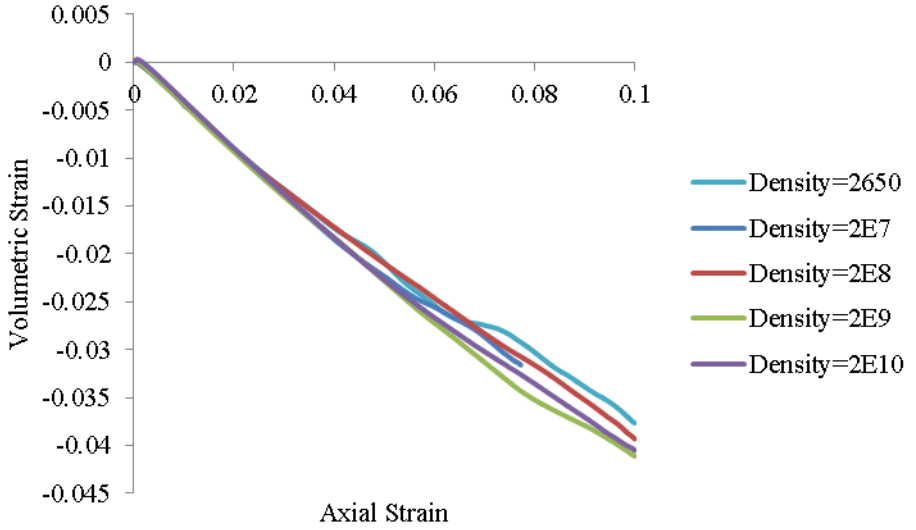

Figure 5-17 The sensitivity of sand response to the different particle density: volumetric strain vs. axial strain when the normal stiffness of particle is of order 10^9

5.4.1.2 The sensitivity of sand system to the inter-particle coefficient friction

Twenty one biaxial tests with rigid boundary particles were carried out to determine the effect the inter particle coefficient of friction has upon the macro behaviour of the model. The input data for these 21 tests is listed in table 5-8. The results of the tests in terms of deviatoric stress vs. axial strain and volumetric strain vs. axial strain are shown in Appendix 3. The

interpretation of the tests to show the effect of the inter particle coefficient of friction upon the average coordination number, average fabric anisotropy, average normal contact force anisotropy, average shear contact force anisotropy, average symmetric geometric deviation index is show in Appendix 3.

Figures 5.18 to 5.21 show the effect of the inter particle friction on the macro properties the angle of friction, the peak stress, the secant stiffness at 50% of the peak stress and Poisson's ratio.

$k_n\ [\frac{N}{m}]$	$k_s\ [\frac{N}{m}]$	μ	$\rho\ [\frac{kg}{m^3}]$	n
$1.24*10^7$	$1.24*10^7$			
$8.45*10^7$	$8.45*10^7$			
$17.1*10^7$	$17.1*10^7$			
$46.0*10^7$	$46.0*10^7$	0.5,0.9,1.2	$2*10^8$	0.12
$133.0*10^7$	$133.0*10^7$			
$150.0*10^7$	$150.0*10^7$			
$160.0*10^7$	$160.0*10^7$			

Table 5:8 The micro-mechanical parameters for performing a series of biaxial tests of sand system to investigate the sensitivity of system to the particle friction.

The peak stress (Figure 5.18) increases as the inter-particle friction increases though it is independent on the inter particle stiffness. Note that in *PFC^{2D}*, there is no rolling friction between the particles. This is compensated by increasing the inter-particle friction.

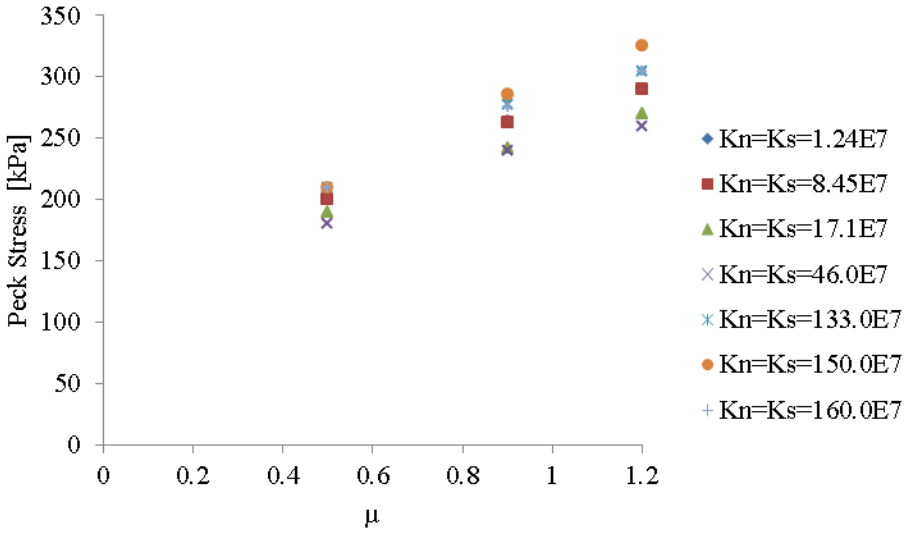

Figure 5-18 The sensitivity analysis: μ vs. Peak stress.

The angle of friction (Figures 5-19) increases as the inter particle friction increases but is not affected by the inter particle stiffness. The angle of friction between 28° and 37° is typical for medium and dense sand. The angle of friction was computed using Eq. 5.8.

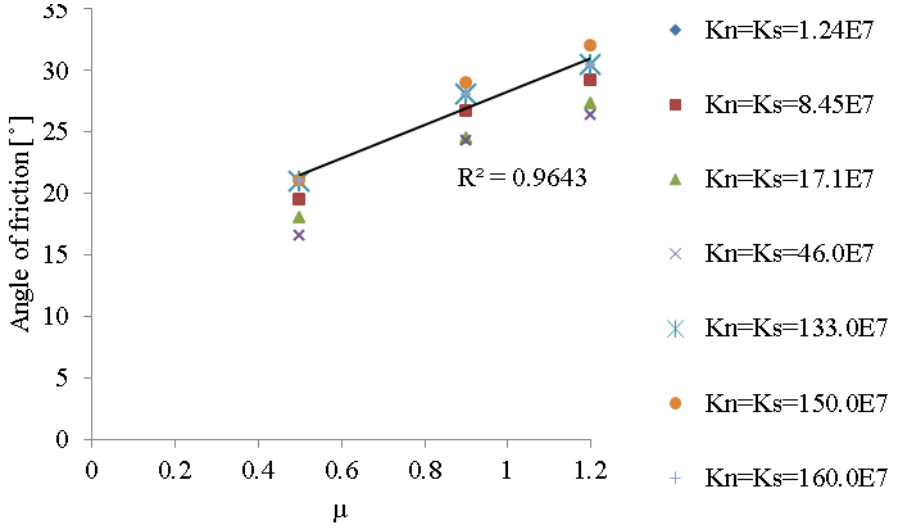

Figure 5-19 The sensitivity analysis: μ vs. angle of friction.

Based on the data provided for this study, a relationship between inter-particle friction and angle of friction can be developed as follows:

$$\theta = 13.5\mu + 14.8 \qquad 5.9$$

where θ and μ are angle of friction and inter-particle coefficient friction. Note, this relationship is developed for inter-particle coefficient between 0.5 and 1.2. Figure 5.20 shows E_{50} vs. inter-particle friction, for both plane stress and plane stress conditions, that the sample stiffness is more dependent on the inter particle stiffness than the inter particle friction. The relationship between the inter particle friction changes as the inter particle stiffness increases.

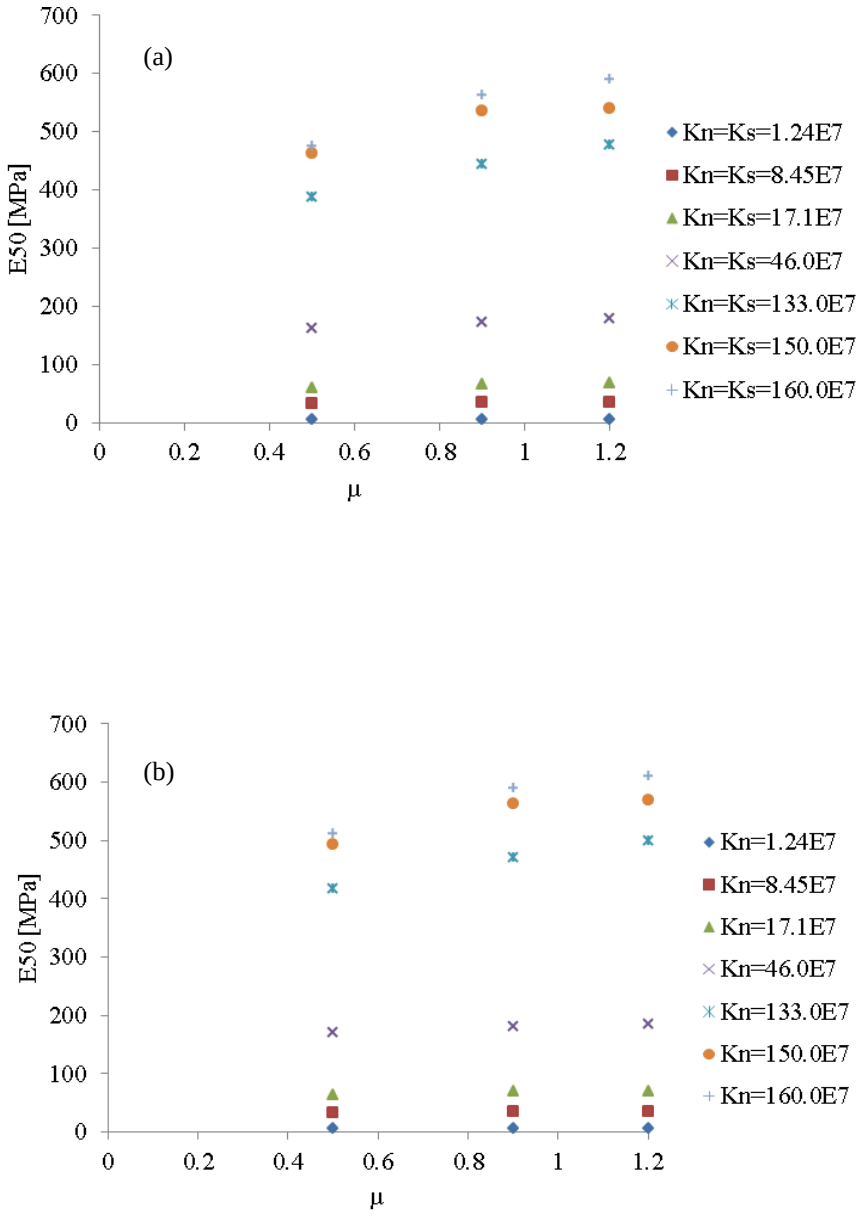

Figure 5-20 The sensitivity analysis: μ vs. E_{50}. (a) Plane-strain (b) Plane-stress

Figure 5-21 shows that increasing the inter-particle coefficient friction leads to a slight increase in Poisson's ratio. As inter-particle coefficient friction leads to increase the magnitude of inter-particle forces, the contact deformations and particles displacements increases. This leads to increase the lateral deformation of system.

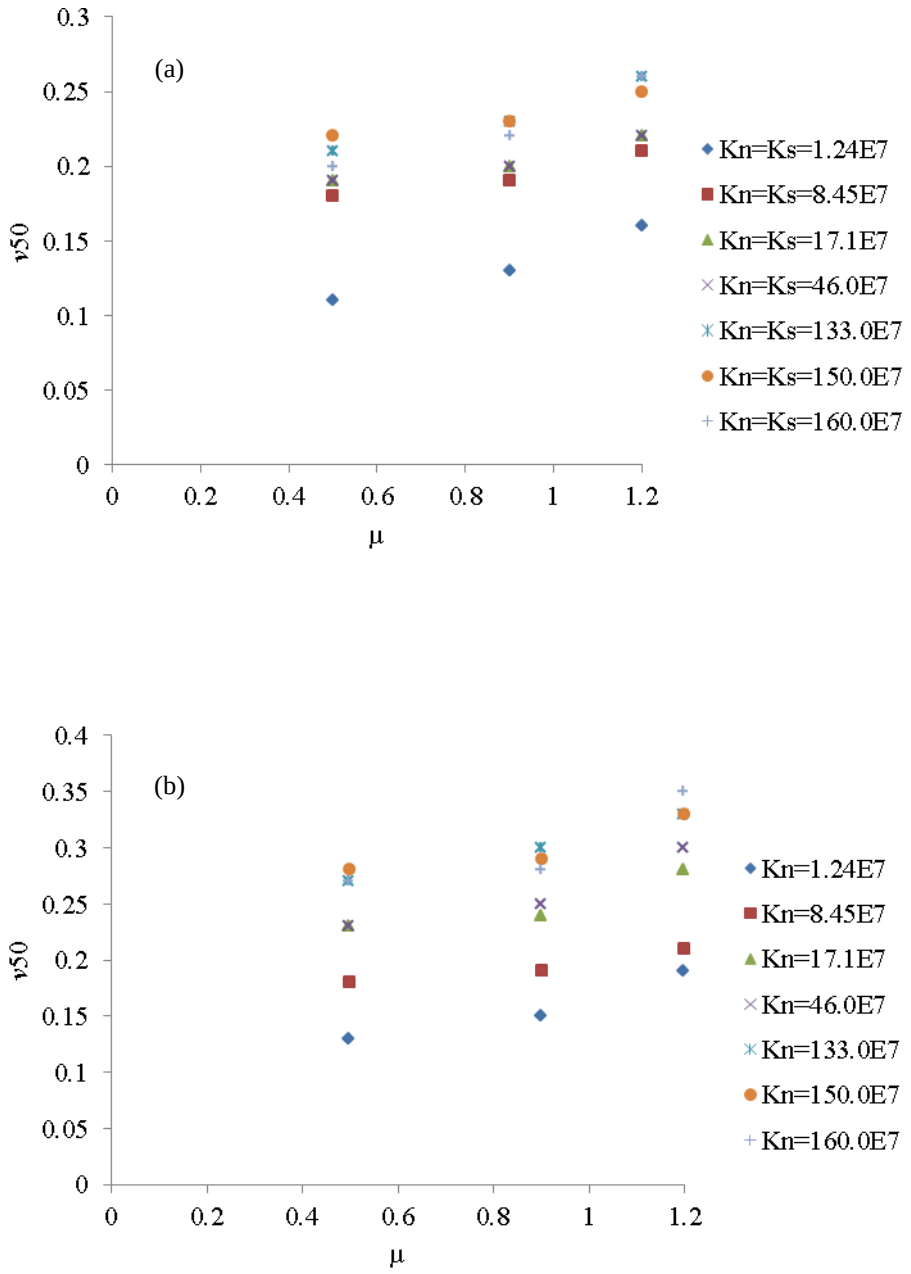

Figure 5-21 The sensitivity analysis: Inter-particle coefficient friction vs. Poisson's ratio: (a) Plane-strain (b) Plane-stress

Figures 5.22 to 5.25 show the effect of the inter particle friction on the anisotropic behaviour with axial strain for a fixed value of inter particle stiffness.

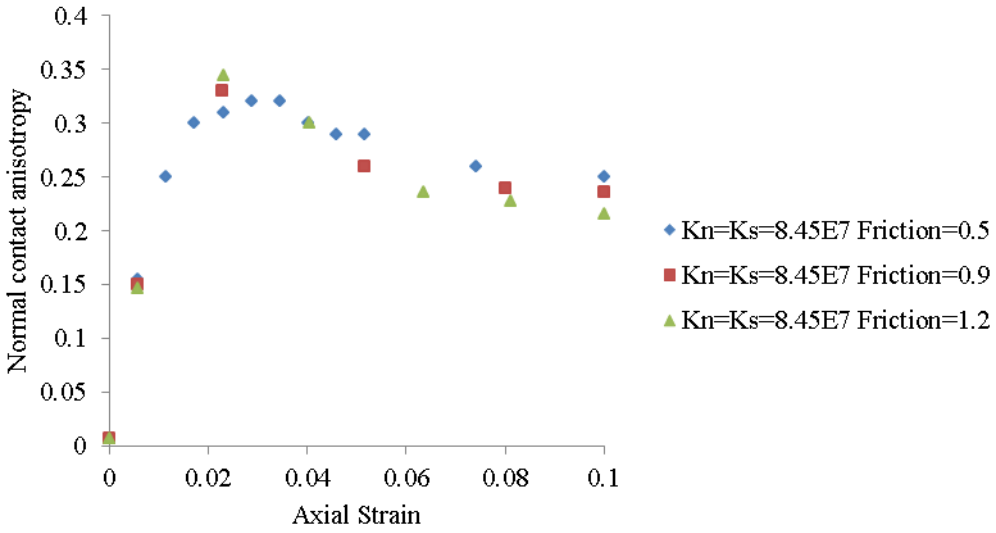

Figure 5-22 The sensitivity of normal contact anisotropy to the various inter-particle coefficient friction when normal and shear stiffnesses are constant

The normal contact anisotropy (Figure 5.22) increases until a maximum at the peak stress and then reduces with further strain for all inter-particle frictions. The trend of this fabric quantity is similar to the trend of deviatoric stress-axial stain (see Appendix 3). This clearly shows that the inter particle friction has little effect on the results. The maximum normal contact anisotropy which is approximately 0.3 shows how much the contact arrangement drifts from the isotropic state (i.e. a=0). Indeed, this term shows how much the system being loaded can develop anisotropy in contact networks. It is also a variance term that can be statistically shown as to how well the contact networks are changing during loading. The more normal contact anisotropy there is, the more shear strength capacity can be attained.

The variation of normal contact force anisotropy is shown in figure 5-23. As seen, it increases until a maximum at the peak stress and then reduces with further strain for all inter-particle frictions. This clearly shows that the inter particle friction has little effect on the results. The maximum value of normal

contact force anisotropy is 0.8 for these three models. That is, the ability of the system to develop the normal contact forces during loading for these inter-particle properties and pack is 0.8. The trend of this is normal contact force anisotropy is similar with the trend of normal contact anisotropy behaviour.

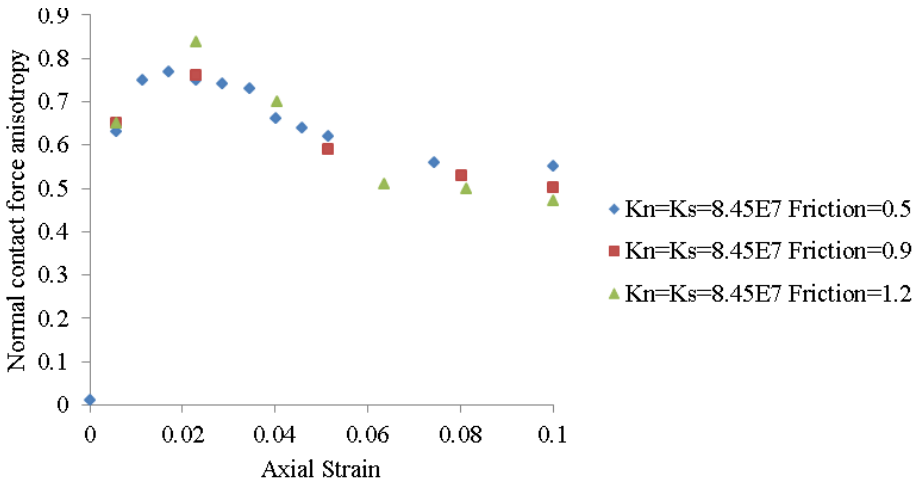

Figure 5-23 The sensitivity of normal contact force anisotropy to the various inter-particle coefficient friction when normal and shear stiffnesses are constant

Figure 5.24 shows that the shear contact force anisotropy is dependent on the inter-particle friction and the amount of axial strain. The anisotropy reduces to a constant value of 0.05 for all three samples. It is also seen that the peak of shear contact force anisotropies are not at the same strain as those for the normal contact and normal contact force anisotropies.

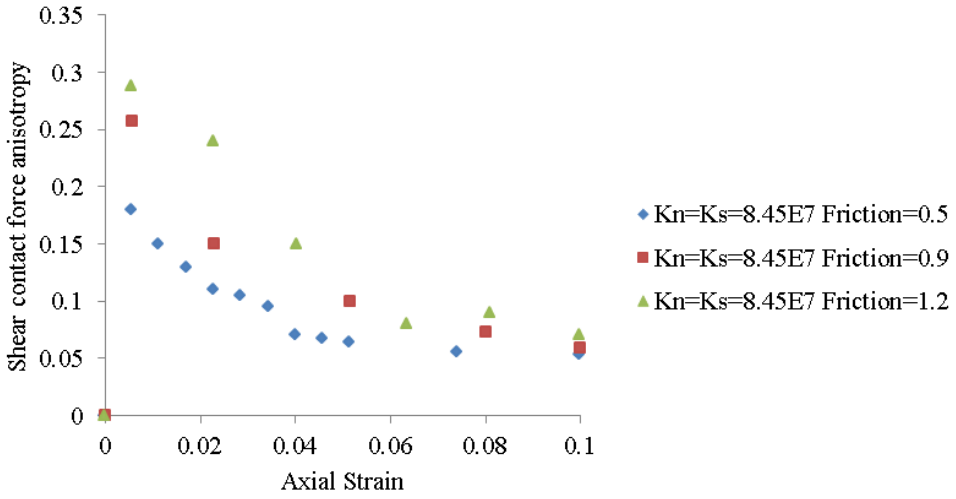

Figure 5-24 The sensitivity of shear contact force anisotropy to the various inter-particle coefficient friction when normal and shear stiffnesses are constant

Figure 5.25 shows that the average symmetric deviation index increases with axial strain but the inter-particle friction has little effect. The graph qualitatively shows that the models were not in symmetric state at the initial (λ = 0.1 at ε_{22} = 0). At peak deviatoric stress (see figure 100 in Appendix 3), the slope of λ significantly decrease, showing the stability of bulk decreases. However, at post-peak the slope of λ slightly increases, showing that the stability of bulk increases. λ = 0 corresponds with a fully symmetric contact configuration and λ = 1 corresponds the floating particles.

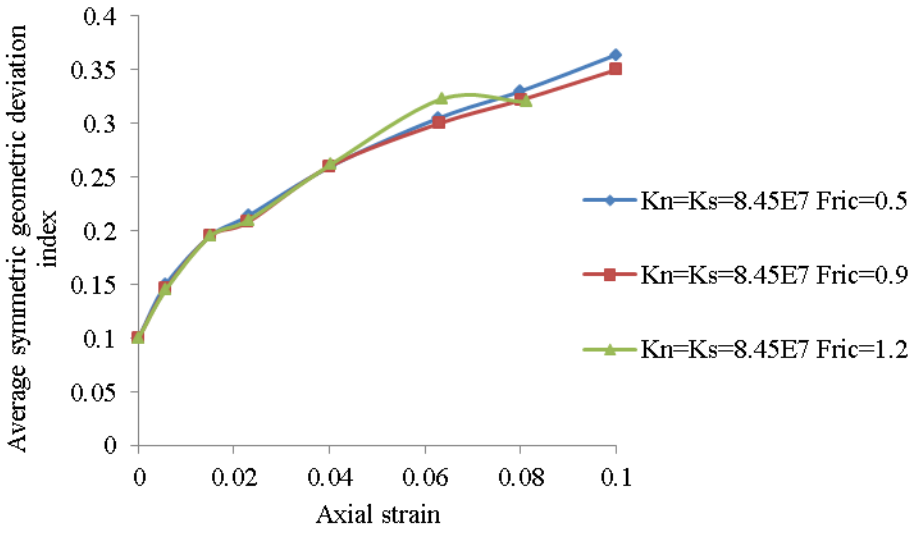

Figure 5-25 The sensitivity of average geometric symmetric deviation index of sand to the various particle coefficient friction.

Figure 5-26 shows that an increase in inter-particle friction has little effect on the average coordination number to peak deviatoric stress. The coordination number is constant after that though the value depends on the inter particle friction.

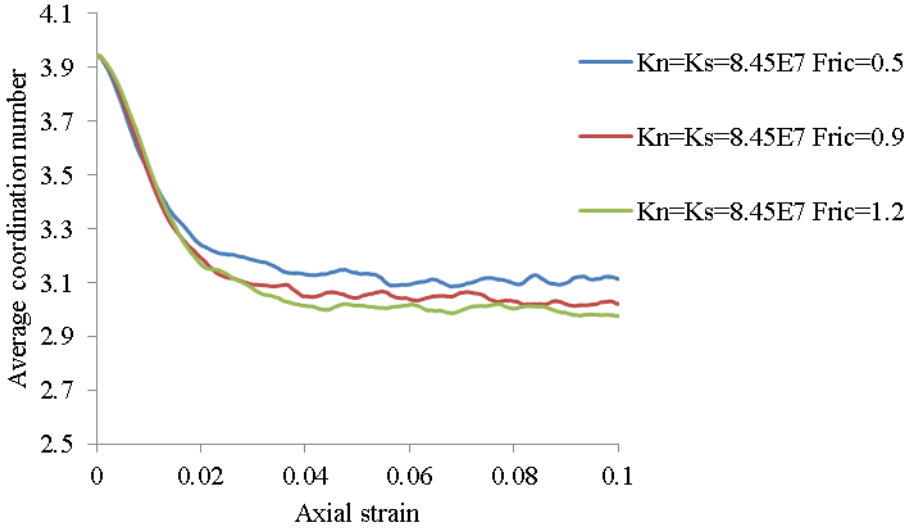

Figure 5-26 The sensitivity of average coordination number of sand to the various particle coefficient friction.

Comparing the stress-strain behaviour obtained from μ=0.2 (see figure 5-8) and those obtained from μ=0.5, 0.9 and 1.2 (for example figure 100 in Appendix 3) shows that inter-particle friction is also mainly controlled the hardening and softening strain behaviour. Therefore, μ = 0.2 used to study the sensitivity of bulk to the various particle densities shows no clear peak deviatoric stress, corresponding typical loose behaviour of dry sand (Atkinson and Bransby, 1978), while μ=0.5, 0.9 and 1.2 used to study the sensitivity of bulk to the inter-particle coefficient friction indicates the clear peak deviatoric stress, corresponding typical dense and medium behaviour of dry sand (Atkinson and Bransby, 1978).

5.4.1.3 The sensitivity of sand system to normal contact stiffness

A series of 21 biaxial tests were performed to determine the effect of the normal particle stiffness on the macro properties of the sample. The input data for these 21 tests is listed in table 5-8. The results of the sensitivity of

the particulate system to the normal contact stiffness is shown as deviatoric stress vs. axial strain, volumetric strain vs. axial strain, average coordination number, average fabric anisotropy, average normal contact force anisotropy, average shear contact force anisotropy, average symmetric geometric deviation index in Appendix 3 (see tables 19 to 20 and figures 139 to 159).

The sensitivity of macro-mechanical behaviour for these 21 tests to the different particle normal stiffness are shown in Figures 5-27 to 5-30. Figure 5-27 shows that an increase in normal particle stiffness results in an increase in the elastic modulus of the sample (i.e. E_{50}). The linear relationship can be established for each inter-particle friction (in the case of plane-strain):

$E_{50} = 2.94k_n$ for inter-particle friction 0.5

$E_{50} = 3.45k_n$ for inter-particle friction 0.9 5.10

$E_{50} = 3.60k_n$ for inter-particle friction 1.2

A linear relationship can be also established for each inter-particle friction (in the case of plane-stress):

$E_{50} = 3.15k_n$ for inter-particle friction 0.5

$E_{50} = 3.63k_n$ for inter-particle friction 0.9 5.11

$E_{50} = 3.76k_n$ for inter-particle friction 1.2

The values of normal stiffness, which are between $8.45*10^7$ and $17.1*10^7$ (N/m) lead to values of E_{50} which are typical for medium and dense sand; i.e. between 25 and 50 [MPa] and 50 and 80 [MPa], respectively.

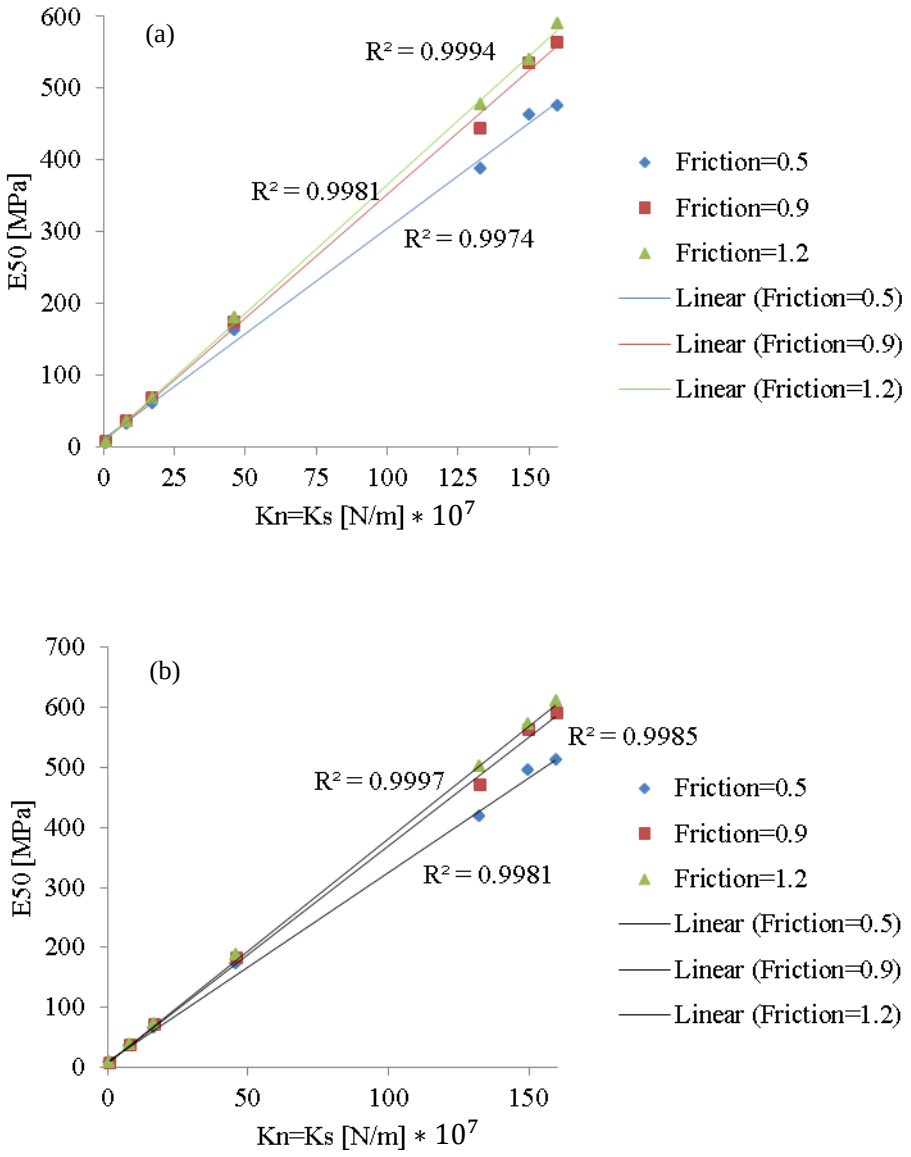

Figure 5-27 The sensitivity of E_{50} to the various particle normal stiffness: (a) Plane-strain (b) Plane-stress

Figure 5-28 shows that an increase in the normal particle stiffness leads to an increase in Poisson's ratio. The value increases from 0.1 to 0.25. The typical range of v_{50} for medium and dense sand (see table 5-2) is between 0.2 and 0.35 and 0.3 and 0.4, respectively. However, if the normal stiffness of particles is between $8.45*10^7$ and $17.1*10^7$ [N/m], which produces a sensible value of E_{50} for any inter-particle friction used in this work, these values of normal stiffness will also produce a sensible range for Poisson's ratio of medium sand only for inter-particle friction between 0.9 and 0.5. For the

higher values of inter-particle coefficient friction, the interpreted value of Poisson's ratio is less than typical values.

A non-linear relationship can be also established for each inter-particle friction (in the case of plane-strain):

$$v_{50} = 0.163{k_n}^{0.091} \quad \text{for inter-particle friction 0.5}$$

$$v_{50} = 0.136{k_n}^{0.102} \quad \text{for inter-particle friction 0.9} \qquad 5.12$$

$$v_{50} = 0.122{k_n}^{0.115} \quad \text{for inter-particle friction 1.2}$$

A non-linear relationship can be also established for each inter-particle friction (in the case of plane-stress):

$$v_{50} = 0.18{k_n}^{0.126} \quad \text{for inter-particle friction 0.5}$$

$$v_{50} = 0.14{k_n}^{0.137} \quad \text{for inter-particle friction 0.9} \qquad 5.13$$

$$v_{50} = 0.13{k_n}^{0.15} \quad \text{for inter-particle friction 1.2}$$

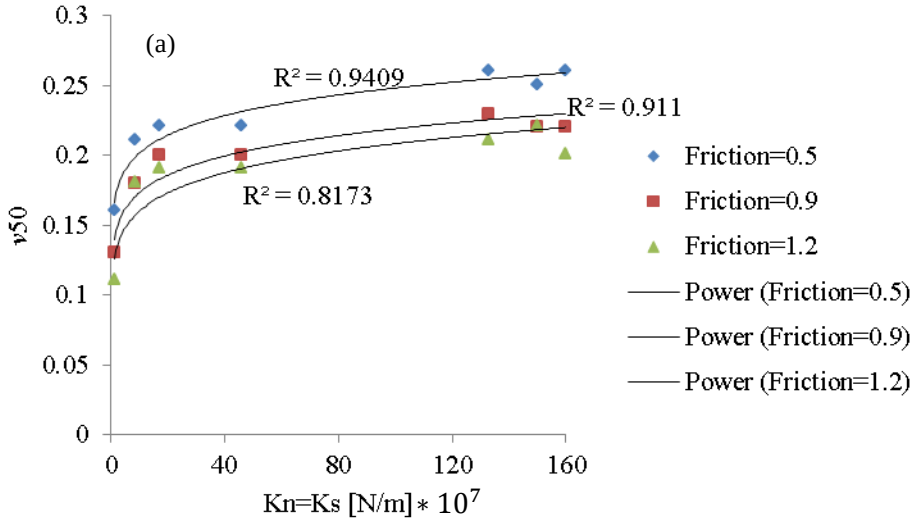

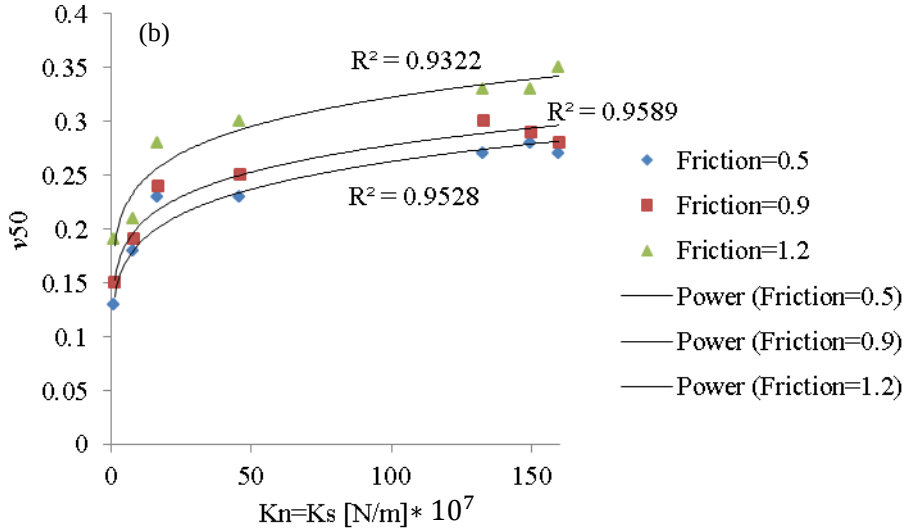

Figure 5-28 The sensitivity of v_{50} to the various particle normal stiffness: (a) Plane-strain (b) Plane-stress

Figures 5-29 and 5-30 shows that an increase in the normal stiffness of particles has little effect on the angle of friction and peak deviatoric stress.

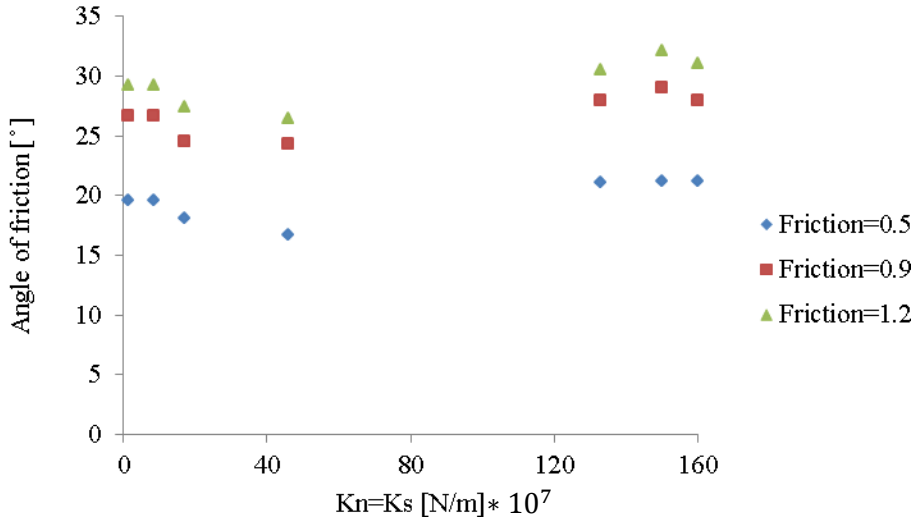

Figure 5-29 The sensitivity of angle of friction to the various particle normal stiffness

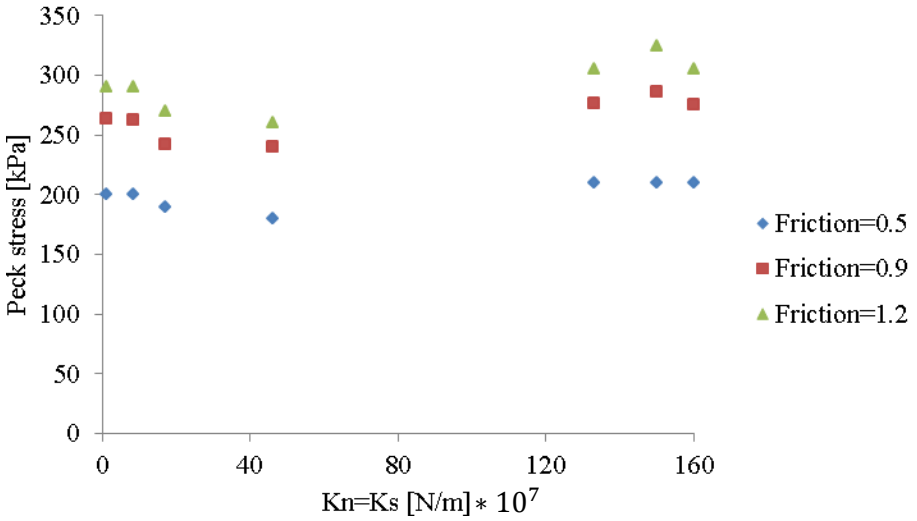

Figure 5-30 The sensitivity of peak stress to the various particle normal stiffness

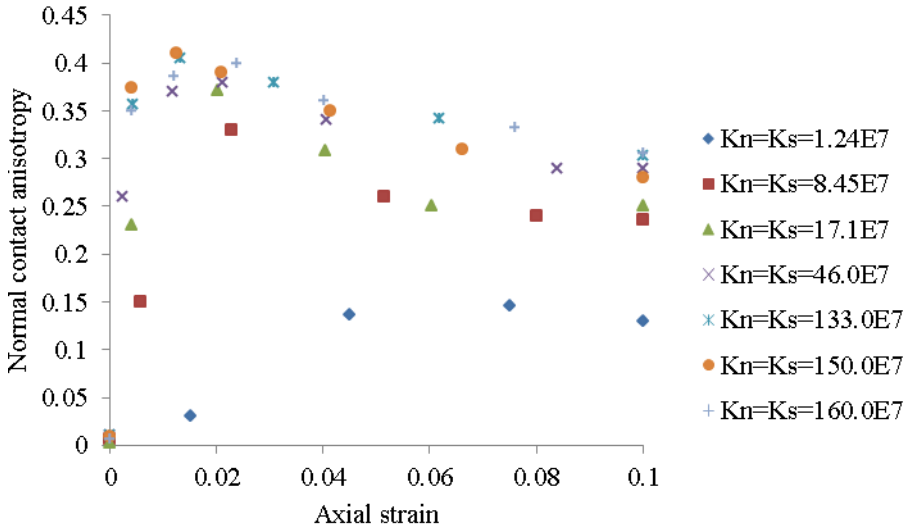

Figure 5-31 The sensitivity of sand to the different normal particle stiffness when inter-particle friction is 0.9: Normal contact anisotropy vs. axial strain

An increase in normal particle stiffness from $1.24*10^7$ to $160*10^7$ [N/m] leads to increase in the rate of normal contact anisotropy in the direction of applied deviatoric load. That is, the particles and contacts velocities and displacements in the direction of applied deviatoric load increase. This results in an initial increase in the normal contact anisotropy of the system (see figure 5-31). The maximum value of average fabric anisotropy takes place when the axial strain corresponds to the peak deviatoric stress.

This initial increase in normal contact anisotropy significantly increases the average normal contact force anisotropy (see figure 5-32). It is because the contact networks re-arranges in the direction of major principle stress (σ_{11}) to resist against shearing deformation. The main reason of this rapid rise is to increase the slope of λ significantly, where the contact networks around each particle tends to drift from its symmetric contacts arrangement (or stablest contacts arrangement) to resist against the deviatoric load (see figure 5-34).

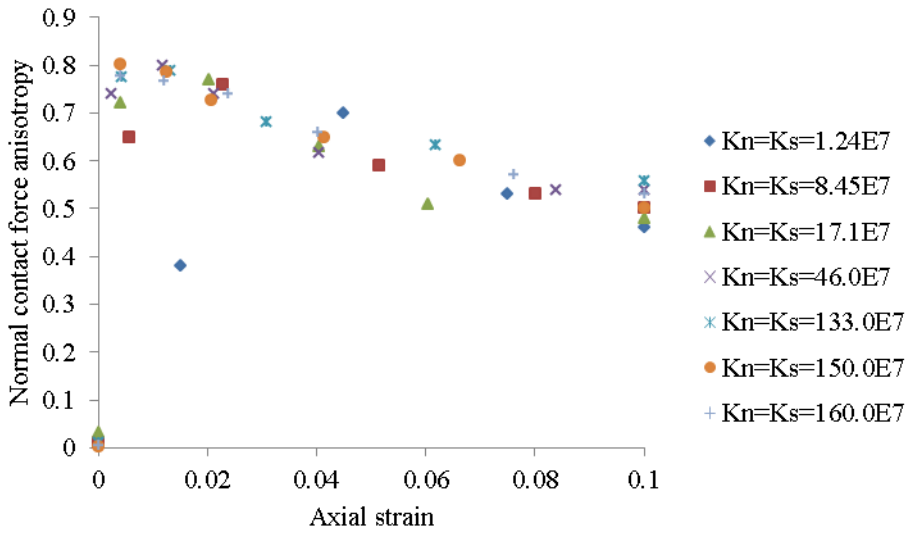

Figure 5-32 The sensitivity of sand to the different normal particle stiffness when inter-particle friction is 0.9: average normal force anisotropy vs. axial strain

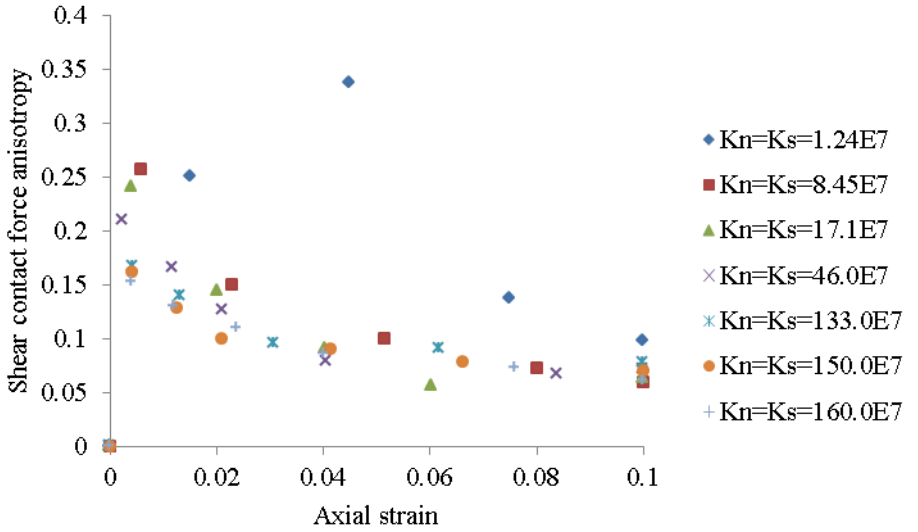

Figure 5-33 The sensitivity of sand to the different normal particle stiffness when inter-particle friction is 0.9: average shear force anisotropy vs. axial strain

Figure 5.33 shows that the shear contact force anisotropy reduces with axial strain for all particle stiffnesses. At post-peak, a_t is independent from contact stiffness.

During the shearing of sand in a biaxial test, the particles are rearranged to represent their higher shear capacity. These changes lead to drift from the initial contact configuration. This is shown in figures 5-34 and 5-35. Figure 5-34 shows that an increase in normal particle stiffness causes the average symmetric geometric deviation of contact points increase due to lose of their contacts because the higher rate of dilation (see figures 142 to 144 in Appendix 3).

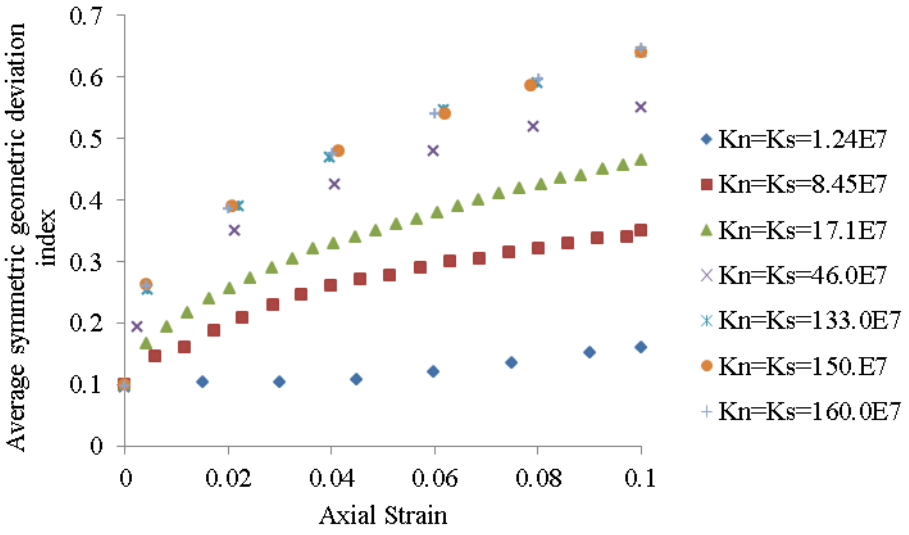

Figure 5-34 The sensitivity of average geometric symmetric deviation index of particles to the normal particle stiffness when inter-particle friction is 0.9

Figure 5-35 shows that increase in normal particle stiffness leads to decrease the average coordination number. In both cases the variation depends on the particle stiffness.

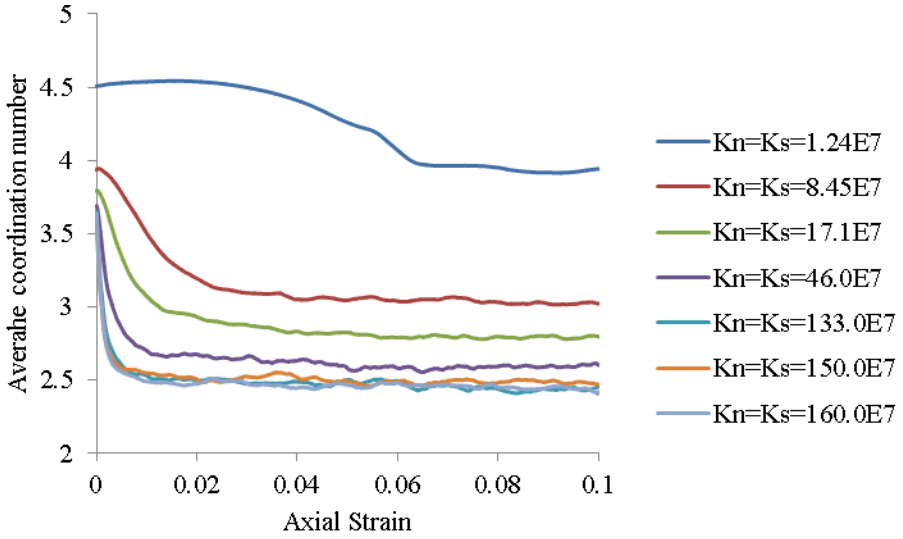

Figure 5-35 The sensitivity of average coordination number of particles to the normal particle stiffness when the inter-particle friction is 0.9

As seen in figure 5-35, the average coordination number after peak deviatoric stress (see figure 140 in Appendix 3) for k_n = 17.1*10^7 to k_n = 160.0*10^7 [N/m] is below 3, which is below the enough restrains to satisfy the static equilibrium of each particle, while their stiffnesses are much higher than that for k_n = 1.24*10^7 to k_n = 8.45*10^7. It is because an increase in contact stiffness or μ leads to increase the inter-particle forces (or shear capacity of particles). Therefore, the chain forces developed for each particle during sharing in order to maintain granular system in static equilibrium increases. This leads to this conclusion that a lower average coordination number is possible for strong network forces to resist against shear deformation.

In the case of lower normal contact stiffness, the average coordination number increases about peak and becomes constant at post-peak. The reason of this increase till peak stress is due to dilation behaviour (see figure 143 in Appendix 3). As seen in this figure, the system contracts till axial strain 0.05. This causes that the system becomes compacted and tendency of particles to lose their contact decreases. Therefore, the average coordination number increases. Also, as the rate of dilation decreases, the ability of system to develop higher anisotropy in comparison to that for higher normal contact stiffnesses decreases.

5.4.1.4 The sensitivity to the shear particle stiffness

The input data of the biaxial tests to determine the effect of shear particle stiffness is listed in table 5-9. The results for a normal particle stiffnesses between $8.45*10^7$ and $17.1*10^7$ [N/m] are presented as these gave produced typical values of deformation modulus. The results of the sensitivity of particulate system to the shear contact stiffness such as deviatoric stress vs. axial strain, volumetric strain vs. axial strain, average coordination number, average fabric anisotropy, average normal contact force anisotropy, average shear contact force anisotropy, average symmetric geometric deviation index for these tests are shown in Appendix 3 (see tables 22 to 42 and figures 160 to 162). The results are shown in figures 5-36 to 5-38.

k_n (N/m)		k_s (N/m)	
		k_s/k_n=1	k_s/k_n=0.5
$1.24*10^7$		$1.24*10^7$	$6.2*10^6$
$8.45*10^7$		$8.45*10^7$	$42.25*10^6$
$17.1*10^7$		$17.1*10^7$	$8.55*10^7$
$46.0*10^7$		$46.0*10^7$	$23*10^7$
$133.0*10^7$		$133.0*10^7$	$66.5*10^7$
$150.0*10^7$		$150.0*10^7$	$75*10^7$
$160.0*10^7$		$160.0*10^7$	$80*10^7$
μ	0.5		
$\rho[\frac{kg}{m^3}]$	$2*10^8$		
n	0.12		

Table 5:9 The micro-mechanical parameters for performing a series of biaxial tests of a particulate system to investigate the sensitivity of system to the normal stiffness of particle.

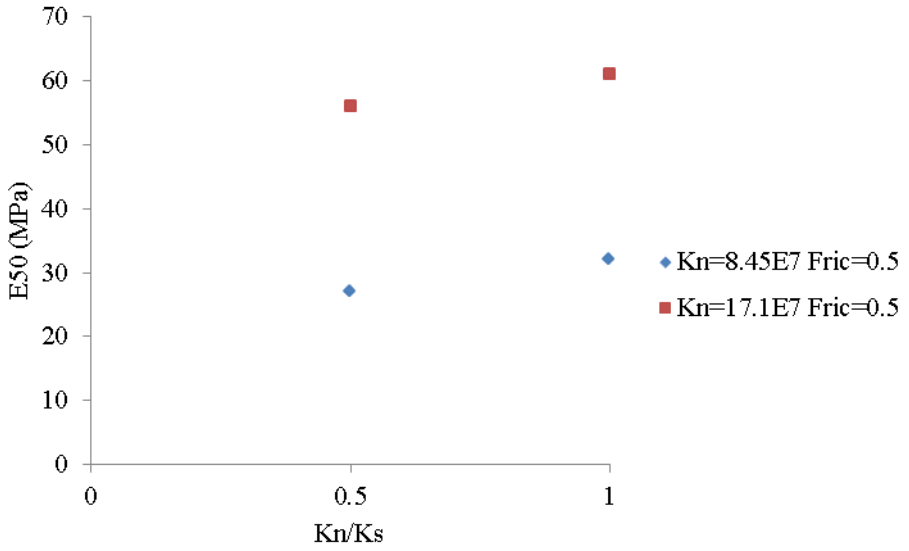

Figure 5-36 The sensitivity of E_{50} to the various particle shear stiffness

Figures 5-36 shows that an increase in k_n/k_s between 0.5 and 1 results in an increase in E_{50} while this increase leads to a decrease in Poisson's ratio (see figure 5-37). As expected increasing E_{50} leads to system that is more brittle. That is the deformability term such as Poisson's ratio should decrease.

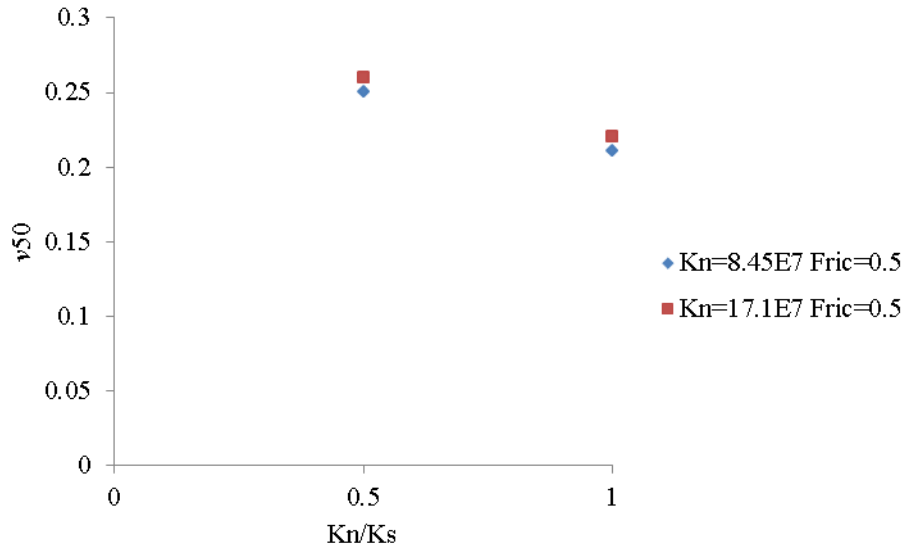

Figure 5-37 The sensitivity of v_{50} to the various particle shear stiffness

Figure 5-38 clearly show that increase in k_s/k_n between 0.5 and 1 has little effect on the angle of friction and peak deviatoric stress. The results show

how the deformation modulus is controlled by particle normal stiffness and shear stiffness while the angle of bulk friction is controlled by particle friction.

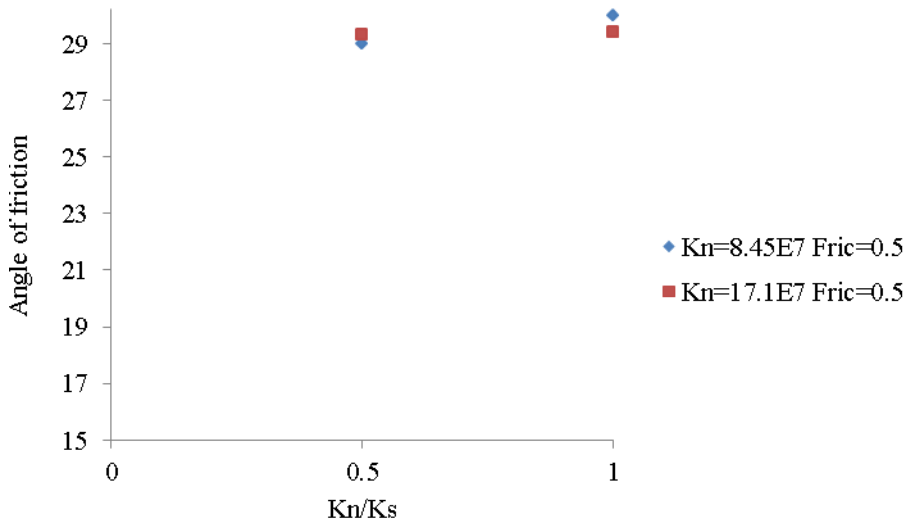

Figure 5-38 The sensitivity of angle of friction to the various particle shear stiffness

Figures 5-39, to 5-43 shows that changes in the ratio of particle normal stiffness to the shear stiffness from 1 to 0.5 do not have any effect on the average coordination number, average symmetric geometric deviation index, average fabric anisotropy, average normal force anisotropy and average shear force anisotropy of sand respectively.

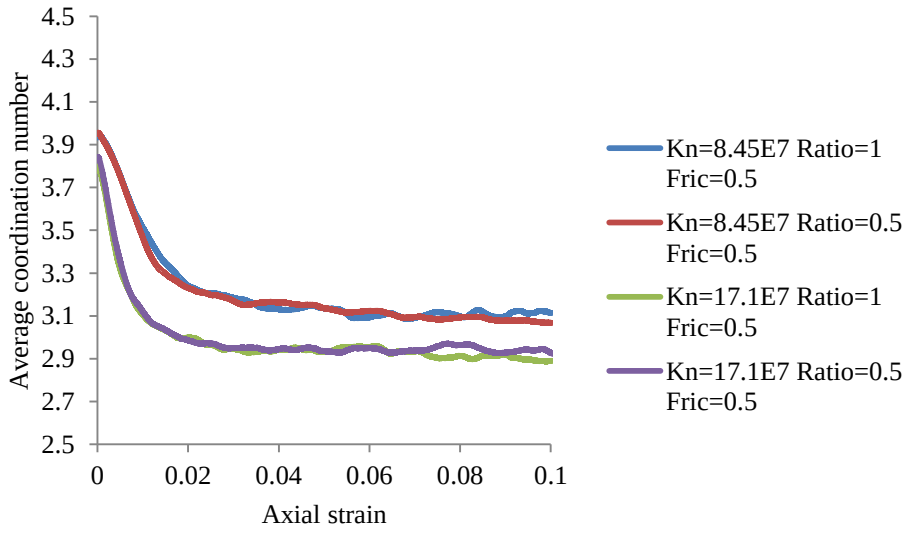

Figure 5-39 The sensitivity of average coordination number of sand to the various particle shear stiffness.

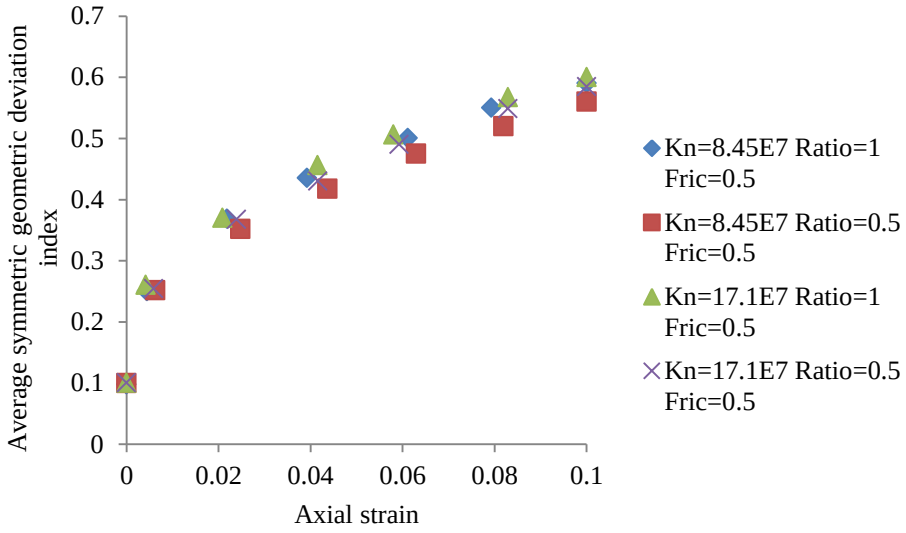

Figure 5-40 The sensitivity of average symmetric geometric deviation index of sand to the various particle shear stiffness.

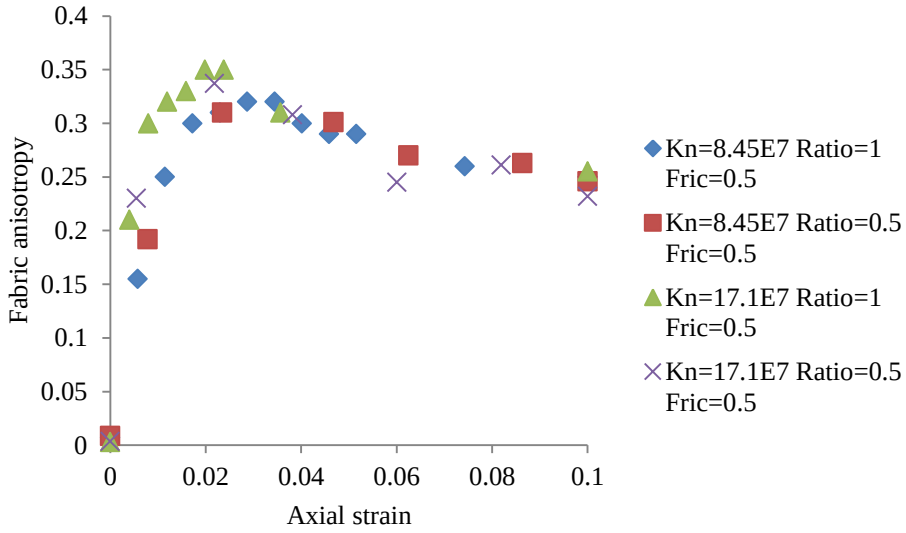

Figure 5-41 The sensitivity of average fabric anisotropy of sand to the various particle shear stiffness.

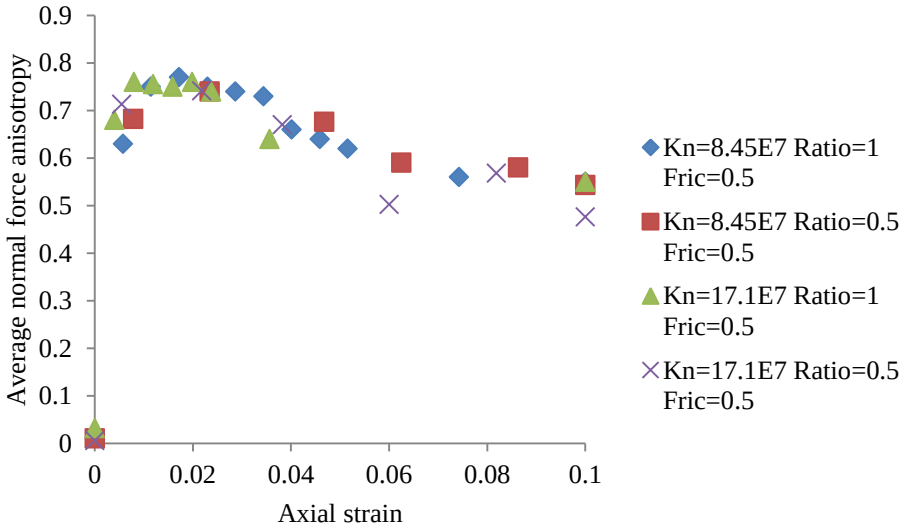

Figure 5-42 The sensitivity of average normal force anisotropy of sand to the various particle shear stiffness.

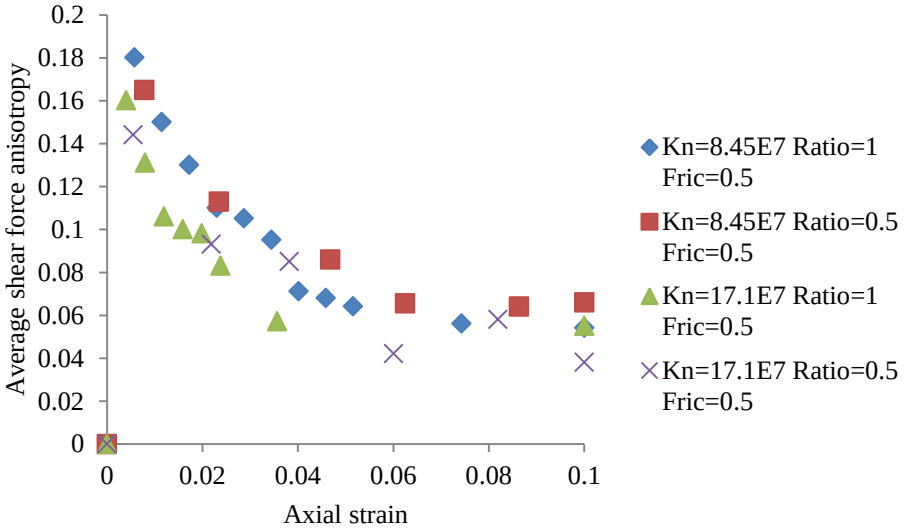

Figure 5-43 The sensitivity of average shear force anisotropy of sand to the various particle shear stiffness.

5.4.1.5 The sensitivity of a particulate system to deformable boundary particles

Two biaxial tests were carried out to investigate the effect of boundary conditions on the mechanical properties of the sample. One test was with deformable boundary particles, discussed in previous chapter, and other was with rigid walls boundary (i.e. non-deformable boundary). Table 5-10 shows

the inter-particle properties, particle size distribution (PSD), initial porosity and confining pressure.

Boundary condition	k_n [N/m] *10^7	k_s [N/m] *10^7	μ	Width [cm]	Height [cm]	n	Range of PSD [mm]	Number of particles	Confining pressure [kPa]
Rigid	8.45	8.45	0.9	7.5	15.0	0.12	1-2	8067	100
Deformable	8.45	8.45	0.9	7.5	15.0	0.12	1-2	8067	100

Table 5:10 The input properties used for sensitivity analysis of sand to the different boundary conditions

The results are shown in figures 5-44 to 5-54 and table 43 in Appendix 3. Figure 5-44 shows that trend of deviatoric stress vs. axial strain between rigid boundary and deformable boundary till peak stress is similar. However, the peak stress with a rigid boundary is higher than that for a deformable boundary. This fact is also shown by (Cheung and O'Sullivan, 2008). The reason of this higher peak stress in the case of rigid boundary is that the rigid side boundaries are a constraint not for those particles in contact the boundary which constrains the whole system. Both samples show a reduction in deviatoric stress to a post peak value. The deviatoric stress remains relatively constant for the deformable boundary, suggesting critical state conditions, but it increases for the rigid boundary. Therefore, the macro stress strain response with deformable boundaries is more representative of actual behaviour than that with rigid boundaries.

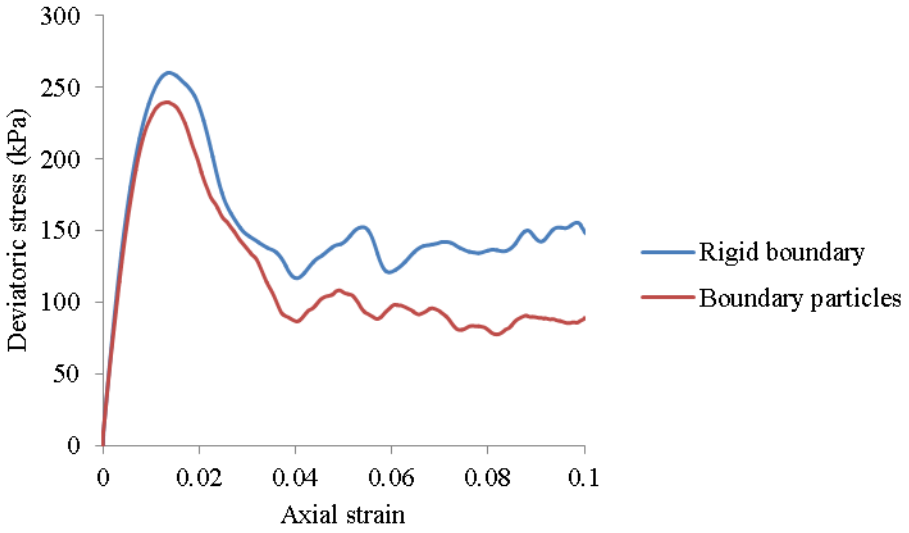

Figure 5-44 The sensitivity of macro-mechanical behaviour of the system to the different boundary condition: deviatoric stress vs. axial strain

The volumetric strain increases in both cases though the dilation rate with deformable boundaries post-peak is more representative of typical soil behaviour than that with rigid boundaries, suggesting critical state conditions (figure 5-45).

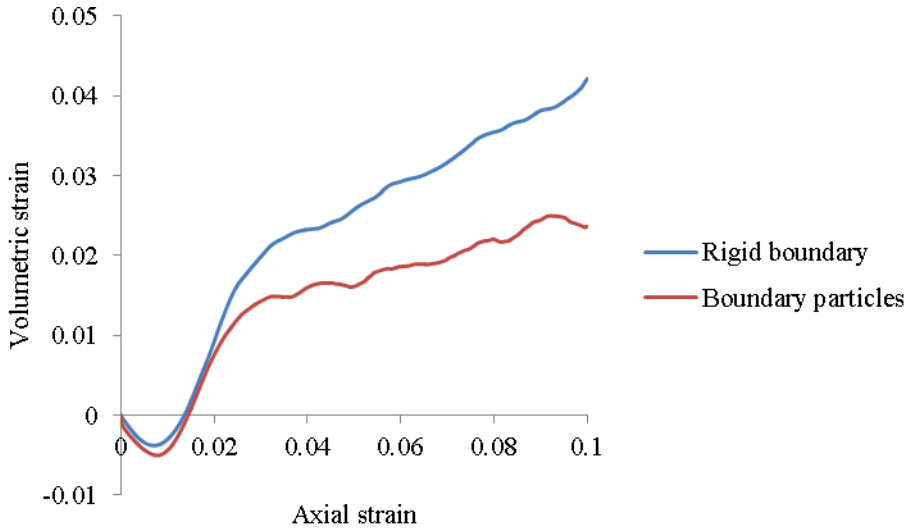

Figure 5-45 The sensitivity of macro-mechanical behaviour of the system to the different boundary condition: volumetric strain vs. axial strain

The average symmetric geometric deviation index, λ is constant at post peak for deformable boundaries (λ = 0.2) (see figure 5-46). Tracking λ clearly shows that the particle stability and bulk stability do not increase after peak stress for deformable boundaries, suggesting critical state conditions, while it increases after peak stress in the case of rigid boundaries.

Figure 5-47 shows the variation of average coordination number against axial strain for different boundary conditions. The trend of average coordination number vs. axial strain between rigid boundary and deformable boundary till peak stress is similar. It remains relatively constant at 3.3 for the deformable boundary which suggests critical state conditions but it slightly decreases for the rigid boundary. The reason of this decrease in average coordination number in the case of rigid boundaries after peak is its dilation behaviour. As the rate of dilation increases, the tendency of particles to move and lose their contacts increases and subsequently their stability decreases.

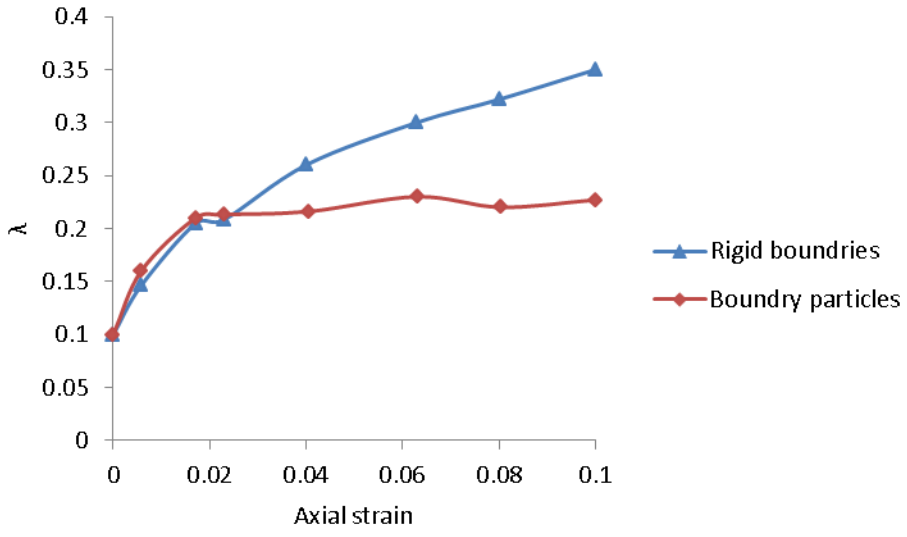

Figure 5-46 The sensitivity of λ to the different boundary condition: volumetric strain vs. axial strain

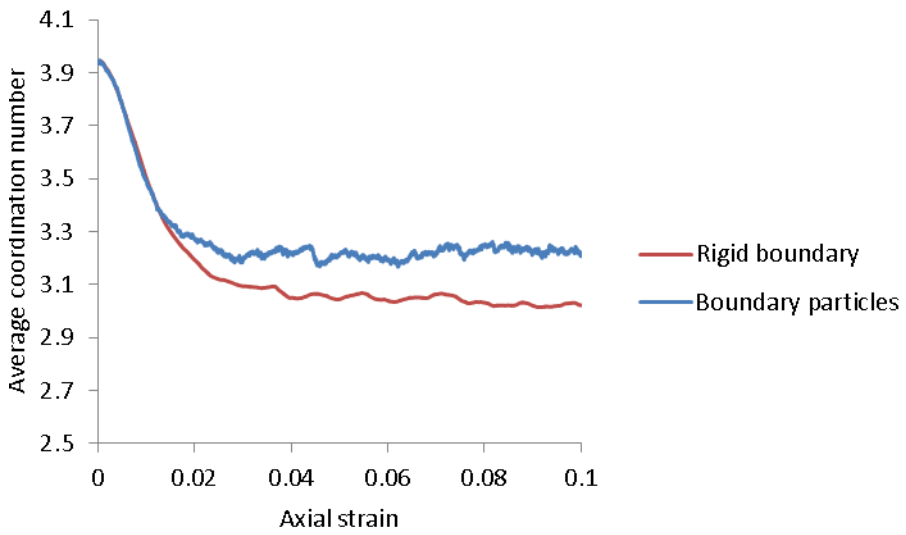

Figure 5-47 The sensitivity of average coordination number to the different boundary condition: volumetric strain vs. axial strain

Thus, if the aim is to find the elastic deformation modulus, rigid side boundaries can be applied as the initial stress-strain and volumetric behaviour are similar for two cases. However, if the critical state behaviour of soil is considered, the deformable boundary particles should be applied.

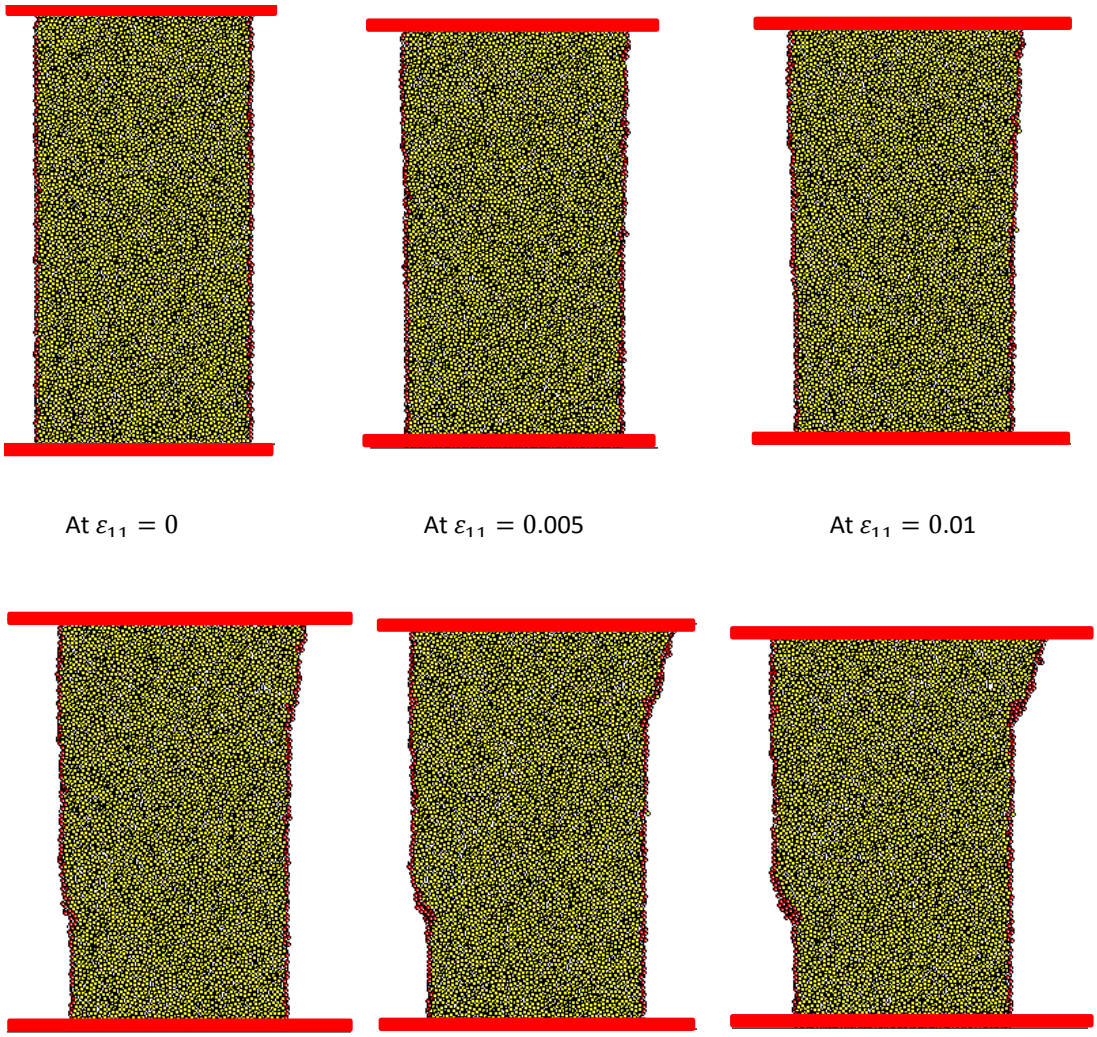

Figure 5-48 The bulk shearing deformation when deformable boundary particles used

Figure 5-48 shows the shearing deformation of sand at different axial strain levels for deformable boundary. It is seen that the use of deformable boundary particles allows the bulk to bulge. According to this figure, the bulk dilation starts about $\varepsilon_{11} = 0.005$. From $\varepsilon_{11} = 0.05$ to $\varepsilon_{11} = 0.1$the bulk deformation seems to be similar, suggesting critical state conditions.

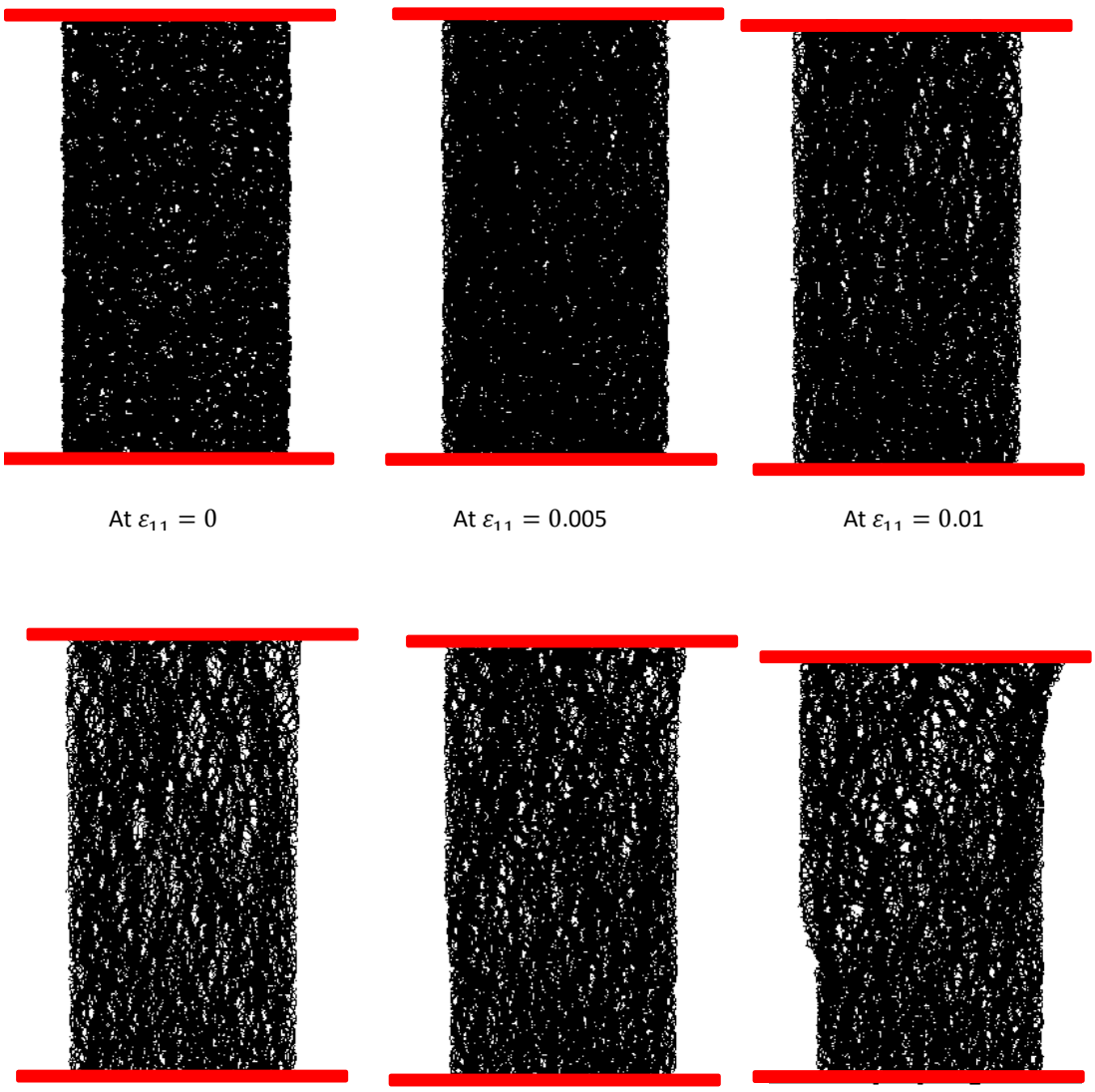

Figure 5-49 The evolution of normal contact forces during shearing when deformable boundary particles used

Figure 5-49 shows the evolution of normal contact forces during shearing deformation at different axial strain levels for deformable boundary. It is noted that the magnitude of normal contact force is proportional to its thickness. From $\varepsilon_{11} = 0.0$ to $\varepsilon_{11} = 0.005$ where the sample mainly contracts the normal contact forces increases. However, once the sample starts to dilate (i.e. above $\varepsilon_{11} = 0.005$) the direction of normal contact forces change and their magnitude is decreasing such that at $\varepsilon_{11} = 0.1$ a clear change in distribution of normal chain forces formed.

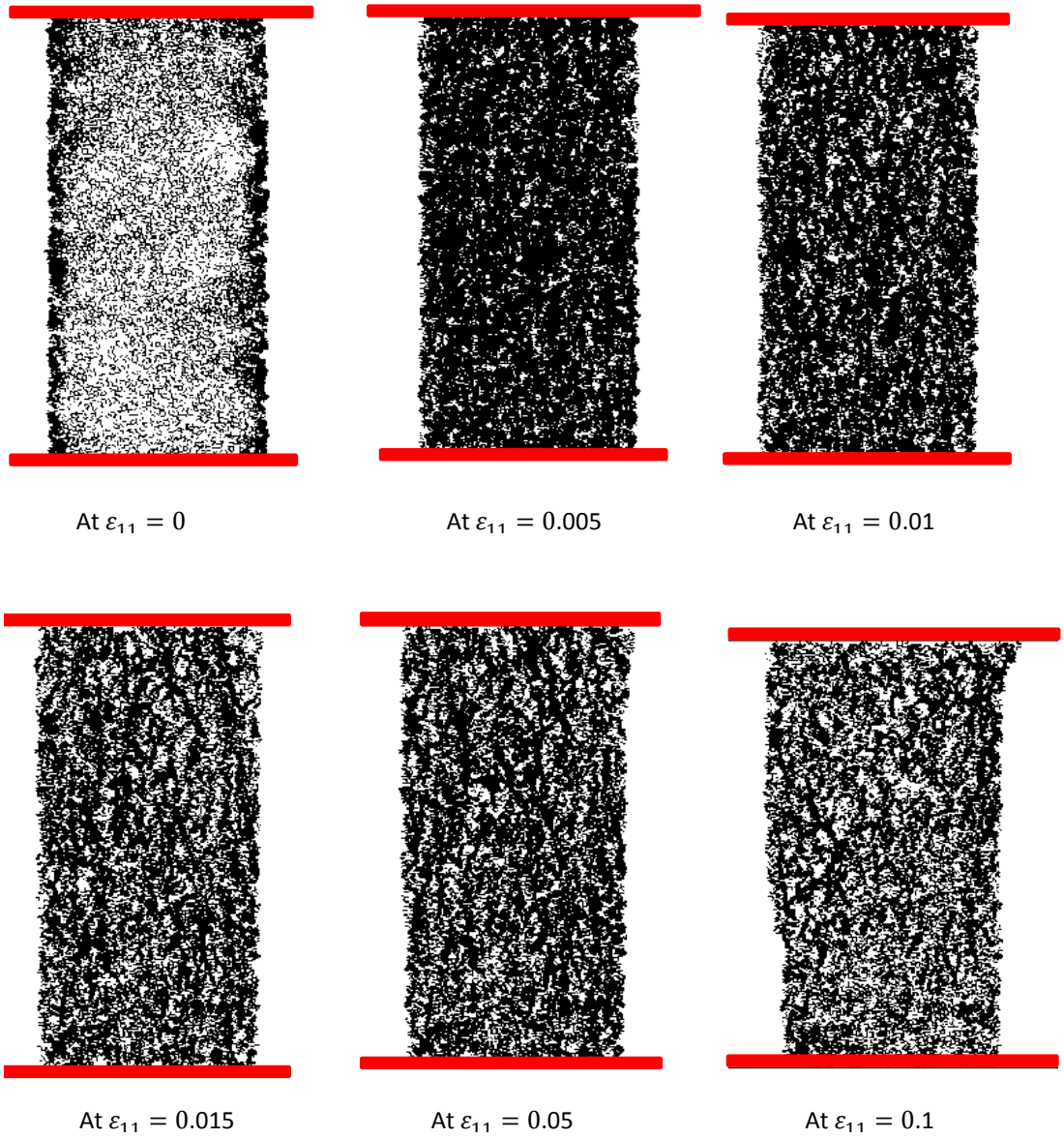

Figure 5-50 The evolution of shear contact forces during shearing when deformable boundary particles used

Figure 5-50 shows the evolution of shear contact forces during shearing deformation at different axial strain levels for deformable boundary. It is noted that the magnitude of normal contact force is proportional to its thickness. From $\varepsilon_{11} = 0.0$ to $\varepsilon_{11} = 0.005$ the magnitude of shear contact forces significantly increases as system is compacted. However, once the sample starts to dilate (i.e. over $\varepsilon_{11} = 0.005$) particle sliding starts. This leads to a reduction in the magnitude of shear contact forces.

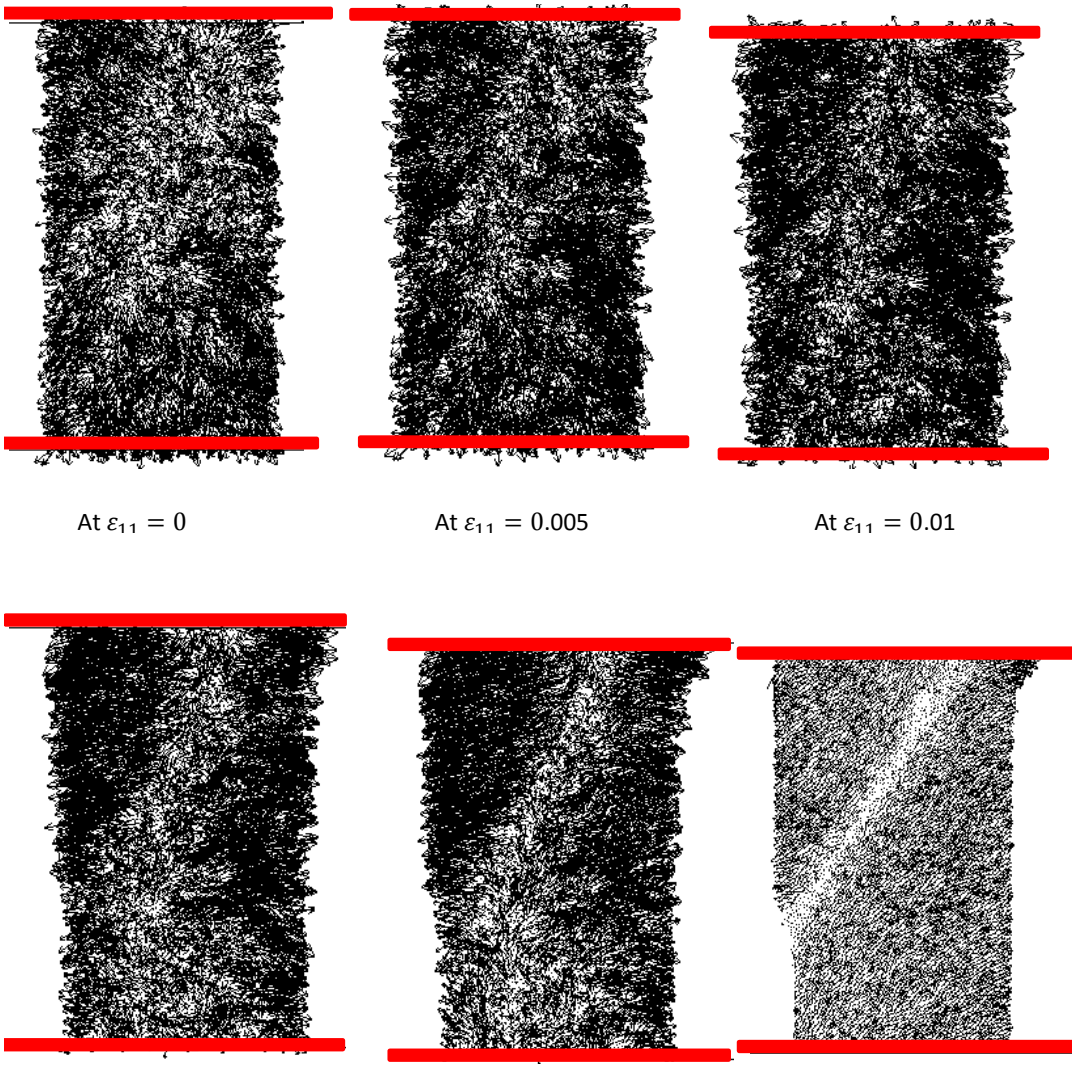

Figure 5-51 The particles displacement during shearing along with shear band taken place at $\varepsilon_{11} = 10\%$ when deformable boundary particles used

Figure 5-51 shows the particles displacement during shearing deformation at different axial strain levels for deformable boundary. It is seen that applying vertical loading causes the particles to move in the horizontal direction. As the system dilates the configuration of particle displacement changes significantly (e.g. compare particles displacements at $\varepsilon_{11} = 0.005$ and $\varepsilon_{11} = 0.015$). From $\varepsilon_{11} = 0.015$ and $\varepsilon_{11} = 0.05$ a wedge failure forms. Eventually, the shear band formed at $\varepsilon_{11} = 0.1$ for deformable boundary is clearly seen.

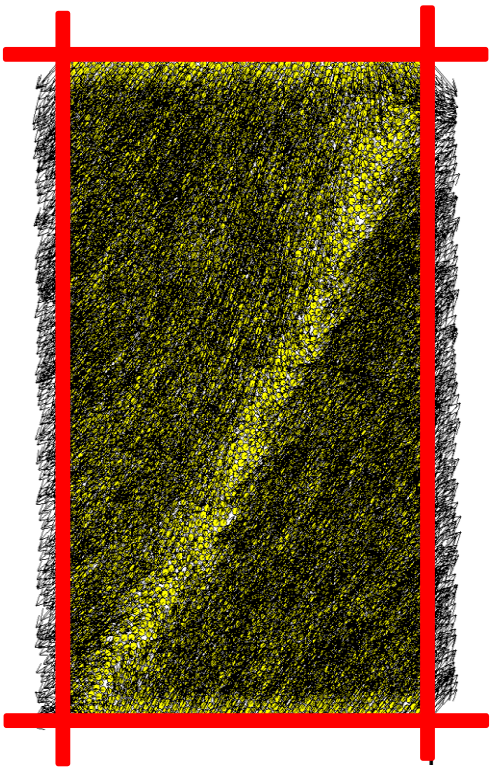

Figure 5-52 The shear band taken place at $\varepsilon_{11} = 10\%$ when rigid boundary used

Figure 5-52 shows the shear band clearly formed at $\varepsilon_{11} = 0.1$ for the rigid boundary is different for that formed for deformable boundary particles.

Figures 5-53 and 5-54 show the polar diagram and analytical form of normal contact distributions for deformable and rigid boundaries at the end of test. These figures show that the orientation of the normal contact at the post peak state at the end of the test for deformable boundary particle is 0.057˚ and it is 4.2˚ for rigid boundary from horizontal direction. This shows the system with rigid boundary has this ability to develop at the failure state while the system with deformable boundary does not have this ability to develop as $\theta_a = 0.057$˚.

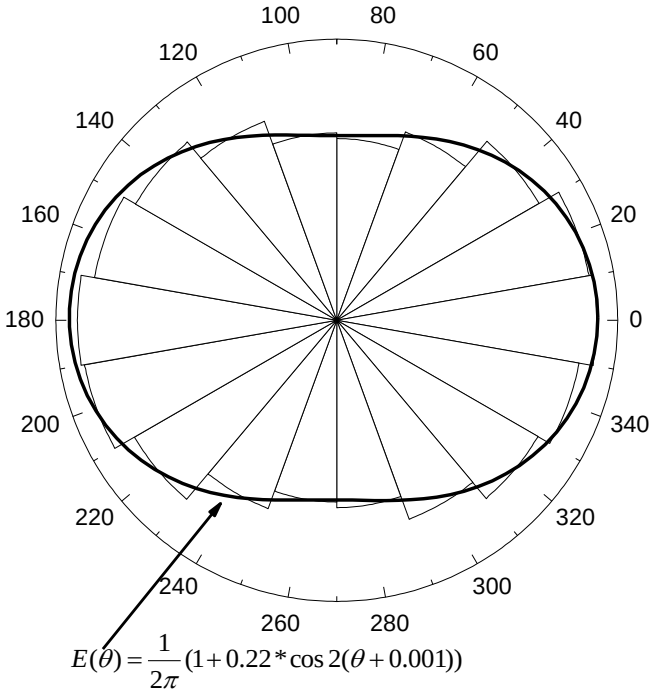

Figure 5-53 Normal contact distribution of deformable boundary particles at $\varepsilon_{11} = 10\%$

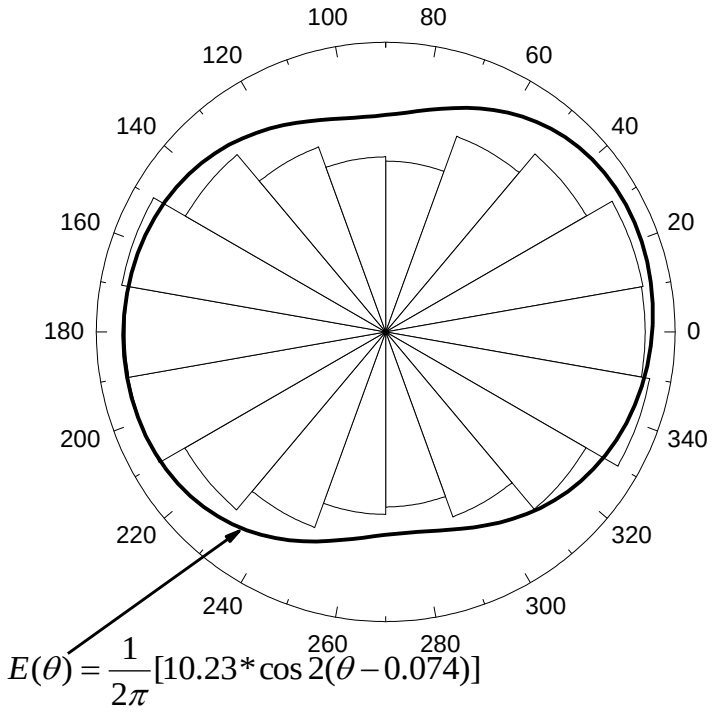

Figure 5-54 Normal contact distribution of rigid boundary particles at $\varepsilon_{11} = 10\%$

Figures 5-55 and 5-56 show the polar diagram and analytical form of normal contact force distributions for the system for deformable and rigid boundaries at the end of the test. These figures show that the orientation of normal contact forces at the residual state is in the horizontal direction. However, the summation of normal contact forces at the end of test is significantly different between deformable and rigid boundaries. For deformable boundaries, the value of $\bar{f}_0^c$ (see Eq. 3.14) is 16082 (N/m) while it is 658277 (N/m) for rigid boundaries, which is possibly due to the effects of interaction between the rigid walls and the neighbouring particles and lack of deformation at the boundaries.

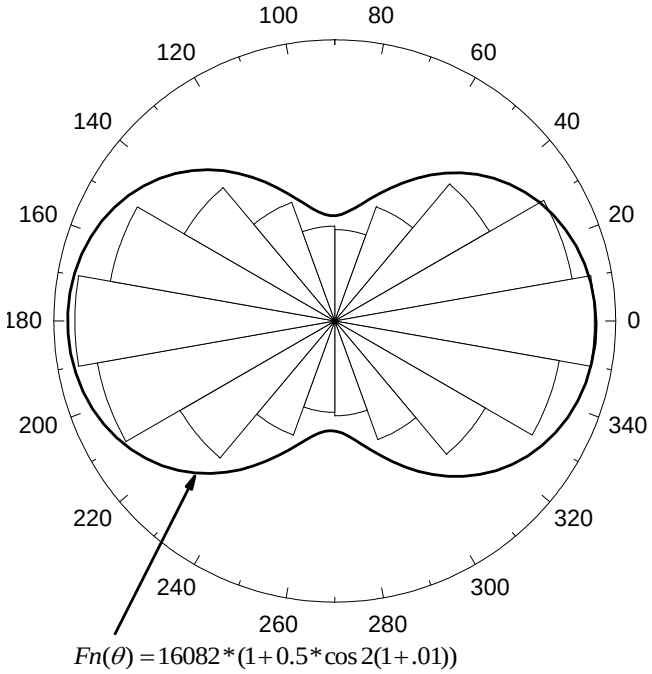

Figure 5-55 Normal contact force distribution of deformable boundary particles at $\varepsilon_{11} = 10\%$

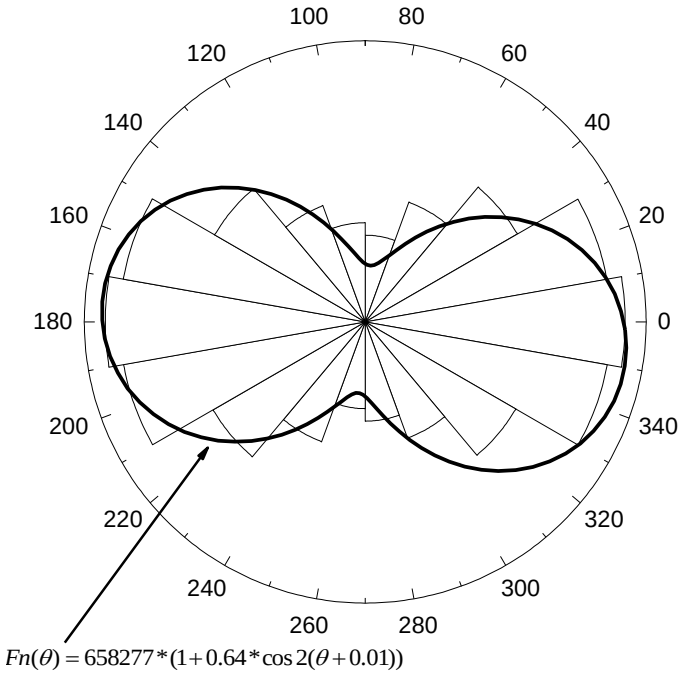

Figure 5-56 Normal contact force distribution of rigid boundary at $\varepsilon_{11} = 10\%$

Figures 5-57 and 5-58 show that the concentration of shear contact forces is about 30˚ for deformable boundary while it is about 40˚ for rigid boundary when shear band formed. As seen in table 44 in Appendix 3, the angle of friction obtained from Mohr-Coulomb envelope is about 27˚ for this system. This shows the direction of the shear band formed in the case of deformable boundary is similar to that in a triaxial test on dense sand.

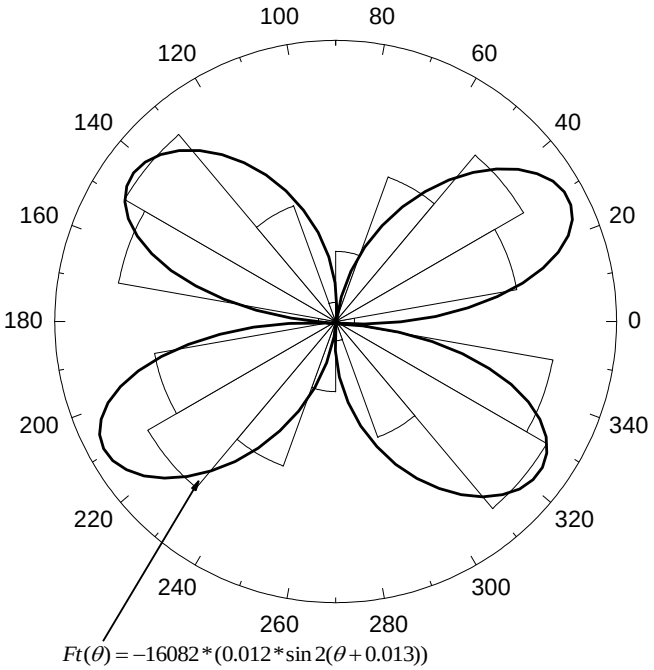

Figure 5-57 Shear force anisotropy of deformable boundary particles at $\varepsilon_{11} = 10\%$

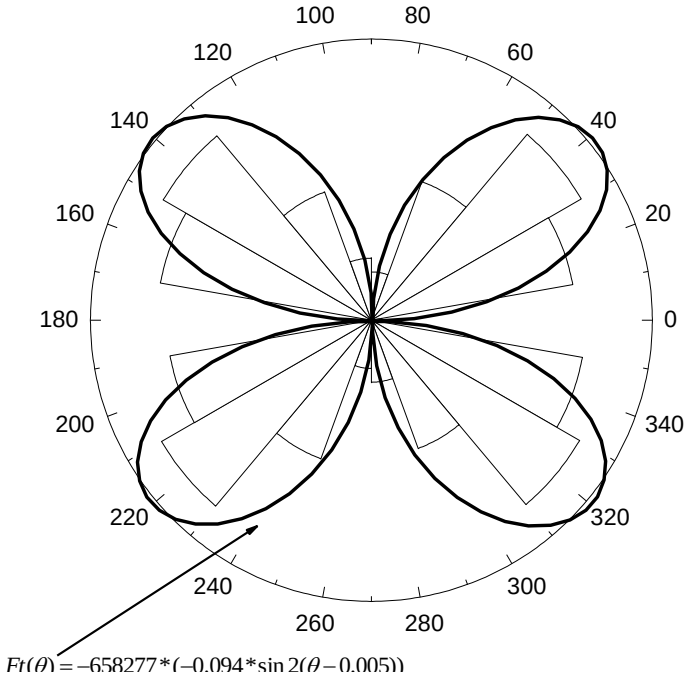

Figure 5-58 Shear force anisotropy of rigid boundary at $\varepsilon_{11} = 10\%$

5.4.1.6 The sensitivity of sand system to the isotropic stress

To investigate the effect of confining pressure on the macro mechanical behaviour of the particulate system, three different confining pressures 100,

200 and 300 [kPa] were applied. Table 5-11 shows the inter-particle properties along with size of sample, initial porosity, PSD, number of particles and confining pressures used for this study. The results are shown in figures 5-59 to 5-64 and table 44 in Appendix 3.

Test No.	k_n [N/m] *10^7	k_s [N/m] *10^7	μ	Width [cm]	Height [cm]	n	Range of PSD [mm]	Number of particles	Confining pressure [kPa]
1	8.45	8.45	0.9	7.5	15.0	0.12	1-2	8067	100
2	8.45	8.45	0.9	7.5	15.0	0.12	1-2	8067	200
3	8.45	8.45	0.9	7.5	15.0	0.12	1-2	8067	300

Table 5:11 The input properties used for sensitivity analysis of sand to the different confining pressures

Figure 5-59 shows the variation of deviatoric stress against axial strain. As expected an increase in confining pressure leads to an increase in the peak stress. For example, the ratio of peak stress in the case of a confining pressure of 300 [kPa] to that for 100 [kPa] is nearly 3.1, the ratio of peak stress for the case of 300 [kPa] to that for 200 [kPa] is almost 1.5 and the ratio of peak stress in the case for 200 [kPa] to that or 100 [kPa] is approximately 1.0. This shows that these ratios are in good agreement with the ratio 300 [kPa]/100 [kPa], 300 [kPa]/200 [kPa], and 200 [kPa]/100 [kPa], respectively. The reduction to post peak stress increases as the confining pressure increases and the post peak stress increases with confining pressure.

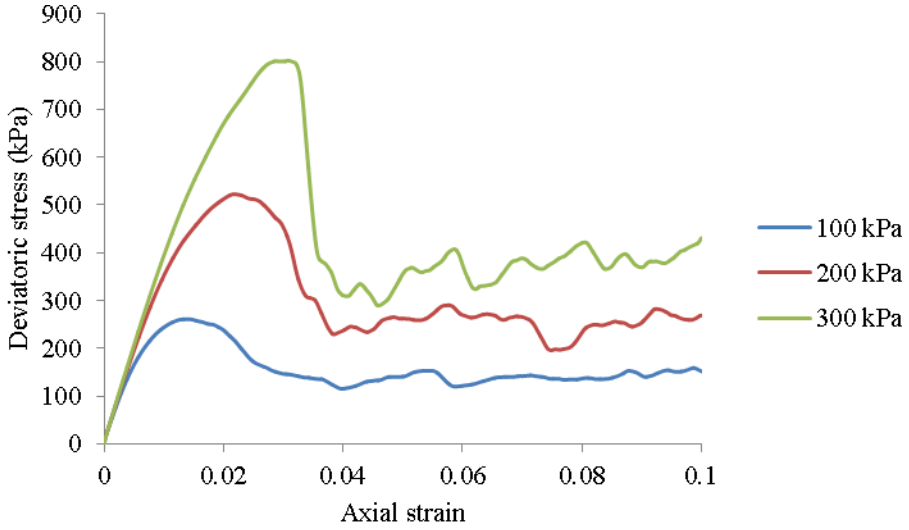

Figure 5-59 The sensitivity of macro-mechanical behaviour of sand to isotropic stress: deviatoric stress vs. axial strain

Figure 5-60 shows the variation of volumetric strain against axial strain for different confining pressures. As expected increasing the confining pressure leads to an increase in the degree of compaction or contraction of sand. This leads to an increase of the secant elastic modulus of sand E_{50}.

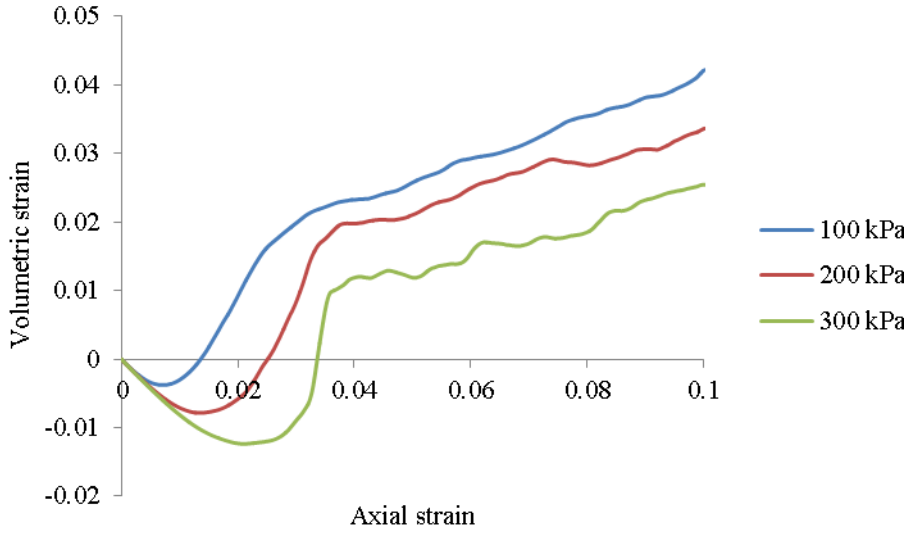

Figure 5-60 The sensitivity of macro-mechanical behaviour of sand to isotropic stress: volumetric strain vs. axial strain

Figure 5-61 shows the variation of E_{50} against confining pressures in terms of plane-strain and plane-stress. As expected increasing the confining pressure

leads to increase the degree of compaction E_{50} and angle of friction (figure 6-62).

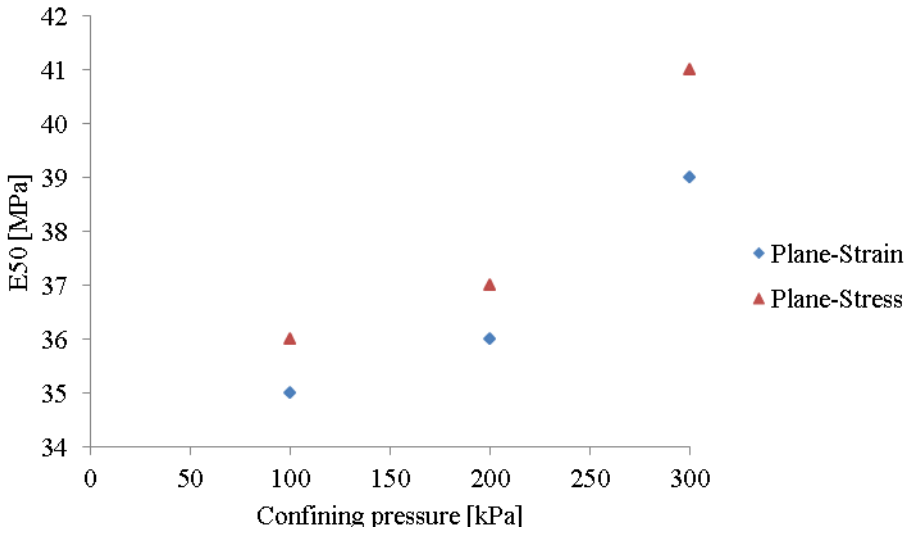

Figure 5-61 E_{50} against confining pressure for both plane-strain and plane-stress

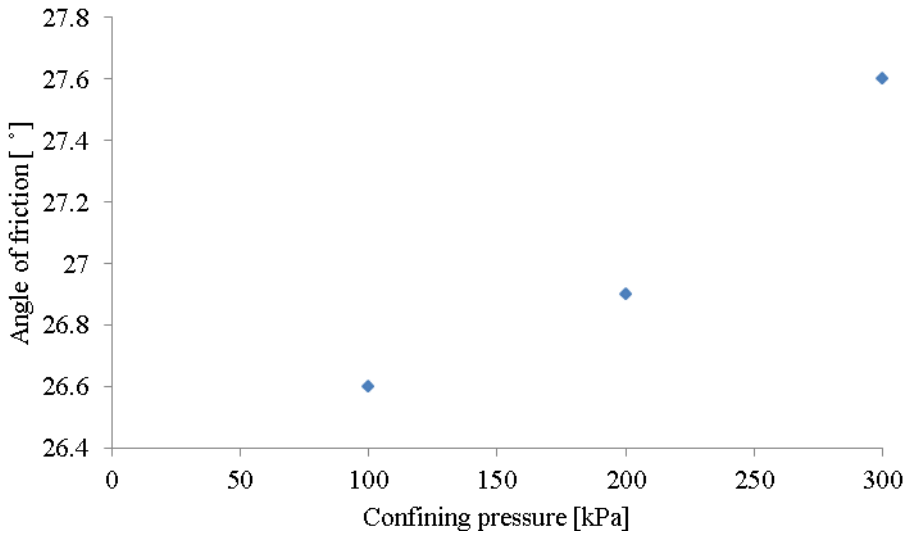

Figure 5-62 Angle of friction against confining pressure

Figure 5-63 shows that increase in confining pressure results in a decrease in Poisson's ratio. It is because the system shows more contraction by increasing the confining pressure.

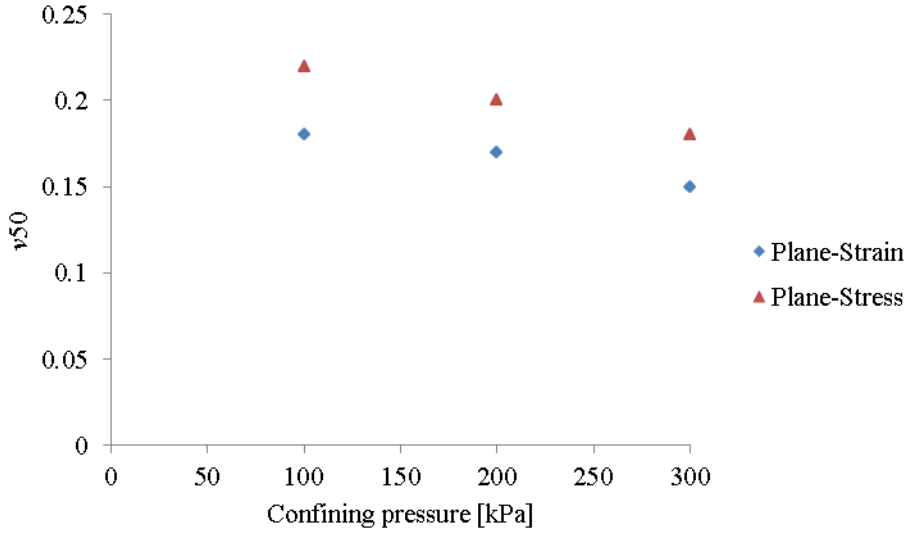

Figure 5-63 Poisson's ratio against confining pressure

Figure 5-64 demonstrates the Mohr-Coulomb failure envelope of sand. It can be seen from this figure that the cohesion term is zero.

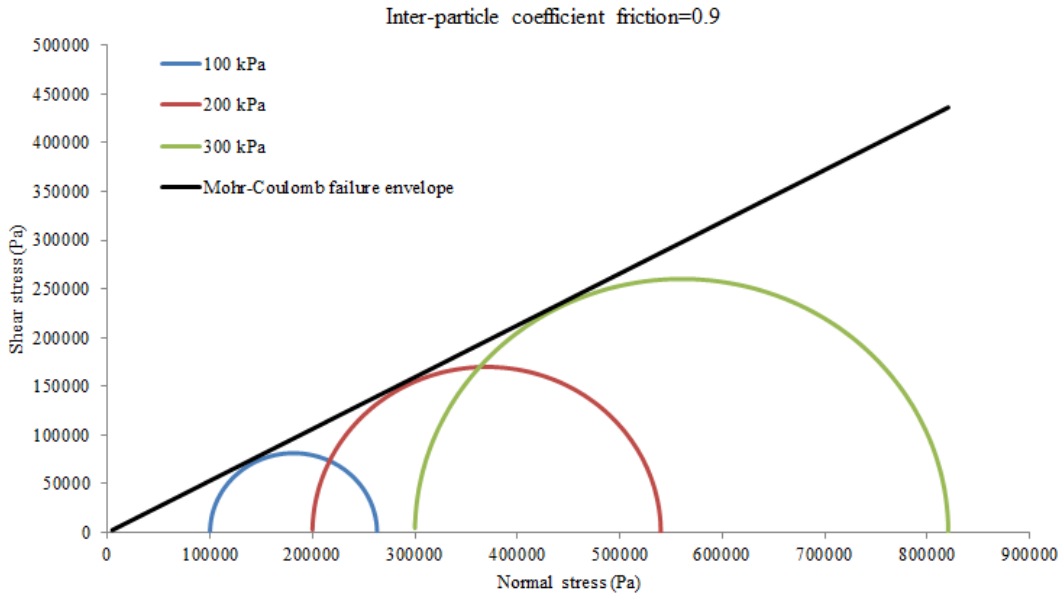

Figure 5-64 Mohr-Coulomb failure envelope.

5.5 Conclusion

In this chapter the sensitivity of an idealised particulate system to the inter-particle friction and normal and shear particle stiffnesses was investigated. 42 biaxial tests with rigid walls were investigated. For this purpose, more than 5800 lines code were written by Fish language programming. The values of inter-particle properties for these 42 tests were extracted from table 4-1.

The results show that elastic parameters, Young's modulus and Poisson's ratio, with particle diameters varying between 1.25 [mm] and 2.0 [mm], are greatly dependent on the normal particle stiffness while the angle of friction is strongly dependent on the inter particle friction. It was seen that an inter-particle friction between 0.5 and 1.2 produced an angle of friction between 30˚ and 37˚ such that the relationship between them seems to be linear. These values are compatible with typical ranges of angle of friction of medium sand. That is, to produce the angle of friction for dense sand, a higher inter-particle coefficient friction (i.e. more than 1.2) should be applied. It was also seen that the values of normal particle stiffnesses between 8.45*10^7 and 17.1*10^7 with ratio k_s/k_n=1 results in sensible values of E_{50} of medium sand. However, Poisson's ratio obtained from these ranges produced a lower value than typical values for sand. That is, to produce E_{50} for dense sand, higher values for k_n should be applied. The sensitivity of Poisson's ratio to shear stiffness was investigated with a number of biaxial tests within ranges of normal particle stiffnesses between 8.45*10^7 and 17.1*10^7 and ratio k_s/k_n= 0.5. The results show that a decrease in shear particle stiffness produces sensible ranges of Poisson ratio for idealised sand which are compatible with those mentioned for typical medium sand while this decrease does not have any effect on E_{50}.

In terms of micro-mechanics, changes in inter-particle friction from 0.5 to 1.2 do not have any significant effect on the average fabric anisotropy and average normal force anisotropy, while this increase leads to increase the average shear force anisotropy. An increase in k_n results in an increase in average fabric anisotropy, while this increase results in initial rise in average normal force anisotropy. The average shear force anisotropy decreases

slightly when k_n increases. The deviation from the average symmetric of contact topology increase significantly when k_n increase. That is, the average coordination number decreases considerably when k_n increases. An increase in the ratio k_s/k_n from 0.5 to 1 does not have any effect on the micro-structure.

To investigate the macro-mechanical behaviour of idealised sand to the different boundary conditions two biaxial tests with the same initial condition and inter-particle properties were implemented, one with rigid walls and the other with deformable boundary particles. For the later one, a novel Fish code with approximately 1500 lines was written. The results show that the macro mechanical behaviour of sand obtained from these two different boundary conditions demonstrates the same behaviour till peak deviatoric stress.

To investigate the macro-mechanical behaviour of idealised sand to the different confining pressure three biaxial tests with the same initial condition and inter-particle properties were implemented with three confining pressure 100 [kPa] 200 [kPa] and 300 [kPa]. The results show that the E_{50} and angle of friction increase as the confining pressure increases.

Chapter 6

6 Studying the fabric of sand during earthquake

6.1 Introduction

The evolution of idealized sand fabric serves as a powerful tool to investigate its response during an intricate phenomenon earthquake. By monitoring the fabric components, a qualitative assessment of the response of granular sand to seismic loading can be attained. However, the fabric quantities such as “normal contact distribution”, “normal contact force distribution”, “shear contact force distribution”, “average coordination number” and “average symmetric geometric deviation index” are material-geometric-dependent quantities. That is, the geometry of contacts and contact forces are greatly dependent on inter-particle properties and the initial geometry of system. Additionally, the frequency and amplitude of an earthquake has a profound influence on the geometrical arrangement of contacts and contact forces such that a change in the contacts topology will influence the seismic micro-macro behaviour of particulate system. Therefore, a series of sensitivity analysis was undertaken to examine the effect of inter-particle properties such as normal and shear contact stiffness and inter-particle coefficient friction on the behaviour of idealized sand fabric during earthquake. The sensitivity of idealized sand fabric to different frequencies and amplitudes of earthquake load was also studied by performing a series of DEM simulations.

To study the evolution of the fabric quantities of a granular element using DEM simulations due to seismic activity, a novel deformable boundary particles algorithm was defined. The applied assumptions and limitations of this algorithm regarding seismic wave propagation through the sand media are presented in section 6.2. To apply this dynamic deformable boundary, the average shear velocity of particulate sand system is required. Section 6.3 investigates the sensitivity of seismic shear wave speed to the various earthquake frequencies. The validation of this new method is also described in section 6.4. The sensitivity of shear wave propagation to the different boundary conditions is also discussed in section 6.5. The influence of

different sample ratios on the shear wave propagation and fabric evolution of idealized sand is investigated in section 6.6. Section 6.7 studies the sensitivity of fabric quantities of sand system to the various earthquakes' frequencies. Section 6.8 studies the sensitivity of fabric quantities of sand system to the various earthquakes' amplitudes. Section 6.9 explores the sensitivity of fabric quantities of sand system to the various initial porosities. Section 6.10 explores the sensitivity of fabric quantities of sand system to the various normal particle stiffnesses. Section 6.11 presents the sensitivity of fabric quantities of sand system to the various inter-particle frictions. The influence of pile element on the fabric evolution will be studied in section 6.12. The conclusion is presented in section 6.13.

6.2 Assumptions and limitations of dynamic deformable boundary particles

One of the main differences between a quasi-static analysis and a dynamic analysis using DEM is that damping should be reduced to a physically realistic value when the aim is to simulate a dynamic problem (Marketos and O'Sullivan, 2013, Itasca, 2008). However, before applying dynamic loading, the particulate system being considered must be in relative static equilibrium. That is, the ratio of average unbalanced force to the maximum contact force must be below 0.005. The contact law used in this work is a linear elastic spring acting in parallel with a contact viscous dashpot, both in the normal and shear directions (see chapter 2 for more details). The damping force, *D*, is added to the contact force at each time step to absorb the kinetic energy of the particles. The magnitude of this force, whose direction is always opposite to the velocity vector, is calculated through $D = 2\beta\sqrt{mk}|V|$, where β is the critical damping ratio, m is the effective mass of the two particles in contact, k is the normal or shear contact stiffness and V is the relative normal or shear contact velocity. As mentioned in chapter four, the magnitude of critical damping ratio β for dynamic problems should be set to a low value in order to show the dynamic behaviour of system. (Marketos and O'Sullivan, 2013) applied 0.01 and 0.0 for the magnitude of normal and shear critical damping ratio for their DEM simulations, respectively, while (Zamani and El Shamy,

2012) applied 0.1 and 0.1 for the magnitude of normal and shear critical damping ratio, respectively. Thus, a sensitivity analysis is required to examine the effect of different normal and shear critical damping on the micro-macro-mechanical behaviour of idealized sand.

6.2.1 Boundary condition

As discussed in section 3.2, in reality seismic earthquake waves are produced at bedrock then they radiate to the soil media (see figure 3-7). Due to the limiting computing power of the current computers it is impossible to fully study the phenomena of wave propagation through idealized sand media using DEM simulations. Thus, the particulate sand media must be discretized into small elements (see figure 6-1). DEM simulation can be then applied for each element. If the seismic behaviour of the particulate element near the ground surface requires to be investigated, the impedance ratio of top boundary particles should be set to zero, while the impedance ratio of base and lateral boundary particles should be set to one to represent infinite media. If the seismic behaviour of the particulate element near the bed rock is investigated, the proper impedance ratio for those base boundary particles should be set to a very high value (Kramer, 1996), while the impedance ratio of the top and lateral boundary particles should be set to one to represent infinite media. This reflects any downward-traveling waves to the soil media, thereby trapping all of the elastic wave energy within the soil layer. In terms of an elastic bed rock, part of the seismic wave energy will be transmitted through the interface and continue traveling through the elastic base, whereas the remainder will be reflected at the interface and will travel back through the soil media. For this purpose, the impedance ratio of base particles should be greater than one. In the case of an infinite medium, all the energy of the wave will be transmitted through the interface, and there will be no reflection at the boundary. For this purpose, the impedance ratio of base particles should be set to one. In this research it is assumed that the bed rock is an infinite medium. The effect of other bed rock conditions on the propagation and fabric is recommended for further work. For those elements which are neither in contact with bedrock nor the free ground surface, the

impedance ratio should be set to one so that seismic waves travel across them without any reflection.

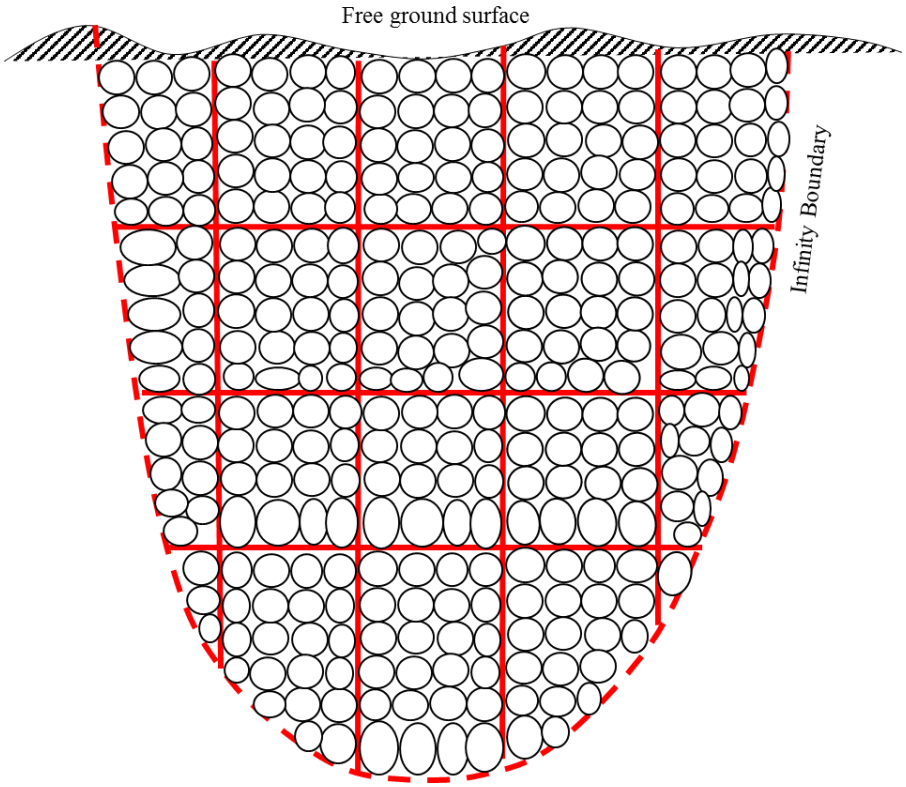

Figure 6-1 Discretization of half-space schematically

6.2.1.1 The dynamic deformable boundary condition

The numerical algorithm which is used to create a dynamic deformable boundary for seismic application in granular soil dynamics is different to that for deformable boundary particles for a static loading discussed in chapter 4. In the latter, once a particulate system reaches to isotropic state, the lateral rigid walls are removed and numerical deformable boundary particles are applied. This models the latex that is used for the standard triaxial test. It applies an external force corresponding to a uniform pressure in x and y direction to each boundary particle in order to maintain the confining pressure. For seismic application where the wave-induced grain velocities are considerable during an earthquake, the external force applied through the deformable boundaries is not constant. Therefore, the algorithm of

deformable boundary particles should be modified to take into account the effect of dynamic boundary condition (see chapter 3 for more details). The framework of this algorithm is as follows:

1- Create four rigid walls to build up the initial geometry of the model (see figure 6-2).

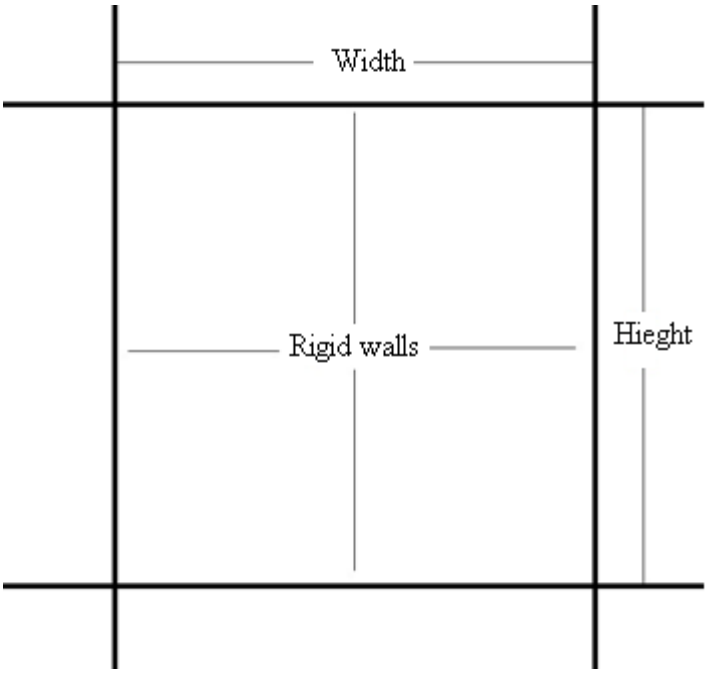

Figure 6-2 The four rigid walls were created to establish the initial geometry of the model

2- Generate uniform random sand particles between 1.5 to 2.0 [mm] in size and expand their radius to reach the porosity of the system to the desired value as discussed in chapter 4. Then allow the system to reach to static equilibrium (see figure 6-3). The global or mass damping is applied at this stage to bring the system to static equilibrium more rapidly. The value of mass damping ratio is, therefore, set to 0.75.

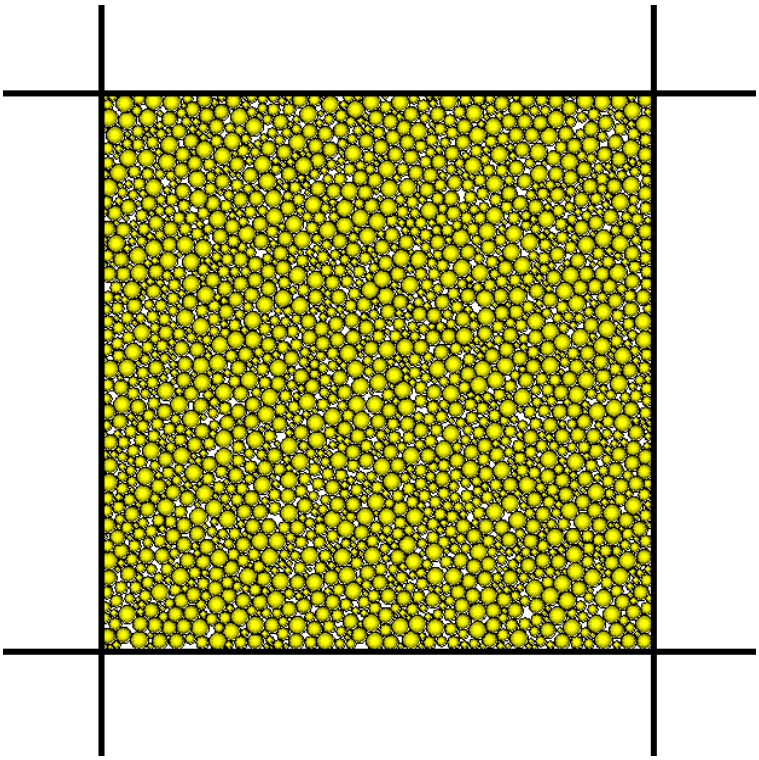

Figure 6-3 Generation of uniform randomly ideal sand particle

3- In this stage, the rigid boundaries are moved by applying servo-mechanism control discussed in section 4.3.5.1 to apply the required confining stress. It is to be noted that at this stage the inter-particle coefficient friction is set to zero so that the isotropically consolidation process can be achieved rapidly. When the system reaches to the desired confining pressure, extra mechanical cycles are executed to bring the system to static equilibrium.

4- Next, the dynamic deformable boundary particles algorithm is run. To apply dynamic deformable boundary particles after terminating stage 3, those particles in contact with the rigid walls are recognised and their addresses are stored in four separate arrays. At the same time, the un-balanced forces of these particles are stored into four different arrays. Next, the four rigid walls are removed. Once these walls are removed, an external force exists, which is equivalent to the un-balanced force on each particle. Extra mechanical cycles are required to bring the system to static equilibrium (see figure 6-4).

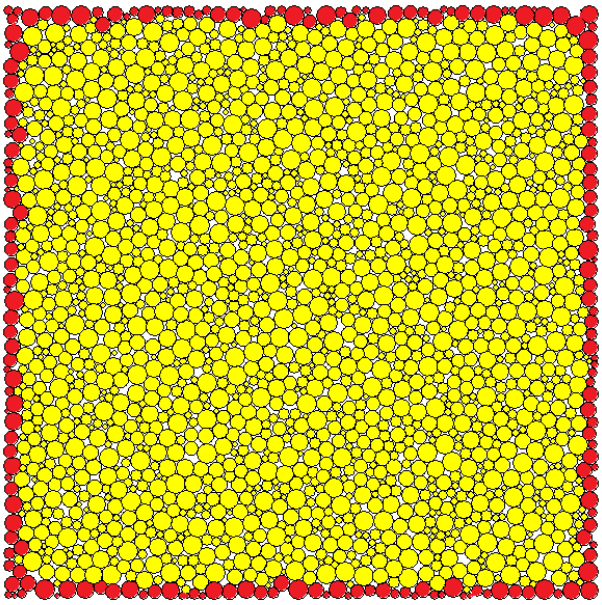

Figure 6-4 applying top and bottom deformable boundary

5- When the system reaches the equilibrium, the shear wave component of an earthquake load is applied to the base of the model. The stages of applying a seismic shear wave force to the base deformable boundary particles and applying a dynamic boundary condition to the top and lateral deformable boundary particles are as follows:

5-1- In this stage, the global damping is set to zero. Normal and shear contact viscous damping is added (see figure 6-5). In this figure, k_n, k_s, c_s and c_n are the normal contact stiffness, shear contact stiffness, normal contact viscous damping ratio and shear contact viscous damping ratio. The values of c_s and c_n are set to 0.01. The inter-particle coefficient friction value is also set in this section.

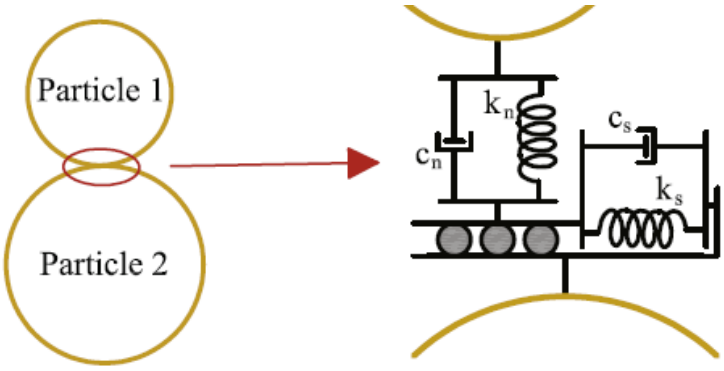

Figure 6-5 The rheological model for the inter particle contact for seismic application

5-2- At each time step, a dynamic force is applied to each base particle. This external dynamic force is superimposed on the static external force of each base boundary particle (see figure 6-6). The dynamic force is as follows:

$$F_{earthquake:shear} = \alpha * \rho * V_S * A * \left(2 * \dot{U}_x - \dot{x}\right) \quad 6.1$$

where A is the base particle disk area (for 2D) perpendicular to the shear wave.

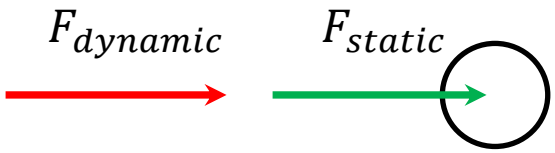

Figure 6-6 Apply both static and dynamic forces to a base particle

5-3- If P-wave propagation is to be studied then a dynamic normal force is applied to the base particles at each time step as follows (see figure 6-7):

$$F_{earthquake:normal} = \alpha * \rho * V_P * A * \left(2 * \dot{U}_y - \dot{y}\right) \quad 6.2$$

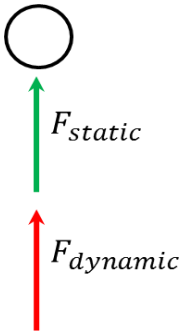

Figure 6-7 Apply both static and dynamic forces to a base particle

5-4- To consider dynamic boundary on the lateral deformable boundary particles, the following shear and normal dynamic forces should be applied on each particle at each time step as follows:

$$F_{dynamic;shear} = \alpha * \rho * V_S * A * \dot{x} \quad 6.3$$

$$F_{dynamic;normal} = \alpha * \rho * V_P * A * \dot{y} \quad 6.4$$

The ratio of P-wave velocity to S-wave velocity $\frac{V_P}{V_S}$ is between 1.5 and 2.0 for dry sand (Osman, 2010). A ratio of 1.75 was used.

5-5- To consider dynamic boundary on the top deformable boundary particles, the following shear and normal dynamic forces were applied to each particle at each time step as follows:

$$F_{dynamic;shear} = \alpha * \rho * V_S * A * \dot{x} \quad 6.5$$

$$F_{dynamic;normal} = \alpha * \rho * V_P * A * \dot{y} \quad 6.6$$

These dynamic forces simulate an infinite media and transmit the whole energy to them (see figure 6-8).

5-6- The stages 4 and 5 are invoked every time step.

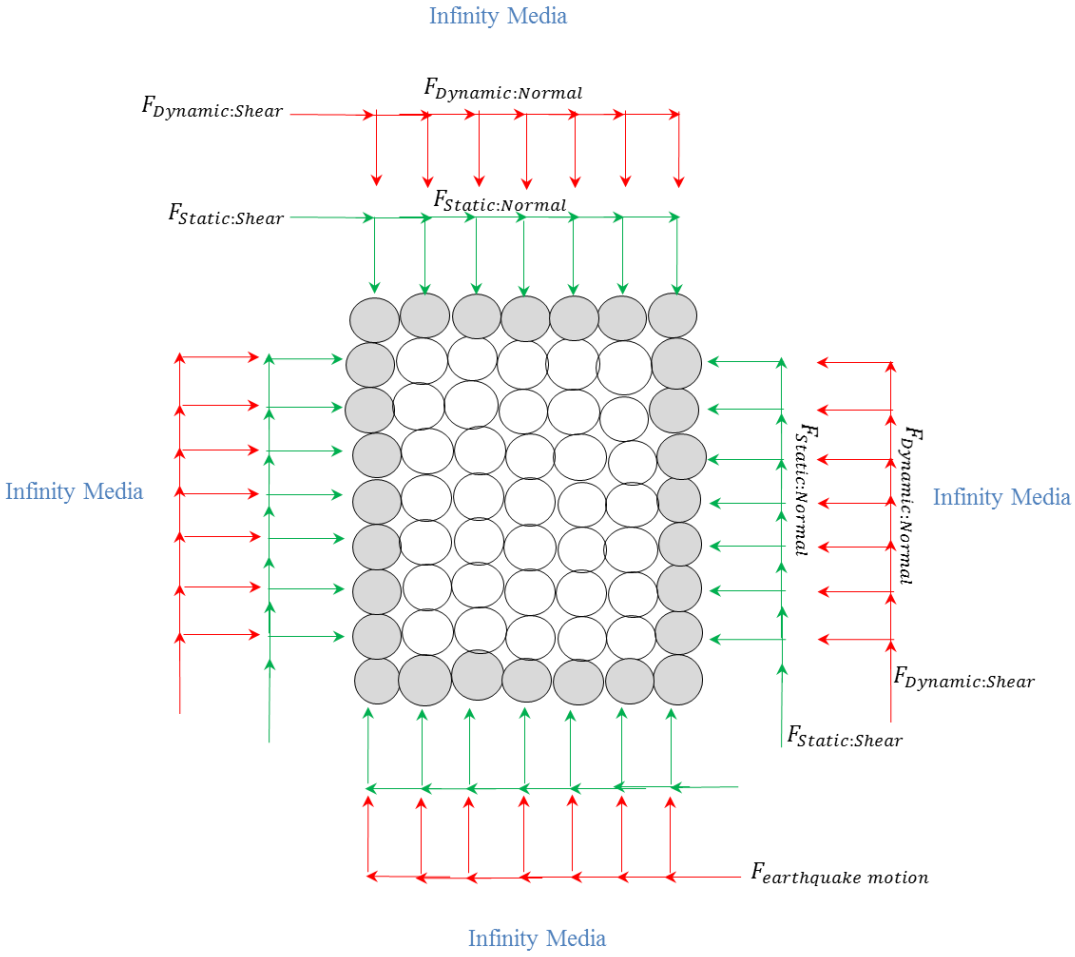

Figure 6-8 Dynamic deformable boundary particles

6.3 The sensitivity of shear wave velocity to the various earthquake frequencies

An earthquake produces two modes of propagation which are distinguished by the relative directions of particle oscillation. P-waves have particle motion parallel to the direction of propagation and S-waves have particle motion perpendicular to the direction of propagation. However, shear wave propagation has a more destructive effect on the stability of both soil media and structures in comparison to P-wave propagation. It is because during P-wave propagation, the weight of ground and superstructure resists the vertical ground motion. O'Donovan et al. (2012) showed that the value of shear wave speed significantly changes between the frequencies 4 [kHz] and 12 [kHz] for hexagonal pack when the material is in fully elastic mode. However, these frequencies are not in the range of typical earthquake frequencies. The aim of this section is to compute and measure the sensitivity of shear wave speed with various seismic earthquakes' frequencies. As the maximum value of shear wave velocity is obtained when the material is in elastic mode, the input motion should be small. To assure that the system is in elastic mode, the amplitude of input velocity is set to 1μm/s. The same scenario applied by (O'Donovan et al., (2012) and Marketos and O'Sullivan, (2013) (see chapter three for more details) to calculate shear wave velocity is investigated but using dynamic boundaries and irregular packing. For this purpose, a velocity-sine wave with the frequencies between 1 and 6 [Hz] are applied to the base particles (i.e. transmitter particles) and the average velocities of top particles (or receiver particles) (see figure 6-9) are recorded. Table 6-1 shows the input inter-particle properties for the DEM simulations. k_n, k_s and μ are normal and shear contact stiffness and inter-particle coefficient friction. In *PFC*^{2D}, there are three ways to import input motion to the particle: applying velocity, applying displacement and applying external force to the particles. External load (see Eq. 6.1) cannot be used to compute the shear wave velocity. It is because the value of shear wave velocity is one of the required parameters for equation 6.1. Therefore, velocity and displacement can be applied. Only velocity is considered in this research because it is more compatible with the

algorithm and is suggested by *PFC*^{2D} (Itasca, 2008) when the aim is to apply dynamic load to a group of particles. A velocity-sine wave was applied to the base particles. They were initially fixed in a horizontal direction then the sine velocity wave was prescribed to them. To allow that input motion to be fully transmitted to the soil element, the base particles were not allowed to rotate. Figure 6-10 shows that the velocity-time history at the receiver particle for different frequencies when the amplitude of input motion for whole simulations was similar. T in horizontal axis in figure 6-10 is period which is $\frac{1}{f}$, where *f* is frequency.

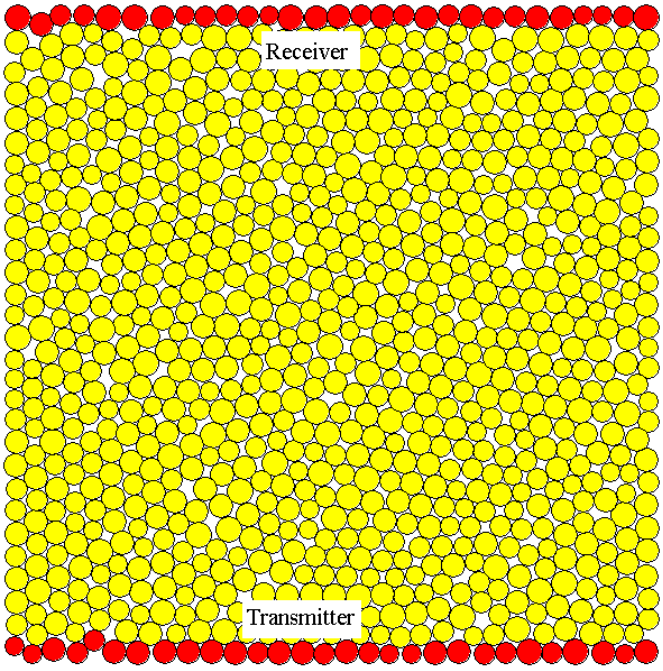

Figure 6-9 The transmitter and receiver particles

To compute V_S, the travel distance and travel time of the shear component of the seismic wave must be known. The travel distance of the shear wave component is taken as the distance between the transmitting and receiving particles. To compute the travel time two methods are generally applied which are:

- Start–start,

- Peak–peak,

In the first method, the start time of the propagating wave at the transmitter is subtracted from the start time of the propagating S-wave at the receiver particle. Toomey and Bean (2000) and (El Shamy and Zamani, 2012) applied this method to measure arrival time for their work.

The peak–peak travel time is taken as the difference of the peak time of the propagating wave at the transmitter and the peak time of the propagating S-wave at the receiver particle. However, the peak time cannot be easily distinguished for discrete systems Marketos and O'Sullivan, (2013) therefore the start–start approach was used to compute the travel distance.

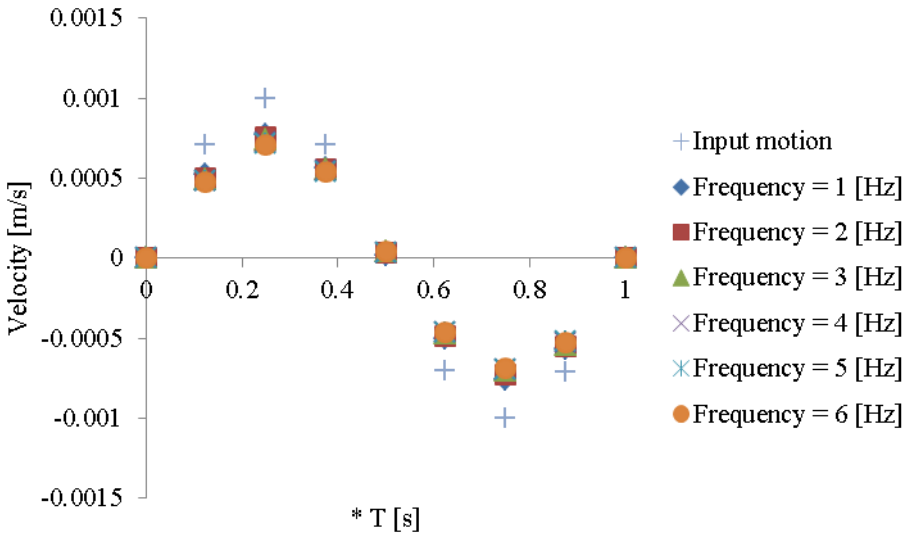

Figure 6-10 The velocity-time history of receiver particle for various frequencies

Figure 6-11 shows that the trend of average shear velocities of receiver particles from t = 0 to arrival times of these six DEM models are the same. Figure 6-12 shows the variation of shear wave velocity of the idealized system to the various earthquake frequencies. The figure demonstrates that shear wave velocity is constant when the frequencies are between 1 and 6 [Hz]. (Thomas et al., 2009, O'Donovan et al., 2012) measured the variation of shear wave velocity of between 4 to 12 [kHz] for hexagonal packing and found that the shear wave velocity increases.

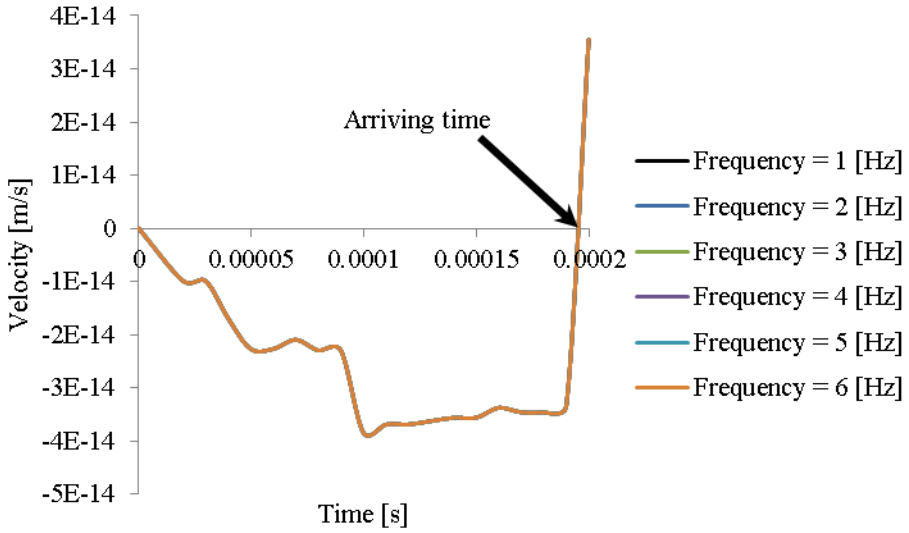

Figure 6-11 Comparing the arrival time of these six DEM models in order to compute the shear wave velocity

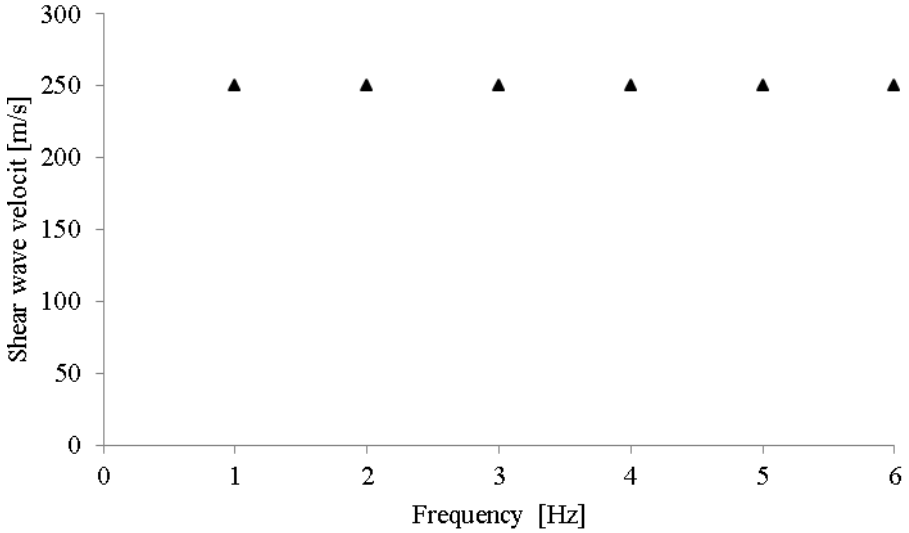

Figure 6-12 Sensitivity of shear wave velocity to the earthquake frequencies

The maximum value of G_{max}, the small-strain shear modulus is as follows:

$$V_s = \sqrt{\frac{g * G_{max}}{\rho_{bulk}}} \qquad 6.7$$

where G_{max}, g and ρ_{bulk} are the small-strain shear modulus, gravity acceleration and bulk density. The values of G_{max} from these simulations were compared with G_{max} from biaxial test with similar inter-particle

properties (Table 6.1). The results show that G_{max} obtained from these six tests are in good agreement with that obtained from biaxial test in chapter 5. Only 4.9% error is between these values.

f [Hz]	V_s [m/s]	k_n [N/m] *10^7	k_s [N/m] *10^7	μ	ρ_{bulk}[kg/m^3]	G_{max} [MPa]	G_{max} [MPa] Obtained from biaxial test	Error [%]
1	250.37	8.45	8.45	0.9	2250	14.1	14.8	4.9
2	250.37	8.45	8.45	0.9	2250	14.1		
3	250.37	8.45	8.45	0.9	2250	14.1		
4	250.37	8.45	8.45	0.9	2250	14.1		
5	250.37	8.45	8.45	0.9	2250	14.1		
6	250.37	8.45	8.45	0.9	2250	14.1		

Table 6:1 The values of G_{max} vs. frequency

6.4 The verification of the proposed algorithm

To verify the code provided for this study as well as those results shown in table 6-1, the displacement-time history of the receiver particle obtained from this method was compared to that obtained by O'Donovan et al., (2012). Table 6-2 shows the dimension of the model, inter-particle properties, particle radius, frequency and amplitude of input motion used by O'Donovan et al., (2012). Figure 6-13 shows the regular DEM mono-size pack created by this method and the lattice hexagonal packed created by O'Donovan et al., (2012).

After generating the particles, the granular system was isotropically consolidated to 1.0 [MPa]. The dynamic deformable boundary particles algorithm was then applied. The input motion applied to the transmitter particle and the displacement-time history of receiver particle was tracked. Figure 6-14 compares the displacement-time history of the receiver particle for these two models. The figure shows that the response of receiver particle for these two models is similar in shape but different in value. The reasons

for this difference are due to the different boundary conditions and the particle arrangement. Those particles in contact with the rigid base including the transmitter cannot move down due to the rigid base constraint. This issue cannot happen with for deformable boundary particles since the base particles can move down which absorbs some of the energy of the system. A lattice hexagonal pack means the seismic wave reaches the receiver particle faster than the irregular pack (see figure 6-15). The shear wave velocity obtained by O'Donovan et al., (2012) was 340 [m/s] compared to 250 [m/s] with irregular packing and deformable boundaries.

Height [m]	0.24
Width [m]	0.12
k_n *(N/m)*	$1*10^9$
k_s *(N/m)*	$1*10^9$
μ	0.65
Particle radius [m]	0.0029
Global damping ratio	0.01
Frequency [kHz]	8.2
Amplitude [m]	$1.5*10^{-5}$
Confining pressure [MPa]	1.0
Shear wave velocity [m/s]	400.0

Table 6:2 The input data used for validation test (O'Donovan et al., (2012)

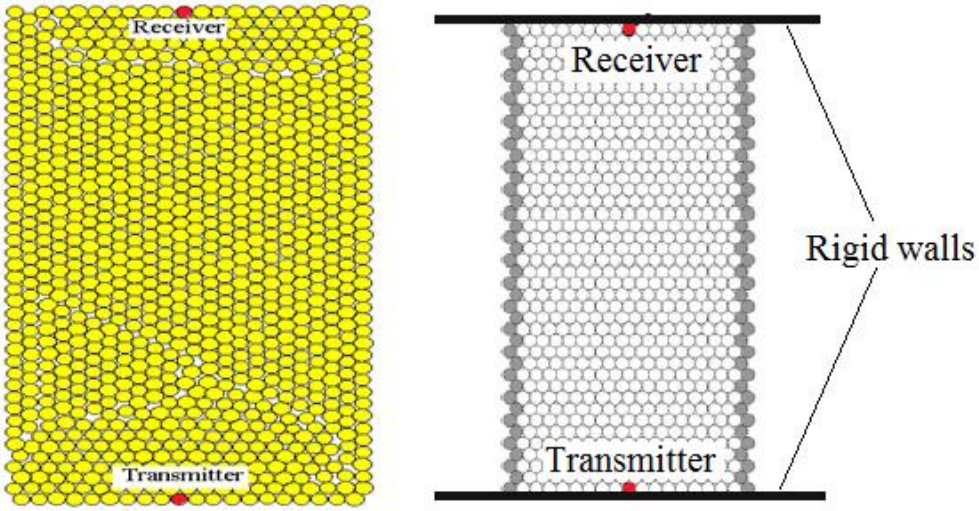

(a) (b)

Figure 6-13 DEM models: (a) Dynamic deformable boundary condition, (b) mixed boundary condition (after O'Donovan et al., (2012))

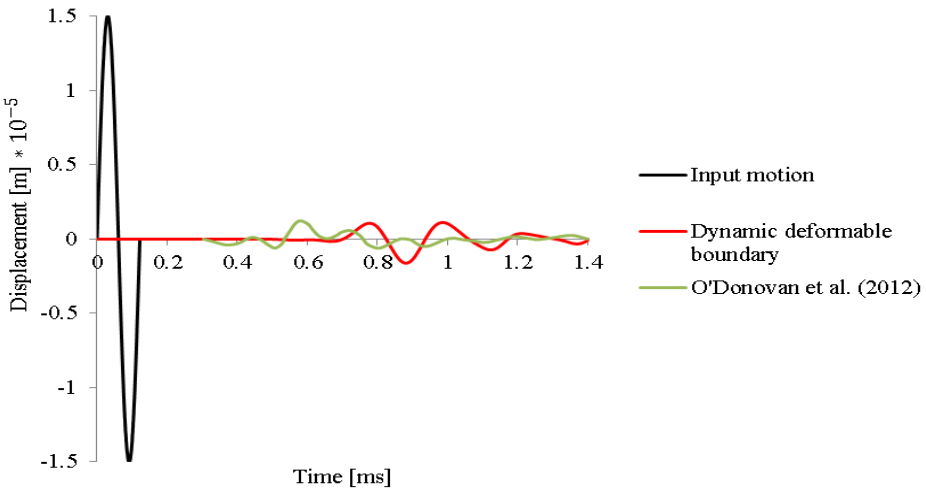

Figure 6-14 The displacement-time history of the receiver particle for two different methods with the same input motion

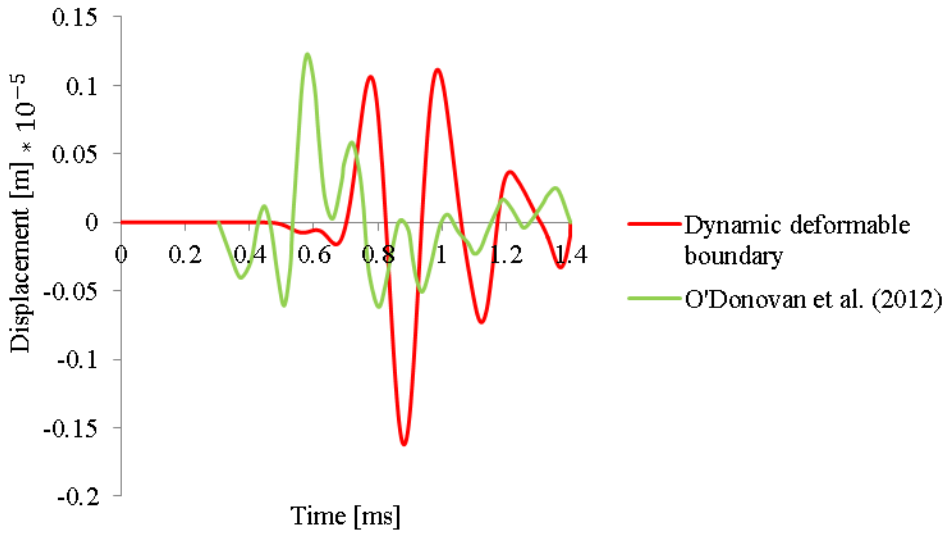

Figure 6-15 The displacement-time history of the receiver particle for two different methods

6.5 The sensitivity of shear wave propagation to the different boundary conditions

In the previous section, it was seen that the existence of horizontal rigid walls and hexagonal pack leads to an increase in shear wave velocity in comparison with that obtained from dynamic deformable boundary particles. A sensitivity test is required to distinguish how the side boundaries affect the base and top particles velocities. For this purpose, two DEM simulations with the similar initial condition but with different boundary conditions: rigid boundaries and dynamic deformable boundary particles were executed (see figure 6-16). A single sine load with the frequency 6.0 [Hz] and amplitude $1*10^{-3}$ [m/s] was considered. Table 6-3 show the details relating to these two simulations.

Test No.	Boundary condition	k_n and k_s [N/m] * 10^7	μ	Confining pressure [kPa]	n	Range of PSD [mm]
1	Rigid	8.45	0.9	100.0	0.12	1.5-2
2	Deform.	8.45	0.9	100.0	0.12	1.5-2

Table 6:3 The properties of the two DEM models used to study the effect of the type of boundaries

After generating the particles within a chamber with sample ratio 4 (width/height=4.0), the system was isotropically consolidated to reach 100 [kPa]. In the case of the rigid boundaries, the bottom rigid boundary was moved by applying a sine wave and a servo-control mechanism simultaneously applied to maintain the confining pressure on these four boundaries. The average base and top velocities of the particles were recorded. Figure 6-17 clearly shows that the velocities of base and top particles are similar. As the chamber is enclosed with rigid boundaries, the induced waves cannot be transmitted over the boundaries due to high impedance ratio. Thus, the energy of the system cannot be absorbed at the boundaries. This means the waves are reflected and the waves amplified.

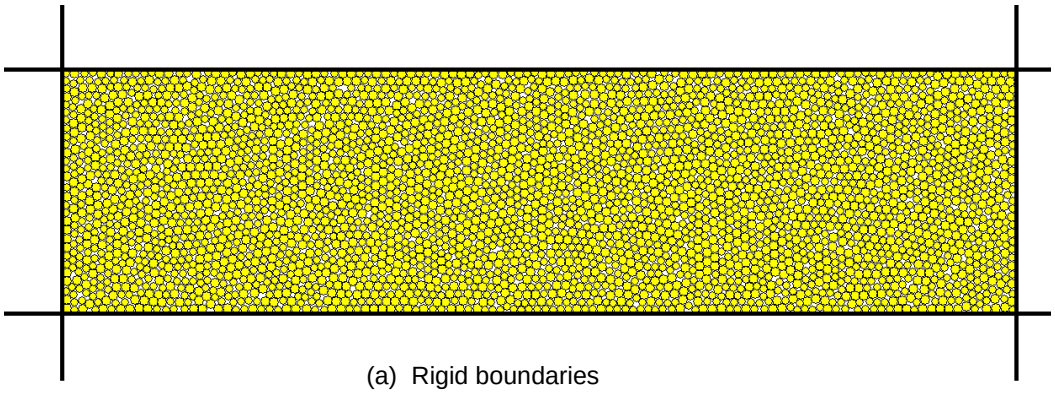

(a) Rigid boundaries

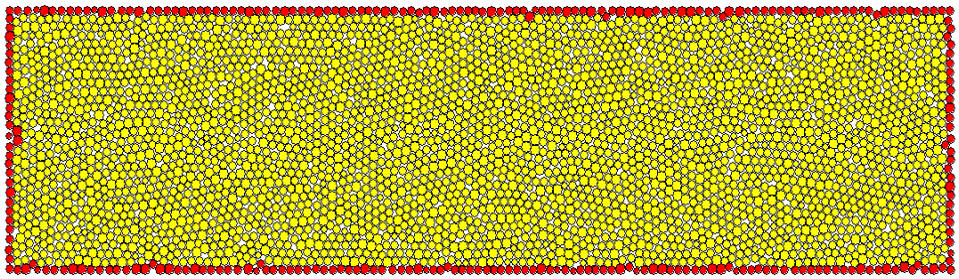

(b) Dynamic deformable boundaries

Figure 6-16 DEM model: (a) rigid boundaries, (b) dynamic deformable boundary particles

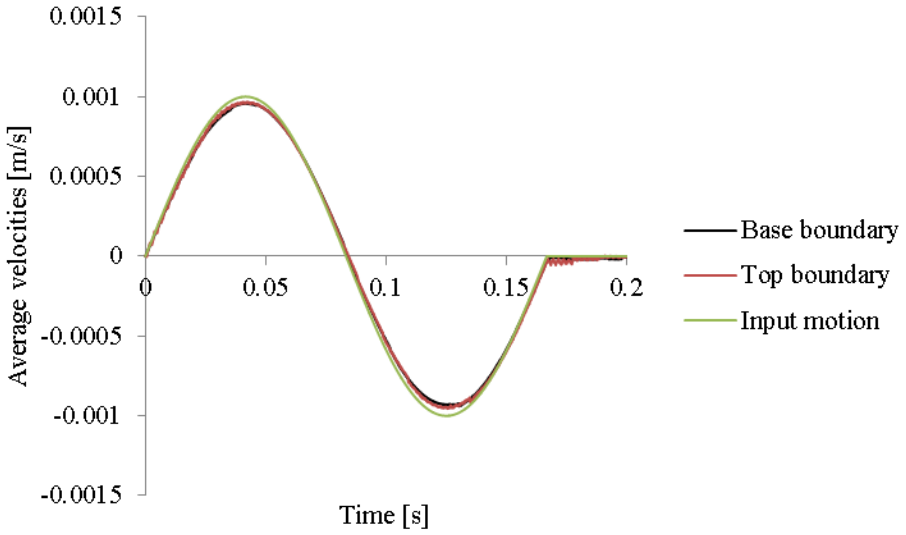

Figure 6-17 Average velocity-time history of top and bottom boundaries

Figure 6-18 compares the time-history of the average velocities of the top particles obtained from these two models. The average velocity of the top particles is similar to the input velocity; that is the amplification factor was 1.01 (Table 6.4). It is to be noted that the amplification factor is ratio $\frac{\text{Average maximum top boundary velocities}}{\text{Average maximum base boundary velocities}}$. The amplification factor for the deformable boundary was 0.85 showing that the deformable boundaries absorbed some of the energy.

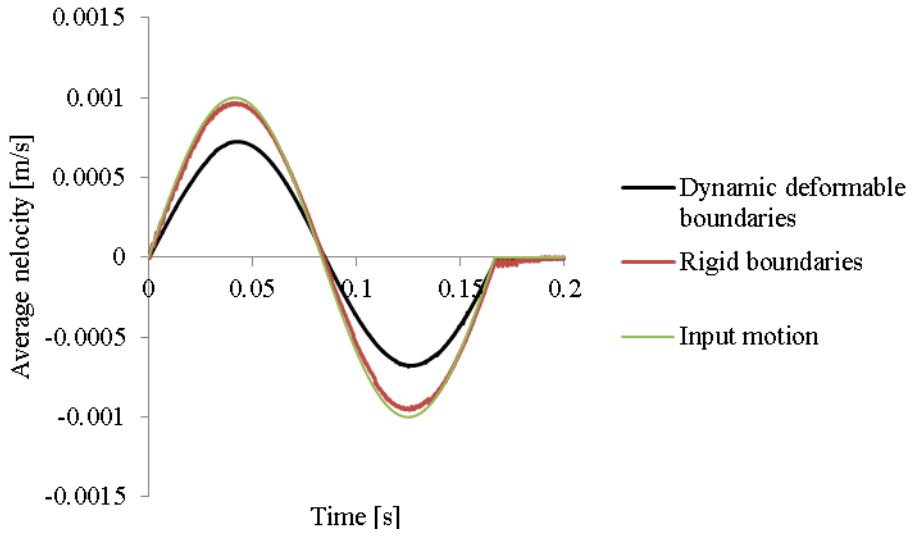

Figure 6-18 A comparison of the average top particles velocities vs. time

Boundary condition	Dynamic deformable boundaries	Rigid boundaries
Average maximum base boundary velocity [m/s]	0.000853	0.000958
Average maximum top boundary velocity [m/s]	0.000725	0.000968
Amplification factor	0.849941	1.010194

Table 6:4 The seismic characterization of average top and bottom velocities for two different boundary conditions for sample ratio = 4

This leads to the conclusion that applying rigid boundaries may amplify seismic waves, while applying dynamic deformable boundaries absorb the seismic waves. Further work is needed to establish whether this is always the case.

6.6 The influence of sample ratio

In reality, the earthquake wave propagates within a semi-infinite media (i.e. the width of the soil layer is much greater than its depth). Thus an earthquake waves naturally travel to infinity. However, due to the cost of DEM simulations, it is impossible to simulate a semi-infinite particulate media with current computers. Thus, the DEM model should be necessarily bounded but this may lead to changes in the micro-scale responses such that this alteration may influence the fabric of system.

6.6.1 The sensitivity of sample ratio on the micro-scale responses

The aim of this section is to investigate the effect of various sample ratios on the propagation of the shear wave through the idealized sand by measuring the particle-scale responses such as particle velocity and kinetic energy. This issue was initially investigated by Marketos and O'Sullivan (2013). They showed that with a uniform hexagonal lattice DEM pack and no slippage between the contacts (i.e. the work done by friction between particles are zero), the velocity of a receiver particle in horizontal and vertical directions was then tracked during the shear wave propagation. The results showed that if the width of sample is 2.25 times bigger than the height of sample, the reflecting waves due to the side boundaries during seismic shear wave propagation will not significantly effect the micro-scale responses such as particle velocity. Furthermore, in their work, the applied frequency was 40

[kHz] while the frequencies of earthquake are between 1 and 6 [Hz]. Moreover, the input motion in that study was only applied to one particle, the transmitter particle (see chapter 2 for more detail).

To investigate the effect of shear earthquake wave propagation on idealized sand system, four different sample ratios were used for this study (see figure 6-19). Table 6-5 shows the inter-particle properties, height, initial porosity, range of particle size distribution (PSD), frequency and amplitude of these four samples ratios. The inter-particle properties used for these DEM simulations were obtained from the sensitivity analysis in chapter 5. A single periodic sine load with frequency 6.0 [Hz] and input velocity amplitude $1*10^{-3}$ [m/s] was applied in horizontal direction to the base boundary particles for the four DEM models. The average velocities of the top boundary particles in x and y directions was then recorded (see figure 6-20 and figure 6-21). Figure 6-20 shows that the amplitudes of the average velocities at the top of the samples were different. It is because the total kinetic energy of the system obtained from the summation of the micro-scale kinetic energy of each particle at the based boundary particles increases by increasing the width of sample (see figure 6-22). However, this increase slightly increase after sample ratio = 3. The micro-scale kinetic energy of system obtained from the following equation:

$$E_{kinitic} = \sum_{t=0}^{T} \sum_{N=1}^{p} \frac{1}{2} m_p \mathrm{v}^2 + \frac{1}{2} I_p \dot{\theta}^2 \qquad 6.8$$

where t, T, p, m_p, v, I_p and $\dot{\theta}$ are time, period, number of particles, particle mass, particle translational velocity, moment of inertia of particle and rotational velocity of particle, respectively. Marketos and O'Sullivan (2013) suggested that the reason for this increase in amplitude is because of side boundaries wave reflection. This should mean that increasing the width of the sample should reduce the effect of the boundaries. Figure 6-20 shows that the difference in amplitude between sample ratio 3 and 4 is lower than that for sample ratio 1 and 1.5. This suggests that an increase in the sample ratio leads to a decrease in the effect of reflecting wave due to the side boundaries. Figure 6-23 clearly shows that an increase in sample ratio leads to an increase in average velocity but the increase reduces as the sample

ratio increases. It also shows that there is a sample ratio such that boundaries have no effect. Figure 6-24 shows the influence of sample ratio on the amplification factor. Figure 6-24 also shows that there is a sample ration such that the boundaries have no further effect on the amplification factor. This investigation leads to this conclusion that the minimum sample ratio required to decrease the effect of side boundaries should be 4. The influence of sample ratios on fabric of sand during a sine load will be investigated in the following section.

Sample ratio (width/height)	Height [cm]	k_n [N/m] * 10^7	k_s [N/m] * 10^7	μ	n	Range of PSD [mm]	f [Hz]	Amplitude [m/s] *10^{-3}
1.0	5.0	8.45	8.45	0.9	0.12	1.5-2	6.0	1.0
1.5	5.0	8.45	8.45	0.9	0.12	1.5-2	6.0	1.0
3.0	5.0	8.45	8.45	0.9	0.12	1.5-2	6.0	1.0
4.0	5.0	8.45	8.45	0.9	0.12	1.5-2	6.0	1.0

Table 6:5 various samples ratio and inter-particle properties considered in this study

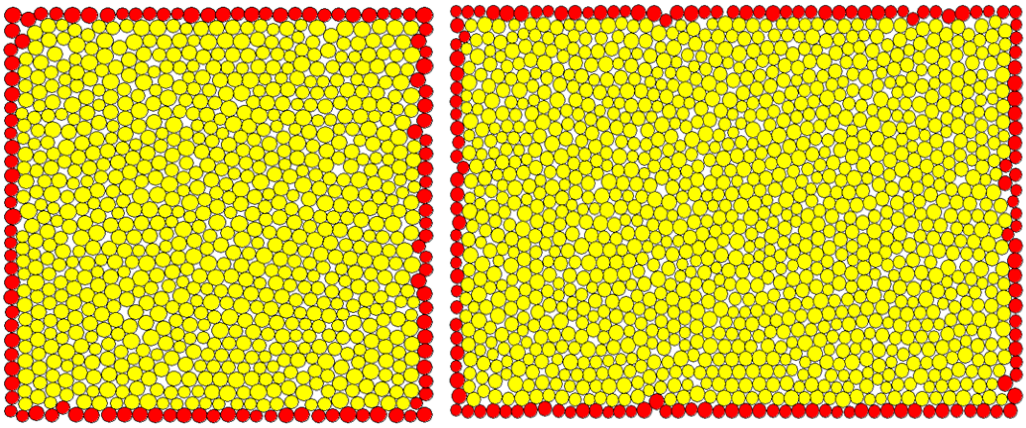

(b) Sample ratio=1.0 (a) Sample ratio=1.5

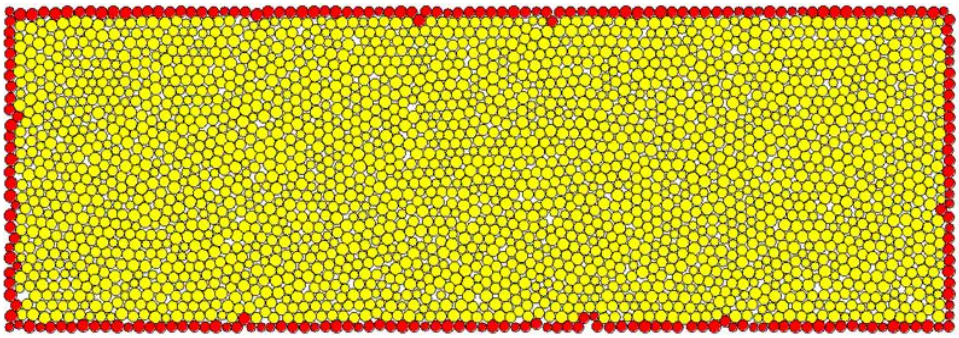

(c) Sample ratio=3.0

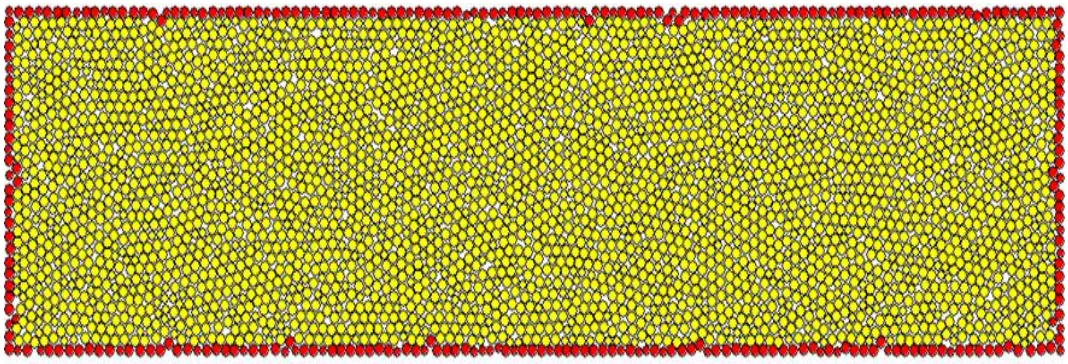

(d) Sample ratio=4.0

Figure 6-19 Four DEM simulations in order to investigate the effect of sample ratio on overall seismic behaviour of idealized sand (a) Sample ratio=1.0, (b) Sample ratio=2.0, (c) Sample ratio=3.0 and (d) Sample ratio=4.0

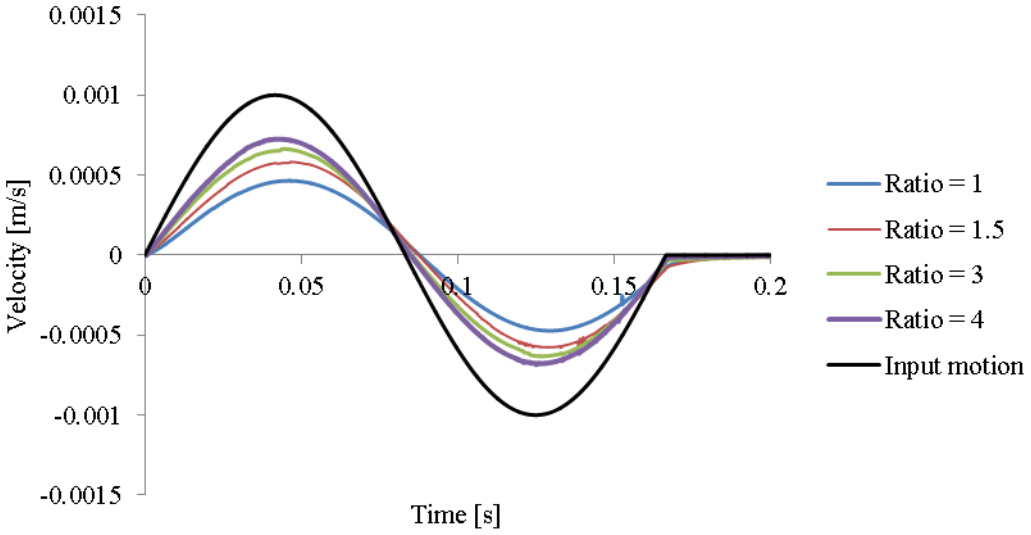

Figure 6-20 Average shear velocity of top boundary particles vs. time for four samples ratio

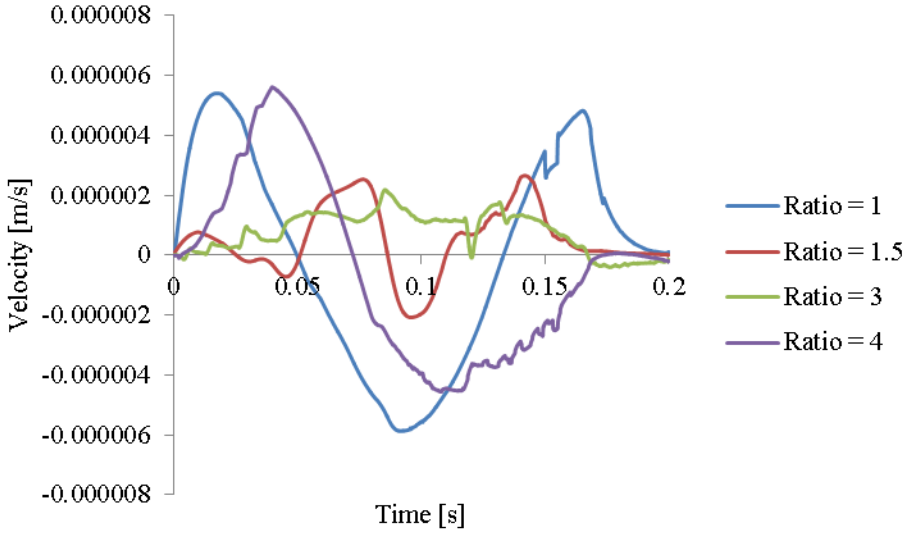

Figure 6-21 The recorded vertical average top boundary particles velocity for four samples ratio

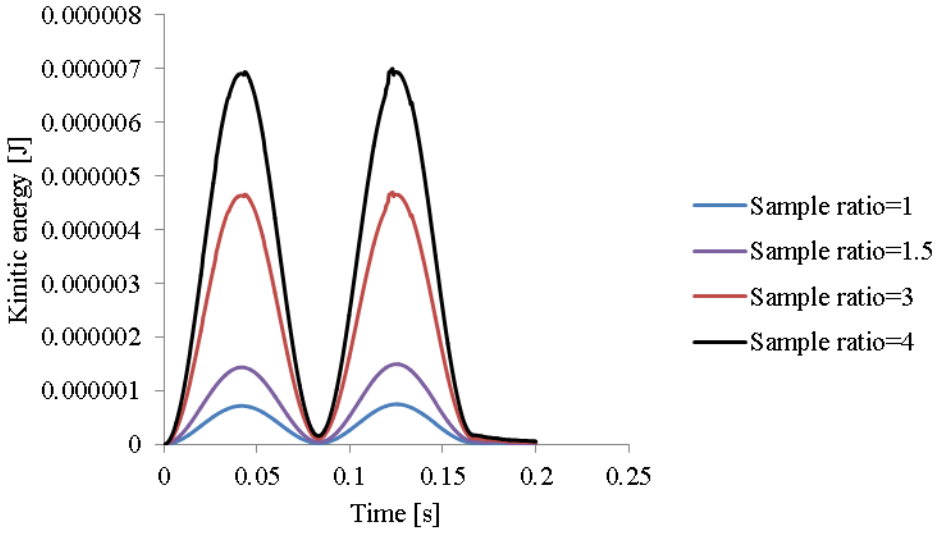

Figure 6-22 The total kinetic energy-time history of system obtained from each kinetic energy of particle

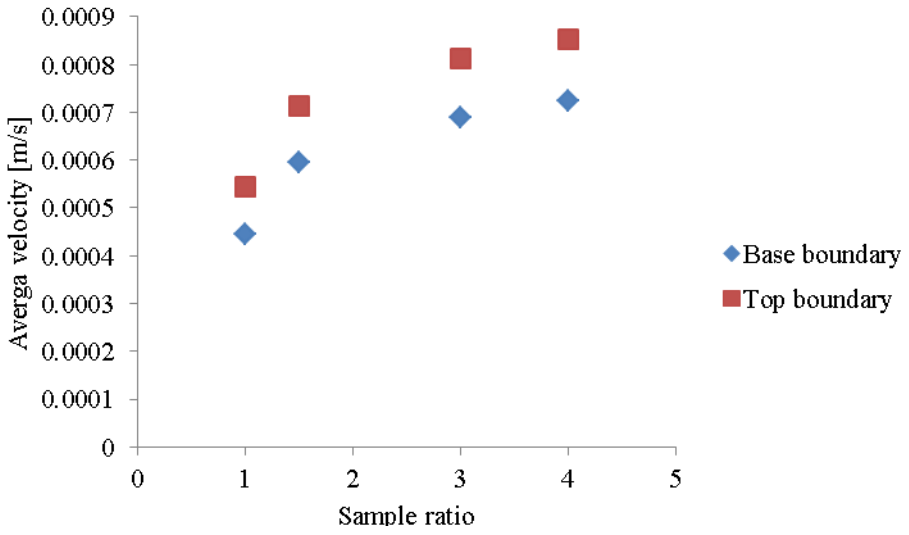

Figure 6-23 Average maximum velocities of top and bottom boundaries vs. sample ratio

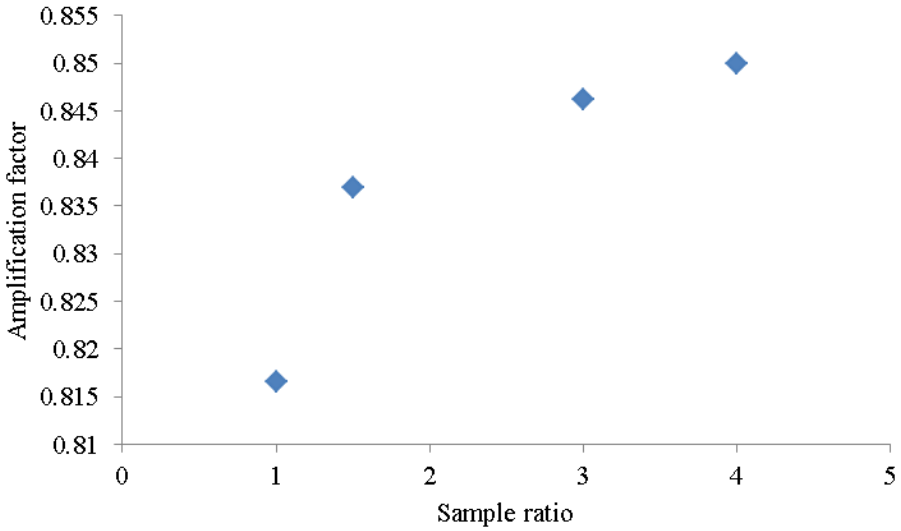

Figure 6-24 Amplification factor vs. sample ratio

Figure 6-21 displays that the propagation of pure shear wave results in vertical wave propagation. To illustrate this problem, consider two different contact topology of configuration in figure 6-25. Let's assume particles are in touch (i.e. the initial contact forces between particles are zero). When an external force or velocity applies to the particle A (see figure 6-25a) in a time step, it starts to move in only x direction. The value of this displacement is calculated by solving its dynamic equilibrium equation at the end of this time step. This displacement leads to produce the contact normal and shear forces to its neighbouring particles. The dynamic equilibrium solution of these particles in next time step results in generates the displacement in horizontal and vertical directions and rotation for them. In contrast, applying an external force or velocity to the particle, A, does not induce any vertical displacement to other particles (see figure 6-25b) because contacts are in net form.

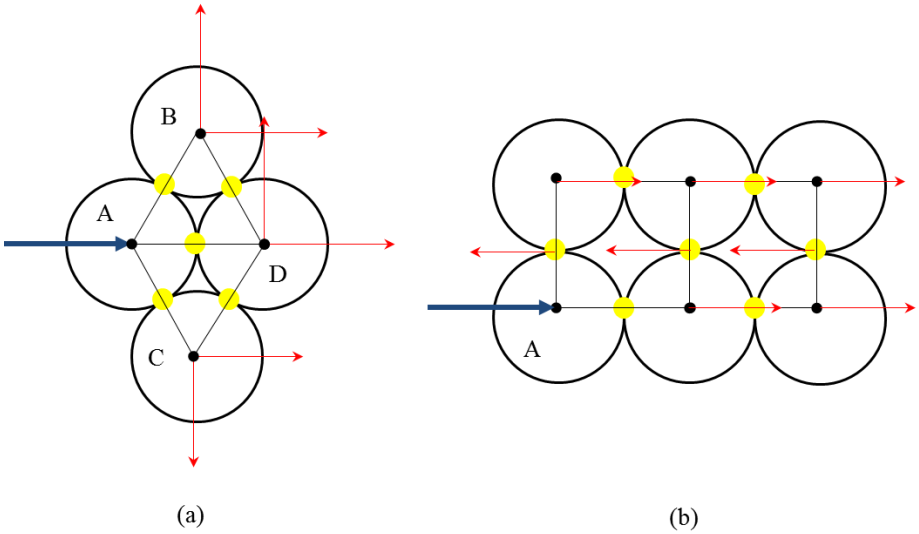

Figure 6-25 Two different contact topology of configurations

6.6.2 The sensitivity of sand fabric to the different sample ratios during earthquake

Seismic waves propagate through the inter-particle contacts network changing the fabric which affects the subsequent response to the seismic waves and the magnitude of the stress tensor. Thus, by studying the fabric evolution of the system during the propagation of the shear component of a seismic earthquake wave provides an insight into the seismic behaviour of sand. The aim of this section is to investigate the effect of sample ratio on evolution of fabric quantities during the propagation of shear component of seismic earthquake wave and the influence of this fabric evolution on the seismic micro-macro-mechanical behaviour of sand. According to the literature review, there have been no researches carried out in the area into the effect of fabric evolution during the propagation of both shear and longitude components of seismic earthquake wave using DEM. Two sample ratios 1 and 4 were considered for this study. The fabric evolution of whole system called hereafter RVE is investigated in this research. Figure 6-26 shows the RVE for these two DEM samples. The influence of the RVE size and its location on the fabric quantities and macro-mechanical parameters such as stress tensors requires further study.

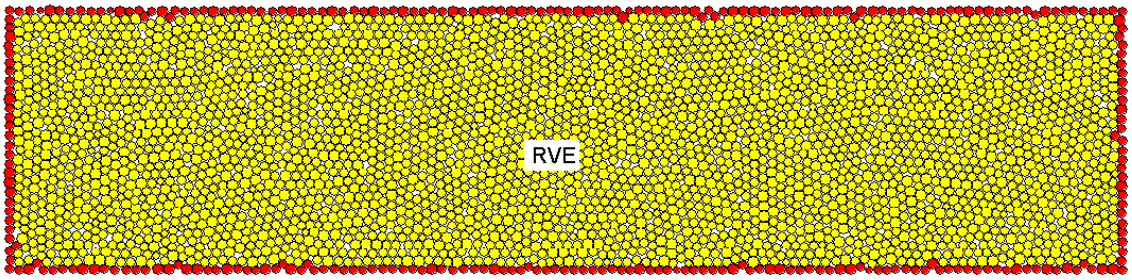

(a) Sample ratio = 4

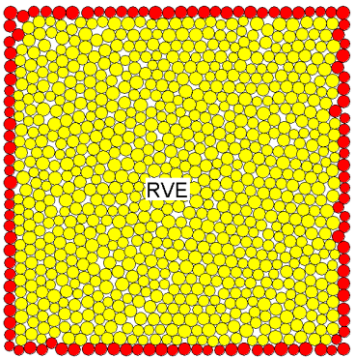

(b) Sample ratio = 1

Figure 6-26 RVE: (a) Sample ratio=4, (b) Sample ratio=1

The inter-particle properties, initial, porosity, range of PSD, frequency and amplitude of periodic loading for these two samples are listed in table 6-5. The input motion for this study is the same as shown in figure 6-20.

A sine periodic load with frequency 6 [Hz] and input velocity amplitude $1*10^{-3}$ [m/s] (i.e. v = *V* * Sin (2*π*6*t)), which is equal to the maximum acceleration 0.037 [m/s^2], was applied in the horizontal direction to the base boundary particles. The maximum acceleration takes place when t=0. As acceleration is the derivative of velocity function to time (i.e. a = (2*π*6) * *V* * Cos (2*π*6*t)), the velocity amplitude (i.e. *V*) at the maximum acceleration a=0.037 [m/s^2] is $1*10^{-3}$ [m/s]. The evolution of fabric quantities such as "normal contact distribution", "normal contact force distribution", "shear contact force distribution", "average coordination number", "bulk density" and "average symmetric geometric deviation index" of the RVE were studied at five different times during seismic excitation: t = 0.0 [s], 0.25T [s], 0.5T [s], 0.75T [s] and T [s]. T is the period of sine load. For this purpose, 18 bins were considered for each polar diagram each with an angular interval $\Delta\theta$ =

20°. The radius of each bin in the polar diagram of average normal contact, average normal contact force and shear contact force distribution corresponds to the number of contacts, summation of normal contact forces and summation of shear contact forces within each angular interval. Changes in contacts, normal contact force and shear contact force alter the radius of bins. Thus, following these fabric quantities through the polar diagrams shows how the fabric of the system is changing during loading. The polar diagram of normal contact, normal contact force, and shear contact force distribution are shown in 6-27, 6-32 and 6-34 against time for both sample ratios. As seen in these figures, the number of contacts, the magnitude of normal contact force and shear force per bin increases significantly when the sample ratio increase from 1 to 4 because the number of contacts within a RVE in sample ratio 4 is larger than that in sample ratio=1. For example, compare the number of contacts at 0.5T in Figure 6.27. Number contact anisotropy is greater in Figure 6.28 for the sample ratio of 4 and the distribution of the number of contacts is more uniform in the smaller sample. This applies to all the other diagrams for the normal contact force distribution.

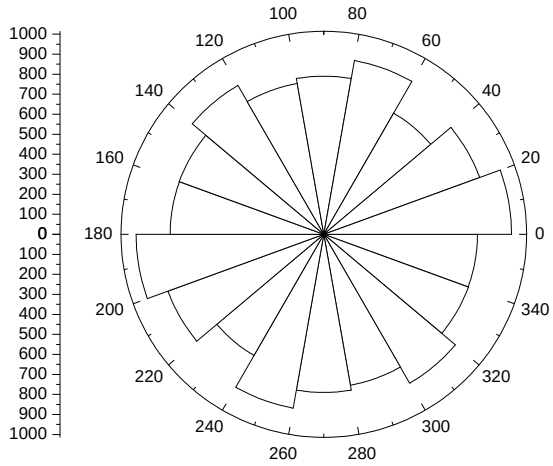

Ratio=4: Normal contact distribution at t = 0 [s]

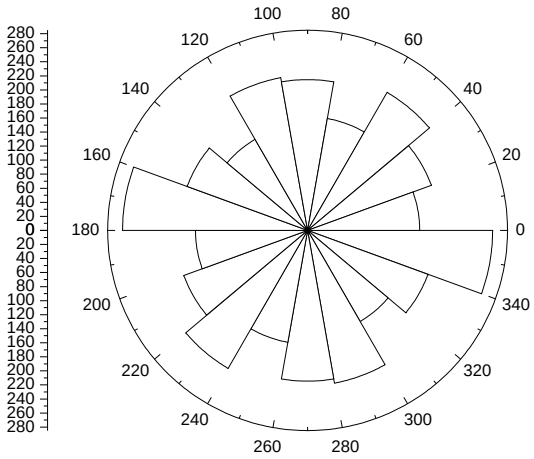

Ratio=1: Normal contact distribution at t = 0 [s]

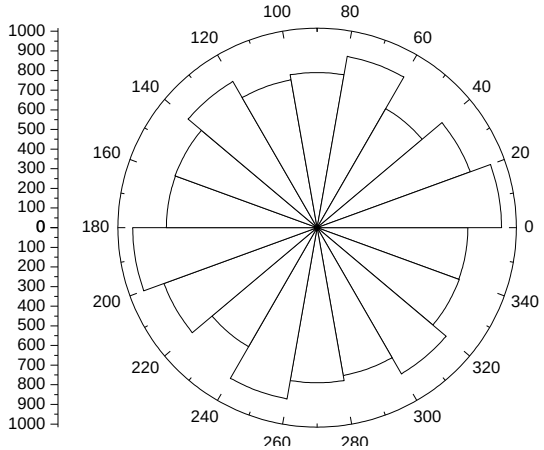

Ratio=4: Normal contact distribution at t = 0.25T [s]

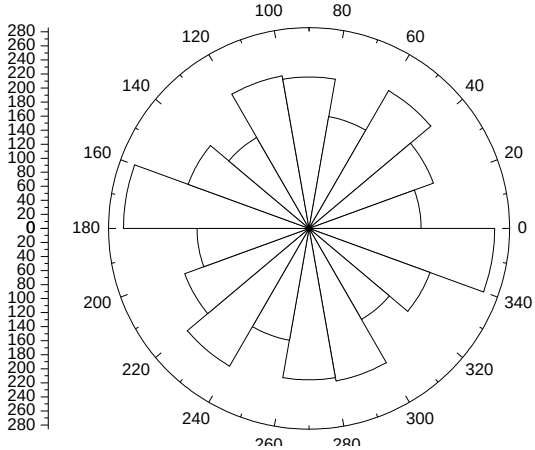

Ratio=1: Normal contact distribution at t = 0.25T [s]

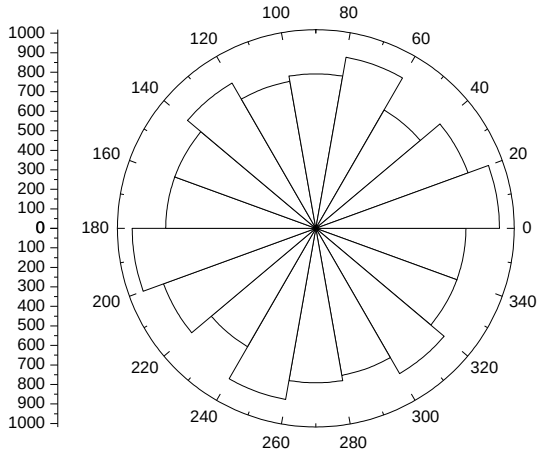

Ratio=4: Normal contact distribution at t = 0. 5T [s]

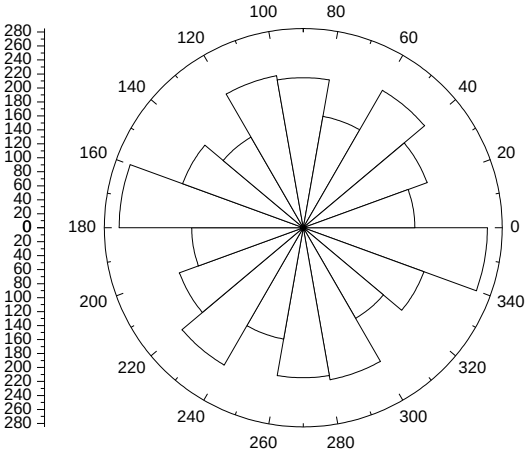

Ratio=1: Normal contact distribution at t = 0.5T [s]

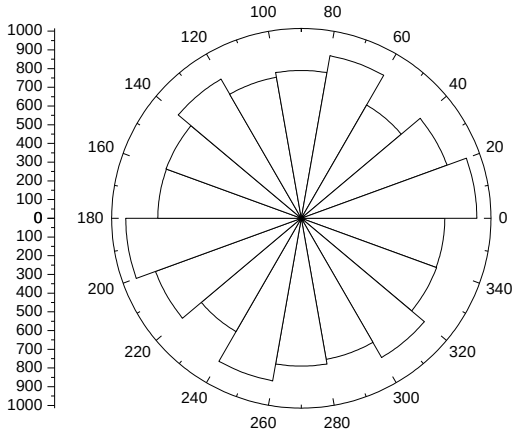

Ratio=4: Normal contact distribution at t = 0.75T [s]

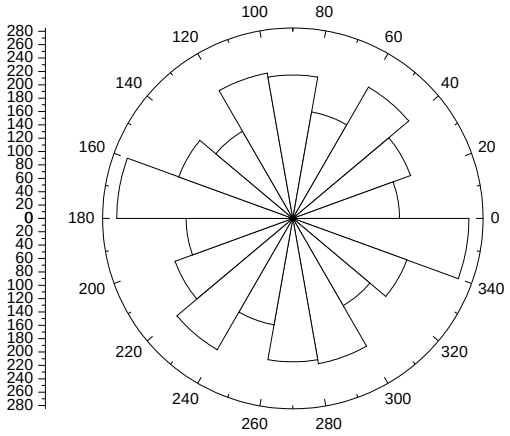

Ratio=1: Normal contact distribution at t = 0.75T [s]

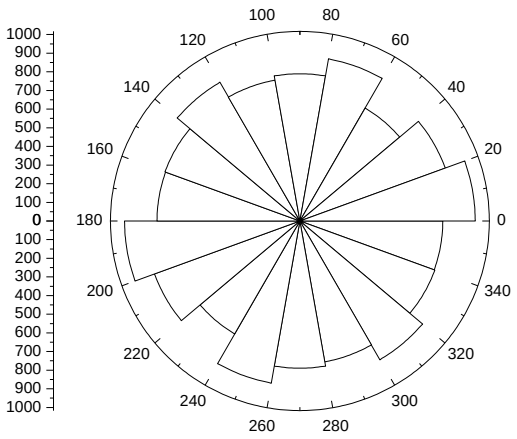

Ratio=4: Normal contact distribution at t = T [s]

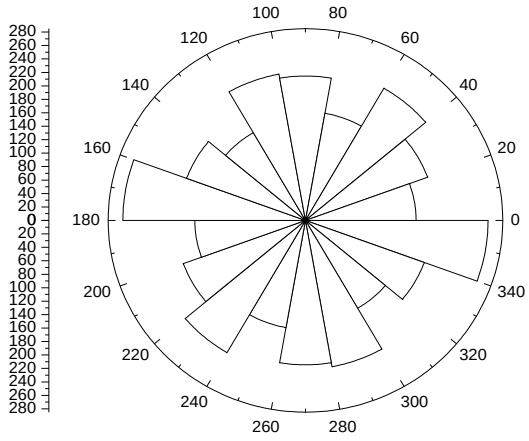

Ratio=1: Normal contact distribution at t = T [s]

Figure 6-27 Comparison of normal contact distribution for two samples ratio during earthquake

The polar diagrams of normal contact distribution for sample ratios 4 and 1 are not in an isotropic state before applying the periodic load as shown in the normal force contact distribution for 0T in Figure 6.27. This is more evident for sample ratio = 1 such that the ratio of normal contact anisotropy of sample ratio 1 to 4 at t = 0 [s] is 1.74 (see figure 6-28). The evolution of fabric anisotropies are shown in 6-28, 6-33 and 6-35 in which the normal contact anisotropy, normal contact force distribution and shear contact distribution are plotted against time for both sample ratios.

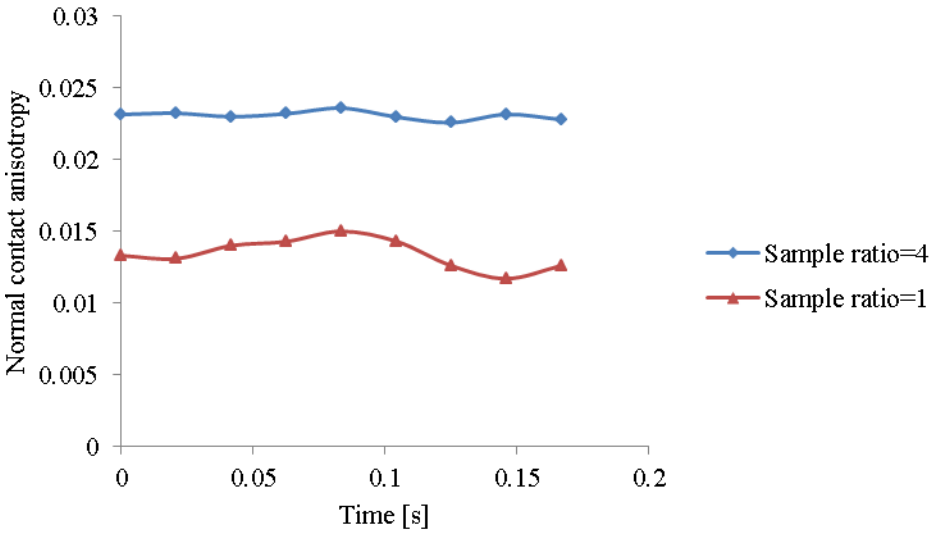

Figure 6-28 The variation of normal contact distribution vs. time for two different sample ratios

Figure 6-29 shows that the larger sample is more stable than the smaller one.

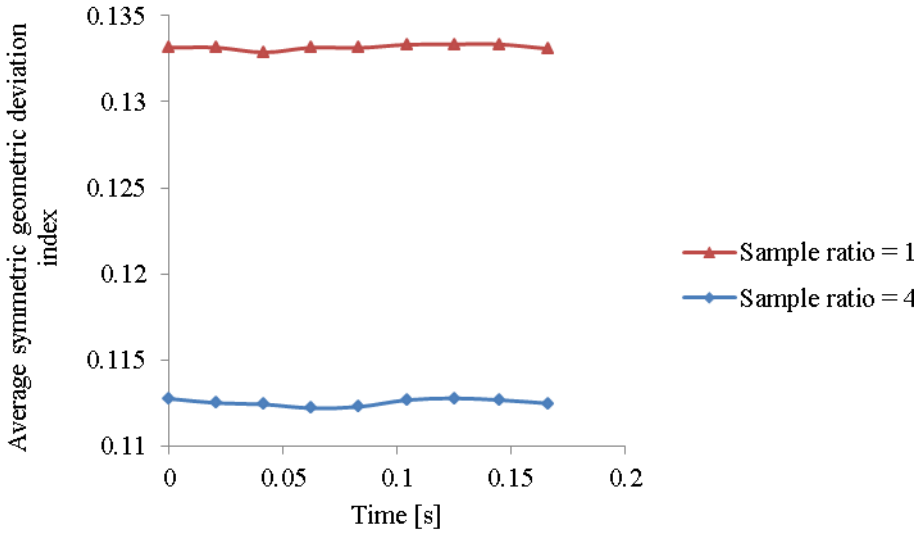

Figure 6-29 Variation of average symmetric geometric deviation index vs. time for two different sample ratios

Indeed, if the distribution of contact around each particle approaches to the isotropic state, the deviation of contacts arrangement around the particle

from symmetric configuration decreases. Thus, a meaningful relationship can be established between these two fabric quantities. This will be recommended as a research gap.

Tracking the evolution of polar diagram of normal contact distribution and the evolution of normal contact anisotropy for these two sample ratios from 0T to T shows that applied sine shear wave load does not have a significant effect on the arrangement of the average normal contact distribution of both DEM models (Figures 6.27 and 6-28). This means that the contact distribution is similar to that for a static state. Thus, the contact network generated during the static loading dominates the average coordination number and therefore the average symmetric geometric deviation index is very nearly constant though different for the two models (see figures 6-29 and 6-30.

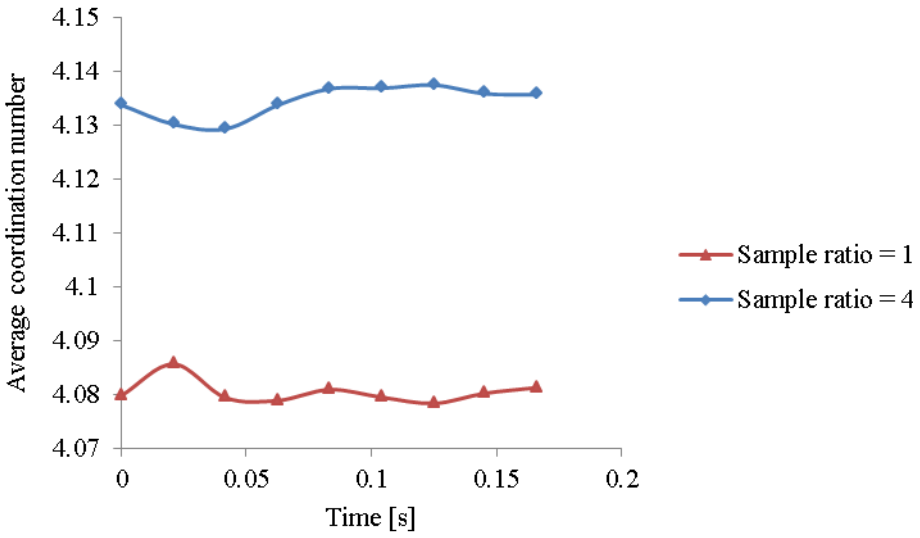

Figure 6-30 Variation of average coordination number vs. time for two different sample ratios

The bulk density of these two systems is very high and is little influenced by the periodic load (see figure 6-31). This leads to the conclusion that the contact network created at the static state for two DEM models dominates its behaviour during seismic loading such that the given amplitude does not have a major effect on average normal contact distribution, coordination number and average symmetric geometric deviation index of system.

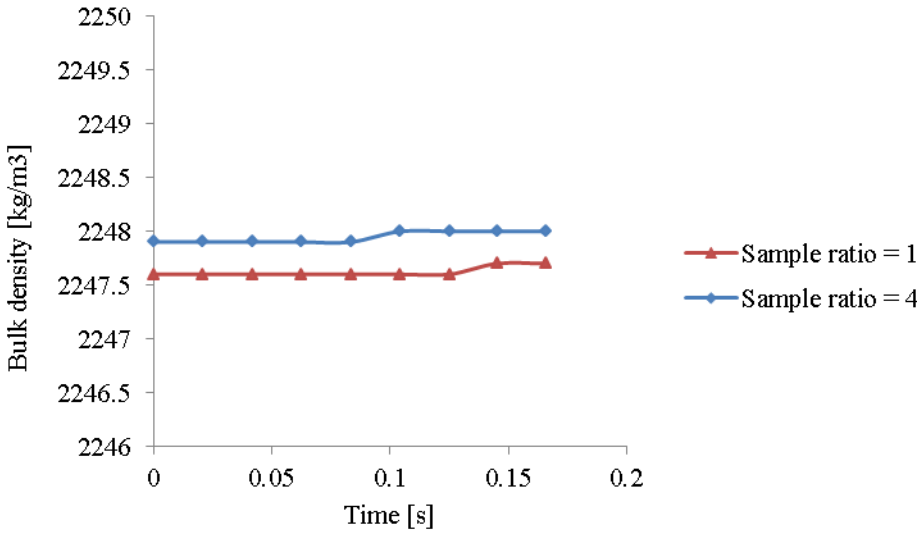

Figure 6-31 Bulk density of two DEM model during shear wave propagation

Increasing the size of samples increases the number of contacts within the RVE. This increases the magnitude of normal contact force within each segment in the polar diagram of normal contact force distribution. For example, compare the normal contact distribution at 0.5T from Figure 6-32.

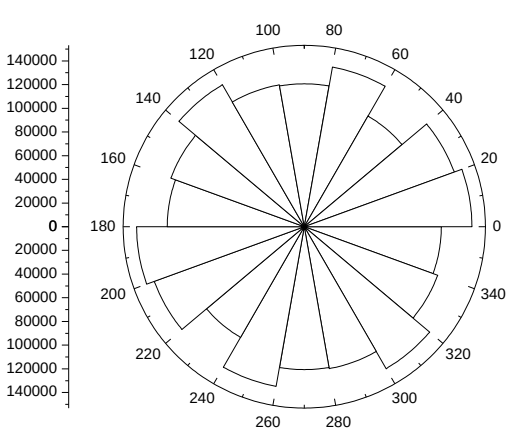

Ratio=4: Normal contact force distribution at t = 0 [s]

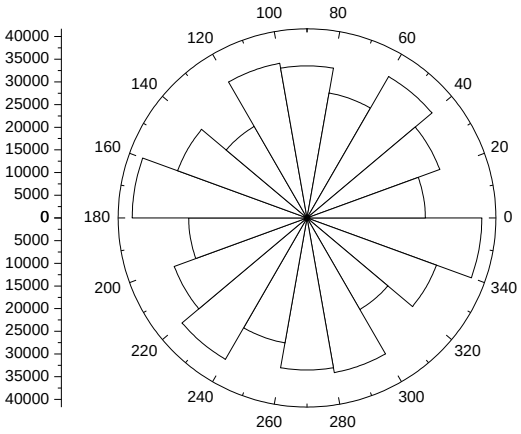

Ratio=1: Normal contact force distribution at t = 0 [s]

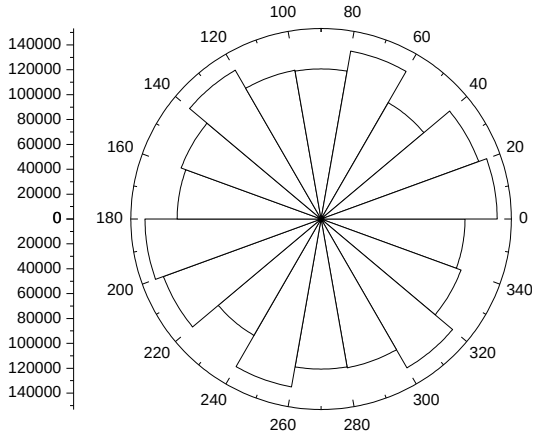

Ratio=4: Normal contact force distribution at t = 0.25T [s]

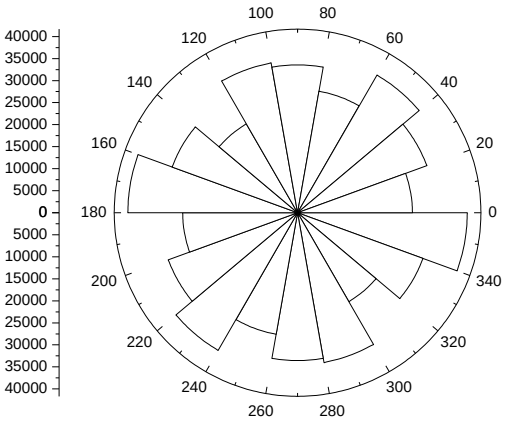

Ratio=1: Normal contact force distribution at t = 0.25T [s]

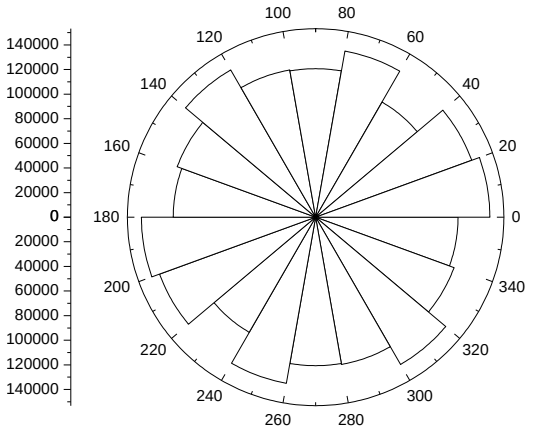

Ratio=4: Normal contact force distribution at t = 0.25T [s]

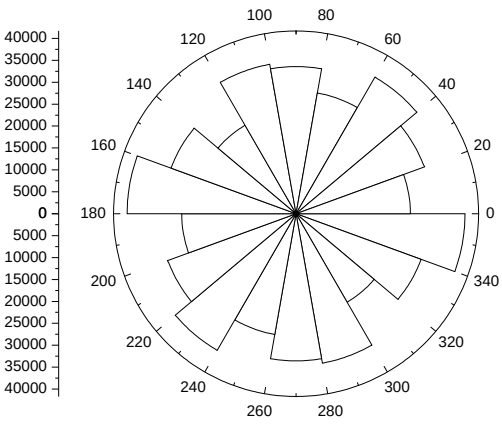

Ratio=1: Normal contact force distribution at t = 0.5T [s]

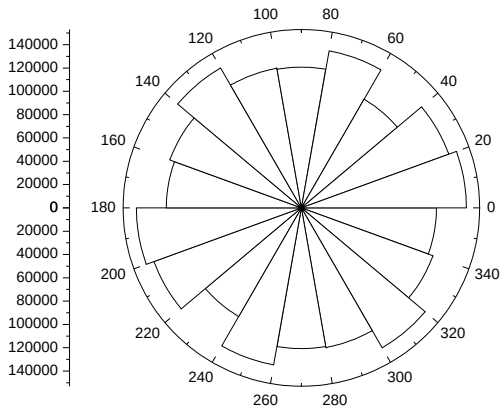

Ratio=4: Normal contact force distribution at t = 0.5T [s]

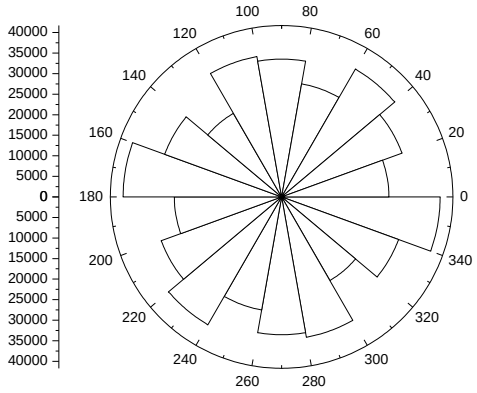

Ratio=1: Normal contact force distribution at t = 0.75T [s]

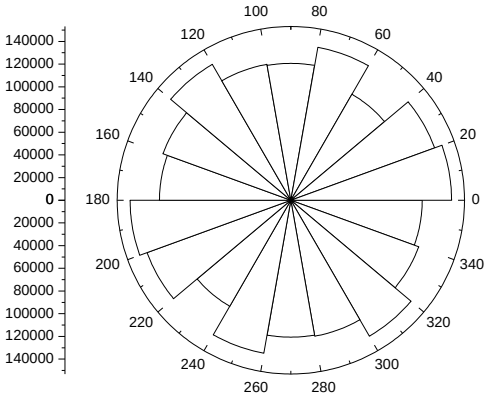

Ratio=4: Normal contact force distribution at t = T [s]

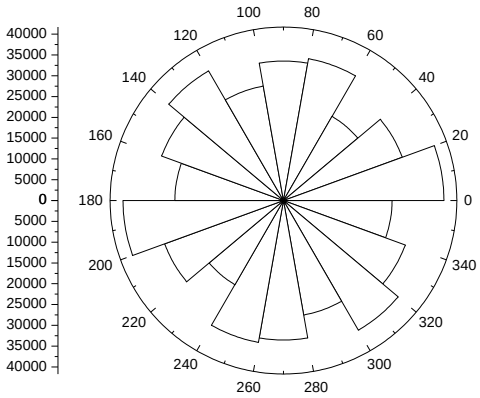

Ratio=1: Normal contact force distribution at t = T [s]

Figure 6-32 Comparison of normal contact force distribution for two samples ratio during earthquake

Moreover, this increase in sample size results in smoothing the polar diagram of normal contact force distribution. As the chain force established during static state is strong, the applied dynamic load on the particulate system has a little influence on anisotropy of normal contact force, it can be concluded that normal contact distribution during wave propagation does not change significantly for the systems being considered. The positive sign of average normal contact force anisotropy (i.e. a_{n}) in figure 6-33 implies this fact that the average normal contact forces of particles within RVE is larger than the ideal isotropic state i.e. a_{n}=0. A similar argument is also used to justify the positive sign of average normal contact anisotropy (i.e. a). As the system was isotropically consolidated before applying the earthquake (i.e. t = 0 [s]), the

positive sign of "a_n" and "a" presents this fact that in micro-scale point of view the particulate system is not in isotropic state.

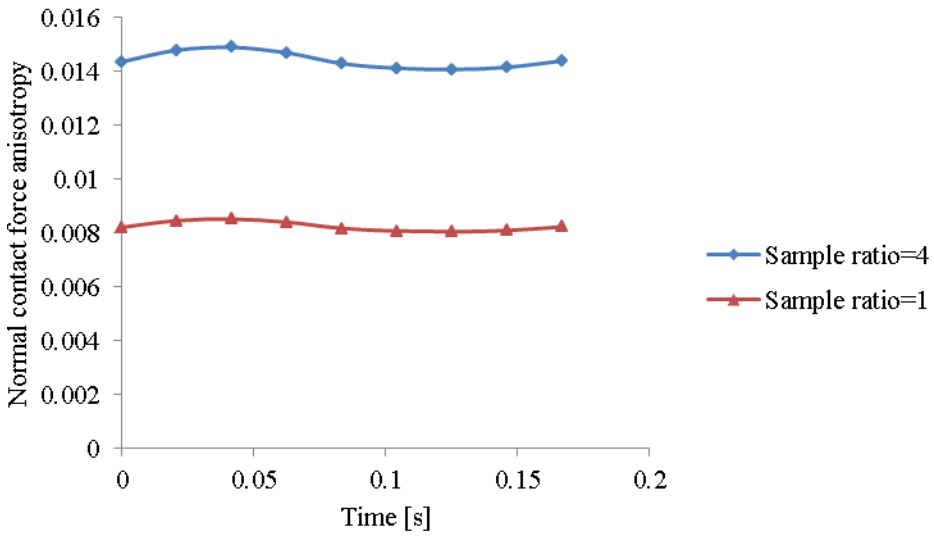

Figure 6-33 The variation of normal contact force distribution vs. time for two different sample ratios

The normal contact forces are always in compression, while the direction of shear contact force is positive if it produces a clockwise moment and is negative if it produces a counter clockwise moment. The shear contact forces developed within RVE for these two samples during the static stages (i.e. t = 0 [s]) were approximately zero (see the axial axis in the left hand side of shear contact force distribution of these two models at t = 0 [s] in figure 6-34).

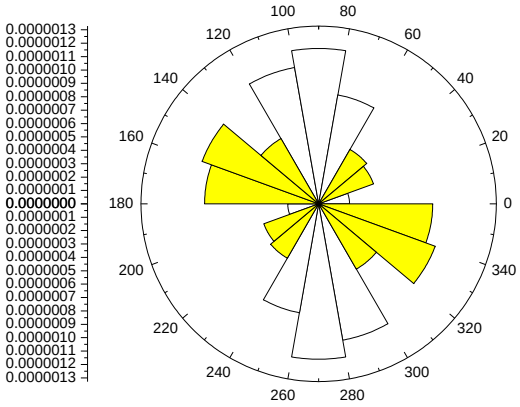

Ratio=4: Shear contact force distribution at t = 0 [s]

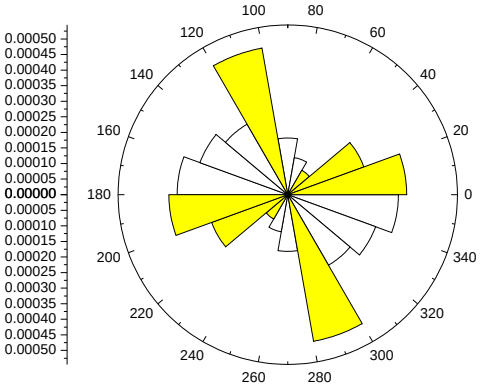

Ratio=1: Shear contact force distribution at t = 0 [s]

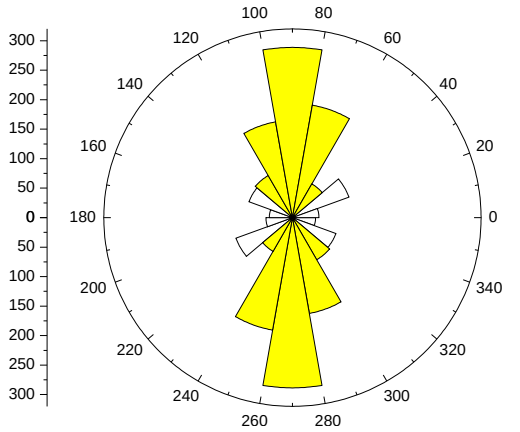

Ratio=4: Shear contact force distribution at t = 0.25T [s]

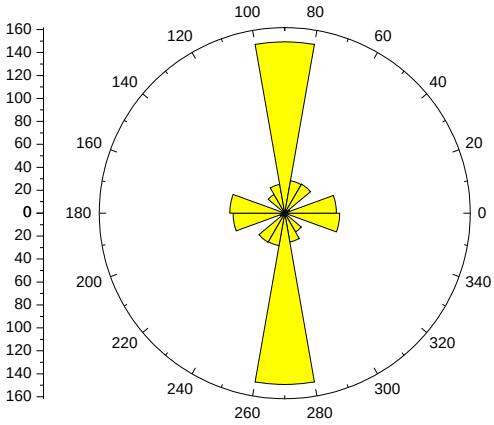

Ratio=1: Shear contact force distribution at t = 0.25T [s]

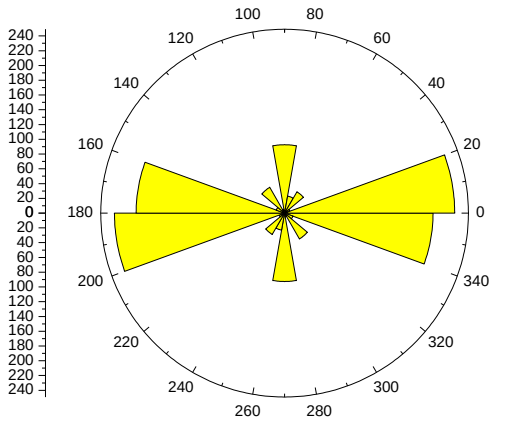

Ratio=4: Shear contact force distribution at t = 0.5T [s]

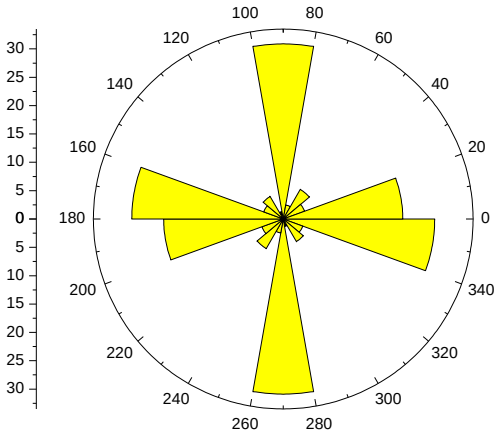

Ratio=1: Shear contact force distribution at t = 0.5T [s]

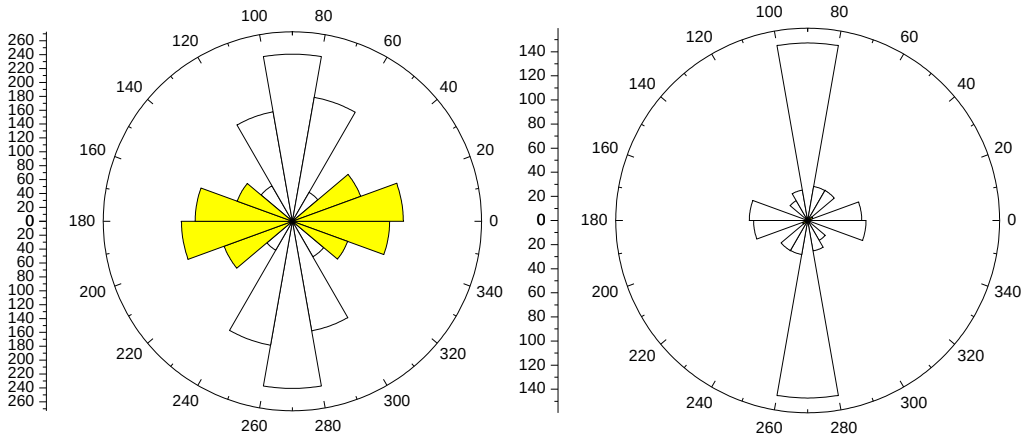

Ratio=4: Shear contact force distribution at t = 0.75T [s] Ratio=1: Shear contact force distribution at t = 0.75T [s]

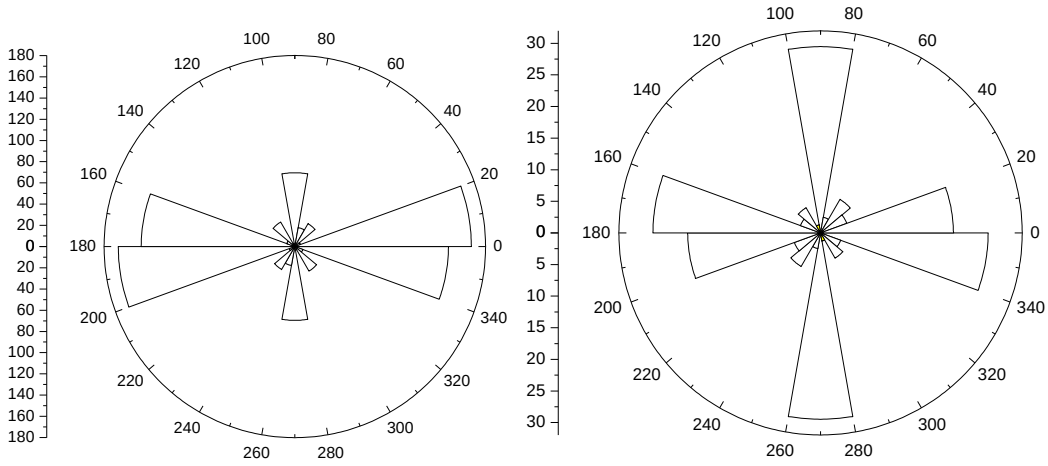

Ratio=4: Shear contact force distribution at t = T [s] Ratio=1: Shear contact force distribution at t = T [s]

Figure 6-34 Comparison of shear contact force distribution for two samples ratio during earthquake

As seen in this figure, some contacts have negative shear forces and the rest has a positive shear contact force. Note that white bins correspond to positive shear contact force and yellow bins correspond to negative shear contact forces. It is known that the activation of shear contact force is only related to the shear contact deformation when the linear elastic contact model is applied. The shear contact deformation is also related to the relative shear motion at the contact, or the shear contact velocity, which is defined as the shear velocity of two particles in contact (see Eq. 2.5). The velocity of each particle is also related to the resultant of the normal and shear contact

forces applied to the particle. Thus, both the evolution in normal and shear contact forces has a profound influence on the shear contact velocity. As the particles velocities are almost zero at t = 0 [s], it can be argued that the induced resultant forces of particles are approximately zero. That is, the system is in static state (see chapter 4). This also leads to the conclusion that the stability of granular system is greatly dependent on the normal contact forces rather than shear contact forces.

Tracking the polar diagram of shear contact force of these two sample ratios from t = 0 [s] to t = T [s] (see figure 6-34) shows that the magnitude of shear contact force distribution is greater at t = 0.25T [s] when the shear load reaches to its maximum value. From t = 0 [s] to t = 0.25T [s], shear seismic load moves to the right. The majority of shear contact forces are negative and distributed in a vertical direction.

From t = 0.25T [s] to t = 0.5T [s], when the direction of shear load reverses and the shear load approaches to zero, the distribution of shear contact forces is different for the two samples. As particles have already experienced higher shear contact forces at t = 0.25T [s], decreasing the shear seismic load cannot alter the magnitude of shear contact forces of whole contacts to zero at t = 0.5T [s]. This shows that samples experienced plastic deformation. Instead, the direction of whole shear contact forces is negative.

From t = 0.5T [s] to t = 0.75T [s], when the seismic load increases to its maximum value at t = 0.75 [s], the distribution and the magnitude of shear contact force changed. In the case of sample ratio = 4 positive shear contact forces dominated, while in the case of sample ratio = 1 negative shear contact forces dominated.

From 0.75T to T, when the load is terminated there is residual shear contact forces for both samples. It is because when the loading process is terminated, the individual particles are still vibrating due to free-vibration (see chapter 4). Thus, more cycles after termination of load are required to dampen the free-vibration of whole particles.

Another result can be deduced by following the polar diagrams of shear contact force distribution during wave propagation are to track the radius of bins. For, example, when the seismic wave reaches to the maximum value, the majority of shear contact forces is concentrated between 260° and 280°, 80° and 100° for two cases (i.e. in the direction of wave propagation).

The shear contact velocity of any contact point is related to the velocities of those two particles which create this contact. Figures 6-20 and 6-21 show the horizontal and vertical average velocities of the top boundary particles. As seen from these two figures, the trend of horizontal average particles velocities is similar to the trend of the input motion, while the magnitude of the vertical average particles velocities is very small and can be ignored in comparison with the horizontal velocity. The normal contact forces are almost constant during loading, while shear contact forces vary significantly during loading. Thus, it is changes in the shear contact forces that accelerate the particles not changes in normal contact forces.

The changes in shear contact force distribution from t = 0 [s] to t = T [s] shows that these variation in this distribution is almost periodic. However, the magnitude of shear contact forces within each bin is being altered during loading. This indicates that the plastic deformation is being developed within RVE from t = 0 [s] to t = T [s]. Comparing the magnitude of shear contact force distribution developed during earthquake for these two samples also shows that an increase in sample ratio results in increasing the shear contact force capacity when the same load is applied for these two models. In contrast to the normal contact force distribution, the shear contact distribution at t = 0 [s] and t = T [s], when the magnitude of the earthquake load is zero, is not similar. The shear contact distribution is also not similar at t = 0.25T [s] and t = 0.75T [s] when the magnitude of the earthquake load is maximum. This indicates the natural of shear contact force distribution is more complicated than the normal contact force during earthquake. As the magnitude of shear contact force is greatly dependant on the shear contact velocity, the reason for this discrepancy in shear contact force distribution should be explored to understand how the shear contact velocity is developed during the earthquake. This is recommended as further work.

The evolution of shear contact force anisotropy is shown in figure 6-35. This figure clearly shows that the trend of changes in shear contact anisotropy is a sine form during loading such that the maximum shear contact anisotropy takes place when the shear seismic load is at its peak and the minimum shear contact anisotropy takes place when the shear seismic load is in its negative maximum value.

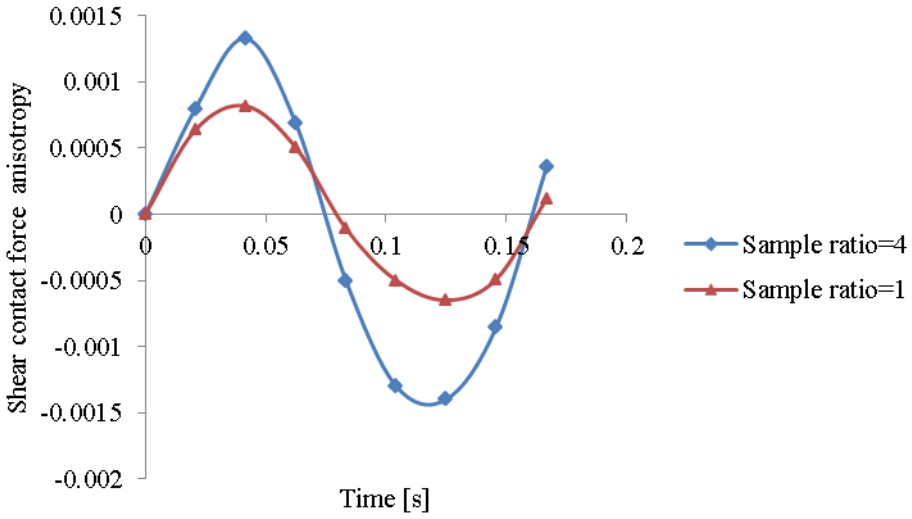

Figure 6-35 The variation of shear contact distribution vs. time for two different sample ratios

According to Eq. 3.15, the shear contact force anisotropy at each time step is related to the summation of shear contact forces of each bin and average normal contact forces of the RVE. As the average normal contact forces are approximately constant between t = 0 [s] and t = T [s], changes in the shear contact forces in each segment is the main influence on shear contact force anisotropy. Figure 6-35 also shows that the maximum shear contact force anisotropy of ratio 4 is 1.62 times bigger than the maximum shear contact force anisotropy of ratio 1.

As the contact arrangement and normal contact forces during loading is almost constant, it can be expected that the bulk density is constant during loading (see figure 6-31).

Figures 3-38, 3-39 and 3-40 show the effect of fabric evolution on the micro-mechanical stress tensor RVE obtained from Eq. 3.16 and 3.17 where the magnitude of stress tensors is mainly related to D_{50} (it is $8.75*10^{-4}$ [m] for two models), average normal contact force ($\bar{f}_0^c$), normal contact, normal contact force and shear contact force anisotropies, the orientation of normal contact distribution (θ_a) and m_v. m_v is dependent on the average coordination number, (see figure 6-30), the number of particles and the volume of RVE which were all constant during these two simulations (it is 0.01 [m^2] for sample ratio 4 and it is 0.0025 [m^2] for sample ratio 2). The number of particles in the RVE for samples ratio=4 and ratio=1 is 3658 and 914, respectively. Thus, the trend of m_v is similar to the trend of average coordination number for each case. The maximum deviation in the variations of θ_a (i.e. the relative rotation of normal contact distribution) during loading is 2.8° and 2.4° for ratio=4 and ratio=1, respectively (see figure 6-37). This indicates that the rotation of contact points at each time step during loading is very small relative to the previous time step. The variations of average normal contact forces during time for two cases are shown in figure 6-36. It is also seen that the ratio of the average contact normal force of sample ratio=4 to the average contact force sample ratio=1 is 4, which is equal to the sample ratio of these two samples.

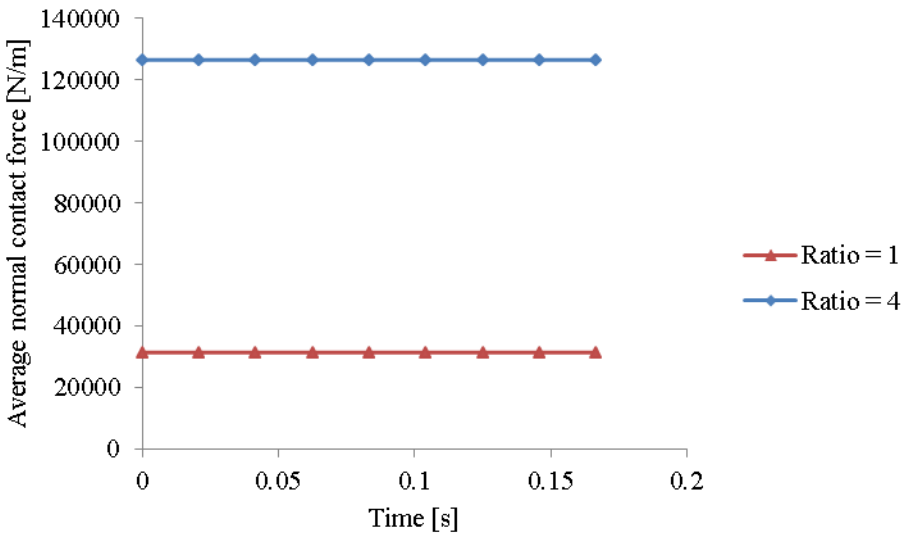

Figure 6-36 The variation of average normal contact force

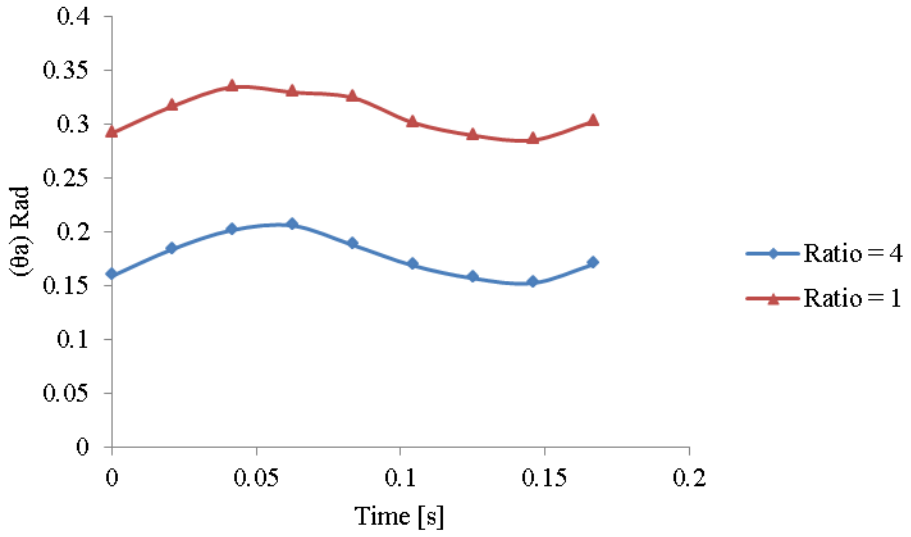

Figure 6-37 The variations of θ vs. time

Thus, changing in shear contact force anisotropy developed during earthquake mainly has a significant role on developing and evolution of stress tensor quantities.

Figure 6-38 shows the variations of micro-force-fabric shear stress tensor vs. time. It is seen that the evolution of fabric quantities, number of particles, volume of RVE and inter-particle contact forces can show the development of shear stress tensor. It can be argued that the trend of this variable is strongly dependent on the trend of combination of fabric anisotropies, while the magnitude of this variable at each time is mainly related to the average normal contact forces of particles within RVE at that time. For instance, the ratio of maximum shear stress developed for sample ratio=4 to that developed for sample ratio=1 is nearly 4.1. Thus, increasing the average normal contact forces leads to increase the shear stress demand during the earthquake. Moreover, increase in fabric anisotropies during earthquake result in raise the shear stress demand of RVE. Thus, if the ability of particulate system to develop the fabric anisotropies rises, the shear demand of RVE during an earthquake therefore increases.

The trend of micro-force-fabric principle stresses is shown in figures 6-39 and 6-40. The confining pressure in the static situation during loading is 100 [kPa] for the two samples. Applying earthquake leads to oscillate the confining

pressure and principle stresses around confining pressure due to static situation. However, the derived principle stresses for the sample with a ratio of 1 are significantly less than the confining pressure suggesting that this sample size is too small. The principle stresses for the sample with a ratio of 4 are similar to the confining pressure.

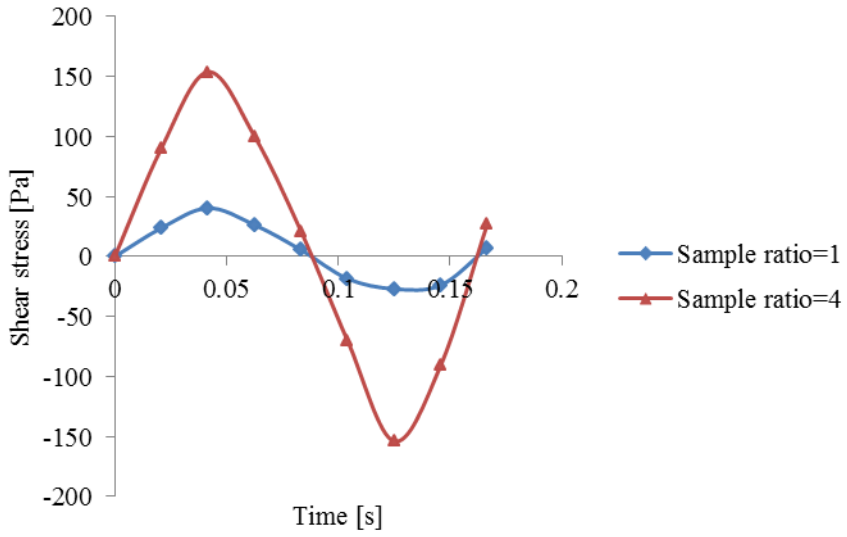

Figure 6-38 The micro-mechanical shear stress vs. time for two different sample ratios

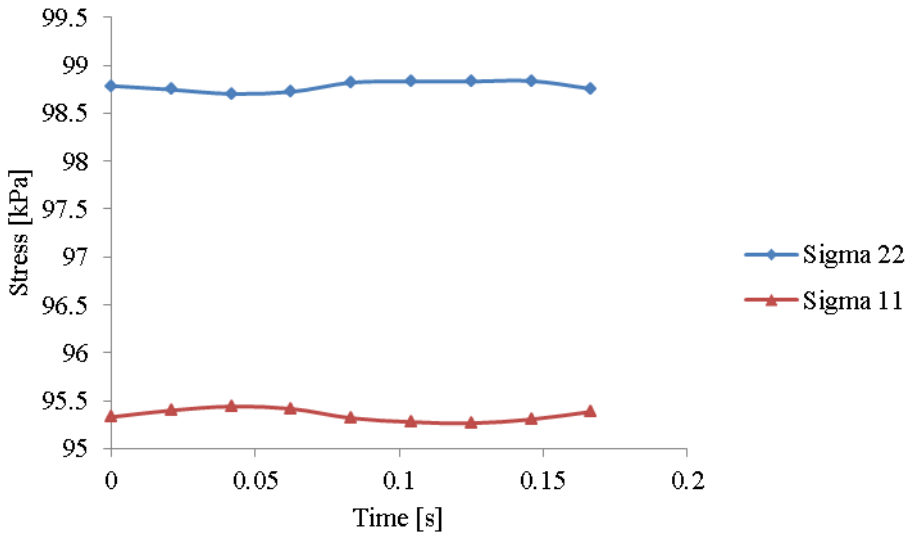

Figure 6-39 Principle stress of ratio 4 vs. time

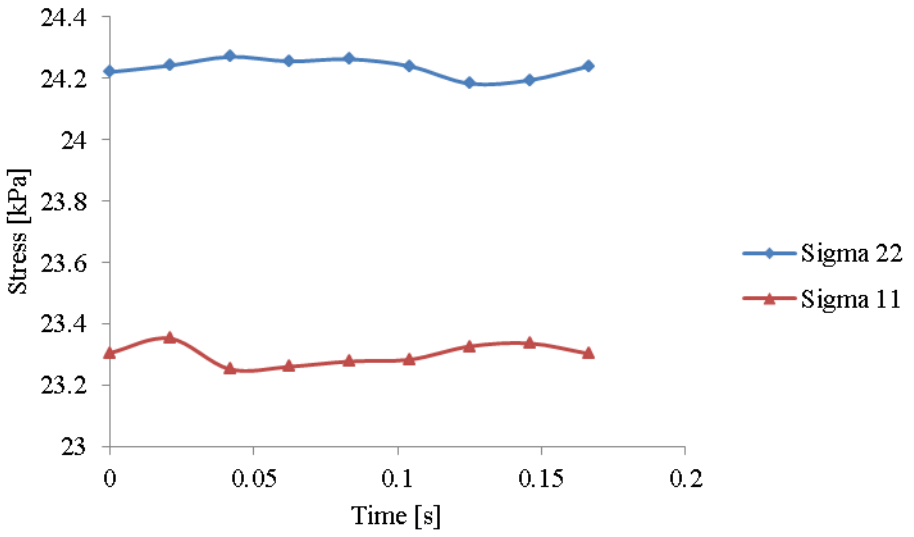

Figure 6-40 Principle stress of ratio 1 vs. time

It is necessary to investigate the effect of amplitude and frequency on the normal contact forces and fabric for different inter particle properties and porosity. These tests show that there was little change in the normal contact forces which may be related to the amplitude and frequency of the input.

6.7 The sensitivity of sand fabric to the various frequencies during earthquake

An earthquake signal includes various frequencies. The Fast Fourier transformation of 10 well-known earthquakes, which was shown in chapter 3, shows that earthquakes generally produce low frequencies (Marketos and O'Sullivan, 2013). The frequencies of these ten earthquake's was generally between 1 and 6 [Hz]. It is more precise to apply an earthquake signal for DEM simulations but given the diverse range of signals and the complex pattern of a single earthquake. However, it is necessary to study the effect of a single periodic wave to understand the impact of dynamic loading of sand. Six DEM simulations were performed. The initial conditions of these six models were similar. The samples were isotropically consolidated to 100 [kPa] after generating a uniform particle size distribution of particles ranging from 1.5 [mm] to 2 [mm]. Dynamic deformable boundary particles were used.

Table 6-6 displays the input parameters of these DEM simulations. The variation in the normal contact anisotropy with time for the six frequencies is

shown in Figure 6.41. The normal contact force anisotropy is shown in figure 6.42 and the shear force contact force anisotropy in figure 6.43. The evolution of the shear contact force distribution is shown in figure 6-44. The variations in bulk density, average coordination number and average symmetric geometric deviation index with time for the six frequencies are shown in figures 6-45 to 6-47.

Test No.	k_n [N/m] *10^7	k_s [N/m] *10^7	μ	c_n	c_s	n	Range of PSD [mm]	Amplitude [m/s]	Sample ratio	f [Hz]
1	8.45	8.45	0.9	0.01	0.01	0.12	1.5-2	$1*10^{-3}$	4	1
2	8.45	8.45	0.9	0.01	0.01	0.12	1.5-2	$1*10^{-3}$	4	2
3	8.45	8.45	0.9	0.01	0.01	0.12	1.5-2	$1*10^{-3}$	4	3
4	8.45	8.45	0.9	0.01	0.01	0.12	1.5-2	$1*10^{-3}$	4	4
5	8.45	8.45	0.9	0.01	0.01	0.12	1.5-2	$1*10^{-3}$	4	5
6	8.45	8.45	0.9	0.01	0.01	0.12	1.5-2	$1*10^{-3}$	4	6

Table 6:6 Input parameters of six different DEM simulations with various frequencies in order to study the fabric response

A sinusoidal shear wave was applied to the base of the sample. The figures are expressed in terms of the total time, T, for one cycle.

Figure 6.41 shows that the normal contact anisotropy follows the input motion with the maximum anisotropy at 0.25T and 0.75T. Figure 6.41 shows that the maximum normal anisotropy increases as the frequency reduces. This may be due to the fact that at low frequencies the system has enough time to redistribute the external shear load through the sample. The minimum anisotropy occurs a 0T, 0.5T and T and is not affected by the frequency.

Changes in normal contact distribution are also the result of changes in normal and shear contact forces. Figures 6-43 and 6-44 show the shear

contact force anisotropy and shear contact force distribution of these six DEM models. Figure 6.43 shows that the variation in shear contact force anisotropy differs between the frequencies.

Figure 6.44 shows that the shear contact force distribution is similar for each of the frequencies at each point investigated. For example, compare the distribution at 0.5T for the six frequencies. The figure also shows that the shear contact force distribution aligns with the input motion. The initial distribution shows a preferential alignment in the vertical and horizontal directions. At 0.25T, when the input motion is a maximum the shear force is strongly aligned with the vertical direction. This rotates to the horizontal direction at 0.5T and then reverses at 0.75T and T. While the shear contact force distribution at each time interval is similar in shape between each frequency, the number of contacts slightly varies. The shear contact force distribution at a frequency of 1Hz is a maximum of 400; 340 at 2Hz, 325 at 3Hz, 310 at 4Hz, 300 at 5Hz and 275 at 6Hz.

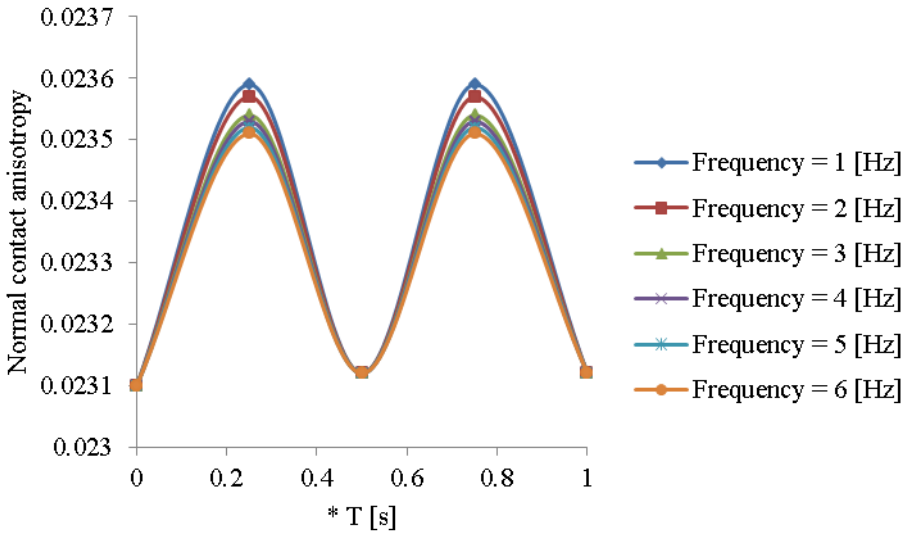

Figure 6-41 Normal contact anisotropy of six DEM simulations vs. time

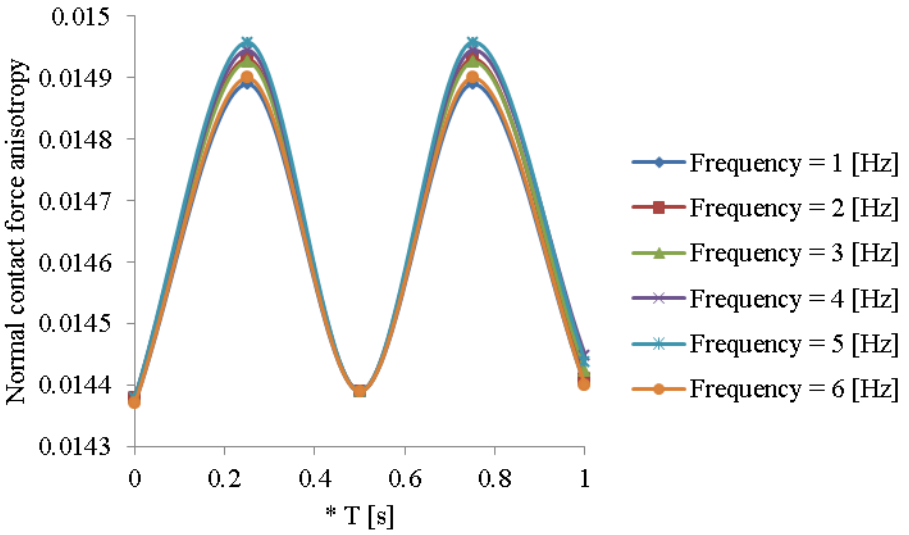

Figure 6-42 Normal contact force anisotropy of six DEM simulations vs. time

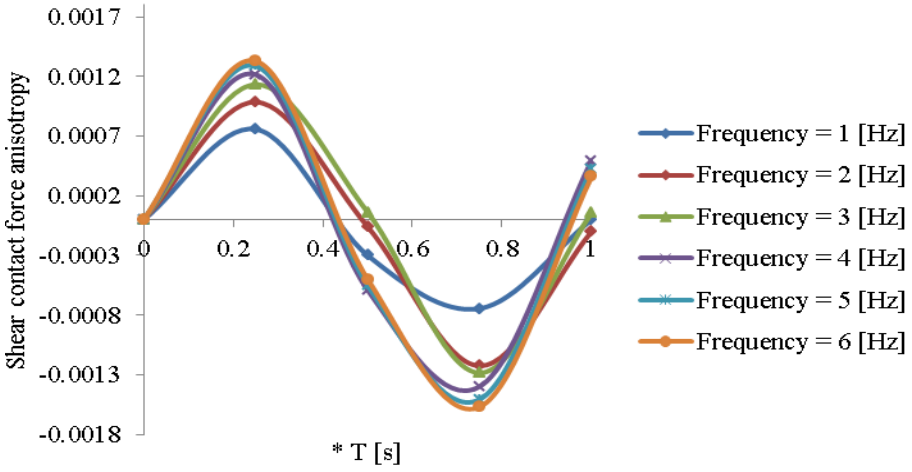

Figure 6-43 Shear contact force anisotropy of six DEM simulations vs. time

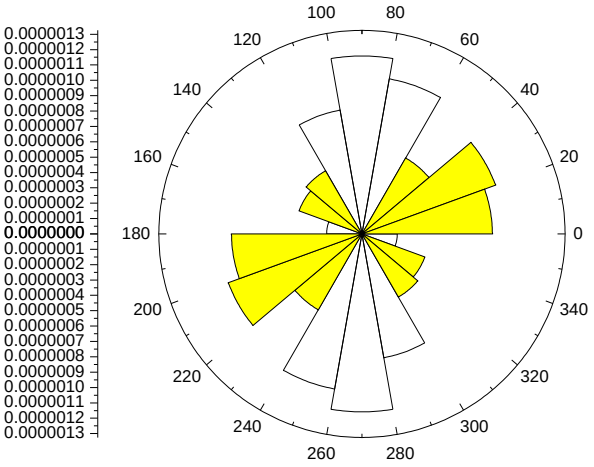

Shear contact force distribution at t = 0 [s]

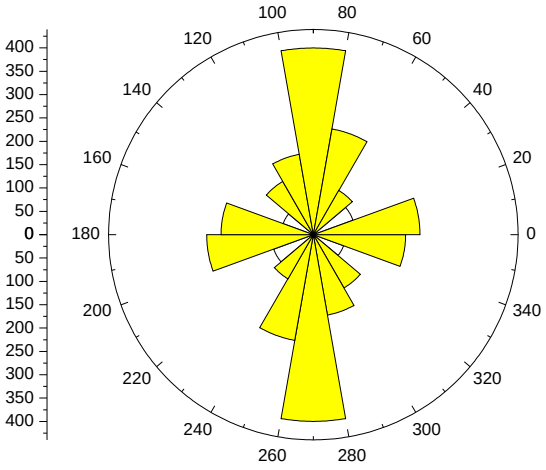

Shear contact force distribution at t = 0.25T [s]

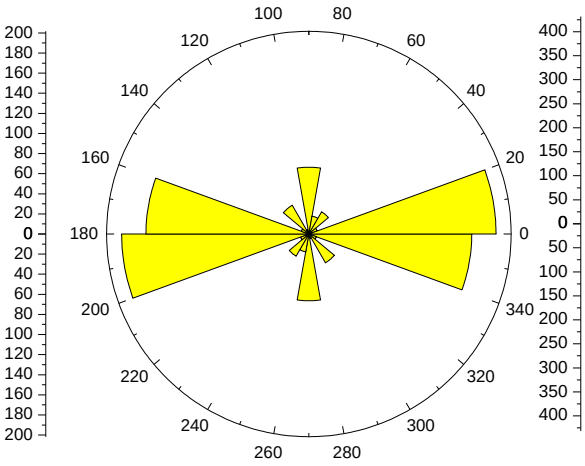

Shear contact force distribution at t = 0.5T [s]

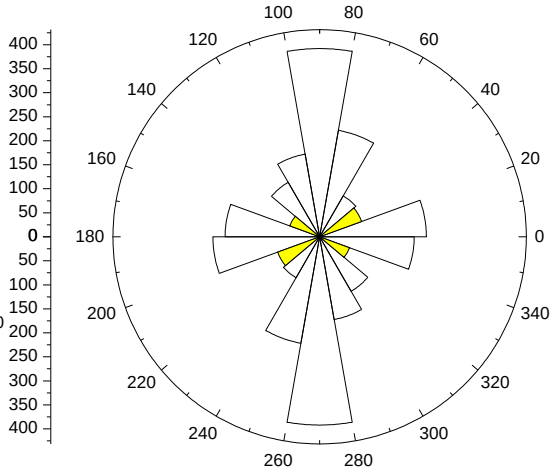

Shear contact force distribution at t = 0.75T [s]

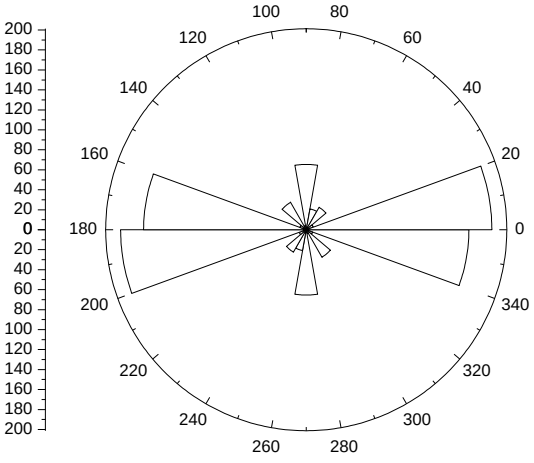

Shear contact force distribution at t = T [s]

(a) Frequency = 1 [Hz]

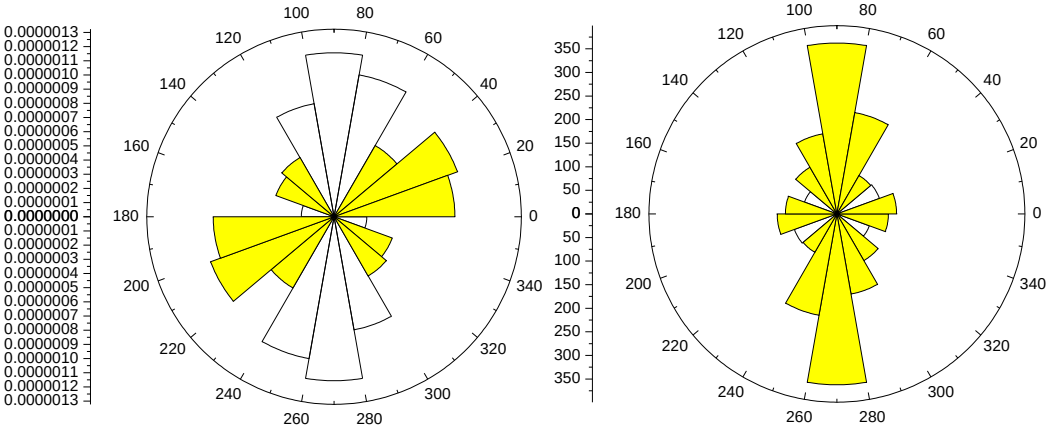

Shear contact force distribution at t = 0 [s]

Shear contact force distribution at t = 0.25T [s]

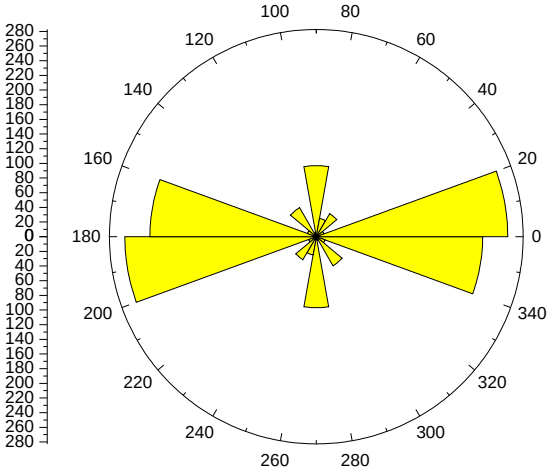

Shear contact force distribution at t = 0.5T [s]

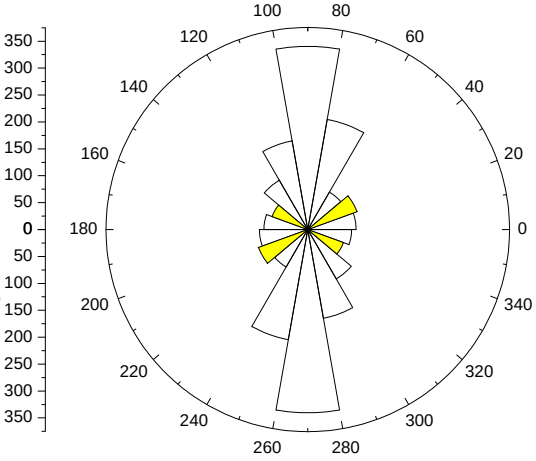

Shear contact force distribution at t = 0.75T [s]

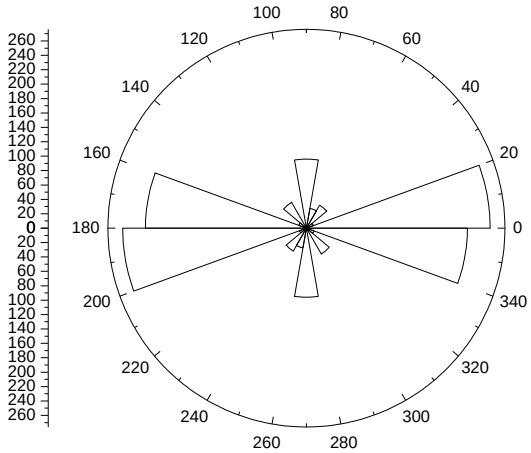

Shear contact force distribution at t = T [s]

(b) Frequency = 2 [Hz]

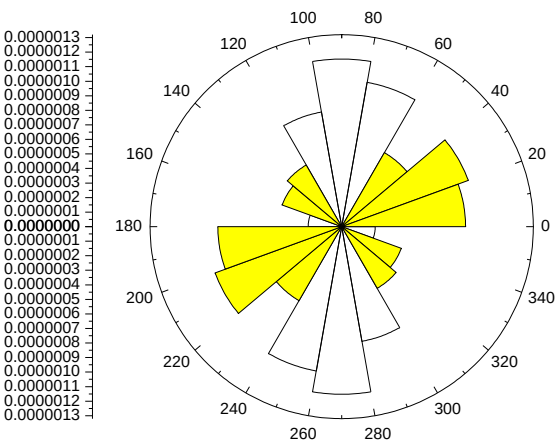

Shear contact force distribution at t = 0 [s]

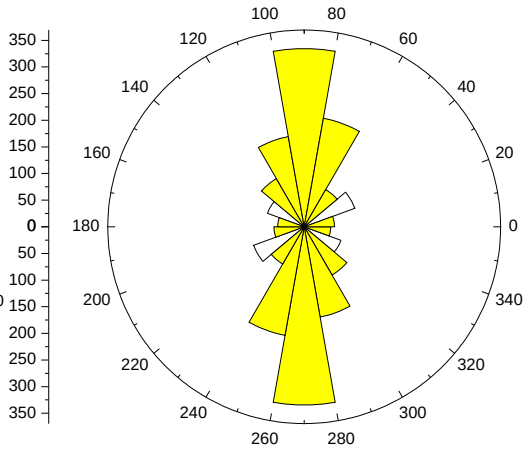

Shear contact force distribution at t = 0.25T [s]

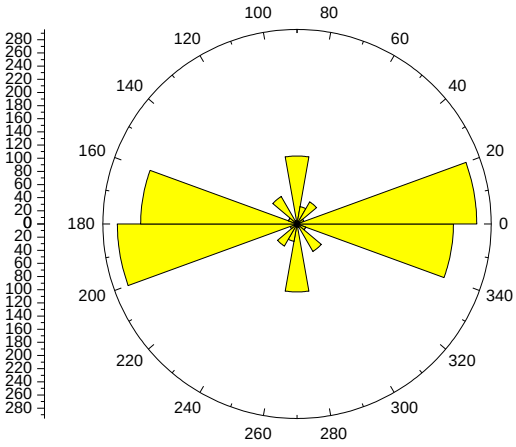

Shear contact force distribution at t = 0.5T [s]

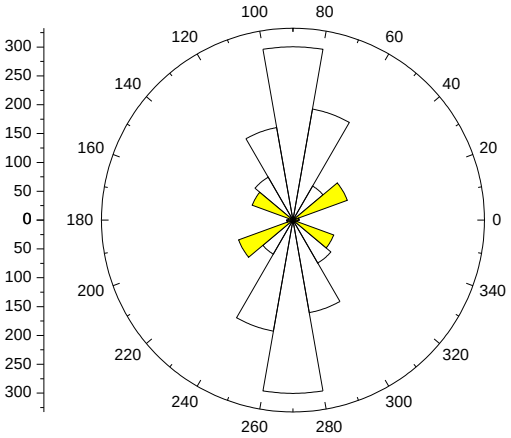

Shear contact force distribution at t = 0.75T [s]

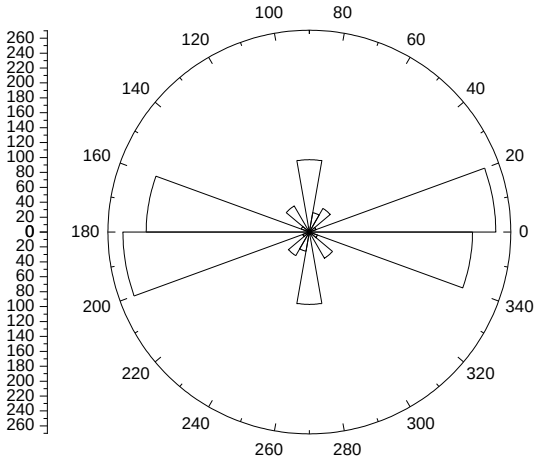

Shear contact force distribution at t = T [s]

(c) Frequency = 3 [Hz]

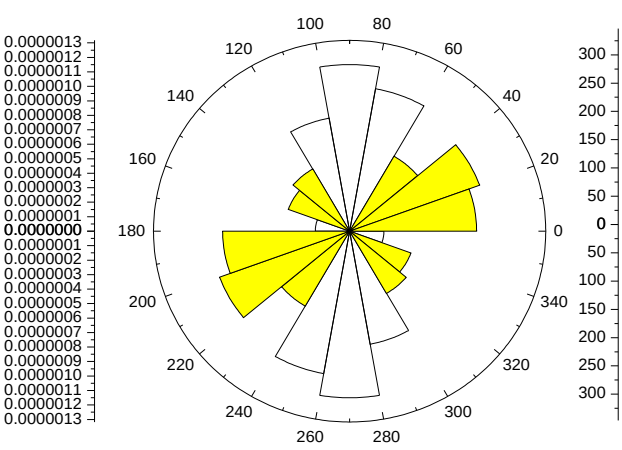

Shear contact force distribution at t = 0 [s]

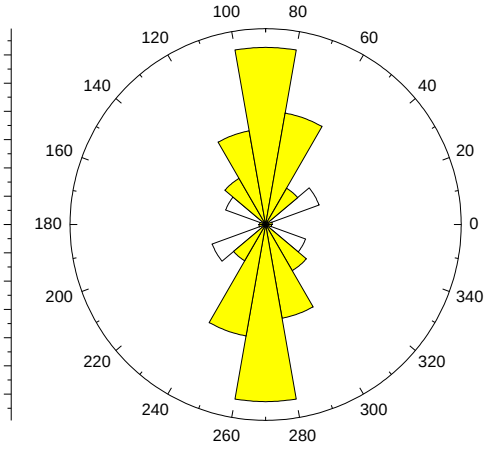

Shear contact force distribution at t = 0.25T [s]

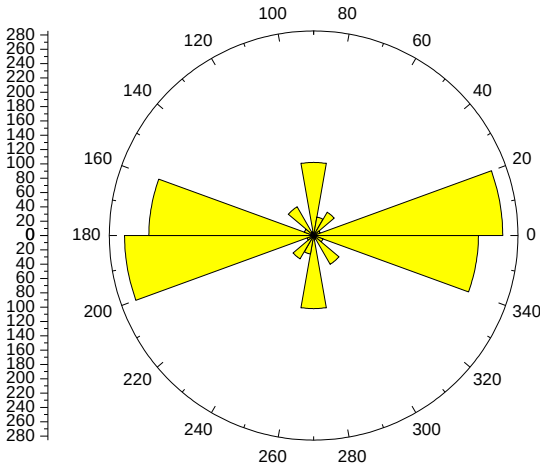

Shear contact force distribution at t = 0.5T [s]

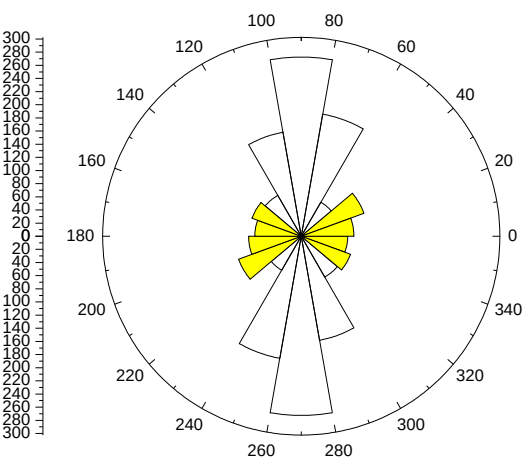

Shear contact force distribution at t = 0.75T [s]

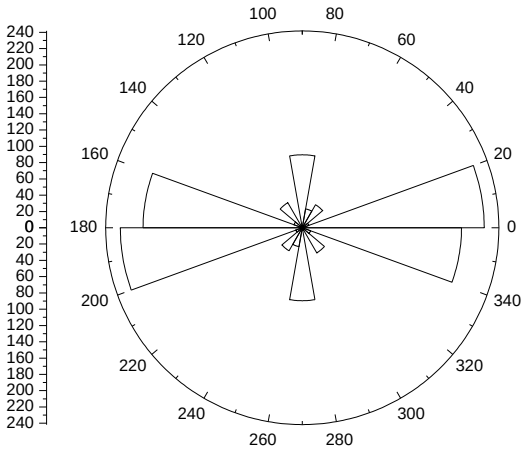

Shear contact force distribution at t = T [s]

(d) Frequency = 4 [Hz]

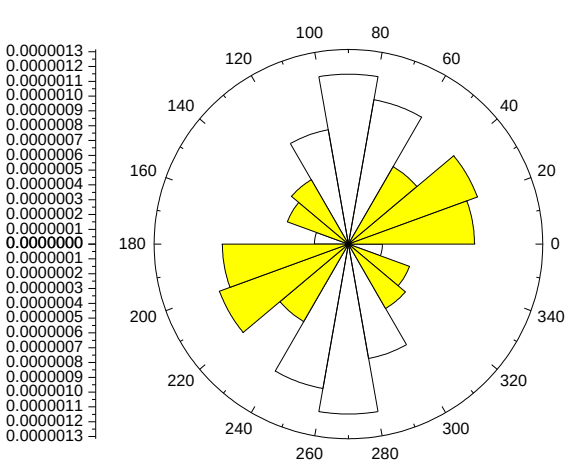

Shear contact force distribution at t = 0 [s]

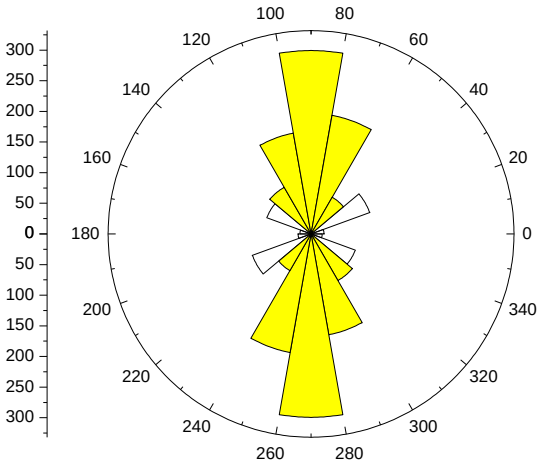

Shear contact force distribution at t = 0.25T [s]

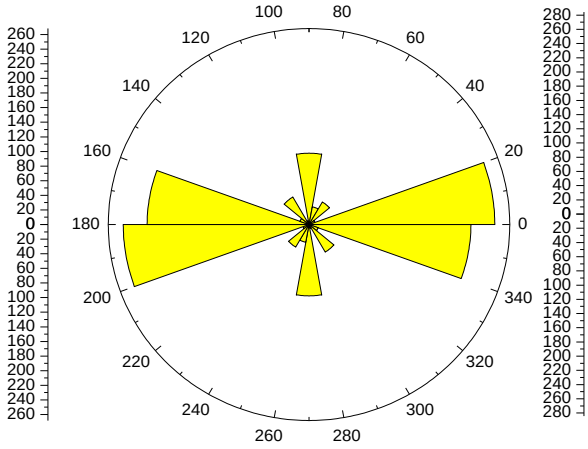

Shear contact force distribution at t = 0.5T [s]

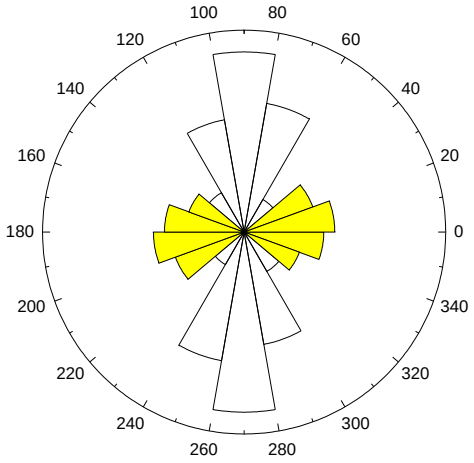

Shear contact force distribution at t = 0.75T [s]

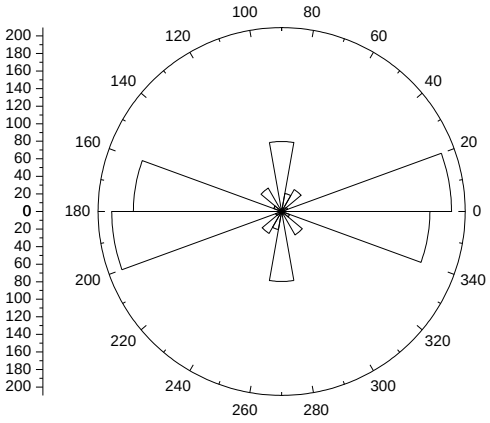

Shear contact force distribution at t = T [s]

(e) Frequency = 5 [Hz]

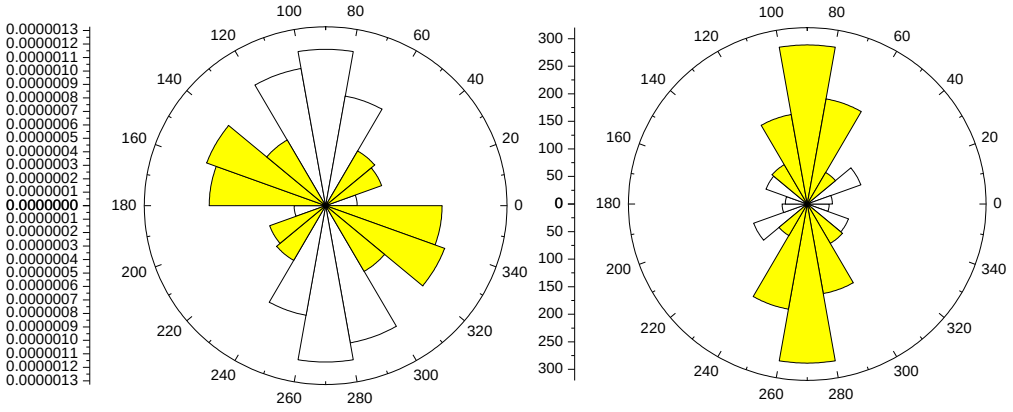

Shear contact force distribution at t = 0 [s]

Shear contact force distribution at t = 0.25T [s]

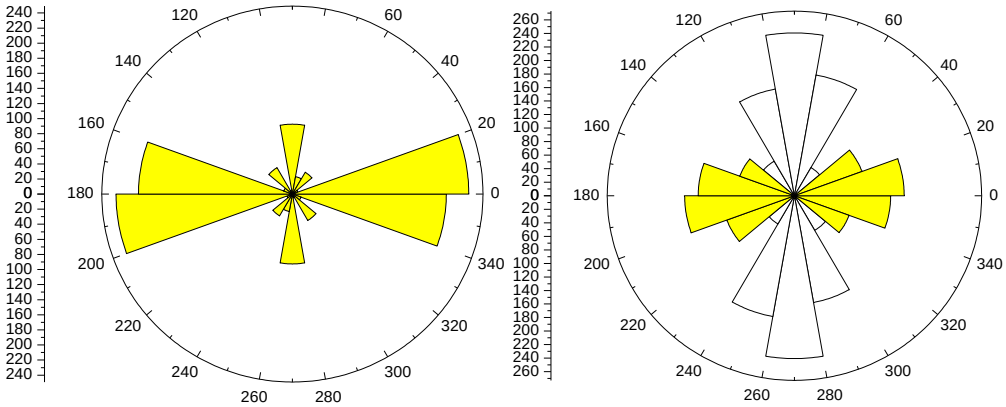

Shear contact force distribution at t = 0.75T [s]

Shear contact force distribution at t = T [s]

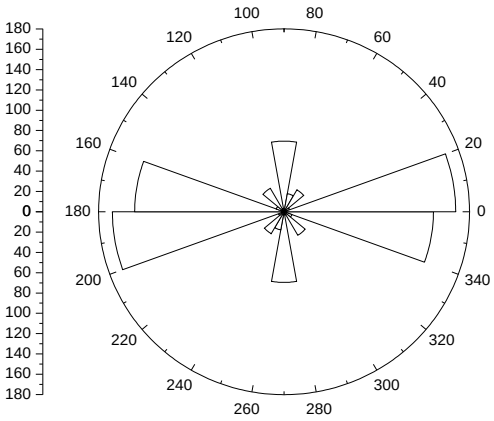

Shear contact force distribution at t = T [s]

(f) Frequency = 6 [Hz]

Figure 6-44 Shear contact force distribution for various frequencies: (a) Frequency=1 [Hz], (b) Frequency=2 [Hz], (c) Frequency=3 [Hz], (d) Frequency=4 [Hz], (e) Frequency=5 [Hz] and (f) Frequency=6 [Hz],

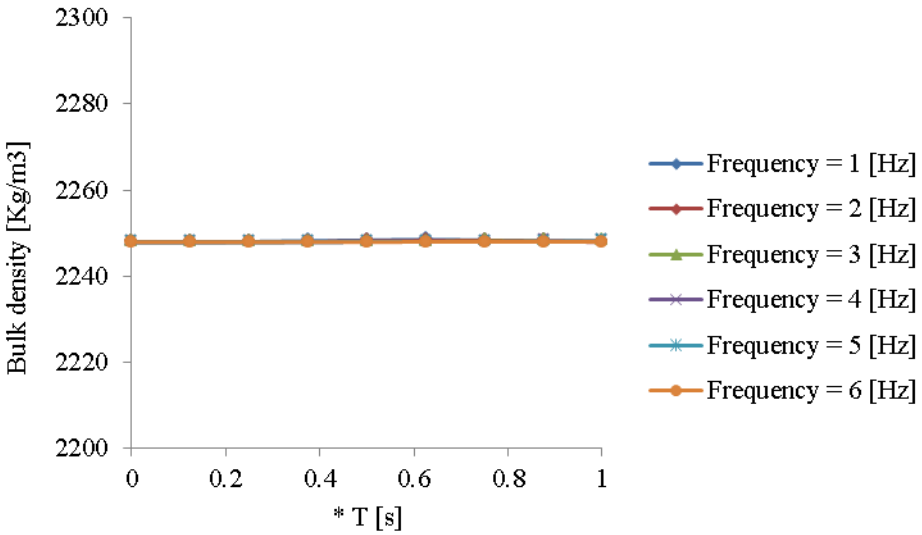

Figure 6-45 Bulk density vs. time

Figure 6-45 shows the variation of bulk density with time. As seen in this figure there is very little change 0T to T for all frequencies and there is no difference between the frequencies. This is because the normal contact force anisotropy remains constant within this range as the normal contact forces controls the stability of the particulate system (see chapter 5). The variation of average coordination number with time is drawn in figure 6-46. As seen in this figure the variation in average coordination number follows the input motion and is different between the frequencies. The trend of this micro-scale behaviour is in good agreement with the trend of normal contact anisotropy. This leads to a change in average symmetric geometric deviation index which is shown in Figure 6-47. The average symmetric geometric deviation index decreases with time though the actual variation depends on the frequency.

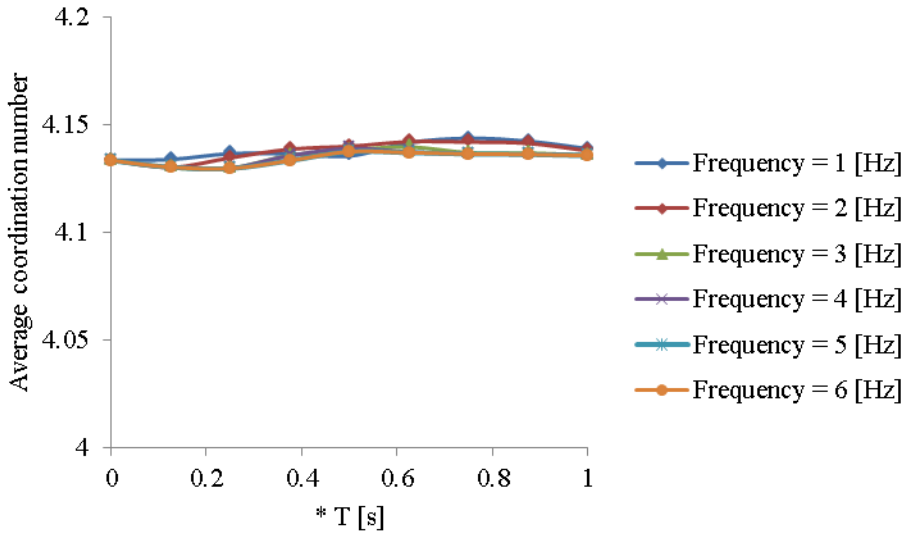

Figure 6-46 Average coordination number vs. time

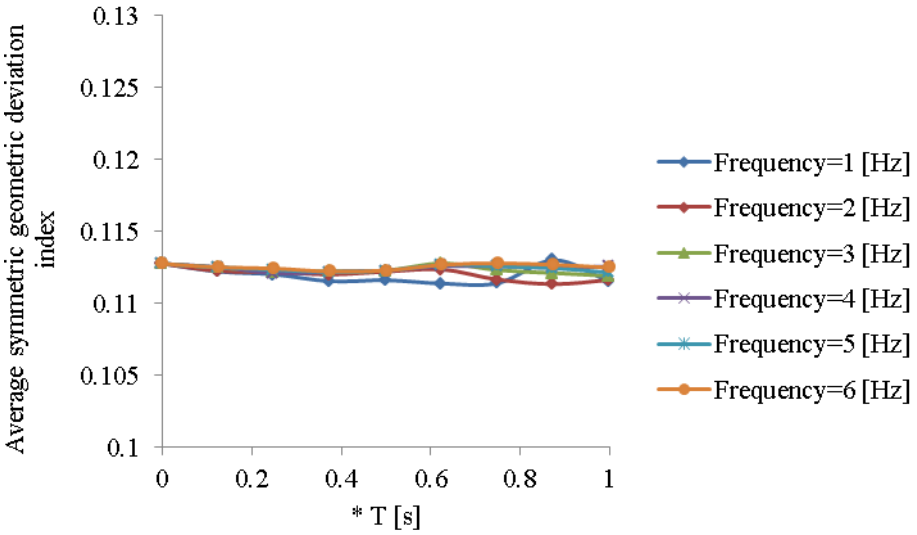

Figure 6-47 Average symmetric geometric deviation index vs. time

Figures 6-49, 6-50 and 6-51 show the effect of fabric evolution on the micro-mechanical stress tensor of RVE. Figure 6-48 shows the variations of average normal contact force with time. The frequency has a negligible influence on this parameter. In addition, the variation of average coordination number within the RVE is negligible and the number of particles within the RVE is similar for these six DEM models. Thus, changes in m_v during the simulation are small for these six models. This leads to the conclusion that the magnitude of micro-mechanical stress tensor values is mainly a function of the average normal contact force and a combination of fabric anisotropies.

The magnitude of normal contact and normal contact force anisotropies are larger than the magnitude of shear contact force anisotropy. Increasing the frequencies from 1 to 6 [Hz] leads to a slight reduction in the shear stress tensor (see figure 6-49). The trend of micro-mechanical shear stress (figures 6-49) is in good agreement with the trend of shear contact force anisotropy.

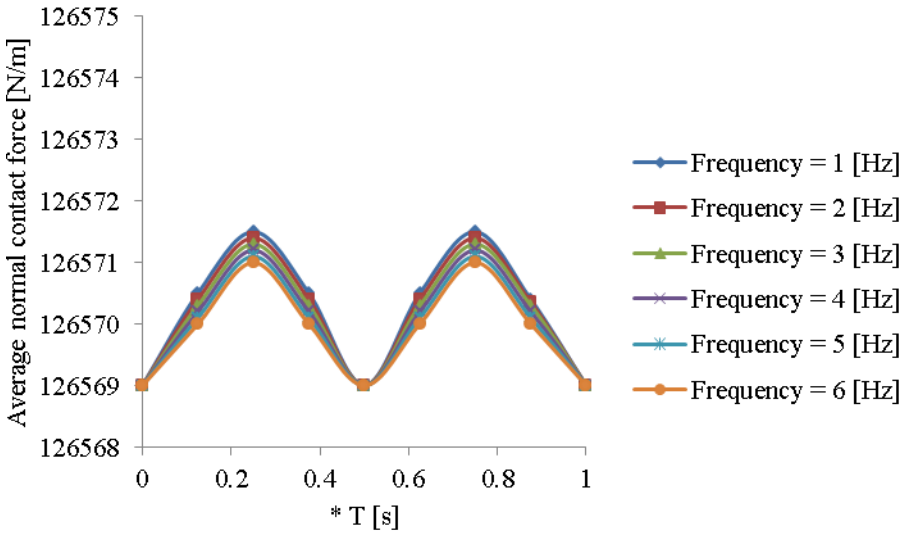

Figure 6-48 The variation of average normal contact force vs. time

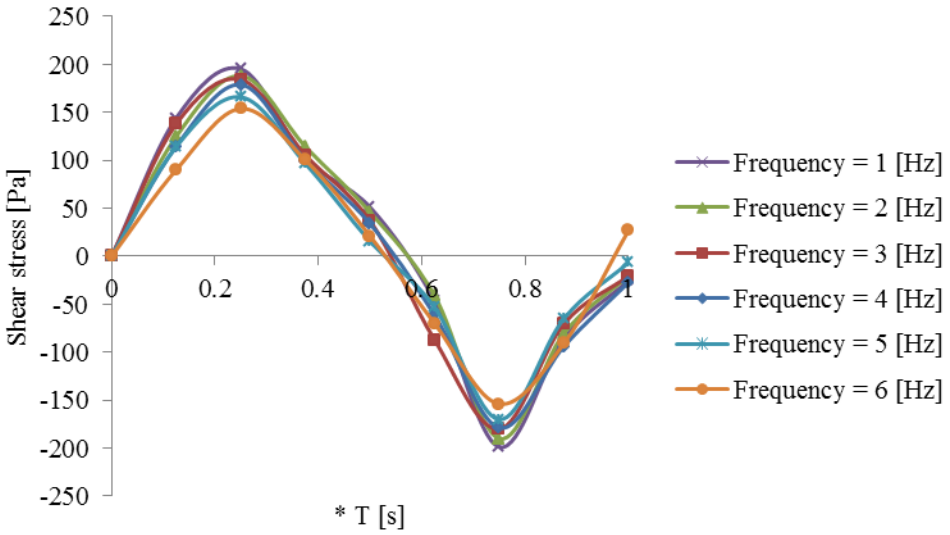

Figure 6-49 Micro-mechanical shear stress vs. time

The trend of micro-mechanical principle stresses of RVE is shown in figures 6-50 and 6-51. As can be seen increasing the frequency has little influence on their magnitude oat any time. It is because the average normal contact forces which control the stability of particulate system do not change considerably. The trend of these stresses is in good agreement with the trend of fabric anisotropies.

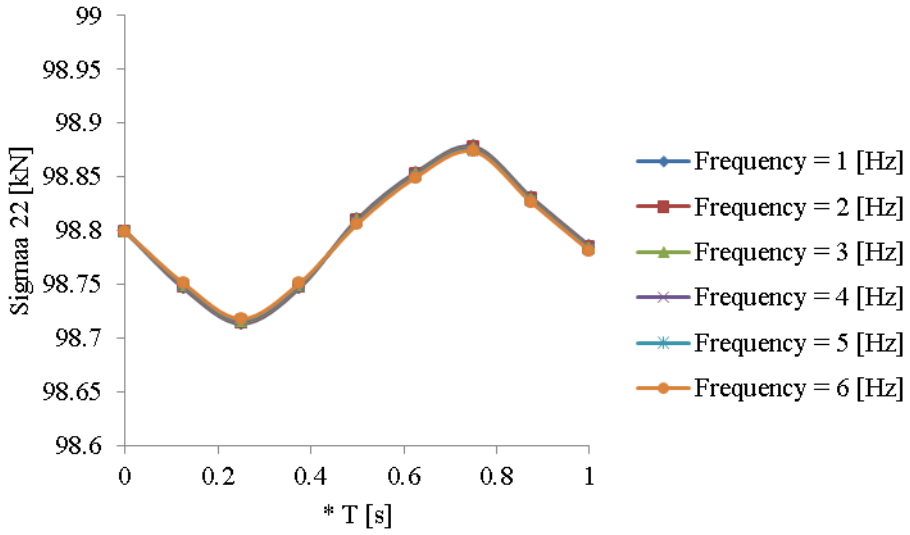

Figure 6-50 Micro-mechanical stress 22 vs. time

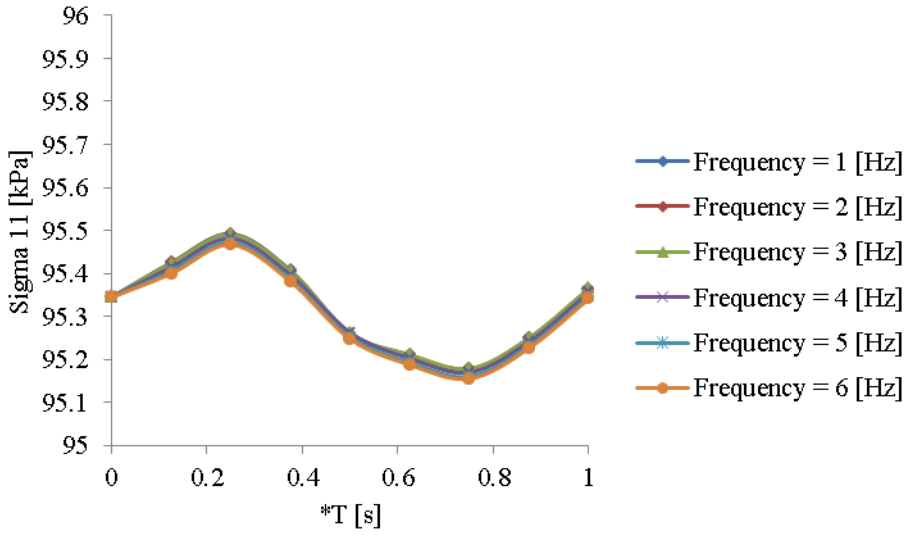

Figure 6-51 Micro-mechanical stress 11 vs. time

6.8 The sensitivity of sand fabric to the various amplitudes during earthquake

The range of acceleration of the 10 earthquake signals used to determine the frequency range is approximately between 0.03 and 0.5 [m/s^2]. In addition to this range, a greater acceleration was investigated to establish the influence of rare, greater acceleration on fabric evolution and micro-mechanical behaviour of idealized sand. The same approach was used; i.e. a single sine periodic wave with a unique amplitude and frequency. To study the influence of earthquake's amplitudes on fabric evolution of granular sand, three DEM simulations with three different amplitudes were performed. The initial conditions of these three models were the same. After generation of uniform particle size distribution within sand range - i.e. 1.5 [mm] to 2 [mm], all these models were isotropically consolidated to 100 [kPa]. The amplitude of input motion was between 0.0377 and 3.77 [m/s^2]. The input frequency of these three DEM simulations is 6 [Hz]. Table 6-7 displays the input parameters of these DEM simulations. The normal contact, normal contact force and shear contact force distribution of amplitudes of 3.77 [m/s^2] and 0.37 [m/s^2] models is drawn in figures 6-52(a), 6-52(b), 6-53(a), 6-53(b), 6-54(a), 6-54(b), respectively. The normal contact, normal contact force and shear contact force distribution of amplitudes of 0.0377 [m/s^2] is drawn in figures 6-27, 6-32 and 6-34 when the sample ratio is 4. The variation of normal contact, normal contact force and shear contact force anisotropies with time of these three simulations is shown in figures 6-55, 6-56 and 6-57, respectively. The average coordination number, average symmetric geometric deviation index and bulk density of these three DEM simulations are shown in figures 6-58 to 6-60.

Test No.	k_n [N/m] *10^7	k_s [N/m] *10^7	μ	c_n	c_s	n	Range of PSD [mm]	Amplitude [m/s]	Sample ratio	f [Hz]
1	8.45	8.45	0.9	0.01	0.01	0.12	1.5-2	$1*10^{-3}$	0.0377	6
2	8.45	8.45	0.9	0.01	0.01	0.15	1.5-2	$1*10^{-2}$	0.377	6
3	8.45	8.45	0.9	0.01	0.01	0.16	1.5-2	$1*10^{-1}$	3.77	6

Table 6:7 Input parameters of three different DEM simulations with various amplitudes in order to study the fabric response

From t=0 [s] to t=0.25T [s] when the magnitude of external load reaches to its positive maximum value, increasing the amplitude has a significant influence on the evolution of normal contact distribution of higher amplitude while this rise in amplitude has a less effect on the re-arrangement of contacts in the case of lower amplitudes (see figure 6-52(a), 6-52(b) and 6-27). That is, increasing the amplitude causes that the radius of each bin and the orientation of the polar diagram of higher the higher amplitude considerably changes. It is to be noted that the radius of each bin corresponds to the number of contacts that bin. This indicates that the re-arrangement in contacts is being formed to represent the maximum bearing capacity, which is more evidence in the case of higher amplitude. Thus, the normal contact anisotropy in the case of higher amplitude considerably alters in comparison to lower amplitudes (see figure 6-55). As the principle axes in normal contact distribution corresponds to the principle stresses (see chapter 5 and (Yimsiri and Soga, 2010)), the principle stresses in the case of higher amplitude in figure 6-52(a) is clearly rotated at t = 0.25T [s]. Increasing the amplitude also results in rise the speed of loading. For example, $\frac{a:amplitude=0.037}{t=0.25\mathrm{T}} = 0.55\ [\frac{1}{s}]$, $\frac{a:amplitude=0.37}{t=0.25\mathrm{T}} = 0.65\ [\frac{1}{s}]$ while the ratio $\frac{a:amplitude=3.7}{t=0.25\mathrm{T}} = 2.0\ [\frac{1}{s}]$. It is to be noted that "a" is normal contact anisotropy. This indicates in the same time, the rate of re-arrangement in contacts considerably increases by elevating the amplitude. For instance, considering the normal contact distribution of lower and higher amplitudes in figures 6-27

and 6-52, respectively. As discussed already, the reason of contact re-arrangement is back to the arrangement of contact forces. Figures 6-53and 6-32 show the normal contact force distribution of these three DEM models. As seen, normal contact force distribution within each bin in the case of higher amplitude significantly changes in comparison to lower amplitudes. Thus, normal contact force anisotropy in the case of higher amplitude is considerably bigger than that in lower amplitudes (see figure 6-56). Comparing the normal contact force anisotropies of these three simulations shows that changing the anisotropy degree of normal contact force of amplitude = 3.7 [m/s^2] is 19.0 and 9.5 times bigger than the anisotropy degree of normal contact force of amplitude = 0.037 [m/s^2] and amplitude = 0.37 [m/s^2], respectively at t = 0.25T [s]. Since, the sliding friction at each contact is greatly dependant on its counterpart normal contact force, the shear capacity of the idealized sand significantly increases by increasing the contact force and the rate of re-arrangement in contacts. This orientation of normal contact force distribution at t = 0.25T [s] is qualitatively the same as the orientation of normal contact distribution at t = 0.25T [s]. As the direction of normal contact force distribution alters at t = 0.25T [s] in the case of higher amplitude, the ordination of force chains change.

In terms of shear contact force distribution, increasing the amplitude leads to considerably rise in shear contact force in each segment (see figures 6-54 and 6-34). It is because the input motion imported to the system is in shear direction so that increase in the amplitude of this motion leads to generate the higher shear contact force across the particulate media. Thus, another reason with respect to contact re-arrangement is to re-distribute shear contact forces beside the re-distribution of normal contact forces. Figure 6-57 shows the variation of shear contact anisotropy. As seen in this figure, the anisotropy degree of shear contact force from t = 0 [s] significantly increases by increasing the amplitude of input motion. That, is the value of shear contact forces at t = 0.25T [s] increases significantly from t = 0 [s] (i.e. static state) when the amplitude of input motion rises from 0.037 to 3.7 [m/s^2] (see figure 6-53). Increasing this anisotropy also represents the increase in shear strength of system.

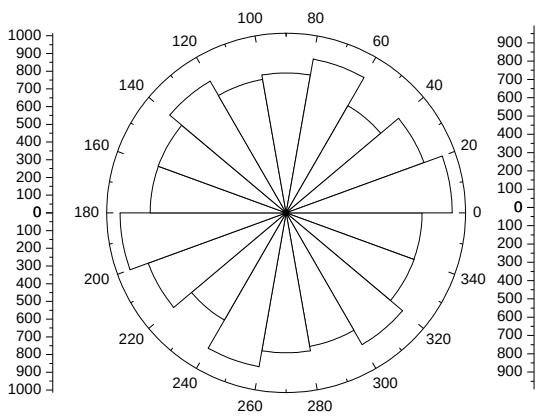

Normal contact distribution at t = 0 [s]

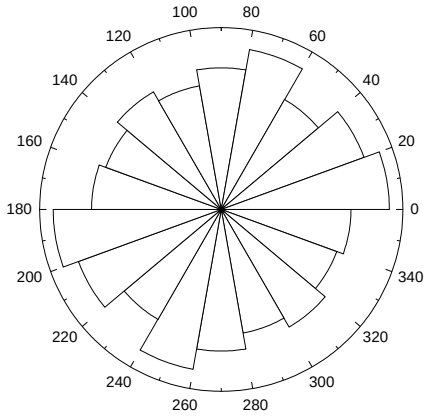

Normal contact distribution at t = 0.25T [s]

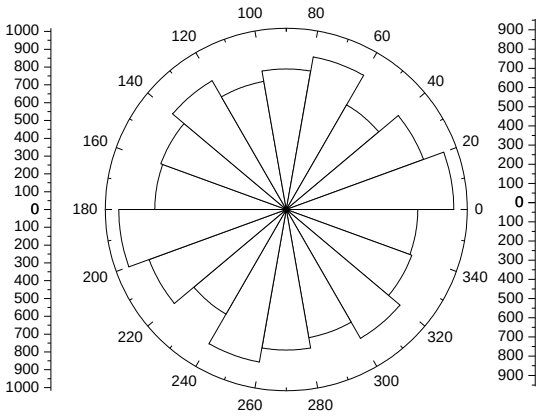

Normal contact distribution at t = 0.5T [s]

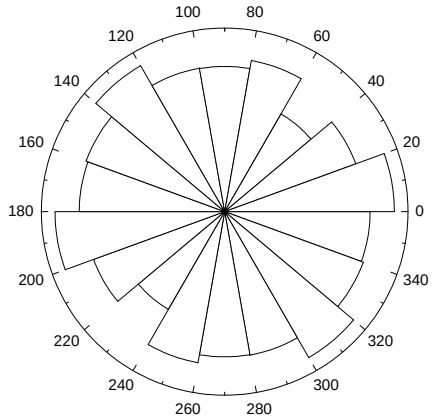

Normal contact distribution at t = 0.75T [s]

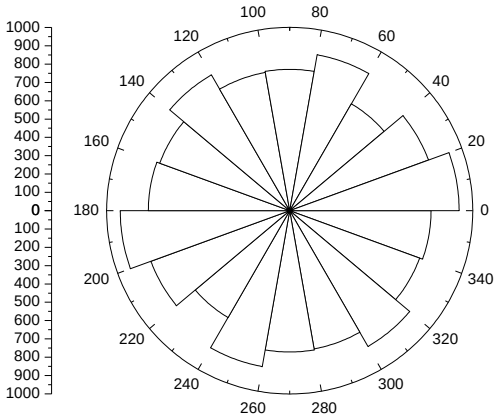

Normal contact distribution at t = T [s]

(a) Amplitude=3.7[m/s^2]

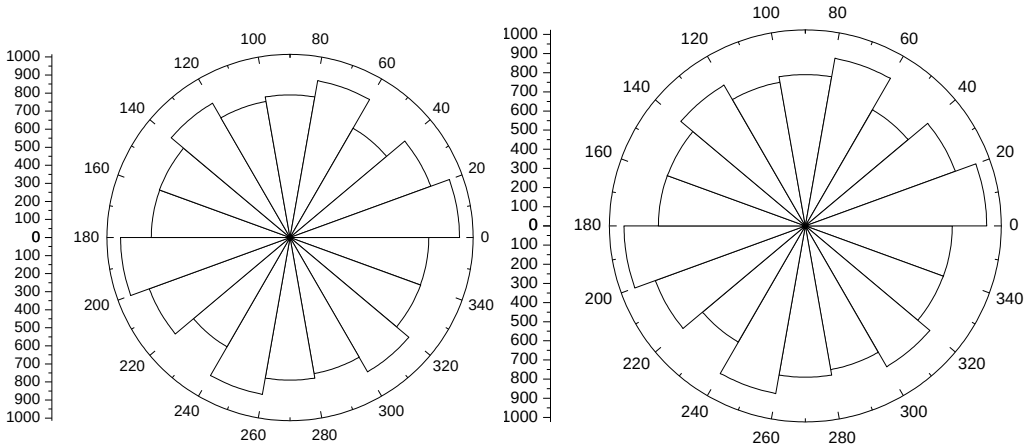

Normal contact distribution at t = 0 [s]

Normal contact distribution at t = 0.25T [s]

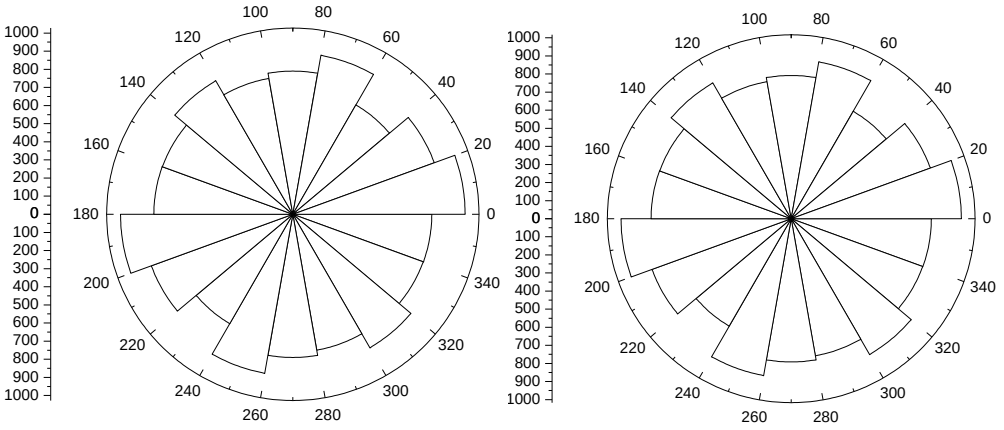

Normal contact distribution at t = 0.5T [s]

Normal contact distribution at t = 0.75T [s]

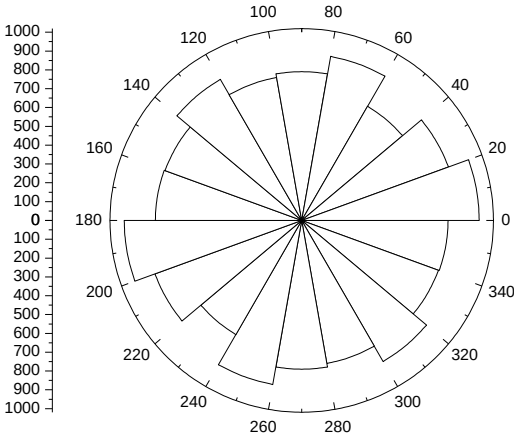

Normal contact distribution at t = T [s]

(a) Amplitude=0.37[m/s^2]

Figure 6-52 The evolution of normal contact distribution vs. time: (a) Amplitude=3.7[m/s^2], (b) Amplitude=0.37[m/s^2]

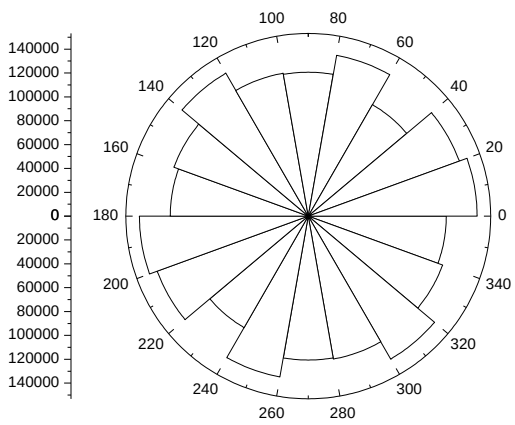

Normal contact force distribution at t=0 [s]

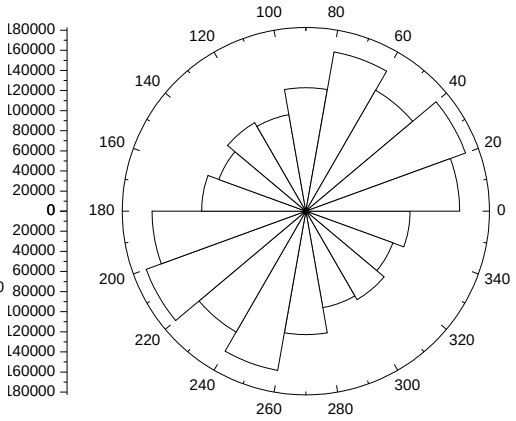

Normal contact force distribution at t=0.25T [s]

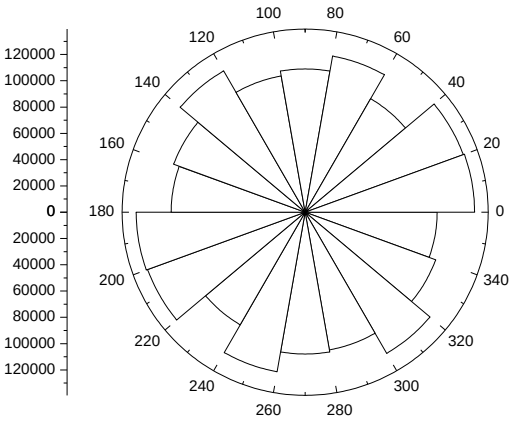

Normal contact force distribution at t=0.5T [s]

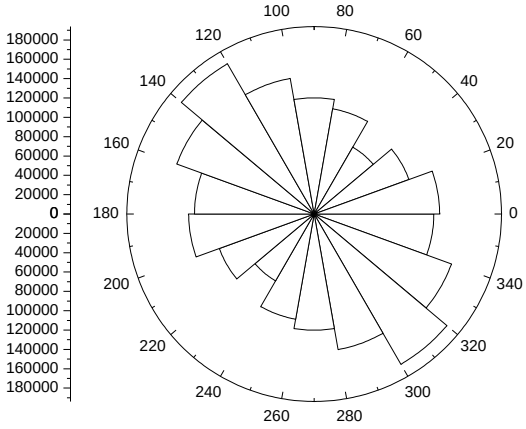

Normal contact force distribution at t=0.75T [s]

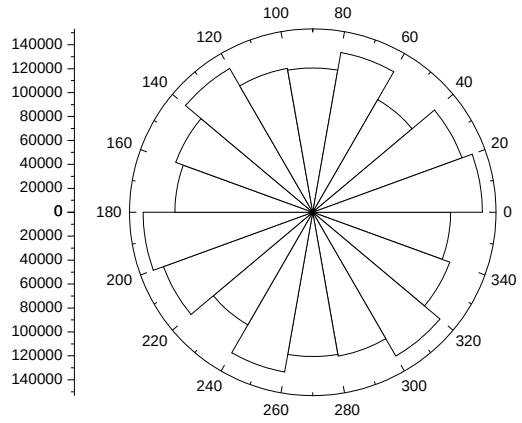

Normal contact force distribution at t=T [s]

(a) Amplitude=3.7[m/s^2]

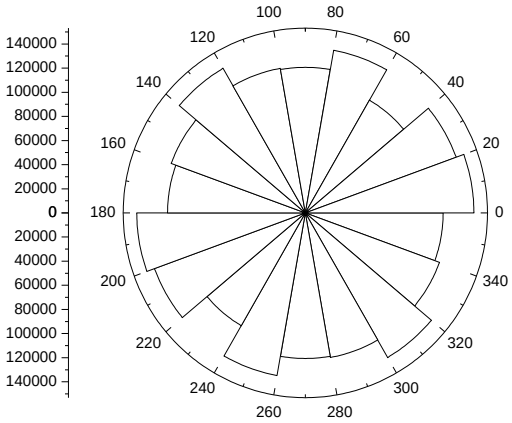

Normal contact force distribution at t = 0 [s]

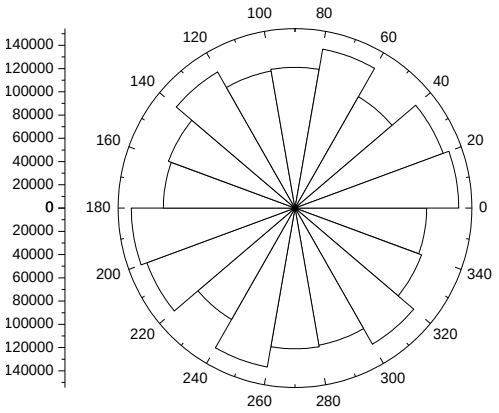

Normal contact force distribution at t = 0.25T [s]

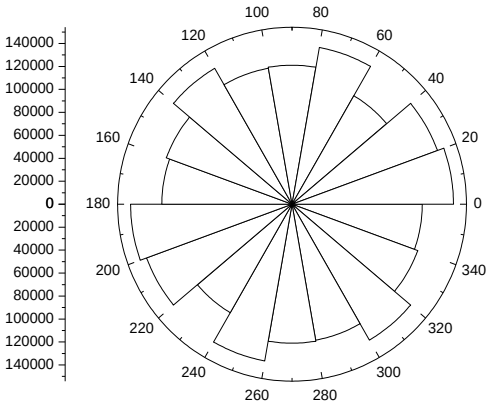

Normal contact force distribution at t = 0.5T [s]

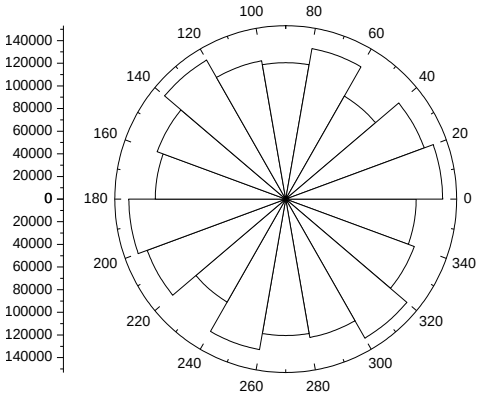

Normal contact force distribution at t = 0.75T [s]

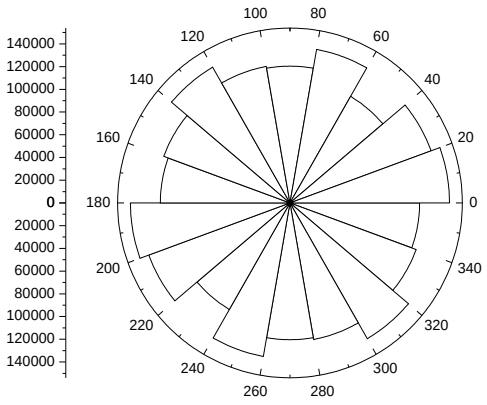

Normal contact force distribution at t = 0T [s]

(b) Amplitude=0.37[m/s^2]

Figure 6-53 The evolution of normal contact force distribution vs. time: (a) Amplitude=3.7[m/s^2], (b) Amplitude=0.37[m/s^2]

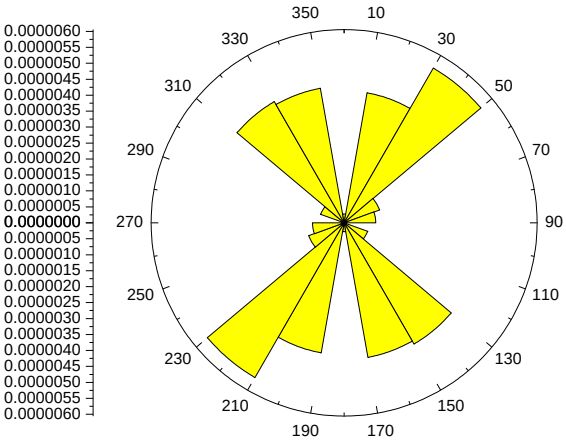

Shear contact force distribution at t = 0 [s]

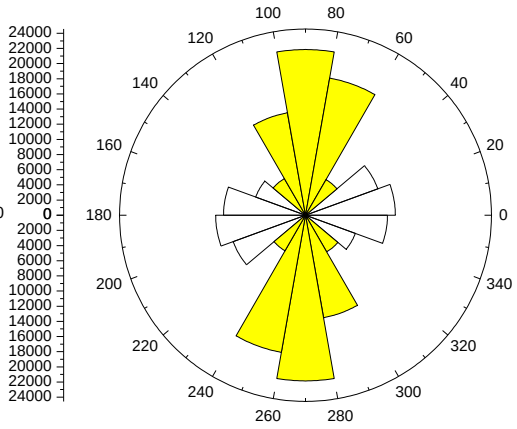

Shear contact force distribution at t = 0.25T [s]

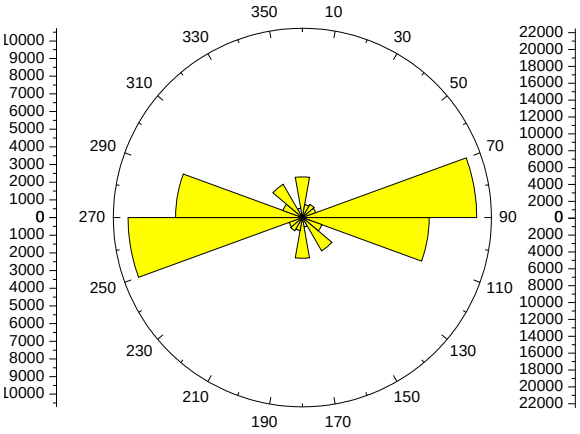

Shear contact force distribution at t = 0.5T [s]

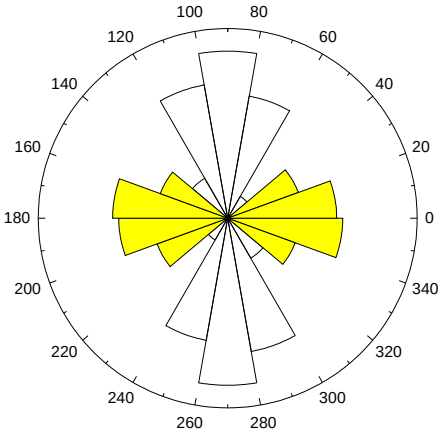

Shear contact force distribution at t = 0.75T [s]

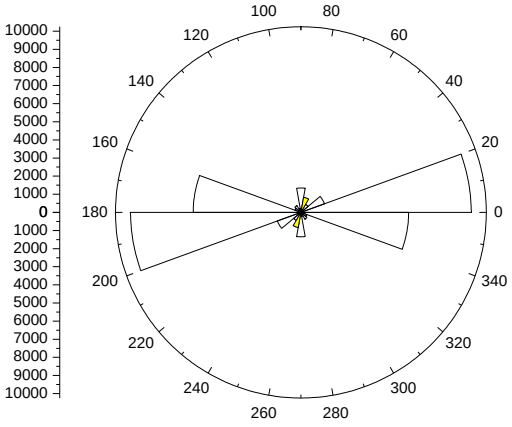

Shear contact force distribution at t = T [s]

(a) Amplitude=3.7[m/s^2]

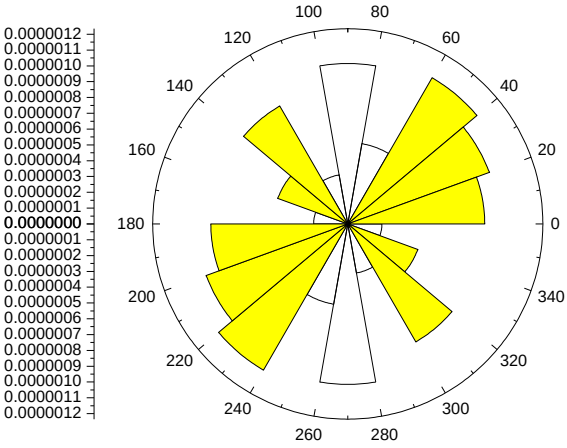

Shear contact force distribution at t = 0 [s]

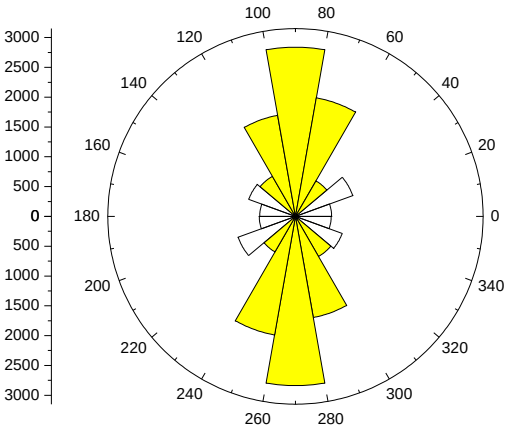

Shear contact force distribution at t = 0.25T [s]

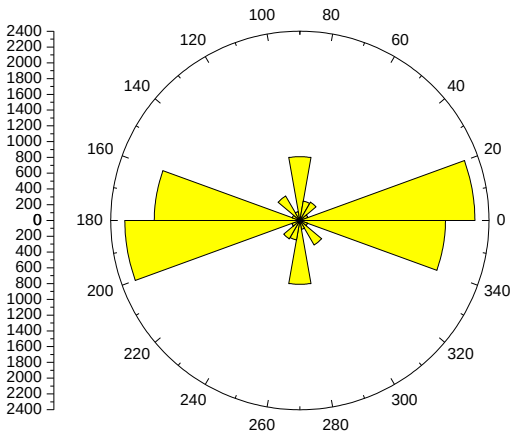

Shear contact force distribution at t = 0.5T [s]

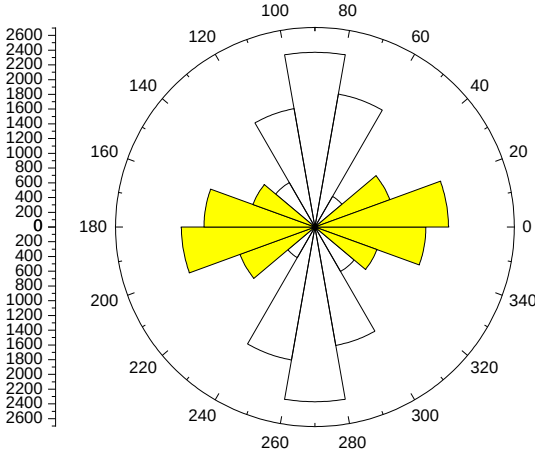

Shear contact force distribution at t = 0.75T [s]

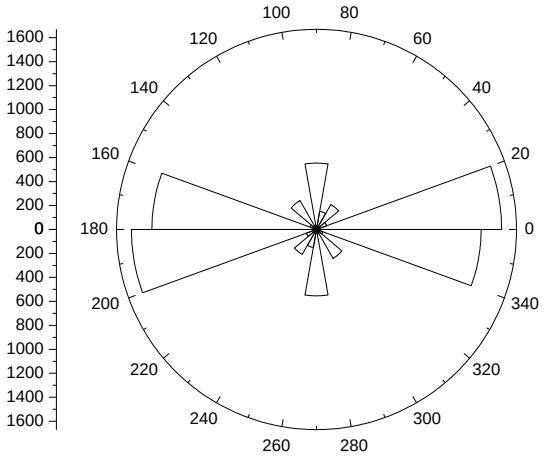

Shear contact force distribution at t = T [s]

(b) Amplitude=0.37[m/s^2]

Figure 6-54 The evolution of shear contact force distribution vs. time: (a) Amplitude=3.7[m/s^2], (b) Amplitude=0.37[m/s^2]

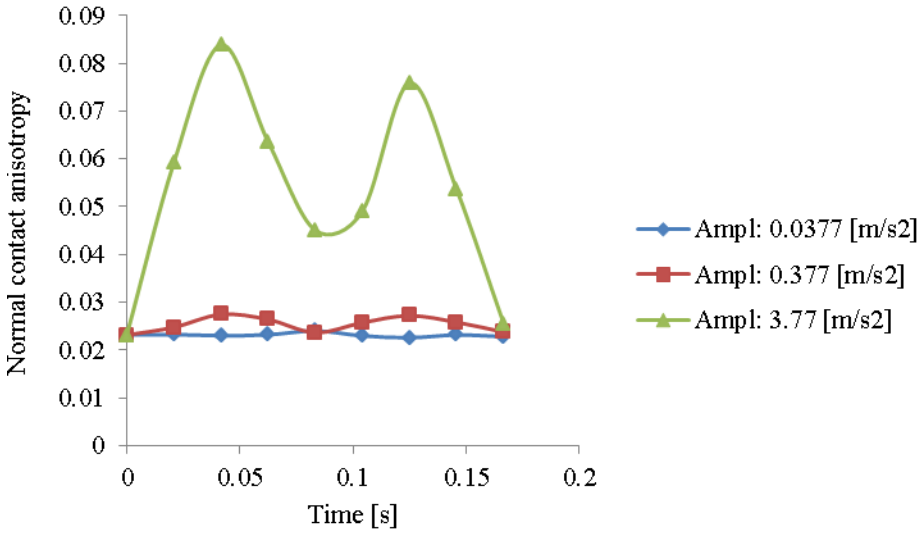

Figure 6-55 Normal contact anisotropy of these three DEM simulations vs. time

Figure 6.55 shows that the normal contact anisotropy follows the input motion but as the amplitude increases there is a significant change to the normal contact anisotropy.

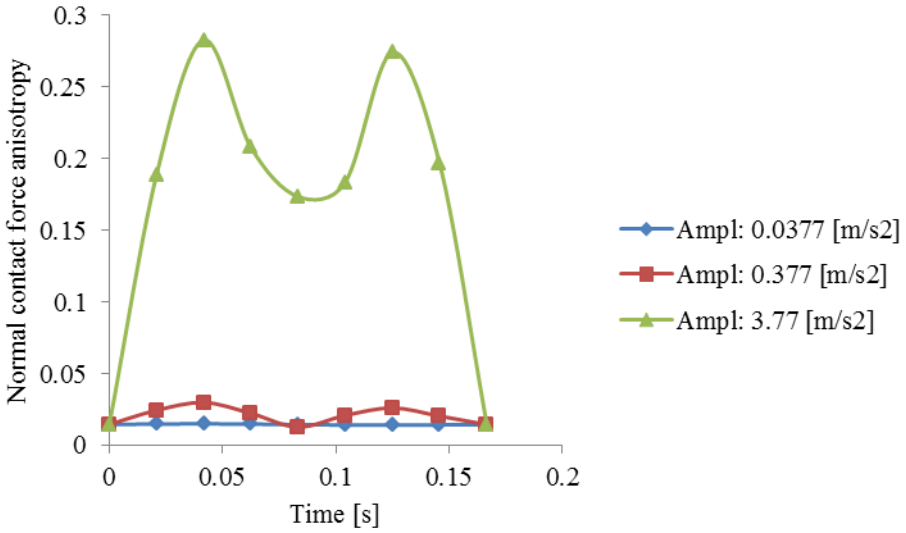

Figure 6-56 Normal contact force anisotropy of these three DEM simulations vs. time

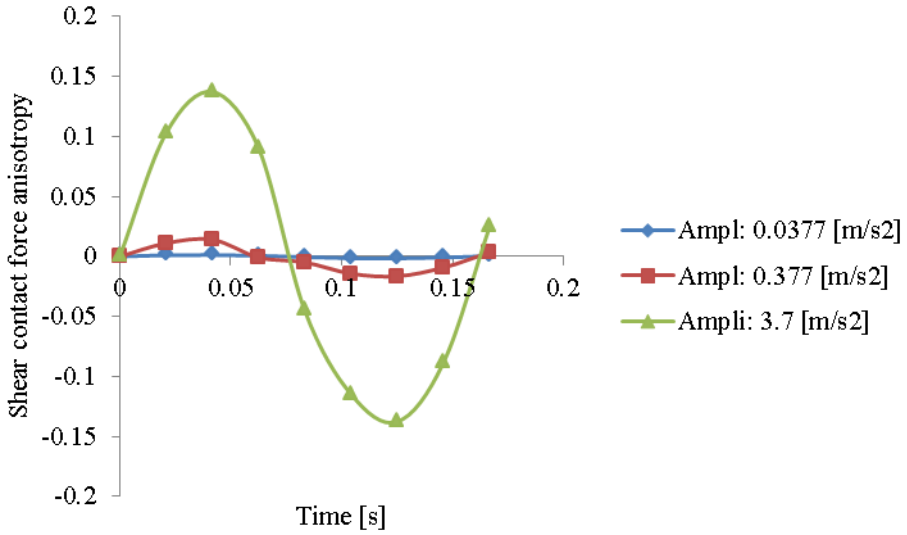

Figure 6-57 Shear contact force anisotropy of these three DEM simulations vs. time

The average coordination number of the system for 0.037 [m/s^2] and 0.37 [m/s^2] is very nearly constant over the cycle of loading (figure 6.58) but for 3.7 [m/s^2] the number decreases. Figure 6-59 shows that by increasing the amplitude, the arrangement of contacts around each particle remains the same for 0.037 [m/s^2] and 0.37 [m/s^2] but fluctuates for 3.7 [m/s^2]. Figure 6-60 shows that by increasing the amplitude, the bulk density reduces by a small amount for 0.037 [m/s^2] and 0.37 [m/s^2] but drops for 3.7 [m/s^2]. This means that the sample expands and, more importantly, leads to a significant loss of strength since strength is related to density.

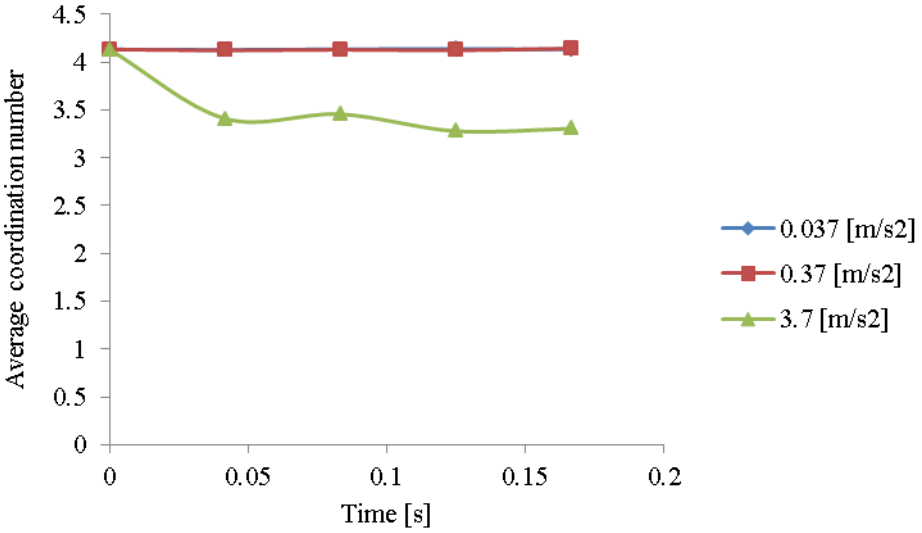

Figure 6-58 The evolution of bulk density of these three DEM simulations vs. time

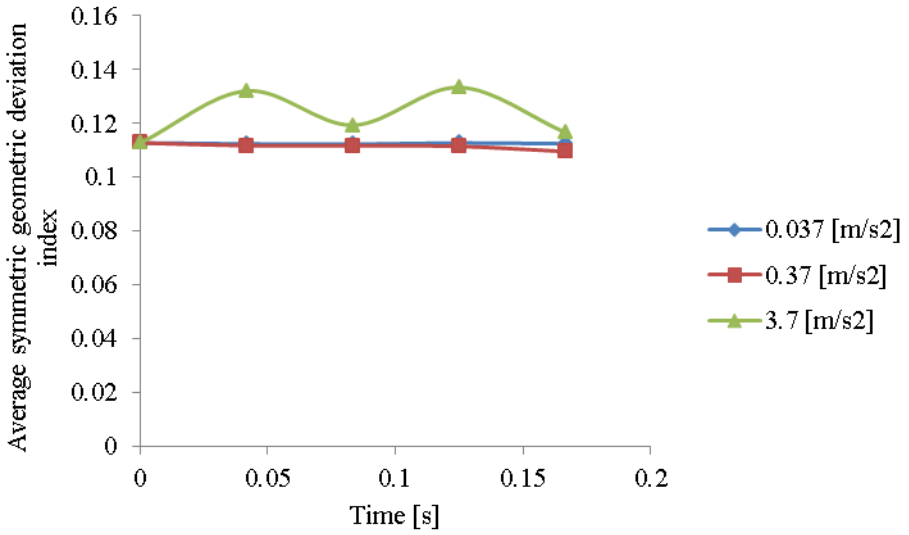

Figure 6-59 The evolution of average symmetric geometric deviation index of these three DEM simulations vs. time

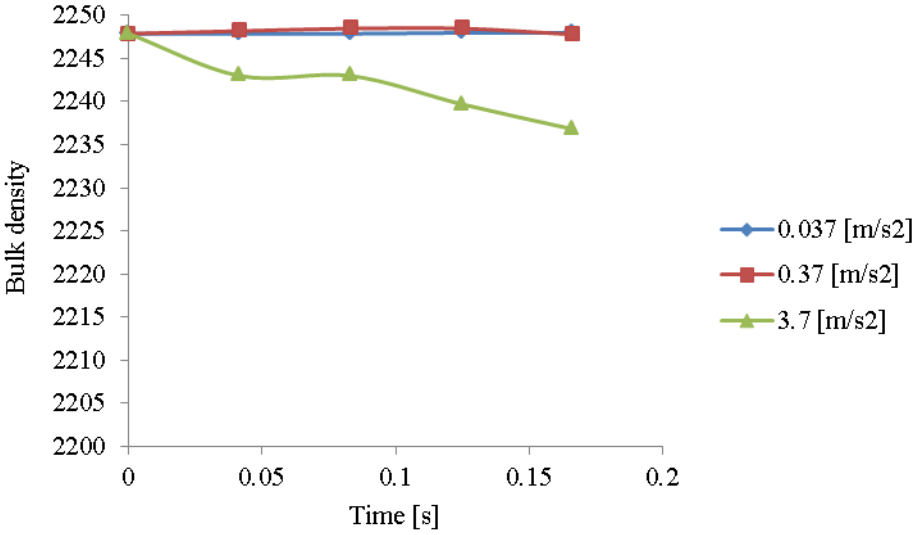

Figure 6-60 The evolution of average coordination number of these three DEM simulations vs. time

Figure 6-61 shows the variation of average normal contact force with time. The change in average normal contact force follows the input motion with the amplitude increasing with the acceleration. As seen increasing the amplitude has a considerable influence on this parameter especially in the case of higher amplitude.

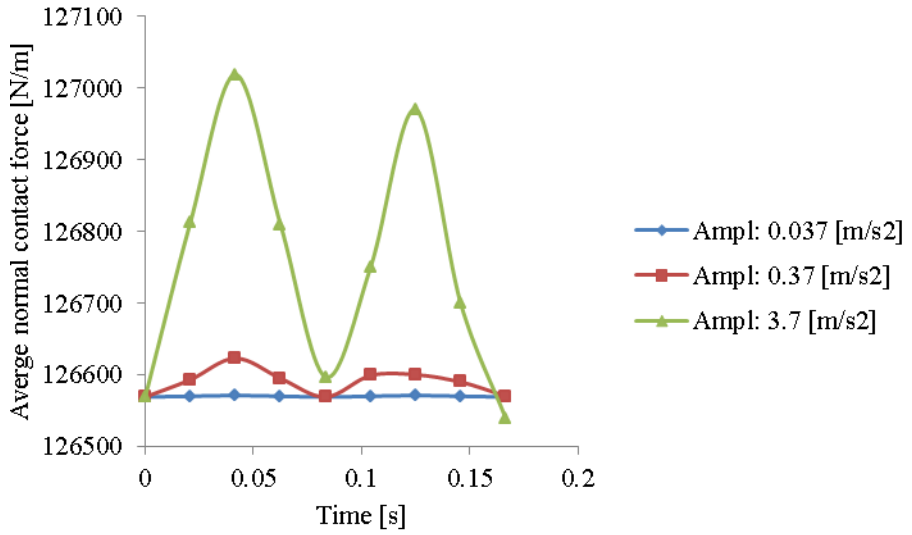

Figure 6-61 The variation of average normal contact force vs. time

The shear stress of the RVE for 0.037 [m/s^2] and 0.37 [m/s^2] is very nearly zero but for 3.7 [m/s^2] there is a significant change in shear stress.

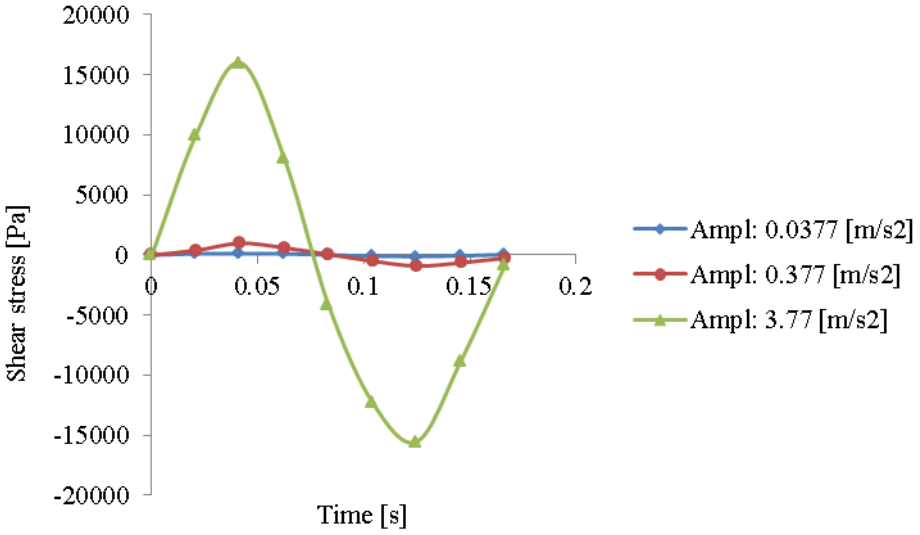

Figure 6-62 The variation of micro-mechanical shear stress vs. time

The change in shear stress is also reflected in the change in the vertical and horizontal stresses (figures 6-63 and 6-64). The mean stress is similar to the confining stress but, in the case of 3.7 [m/s^2] the vertical and horizontal

stresses change suggesting that the sample is undergoing cyclic behaviour driven by the change in normal stresses.

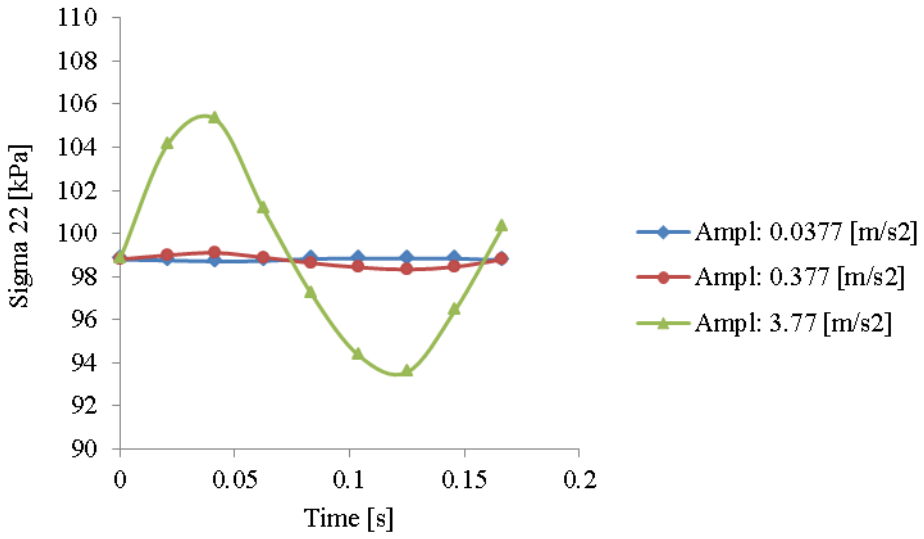

Figure 6-63 Micro-mechanical stress 22 vs. time

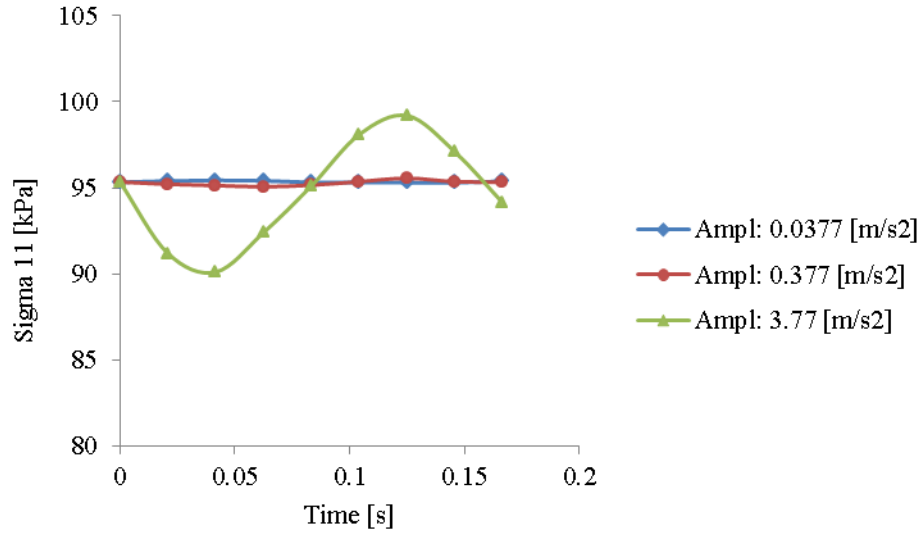

Figure 6-64 Micro-mechanical stress 11 vs. time

6.9 The sensitivity of sand fabric to the various confining pressures during earthquake

In this section, the influence of the confining pressure on a system subject to seismic loading was investigated. The initial conditions of these two models are shown in Table 6-8.

Test No.	k_n [N/m] *10^7	k_s [N/m] *10^7	μ	c_n	c_s	n	Range of PSD [mm]	Amplitude [m/s]	Confining pressure [kPa]	f [Hz]
1	8.45	8.45	0.9	0.01	0.01	0.12	1.5-2	$1*10^{-3}$	100.0	6
2	8.45	8.45	0.9	0.01	0.01	0.12	1.5-2	$1*10^{-3}$	50.0	6

Table 6:8 The input properties used for the sensitivity analysis of the system subject to different confining pressures

Figure 6-65 shows that increasing the confining pressure reduces the initial normal contact anisotropy. In both cases the normal contact anisotropy varies with time.

Figure 6.66 shows that the normal contact force anisotropy changes, the change reflecting the input motion. However, the magnitude of the change is much greater for 50 [kPa] than 100 [kPa] showing the confining pressure influences the behaviour of the system.

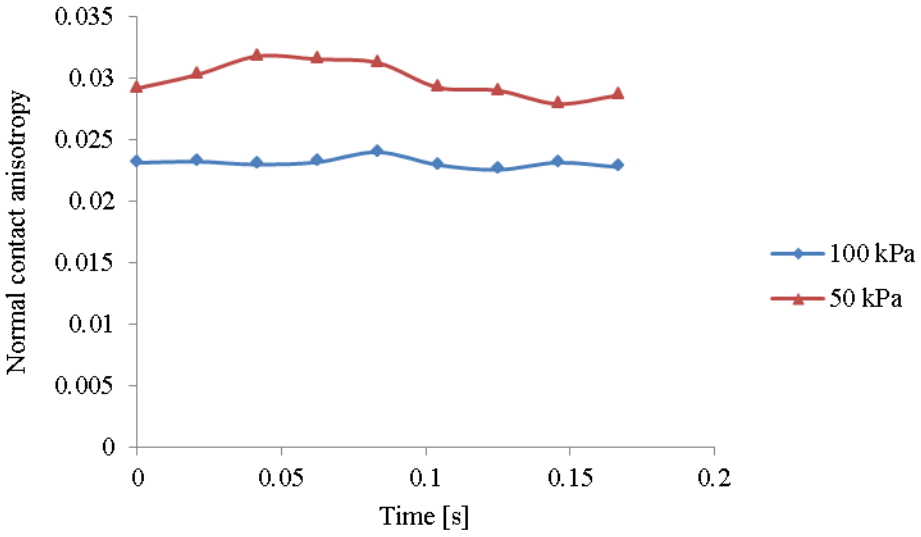

Figure 6-65 The variation of normal contact anisotropy vs. time

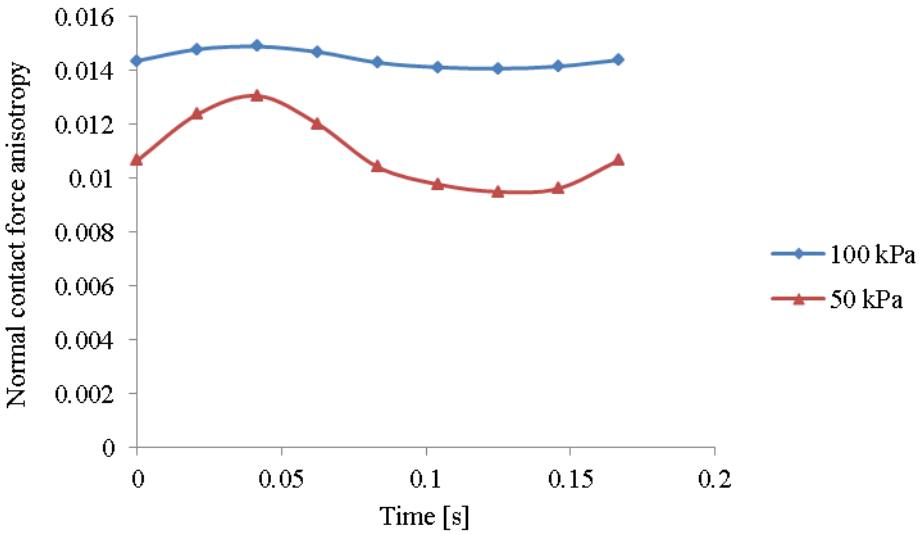

Figure 6-66 The variation of normal contact force anisotropy vs. time

Figures 6-66 and 6-73 shows the variation of normal contact force anisotropy and average normal contact force (i.e. $\bar{f}_0^c$) during the periodic loading for these two DEM samples. As seen increasing the confining pressure leads to significant rise in $\bar{f}_0^c$. The ratio $\frac{\bar{f}_{0\,100\,[kPa]}^c}{\bar{f}_{0\,50\,[kPa]}^c}$ is exactly equal 2.0. The initial normal contact force anisotropy for 100 [kPa] confining pressure is 1.3 times larger than that for the confining pressure of 50 [kPa].

Since the systems are dense and $\bar{f}_0^c$ is constant during loading, the contact shear forces produced due to the same earthquake load through the models are similar (see figure 6-68 and 6-44(f)). As the evolution of shear contact force anisotropy is directly related to the shear contact force and inversely related to $\bar{f}_0^c$, the ratio of maximum $\frac{a_s:50\,[kPa]}{a_s:100[\mathrm{kPa}]}$ is nearly equal 2.0 which inversely corresponds to ratio $\frac{100\,[kPa]}{50\,[kPa]}$ and $\frac{\bar{f}_{0\,100\,[kPa]}^c}{\bar{f}_{0\,50\,[kPa]}^c}$ (see figure 6-67). Thus, increasing the confining pressure leads to a reduction in the shear contact force anisotropy.

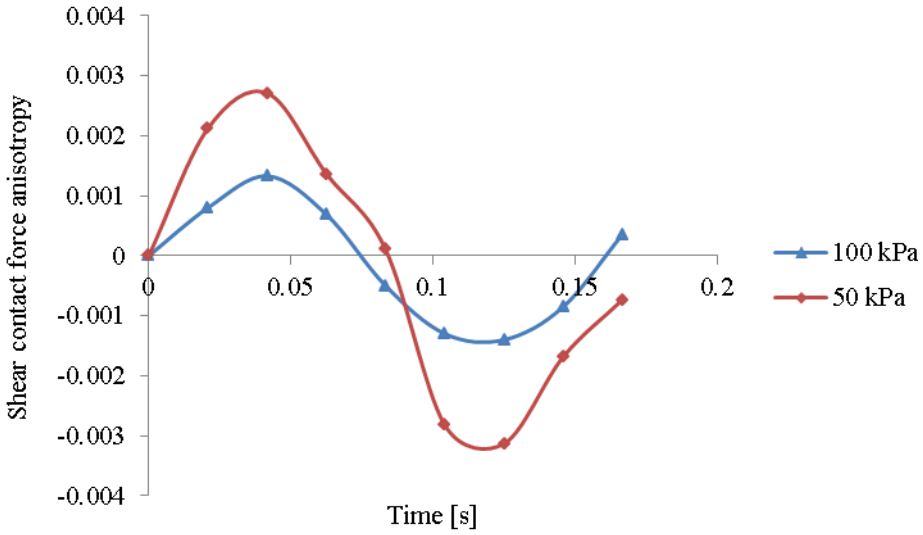

Figure 6-67 The variation of shear contact force anisotropy vs. time

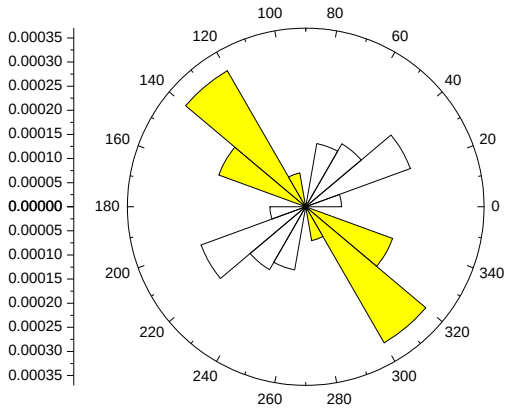

Shear contact force distribution at t = 0 [s]

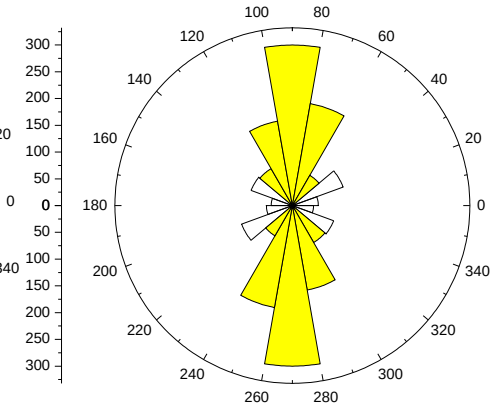

Shear contact force distribution at t = 0.25T [s]

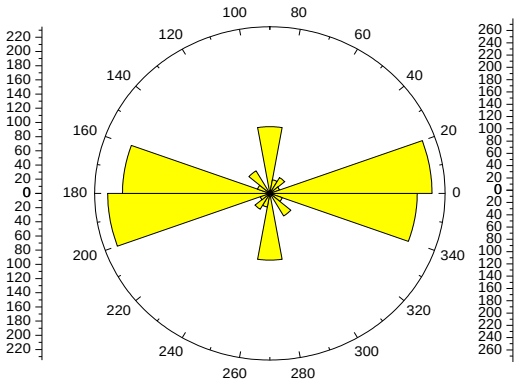

Shear contact force distribution at t = 0.5T [s]

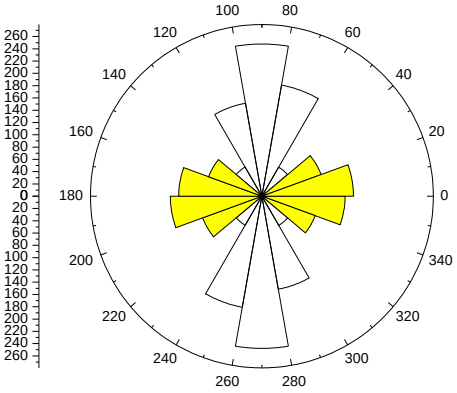

Shear contact force distribution at t = 0.75T [s]

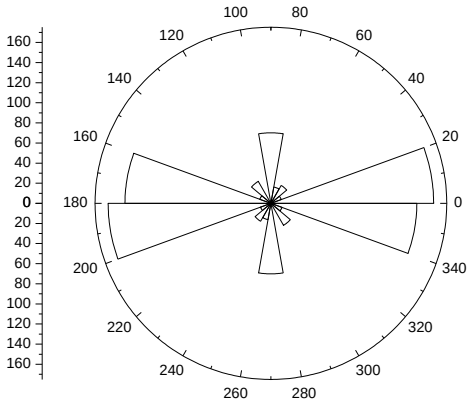

Shear contact force distribution at t = T [s]

Figure 6-68 Shear contact force distribution of 50 [kPa] vs. time

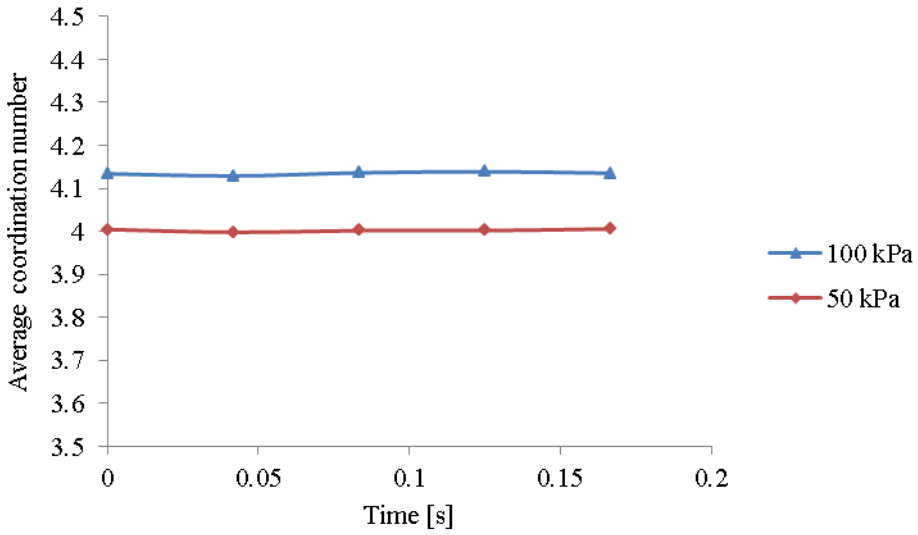

Figure 6-69 Average coordination number vs. time

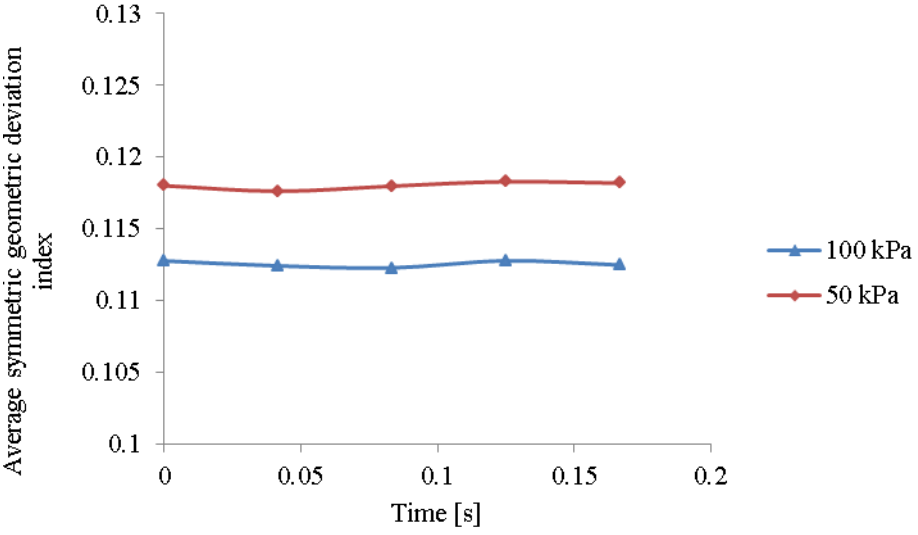

Figure 6-70 Average symmetric geometric deviation index vs. time

The bulk density remains constant during dynamic loading (figure 6-71).

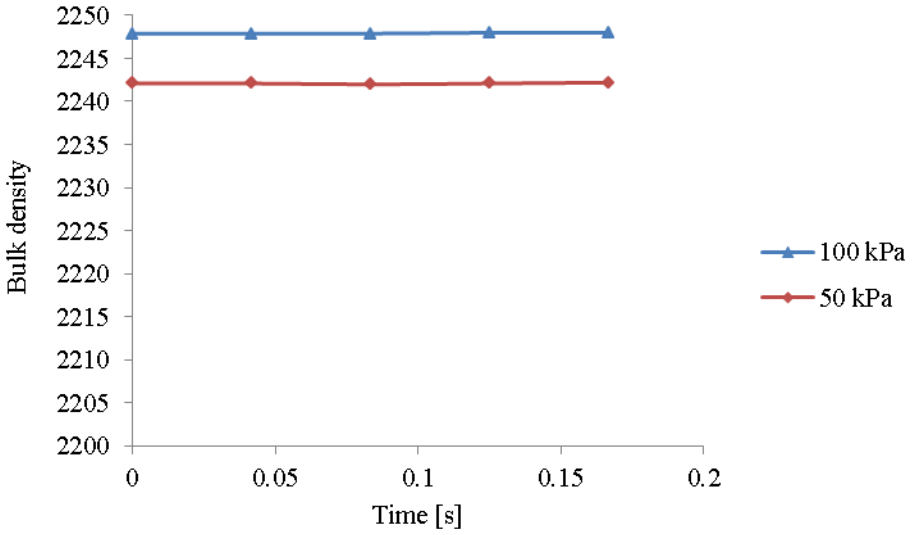

Figure 6-71 Bulk density vs. time

Figure 6-72 shows the variation of micro-shear stress with time. The maximum shear stress for a confining pressure of 100 [kPa] is nearly twice as large as the magnitude of maximum shear stress for a confining pressure of 50 [kPa], which corresponds to the $\frac{\bar{f}_{0\ 100\ [kPa]}^{c}}{\bar{f}_{0\ 50\ [kPa]}^{c}} = 2.0$. The trend of shear contact stresses are in good agreement with their counterpart shear contact force anisotropies. Thus, increasing the normal contact force and fabric anisotropies leads to increase the micro-shear stress.

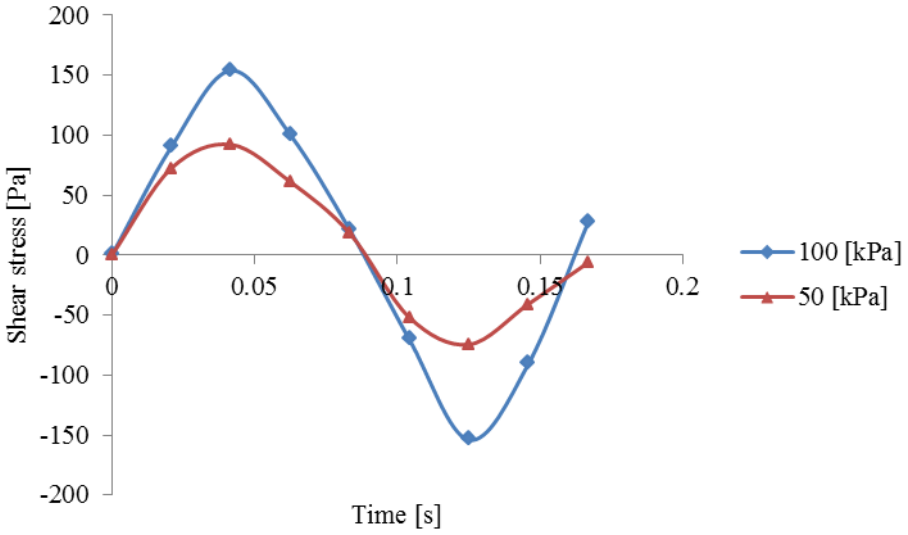

Figure 6-72 The variation of shear stress vs. time

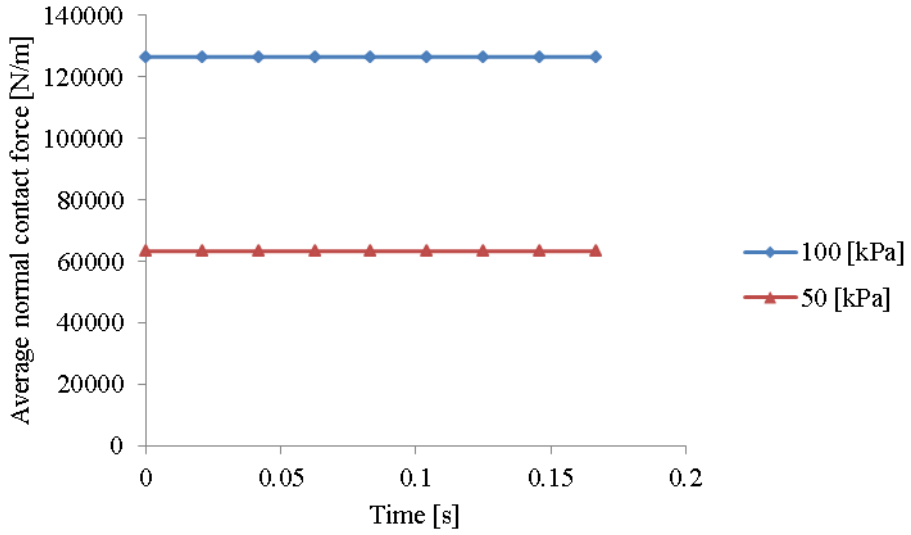

Figure 6-73 Average normal contact force ($\bar{f}_0^c$) vs. time

The variation of the principle stresses is displayed in figures 6-74 and 6-75, respectively. They show that for both confining pressures they remain constant.

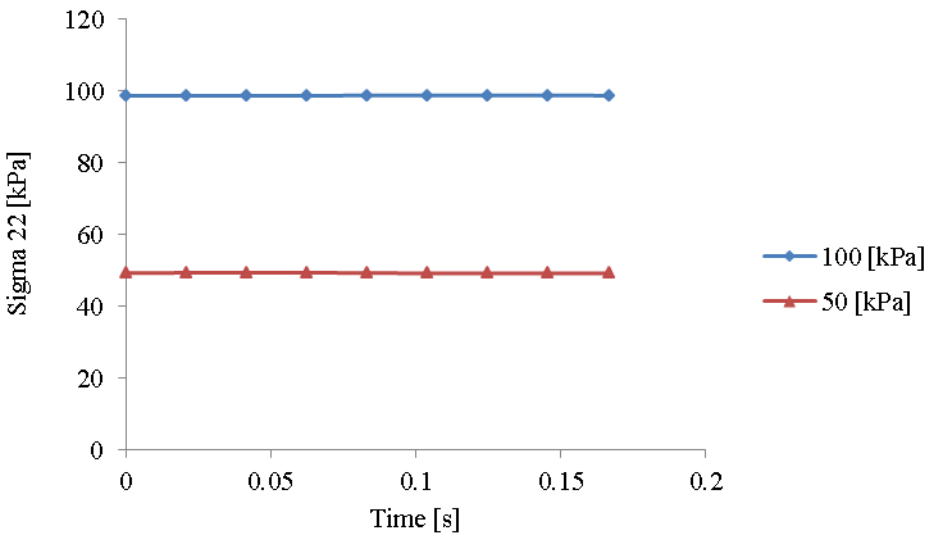

Figure 6-74 The variation of normal principle stress 22 vs. time

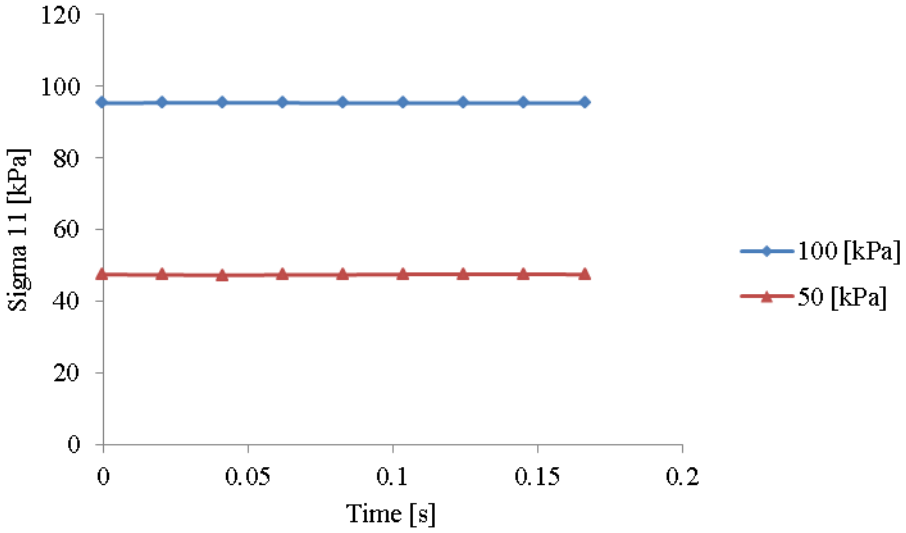

Figure 6-75 The variation of normal principle stress 11 vs. time

6.10 The sensitivity of sand fabric to the inter-particle coefficient friction

In this section, the influence of seismic loading on two DEM samples with two different inter-particle coefficient of friction was investigated. The initial conditions of these two models are shown in Table 6-9. It is known from

micro-mechanical point of view that an increase in the inter-particle coefficient friction leads to elevate the shear strength of the contact points (see Eq. 2.8) and consequently increasing the shear demand of particulate system. It is to be noted that inter-particle coefficient friction for sand is normally between 0.9 and 1.2.

Test No.	k_n [N/m] *10^7	k_s [N/m] *10^7	μ	c_n	c_s	n	Range of PSD [mm]	Amplitude [m/s]	Confining pressure [kPa]	f [Hz]
1	8.45	8.45	0.9	0.01	0.01	0.12	1.5-2	$1*10^{-3}$	100	6
2	8.45	8.45	1.2	0.01	0.01	0.12	1.5-2	$1*10^{-3}$	100	6

Table 6:9 The input properties used for sensitivity analysis of sand fabric to the different friction

As friction between particles helps to propagate the induced shear wave across the particulate media, changing this inter-particle property may have an influence on the phenomena of wave propagation. Eq. 2.8, shows that $((F^s_{totall})_t = (F^s_{totall})_{t-1} + (\Delta F_s)_t < \mu(F^n_{totall})_t)$, so at each time step the shear contact force (F^s_{totall}) can be compared with the Coulomb friction $(\mu(F^n_{totall})_t)$ by *PFC* compiler. Since the shear contact force in the case of a linear elastic contact model is only related to the shear contact stiffness and shear contact deformation, the only parameter can increase the magnitude of shear contact force is the shear contact deformation. As the evolution of normal contact anisotropy (see figure 6-76), normal contact force anisotropy (see figure 6-77) and shear contact force anisotropy (see figure 6-78) are similar during loading, it can be concluded that the shear contact forces developed for these two models during loading cannot exceed the sliding friction capacity. Thus, the contacts network during seismic excitation is similar is independent of the inter-particle friction which means the micro-mechanical stress tensors of the RVE are unaffected (see figures 6.79 to 6-81).

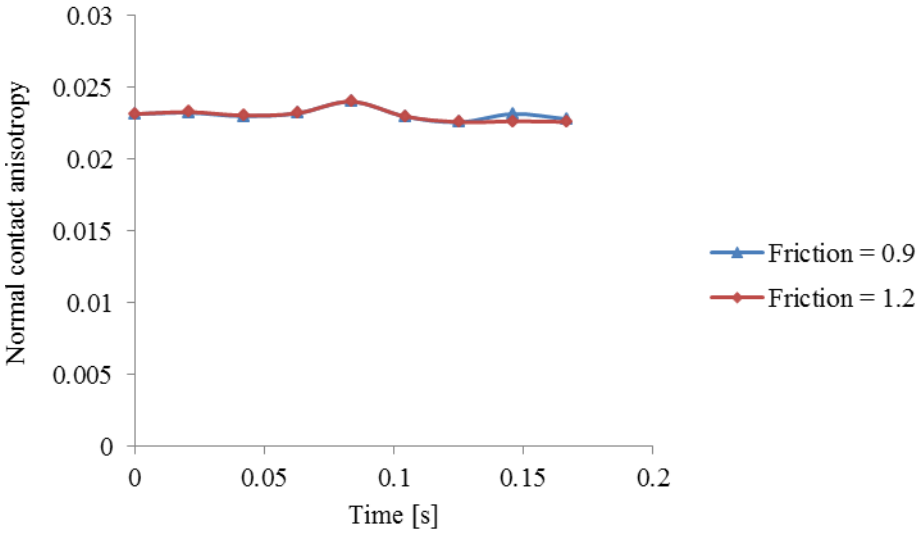

Figure 6-76 The variation of normal contact anisotropy vs. time

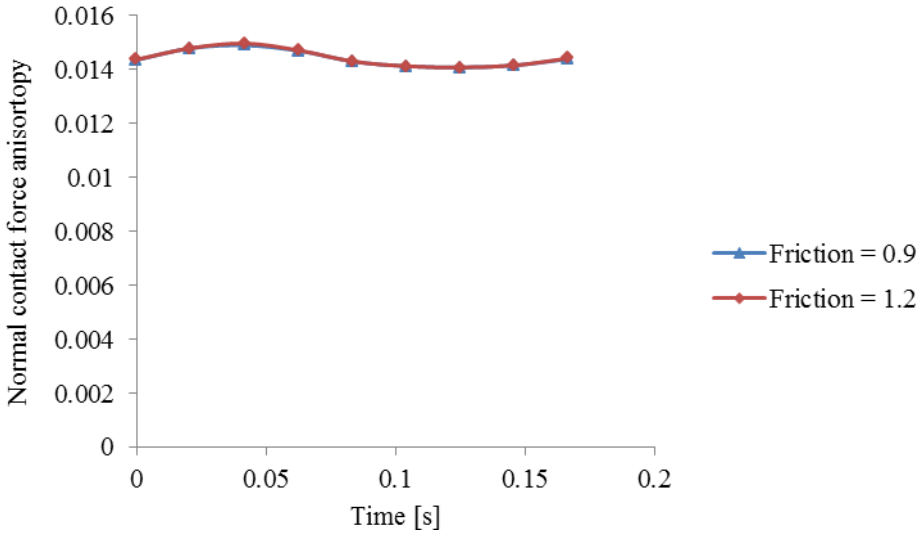

Figure 6-77 The variation of normal contact force anisotropy vs. time

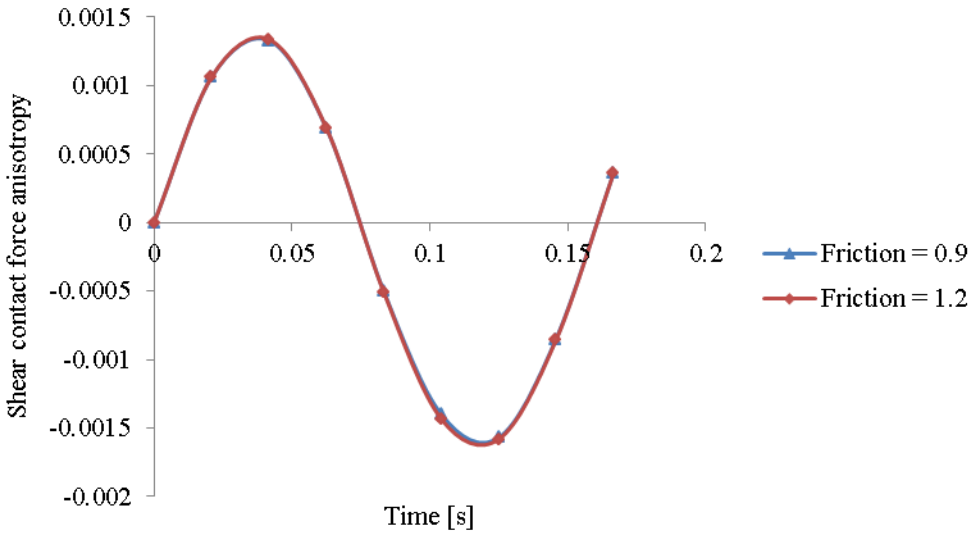

Figure 6-78 The variation of shear contact force anisotropy vs. time

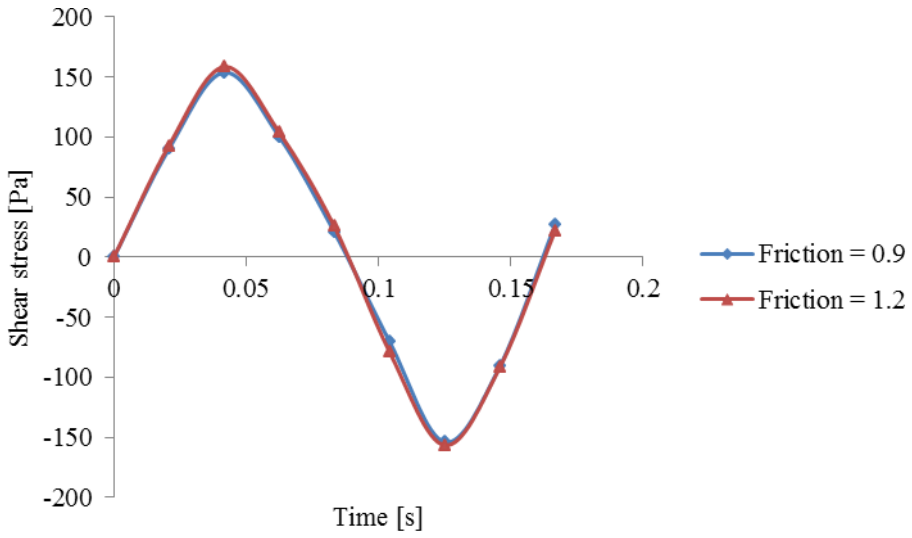

Figure 6-79 The variation of micro-mechanical shear stress vs. time

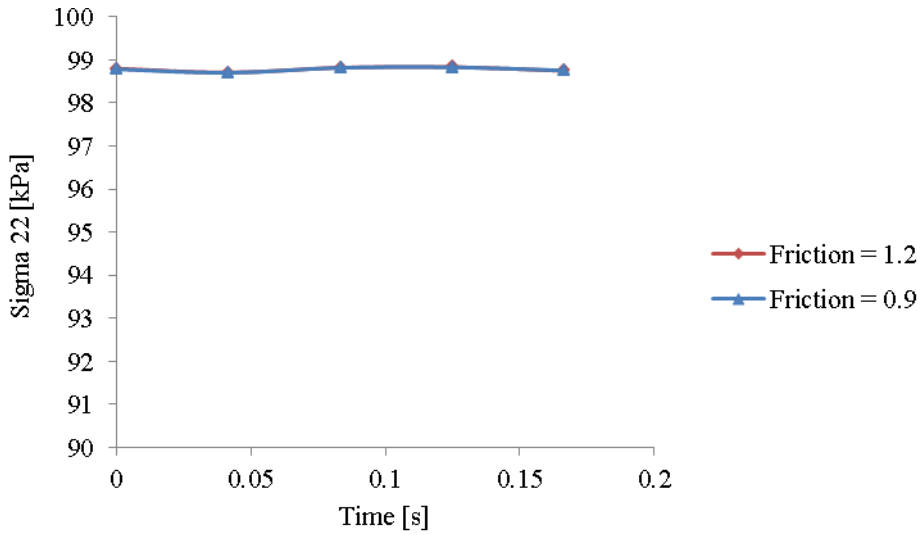

Figure 6-80 The variation of principle micro-mechanical normal stress 22 vs. time

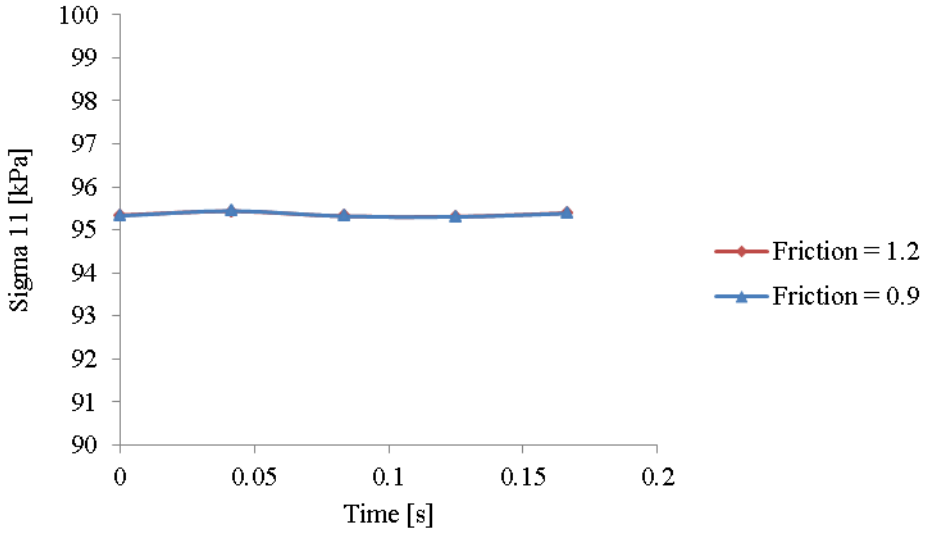

Figure 6-81 The variation of principle micro-mechanical normal stress 11 vs. time

6.11 The sensitivity of sand fabric to the normal particle stiffnesses

In this section, the influence of the inter particle stiffness on the behaviour of the system subject to seismic loading was investigated. The initial conditions of these two models are shown in Table 6-10.

Test No.	k_n [N/m] *10^7	k_s [N/m] *10^7	μ	c_n	c_s	n	Range of PSD [mm]	Amplitude [m/s]	Confining pressure [kPa]	f [Hz]
1	8.45	8.45	0.9	0.01	0.01	0.12	1.5-2	$1*10^{-3}$	100	6
2	100	100	0.9	0.01	0.01	0.12	1.5-2	$1*10^{-3}$	100	6

Table 6:10 The input properties used for sensitivity analysis of sand fabric to the different normal stiffness

Figure 6-82 shows that an increase in the normal contact stiffness leads to an increase in the normal contact anisotropy. This is because an increased stiffness increases the confinement of the particles; i.e. the particles are less able to move. In the case of the normal contact force anisotropy (figure 6-83) there is no difference during the static loading but there are differences during the dynamic loading with the system with higher inter particle stiffness responding more.

Figure 6-84 shows the trend of shear contact force anisotropy during loading. It is seen that for the same imposed dynamic load, the particulate system having lower normal stiffness has larger shear contact anisotropy.

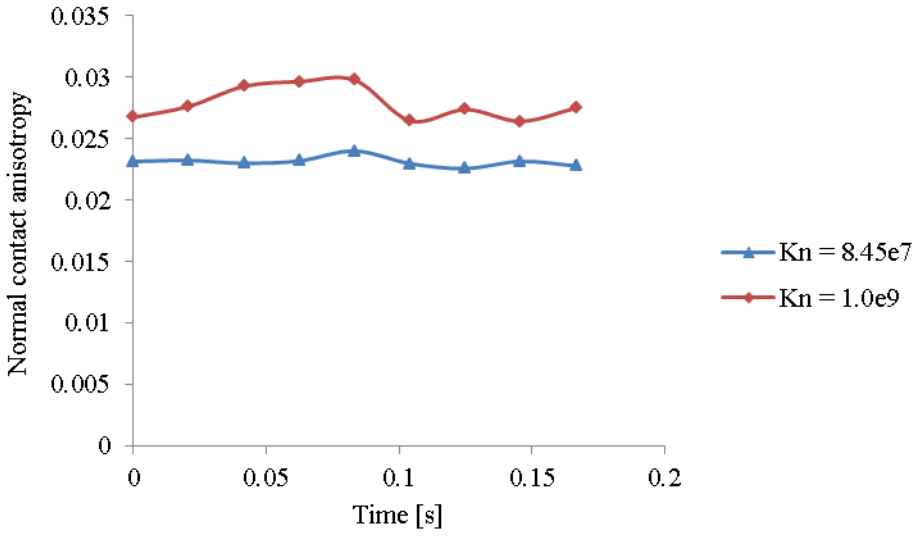

Figure 6-82 The variation of normal contact anisotropy vs. time

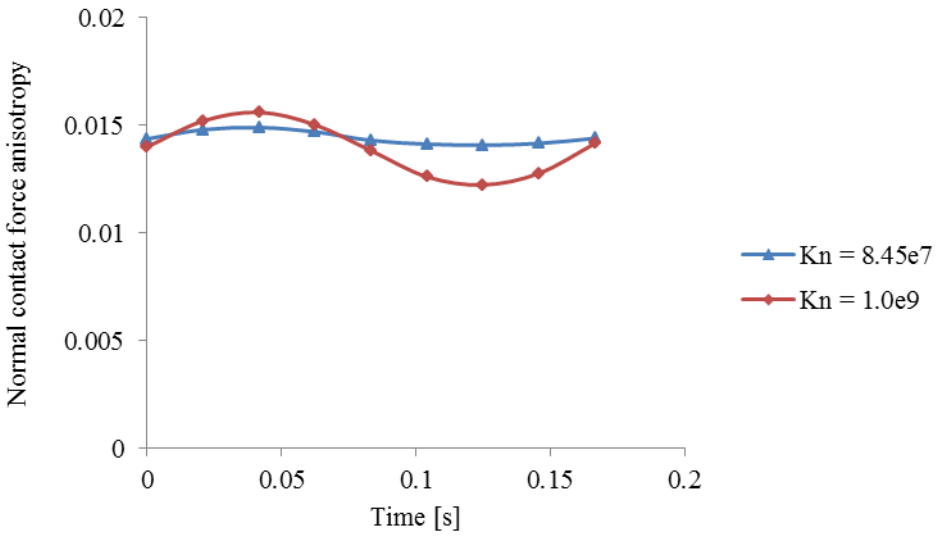

Figure 6-83 The variation of normal contact force anisotropy vs. time

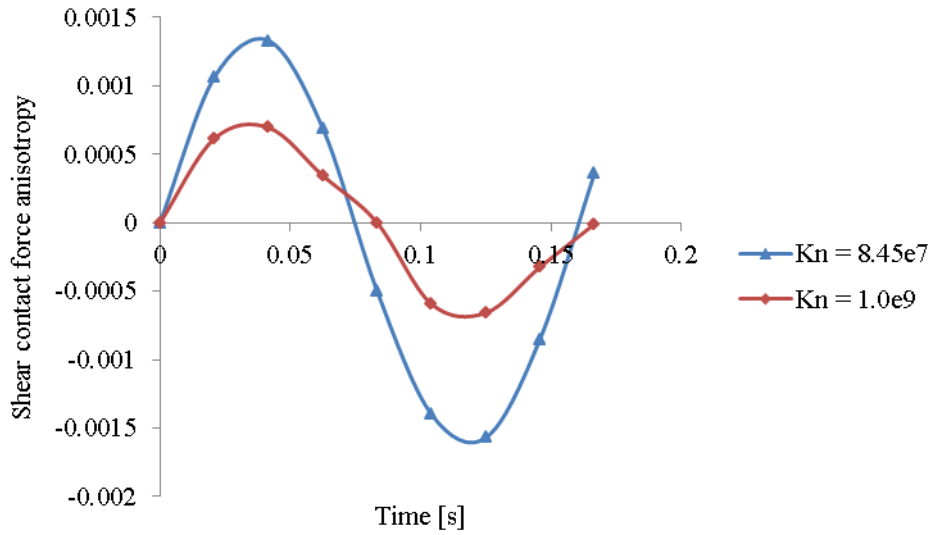

Figure 6-84 The variation of shear contact force anisotropy vs. time

Figure 6-85 shows the variation in micro-mechanical shear stress with time. It was seen that the peak shear stress at 0.25T is greater than that for 0.75T. This figure also shows that increase in normal contact stiffness leads to a_n increase in the micro-mechanical shear stress of the RVE.

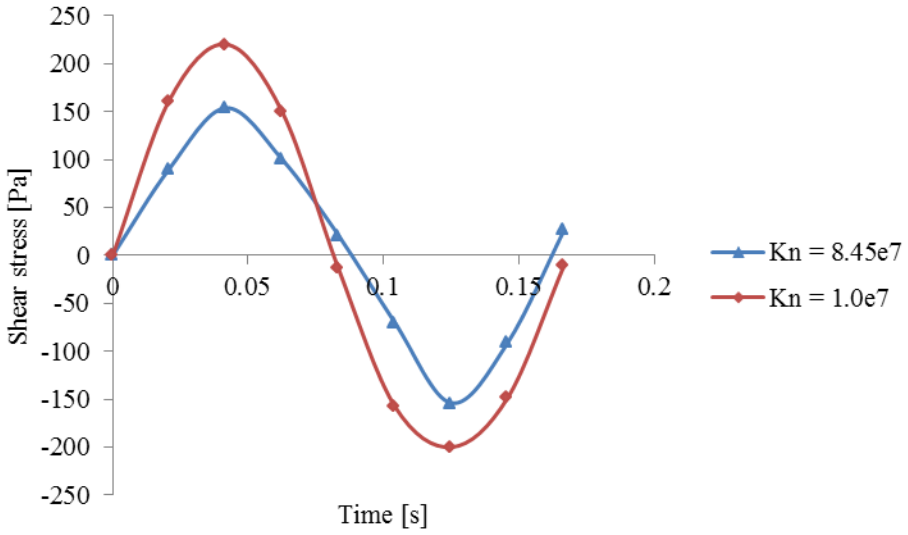

Figure 6-85 Micro-mechanical shear stress vs. time

The variations in principle stresses are shown in figures 6-86 and 6-87. As seen their trends more follows the trend of normal contact anisotropy (figure 6-82).

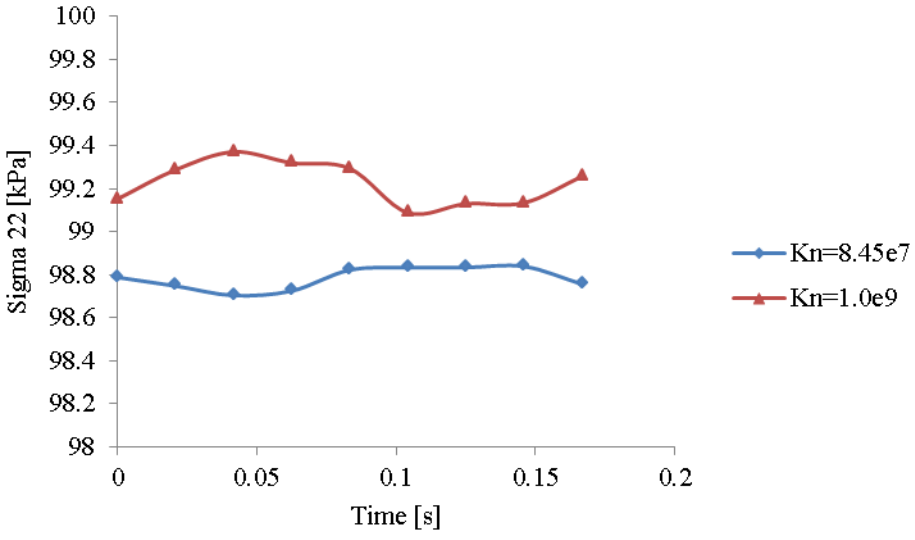

Figure 6-86 Micro-mechanical normal principle stress 22 vs. time

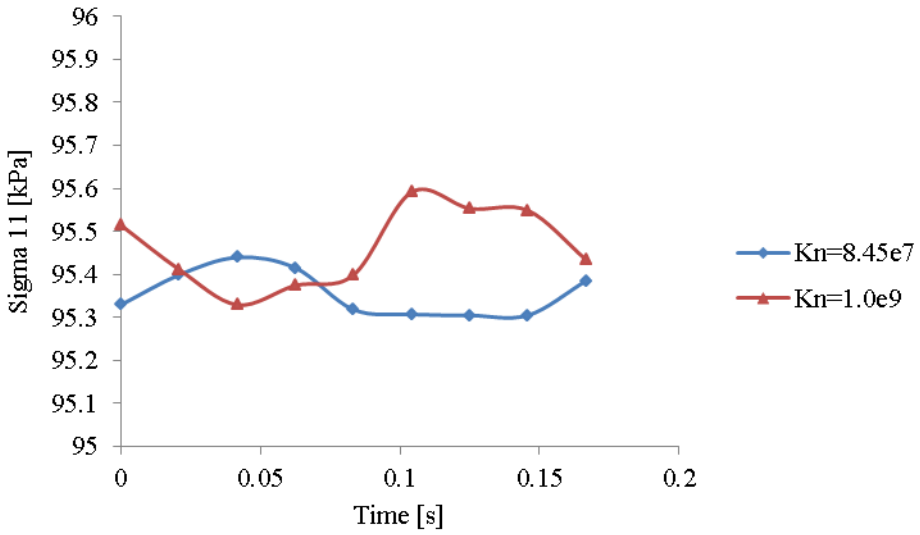

Figure 6-87 Micro-mechanical normal principle stress 11 vs. time

6.12 The sensitivity of sand fabric in the present of rigid pile element during earthquake

As mention the pile foundation at seismic hazardous regions has been damaged by earthquakes due to the effect of seismic soil-pile interaction on the fabric of soil-pile system and the development of sand particles' instability adjacent to the pile during earthquake. To understand the seismic soil-pile interaction, a DEM model was developed to simulate section of an inflexible pile-soil system subjected to cyclic shear load. As seen above the macro-mechanical behaviour of granular system is directly related to its fabric quantities. Thus, by investigating the macro-mechanical stress tensor obtained from the its fabric in the presence of a pile element and then comparing these variables to those obtained without the pile, the effect of seismic soil-pile interaction on the fabric and macro-mechanical behaviour of RVE will be clearer.

In this section, the effect of pile foundation on the fabric evolution including fabric anisotropies of the system and consequently the evolution of micro-mechanical shear stress during single shear sine load is investigated. The graphical normal and shear contact force distributions and the shear wave propagation with and without a pile element is also considered to gain an insight into the phenomena of wave propagation with and without a pile.

Similar boundary conditions were applied for wave propagation as discussed in previous sections (see figure 6-88). The pile foundation is assumed to be inflexible. The scale of the model is shown in figure 6-89. Table 6-11 displays the input properties used for this simulation. Note that the normal and shear contact stiffnesses and pile coefficient friction are assumed to be similar to those of the soil particles. The input motion is the same as shown in figure 6-20. Only one DEM simulation was performed for this problem.

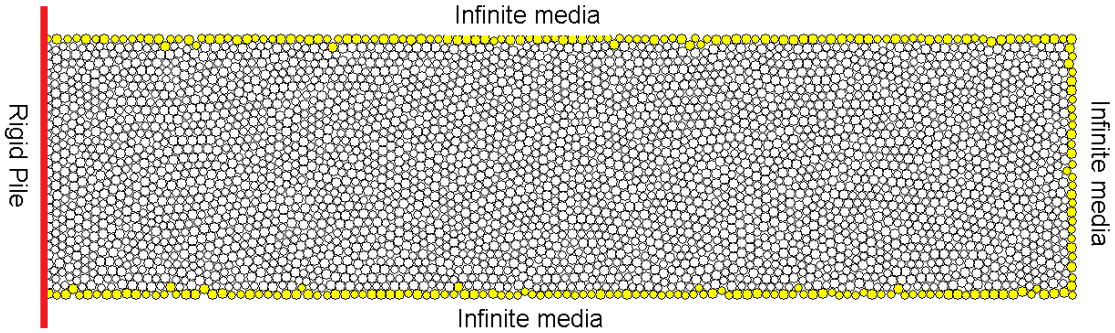

Figure 6-88 The soil-pile system

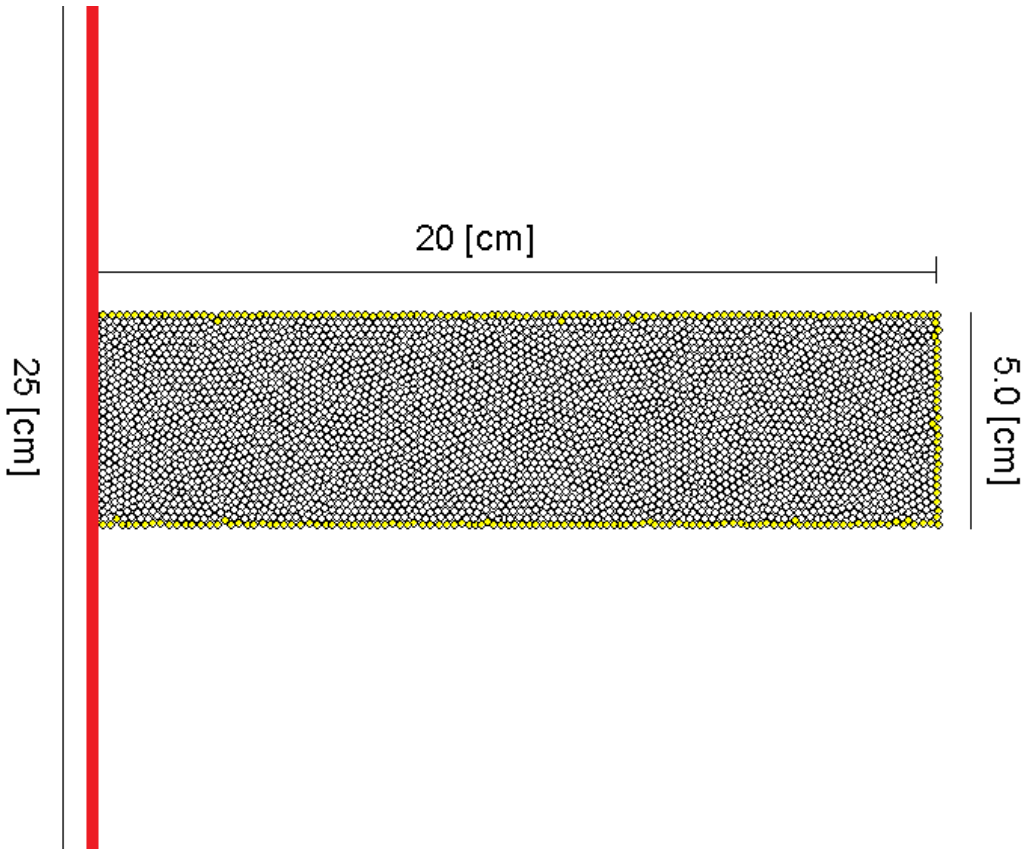

Figure 6-89 The scale of the soil-pile system

k_n [N/m] *10^7	k_s [N/m] *10^7	μ	c_n	c_s	n	Range of PSD [mm]	Amplitude [m/s]	Confining pressure [kPa]	f [Hz]
8.45	8.45	0.9	0.01	0.01	0.12	1.5-2	0.1	100	6

Table 6:11 The input properties used for sensitivity analysis of sand fabric to the different normal stiffness

After generation of particles, their radiuses were expanded so that the system achieved an initial porosity of 0.12. Four rigid walls were then moved to apply the confining pressure (100 [kPa]). Next, three walls were removed and replaced with deformable boundary particles. The left rigid wall (red boundary in figure 6-88) is considered as a pile element. Extra cycles were then performed to bring the system to equilibrium. The servo-mechanism, mentioned in section 4.3.5.1, was applied to maintain the confining stress at 100 [kPa] on the pile element. In the next stage, the external shear single sine load was applied. The fabric anisotropies evolution and macro-mechanical stress tensor were recorded at five times: t = 0 [s], t = 0.25T [s], t = 0.5T [s], t = 0.75T [s] and t = T [s].

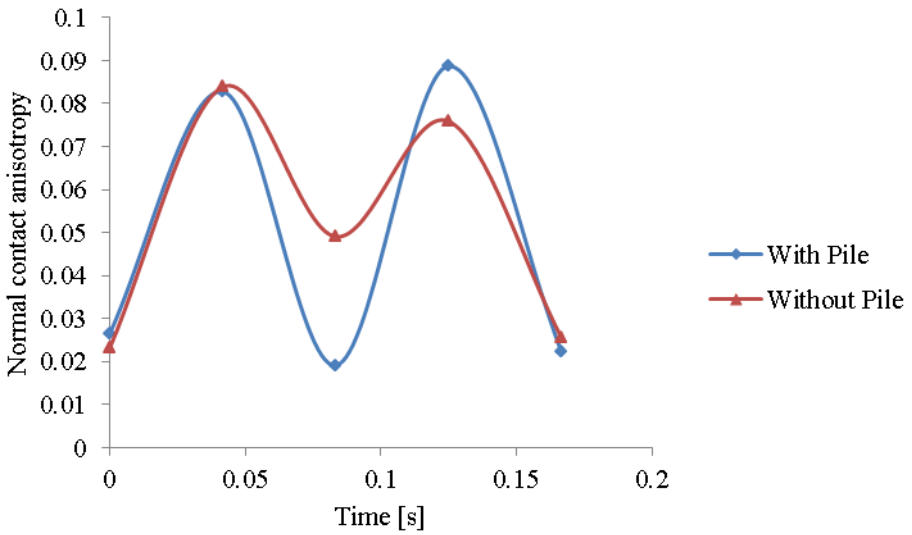

Figure 6-90 Normal contact anisotropy against time

Figure 6-90 shows the evolution of normal contact anisotropy during earthquake. It is seen from 0T [s] to 0.25T [s] (T is the period of load) the trend of normal contact anisotropy in the case of presence of pile and without pile are similar. This is also seen for normal contact force anisotropies in figure 6-91. From 0.25T [s] to 0.5T [s] the change in normal contact anisotropy with the pile is significantly more than that without the pile. Normal contact force anisotropies with and without pile in this period also reduces but the reduction in the case of no pile is slightly bigger than that with pile (see figure 6-91). When the seismic load is reversed, a re-arrangement of contacts took place so that the slope of normal contact anisotropies in the case of with pile is deeper than that for no pile. It is seen that peak of normal contact and normal contact force anisotropies at 0.75T [s] in the case of pile is larger than that at 0.25T [s]. This leads to the conclusion that the effect of inflexible pile increases the normal contact and normal contact force anisotropies.

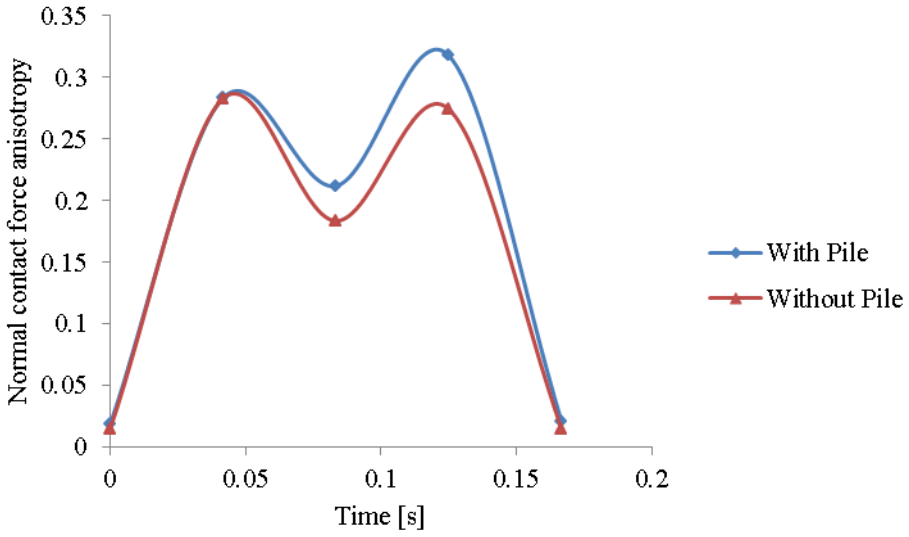

Figure 6-91 Normal contact force anisotropy against time

Figure 6-92 shows the evolution of shear contact force anisotropy during the periodic loading. It is seen that the effect of inflexible pile element leads to an increase of the shear contact force anisotropy during the periodic loading.

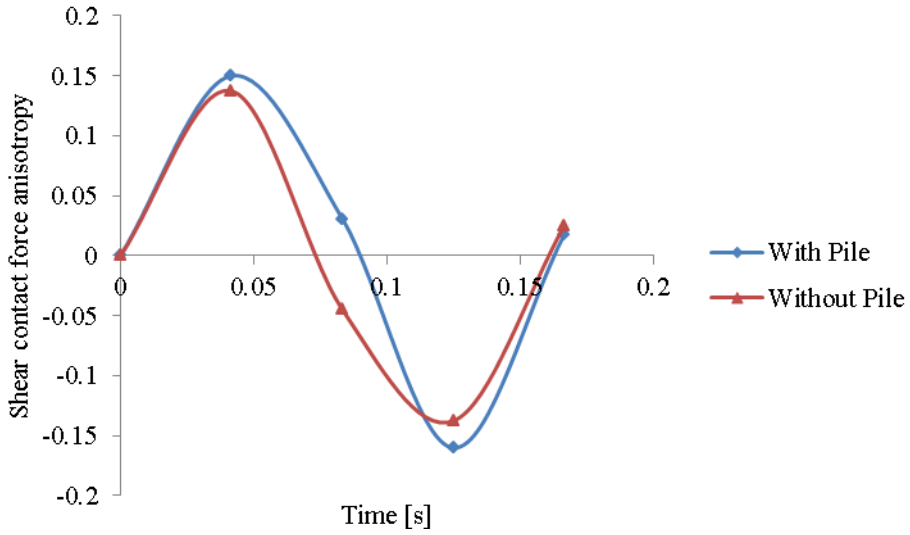

Figure 6-92 Shear contact force anisotropy against time

Figure 6-93 shows the variation of average coordination number during seismic loading. It seen from this figure that the presence of an inflexible pile has a positive effect on the average coordination number as it is the same as that for the static state. This fact is also shown in figure 6-94 where the stability of particles increases with rigid pile. Indeed, the presence of a_n inflexible pile element acts as obstacle. That is, the movements of particles are influenced by the pile, while deformable boundary particles allow the particulate system to move more freely.

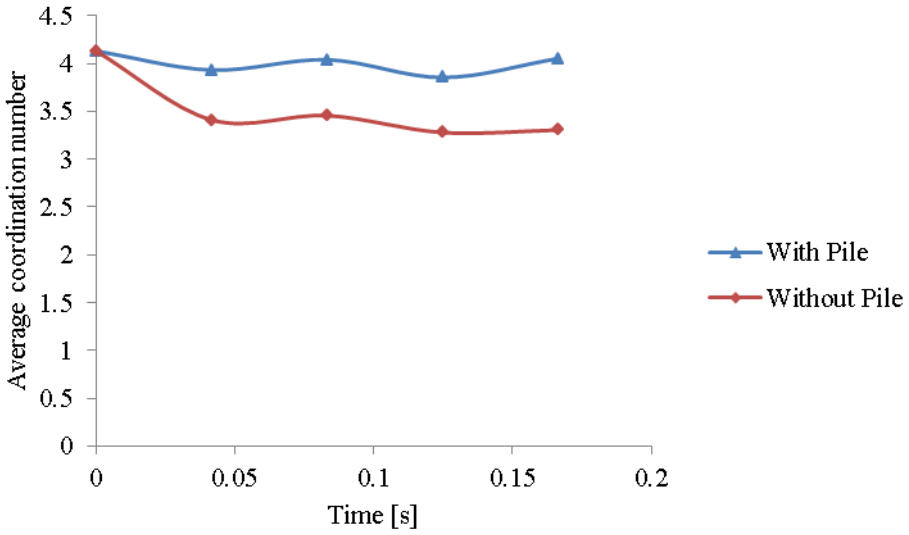

Figure 6-93 Average coordination number against time

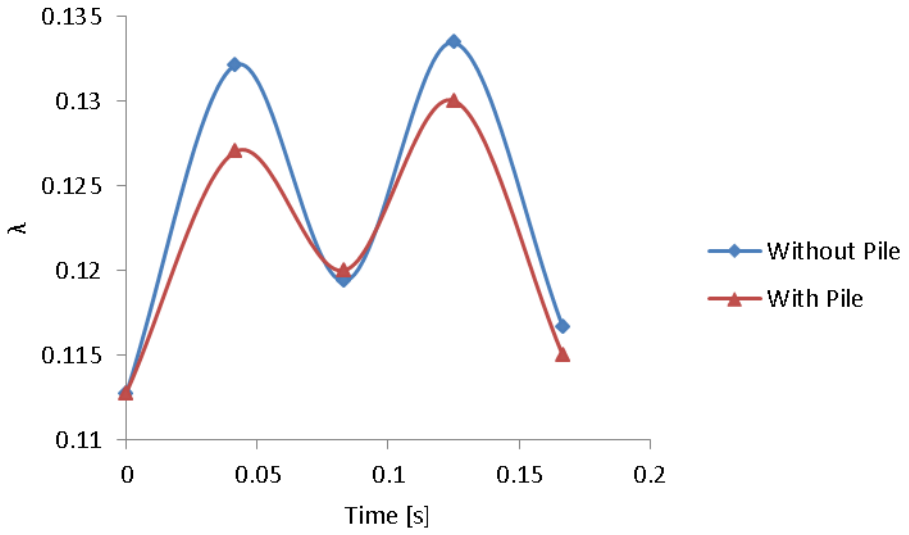

Figure 6-94 Average symmetric geometric deviation index against time

As the presence of rigid pile causes to increase the stability of its adjacent sand particles, the shear stress capacity of soil-pile system increases. Figure 6-95 clearly shows that the effect of inflexible pile leads to an increase in the shear capacity.

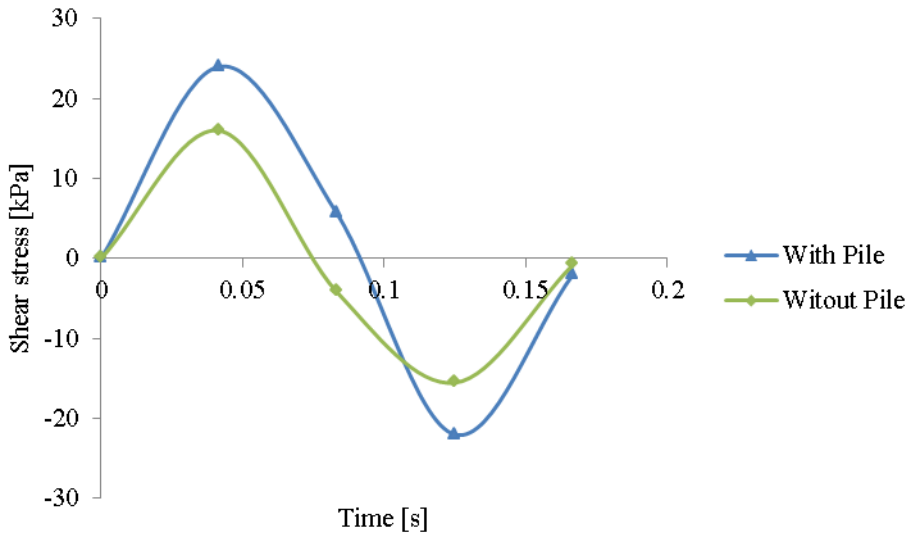

Figure 6-95 Shear stress vs. time

The arrangements of normal and shear chain forces with and without a pile at the five increments during are the periodic loading is shown in figures 5-96 and 5-97. The particles velocities during seismic shear wave propagation with and without pile are also shown in figure 5-97. Tracking the figures shows that the presence of a pile leads to an expansion of the system. Comparing figures 5-96 (a) and 5-96 (b) shows that the density of normal contact forces in the case of pile is more than that in the case of no pile. It also seen that the normal chains force at t = 0T and at t =T [s] are similar for two cases. Note, the thickness of normal and shear contact forces is proportional to their magnitude.

Comparing the figures 5-97 (a) and 5-97 (b) shows that the presence of the inflexible pile has a significant effect on the density and distributions of shear contact forces at t = 0T. Afterwards, the increase in the magnitude of shear chains force in the case of pile is more than that for no pile. It was seen that

the shear contact forces at the circumference of the sample were more than the rest of sample. It is because the load including static and dynamic loads.

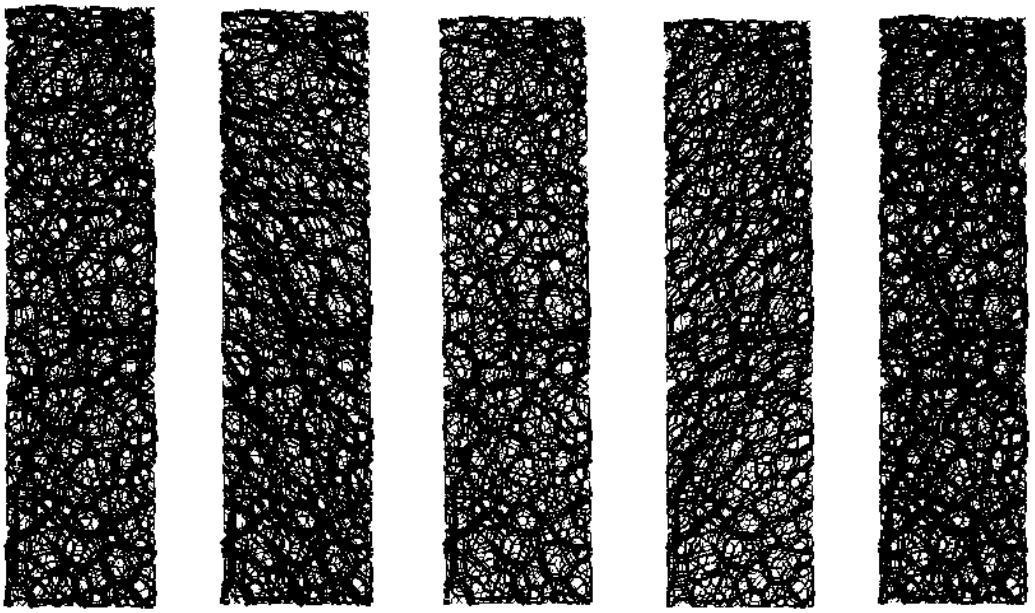

At t = 0 [s] At t = 0.25T [s] At t = 0.5T [s] At t = 0.75T [s] At t = T [s]

(a) Normal contact forces without pile

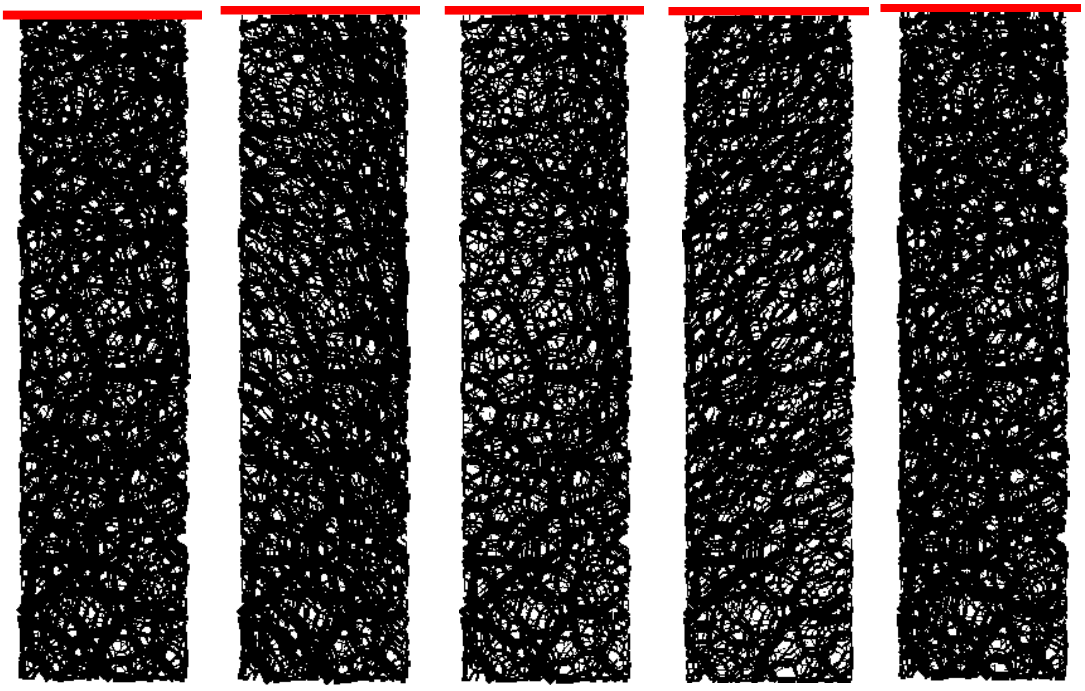

At t = 0 [s] At t = 0.25T [s] At t = 0.5T [s] At t = 0.75T [s] At t = T [s]

(b) Normal contact forces with pile

Figure 6-96 The arrangement of normal chains forces with and without pile at five times during earthquake: (a) without pile (b) with pile

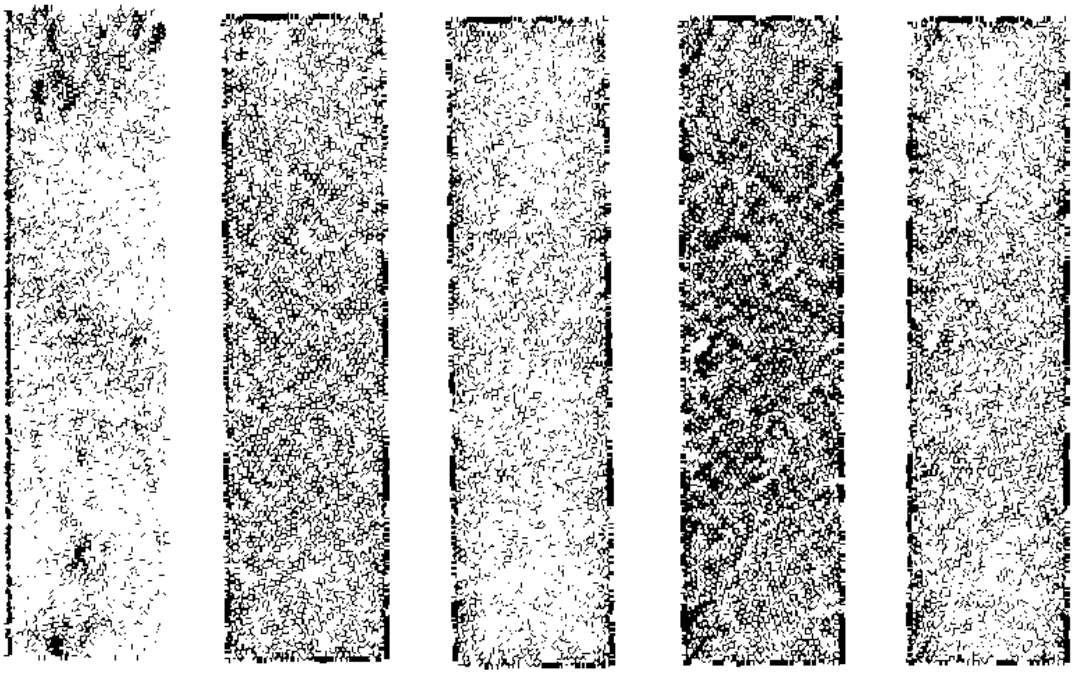

At t = 0 [s] At t = 0.25T [s] At t = 0.5T [s] At t = 0.75T [s] At t = T [s]

(a) Shear contact forces without pile

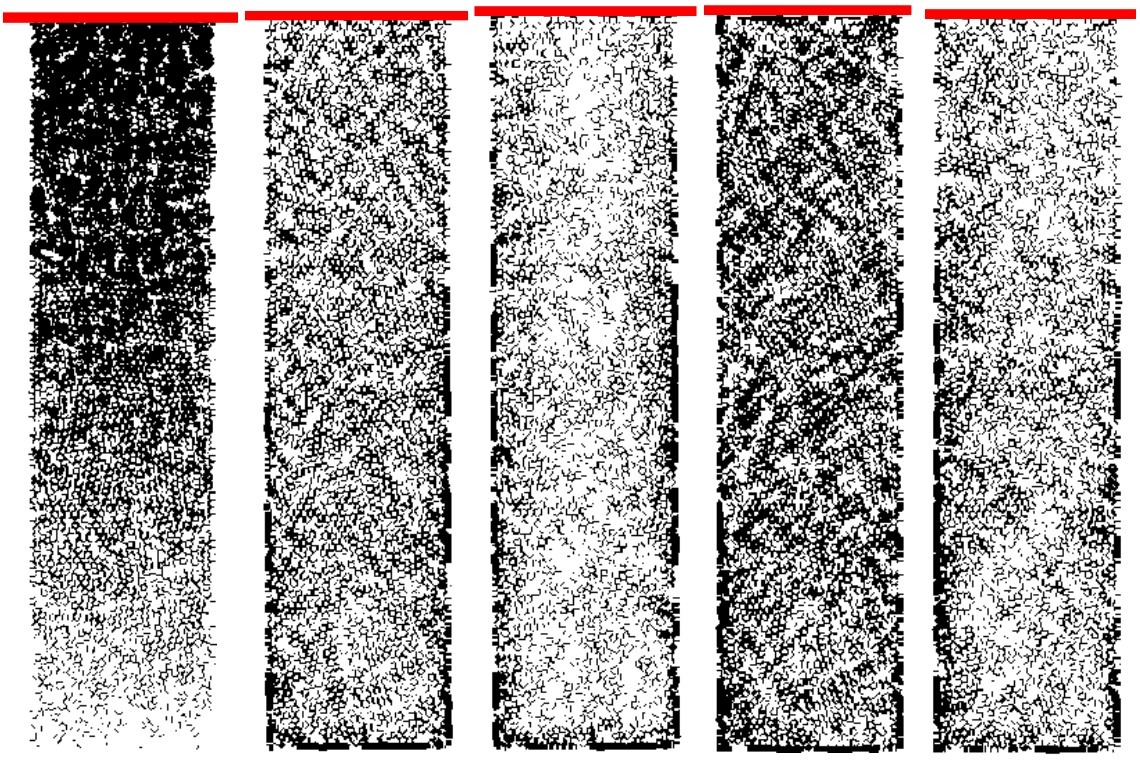

At t = 0 [s] At t = 0.25T [s] At t = 0.5T [s] At t = 0.75T [s] At t = T [s]

(b) Shear contact forces with pile

Figure 6-97 The arrangement of shear chains forces with and without a pile at five times during earthquake: (a) without pile (b) with pile

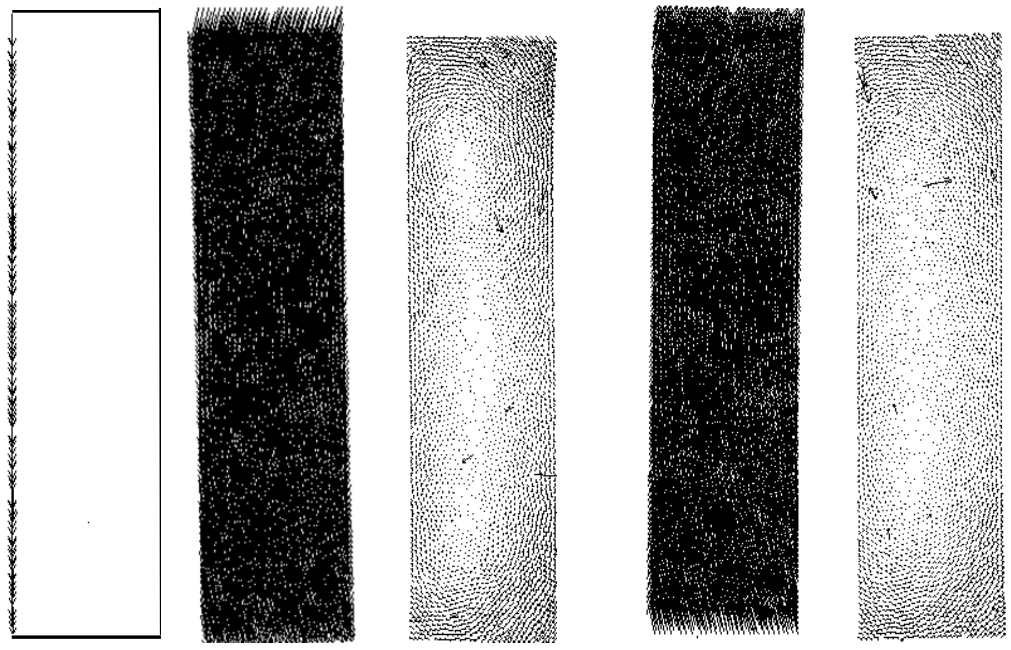

(a) Shear wave propagation without pile

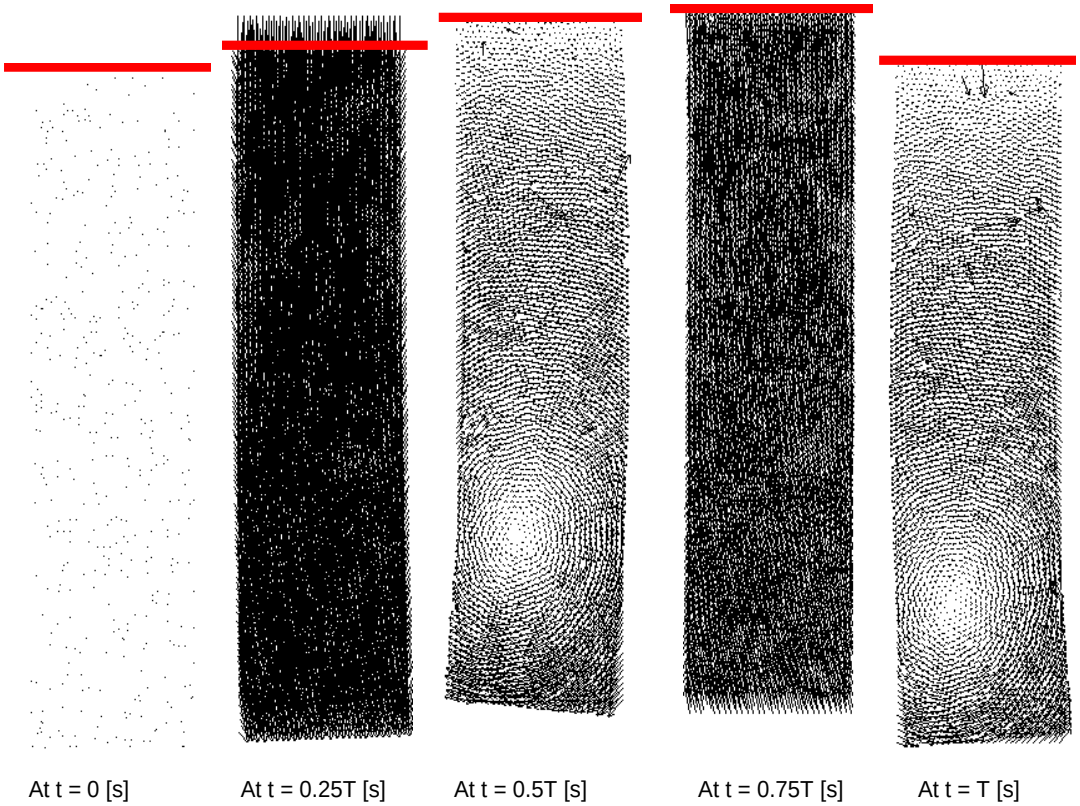

(b) Shear wave propagation with pile

Figure 6-98 Particle velocities during seismic shear wave propagation with and without pile: (a) no pile (b) with pile

The following issues can be derived from snapshots of particles velocities for these two cases.

- The trends of particles velocities at 0.25T were similar for the two cases. However, the velocity of those particles in contact with the pile is horizontal while the velocities of left boundary particles are oblique. It is because the pile is rigid and cannot rotate. A rotation in those particles velocities near the right deformable boundary can be seen.
- At t = 0.5T where the magnitude of external load is zero, a vortex-like motion was taking place adjacent to the right boundary in the case of pile. In addition, the velocities of those particles adjacent to the pile are lower in comparison to the rest of sample. Moreover, a rotation for those particles adjacent to the right boundary was seen, while this was not seen in the case of no pile.
- At t = 0.75T where the external load reverses, the conditions are similar for the two cases but a rotation in the left boundary particles (in the case of no pile) can be seen.
- At t = T where the earthquake was terminated, a vortex-like motion was taking place adjacent to the right boundary in the case of a pile. In addition, the velocities of those particles adjacent to the pile are lower in comparison to the rest of sample. Moreover, a rotation for those particles adjacent to the right boundary was seen, while this was not seen in the case of no pile.

6.13 Conclusion

As boundary forces are transmitted through the contact networks in granular material, a change in these networks has a profound influence on its macro-mechanical behaviour. The ability of DEM to model dynamic problems such as earthquakes has not been proved well (Marketos and O'Sullivan, 2013). The fabric quantities applied for static problems describe how well changes at micro-scale take place at each time step during loading. Thus, following the fabric evolution increases our insight into the micro-macro-scale behaviour of granular sand during earthquake. The main aims of this chapter were to investigate the fabric evolution and consequently the micro-fabric-

stress of idealized two-dimensional sand using DEM and understand how DEM is able to study the seismic behaviour of granular sand. The effect of pile element on the fabric evolution of sand adjusted to the pile was also investigated. For this purpose, a new algorithm of dynamic deformable boundary particles with nearly 1300 lines was proposed to simulate the seismic wave propagation problems including seismic soil-pile system. The accuracy of the shear wave velocity obtained from this approach to compute $G_{\max}$ has only 4.9% error in comparison with $G_{\max}$ obtained from biaxial test simulation in chapter 5.

The influence of rigid boundaries on the phenomena of wave propagation was also investigated. It was seen that applying rigid boundaries amplifies the seismic waves while dynamic deformable boundary particles absorbs the wave when waves travels upward. The effect of various sample ratios on the horizontal and vertical particle velocities and kinetic energy of each particle subjected to a similar single period sine load was also studied. It was seen that increasing the sample ratio results in a decrease in the effect of side boundaries. Moreover, applying this periodic shear load develops vertical particle motion. It was shown that applying a sample ratio=1 produces unrealistic micro-macro stress tensors while the micro-macro stresses tensors obtained from sample ratio = 4 were more reasonable.

It was also seen that the trend of stress tensor is greatly dependent on the combination of fabric anisotropies such that a change in this combination alters the trend of macro-mechanical stress tensors. Tracking the fabric anisotropies of these two samples also shows that plastic deformation is developed during an earthquake is mainly based on the evolution of shear contact force distribution. The effects of six common earthquake frequencies on the fabric evolution and micro-mechanical stress tensors were studied. It was seen that increasing the frequency leads to a slight decrease in the normal contact and normal contact force distributions as the shear contact force anisotropy increases. However, the macro-mechanical stress tensor is similar for these six cases. Tracking the fabric anisotropies of these six samples also shows that the plastic deformation is mainly due to the evolution of the shear contact force distribution during an earthquake.

The effect of various earthquake amplitudes on the fabric evolution and micro-mechanical stress tensors was investigated. In contrast to frequency effects, increasing the amplitude leads to a considerable change in fabric anisotropies. It was also found that a relationship can be established between plastic deformation of idealized sand and their fabric anisotropies. It is also seen that the periodic change in the fabric of a RVE produces a periodic micro-mechanical stress tensor. Moreover, it was found that there is a reasonable link between fabric anisotropy and rate of loading.

The effect of various confining pressures on the fabric evolution and micro-fabric stress tensors was investigated. It was seen that a change in confining pressure has a profound influence on the fabric evolution and micro-mechanical behaviour. The effect of various inter-particle coefficient frictions on the fabric evolution and micro-fabric stress tensors was also investigated. It was seen when the amplitude of load is small increasing this parameter between 0.9 and 1.2 does not influence the fabric evolution and micro-mechanical behaviour. The effect of various contact stiffnesses on the fabric evolution and micro-fabric stress tensors was also investigated.

The presence of a rigid pile element on the fabric evolution of sand during seismic loading was investigated. It was seen that the presence of a pile element increases the fabric anisotropies and average normal contact forces. It is also seen that the average coordination number in the presence of a pile fluctuates around that in a static state. Moreover, the shear capacity of dense sand is significantly increased in the presence of rigid pile during seismic load. Tracking the chains force showed that the shear contact forces at the circumference of the samples were more than the rest of samples. A vortex-like motion takes place adjacent to the opposite boundary to the pile boundary; this does not happen when there is no pile.

Chapter 7

7 Conclusions and Recommendations

7.1 Introduction

Piled foundations in seismic hazardous regions are damaged by earthquakes because of the effect of seismic loads on the soil-pile interaction and the development of sand particles' instability adjacent to the pile. Therefore, in order to understand how a seismic load affects the capacity of a pile it is necessary to study the changes in that interaction which is affected by the volume changes in the soil. The pile capacity is formed of the interface friction and end bearing capacity. This research focused on the interface friction because the visual evidence suggests that a seismic load has a dramatic effect on the volume of the soil adjacent to a pile. Since the pile capacity is a function of the interaction between individual soil particles and the pile, the discrete element method of analysis was considered to be the most appropriate method. Thus a DEM model of an element of soil adjacent to a pile was created and that model was subjected to cyclic shear load. This meant developing appropriate boundary conditions that allowed not only shear to be applied but also a viscous boundary to absorb the reflecting energy. This had to be carried out in stages. The first stage was to determine the characteristic inter particle properties of the particles using a sensitivity analysis to investigate the impact the properties had upon the mass behaviour. Mass behaviour was used as the outcome as it provided a link to experimental behaviour, which provides the macro mechanical properties. The second stage was to create an appropriate stress controlled boundary which allowed the soil model to deform in a similar manner to experimental studies of soil behaviour. The third stage was to subject the soil model to a cyclic shear load to represent a seismic load. Finally a study of an element of soil adjacent to a pile was studied under that same cyclic shear load. This chapter summarises the main conclusions of this thesis and provides recommendations for further works in this field.

7.2 The conclusions

7.2.1 The analysis of granular sand media

An axially loaded pile can be considered to be an axisymmetric problem which means it is possible to consider a 2D analysis of an element of soil adjacent to a pile. However, when a shear load is applied this is no longer the case. Ideally 3D analysis would be undertaken. DEM assumes unbreakable disk or spherical particles but sand particles are neither disks nor spheres and can break. However, it is possible to create DEM particles to represent that type of behaviour by agglomeration of disks and spheres. There are two methods to validate a DEM analysis; adjusting the inter particle properties to fit the macro response to experimental data and varying the inter-particle properties to determine the relationship between the inter particle properties and the macro properties and comparing those macro properties with published data.

The literature review highlighted the fact that there were very few DEM studies into seismic behaviour of soils and none addressing soils adjacent to piles. The literature review did highlight the need to generate appropriate boundary conditions if realistic results were to be generated. Since the focus of this research was to study the use of DEM to analyse seismic loading which meant selecting the most appropriate inter particle properties, a sensitivity analysis was considered most appropriate. Curve fitting would only be relevant to a particular test and a number of combinations of inter-particle properties would produce that fit. In order to produce the macro properties of the element it was necessary to use a homogenisation method. Given that macro properties are normally determined from triaxial tests this meant it was necessary to create a deformable vertical boundary and rigid horizontal boundaries to replicate the test conditions. The range of inter particle properties were selected from published data.

2D DEM analysis was studied. This was acceptable for the axisymmetric case under static loading. In the case of seismic loading it was assumed that the element was in line with the direction of loading so a 2D analysis was considered acceptable. The main limitation of a DEM model is that the

simulation is limited by the speed of the computer. This limits the number of particles that can be analysed and the number of agglomerated particles that can be created. It was necessary to balance the number of particles with the speed of the analysis and ensure that the outcome was acceptable. Given that the focus of the research was on the seismic response in which volume changes are associated with changes in direction of applied load rather than the value of the applied load, it was considered acceptable to study the behaviour of a randomly generated assembly of disks. The strains in the soils should not generate sufficient load to crush or break the particles.

7.2.2 The development of the DEM model for static loads

Recent developments in computational technology have allowed the simulation of sand as a heterogeneous material using DEM. *PFC*^{2D} has been shown to be a powerful numerical program for modelling soil, thus, it was chosen as the DEM programming code for this research. A number of user-defined functions had to be developed including algorithms for homogenisation, a flexible continuous boundary, a dynamic boundary and the application of a seismic cyclic load. *PFC*^{2D} included an in built scripting language, FISH, which allowed these functions to be created.

The outcome of the sensitivity analysis was to compare the macro behaviour of the element with published intrinsic properties of sand (stiffness and strength). These are normally obtained from triaxial tests on samples of sand. It was assumed that the results of biaxial tests and triaxial tests are similar so the biaxial modelling used in the sensitivity analysis would be acceptable. It is appreciated that this assumption is not correct but given the fact that there are no unique values of strength or stiffness for sand, the 2D sensitivity analysis would indicate the trend. However, this would only be acceptable if the vertical boundaries were flexible. Therefore it was necessary to create an algorithm to numerically simulate the latex membrane of a biaxial test (section 4.3.5.2). This produced a continuous membrane latex to which a constant external load could be applied to simulate the cell pressure in a triaxial test.

It was found that applying the Hertz contact model used in granular mechanics to disk-shaped particles in a DEM analysis produces an unrealistic response. For this reason, a non-linear normal contact model, which takes into account the inter-particle parameters, elastic modulus and Poisson's ratio, was used (figures 4-7 and 4-8).

The method chosen to create the model was to generate a random particle size distribution of particles specifying the number of particles and the porosity. The soil element was filled with the specified number of particles but in the first stage the size of the particles was reduced to prevent any overlap. The particle diameter was increased until the element was filled. This meant the final particle size distribution was different from the initial distribution though it was still random. The external load (confining pressure) was then applied.

A number of fabric quantities (e.g. average coordination number, contact force distribution, normal contact distribution) can be used to study the response of the element to external loads. These are average values thus give an indication of the response and bulk instability. However, instability can occur at a particle level which may progress causing local instability. Therefore, a new fabric quantity called "symmetric geometric deviation index" was developed to show the deviation of the contact points from a symmetric, stable distribution (see section 4.3.2). The threshold of bulk instability (e.g. peak deviatoric stress) can be observed by tracking this quantity (see figures 5-44 and 5-46).

Forty four biaxial tests with rigid and deformable boundaries were conducted to establish the effect of the type of boundary and the inter particle parameters had upon the macro response of the soil element. Particles of between 0.25 [mm] to 1.0 [mm], that is medium to coarse sand, were used in each of the tests. In order to reduce the processing time an investigation was undertaken to determine the effect of particle density on the macro mechanical behaviour. An increase in particle density reduces the processing time. It was found (Figures 5-8 – 5-17) using an initial porosity of 0.12, inter-particle stiffness 4.62 * 10^8 [N/m]; inter-particle friction of 0.2; and particle's

Poisson's ratio of 0.15 that a particle density from 2650 [kg/m^3] to 2*10^8 [kg/m^3] had little effect on the macro response. Therefore, particle density of 2*10^8 [kg/m^3] was used for biaxial tests to significantly decrease the time of simulations.

The effect of inter particle stiffness for an initial porosity of 0.12, density of 2*10^8 [kg/m^3] and inter particle friction of 0.5, 0.9 and 1.2 (figure 5-18 to 5-21) was studied using a rigid wall biaxial test. They showed that the inter particle friction affected the angle of friction of the soil element which varied between 25^o and 35^o (figure 5-19) and the inter particle stiffness affected the stiffness of the soil element (figure 5-20) for both plane stress and plane strain conditions. It was also found that the relationship between macro stiffness, E_{50} and the inter particle normal stiffness was linear with the constant increasing with inter particle friction. The inter particle stiffness varied between 1.24 *10^7 [N/m] and 160 *10^7 [N/m] giving values of E_{50} of between 5.8 [MPa] and 590 [MPa] though for values of normal stiffness between 8.45*10^7 and 17.1*10^7 (N/m), this leads to values of E_{50} which are typical for medium and dense sand; i.e. between 25 and 50 [MPa] and 50 and 80 [MPa], respectively (figure 5-27).

The inter-particle stiffness also affects Poisson's ratio though in order to obtain realistic values the inter particle parameters have to be restricted. Using a stiffness of between 8.45 and 17.1 * 10^7 [N/m] that produces realistic values of E_{50} means that the inter particle friction must lie between 0.5 and 0.9.

In these analyses the ratio k_s/k_n was kept constant and equal to 1. An investigation of the effect of this ratio showed that increasing the ratio increased E_{50} (figure 5-36) though the increase was less significant than an increase in the inter particle normal stiffness.

The stability of the soil element can be expressed in terms of the average symmetric geometric deviation index which is the difference between the current contact distribution and that required for stability. Figure 5-34 and 5-

35 shows that increasing the inter particle stiffness reduces the stability as the index increases.

The effect of the inter particle properties was assessed using rigid boundaries yet the outcome was compared to macro properties measured in triaxial tests. A comparison between a biaxial test with rigid boundaries and flexible boundaries (figure 5-44 and 5-45) showed that the macro stress strain response with deformable boundaries was more representative of the actual behaviour than that with rigid boundaries since the post peak deviator stress was very nearly constant with the deformable boundaries and with the rigid boundaries it continued to increase. It is noted that the macro stiffness (E_{50}) for deformable and rigid boundaries are similar so the conclusions of the sensitivity analysis on macro stiffness carried out using the rigid boundaries applies to deformable boundaries. This is not the case for the strength as the deformable boundaries give a lower value of peak stress than tests with rigid boundaries. This means that angles of friction for the rigid boundaries were probably an overestimate of typical values. Further the shear surface shown with deformable boundaries is similar to that for a brittle sample.

7.2.3 Studying the fabric of sand during earthquake

The issues to be addressed when studying the effect of seismic loading on the pile/soil interface friction and, therefore, capacity, are the size of the element, the type of boundary. Once these were established it was possible to assess the behaviour of the model for different frequencies and amplitudes of a cyclical shear load confining pressures, normal contact stiffness and inter-particle friction

A deformable boundary was created that could absorb the seismic energy due to a horizontal cyclic shear load applied to the base of the element. It is noted that the deformable boundary for the dynamic case is different from that for a static case since the external force in the static case is constant whereas in the dynamic case it varies. The input shear wave velocity was selected to ensure the response was elastic and the frequency typical of earthquakes. The optimum length to height of the element was 4. The

deformable boundaries (Figure 6-18) showed that the deformable boundaries absorbed some of the energy when compared to the rigid boundaries with the possibility that rigid boundaries amplify the signal.

Typical frequencies of earthquakes at a constant amplitude have little effect on the magnitude of shear wave velocity (figure 6-12) and particle stability expressed in terms of the average symmetric geometric deviation index (figure 6-47). The shear stress developed during the seismic excitation within the element (figure 6-49) does change with frequency and for a six fold increase in frequency there is a 25% change in the peak shear stress.

The amplitude and at a constant frequency of the input signal did have a significant effect on the particle stability (figure 6-59) and shear stress (figure 6-62) suggesting that the it is the amplitude of the signal that is critical and that can lead to plastic deformation which is shown in figure 6-60 as a reduction in bulk density.

It was found that depth of sample (expressed in terms of the confining stress) played a major role on the particle stability (figure 6-70) because the deviatoric index for 100 [kPa] confining stress was less than that for 50 [kPa] confining stress and average shear stress within the soil (figure 6-72).
An increase in μ from 0.9 to 1.2 does not have any effect on the fabric evolution and micro-mechanical behaviour (see figures from 6-76 to 6-81), while the seismic micro-macro mechanical behaviour of soil is greatly dependent on k_n (see figures from 6-82 to 6-87). This means that for the conditions applied in this analysis it is the inter particle stiffness that is critical.

Installing a pile within the soil would be expected to change the response of the soil to a seismic load. This is the case. For example, figure 6-94 shows that the average symmetric geometric deviation index reduces because of the pile. This means the soil is more stable. The average shear stresses within the soil element also increase (figure 6-95) suggesting even the soil is more stable the stresses increase causing more deformation and possibly failure. This is consistent with observations with failure of piled foundations in seismic regions.

7.3 Recommendations for further work

The following issues were identified during this research and, therefore, are recommendations for further research:

7.3.1 The soil model

The responses of granular material are highly dependent on the contact model. A simple elastic disk was selected. In practice, sand particles are three dimensional irregular shaped particles. It is possible to model as these agglomerates of spheres. This is important in simulating seismic loading because the particles may crush because of locally high contact forces.

7.3.2 Saturated soil

The DEM modelled developed for performing a biaxial test in this research was limited to dry particulate sand. However, in reality many sands are saturated or semi-saturated. Thus, an aim is to execute biaxial tests on saturated and semi-saturated sands taking into account the effect of pore water pressure.

7.3.3 The sensitivity of sand fabric during an earthquake

This research demonstrated that it is possible to simulate the seismic behaviour of an element of soil and the pile/soil interface behaviour but the study was limited. It is necessary to undertake a sensitivity analysis to the effect of particle shape, pore water, inter particle properties and the inter particle model under a variety of seismic loads. This will help explain the response of the soil using the macro response and change in fabric to monitor that response.

The ultimate aim of this work is to develop a constitutive relationship for the pile/soil interaction which can be used in a continuum analysis to model piled foundations. Therefore it will be necessary to generate data against which these predictions can be validated.

Appendix 1: Fast Fourier Transform of 10 well-known earthquakes

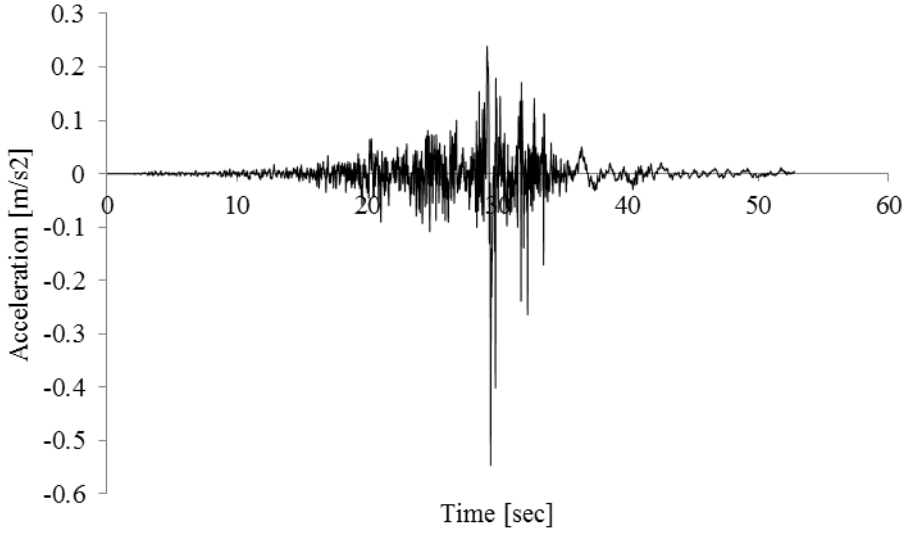

Appendix [1] Figure 1 acceleration-time history of ChiChi earthquakes

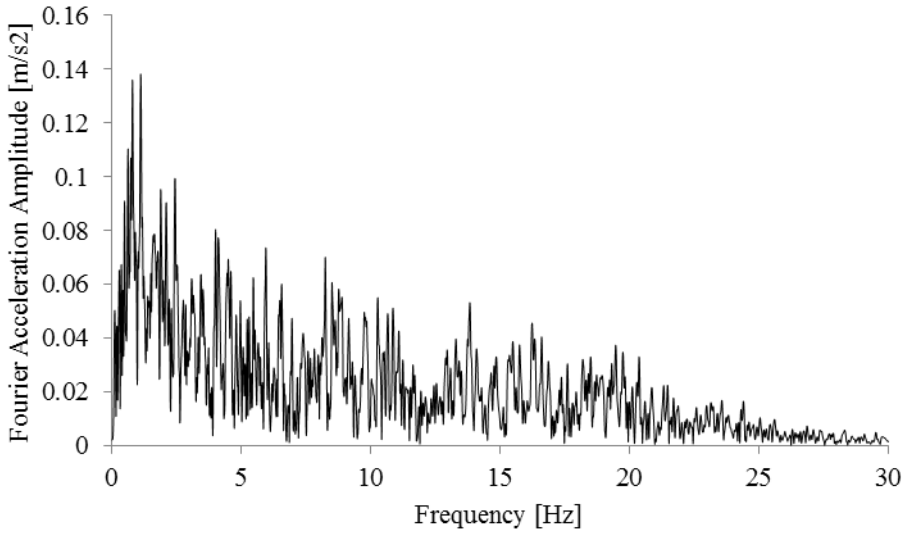

Appendix [1] Figure 2 frequency contents of ChiChi earthquakes

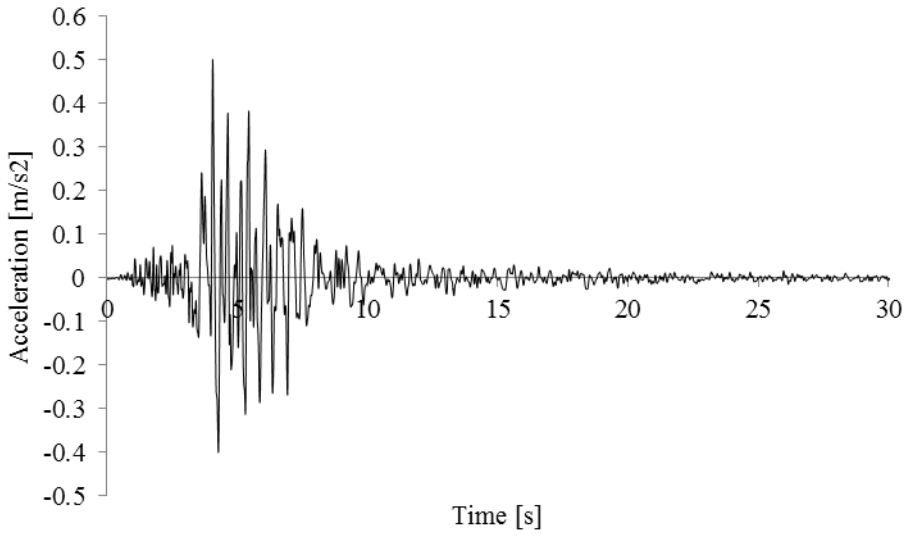

Appendix [1] Figure 3 acceleration-time history of Friuli earthquakes

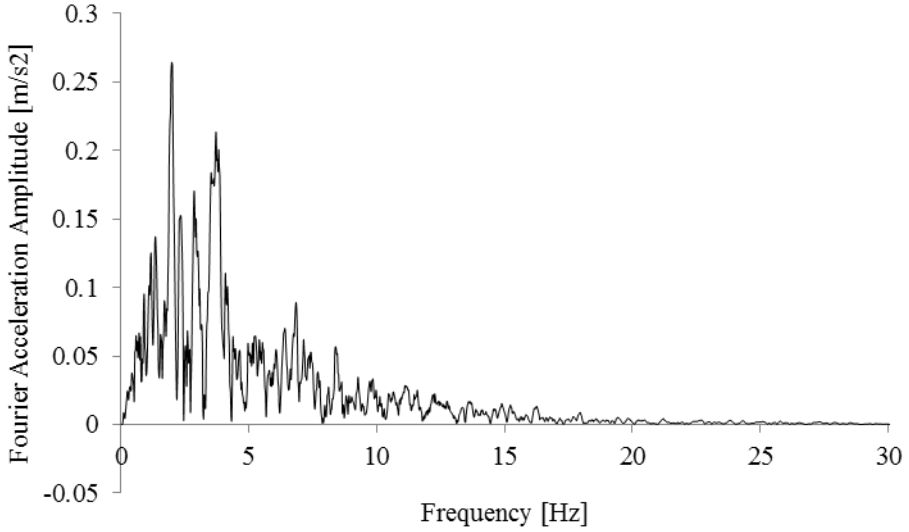

Appendix [1] Figure 4 frequency contents of Friuli earthquakes

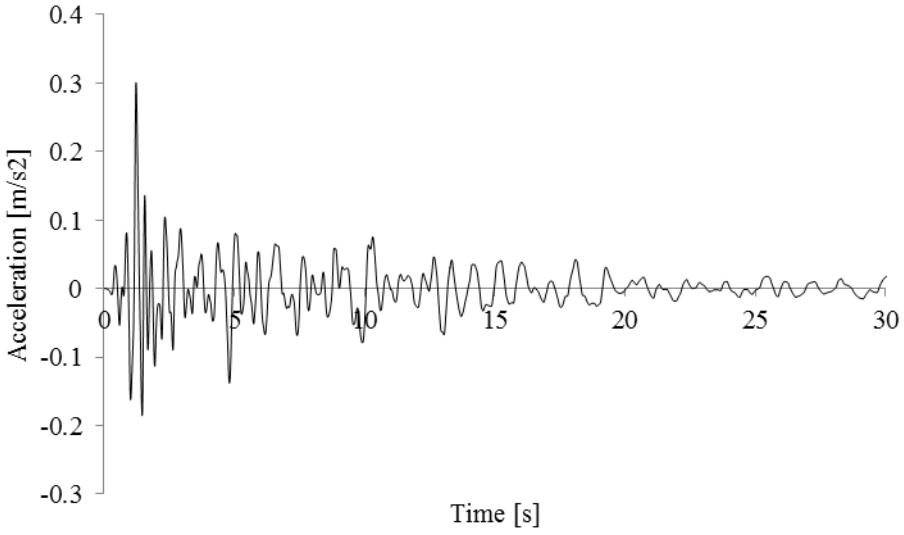

Appendix [1] Figure 5 acceleration-time history of Hollister earthquakes

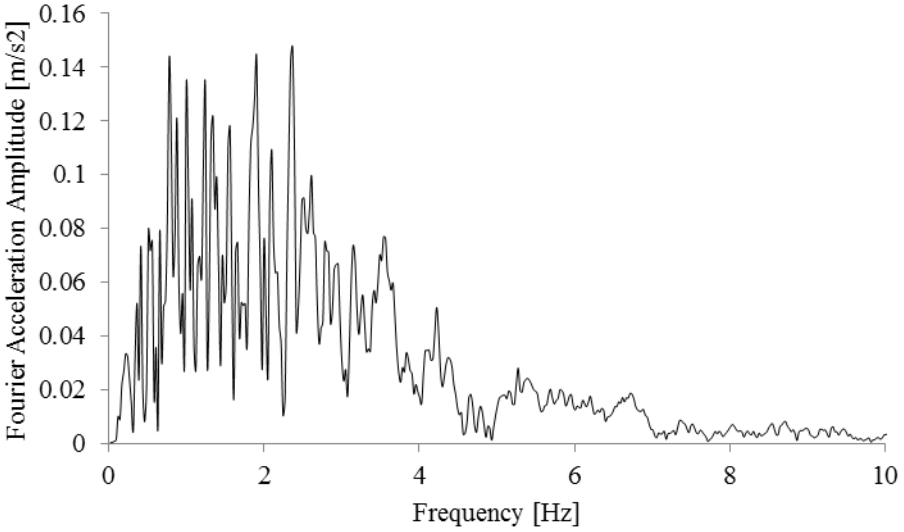

Appendix [1] Figure 6 frequency contents of Hollister earthquakes

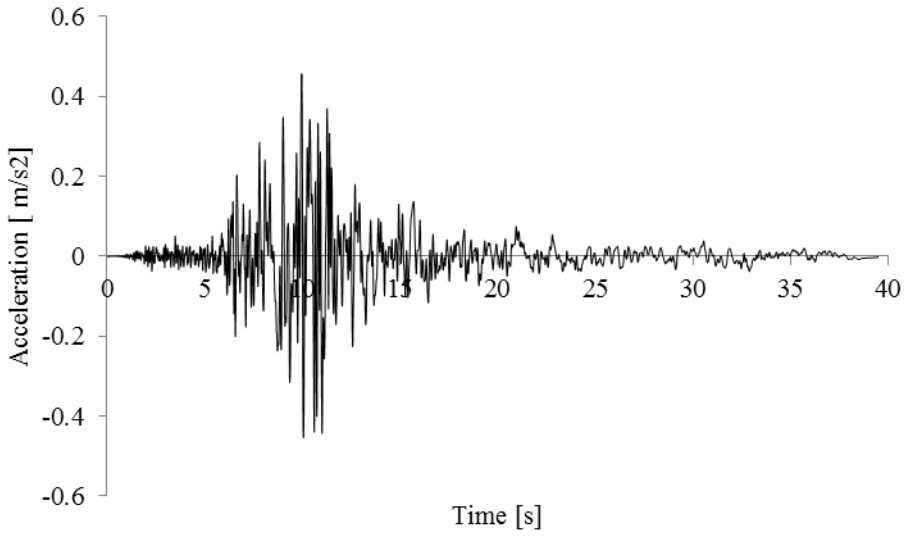

Appendix [1] Figure 7 acceleration-time history of Imperial Valley earthquakes

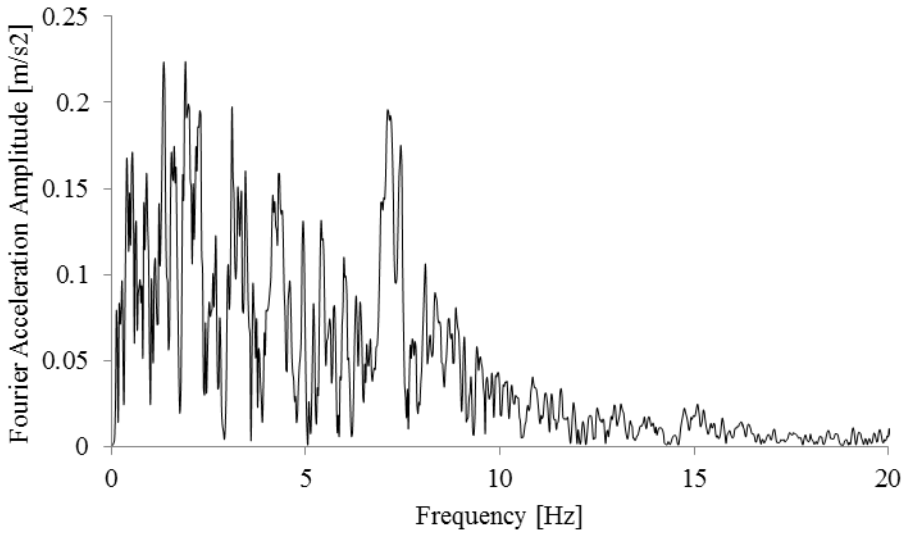

Appendix [1] Figure 8 acceleration-time history of Imperial Valley earthquakes

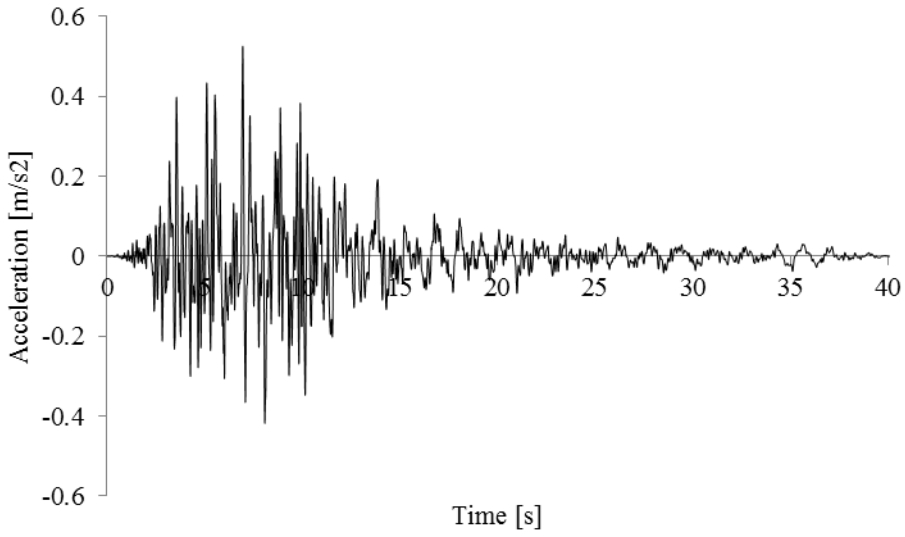

Appendix [1] Figure 9 acceleration-time history of Kobe earthquakes

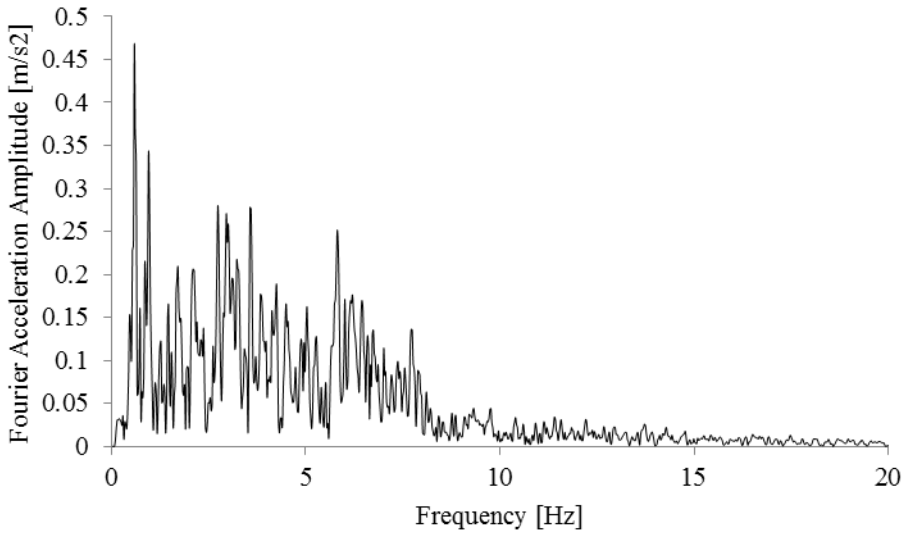

Appendix [1] Figure 10 acceleration-time history of Kobe earthquakes

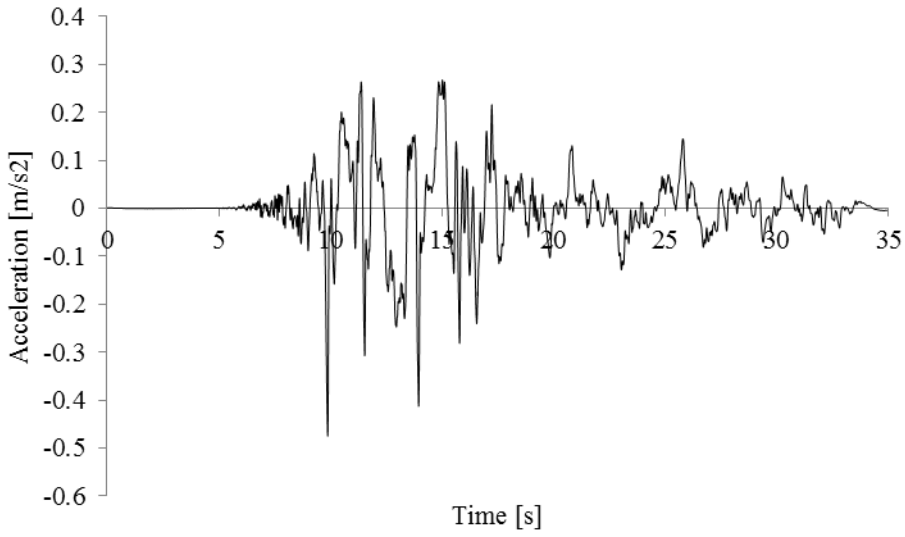

Appendix [1] Figure 11 acceleration-time history of Kocaeli earthquakes

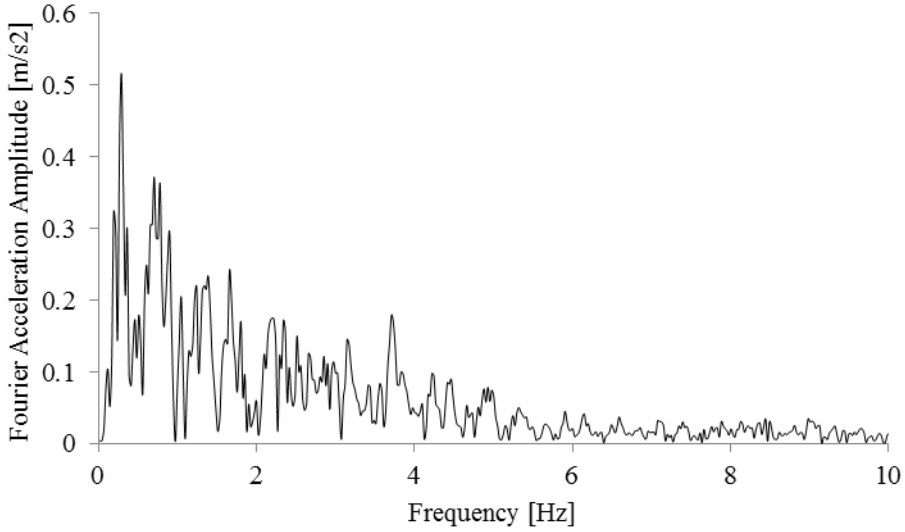

Appendix [1] Figure 12 acceleration-time history of Kocaeli earthquakes

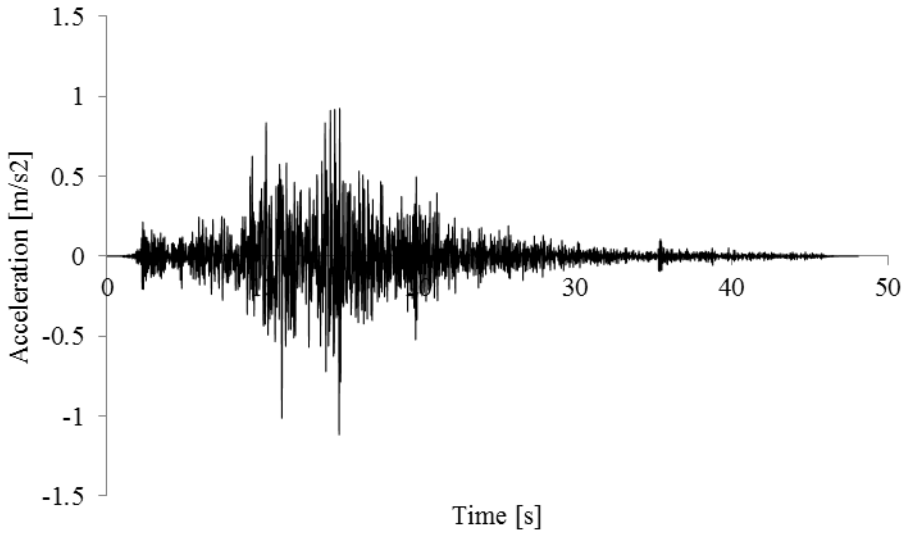

Appendix [1] Figure 13 acceleration-time history of Landers earthquakes

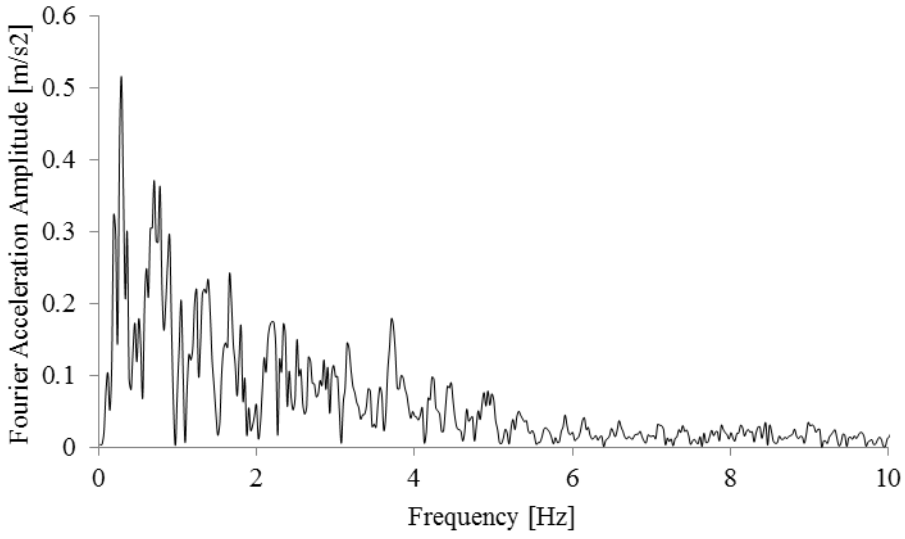

Appendix [1] Figure 14 acceleration-time history of Landers earthquakes

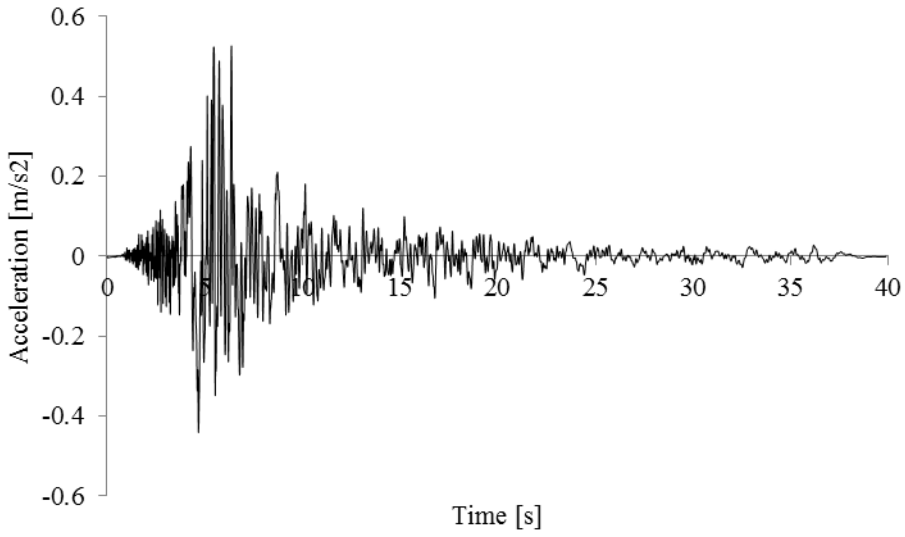

Appendix [1] Figure 15 acceleration-time history of Loma Prieta earthquakes

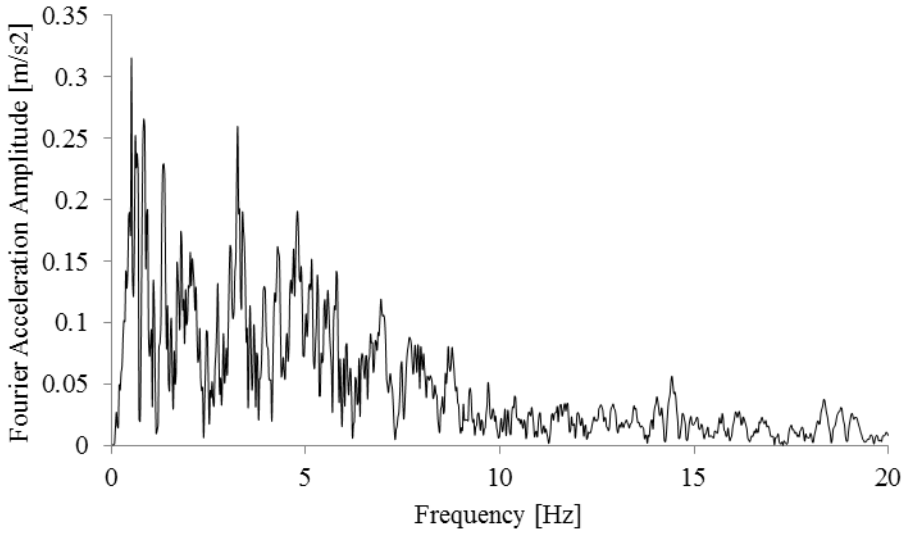

Appendix [1] Figure 16 acceleration-time history of Loma Prieta earthquakes

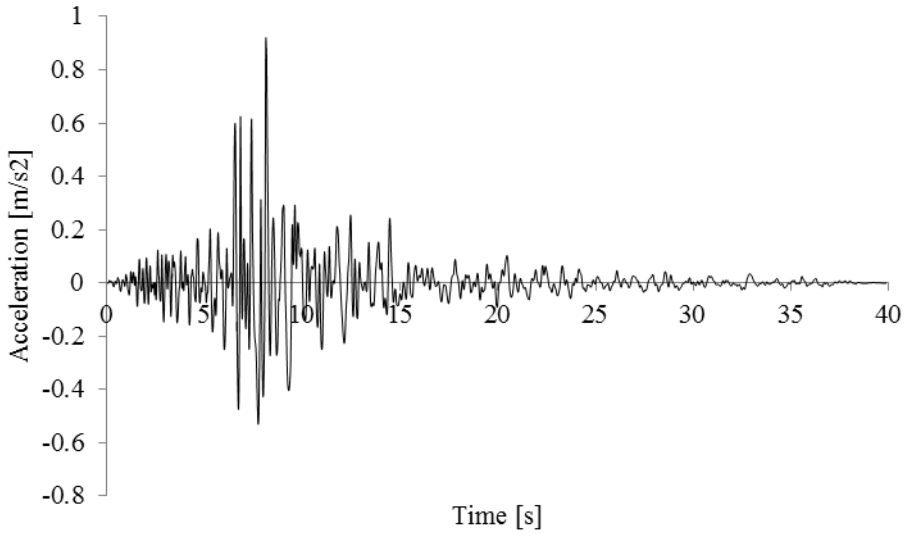

Appendix [1] Figure 17 acceleration-time history of Northridge earthquakes

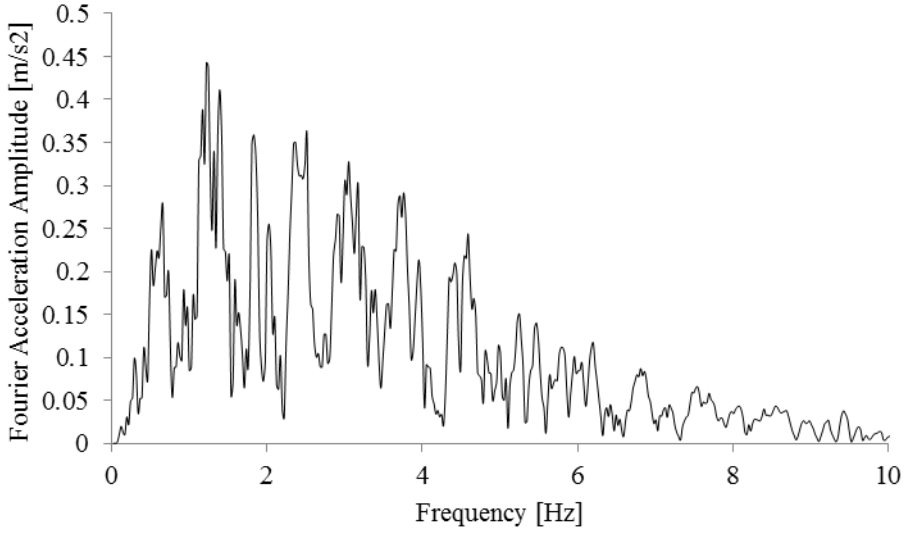

Appendix [1] Figure 18 acceleration-time history of Northridge earthquakes

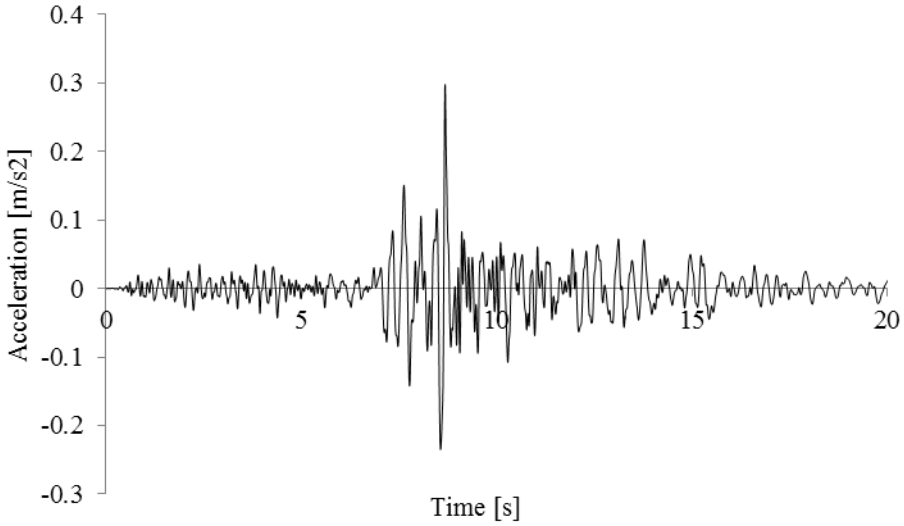

Appendix [1] Figure 19 acceleration-time history of Trinidad earthquakes

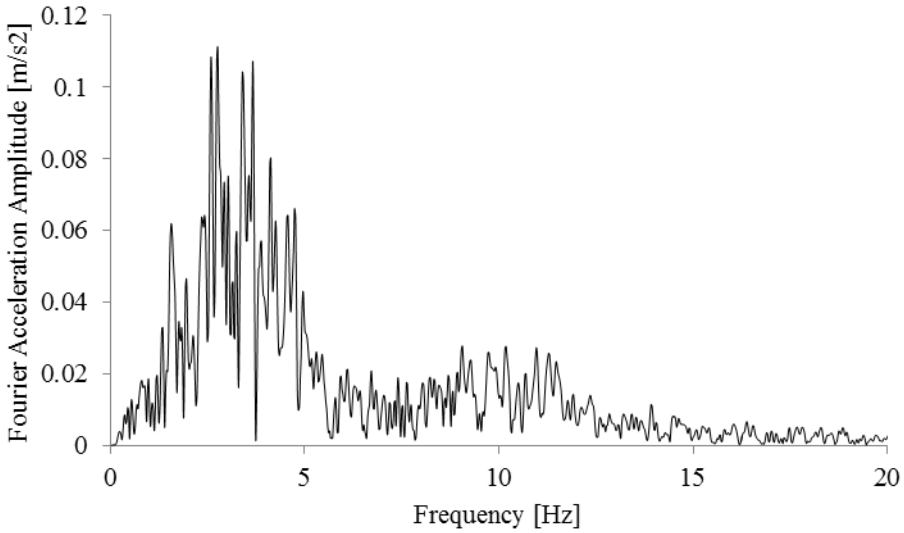

Appendix [1] Figure 20 acceleration-time history of Trinidad earthquakes

Appendix 2- Inter-particle properties of quartz sand

θ	30°	(Belheine et al., 2009)
$shear\ modulus$	$2e8\ (Pa)$	(Soroush and Ferdowsi, 2011)
θ	26.56°	
$Poisson's\ ratio$	0.35	
θ	26.56°	(Sazzad and Suzuki, 2010, Zamani and El Shamy, 2012, Sitharam, 2003, El Shamy and Zeghal, 2007, El Shamy and Denissen, 2010, Jiang et al., 2011, Iwashita and Oda, 1998)
$shear\ modulus$	$29e9(Pa)$	(Yimsiri and Soga, 2010)
θ	$45^{\circ}, 63^{\circ}, 84^{\circ}$	
$Poisson's\ ratio$	0.35	
$Young's\ modulus$	$8.34\ GPa$	(Thornton and Zhang, 2003)
θ	26°	
$Poisson's\ ratio$	0.35	
$Young's\ modulus$	$7.9e10\ (Pa)$	(O'Sullivan et al., 2008)
θ	5.4°	
$Poisson's\ ratio$	0.28	
$Young's\ modulus$	$7e10\ (Pa)$	(Zamani and El Shamy, 2011)
θ	35°	
$Poisson's\ ratio$	0.15	
$Young's\ modulus$	$46.9e\ GPa$	(Karrech et al., 2008)
θ	38.6°	
$Poisson's\ ratio$	0.25	
$Shear\ modulus$	$34\ GPa$	(Van Baars, 1996)
θ	30°	
$Poisson's\ ratio$	0.16	
$Shear\ modulus$	$10\ GPa$	(Pruiksma and Bezuijen, 2002)
θ	52°	
$Poisson's\ ratio$	0.16	
θ	42°	(Pruiksma and Bezuijen, 2002)
$Young's\ modulus$	$80 - 85\ (GPa)$	Bardet (1998)
θ	37	
$Poisson's\ ratio$	0.29	

Appendix [2] Table 1 The values of elastic modulus, Poisson's ratio and inter-particle friction in literature

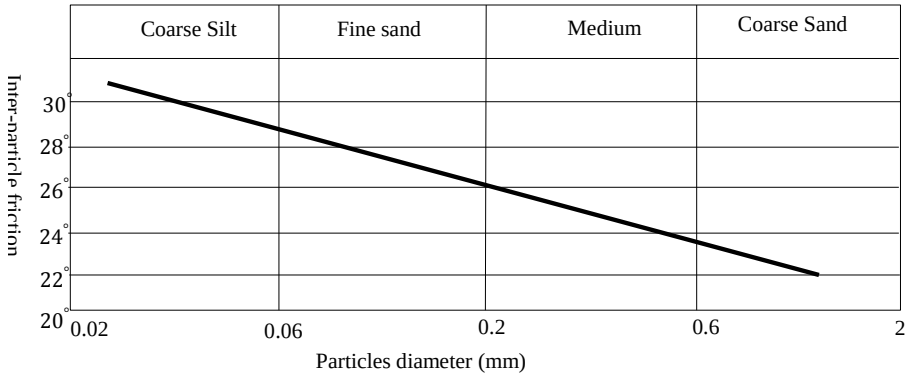

Appendix [2] Table 2 The values of inter-particle friction for quartz sand After (Rowe, 1962)

Appendix 3- The results of biaxial simulations tests

Shear Stiffness (N/m)	$1.24*10^7$	$1.24*10^7$	$1.24*10^7$
Normal Stiffness (N/m)	$1.24*10^7$	$1.24*10^7$	$1.24*10^7$
Coefficient friction	0.5	0.9	1.2
E_{50} (P.Strain) (MPa)	5.8	6.30	6.55
E_{50} (P.Stress) (MPa)	6.0	6.5	6.65
v_{50} (P.Strain)	0.16	0.13	0.11
v_{50} (P.Stress)	0.19	0.15	0.13
σ_{max} (kPa)	200.0	264.0	290.0
ε_{11} at σ_{max}	0.04	0.05	0.05
θ(°)	19.5	26.8	29.1

Appendix [3] Table 1 The sensitivity of sand to the different inter-particle friction when normal and shear stress is $1.24*10^7$ (N/m)

Shear Stiffness (N/m)	$8.45*10^7$	$8.45*10^7$	$8.45*10^7$
Normal Stiffness (N/m)	$8.45*10^7$	$8.45*10^7$	$8.45*10^7$
Coefficient friction	0.5	0.9	1.2
E_{50} (P.Strain) (MPa)	32.0	35.0	35.0
E_{50} (P.Stress) (MPa)	34.0	36.0	36.0
v_{50} (P.Strain)	0.21	0.18	0.18
v_{50} (P.Stress)	0.27	0.23	0.22
σ_{max} (kPa)	200.0	263.0	290.0
ε_{11} at σ_{max}	0.01	0.01	0.01
θ(°)	19.5	26.8	29.1

Appendix [3] Table 2 The sensitivity of sand to the different inter-particle friction when normal and shear stress is $8.45*10^7$ (N/m)

Shear Stiffness (N/m)	$17.1*10^7$	$17.1*10^7$	$17.1*10^7$
Normal Stiffness (N/m)	$17.1*10^7$	$17.1*10^7$	$17.1*10^7$
Coefficient friction	0.5	0.9	1.2
E_{50} (P.Strain) (MPa)	61.0	67.0	68.0
E_{50} (P.Stress) (MPa)	64.0	70.0	71.0
v_{50} (P.Strain)	0.22	0.20	0.19
v_{50} (P.Stress)	0.28	0.24	0.23
σ_{max} (kPa)	190.0	242.0	270.0
ε_{11} at σ_{max}	0.01	0.007	0.007
θ(°)	18.0	24.5	27.3

Appendix [3] Table 3 The sensitivity of sand to the different inter-particle friction when normal and shear stress is $17.1*10^7$ (N/m)

Shear Stiffness (N/m)	$46.0*10^7$	$46.0*10^7$	$46.0*10^7$
Normal Stiffness (N/m)	$46.0*10^7$	$46.0*10^7$	$46.0*10^7$
Coefficient friction	0.5	0.9	1.2
E_{50} (P.Strain) (MPa)	162.0	173.0	180.0
E_{50} (P.Stress) (MPa)	170.0	181.0	186.0
v_{50} (P.Strain)	0.22	0.20	0.19
v_{50} (P.Stress)	0.30	0.25	0.23
σ_{max} (kPa)	180.0	240.0	260.0
ε_{11} at σ_{max}	0.01	0.005	0.004
$\theta(°)$	16.6	24.3	26.4

Appendix [3] Table 4 The sensitivity of sand to the different inter-particle friction when normal and shear stress is $46.0*10^7$ (N/m)

Shear Stiffness (N/m)	$133.0*10^7$	$133.0*10^7$	$133.0*10^7$
Normal Stiffness (N/m)	$133.0*10^7$	$133.0*10^7$	$133.0*10^7$
Coefficient friction	0.5	0.9	1.2
E_{50} (P.Strain) (MPa)	388.0	444.0	478.0
E_{50} (P.Stress) (MPa)	417.0	470.0	500.0
v_{50} (P.Strain)	0.26	0.23	0.21
v_{50} (P.Stress)	0.33	0.3	0.27
σ_{max} (kPa)	210.0	277.0	305.0
ε_{11} at σ_{max}	0.01	0.045	0.004
$\theta(°)$	20.8	28.0	30.4

Appendix [3] Table 5 The sensitivity of sand to the different inter-particle friction when normal and shear stress is $133.0*10^7$ (N/m)

Shear Stiffness (N/m)	$150.0*10^7$	$150.0*10^7$	$150.0*10^7$
Normal Stiffness (N/m)	$150.0*10^7$	$150.0*10^7$	$150.0*10^7$
Coefficient friction	0.5	0.9	1.2
E_{50} (P.Strain) (MPa)	463.0	535.0	540.0
E_{50} (P.Stress) (MPa)	494.0	563.0	570.0
v_{50} (P.Strain)	0.25	0.22	0.22
v_{50} (P.Stress)	0.33	0.28	0.28
σ_{max} (kPa)	213.0	286.0	325.0
ε_{11} at σ_{max}	0.01	0.003	0.003
$\theta(°)$	21.1	29.0	32.0

Appendix [3] Table 6 The sensitivity of sand to the different inter-particle friction when normal and shear stress is $150.0*10^7$ (N/m)

Shear Stiffness (N/m)	$160.0*10^7$	$160.0*10^7$	$160.0*10^7$
Normal Stiffness (N/m)	$160.0*10^7$	$160.0*10^7$	$160.0*10^7$
Coefficient friction	0.5	0.9	1.2
E_{50} (P.Strain) (MPa)	476.0	564.0	590.0
E_{50} (P.Stress) (MPa)	511.0	590.0	610.0
v_{50} (P.Strain)	0.26	0.22	0.20
v_{50} (P.Stress)	0.35	0.28	0.27
σ_{max} (kPa)	213.0	275.0	305.0
ε_{11} at σ_{max}	0.01	0.003	0.003
$\theta(^\circ)$	21.1	27.8	30.4

Appendix [3] Table 7 The sensitivity of sand to the different inter-particle friction when normal and shear stress is $160.0*10^7$ (N/m)

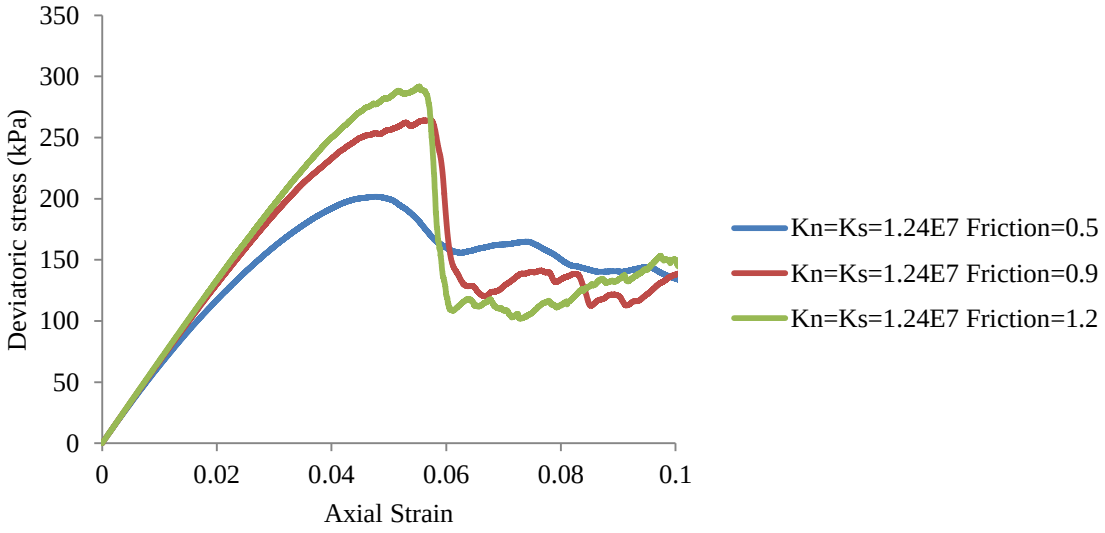

Appendix [3] Figure 1 The sensitivity of sand to the different inter-particle friction when normal and shear stress is $1.24*10^7$ (N/m): deviatoric stress vs. axial strain

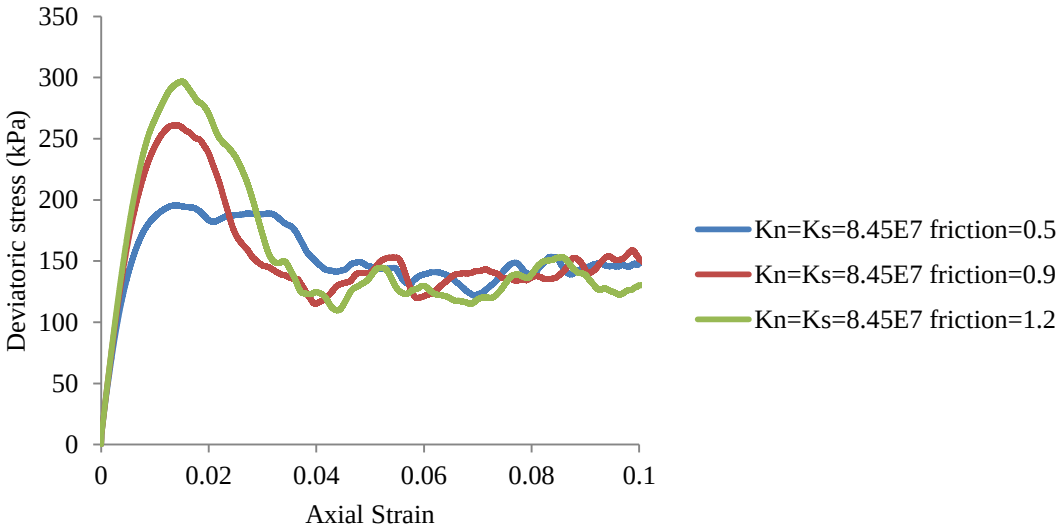

Appendix [3] Figure 2 The sensitivity of sand to the different inter-particle friction when normal and shear stress is $8.45*10^7$ (N/m): deviatoric stress vs. axial strain

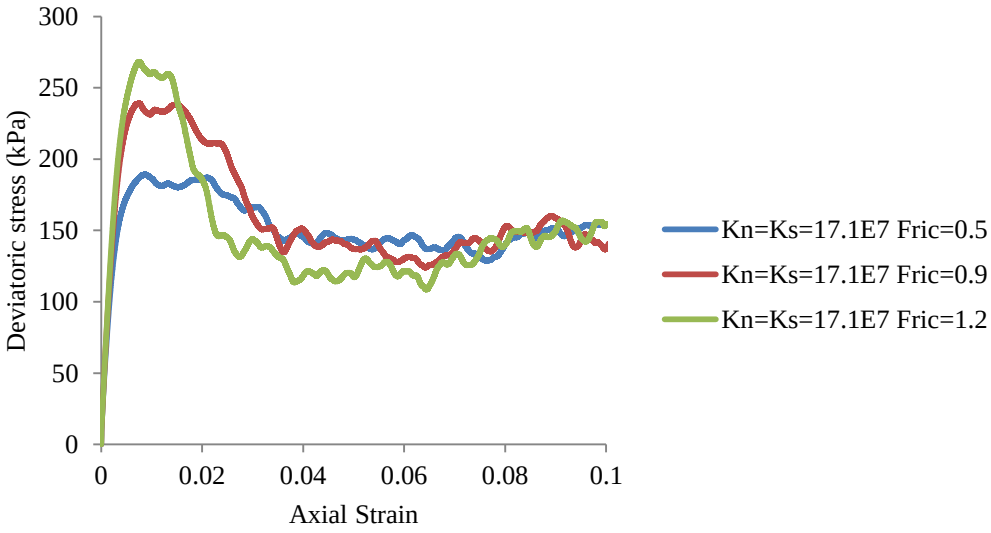

Appendix [3] Figure 3 The sensitivity of sand to the different inter-particle friction when normal and shear stress is $17.1*10^7$ (N/m): deviatoric stress vs. axial strain

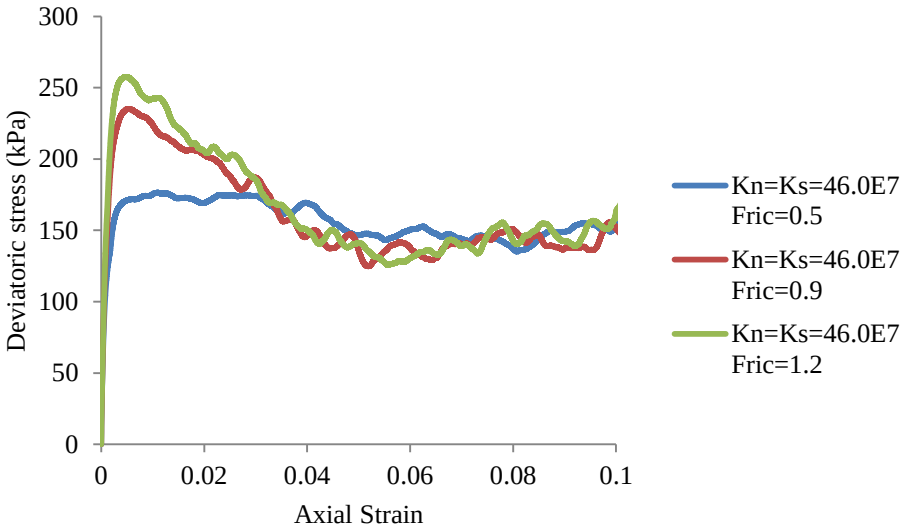

Appendix [3] Figure 4 The sensitivity of sand to the different inter-particle friction when normal and shear stress is $46.0*10^7$ (N/m): deviatoric stress vs. axial strain

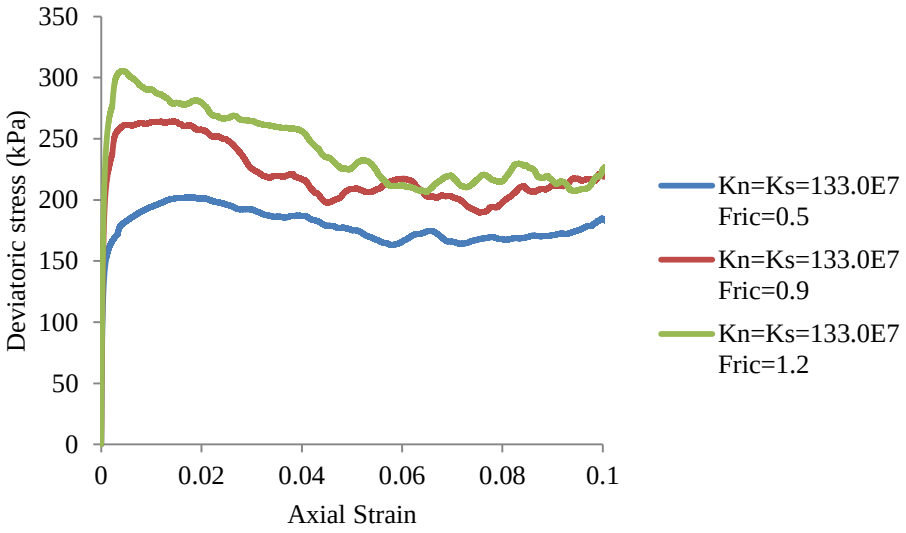

Appendix [3] Figure 5 The sensitivity of sand to the different inter-particle friction when normal and shear stress is $133.0*10^7$ (N/m): deviatoric stress vs. axial strain

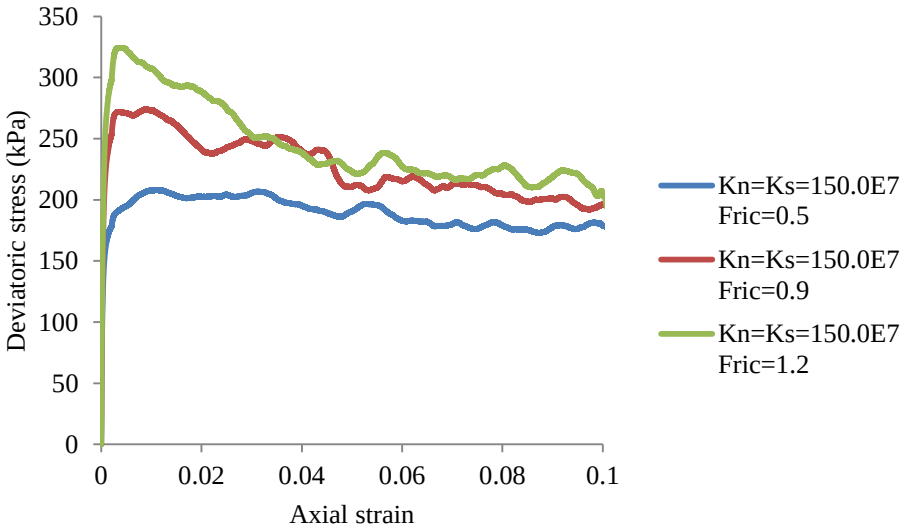

Appendix [3] Figure 6 The sensitivity of sand to the different inter-particle friction when normal and shear stress is $150.0*10^7$ (N/m): deviatoric stress vs. axial strain

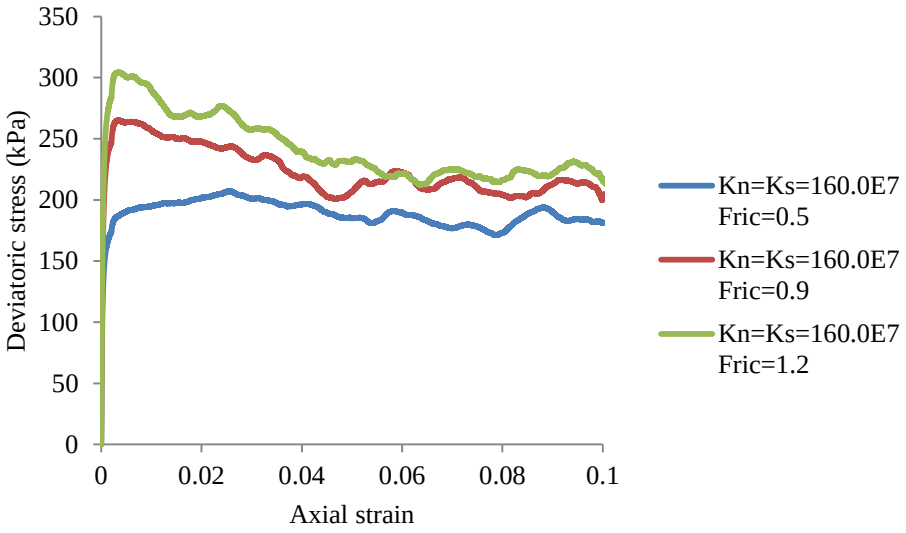

Appendix [3] Figure 7 The sensitivity of sand to the different inter-particle friction when normal and shear stress is $160.0*10^7$ (N/m): deviatoric stress vs. axial strain

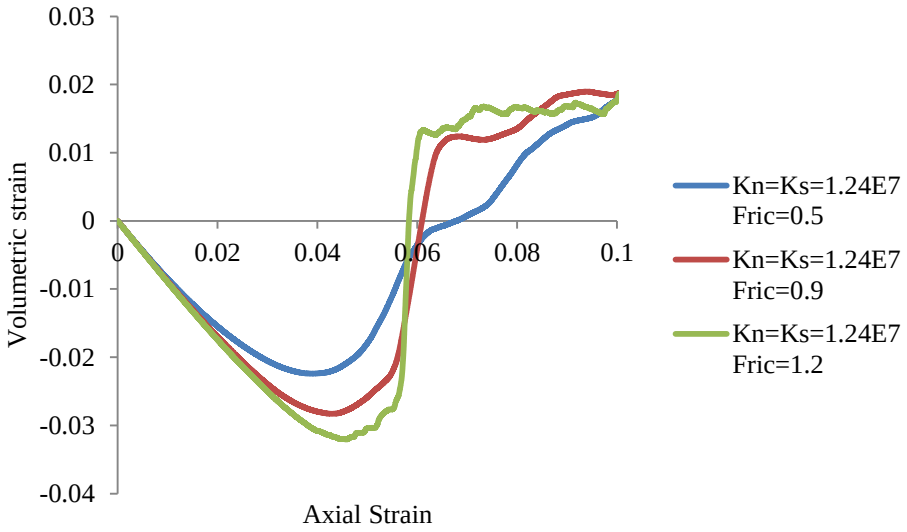

Appendix [3] Figure 8 The sensitivity of sand to the different inter-particle friction when normal and shear stress is $1.24*10^7$ (N/m): volumetric strain vs. axial strain

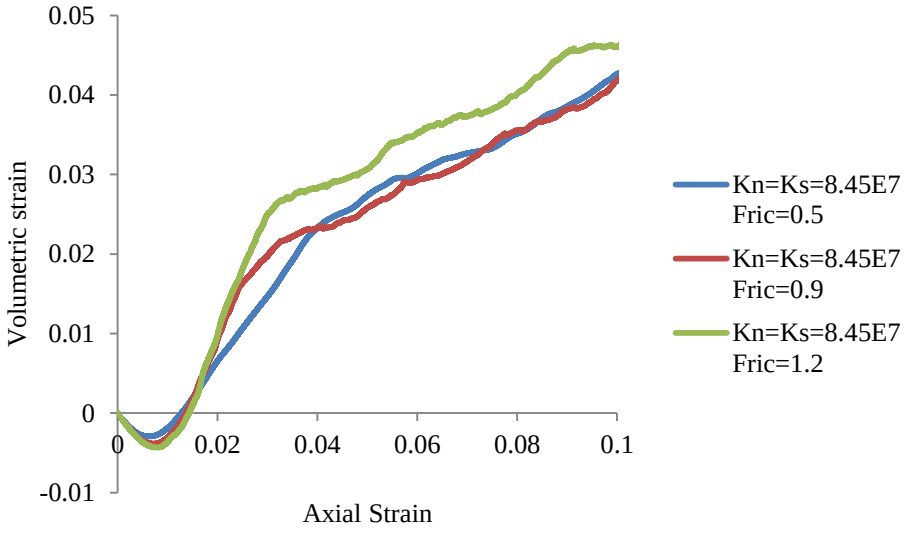

Appendix [3] Figure 9 The sensitivity of sand to the different inter-particle friction when normal and shear stress is $8.45*10^7$ (N/m): volumetric strain vs. axial strain

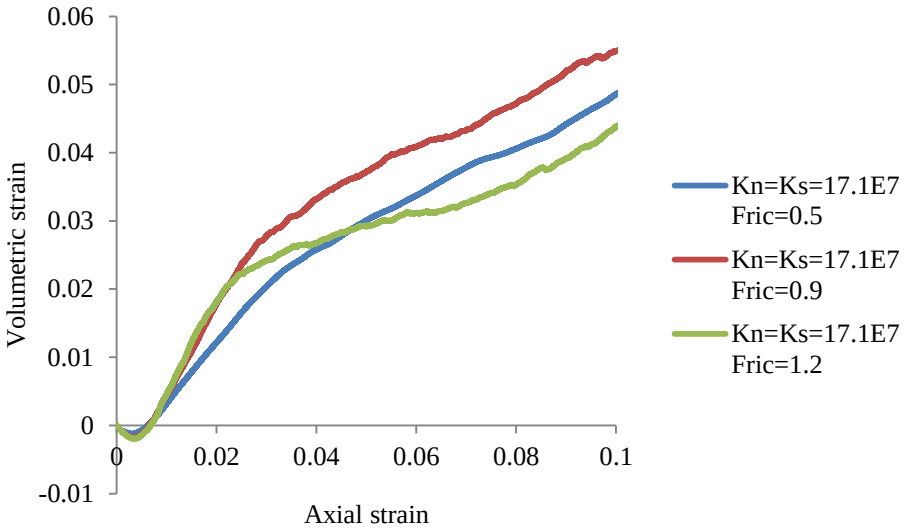

Appendix [3] Figure 10 The sensitivity of sand to the different inter-particle friction when normal and shear stress is $17.1*10^7$ (N/m): volumetric strain vs. axial strain

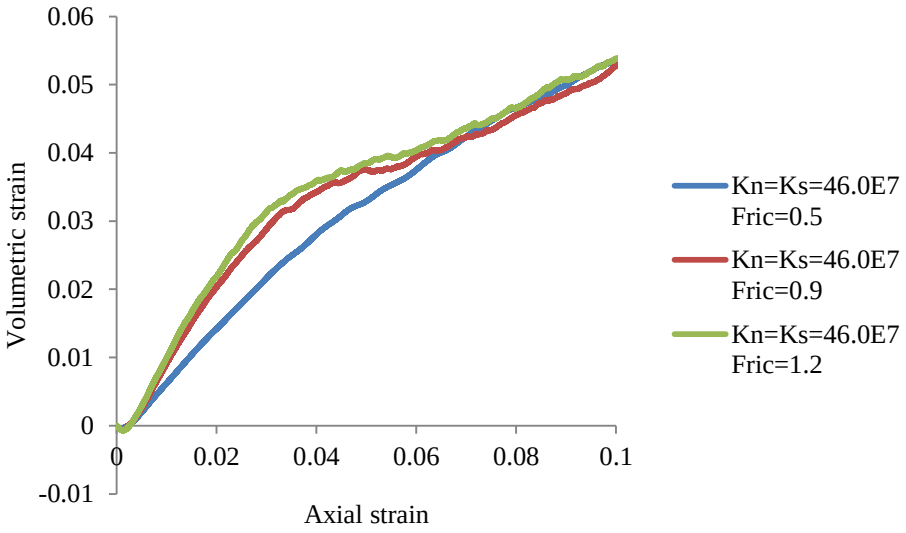

Appendix [3] Figure 11 The sensitivity of sand to the different inter-particle friction when normal and shear stress is $46.0*10^7$ (N/m): volumetric strain vs. axial strain

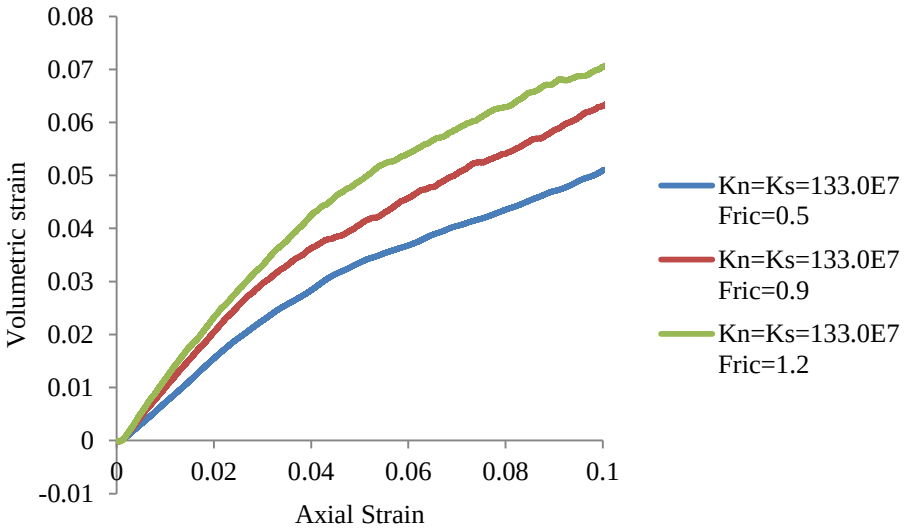

Appendix [3] Figure 12 The sensitivity of sand to the different inter-particle friction when normal and shear stress is $133.0*10^7$ (N/m): volumetric strain vs. axial strain

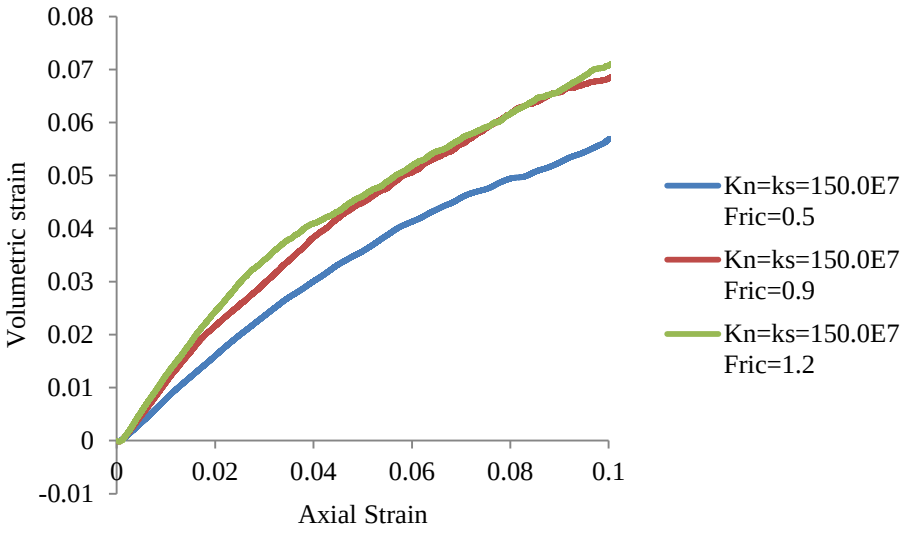

Appendix [3] Figure 13 The sensitivity of sand to the different inter-particle friction when normal and shear stress is $150.0*10^7$ (N/m): volumetric strain vs. axial strain

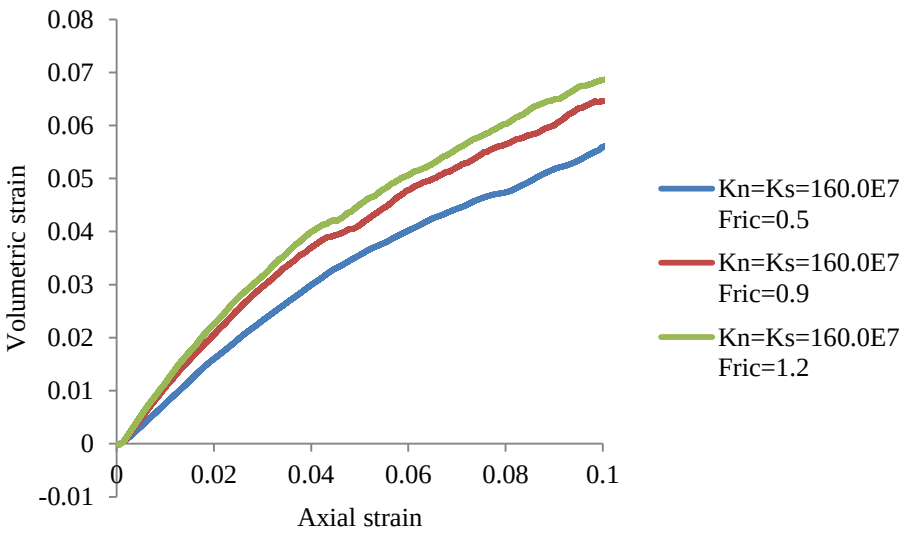

Appendix [3] Figure 14 The sensitivity of sand to the different inter-particle friction when normal and shear stress is $160.0*10^7$ (N/m): volumetric strain vs. axial strain

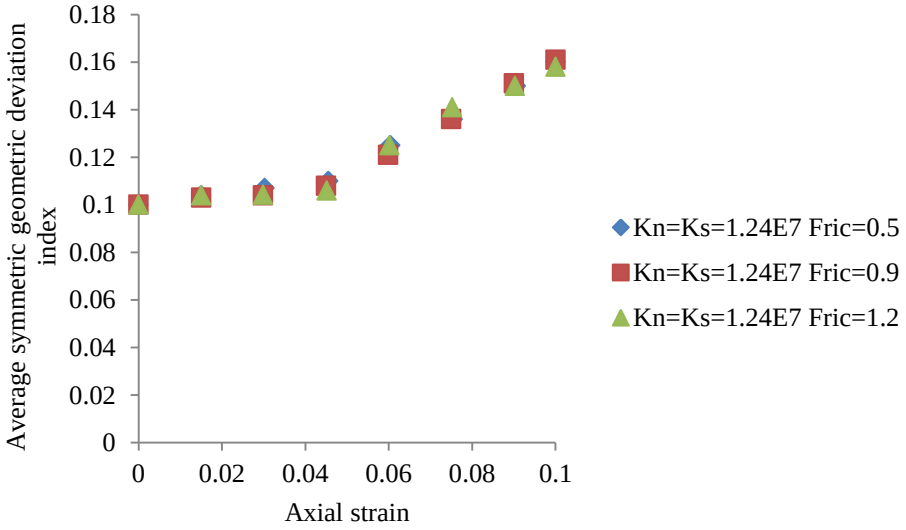

Appendix [3] Figure 15 The sensitivity of sand to the different inter-particle friction when normal and shear stress is $1.24*10^7$ (N/m): Average symmetric geometric deviation index vs. axial strain

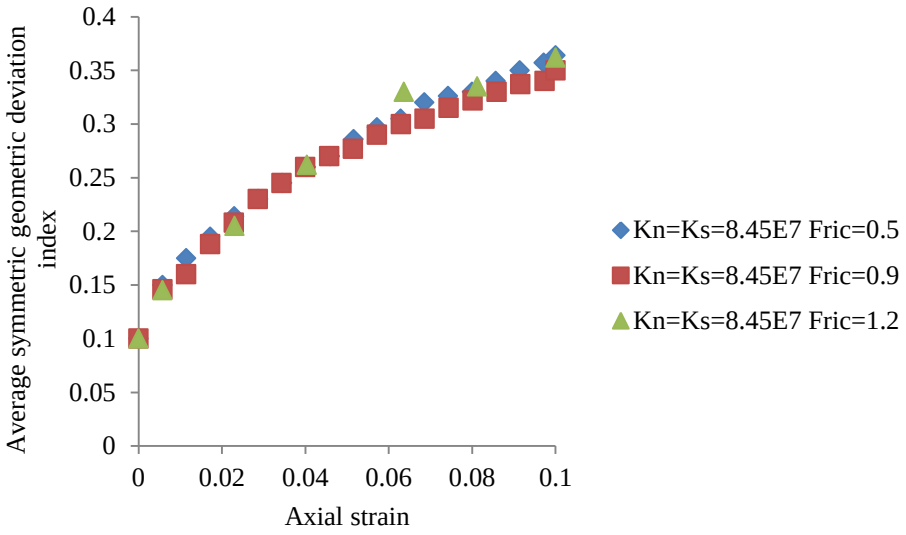

Appendix [3] Figure 16 The sensitivity of sand to the different inter-particle friction when normal and shear stress is $8.45*10^7$ (N/m): Average symmetric geometric deviation index vs. axial strain

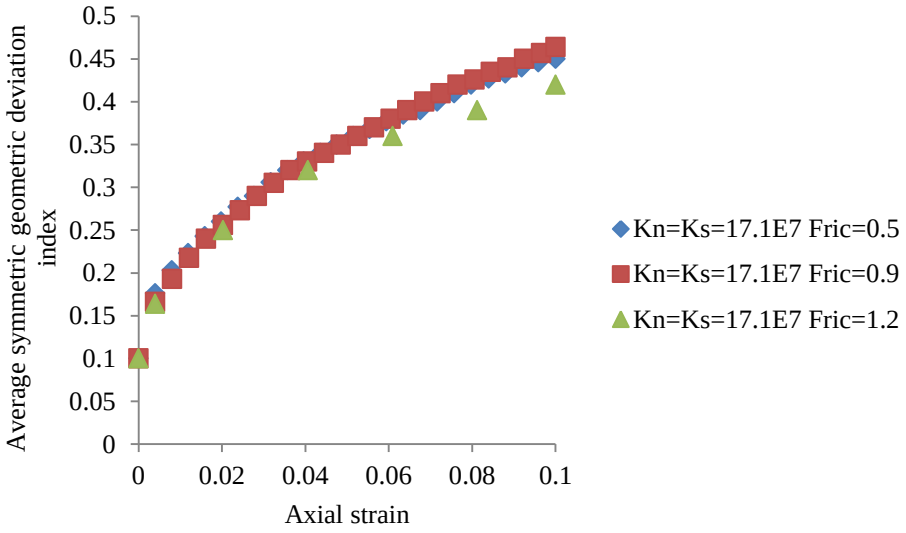

Appendix [3] Figure 17 The sensitivity of sand to the different inter-particle friction when normal and shear stress is $17.1*10^7$ (N/m): Average symmetric geometric deviation index vs. axial strain

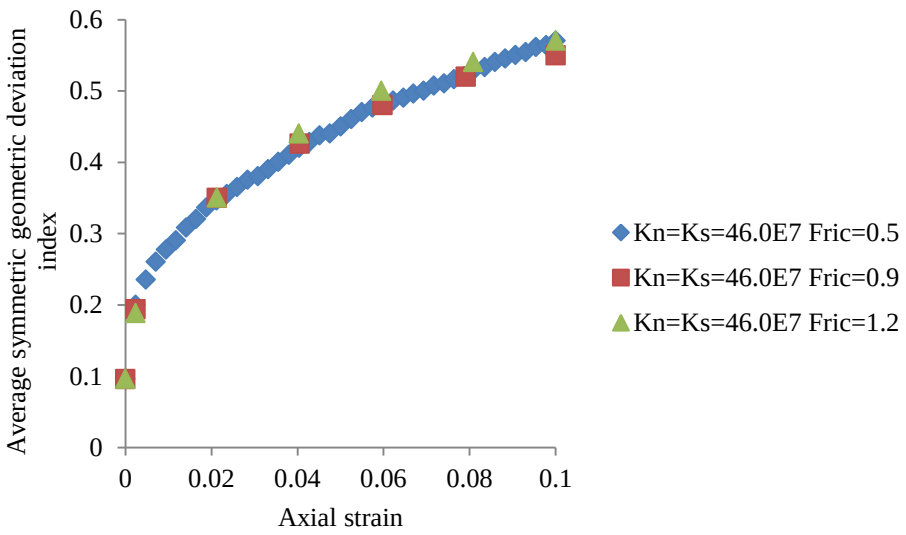

Appendix [3] Figure 18 The sensitivity of sand to the different inter-particle friction when normal and shear stress is $46.0*10^7$ (N/m): Average symmetric geometric deviation index vs. axial strain

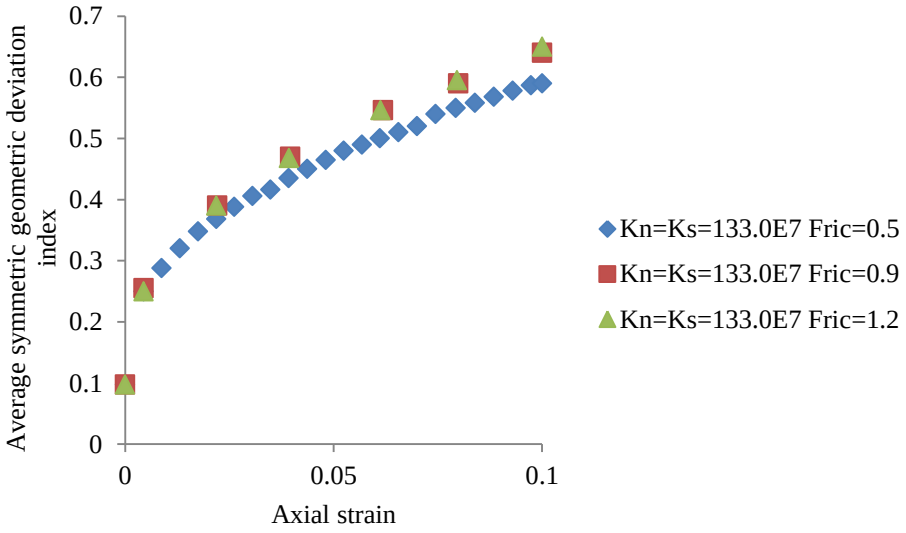

Appendix [3] Figure 19 The sensitivity of sand to the different inter-particle friction when normal and shear stress is $133.0*10^7$ (N/m): Average symmetric geometric deviation index vs. axial strain

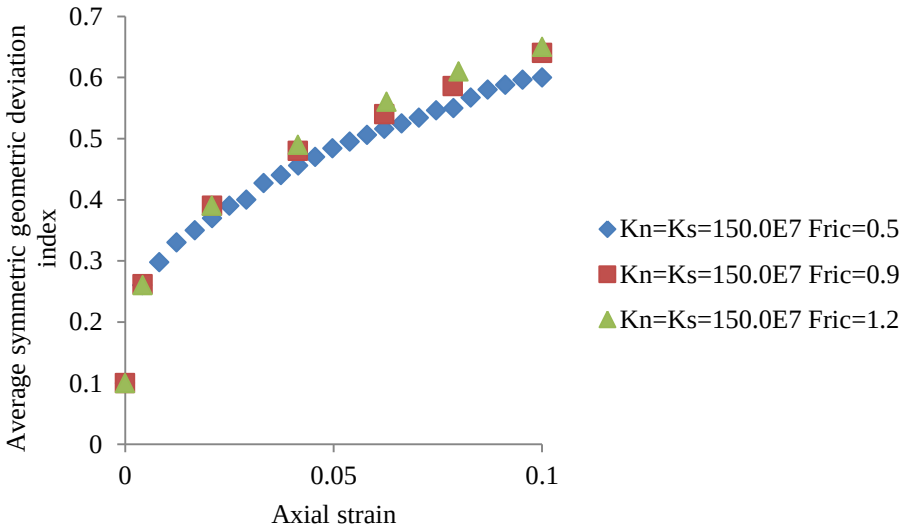

Appendix [3] Figure 20 The sensitivity of sand to the different inter-particle friction when normal and shear stress is $150.0*10^7$ (N/m): Average symmetric geometric deviation index vs. axial strain

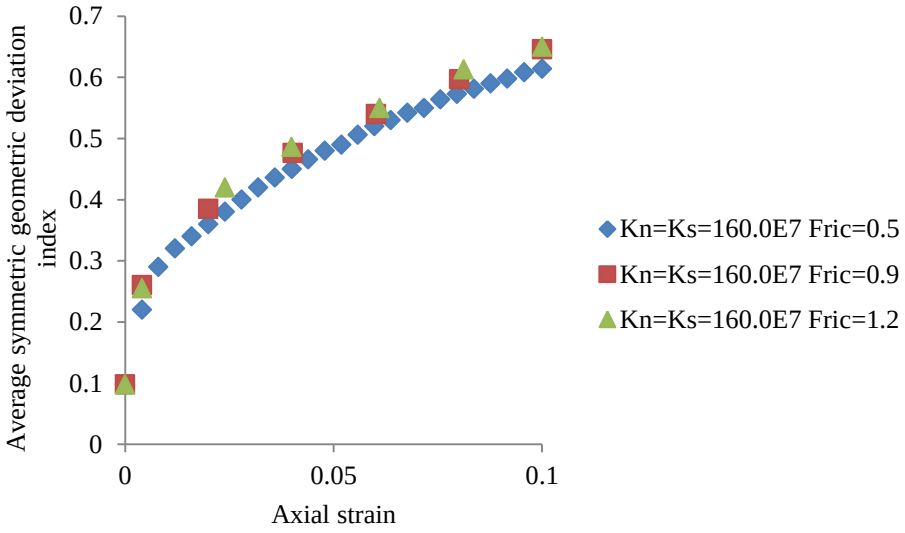

Appendix [3] Figure 21 The sensitivity of sand to the different inter-particle friction when normal and shear stress is $160.0*10^7$ (N/m): Average symmetric geometric deviation index vs. axial strain

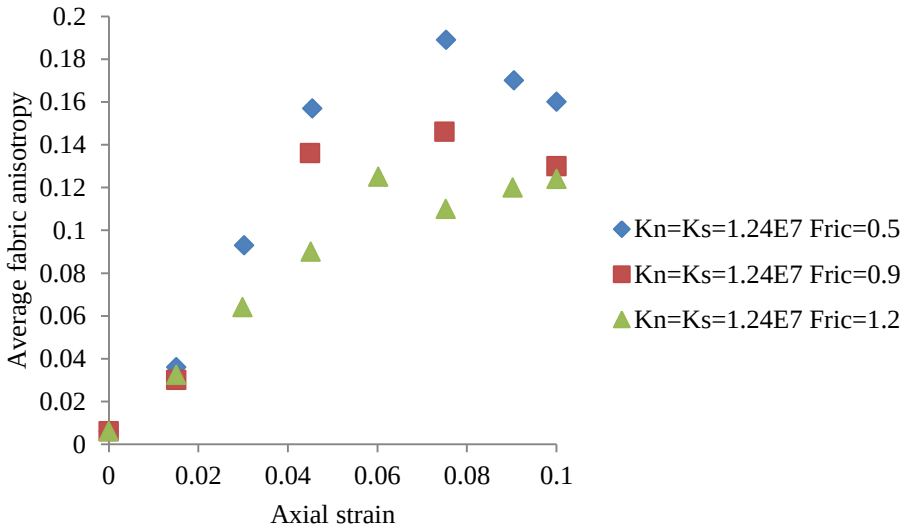

Appendix [3] Figure 22 The sensitivity of sand to the different inter-particle friction when normal and shear stress is $1.24*10^7$ (N/m): Average fabric anisotropy vs. axial strain

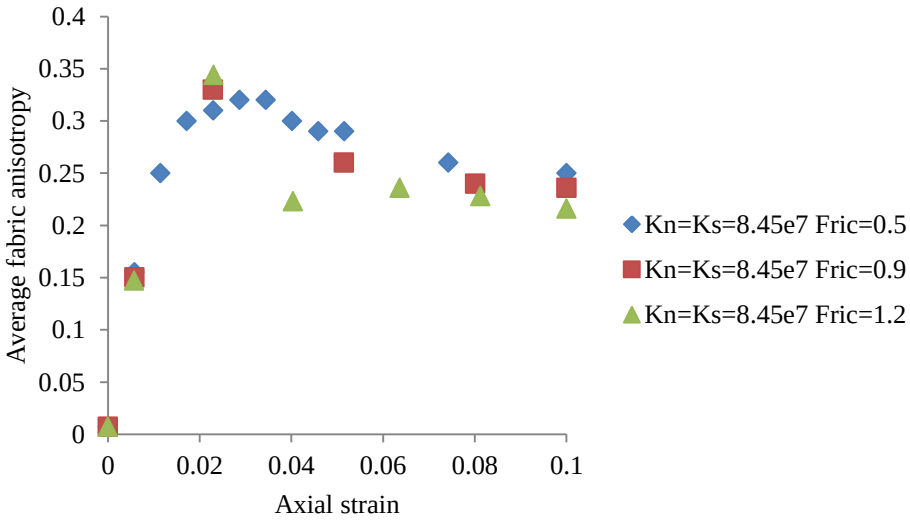

Appendix [3] Figure 23 The sensitivity of sand to the different inter-particle friction when normal and shear stress is $8.45*10^7$ (N/m): Average fabric anisotropy vs. axial strain

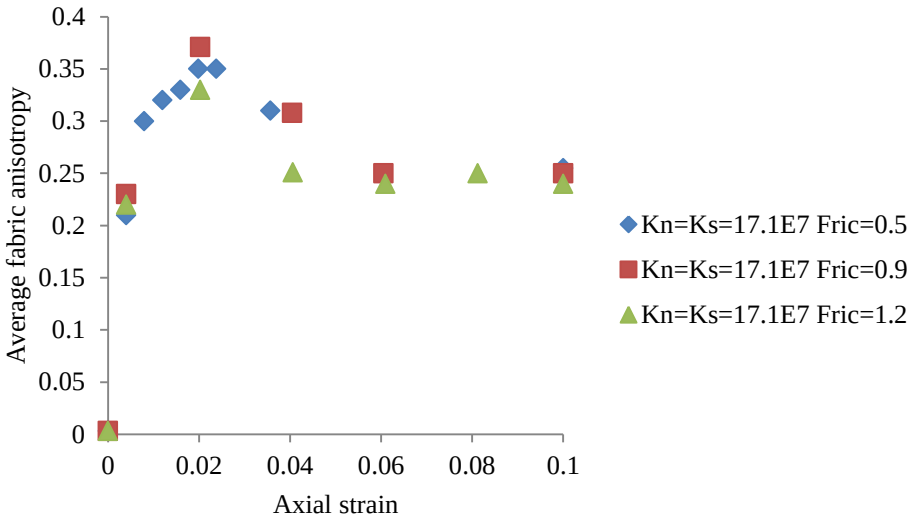

Appendix [3] Figure 24 The sensitivity of sand to the different inter-particle friction when normal and shear stress is $17.1*10^7$ (N/m): Average fabric anisotropy vs. axial strain

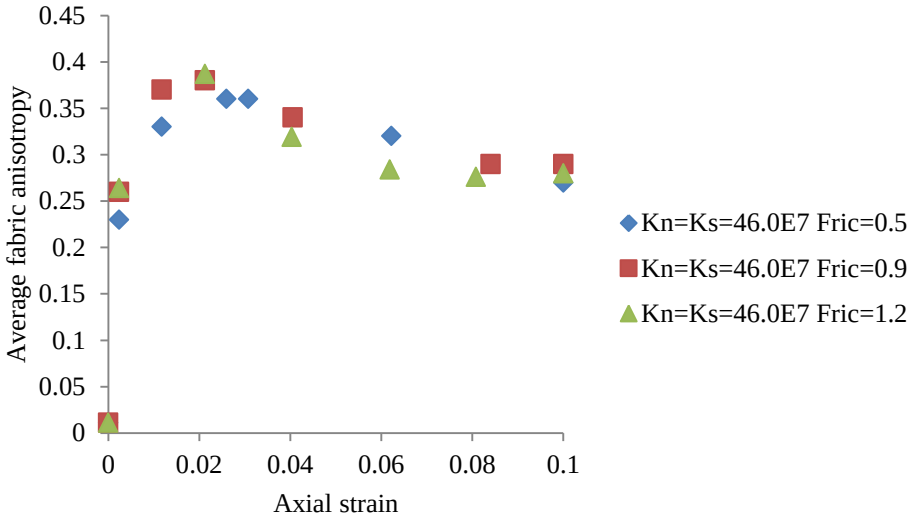

Appendix [3] Figure 25 The sensitivity of sand to the different inter-particle friction when normal and shear stress is $46.0*10^7$ (N/m): Average fabric anisotropy vs. axial strain

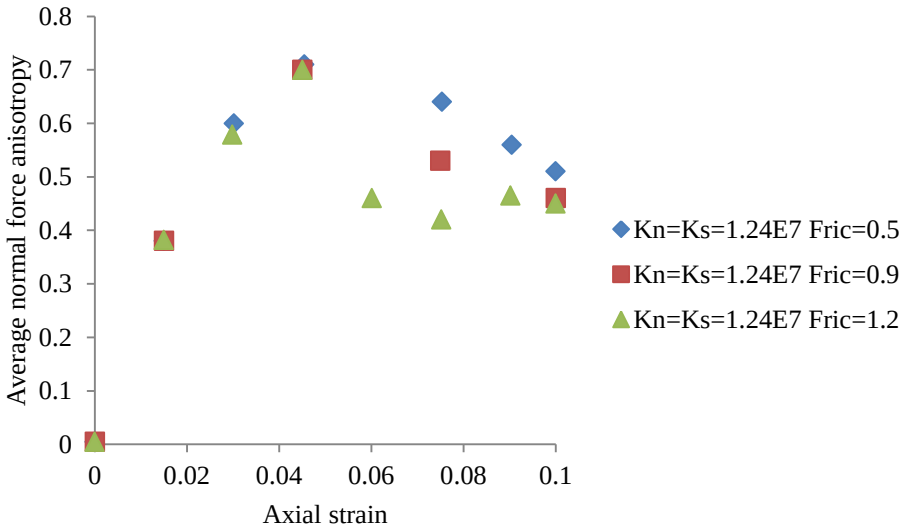

Appendix [3] Figure 26 The sensitivity of sand to the different inter-particle friction when normal and shear stress is $1.24*10^7$ (N/m): Average normal force anisotropy vs. axial strain

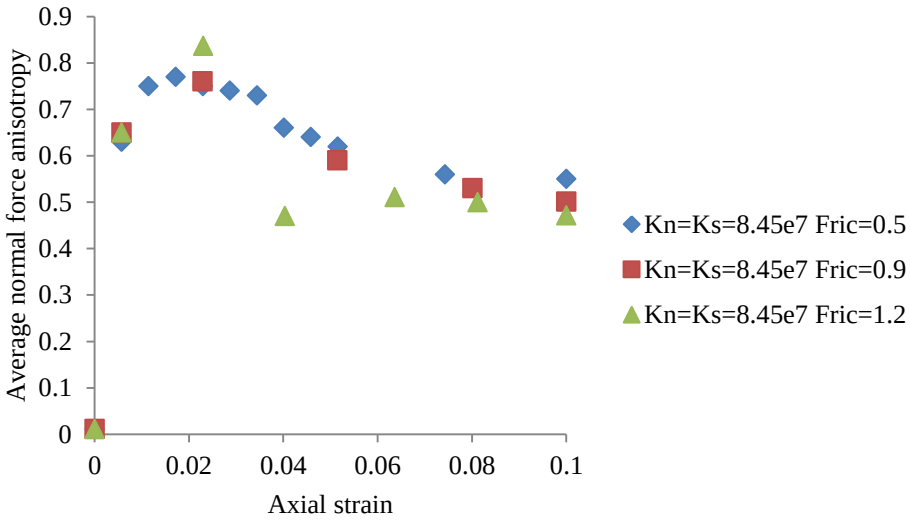

Appendix [3] Figure 27 The sensitivity of sand to the different inter-particle friction when normal and shear stress is $8.45*10^7$ (N/m): Average normal force anisotropy vs. axial strain

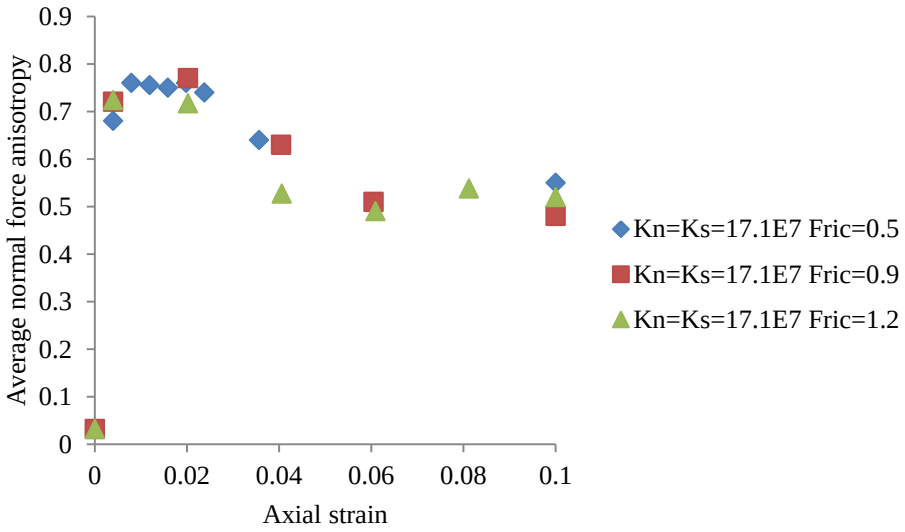

Appendix [3] Figure 28 The sensitivity of sand to the different inter-particle friction when normal and shear stress is $17.1*10^7$ (N/m): Average normal force anisotropy vs. axial strain

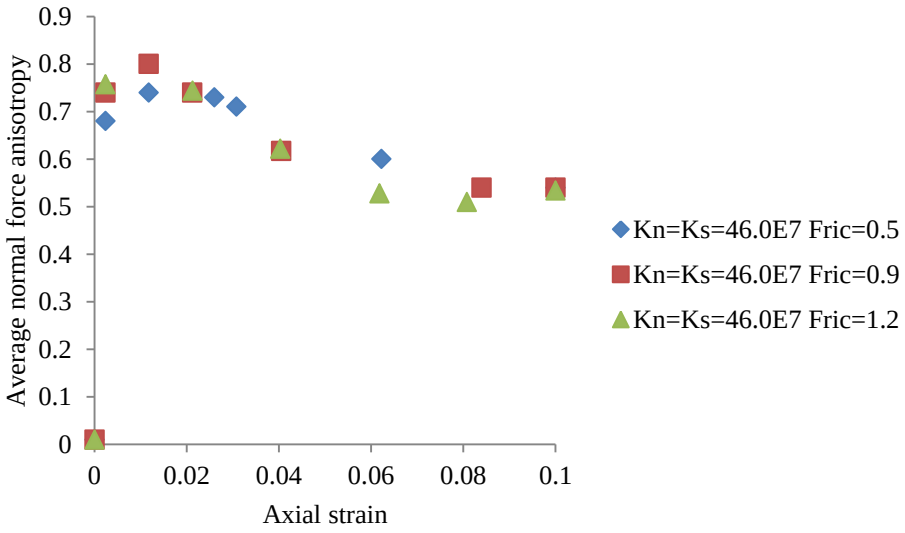

Appendix [3] Figure 29 The sensitivity of sand to the different inter-particle friction when normal and shear stress is $46.0*10^7$ (N/m): Average normal force anisotropy vs. axial strain

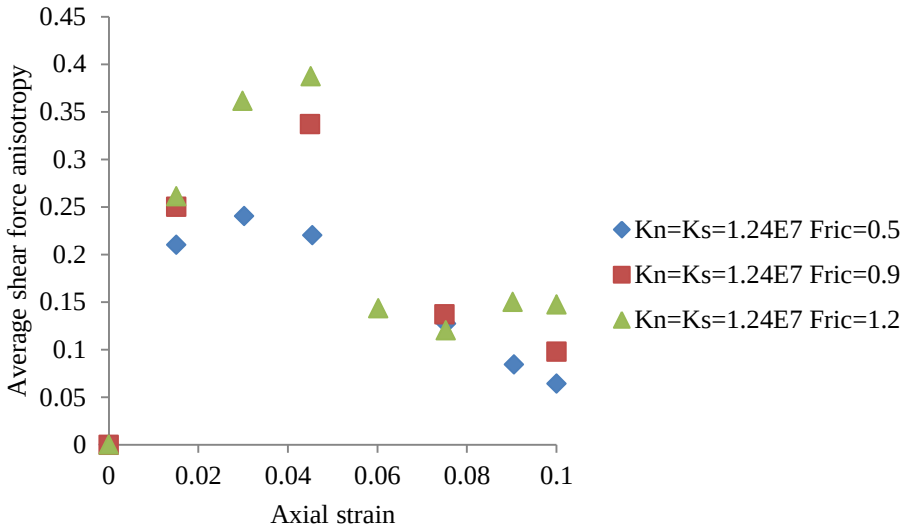

Appendix [3] Figure 30 The sensitivity of sand to the different inter-particle friction when normal and shear stress is $1.24*10^7$ (N/m): Average shear force anisotropy vs. axial strain

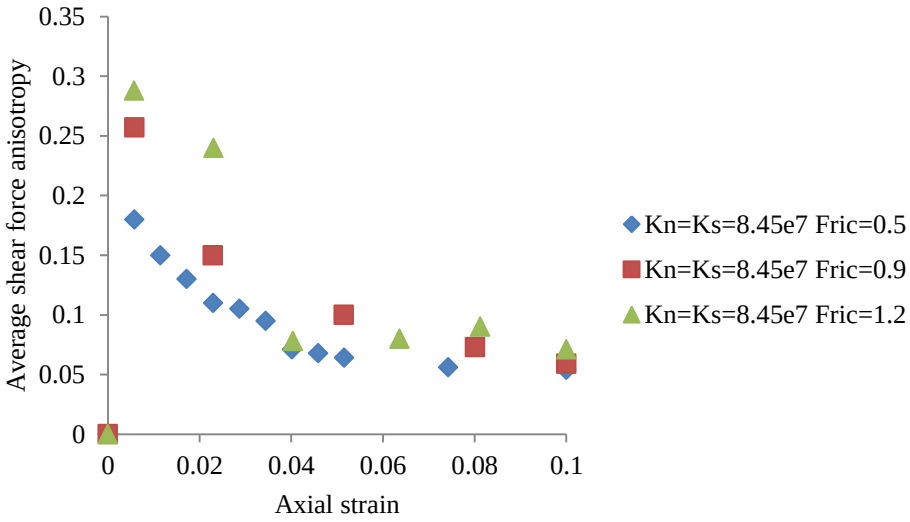

Appendix [3] Figure 31 The sensitivity of sand to the different inter-particle friction when normal and shear stress is $8.45*10^7$ (N/m): Average shear force anisotropy vs. axial strain

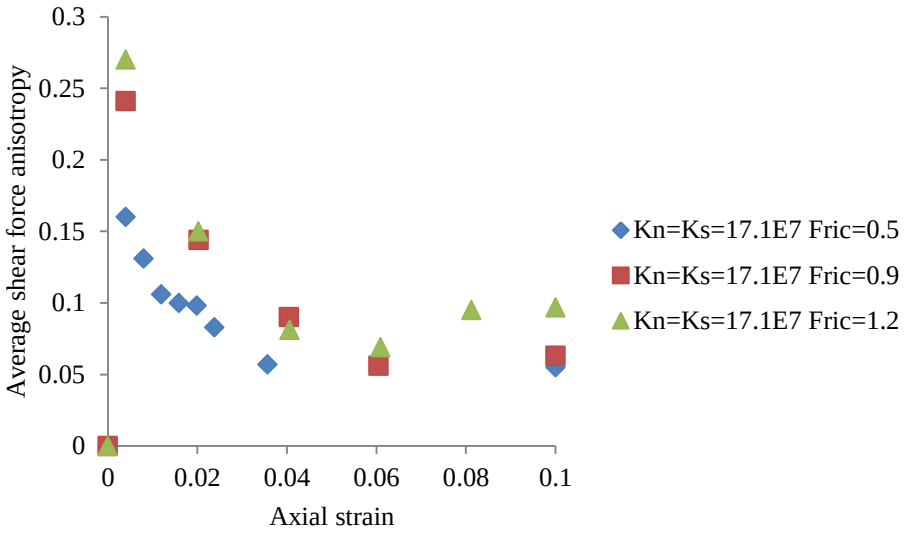

Appendix [3] Figure 32 The sensitivity of sand to the different inter-particle friction when normal and shear stress is $17.1*10^7$ (N/m): Average shear force anisotropy vs. axial strain

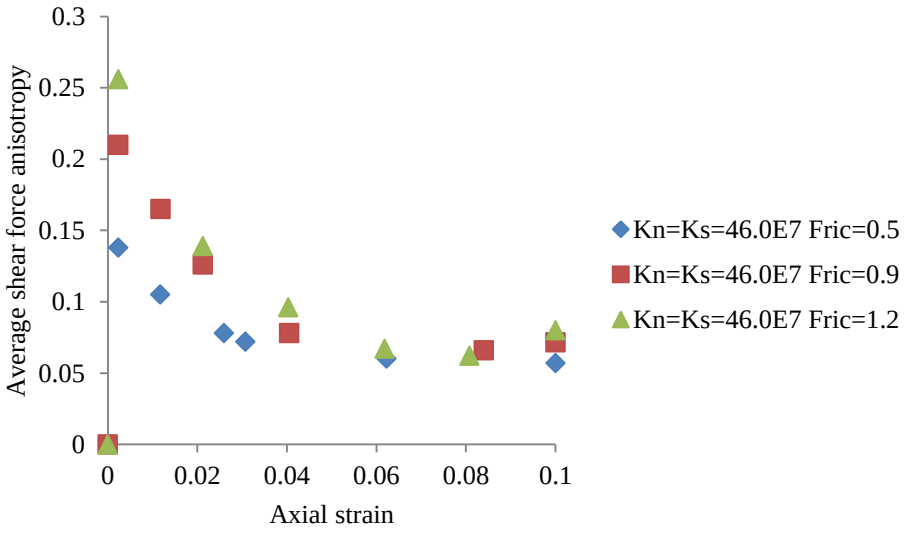

Appendix [3] Figure 33 The sensitivity of sand to the different inter-particle friction when normal and shear stress is $46.0*10^7$ (N/m): Average shear force anisotropy vs. axial strain

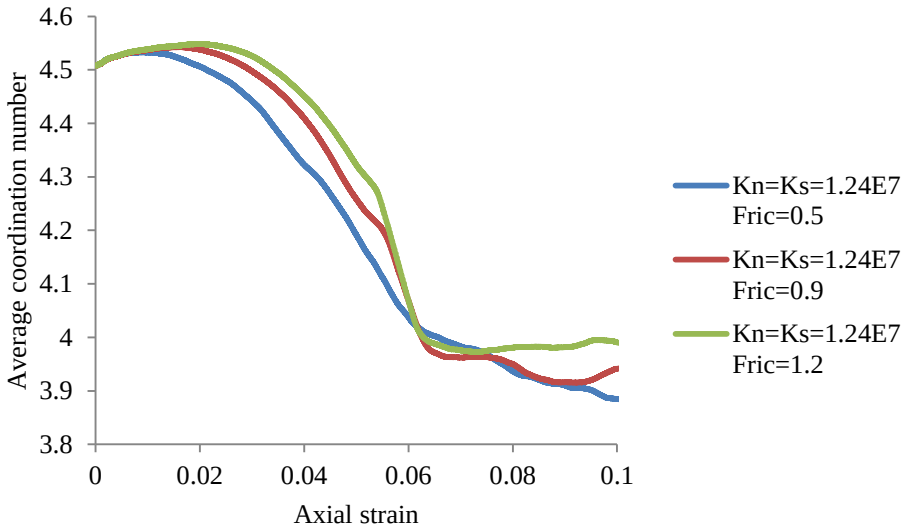

Appendix [3] Figure 34 The sensitivity of sand to the different inter-particle friction when normal and shear stress is $1.24*10^7$ (N/m): Average coordination number vs. axial strain

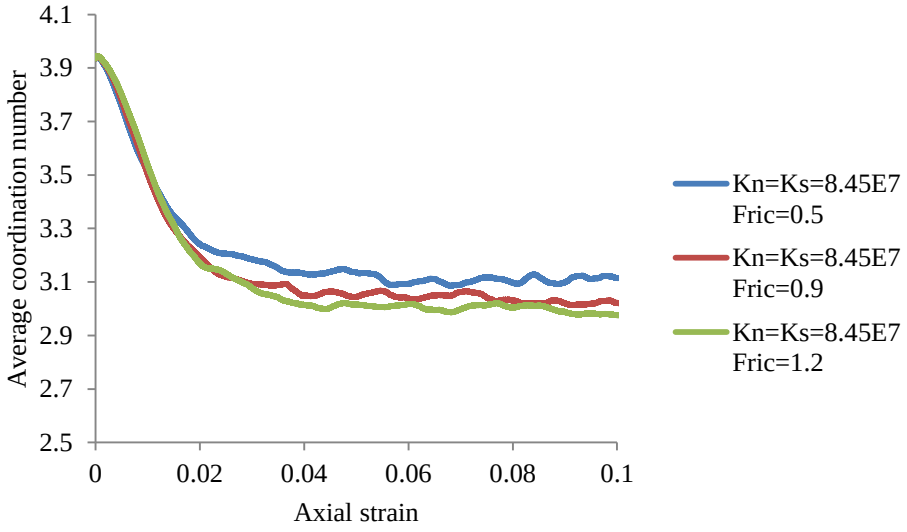

Appendix [3] Figure 35 The sensitivity of sand to the different inter-particle friction when normal and shear stress is $8.45*10^7$ (N/m): Average coordination number vs. axial strain

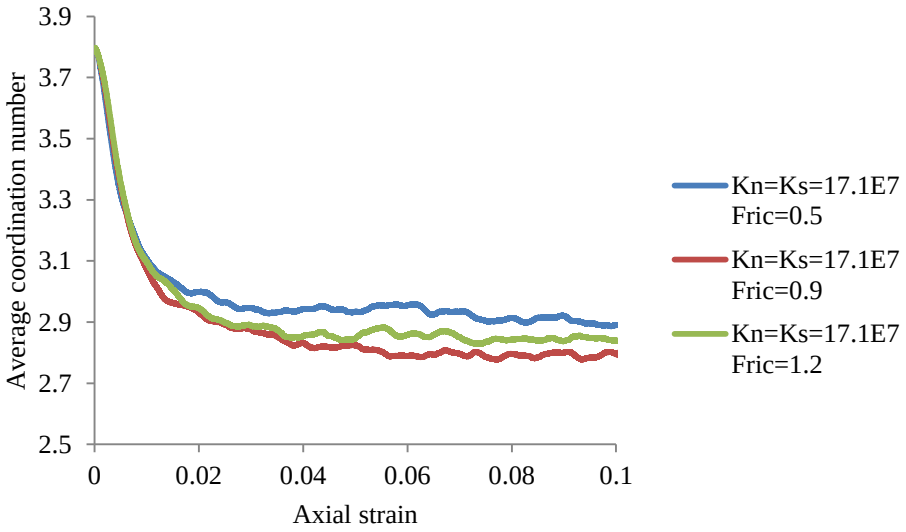

Appendix [3] Figure 36 The sensitivity of sand to the different inter-particle friction when normal and shear stress is $17.1*10^7$ (N/m): Average coordination number vs. axial strain

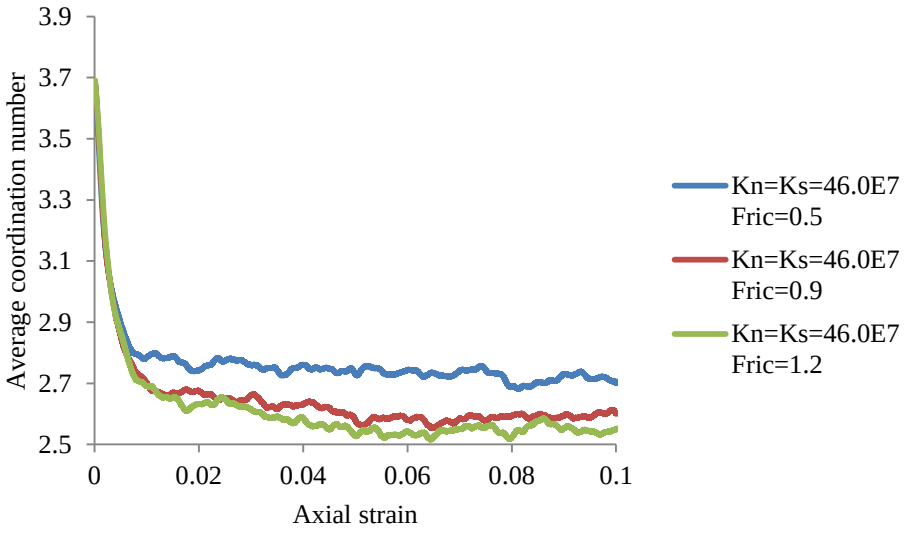

Appendix [3] Figure 37 The sensitivity of sand to the different inter-particle friction when normal and shear stress is $46.0*10^7$ (N/m): Average coordination number vs. axial strain

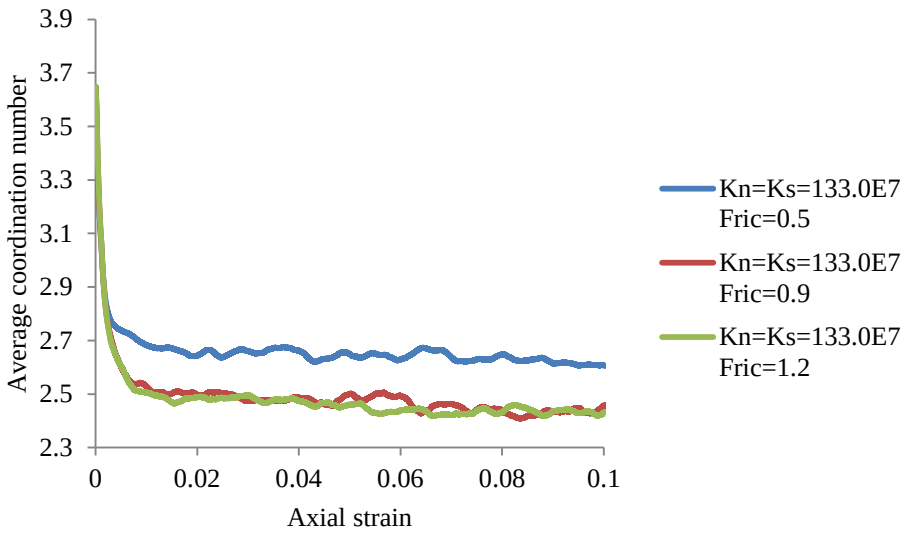

Appendix [3] Figure 38 The sensitivity of sand to the different inter-particle friction when normal and shear stress is $133.0*10^7$ (N/m): Average coordination number vs. axial strain

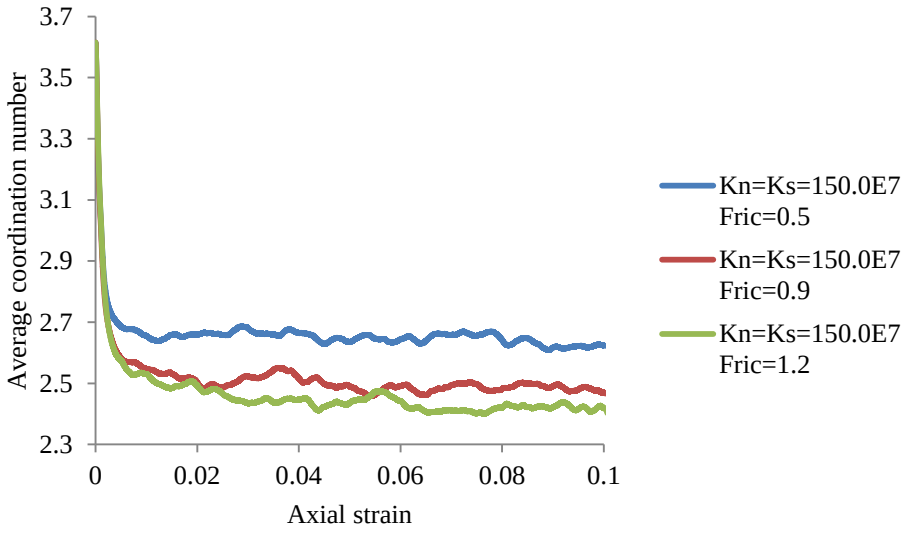

Appendix [3] Figure 39 The sensitivity of sand to the different inter-particle friction when normal and shear stress is $150.0*10^7$ (N/m): Average coordination number vs. axial strain

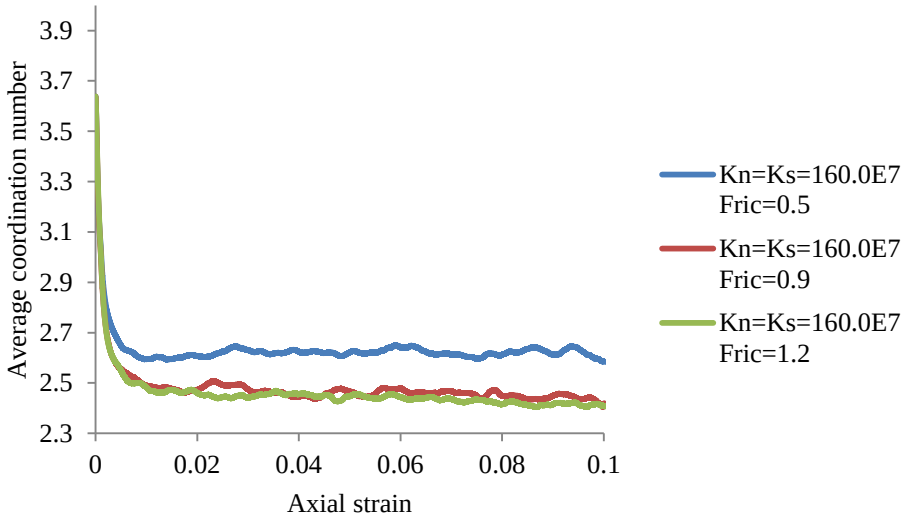

Appendix [3] Figure 40 The sensitivity of sand to the different inter-particle friction when normal and shear stress is 160.0*10^7 (N/m): Average coordination number vs. axial strain

Shear Stiffness (N/m)	1.24*10^7	8.45*10^7	17.1*10^7	46.0*10^7	133.0*10^7	150.0*10^7	160.0*10^7
Normal Stiffness (N/m)	1.24*10^7	8.45*10^7	17.1*10^7	46.0*10^7	133.0*10^7	150.0*10^7	160.0*10^7
Coefficient friction	0.5	0.5	0.5	0.5	0.5	0.5	0.5
E_{50} (P.Strain) (MPa)	5.8	32.0	61.0	162.0	388.0	463.0	476.0
E_{50} (P.Stress) (MPa)	6.0	34.0	64.0	170.0	417.0	494.0	511.0
v_{50} (P.Strain)	0.16	0.21	0.22	0.22	0.26	0.25	0.26
v_{50} (P.Stress)	0.19	0.27	0.28	0.30	0.33	0.33	0.35
σ_{max} (kPa)	200.0	200.0	190.0	180.0	210.0	213.0	213.0
ε_{11} at σ_{max}	0.04	0.01	0.01	0.01	0.01	0.01	0.01
θ(°)	19.5	19.5	18.0	16.6	21.0	21.1	21.1

Appendix [3] Table 8 The sensitivity of sand to the different particle normal stiffness when inter-particle friction is 0.5

Shear Stiffness (N/m)	1.24*10^7	8.45*10^7	17.1*10^7	46.0*10^7	133.0*10^7	150.0*10^7	160.0*10^7
Normal Stiffness (N/m)	1.24*10^7	8.45*10^7	17.1*10^7	46.0*10^7	133.0*10^7	150.0*10^7	160.0*10^7
Coefficient friction	0.9	0.9	0.9	0.9	0.9	0.9	0.9
E_{50} (P.Strain) (MPa)	6.30	35.0	67.0	173.0	444.0	535.0	564.0
E_{50} (P.Stress) (MPa)	6.5	36.0	70.0	181.0	470.0	563.0	590.0
v_{50} (P.Strain)	0.13	0.18	0.20	0.20	0.23	0.22	0.22
v_{50} (P.Stress)	0.15	0.23	0.24	0.25	0.3	0.28	0.28
σ_{max} (kPa)	264.0	264.0	242.0	240.0	277.0	286.0	275.0
ε_{11} at σ_{max}	0.05	0.01	0.007	0.005	0.045	0.003	0.003
θ(°)	26.7	26.7	24.5	24.3	28.0	29.0	28.0

Appendix [3] Table 9 The sensitivity of sand to the different particle normal stiffness when inter-particle friction is 0.9

Shear Stiffness (N/m)	$1.24*10^7$	$8.45*10^7$	$17.1*10_7$	$46.0*10^7$	$133.0*10^7$	$150.0*10^7$	$160.0*10^7$
Normal Stiffness (N/m)	$1.24*10^7$	$8.45*10^7$	$17.1*10_7$	$46.0*10^7$	$133.0*10^7$	$150.0*10^7$	$160.0*10^7$
Coefficient friction	1.2	1.2	1.2	1.2	1.2	1.2	1.2
E_{50} (P.Strain) (MPa)	6.55	35.0	68.0	180.0	478.0	540.0	590.0
E_{50} (P.Stress) (MPa)	6.65	36.0	71.0	186.0	500.0	570.0	610.0
v_{50} (P.Strain)	0.11	0.18	0.19	0.19	0.21	0.22	0.20
v_{50} (P.Stress)	0.13	0.22	0.23	0.23	0.27	0.28	0.27
σ_{max} (kPa)	290.0	290.0	270.0	260.0	305.0	325.0	305.0
ε_{11} at σ_{max}	0.05	0.01	0.007	0.004	0.004	0.003	0.003
θ(°)	29.15	29.15	27.35	26.4	30.4	32.0	30.4

Appendix [3] Table 10 The sensitivity of sand to the different particle normal stiffness when inter-particle friction is 1.2

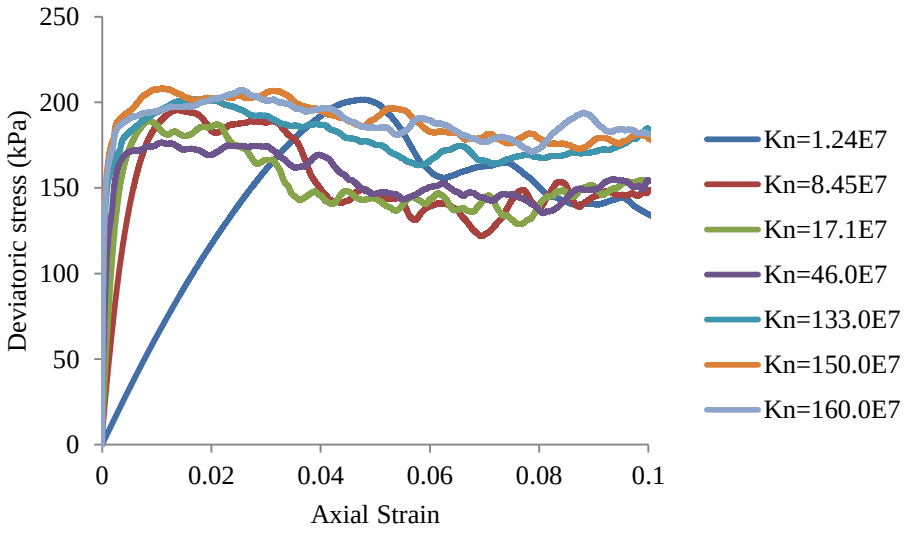

Appendix [3] Figure 41 The sensitivity of sand to the different normal particle stiffness when inter-particle friction is 0.5- deviatoric stress vs. axial strain

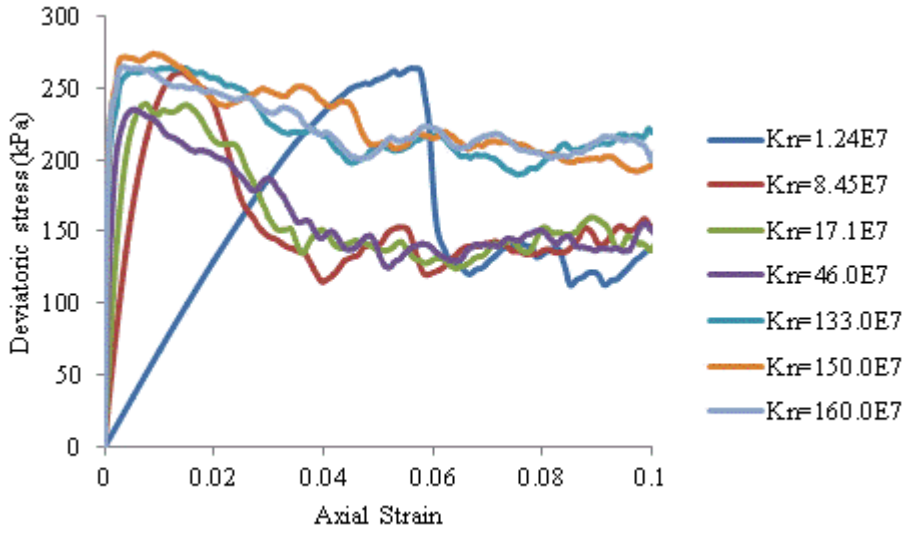

Appendix [3] Figure 42 The sensitivity of sand to the different normal particle stiffness when inter-particle friction is 0.9: deviatoric stress vs. axial strain

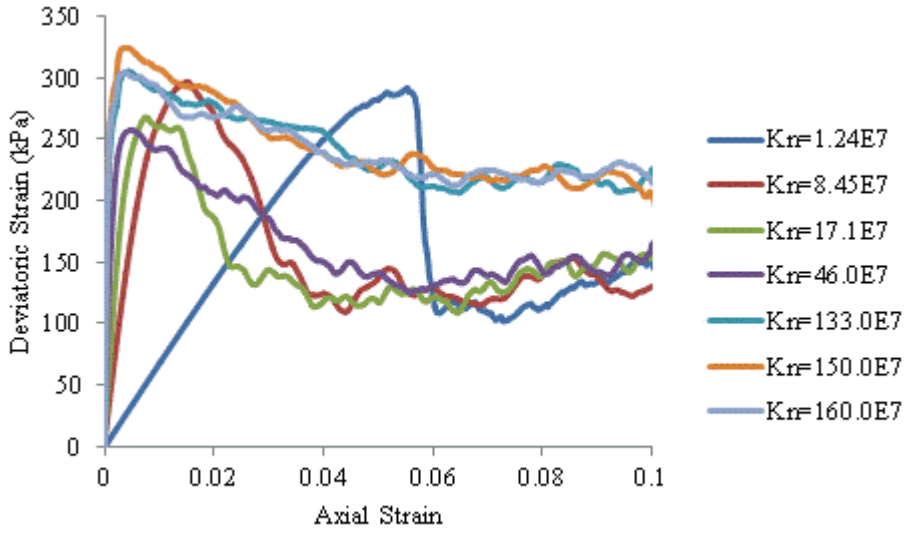

Appendix [3] Figure 43 The sensitivity of sand to the different normal particle stiffness when inter-particle friction is 1.2- deviatoric stress vs. axial strain

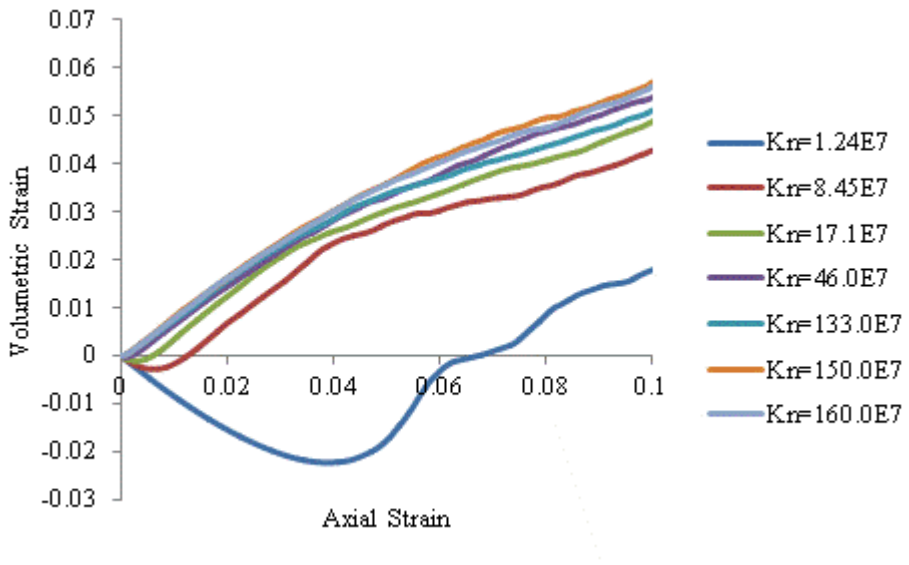

Appendix [3] Figure 44 The sensitivity of sand to the different normal particle stiffness when inter-particle friction is 0.5- volumetric strain vs. axial strain

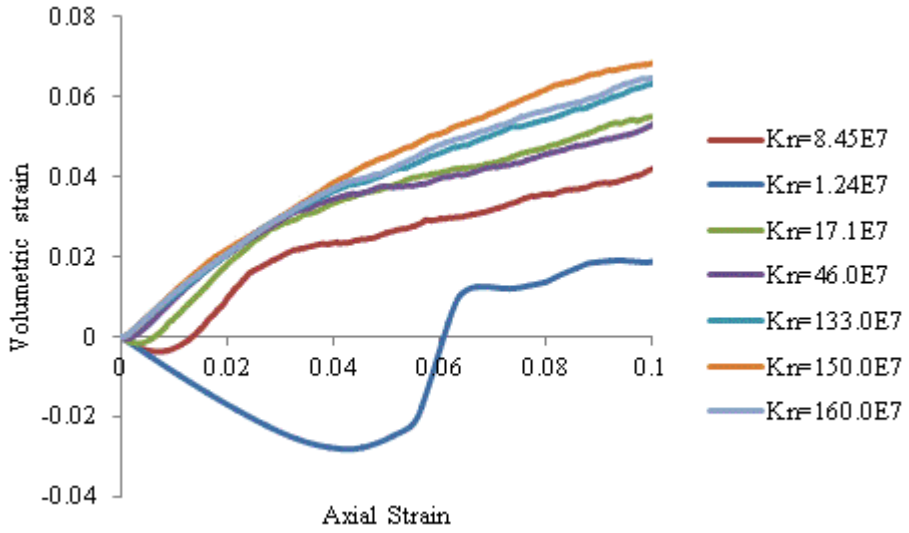

Appendix [3] Figure 45 The sensitivity of sand to the different normal particle stiffness when inter-particle friction is 0.9: volumetric strain vs. axial strain

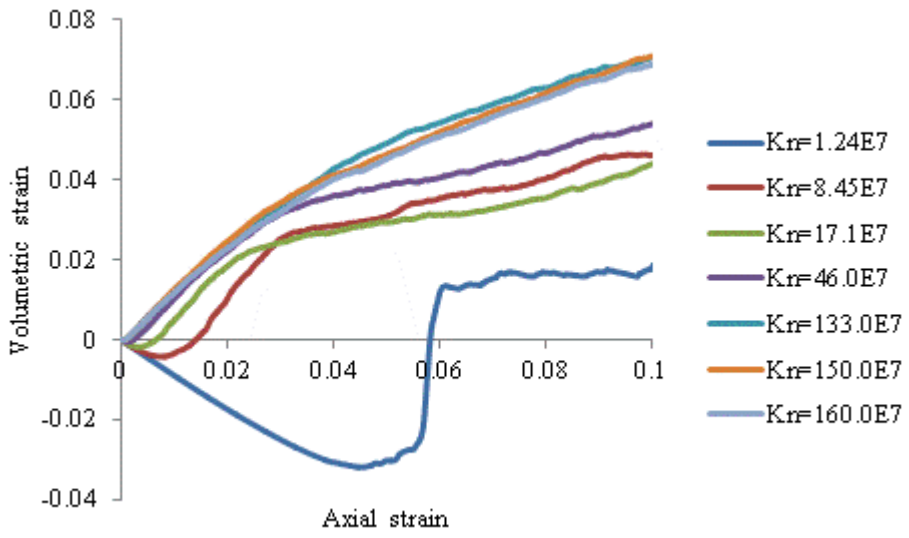

Appendix [3] Figure 46 The sensitivity of sand to the different normal particle stiffness when inter-particle friction is 1.2- volumetric strain vs. axial strain

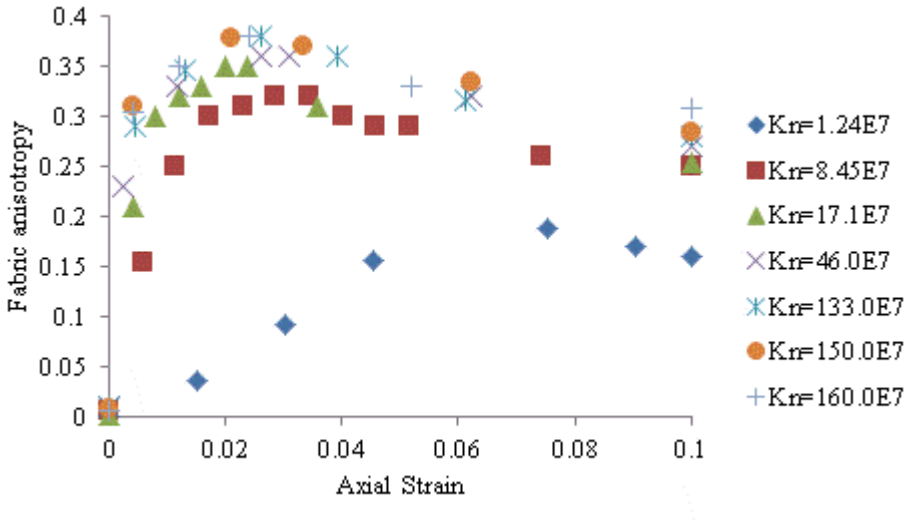

Appendix [3] Figure 47 The sensitivity of sand to the different normal particle stiffness when inter-particle friction is 0.5- average fabric anisotropy vs. axial strain

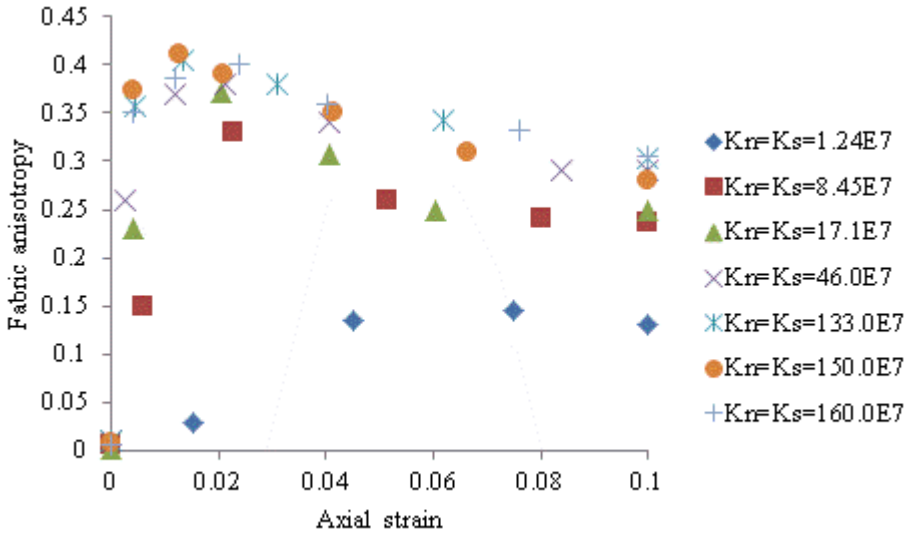

Appendix [3] Figure 48 The sensitivity of sand to the different normal particle stiffness when inter-particle friction is 0.9: average fabric anisotropy vs. axial strain

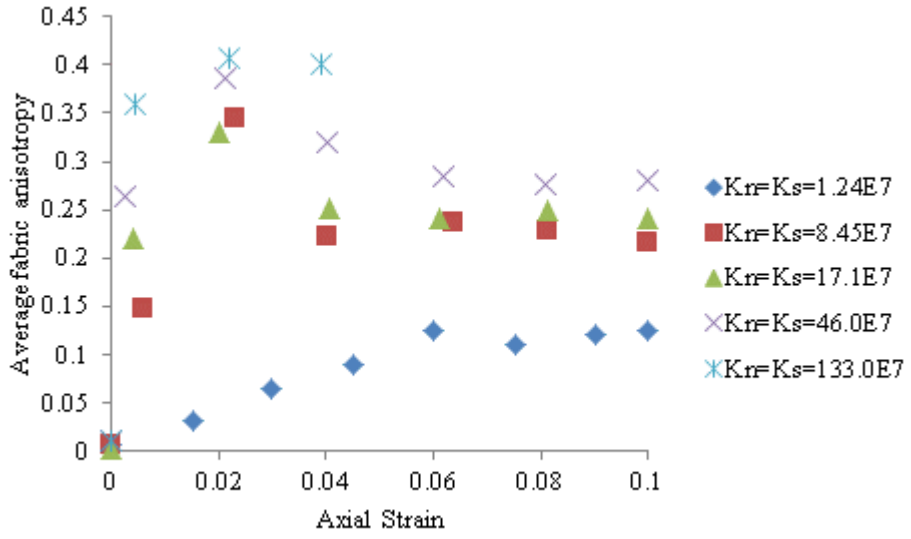

Appendix [3] Figure 49 The sensitivity of sand to the different normal particle stiffness when inter-particle friction is 1.2- average fabric anisotropy vs. axial

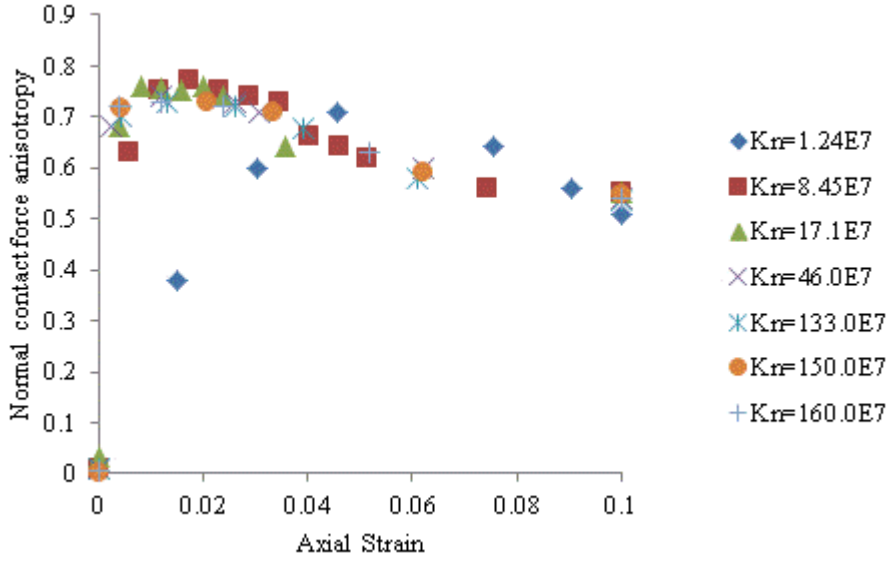

Appendix [3] Figure 50 The sensitivity of sand to the different normal particle stiffness when inter-particle friction is 0.5- average normal force anisotropy vs. axial strain

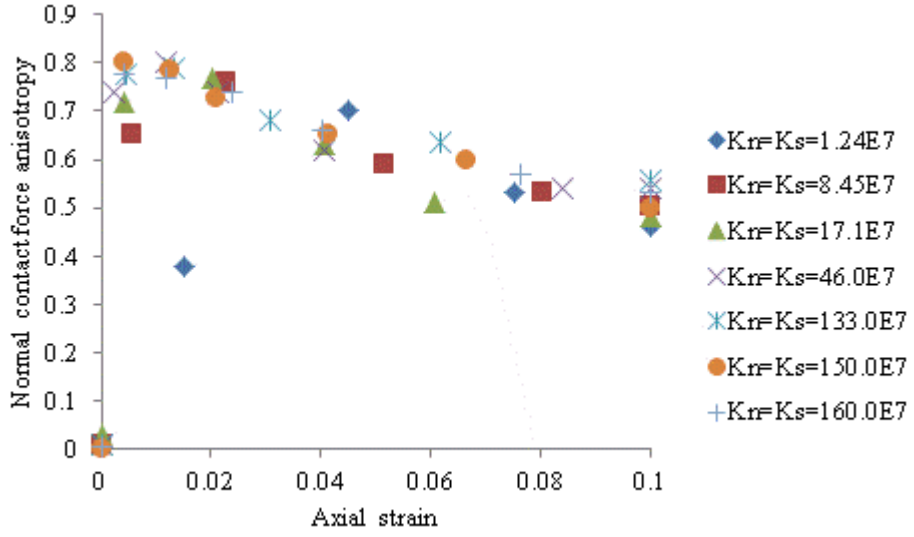

Appendix [3] Figure 51 The sensitivity of sand to the different normal particle stiffness when inter-particle friction is 0.9: average normal force anisotropy vs. axial strain

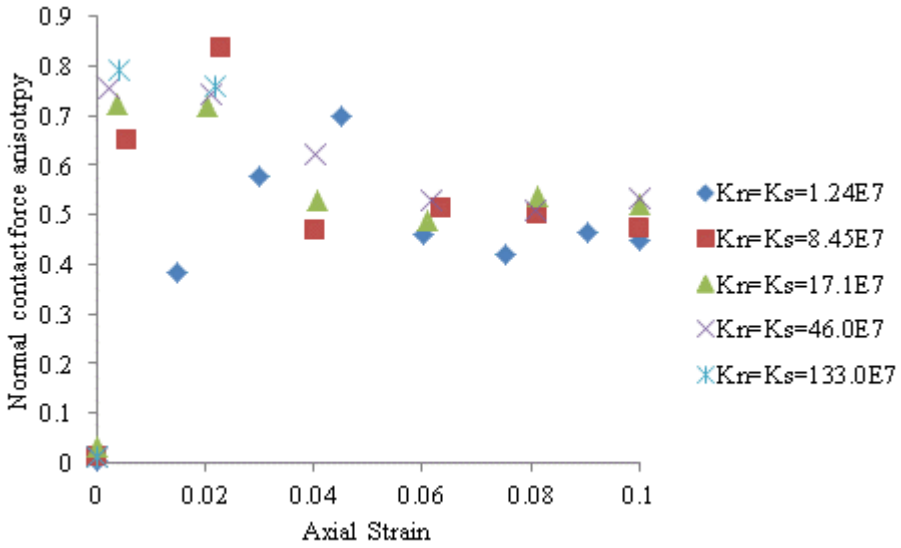

Appendix [3] Figure 52 The sensitivity of sand to the different normal particle stiffness when inter-particle friction is 1.2- average normal force anisotropy vs. axial strain

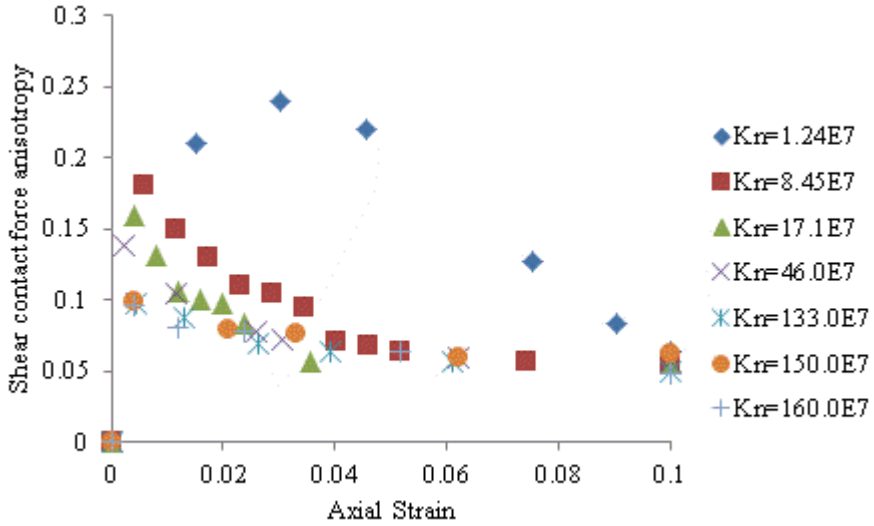

Appendix [3] Figure 53 The sensitivity of sand to the different normal particle stiffness when inter-particle friction is 0.5- average shear force anisotropy vs. axial strain

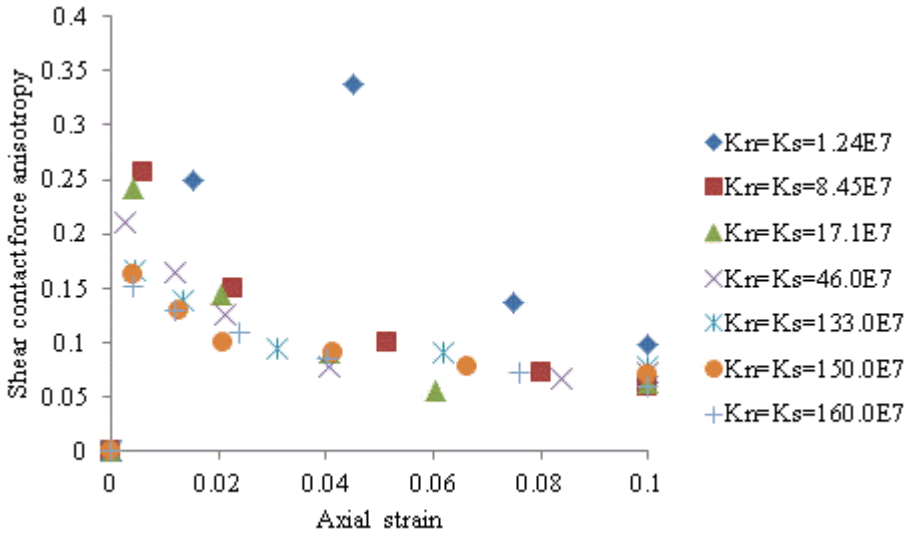

Appendix [3] Figure 54 The sensitivity of sand to the different normal particle stiffness when inter-particle friction is 0.9: average shear force anisotropy vs. axial strain

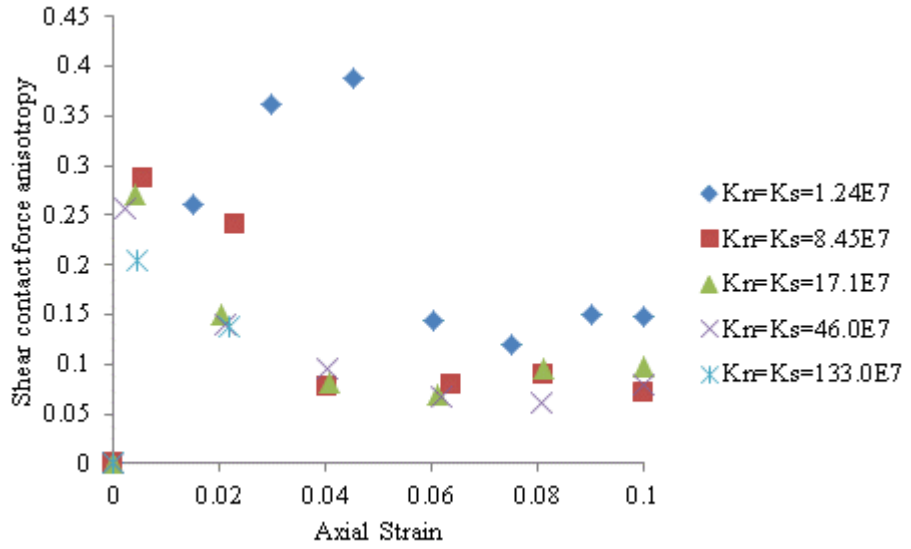

Appendix [3] Figure 55 The sensitivity of sand to the different normal particle stiffness when inter-particle friction is 1.2- average shear force anisotropy vs. axial strain

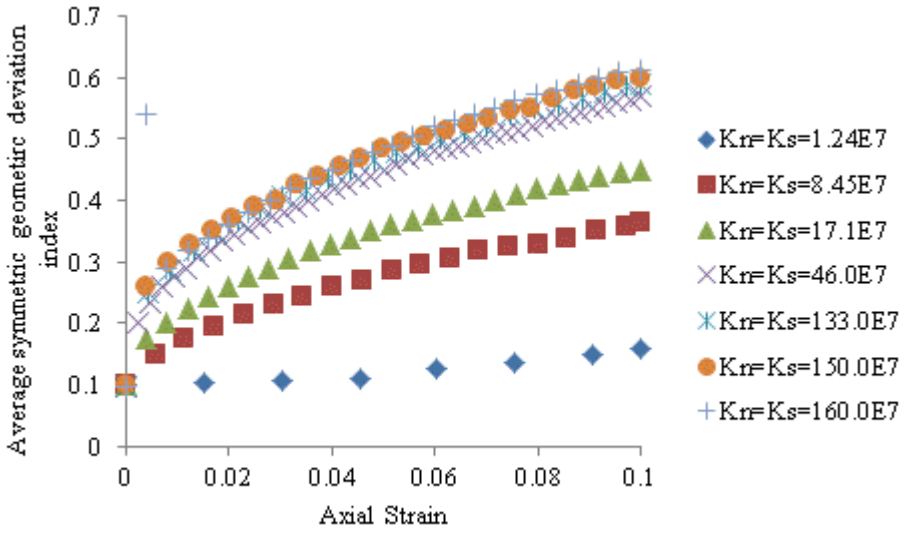

Appendix [3] Figure 56 The sensitivity of sand to the different normal particle stiffness when inter-particle friction is 0.5- average symmetric geometric deviation index vs. axial strain

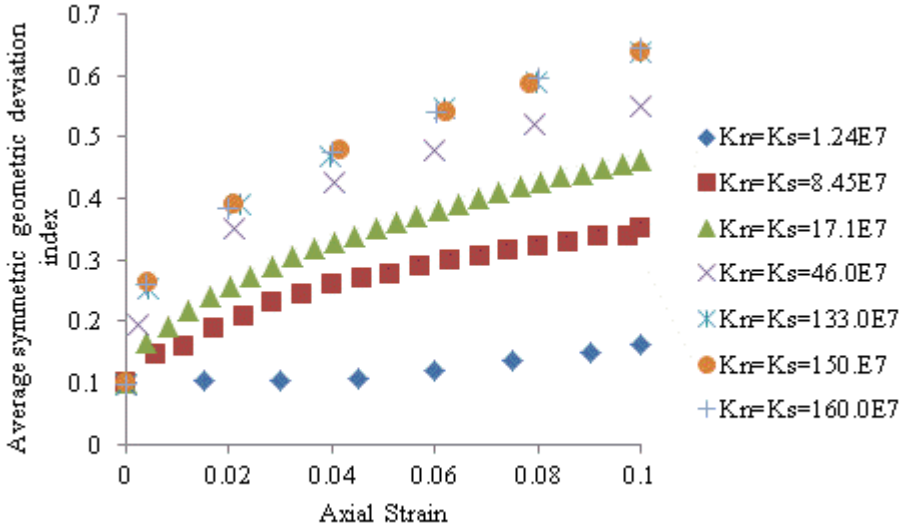

Appendix [3] Figure 57 The sensitivity of sand to the different normal particle stiffness when inter-particle friction is 0.9: average symmetric geometric deviation index vs. axial strain

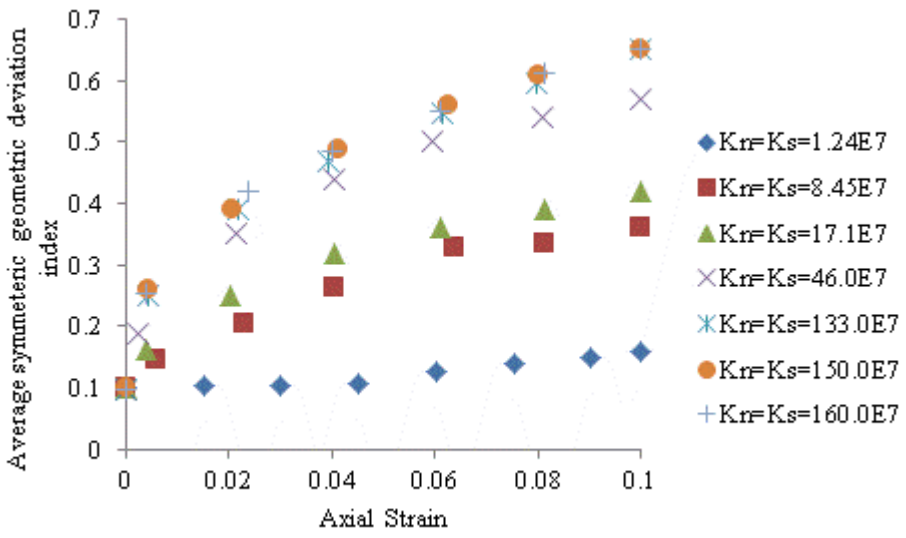

Appendix [3] Figure 58 The sensitivity of sand to the different normal particle stiffness when inter-particle friction is 1.2- average symmetric geometric deviation index vs. axial strain

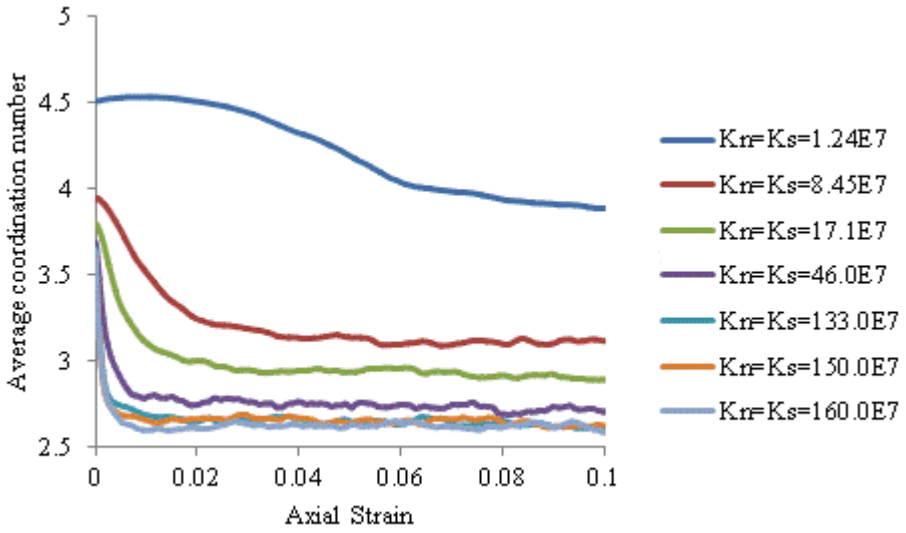

Appendix [3] Figure 59 The sensitivity of sand to the different normal particle stiffness when inter-particle friction is 0.5- average coordination number vs. axial strain

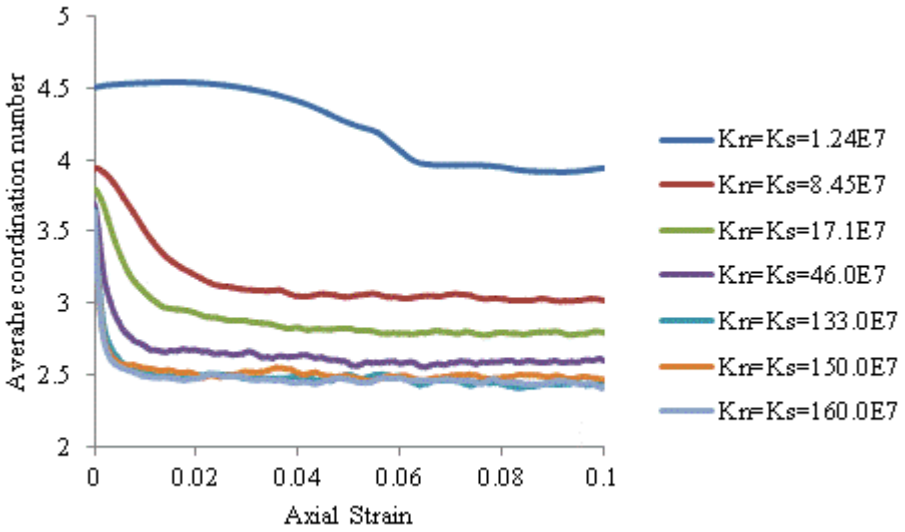

Appendix [3] Figure 60 The sensitivity of sand to the different normal particle stiffness when inter-particle friction is 0.9: average coordination number vs. axial strain

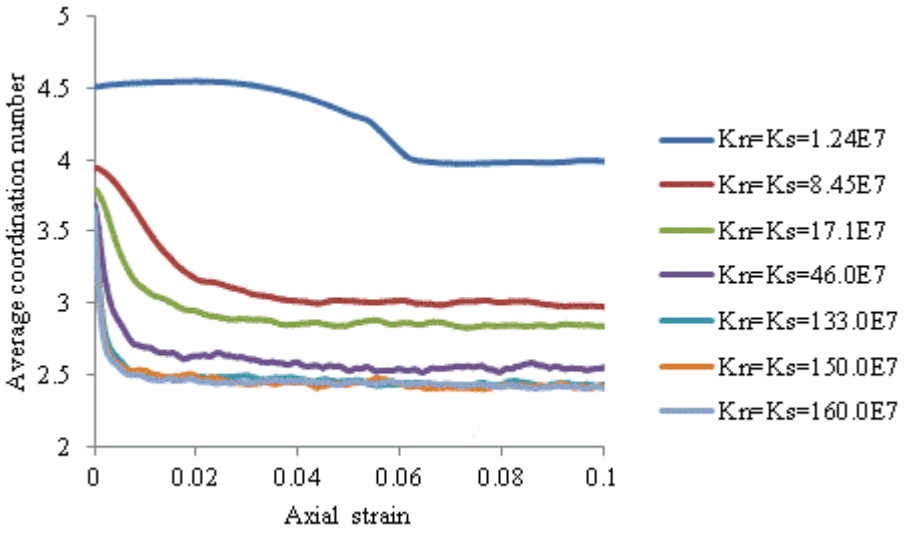

Appendix [3] Figure 61 The sensitivity of sand to the different normal particle stiffness when inter-particle friction is 1.2- average coordination number vs. axial strain

Normal Stiffness (N/m)	$1.24*10^7$	$1.24*10^7$
Kn/Ks	1.0	0.5
Coefficient friction	0.5	0.5
E_{50} (P.Strain) (MPa)	5.8	5.3
E_{50} (P.Stress) (MPa)	6.0	5.5
v_{50} (P.Strain)	0.16	0.21
v_{50} (P.Stress)	0.19	0.26
σ_{max} (kPa)	200.0	190.0
ε_{11} at σ_{max}	0.04	0.05
θ(°)	19.5	18.0

Appendix [3] Table 11 The sensitivity of sand to the different shear particle stiffness

Normal Stiffness (N/m)	$1.24*10^7$	$1.24*10^7$
Kn/Ks	1.0	0.5
Coefficient friction	0.9	0.9
E_{50} (P.Strain) (MPa)	6.30	5.54
E_{50} (P.Stress) (MPa)	6.5	5.76
v_{50} (P.Strain)	0.13	0.20
v_{50} (P.Stress)	0.15	0.25
σ_{max} (kPa)	264.0	250.0
ε_{11} at σ_{max}	0.05	0.05
θ(°)	26.7	25.4

Appendix [3] Table 12 The sensitivity of sand to the different shear particle stiffness

Normal Stiffness (N/m)	$1.24*10^7$	$1.24*10^7$
Kn/Ks	1.0	0.5
Coefficient friction	1.2	1.2
E_{50} (P.Strain) (MPa)	6.55	5.60
E_{50} (P.Stress) (MPa)	6.65	5.80
v_{50} (P.Strain)	0.11	0.19
v_{50} (P.Stress)	0.13	0.24
σ_{max} (kPa)	290.0	290.0
ε_{11} at σ_{max}	0.05	0.05
θ(°)	29.15	29.15

Appendix [3] Table 13 The sensitivity of sand to the different shear particle stiffness

Normal Stiffness (N/m)	$8.45*10^7$	$8.45*10^7$
Kn/Ks	1.0	0.5
Coefficient friction	0.5	0.5
E_{50} (P.Strain) (MPa)	32.0	27.0
E_{50} (P.Stress) (MPa)	34.0	29.0
v_{50} (P.Strain)	0.21	0.25
v_{50} (P.Stress)	0.27	0.29
σ_{max} (kPa)	200.0	190.0
ε_{11} at σ_{max}	0.01	0.01
θ(°)	19.5	18.0

Appendix [3] Table 14 The sensitivity of sand to the different shear particle stiffness

Normal Stiffness (N/m)	$8.45*10^7$	$8.45*10^7$
Kn/Ks	1.0	0.5
Coefficient friction	0.9	0.9
E_{50} (P.Strain) (MPa)	35.0	28.0
E_{50} (P.Stress) (MPa)	36.0	30.0
v_{50} (P.Strain)	0.18	0.24
v_{50} (P.Stress)	0.23	0.32
σ_{max} (kPa)	263.0	250.0
ε_{11} at σ_{max}	0.01	0.01
θ(°)	26.7	25.4

Appendix [3] Table 15 The sensitivity of sand to the different shear particle stiffness

Normal Stiffness (N/m)	$8.45*10^7$	$8.45*10^7$
Kn/Ks	1.0	0.5
Coefficient friction	1.2	1.2
E_{50} (P.Strain) (MPa)	35.0	29.0
E_{50} (P.Stress) (MPa)	36.0	31.0
v_{50} (P.Strain)	0.18	0.24
v_{50} (P.Stress)	0.22	0.31
σ_{max} (kPa)	290.0	280.0
ε_{11} at σ_{max}	0.01	0.01
θ(°)	29.15	29.15

Appendix [3] Table 16 The sensitivity of sand to the different shear particle stiffness

Normal Stiffness (N/m)	$17.1*10^7$	$17.1*10^7$
Kn/Ks	1.0	0.5
Coefficient friction	0.5	0.5
E_{50} (P.Strain) (MPa)	61.0	56.0
E_{50} (P.Stress) (MPa)	64.0	60.0
v_{50} (P.Strain)	0.22	0.26
v_{50} (P.Stress)	0.28	0.35
σ_{max} (kPa)	190.0	190.0
ε_{11} at σ_{max}	0.01	0.007
θ(°)	18.0	18.0

Appendix [3] Table 17 The sensitivity of sand to the different shear particle stiffness

Normal Stiffness (N/m)	$17.1*10^7$	$17.1*10^7$
Kn/Ks	1.0	0.5
Coefficient friction	0.9	0.9
E_{50} (P.Strain) (MPa)	67.0	60.0
E_{50} (P.Stress) (MPa)	70.0	63.0
v_{50} (P.Strain)	0.20	0.25
v_{50} (P.Stress)	0.24	0.32
σ_{max} (kPa)	242.0	250.0
ε_{11} at σ_{max}	0.007	0.01
θ(°)	24.5	25.3

Appendix [3] Table 18 The sensitivity of sand to the different shear particle stiffness

Normal Stiffness (N/m)	$17.1*10^7$	$17.1*10^7$
Kn/Ks	1.0	0.5
Coefficient friction	1.2	1.2
E_{50} (P.Strain) (MPa)	68.0	60.0
E_{50} (P.Stress) (MPa)	71.0	63.0
v_{50} (P.Strain)	0.19	0.25
v_{50} (P.Stress)	0.23	0.32
σ_{max} (kPa)	270.0	280.0
ε_{11} at σ_{max}	0.007	0.01
θ(°)	27.3	28.3

Appendix [3] Table 19 The sensitivity of sand to the different shear particle stiffness

Normal Stiffness (N/m)	$46.0*10^7$	$46.0*10^7$
Kn/Ks	1.0	0.5
Coefficient friction	0.5	0.5
E_{50} (P.Strain) (MPa)	162.0	128.0
E_{50} (P.Stress) (MPa)	170.0	140.0
v_{50} (P.Strain)	0.22	0.28
v_{50} (P.Stress)	0.30	0.4
σ_{max} (kPa)	180.0	185.0
ε_{11} at σ_{max}	0.01	0.004
θ(°)	16.6	17.3

Appendix [3] Table 20 The sensitivity of sand to the different shear particle stiffness

Normal Stiffness (N/m)	$46.0*10^7$	$46.0*10^7$
Kn/Ks	1.0	0.5
Coefficient friction	0.9	0.9
E_{50} (P.Strain) (MPa)	173.0	141.0
E_{50} (P.Stress) (MPa)	181.0	151.0
v_{50} (P.Strain)	0.20	0.26
v_{50} (P.Stress)	0.25	0.35
σ_{max} (kPa)	240.0	235.0
ε_{11} at σ_{max}	0.005	0.006
θ(°)	24.3	23.7

Appendix [3] Table 21 The sensitivity of sand to the different shear particle stiffness

Normal Stiffness (N/m)	$46.0*10^7$	$46.0*10^7$
Kn/Ks	1.0	0.5
Coefficient friction	1.2	1.2
E_{50} (P.Strain) (MPa)	180.0	143.0
E_{50} (P.Stress) (MPa)	186.0	153.0
v_{50} (P.Strain)	0.19	0.26
v_{50} (P.Stress)	0.23	0.35
σ_{max} (kPa)	260.0	270.0
ε_{11} at σ_{max}	0.004	0.006
θ(°)	26.4	27.35

Appendix [3] Table 22 The sensitivity of sand to the different shear particle stiffness

Normal Stiffness (N/m)	$133.0*10^7$	$133.0*10^7$
Kn/Ks	1.0	0.5
Coefficient friction	0.5	0.5
E_{50} (P.Strain) (MPa)	388.0	353.0
E_{50} (P.Stress) (MPa)	417.0	380.0
v_{50} (P.Strain)	0.26	0.29
v_{50} (P.Stress)	0.33	0.38
σ_{max} (kPa)	210.0	220.0
ε_{11} at σ_{max}	0.01	0.003
θ(°)	21.0	22.0

Appendix [3] Table 23 The sensitivity of sand to the different shear particle stiffness

Normal Stiffness (N/m)	$133.0*10^7$	$133.0*10^7$
Kn/Ks	1.0	0.5
Coefficient friction	0.9	0.9
E_{50} (P.Strain) (MPa)	444.0	416.0
E_{50} (P.Stress) (MPa)	470.0	445.0
v_{50} (P.Strain)	0.23	0.25
v_{50} (P.Stress)	0.3	0.34
σ_{max} (kPa)	277.0	270.0
ε_{11} at σ_{max}	0.045	0.003
θ(°)	28.0	27.3

Appendix [3] Table 24 The sensitivity of sand to the different shear particle stiffness

Normal Stiffness (N/m)	$133.0*10^7$	$133.0*10^7$
Kn/Ks	1.0	0.5
Coefficient friction	1.2	1.2
E_{50} (P.Strain) (MPa)	478.0	417.0
E_{50} (P.Stress) (MPa)	500.0	450.0
v_{50} (P.Strain)	0.21	0.26
v_{50} (P.Stress)	0.27	0.35
σ_{max} (kPa)	305.0	320.0
ε_{11} at σ_{max}	0.004	0.003
θ(°)	30.4	31.6

Appendix [3] Table 25 The sensitivity of sand to the different shear particle stiffness

Normal Stiffness (N/m)	$150.0*10^7$	$150.0*10^7$
Kn/Ks	1.0	0.5
Coefficient friction	0.5	0.5
E_{50} (P.Strain) (MPa)	463.0	380.0
E_{50} (P.Stress) (MPa)	494.0	420.0
v_{50} (P.Strain)	0.25	0.3
v_{50} (P.Stress)	0.33	0.42
σ_{max} (kPa)	213.0	220.0
ε_{11} at σ_{max}	0.01	0.002
θ(°)	21.2	22.0

Appendix [3] Table 26 The sensitivity of sand to the different shear particle stiffness

Normal Stiffness (N/m)	$150.0*10^7$	$150.0*10^7$
Kn/Ks	1.0	0.5
Coefficient friction	0.9	0.9
E_{50} (P.Strain) (MPa)	535.0	445.0
E_{50} (P.Stress) (MPa)	563.0	480.0
v_{50} (P.Strain)	0.22	0.26
v_{50} (P.Stress)	0.28	0.36
σ_{max} (kPa)	286.0	280.0
ε_{11} at σ_{max}	0.003	0.003
θ(°)	29.0	28.3

Appendix [3] Table 27 The sensitivity of sand to the different shear particle stiffness

Normal Stiffness (N/m)	$150.0*10^7$	$150.0*10^7$
Kn/Ks	1.0	0.5
Coefficient friction	1.2	1.2
E_{50} (P.Strain) (MPa)	540.0	447.0
E_{50} (P.Stress) (MPa)	570.0	480.0
v_{50} (P.Strain)	0.22	0.27
v_{50} (P.Stress)	0.28	0.37
σ_{max} (kPa)	325.0	330.0
ε_{11} at σ_{max}	0.003	0.003
θ(°)	32.0	32.3

Appendix [3] Table 28 The sensitivity of sand to the different shear particle stiffness

Normal Stiffness (N/m)	$160.0*10^7$	$160.0*10^7$
Kn/Ks	1.0	0.5
Coefficient friction	0.5	0.5
E_{50} (P.Strain) (MPa)	476.0	440.0
E_{50} (P.Stress) (MPa)	511.0	480.0
v_{50} (P.Strain)	0.26	0.28
v_{50} (P.Stress)	0.35	0.40
σ_{max} (kPa)	213.0	220.0
ε_{11} at σ_{max}	0.01	0.002
θ(°)	21.2	22.0

Appendix [3] Table 29 The sensitivity of sand to the different shear particle stiffness

Normal Stiffness (N/m)	$160.0*10^7$	$160.0*10^7$
Kn/Ks	1.0	0.5
Coefficient friction	0.9	0.9
E_{50} (P.Strain) (MPa)	564.0	500.0
E_{50} (P.Stress) (MPa)	590.0	540.0
v_{50} (P.Strain)	0.22	0.26
v_{50} (P.Stress)	0.28	0.35
σ_{max} (kPa)	275.0	280.0
ε_{11} at σ_{max}	0.003	0.002
θ(°)	28.0	28.2

Appendix [3] Table 30 The sensitivity of sand to the different shear particle stiffness

Normal Stiffness (N/m)	$160.0*10^7$	$160.0*10^7$
Kn/Ks	1.0	0.5
Coefficient friction	1.2	1.2
E_{50} (P.Strain) (MPa)	590.0	516.0
E_{50} (P.Stress) (MPa)	610.0	550.0
v_{50} (P.Strain)	0.20	0.25
v_{50} (P.Stress)	0.27	0.34
σ_{max} (kPa)	305.0	330.0
ε_{11} at σ_{max}	0.003	0.002
θ(°)	30.4	32.3

Appendix [3] Table 31 The sensitivity of sand to the different shear particle stiffness

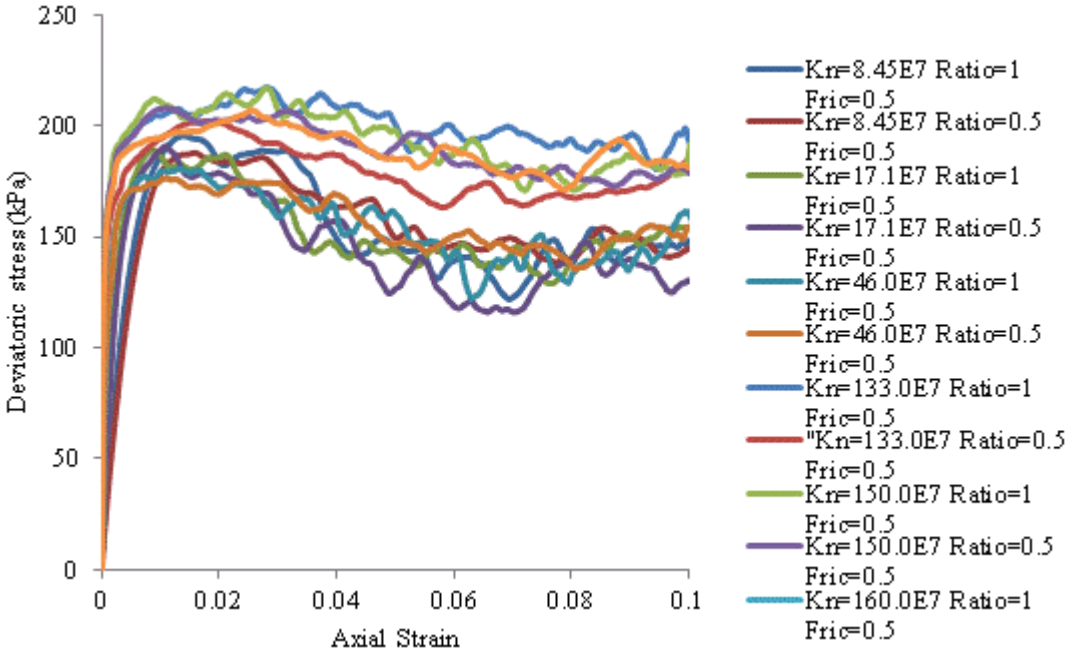

Appendix [3] Figure 62 The sensitivity of sand to the different shear particle stiffness when inter-particle friction is 0.5- deviatoric stress vs. axial strain

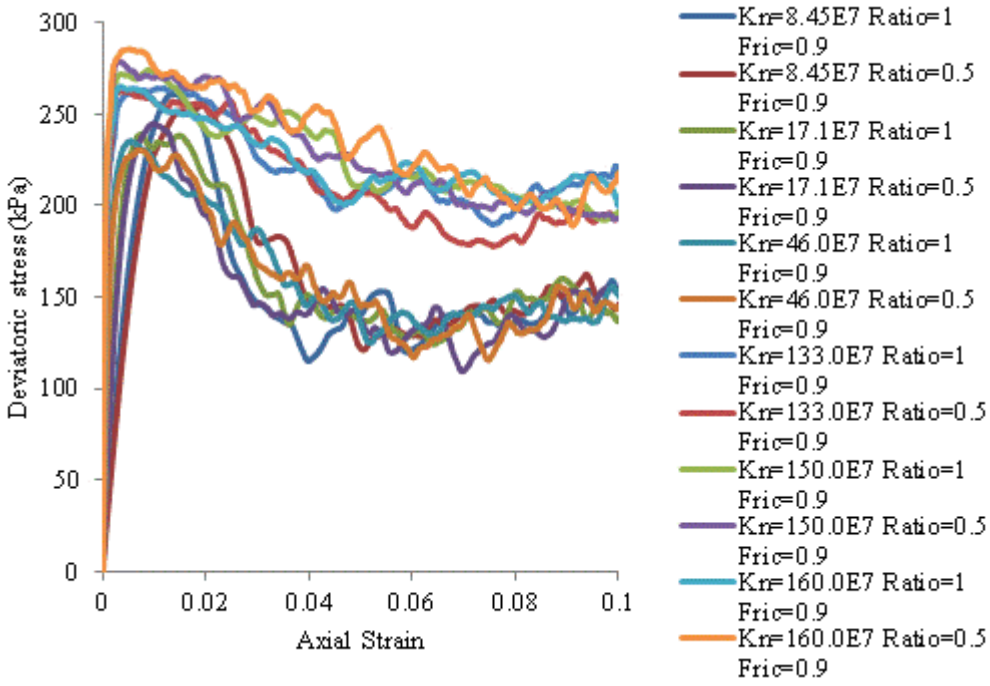

Appendix [3] Figure 63 The sensitivity of sand to the different shear particle stiffness when inter-particle friction is 0.9: deviatoric stress vs. axial strain

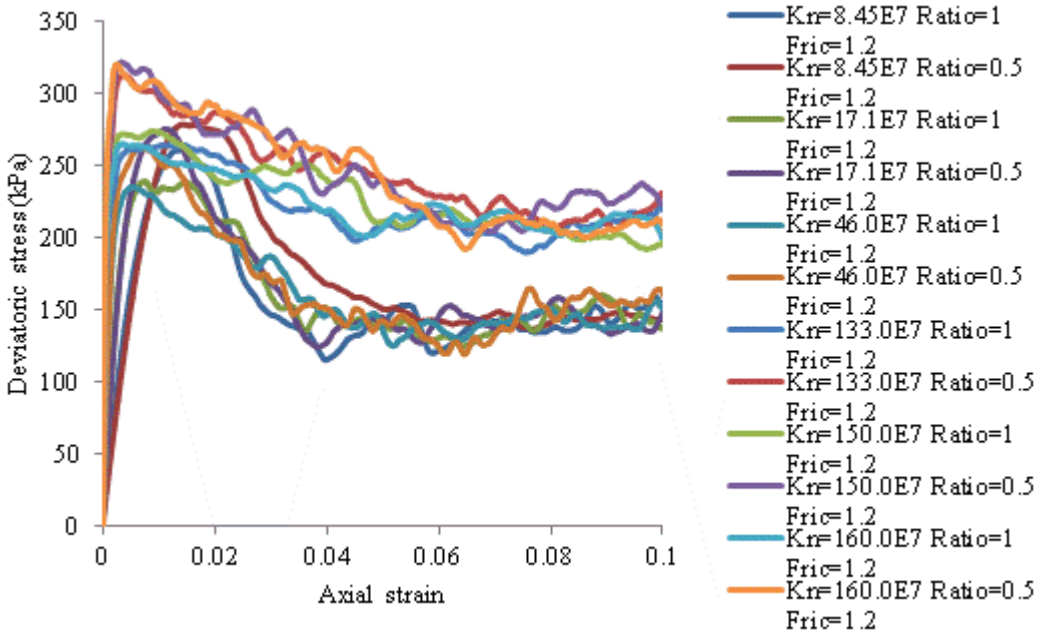

Appendix [3] Figure 64 The sensitivity of sand to the different shear particle stiffness when inter-particle friction is 1.2- deviatoric stress vs. axial strain

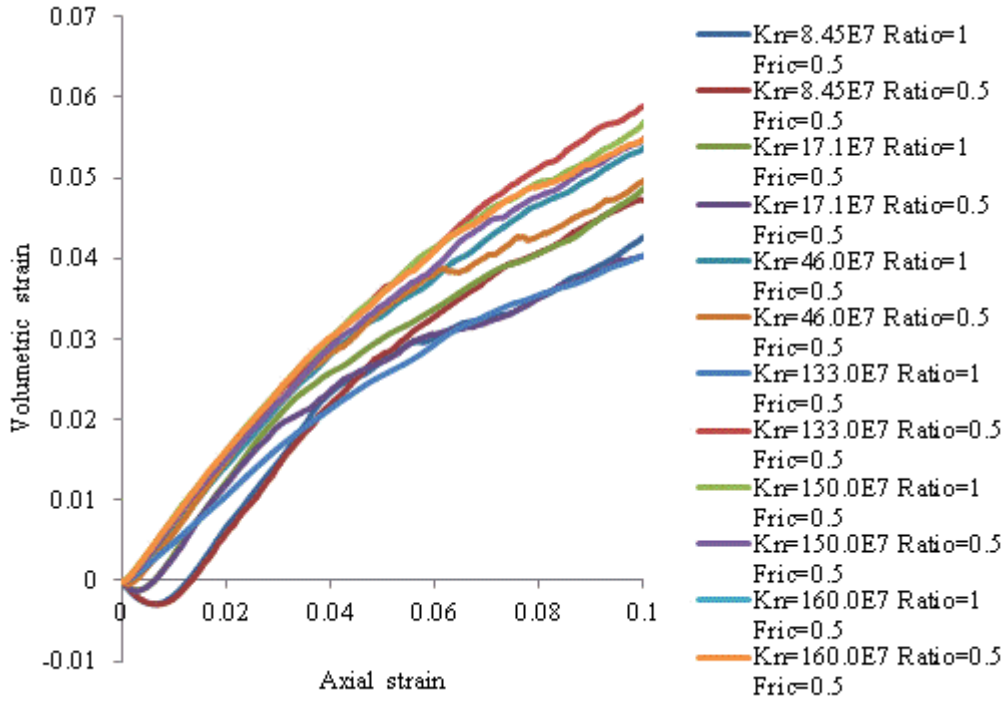

Appendix [3] Figure 65 The sensitivity of sand to the different shear particle stiffness when inter-particle friction is 0.5- volumetric strain vs. axial strain

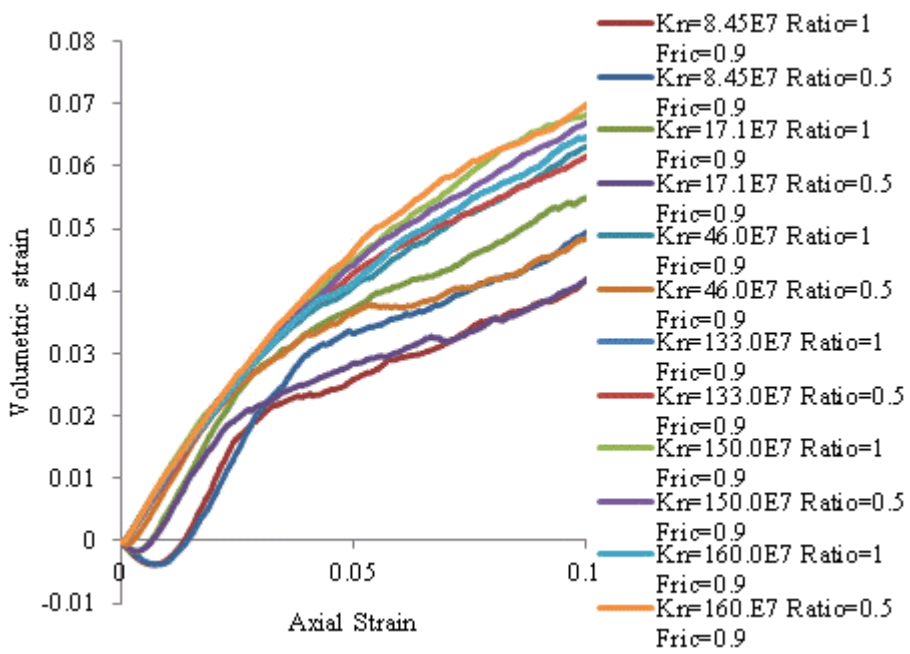

Appendix [3] Figure 66 The sensitivity of sand to the different shear particle stiffness when inter-particle friction is 0.9: volumetric strain vs. axial strain

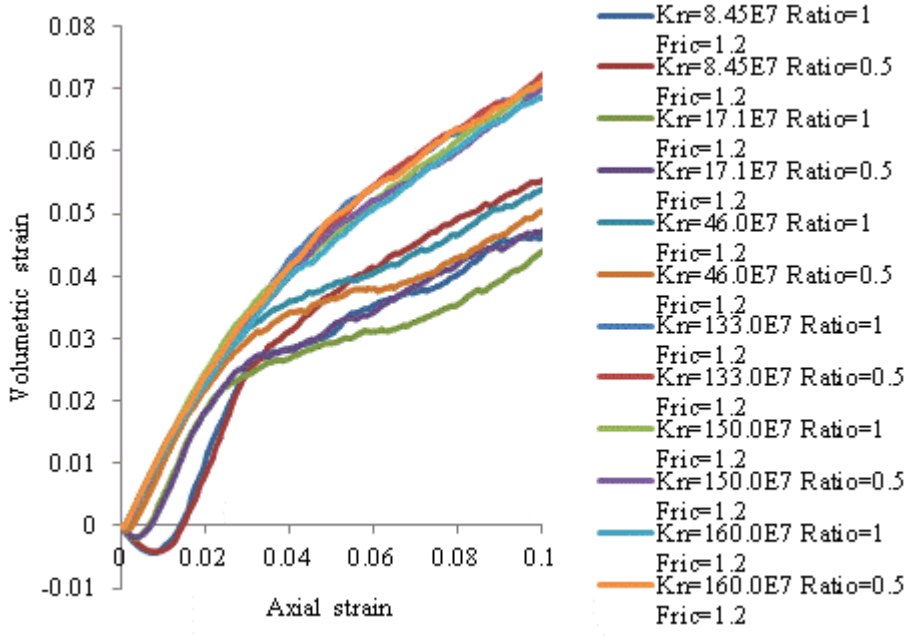

Appendix [3] Figure 67 The sensitivity of sand to the different shear particle stiffness when inter-particle friction is 1.2- volumetric strain vs. axial strain

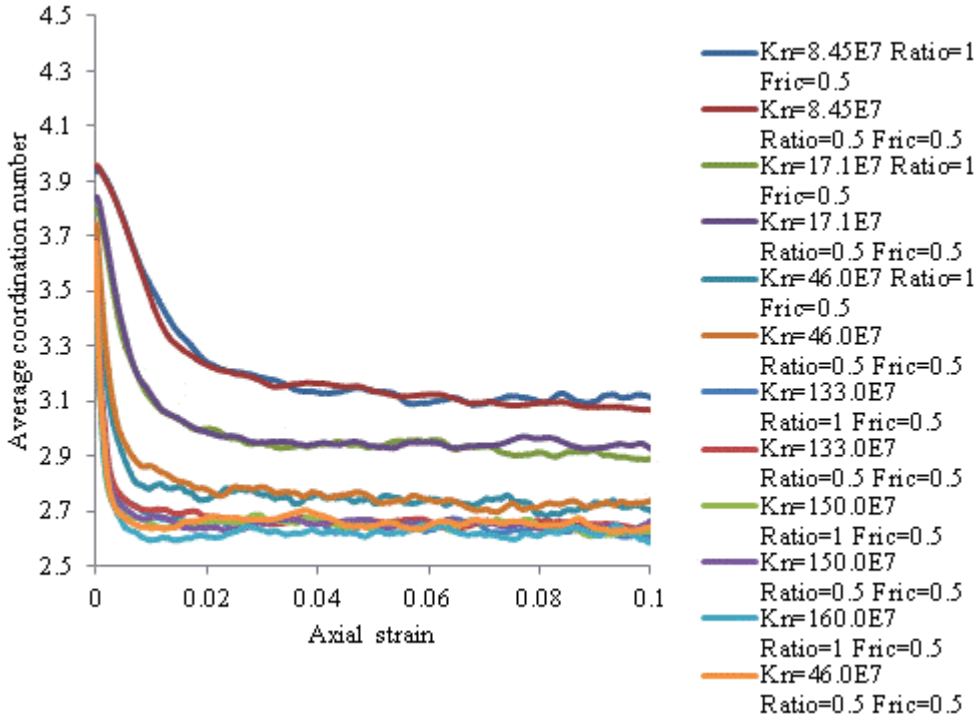

Appendix [3] Figure 68 The sensitivity of sand to the different shear particle stiffness when inter-particle friction is 0.5- average coordination number vs. axial strain

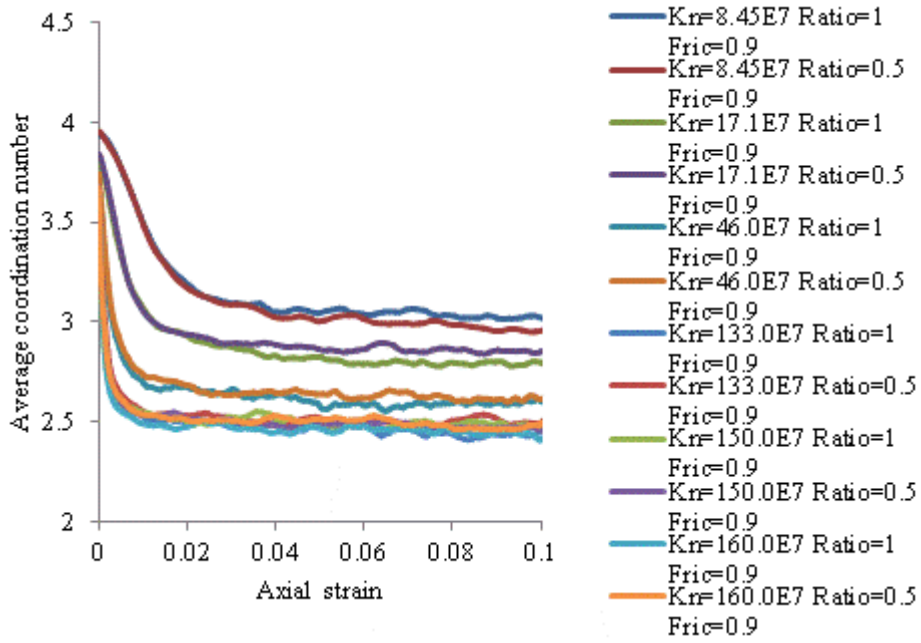

Appendix [3] Figure 69 The sensitivity of sand to the different shear particle stiffness when inter-particle friction is 0.9: average coordination number vs. axial strain

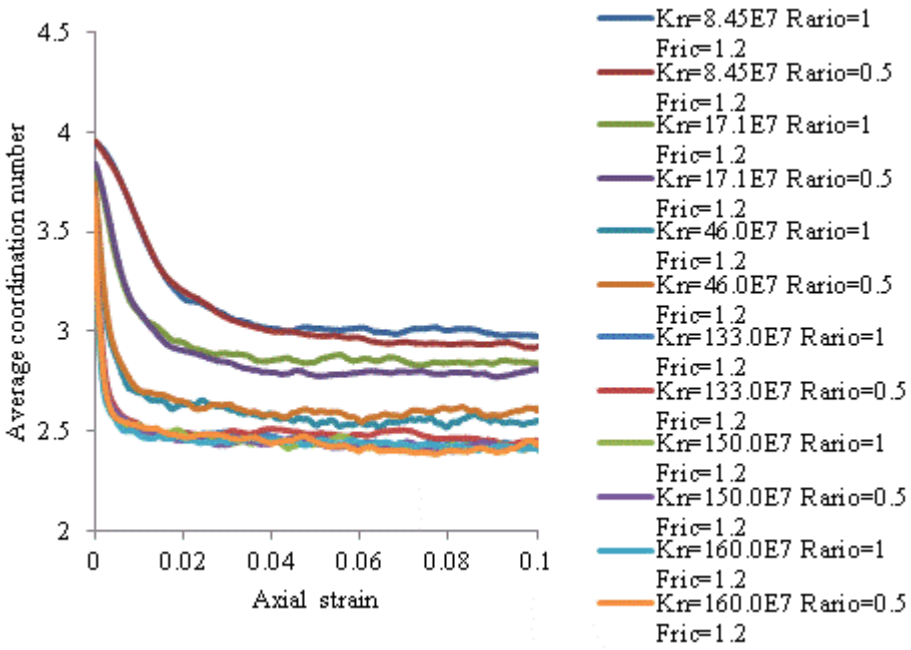

Appendix [3] Figure 70 The sensitivity of sand to the different shear particle stiffness when inter-particle friction is 1.2- average coordination number vs. axial strain

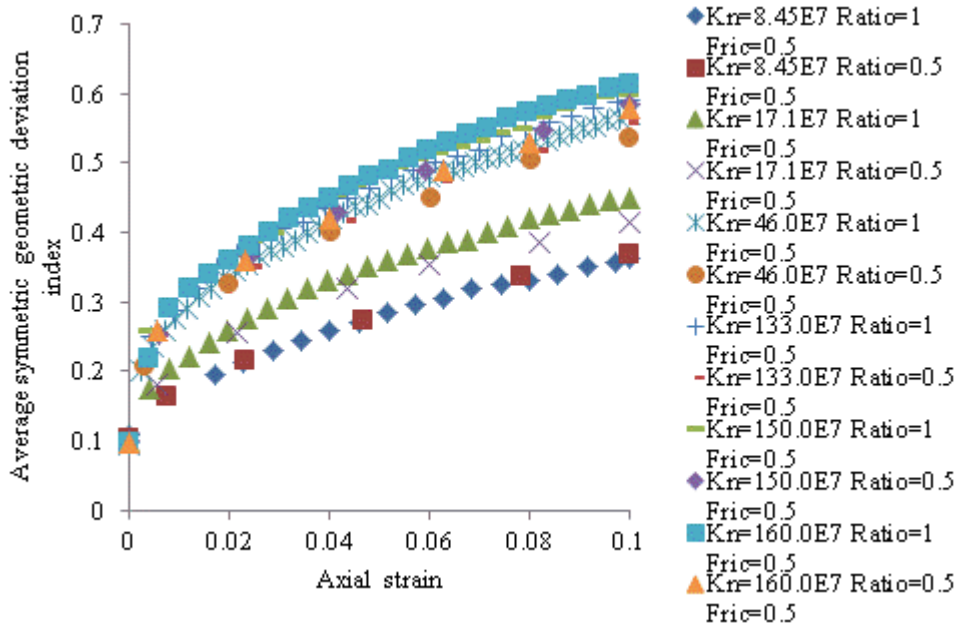

Appendix [3] Figure 71 The sensitivity of sand to the different shear particle stiffness when inter-particle friction is 0.5- average symmetric geometric deviation index vs. axial strain

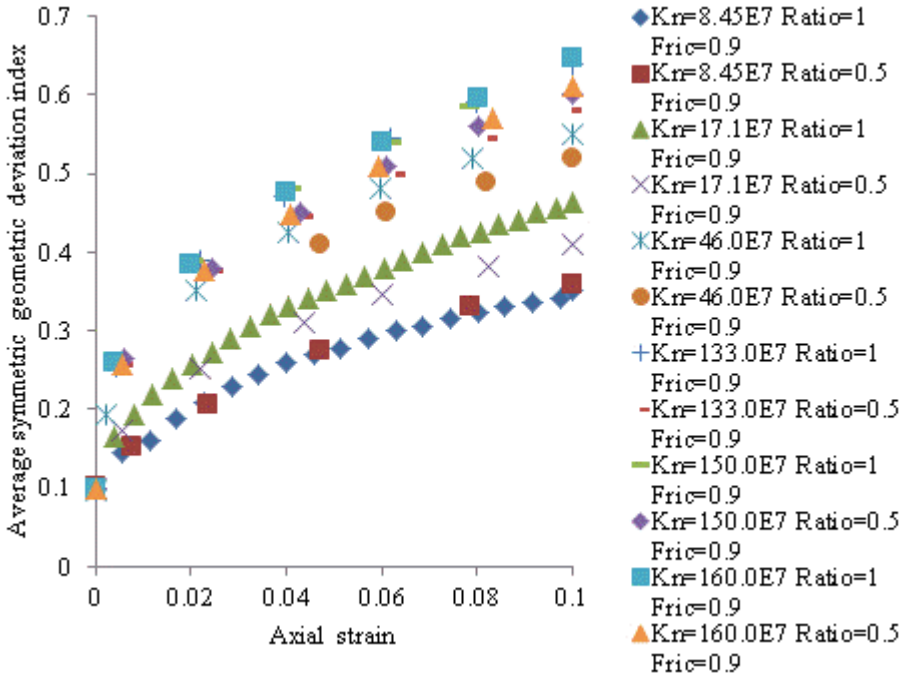

Appendix [3] Figure 72 The sensitivity of sand to the different shear particle stiffness when inter-particle friction is 0.9: average symmetric geometric deviation index vs. axial strain

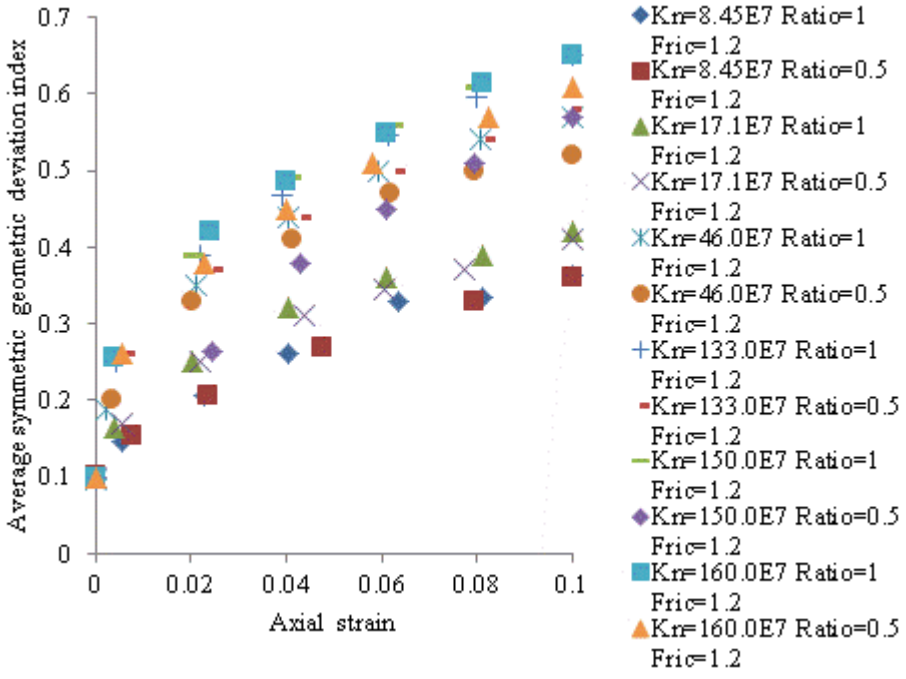

Appendix [3] Figure 73 The sensitivity of sand to the different shear particle stiffness when inter-particle friction is 1.2- average symmetric geometric deviation index vs. axial strain

Shear Stiffness (N/m)	8.4510^{7}	
Normal Stiffness (N/m)	8.4510^{7}	
Boundary Condition	Rigid wall	Deformable boundary
Particle coefficient friction	0.9	0.9
E_{50} (P.Stress) (MPa)	36.0	33.0
E_{50} (P.Strain) (MPa)	35.0	32.0
v (P.Stress)	0.22	0.23
v (P.Strain)	0.18	0.19
σ_{max} (kPa)	260.0	240.0
ε_{11} at σ_{max}	0.01	0.01
θ(°)	26.7	24.3
Initial porosity	0.12	0.12

Appendix [3] Table 32 The macro-mechanical responses of sand: different boundary condition

Confining pressure (kPa)	100	200	300
Shear Stiffness (N/m)	$8.45*10^{7}$	$8.45*10_{7}$	$8.45*10^{7}$
Normal Stiffness (N/m)	$8.45*10^{7}$	$8.45*10_{7}$	$8.45*10^{7}$
Particle coefficient friction	0.9	0.9	0.9
E_{50} (P.Stress) (MPa)	36.0	37.0	38.0
E_{50} (P.Strain) (MPa)	35.0	36.0	39.0
v (P.Stress)	0.22	0.20	0.18
v (P.Strain)	0.18	0.17	0.15
σ_{max} (kPa)	260.0	530.0	820.0
ε_{11} at σ_{max}	0.01	0.01	0.01
θ(°)	26.6	26.9	27.6

Appendix [3] Table 33 The macro-mechanical responses of sand: different confinging pressures

References

AGNOLIN, I. & ROUX, J. 2007. Internal states of model isotropic granular pickings: 1. Assembling progress, geometry and contact networks. *Physical Review E,* 76.

AKI, K. R. 1980. *Quantitative Seismology: Theory and Methods*.

AMIN, M. M. 1976. Effects of earthquakes on dams and embankments.

ANANDARAJAH, A., RASHIDI, H. & ARULANANDAN, K. 1995. Elasto-plastic finite element analyses of a soil-structure system under earthquake excitations. *Computers and Geotechnics,* 17**,** 301-325.

ANTONY, S. 2007. Link between single-particle properties and macroscopic properties in particulate assemblies: role of structures within structures. *Philosophical Transactions of the Royal Society A: Mathematical, Physical and Engineering Sciences,* 365**,** 2879.

ANTONY, S. & KRUYT, N. 2009. Role of interparticle friction and particle-scale elasticity in the shear-strength mechanism of three-dimensional granular media. *Physical Review E,* 79**,** 031308.

ARSOY, S., BARKER, M. R. & DUNCAN, J. M. 1999. The behavior of integral abutment bridges.

ARTHUR, J. & MENZIES, B. 1972. Inherent anisotropy in a sand. *Géotechnique,* 22**,** 115-128.

ATKINSON, J. 2007. *The mechanics of soils and foundations*, CRC Press.

ATKINSON, J. H. & BRANSBY, P. 1978. The mechanics of soils, an introduction to critical state soil mechanics. *McGraw Hill Book Company(UK) Ltd. London,(SW/55), 1978, 375*.

AUBRY, D. & CLOUTEAU, D. A regularized boundary element method for stratified media. Proceedings of the First International Conference on Mathematical and Numerical Aspects of Wave Propagation Phenomena, 1991. Strasbourg, France. SIAM, Philadephia, 660-668.

BAGI, K. 1993. On the definition of stress and strain in granular assemblies through the relation between micro-and macro-level characteristics. *Powders & grains,* 93**,** 117-121.

BAGI, K. 1996. Stress and strain in granular assemblies. *Mechanics of materials,* 22**,** 165-177.

BARDET, J. 1998. Introduction to computational granular mechanics. *COURSES AND LECTURES-INTERNATIONAL CENTRE FOR MECHANICAL SCIENCES***,** 99-170.

BARDET, J. & PROUBET, J. 1991. Numerical investigation of the structure of persistent shear bands in granular media. *Géotechnique,* 41**,** 599-613.

BARDET, J. & VARDOULAKIS, I. 2001. The asymmetry of stress in granular media. *International Journal of Solids and Structures,* 38**,** 353-367.

BELHEINE, N., PLASSIARD, J. P., DONZÉ, F. V., DARVE, F. & SERIDI, A. 2009. Numerical simulation of drained triaxial test using 3D discrete element modeling. *Computers and Geotechnics,* 36**,** 320-331.

BHANDARI, A., HAN, J. & PARSONS, R. L. 2014. Two-dimensional DEM analysis of behavior of geogrid-reinforced uniform granular bases under a vertical cyclic load. *Acta Geotechnica***,** 1-12.

BIAREZ, J. 1962. *Contribution à l'étude des propriétés mécaniques des sols et des matériaux pulvérulents.* PhD, University of Grenoble, France.
BOLTON, M. 1986. Strength and dilatancy of sands. *Geotechnique,* 36**,** 65-78.
BOLTON, M., NAKATA, Y. & CHENG, Y. 2008. Micro-and macro-mechanical behaviour of DEM crushable materials. *Géotechnique,* 58**,** 471-480.
BONILLA, R. R. O. 2004. *Numerical simulations of undrained granular media.* PhD Thesis University of Waterloo.
BONNET, M. 1999. Boundary integral equation methods for solids and fluids. *Meccanica,* 34**,** 301-302.
BOWLES, J. E. 1988. *Foundation analysis and design*.
BREWER, R. 1964. Fabric and mineral analysis of soils.
CAMBOU, B., CHAZE, M. & DEDECKER, F. 2000. Change of scale in granular materials. *European Journal of Mechanics-A/Solids,* 19**,** 999-1014.
CHANG, C. S. & KUHN, M. R. 2005. On virtual work and stress in granular media. *International Journal of Solids and Structures,* 42**,** 3773-3793.
CHEUNG, G. & O'SULLIVAN, C. 2008. Effective simulation of flexible lateral boundaries in two-and three-dimensional DEM simulations. *Particuology,* 6**,** 483-500.
CHEUNG, L., O'SULLIVAN, C. & COOP, M. 2013. Discrete element method simulations of analogue reservoir sandstones. *International journal of rock mechanics and mining sciences,* 63**,** 93-103.
CHEUNG, Y. & LEE, W. 1991. Elastoplastic analysis of soil-pile interaction. *Computers and Geotechnics,* 12**,** 115-132.
CIVJAN, S. A., BONCZAR, C., BRENA, S. F., DEJONG, J. & CROVO, D. 2007. Integral abutment bridge behavior: parametric analysis of a Massachusetts bridge. *Journal of Bridge Engineering,* 12**,** 64.
CUI, L., O'SULLIVAN, C. & O'NEILL, S. 2007. An analysis of the triaxial apparatus using a mixed boundary three-dimensional discrete element model. *Géotechnique,* 57**,** 831-844.
CUNDALL, P. 1978. BALL-A program to model granular media using the distinct element method. *Technical note. Advanced Technology Group, Dames & Moore, London*.
CUNDALL, P. & STRACK, O. 2008. Particle flow code in 2 dimensions. *Itasca Consulting Group, Inc*.
CUNDALL, P. A. A computer model for simulating progressive large scale movements in blocky rock systems. Proc. Symp. (ISRM), Nancy, 1971.
CUNDALL, P. A. Formulation of a three-dimensional distinct element model—Part I. A scheme to detect and represent contacts in a system composed of many polyhedral blocks. International Journal of Rock Mechanics and Mining Sciences & Geomechanics Abstracts, 1988. Elsevier, 107-116.
CUNDALL, P. A. 1989. Numerical experiments on localization in frictional materials. *Ingenieur-archiv,* 59**,** 148-159.
CUNDALL, P. A. & STRACK, O. 1979. A discrete numerical model for granular assemblies. *Geotechnique,* 29**,** 47-65.
DANGLA, P. 1988. A plane strain soil-structure interaction model. *Earthquake engineering & structural dynamics,* 16**,** 1115-1128.
DANTU, P. 1957. Contribution à l' Étude Mécanique et Géométrique des Milieux Pulvérulents.

DEDECKER, F., CHAZE, M., DUBUJET, P. & CAMBOU, B. 2000. Specific features of strain in granular materials. *Mechanics of Cohesive-frictional Materials,* 5**,** 173-193.

DERESIEWICZ, H. 1957. Stress-strain relations for a simple model of a granular medium. DTIC Document.

DERESIEWICZ, H. 1958. Mechanics of granular materials *Advanced applied mechanics,* 5**,** 233-306.

DICLELI, M. & ERHAN, S. 2010. Effect of soil-bridge interaction on the magnitude of internal forces in integral abutment bridge components due to live load effects. *Engineering Structures,* 32**,** 129-145.

DRESCHER, A. 1976. An experimental investigation of flow rules for granular materials using optically sensitive glass particles. *Géotechnique,* 26**,** 591-601.

DRESCHER, A. & DE JOSSELIN DE JONG, G. 1972. Photoelastic verification of a mechanical model for the flow of a granular material. *Journal of the Mechanics and Physics of Solids,* 20**,** 337-340.

DUFFY, J. & MINDLIN, R. D. 1956. Stress-strain relations and vibrations of a granular medium. DTIC Document.

EL SHAMY, U. & DENISSEN, C. 2010. Microscale characterization of energy dissipation mechanisms in liquefiable granular soils. *Computers and Geotechnics,* 37**,** 846-857.

EL SHAMY, U. & ZAMANI, N. 2012. Discrete element method simulations of the seismic response of shallow foundations including soil-foundation-structure interaction. *International journal for numerical and analytical methods in geomechanics,* 36**,** 1303-1329.

EL SHAMY, U. & ZEGHAL, M. A Micro-Mechanical Study of Soil-Pile Interaction during Dynamic Excitations. Advances in Measurement and Modeling of Soil Behavior, 2007. ASCE, 1-10.

FAN, L., ZHANG, K. Y. & LUO, X. J. 2013. Micro-Study of Soil's Inherent Anisotropy with PFC Simulation. *Applied Mechanics and Materials,* 275**,** 383-386.

FUKUMOTO, T. 1992. Particle breakage characteristics of granular soils. *Soils Found,* 32**,** 26-40.

GAO, Z., ZHAO, J., LI, X. S. & DAFALIAS, Y. F. 2013. A critical state sand plasticity model accounting for fabric evolution. *International journal for numerical and analytical methods in geomechanics*.

GAZETAS, G. & MYLONAKIS, G. Seismic soil-structure interaction: new evidence and emerging issues. 1998. ASCE, 1119-1174.

GOODMAN, R. E. 1980. *Introduction to rock mechanics,* John Wiley.

GUÉGUEN, P., BARD, P. & SEMBLAT, J. From soil-structure to site-city interaction. 12th World Conf. on Earthquake Eng, 2000.

HASAN, A. & ALSHIBLI, K. A. 2010. Experimental assessment of 3D particle-to-particle interaction within sheared sand using synchrotron microtomography. *Géotechnique,* 60**,** 369-379.

HAZZARD, J. F., MAXWELL, S. C. & YOUNG, R. P. Micromechanical of modelling acoustic emissions. Eurorock 98 Conference on Rock Mechanics, 1998 Trondheim, Norway. 519-525.

HOLTZ, R. D., KOVACS, W. D. & SHEAHAN, T. C. 1981. *An introduction to geotechnical engineering,* Prentice-Hall Englewood Cliffs, NJ:.

HUANG, J., SHIELD, C. K. & FRENCH, C. E. W. 2008. Parametric Study of Concrete Integral Abutment Bridges. *Journal of Bridge Engineering,* 13**,** 511.

HUMAR, J. 2012. *Dynamics of structures*, CRC Press.
ISHIHARA, K. 1996. *Soil behaviour in earthquake geotechnics*, Oxford University Press.
ISHIHARA, K. & KNOVEL 1996. *Soil behaviour in earthquake geotechnics*.
ITASCA, C. G. 2008. PFC2D particle flow code in two dimensions. *Itasca Consulting Group, Inc.Minneapolis Minnesota.*
IWASHITA, K. & ODA, M. 1998. Rolling resistance at contacts in simulation of shear band development by DEM. *Journal of engineering mechanics,* 124**,** 285-292.
JENSEN, R. P., BOSSCHER, P. J., PLESHA, M. E. & EDIL, T. B. 1999. DEM simulation of granular media—structure interface: effects of surface roughness and particle shape. *International journal for numerical and analytical methods in geomechanics,* 23**,** 531-547.
JIANG, M., YAN, H., ZHU, H. & UTILI, S. 2011. Modeling shear behavior and strain localization in cemented sands by two-dimensional distinct element method analyses. *Computers and Geotechnics,* 38**,** 14-29.
JOHNSON, K. 1985. *Contact mechanics*.
JONG, D. J. D. & VERRUIJT, A. 1969. *Etude photo-élastique d'un empilement de disques*, Cah. Grepe fr. Etud. Rhèol. 73-86.
JOYNER, W. B. & CHEN, A. T. 1975. Calculation of nonlinear ground response in earthquakes. *Bulletin of the Seismological Society of America,* 65**,** 1315-1336.
KARANTZIKIS, M. & SPYRAKOS, C. C. Seismic analysis of bridges including soil–abutment interaction. 2000.
KARRECH, A., DUHAMEL, D., BONNET, G., CHEVOIR, F., ROUX, J.-N., CANOU, J. & DUPLA, J.-C. 2008. A discrete element study of settlement in vibrated granular layers: role of contact loss and acceleration. *Granular Matter,* 10**,** 369-375.
KHODAIR, Y. A. & HASSIOTIS, S. 2005. Analysis of soil-pile interaction in integral abutment. *Computers and Geotechnics,* 32**,** 201-209.
KIM, W. S. & LAMAN, J. A. 2010. Integral abutment bridge response under thermal loading. *Engineering Structures,* 32**,** 1495-1508.
KOZICKI, J., TEJCHMAN, J. & MŰHLHAUS, H. B. 2014. Discrete simulations of a triaxial compression test for sand by DEM. *International journal for numerical and analytical methods in geomechanics*.
KRAMER, S. L. 1996. *Geotechnical earthquake engineering*, Prentice-Hall.
KRUYT, N. 2003. Statics and kinematics of discrete Cosserat-type granular materials. *International Journal of Solids and Structures,* 40**,** 511-534.
KRUYT, N. & ROTHENBURG, L. 1996. Micromechanical definition of the strain tensor for granular materials. *Journal of applied mechanics,* 63**,** 706-711.
KUCUKARSLAN, S., BANERJEE, P. & BILDIK, N. 2003. Inelastic analysis of pile soil structure interaction. *Engineering Structures,* 25**,** 1231-1239.
KUHN, M. R. Deformation measures for granular materials. Mechanics of Deformation and Flow of Particulate Materials, 1997. ASCE, 91-104.
KUHN, M. R. 1999. Structured deformation in granular materials. *Mechanics of materials,* 31**,** 407-429.
KUWANO, R. & JARDINE, R. 2002. On the applicability of cross-anisotropic elasticity to granular materials at very small strains. *Géotechnique,* 52**,** 727-749.
LAMB, T. W. & WHITMAN, R. V. 1969. Soil mechanics. *Massachusetts Institute of Technology*.

LAMBE, T. & WHITMAN, R. 1969. *Soil Mechanics,* New York, John Wiley & Sons.

LEE, D.-M. 1992. *The angles of friction of granular fills.* PhD, University of Cambridge.

LEE, X., DASS, W. C. & MANZIONE, C. W. Characterization of granular material composite structures using computerized tomography. Engineering Mechanics (1992), 1992. ASCE, 268-271.

LI, X., YU, H. & LI, X. 2009. Macro–micro relations in granular mechanics. *International Journal of Solids and Structures,* 46**,** 4331-4341.

LIU, W. B., SU, L. J., CHEN, Z. Y. & JIANG, H. M. 2012. Use of PFC2D for Simulation of Triaxial Compression Test for Reinforced Earth and Analysis of Sand Particle's Movement. *Advanced Materials Research,* 446**,** 1846-1852.

LUO, S. 2012. Fabric evolution of two-dimensional idealized particle. *Journal of Boston Society of Civil Engineers,* 31**,** 74-81.

LYSMER, J. Finite dynamic model for infinite media. Proc. of ASCE, 1969. 859-877.

MAEDA, K. Critical State-based Geo-micromechanics on Granular Flow. AIP Conference Proceedings, 2009. 17.

MAHMOOD, Z. & IWASHITA, K. 2010. Influence of inherent anisotropy on mechanical behavior of granular materials based on DEM simulations. *International journal for numerical and analytical methods in geomechanics,* 34**,** 795-819.

MAKRIS, N. & GAZETAS, G. 1992. Dynamic pile-soil-pile interaction. Part II: Lateral and seismic response. *Earthquake engineering & structural dynamics,* 21**,** 145-162.

MARKETOS, G. & O'SULLIVAN, C. 2013. A micromechanics-based analytical method for wave propagation through a granular material. *Soil Dynamics and Earthquake Engineering,* 45**,** 25-34.

MCDOWELL, G. & BOLTON, M. 1998. On the micromechanics of crushable aggregates. *Géotechnique,* 48**,** 667-679.

MINDLIN, R. & DERESIEWICA, H. 1953. Elastic spheres in contact under varying oblique forces. *Journal of applied mechanics*.

MISRA, A. 1995. Interfaces in particulate materials. *Studies in Applied Mechanics,* 42**,** 513-536.

MITCHELL, J. K. & SOGA, K. 2005. Fundamentals of soil behavior. John Wiley & Sons, New York.

MIURA, K., MIURA, S. & TOKI, S. 1986. Deformation behavior of anisotropic dense sand under principal stress axes rotation. *Soils and Foundations,* 26**,** 36-52.

MOMENI, A., CLARKE, B. & HASSANPOUR, A. 2012. The effects of particle size distribution and number of particles on the macro response of sand using DEM. *12th British Geotechnical Association Young Geotechnical Engineers' Symposium YGES12.* The University of Leeds: British Geotechnical Association.

MYLONAKIS, G. & GAZETAS, G. 1999. Lateral vibration and internal forces of grouped piles in layered soil. *Journal of geotechnical and geoenvironmental engineering,* 125**,** 16.

MYLONAKIS, G. & GAZETAS, G. 2000. Seismic soil-structure interaction: beneficial or detrimental? *Journal of Earthquake Engineering,* 4**,** 277-302.

MYLONAKIS, G., NIKOLAOU, A. & GAZETAS, G. 1997a. Soil-pile-bridge seismic interaction: kinematic and inertial effects. Part I: soft soil. *Earthquake engineering & structural dynamics,* 26**,** 337-359.

MYLONAKIS, G., NIKOLAOU, A. & GAZETAS, G. 1997b. Soil–pile–bridge seismic interaction: kinematic and inertial effects. Part I: soft soil. *Earthquake engineering & structural dynamics,* 26**,** 337-359.

NAKATA, Y., HYODO, M., HYDE, A. F., KATO, Y. & MURATA, H. 2001a. Microscopic particle crushing of sand subjected to high pressure one-dimensional compression. *Soils and Foundations,* 41**,** 69-82.

NAKATA, Y., HYODO, M., MURATA, H. & A.F.L, H. Single particle crushing and mechanical behaviour of decomposed granite soil. Proc. Int. Symp. On Problematic Soils, IS Tohoku98, 1998 Sendai, Japan. 479-483.

NAKATA, Y., KATO, Y., HYODO, M., MURATA, H. & HYDE, A. F. 2001b. One-dimenesional compression behaviour for sand through single particle ceushing strenght. *Powders & grains*.

NAKATA, Y., KATO, Y. & MURATA, H. Properties of compression and single particle crushing for crushable soil. Proceedings of the Fifteenth International Conference on Soil Mechanics and Geotechnical Engineering, Istanbul, Turkey, 27-31 August 2001. Volumes 1-3., 2001c. AA Balkema, 215-218.

NG, T.-T. 2001. Fabric evolution of ellipsoidal arrays with different particle shapes. *Journal of engineering mechanics,* 127**,** 994-999.

NOVAK, M. & NOGAMI, T. 1977. Soil-pile interaction in horizontal vibration. *Earthquake engineering & structural dynamics,* 5**,** 263-281.

O'SULLIVAN, C. 2011. *Particulate discrete element modelling: a geomechanics perspective*, Taylor & Francis New York.

O'SULLIVAN, C. 2012. Particle-Based Discrete Element Modeling: Geomechanics Perspective. *International Journal of Geomechanics,* 11**,** 449-464.

O'SULLIVAN, C., BRAY, J. D. & RIEMER, M. F. 2002. Influence of particle shape and surface friction variability on response of rod-shaped particulate media. *Journal of engineering mechanics,* 128**,** 1182-1192.

O'SULLIVAN, C. & CUI, L. 2009. Micromechanics of granular material response during load reversals: Combined DEM and experimental study. *Powder Technology,* 193**,** 289-302.

O'SULLIVAN, C., D BRAY, J. & LI, S. 2003. A new approach for calculating strain for particulate media. *International journal for numerical and analytical methods in geomechanics,* 27**,** 859-877.

O'SULLIVAN, C., LIANG, C. & O'NEILL, S. C. 2008. Discrete element analysis of the response of granular materials during cyclic loading. *Soils and Foundations,* 48**,** 511-530.

O'DONOVAN, J., O'SULLIVAN, C. & MARKETOS, G. 2012. Two-dimensional discrete element modelling of bender element tests on an idealised granular material. *Granular Matter,* 14**,** 733-747.

OBRZUD, R. 2010. *The Hardening Soil Model: A Practical Guidebook*, Zace Services.

ODA, M. 1972. Deformation mechanism of sand in triaxial compression tests. *Soils and Foundations,* 12**,** 45-63.

ODA, M. & IWASHITA, K. 1999. *Mechanics of granular materials: an introduction*, Taylor & Francis.

ODA, M., KONISHI, J. & NEMAT-NASSER, S. 1980. Some experimentally based fundamental results on the mechanical behaviour of granular materials. *Géotechnique,* 30**,** 479-495.

ODA, M., NEMAT-NASSER, S. & KONISHI, J. 1985. Stress-induced anisotropy in granular masses. *Soils Found,* 25**,** 85-97.

OKUR, D. & ANSAL, A. 2007. Stiffness degradation of natural fine grained soils during cyclic loading. *Soil Dynamics and Earthquake Engineering,* 27**,** 843-854.

OSMAN, U. 2010. Compressional and shear-wave velocity measurements in unconsolidated top-soil and comparison of the results. *International Journal of Physical Sciences,* 5**,** 1034-1039.

POTYONDY, D. & CUNDALL, P. 2004. A bonded-particle model for rock. *International journal of rock mechanics and mining sciences,* 41**,** 1329-1364.

POULOS, H. & DAVIS, E. 1980. Pile foundation analysis and design. *New York*.

PRAKASH, S. 1981. *Soil dynamics*, McGraw-Hill New York.

PRUIKSMA, J. & BEZUIJEN, A. 2002. Biaxial test simulations with PFC2D. GeoDelft Report CO386730/05. The Netherlands.

PUGASAP, K., KIM, W. & LAMAN, J. 2009. Long-term response prediction of integral abutment bridges. *Journal of Bridge Engineering,* 14**,** 129.

PUJOL, J. 2003. *Elastic wave propagation and generation in seismology*, Cambridge University Press.

ROTHENBURG, L. 1980. *Micromechanics of idealized granular assemblies.* PhD thesis, University of Waterloo.

ROTHENBURG, L. & BATHURST, R. 1989. Analytical study of induced anisotropy in idealized granular materials. *Géotechnique,* 39**,** 601-614.

ROTHENBURG, L. & BATHURST, R. 1993. Influence of particle eccentricity on micromechanical behavior of granular materials. *Mechanics of materials,* 16**,** 141-152.

ROTHENBURG, L. & KRUYT, N. 2004. Critical state and evolution of coordination number in simulated granular materials. *International Journal of Solids and Structures,* 41**,** 5763-5774.

ROWE, P. W. 1962. The stress-dilatancy relation for static equilibrium of an assembly of particles in contact. *Proceedings of the Royal Society of London. Series A. Mathematical and Physical Sciences,* 269**,** 500-527.

SADD, M. H., ADHIKARI, G. & CARDOSO, F. 2000. DEM simulation of wave propagation in granular materials. *Powder Technology,* 109**,** 222-233.

SAZZAD, M. M. & SUZUKI, K. 2010. Micromechanical behavior of granular materials with inherent anisotropy under cyclic loading using 2D DEM. *Granular Matter,* 12**,** 597-605.

SCHNEEBELI, G. 1956. Une analogie mécanique pour les terres sans cohésion. *CR Acad. Sci,* 243**,** 125.

SEMBLAT, J.-F. 2009. Rheological interpretation of Rayleigh damping. *arXiv preprint arXiv:0901.3717*.

SHAMSABADI, A., ROLLINS, K. M. & KAPUSKAR, M. 2007. Nonlinear Soil–Abutment–Bridge Structure Interaction for Seismic Performance-Based Design. *Journal of geotechnical and geoenvironmental engineering,* 133**,** 707.

SHENG, Y., LAWRENCE, C., BRISCOE, B. & THORNTON, C. 2004. Numerical studies of uniaxial powder compaction process by 3D DEM. *Engineering computations,* 21**,** 304-317.

SHIRLEY, D. J. & HAMPTON, L. D. 1978. Shear-wave measurements in laboratory sediments. *The Journal of the Acoustical Society of America,* 63**,** 607-613.
SITHARAM, T. & VINOD, J. 2010. Evaluation of shear modulus and damping ratio of granular materials using discrete element approach. *Geotechnical and Geological Engineering,* 28**,** 591-601.
SITHARAM, T. G. 2003. Discrete element modelling of cyclic behaviour of granular materials. *Geotechnical and Geological Engineering,* 21**,** 297-329.
SOROUSH, A. & FERDOWSI, B. 2011. Three dimensional discrete element modeling of granular media under cyclic constant volume loading: A micromechanical perspective. *Powder Technology*.
SPRINGMAN, S., NORRISH, A. & NG, C. 1996. Cyclic loading of sand behind integral bridge abutments.
SPYRAKOS, C. & LOANNIDIS, G. 2003. Seismic behavior of a post-tensioned integral bridge including soil-structure interaction (SSI). *Soil Dynamics and Earthquake Engineering,* 23**,** 53-63.
TANNANT, D. D. & WANG, C. DEM boundary conditions for modeling uniaxial and biaxial tests. *In:* FRANCIS, T., ed. Proceedings of the 1st Canada-US Rock Mechanics Symposium,, 2007 Vancouver, Canada,. 385–392.
TARDOS, G. I., MCNAMARA, S. & TALU, I. 2003. Slow and intermediate flow of a frictional bulk powder in the Couette geometry. *Powder Technology,* 131**,** 23-39.
THIPPESWAMY, H. K., GANGARAO, H. V. S. & FRANCO, J. M. 2002. Performance evaluation of jointless bridges. *Journal of Bridge Engineering,* 7**,** 276.
THOMAS, C. N., PAPARGYRI-BESKOU, S. & MYLONAKIS, G. 2009. Wave dispersion in dry granular materials by the distinct element method. *Soil Dynamics and Earthquake Engineering,* 29**,** 888-897.
THORNTON, C. 2000. Numerical simulations of deviatoric shear deformation of granular media. *Géotechnique,* 50**,** 43-53.
THORNTON, C. & ANTONY, S. 2000. Quasi-static shear deformation of a soft particle system. *Powder Technology,* 109**,** 179-191.
THORNTON, C. & NING, Z. 1998. A theoretical model for the stick/bounce behaviour of adhesive, elastic-plastic spheres. *Powder Technology,* 99**,** 154-162.
THORNTON, C. & ZHANG, L. 2003. Numerical simulations of the direct shear test. *Chemical engineering & technology,* 26**,** 153-156.
THURSTON, C. W. & DERESIEWICZ, H. 1958. Analysis of a compression test of a model of a granular medium. DTIC Document.
TING, J. M., KHWAJA, M., MEACHUM, L. R. & ROWELL, J. D. 1993. An ellipse-based discrete element model for granular materials. *International journal for numerical and analytical methods in geomechanics,* 17**,** 603-623.
TOOMEY, A. & BEAN, C. J. 2000. Numerical simulation of seismic waves using a discrete particle scheme. *Geophysical Journal International,* 141**,** 595-604.
VAN BAARS, S. Discrete element analysis of granular materials. International Journal of Rock Mechanics and Mining Sciences and Geomechanics Abstracts, 1996. Elsevier, 124A-124A.
VASHEGHANI-FARAHANI, R., ZHAO, Q. & BURDETTE, E. G. 2010. Seismic Analysis of Integral Abutment Bridge in Tennessee, Including Soil-Structure Interaction. *Transportation Research Record: Journal of the Transportation Research Board,* 2201**,** 70-79.

WAKABAYASHI, T. 1957. Photoelastic method for determination of stress in powder mass.
WHITE, W., LEE, I. K. & VALLIAPPAN, S. 1977. Unified boundary for finite dynamic models. *Journal of the Engineering Mechanics Division,* 103**,** 949-964.
WOLF, J. P. 1985. *Dynamic soil-structure interaction,* Prentice-Hall.
WOLF, J. P. & SONG, C. 1996. *Finite-element modelling of unbounded media,* Wiley Chichester.
WOOD, D. M. 1990. *Soil behaviour and critical state soil mechanics,* Cambridge university press.
YAN, W. & ZHANG, L. 2013. Fabric and the critical state of idealized granular assemblages subject to biaxial shear. *Computers and Geotechnics,* 49**,** 43-52.
YANG, Y., HUANG, R. Q., CHENG, Y. M. & WANG, J. F. 2014. Investigation of the Deformable Behavior of Loose and Dense Sand through DEM. *Advanced Materials Research,* 871**,** 124-128.
YIMSIRI, S. & SOGA, K. 2010. DEM analysis of soil fabric effects on behaviour of sand. *Geotechnique,* 60**,** 483-495.
ZAFEIRAKOS, A., GEROLYMOS, N. & GAZETAS, G. The role of soil and interface nonlinearities on the seismic response of caisson supported bridge piers. Proceedings of the 5th international conference on geotechnical earthquake engineering, Santiago, Chile, 2011.
ZAMANI, N. & EL SHAMY, U. 2011. Analysis of wave propagation in dry granular soils using DEM simulations. *Acta Geotechnica,* 6**,** 167-182.
ZAMANI, N. & EL SHAMY, U. 2012. Analysis of the seismic response of soil–foundation–structure systems using a microscale framework. *Soil Dynamics and Earthquake Engineering,* 43**,** 398-412.
ZEGHAL, M., EDIL, T. B. & PLESHA, M. E. 2002. Discrete element method for sand-structure interaction. *GEOTECHNICAL SPECIAL PUBLICATION***,** 317-322.
ZHANG, B. S. A. X. The influence of soil-structure dynamic interaction to the seismic design of integral bridge. Recent Development of Geotechnical and Geo-Environmental Engineering in Asai-Luan

2006 Dalian University of Technology

441-446.
ZHANG, G. & ZHANG, J. 2009. State of the art: Mechanical behavior of soil–structure interface. *Progress in Natural Science,* 19**,** 1187-1196.
ZHANG, G. & ZHANG, J. M. 2006. Monotonic and cyclic tests of interface between structure and gravelly soil. *Soil and foundation,* 46**,** 505-518.
ZHANG, G. Z. A. M. J. 2008. Unified modelling of monotonic and cyclic behaviour of interface between structure and gravelly soil. *Soils and Foundations,* 48**,** 231-245.
ZHU, H. & YU, A. 2002. Averaging method of granular materials. *Physical Review E,* 66**,** 021302.
ZORDAN, T., BRISEGHELLA, B. & LAN, C. 2011. Parametric and pushover analyses on integral abutment bridge. *Engineering Structures*.